Diagrammatic Approach to Frustrated Spin Systems

Benedikt Valentin Schneider

Diagrammatic Approach to Frustrated Spin Systems

Benedikt Valentin Schneider

Dissertation

an der Fakultät für Physik

der Ludwig–Maximilians–Universität München

vorgelegt von

Benedikt Valentin Schneider

aus München

München, den 04.11.2025

Erstgutachter: Prof. Dr. Jan von Delft
Zweitgutachter: Prof. Dr. Johannes Reuther
Tag der mündlichen Prüfung: 09.12.2025

Zusammenfassung (Summary in German)

Diese Arbeit widmet sich diagrammatischen Ansätzen zur Berechnung des dynamischen Strukturfaktors (DSF) und der statischen Suszeptibilität von Spinsystemen bei endlicher Temperatur im thermodynamischen Limes. Wir betrachten zwei komplementäre diagrammatische Methoden. Zunächst untersuchen wir Ansätze der funktionalen Renormierungsgruppe (FRG) auf der Grundlage von Pseudo-Fermion- (pf-FRG) und Pseudo-Majorana- (pm-FRG) Darstellungen. Zweitens entwickeln wir Wechselwirkungs- und Hochtemperatur-Entwicklungen (HTE) zu hohen Ordnungen unter Verwendung von freien und eingeschränkten Graphentechniken.

Um Berechnungen bei endlicher Temperatur in pf-FRG zu ermöglichen, eliminieren wir unphysikalische Zustände durch die Einbeziehung des Popov-Fedotov-Tricks. Innerhalb von pm-FRG führen wir ein Temperatur-Fluss-Schema ein, das die Effizienz und Genauigkeit der Detektion thermischer Phasenübergänge bei Analysen der Skalierung unter Änderung der Systemgöße erheblich verbessert. Wir erweitern pm-FRG um externe Magnetfelder, wodurch die Behandlung von XXZ-Modellen mit einem Feld entlang der z-Richtung ermöglicht wird.

Während die Pseudo-Majorana Darstellung lokale Spin-$\frac{1}{2}$-Operatoren auf freie Majorana-Fermionen abbildet, können höhere Spins $S > \frac{1}{2}$ stattdessen als stark wechselwirkende reelle Bosonen dargestellt werden, eine Idee, die der kürzlich vorgeschlagenen Spin-FRG zugrunde liegt. Anstatt Spin-FRG selbst zu implementieren, analysieren wir die Zugehörige Störungsreihe unter Verwendung einer Wechselwirkungsentwicklung. Um die in dieser Erweiterung auftretenden hochdimensionalen Imaginärzeitintegrale mit effizienter Buchführung analytisch zu berechnen, führen wir den Kernel Trick ein, der jedes Matsubaradiagramm in Form der partiellen Spektralfunktionen seiner konstituierenden greenschen Funktionen umschreibt.

Die resultierende Wechselwirkungsreihe in vierter Ordnung für allgemeine Spinlängen S liefert systematische Korrekturen jenseits der Molekularfeldapproximation für kritische Temperaturen und Magnetfelder sowohl in Entwicklungen um große Dimensionen $1/d$ und lange Wechselwirkungsreichweiten. Noch wichtiger ist, dass sie eine analytische Erklärung für die seit Langem beobachtete Korrespondenz zwischen quantenmechanischen und klassischen Modellen liefert, die in diagrammatischen Monte-Carlo-Simulationen gefunden wurde: Die normierten statischen Suszeptibilitäten quantenmechanischer und klassischer Heisenberg-Modelle stimmen nach einer einfachen Temperaturskalierung überein. Unsere Analyse zeigt, dass dies darauf zurückzuführen ist, dass die statische Suszeptibilität gut durch eine einfache Funktionsform approximiert werden kann, die einer Molekularfeld-Suszeptibilität ähnelt und die wir als renormierte Molekularfeldform bezeichnen.

Um höhere Ordnungen zu erreichen, verallgemeinern wir die HTE zu Matsubarafrequenzaufgelösten Greensche Funktionen (Dyn-HTE). Dies schließt die statische Suszeptibilität (bei verschwindender Matsubarafrequenz) als Sonderfall ein und validiert die renormierte Molekularfeldform bis zur 12. Ordnung in Störungstheorie. Durch die analytische Fortsetzung der aus Dyn-HTE erhaltenen Frequenzabhängigkeit unter Verwendung einer Kettenbruchentwicklung berechnen wir DSFs für Einparameter-Heisenbergmodelle auf beliebigen Gittern, die direkt mit experimentellen inelastischen Neutronenstreuspektren verglichen werden können. Alle Dyn-HTE-Berechnungen sind in einem öffentlich zugänglichen, gut dokumentierten open-source Code implementiert.

Abschließend klären wir die Beziehung zwischen Pseudo-Majorana- und spinbasierten diagrammatischen Ansätzen, indem wir die exakte Pseudo-Majoranawirkung direkt aus dem Spin-Hamiltonoperator ableiten, ohne auf eine Parton-Darstellung zurückzugreifen. Diese Herleitung ebnet den Weg für die Erweiterung Majorana- basierter Methoden auf Systeme mit größerem Spin.

Summary

(Summary in English)

This thesis is devoted to diagrammatic frameworks for computing the dynamic structure factor (DSF) and the static susceptibility of spin systems at finite temperature in the thermodynamic limit. We consider two complementary diagrammatic frameworks. First, we study functional renormalization group (FRG) approaches based on pseudo-fermion (pf-FRG) and pseudo-Majorana (pm-FRG) representations. Second, we develop high-order strong-coupling and high-temperature expansions (HTE) using free and restricted-graph techniques.

To enable finite-temperature calculations in pf-FRG, we eliminate unphysical states by incorporating the Popov–Fedotov trick. Within pm-FRG, we introduce a temperature-flow scheme that significantly improves the efficiency and accuracy of finite-size scaling analyses of thermal phase transitions. We further extend pm-FRG to include external magnetic fields, allowing treatment of XXZ models with a field along the z direction.

While the pseudo-Majorana representation maps local spin-$\frac{1}{2}$ operators to free Majorana fermions, higher spin values $S > \frac{1}{2}$ can instead be represented as strongly interacting real bosons, an idea underlying the recently proposed spin-FRG. Rather than implementing the spin-FRG itself, we analyze its perturbation series using a strong-coupling expansion. To evaluate the high-dimensional imaginary-time integrals arising in this expansion analytically with efficient bookkeeping, we introduce the kernel trick, which rewrites any Matsubara diagram in terms of the partial spectral functions of its constituent Green's functions. The resulting fourth-order strong-coupling expansion for general spin S provides systematic beyond-mean-field corrections to critical temperatures and fields in both $1/d$ and large-interaction-range expansions. More importantly, it provides an analytic explanation of the long-standing quantum-to-classical correspondence observed in diagrammatic Monte Carlo simulations: the normalized static susceptibilities of quantum and classical Heisenberg models coincide after a simple temperature rescaling. Our analysis shows that this arises from the fact that the static susceptibility is well approximated by a simple functional form akin to a mean-field susceptibility, which we call the renormalized-mean-field form.

To reach higher orders, we generalize the HTE to Matsubara-frequency-resolved Green's functions (Dyn-HTE). This includes the static susceptibility (at zero Matsubara frequency) as a special case and validates the renormalized-mean-field form up to 12th order in perturbation theory. By analytically continuing the frequency dependence obtained from Dyn-HTE using a continued-fraction expansion, we compute DSFs for one-parameter Heisenberg models on arbitrary lattices, which can be directly compared with experimental inelastic neutron-scattering spectra. All Dyn-HTE calculations are implemented in a publicly available, well-documented open-source code.

Finally, we clarify the relation between pseudo-Majorana and spin-based diagrammatic approaches by deriving the exact pseudo-Majorana action directly from the spin Hamiltonian, without invoking any parton representation. This derivation paves the way for extending Majorana-based methods to higher-spin systems.

Publications

This dissertation is based on the following publications:

[P1] *Taming pseudofermion functional renormalization for quantum spins: Finite temperatures and the Popov-Fedotov trick*
Benedikt Schneider, Dominik Kiese, Björn Sbierski
Sec. 3.2 / arXiv:2209.13484 Phys. Rev. B 106, 235113 (2022)

[P2] *Temperature flow in pseudo-Majorana functional renormalization for quantum spins*
Benedikt Schneider, Johannes Reuther, Matías G Gonzalez, Björn Sbierski, Nils Niggemann
Sec. 3.3 / arXiv:2312.14838 Phys. Rev. B 109, 195109 (2024)

[P3] *Pseudo-Majorana functional renormalization for frustrated XXZ spin-$\frac{1}{2}$ models with field or magnetization along the spin-Z direction at finite temperature*
Frederic Bippus, **Benedikt Schneider**, Björn Sbierski
Sec. 3.4 / arXiv:2411.18198 Phys. Rev. B 111, 054420 (2025)

[P4] *Spectral representation of Matsubara n-point functions: Exact kernel functions and applications*
Johannes Halbinger, **Benedikt Schneider**, Björn Sbierski
Sec. 4.2 / arXiv:2304.03774 SciPost Phys. 15, 183 (2023)

[P5] *Dipolar ordering transitions in many-body quantum optics: Analytical diagrammatic approach to equilibrium quantum spins*
Benedikt Schneider, Ruben Burkard, Beatriz Olmos, Igor Lesanovsky, Björn Sbierski
Sec. 4.3 / arXiv:2407.18156 Phys. Rev. A 110, 063301 (2024)

[P6] *Taming spin susceptibilities in frustrated quantum magnets: Mean-field form and approximate nature of the quantum-to-classical correspondence*
Benedikt Schneider, Björn Sbierski
Sec. 4.4 / arXiv:2407.09401 Phys. Rev. Lett. 134, 176502 (2025)

[P7] *High-temperature series expansion of the dynamic Matsubara spin correlator*
Ruben Burkard, **Benedikt Schneider**, Björn Sbierski
Sec. 5.2 / arXiv:2505.23699 Phys. Rev. B 113, 075102 (2026)

[P8] *Dynamic correlations of frustrated quantum spins from high-temperature expansion*
Ruben Burkard, **Benedikt Schneider**, Björn Sbierski
Sec. 5.3 / arXiv:2505.14571 Phys. Rev. Lett. 136, 056501 (2026)

[P9] *Dyn-HTE: Initial Code Release of the Dyn-HTE.Jl Package*
Björn Sbierski, **Benedikt Schneider**, Ruben Burkard
Sec. 5 Zenodo (2025)

Over the duration of the project the following related Master and Bachelor projects were (co)-supervised:

B1 *Ward identities in many-body physics*
Julia Bialk (2024)
Supervisors: Nepomuk Ritz, **Benedikt Schneider**, Jan von Delft

B2 *Dynamical high-temperature expansion for quantum magnets: application to XXZ quantum-spin-ice*
Florian Stickdorn (2025)
Supervisors: **Benedikt Schneider**, Jan von Delft

B3 *Dynamical high-temperature expansion for quantum magnets: application to the XX-Model*
Anton Buhic (2025)
Supervisors: **Benedikt Schneider**, Jan von Delft

M1 *XXZ quantum spins in a magnetic field a pseudo-fermion functional renormalization group approach*
Frederic Bippus (2023)
Supervisors: Björn Sbierski, **Benedikt Schneider**, Jan von Delft

M2 *Renormalised interactions of strongly correlated systems via composite fields*
Oleksandr Sulyma (2025)
Supervisors: **Benedikt Schneider**, Jan von Delft

M3 *Dynamical properties of the J_1-J_2 Heisenberg model on the triangular lattice*
Ester Pagès Fontanella (2025)
Supervisors: Oleksandra Kovalska, **Benedikt Schneider**, Jan von Delft

Acknowledgments

First and foremost, I am deeply indebted to Björn Sbierksi for his outstanding supervision. I have benefited enormously from his knowledge and ideas, and his productivity and work ethic have been a constant source of inspiration. His generosity in securing my funding even after his own had run out allowed me to remain in Munich, for which I am profoundly grateful. I am equally thankful to Jan von Delft, who welcomed me into his chair and continued to support me after Björn's departure. I have learned tremendously from the expertise and the inspiring atmosphere fostered within Jan's group. I am deeply grateful to both Björn and Jan for their guidance, while also granting me the freedom to pursue my own ideas.

My sincere thanks go to Matthias Punk, who first sparked my interest in frustrated magnetism, and to Jad Halimeh for his early-career support, which led to my first external seminar talk. I am also deeply grateful to Johannes Reuther for always welcoming me into his group seminar and journal club. It was refreshing to have a place where I could talk to others who shared my enthusiasm for frustrated quantum magnets, especially since, for a while, I was the only one in Munich working on them. Special thanks are due to Nils Niggemann and Dominik Kiese for inspiring me to code in Julia and for their collaboration on the pf-(pm)-FRG projects. I would also like to thank all participants and organizers of the yearly Spin-FRG workshop, each meeting has been a source of stimulating discussions and a powerful boost of motivation.

I am grateful to all my colleagues on the fourth floor for creating such a lively and supportive work environment. This includes, but is not limited to, Johannes Halbinger, Mattia Moroder, Dimitris Saraidaris, Samira Hatoum, Markus Frankenbach, Oleksandra Kovalska, Ming Huang, Matthias Pelz, Héloïse Albot, Rajah Nuttaki, Giovanni Canossa, Nihal Rao, Julia Liebert, Markus Scheeb, and Simon Linsel. Special thanks to Marc Ritter for keeping me sane during Covid and sharing my enthusiasm for frustrated magnets, and to Marcel Gievers for organizing the weekly office game nights. Thank you to Marc, Marcel, Héloïse, and Mattia for the unforgettable trip to Yosemite, and to Gün Günal for founding the office-run club and helping me through my first half-marathon. I owe much to my long-term office mates Andreas Gleis, Nepomuk Ritz, and Anxiang Ge. Our countless discussions about coding, field theory, and physics in general have been invaluable. Special thanks to Nepomuk for always pointing me toward the right textbook whenever I had a question.

I am grateful to my former students, Frederic Bippus, Oleksandr Sulyma, Esther Pagès, Julia Bialk, Anton Buhic, and Florian Stickdorn, for their trust and for choosing me as their (co-)supervisor. Many thanks to Kathrin Higgen for her heroic assistance in navigating the bureaucratic adventures on my quest to obtain Passierschein A38.

A special thank you to Anna, Björn, Nepomuk, Oleksandr, and Marcel for proofreading this thesis. Finally, my deepest gratitude goes to Anna, my family, and Adrian for their constant emotional support, and for keeping me alive through the process of writing this thesis.

Contents

Zusammenfassung (Summary in German) **i**

Summary (Summary in English) **iii**

Publications **v**

Acknowledgments **vii**

1 Introduction **1**

2 Background and Mathematical Methods **5**
2.1 Spin Models and Observables 5
2.2 Majorana Fermions in an Exactly Solvable Spin Liquid 8
2.3 Spin Representations 9
2.3.1 Spinful Fermions 10
2.3.2 Majorana Representation 12
2.3.3 Mixed Representation and Spinless Fermions. 13
2.3.4 Gauge Symmetries 13
2.3.5 Summary 14
2.4 Functional Methods 15
2.4.1 1PI Effective Action Formalism 15
2.4.2 Functional Renormalization Group 16
2.4.3 Functional Renormalization Group for Partons 17
2.5 Strong-Coupling Expansion 20
2.6 Perturbation Theory 21
2.6.1 Generalized Wick's Theorem 23
2.6.2 Restricted Graph Aproach 23
2.7 Spectral Representation of Multipoint Green's Functions and its Use in Perturbation Theory 24
2.7.1 Spectral Representation 24
2.7.2 Kernel Trick 26
2.8 Comparison of Spin Diagrams with SO(3) Majorana Diagrams 27

3 Functional Renormalization Group with Fermionic Spin Representations **29**
3.1 Overview 29
3.2 Publication: *Taming pseudofermion functional renormalization for quantum spins: Finite temperatures and the Popov-Fedotov trick* 31
3.3 Publication: *Temperature flow in pseudo-Majorana functional renormalization for quantum spins* 43
3.4 Publication: *Pseudo-Majorana functional renormalization for frustrated XXZ spin-* $\frac{1}{2}$ *models with field or magnetization along the spin-Z direction at finite temperature* 55

4 Strong-Coupling Perturbation Theory and Quantum-to-Classical Correspondence **71**
4.1 Overview . . . 71
4.2 Publication: *Spectral representation of Matsubara n-point functions: Exact kernel functions and applications* . . . 73
4.3 Publication: *Dipolar ordering transitions in many-body quantum optics: Analytical diagrammatic approach to equilibrium quantum spins* . . . 92
4.4 Publication: *Taming Spin Susceptibilities in Frustrated Quantum Magnets: Mean-Field Form and Approximate Nature of the Quantum-to-Classical Correspondence* . . . 108

5 Dynamic High Temperature Expansion **117**
5.1 Overview . . . 117
5.2 Publication: *High-temperature series expansion of the dynamic Matsubara spin correlator* . . . 118
5.3 Publication: *Dynamic correlations of frustrated quantum spins from high-temperature expansion* . . . 134

6 Summary and Discussion **145**
6.1 Functional Renormalization Group for Partons . . . 145
6.2 Implications of the Connections Between the Pseudo-Majorana and Spin-Diagrams . . . 146
6.3 Spectral Representation and Its Use in Perturbation Theory . . . 146
6.4 Spin-Diagrams Using the Generalized Wick's Theorem . . . 147
6.5 Implications of the Quantum-to-Classical Correspondence . . . 148
6.6 Dynamic High Temperature Series Expansion . . . 150
6.7 Concluding Remarks . . . 151

A Linear Extrapolation of Continued Fraction Expansion **153**

Bibliography **155**

1 Introduction

Condensed matter theory concerns itself with the collective effects arising from the interaction of many elementary constituents. The collective behavior of many particles, however, cannot be understood by simply extending single-particle concepts and instead leads to emergent properties like superconductivity [BCS57], spin-charge separation [Hal81], and spin fractionalization [Kit06], to name a few [And72]. While a large part of condensed matter physics studies electronic systems where electrons can tunnel between overlapping atomic orbitals and interact via Coulomb repulsion, this thesis is dedicated to studying quantum spin systems. Spin degrees of freedom can arise in many ways, for instance, atoms with odd numbers of electrons can have time-reversal protected degenerate states, called Kramers doublets. In Mott insulating phases, these can act like an effective spin-$\frac{1}{2}$ state [AB12].

Historically, the study of quantum spin systems was first able to explain how the collection of microscopic spin degrees of freedom could act together to form macroscopic magnetic moments, known as ferromagnetic order. This explained why household magnets worked and formed the basis of early magnetic storage technologies. In 1930, Louis Néel proposed a new kind of magnetism in bipartite lattices, where the magnetization on the two sublattices has opposite signs, resulting in a net magnetization of zero for the whole material. While Néel himself is often quoted from his Nobel lecture as having found antiferromagnets to be "interesting but useless" [Née71] due to their lack of macroscopic magnetic moment, they have since been used to develop advanced computer memory systems, which represent the next generation of magnetic memories. They provide distinct advantages over conventional ferromagnets, such as access speeds in the vicinity of $\sim$ THz, the absence of stray fields, and high stability under magnetic fields [Xio+22]. More recently, a new class of magnetic order termed *altermagnetism* has been discovered, combining features of both ferromagnetism and antiferromagnetism. Altermagnets exhibit spin-split bands like ferromagnets despite zero net magnetization like antiferromagnets (see Fig. 1.1), and promise $\sim$ THz operation speeds with favorable electronic interface properties [ŠSJ22].

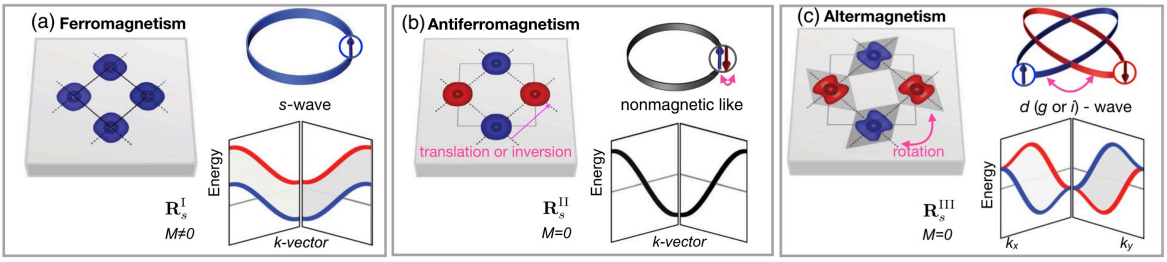

Figure 1.1 Models of collinear ferromagnetism, antiferromagnetism, and altermagnetism in real-space crystal and momentum-space electronic structures. (a) *Ferromagnetism:* one spin sublattice, finite magnetization, momentum-independent spin splitting, and isotropic s-wave Fermi surfaces. (b) *Antiferromagnetism:* opposite-spin sublattices linked by inversion or translation, zero net magnetization, and time-reversal-invariant spin-degenerate bands. (c) *Altermagnetism:* opposite-spin sublattices related by rotation, zero net magnetization, alternating-sign spin splitting, and anisotropic d- (g or i-wave) Fermi surfaces. Figure reproduced from [ŠSJ22].

More interesting than the antiferromagnetic Neel-order of antiferromagnets themselves are their underlying antiferromagnetic spin interactions. When neighboring spins are coupled via antiferromagnetic spin interactions, geometric constraints can prevent antiparallel alignment for all pairs to be satisfied. The spins are then said to be *frustrated* [LM01]. This happens naturally in lattices with antiferromagnetic spin interactions that form triangular patterns, because it is impossible to have three mutually antiparallel vectors (see Fig. 1.2(a)). For classical magnets, this can lead to extensive, disordered ground-state degeneracies [Gin11]. When quantum fluctuations are added, the extensive degeneracy is usually broken. Sometimes this results in an *order by disorder* effect, where states out of the degenerate ground state manifold are selected and long-range order is restored [Vil79; Hen89]. A famous example of this behavior is the nearest-neighbor antiferromagnetic Ising model on the triangular lattice. It remains disordered at all temperatures, leading to a residual ground-state entropy [Wan50]. When quantum fluctuations in terms of a Heisenberg coupling are added, they lead to a ground state with 120° magnetic order [Li+22]. In other cases, the quantum fluctuations lead to the ground state being an extensive superposition of the classical ground states. These so-called *quantum spin liquids* are highly non-trivial disordered ground states whose excitations are fractionalized particles governed by an emergent low-energy gauge theory [SB16] that can have anyonic exchange statistics [Kit06].

Anyonic particles are known to appear in toy models such as the toric code [Kit03]. Still, there are also multiple examples of models that host anyonic quasiparticles and can be realized in nature, such as the Kitaev honeycomb model [Kit06], proposed to be realized in α-$RuCl_3$ [Plu+14] and the XXZ pyrochlore quantum spin-ice [HFB04], which could be realized in pyrochlore materials [BH20; GM14]. The quasiparticles in the low-energy XXZ pyrochlore realize a U(1) gauge theory, which represents a version of three-dimensional quantum electrodynamics with magnetic and electric charges as well as photons that interact with a large fine structure constant [Pac+21]. The topological ground-state degeneracy in the Toric Code, as well as the sought-after Majorana fermions, quasiparticles of the $\mathbb{Z}_2$ spin liquid in the Kitaev honeycomb model, are proposed to be usable for error-corrected, topological quantum computing [Kit03; Kit06]. Similar spin liquid states, such as Anderson's resonating valence bond state, have been proposed to explain features of high-T_c superconductivity [And87; KRS87] in copper oxides.

Unambiguously detecting a quantum spin liquid state is a formidable challenge, both theoretically and experimentally. To date, there is still no conclusive experimental observation of a true quantum spin liquid ground state. While there are direct experimental observables, the so-called Wilson loops, that have well-defined scaling behavior inside quantum spin liquid phases [BF83; Gre+11], they require access to site-resolved high-order observables. Such resolutions are unachievable in solid-state systems but have recently become possible in cold-atom tweezer-array experiments [Sem+21]. However, so far, only renormalized classical spin liquids have been measured this way [WP25]. The current generation of tweezer arrays still suffers from excessive residual entropy during ground-state preparation, and the experiments are typically not in thermal equilibrium [Sbi+24]. While cold-atom tweezer-array experiments are a promising platform to detect quantum spin liquids in the future, they are, with few exceptions, currently limited to two-dimensional lattices [Sch+23]. The search for spin liquids in three-dimensional materials like the pyrochlores is currently conducted via the dynamic structure factor (DSF) obtained from inelastic neutron scattering [Plu+19; Smi+22]. Here, it is possible to work in thermal equilibrium by cooling the sample to low temperatures. However, the absence of site-resolved high-order correlation functions renders the interpretation of the DSF significantly more complex. Typically, if the DSF lacks a sharp

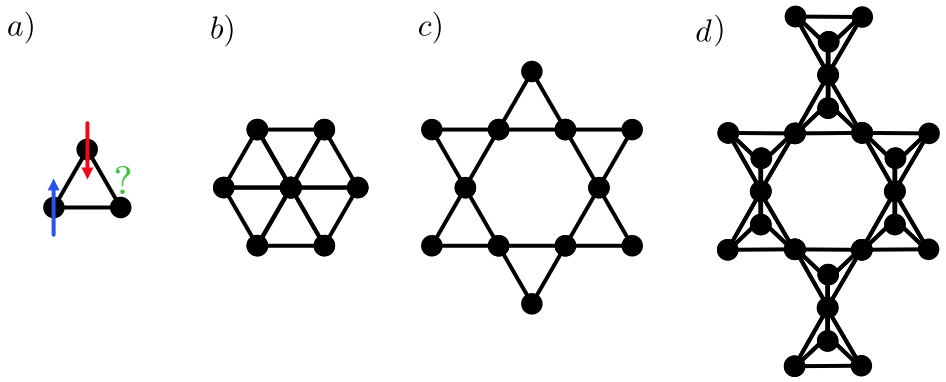

Figure 1.2 a) Symbolic image representing geometric frustration. Not all spins in a triangle can be aligned antiparallelly. Triangular patterns appear in many real-world atomic lattices, including b) the triangular lattice, c) the Kagome lattice, and d) the three dimensional Pyrochlore lattice.

spin-wave mode at low temperatures, it is interpreted as a possible sign of a spin liquid, although other phases, such as valence bond solids, also lack such sharp spin-wave modes. Therefore, the DSF has to be compared with theoretical simulations to make any claims.

Unfortunately, making theoretical predictions for the DSF is challenging in frustrated antiferromagnets. There are currently no quasi-exact methods that can reliably compute DSFs in dimensions $d \geq 2$ for frustrated systems. While quantum Monte Carlo combined with analytical continuation performs well for unfrustrated systems [Sha+17], it fails in frustrated systems due to the infamous sign problem. In $d = 2$, several methods based on the density-matrix renormalization group (DMRG) have been developed. Here, DMRG ground states are either time-evolved [Pae+19; Dre+23; Dre+25] or their spectral functions are calculated via Krylov-based approaches [KDG25]. However, the system sizes accessible to DMRG in two dimensions are limited, and the resulting DSFs suffer from severe finite-size effects. Moreover, all neutron-scattering experiments are conducted at finite temperatures, adding further complications.

In this thesis, we contribute to closing this methodological gap by developing diagrammatic methods for frustrated quantum spin systems. They work with correlation functions instead of wave functions like the DMRG. Diagrammatic methods represent the behavior of interacting quantum systems through diagrams, which graphically encode terms in the perturbative expansion of Green's functions. Beyond plain perturbation theory, the many diagrammatic schemes differ only in their expansion parameter and resummation schemes. Resummation comes in many forms and describes a systematic way to include contributions up to infinite order in the expansion parameter. Popular resummation schemes include, Padé-approximants [OB96], the one-particle-irreducible approach [Dys49], self-consistent perturbation theory [Bay62], the parquet approach [DM64a; DM64b; NGR69; Bic04] or the functional renormalization group (FRG) [KBS10]. The main advantage of diagrammatic methods is that they can be applied directly in the thermodynamic limit and do not suffer from the sign problem, thereby making frustrated-coupling regimes accessible. However, they do come with their own disadvantages, like their perturbative nature and the lack of error-bars.

Here, we focus primarily on high-order perturbation theory and the FRG. In the FRG community, two different strategies have been developed. The pseudo-fermion (pf-FRG) and pseudo-Majorana FRG (pm-FRG) [RW10; NSR21] are based on fermionic, bilinear

spin-$\frac{1}{2}$-representations to map each local spin to free fermions. The spin-spin interactions are then described by non-local quartic fermion interactions. In terms of Majoranas, this mapping is exact. On the other hand, the spin-FRG approach [KK19] does not use any parton representation. Instead, it uses the spin operators directly, which are chosen to commute under time ordering. This leads to an effective description of local spins in terms of strongly interacting, real bosonic systems. While the strong local interactions lead to complications, the spin-spin interactions enter as quadratic boson-boson hopping and the approach generalizes straightforwardly to higher spin values $S > \frac{1}{2}$. Therefore, the spin-spin correlation functions can already be described with full knowledge of the 2-boson correlator instead of the four-fermion correlators needed in the pf-FRG and pm-FRG approaches. The relation of the spin-diagrammatic and parton-diagrammatic approaches is not yet well understood. This thesis will shed some light on their relation.

This thesis is structured as follows: In Chapter 2, we give a concise introduction to the theoretical background of the projects this thesis is based on and fill some conceptual gaps in the current literature about the relation between the spin and parton-diagrammatic approaches. The subprojects are then presented in the following chapters: Chapter 3 focuses on improvements of the pseudo-fermion and pseudo-Majorana functional renormalization group; Chapter 4 generalizes the spectral representation of multi-point functions to bosonic n-point functions and applies it to high-order perturbation-theory calculations, which we use to address the long-standing question of the quantum-to-classical correspondence. Chapter 5 builds upon these advancements to generalize the standard high-temperature series expansion (HTE) to frequency-dependent, dynamic quantities. We use this dynamic HTE (Dyn-HTE) to compute high- and intermediate-temperature DSFs. Finally, in Chapter 6, we summarize the main results, discuss them in the context of the existing literature, provide an outlook for future related projects, and offer concluding remarks.

2 Background and Mathematical Methods

In this chapter, we will review the basic theoretical and mathematical concepts needed for the following chapters. We start by defining the Hamiltonian and main observables for quantum spin systems in Sec. 2.1. Then, after considering the great success of the Majorana representation in the Kitaev spin liquids in Sec. 2.2, we give an in-depth overview of the different possible fermionic spin representations in Sec. 2.3, which we use in Sec. 2.4 to set up a functional renormalization group scheme for pseudo-fermions. Parton representations for spin diagrammatics can be avoided by using the strong-coupling expansion introduced in Sec. 2.5. In Sec. 2.6 we review how the strong-coupling expansion can be used to calculate the perturbative expansion, which we will eventually evaluate with the kernel trick. The kernel trick is a new scheme that uses the spectral representation of multipoint functions for quick, analytic evaluation of Matsubara diagrammatics. This is detailed in Sec. 2.7. Finally, we investigate the direct connection between the fermionic parton and the bosonic strong-coupling approach in Sec. 2.8.

2.1 Spin Models and Observables

The energy landscape of spins in magnetic materials can often be modeled by a Hamiltonian H with two-spin interaction terms encoded by their interaction strength $J_{ij}^{\alpha\beta}$ that both depends on the distance $\mathbf{r}_i - \mathbf{r}_j$ and orientation of $\alpha \in \{x, y, z\}$ of the spins

$$H = \frac{1}{2} \sum_{ij} S_i^\alpha J_{ij}^{\alpha\beta} S_j^\beta. \tag{2.1}$$

If a magnetic field $\mathbf{h}_i$ is applied to the system, it couples directly to the local spins $H_\mathbf{h} = \sum_i h_i^\alpha S_i^\alpha$, which causes a breaking of time-reversal symmetry and can lead to a finite magnetization $M_i^\alpha = \langle S_i^\alpha \rangle$. We write spin operators as S_i^α where we use Greek letters for the direction $\alpha \in \{x, y, z\}$ and i is a site index. The spin operators live in a $(2S+1)$-dimensional Hilbert space and fulfill the spin algebra

$$[S^\alpha, S^\beta] = i\epsilon^{\alpha\beta\gamma} S^\gamma, \tag{2.2a}$$

$$\frac{1}{2}\{S^\alpha, S^\beta\} = \frac{S(S+1)}{3}\delta^{\alpha\beta} + Q^{\alpha\beta}, \tag{2.2b}$$

where $Q^{\alpha\beta}$ is the symmetric traceless quadrupole operator. It is a rank-2 tensor which describes the quadrupole moment of the spin. It can be used to describe biquadratic interactions $H_\text{Biquad} \sim (S_i^\alpha S_j^\alpha)^2 \sim Q_i^{\alpha\beta} Q_j^{\alpha\beta}$ for $S > \frac{1}{2}$ which are not included in Eq. (2.1) but can appear naturally in magnetic materials [PS25].
Hamiltonians like Eq. (2.1) can be derived in the infinite interaction limit from the Hubbard model at half-filling

$$H = \sum_{ij,\sigma} c_{i\sigma}^\dagger t_{ij} c_{i\sigma} + \sum_i U n_{i\uparrow} n_{i\downarrow} \xrightarrow{U\to\infty} \frac{1}{2} \sum_{ij,\beta} S_i^\beta J_{ij} S_j^\beta, \tag{2.3}$$

where $J_{ij} = \frac{4t_{ij}^2}{U}$ [Aro+22]. Similar Hamiltonians also arise in Rydberg atom arrays. Depending on the context, their Hamiltonians are equivalent to transverse-field Ising models [Lab+16; Zei+16]

$$H = \sum_i \frac{\Omega}{2}\sigma_i^x + \sum_{i<j} V_{ij} n_i n_j = \sum_i \Omega S_i^x + \sum_{ij} V_{ij} S_i^z + \sum_{i<j} V_{ij} S_i^z S_j^z, \tag{2.4}$$

where Ω is the Rabi frequency, or to effective XXZ Hamiltonians, the latter can be engineered by a periodic external microwave field interacting on resonance with the Rydberg atoms [Sch+22].

Linear response theory defines the tendency of a system to form magnetic order by its order-parameter susceptibility [BF04]. When a time-dependent magnetic field perturbs a system $h_i^\beta(t')$, the magnetization changes to linear order as

$$\begin{aligned} M_j^\alpha(t) &= M_j^\alpha(t)|_{h=0} + \int_{-\infty}^{\infty} \mathrm{d}t' \frac{\mathrm{d}M_j^\alpha(t)}{\mathrm{d}h_i^\beta(t')}\Big|_{h=0} h_i^\beta(t') + \mathcal{O}(h^2) \\ &= M_j^\alpha(t)|_{h=0} + \int_{-\infty}^{\infty} \mathrm{d}t' (\chi^{\mathrm{R}})_{ij}^{\alpha\beta}(t,t') h_i^\beta(t') + \mathcal{O}(h^2), \end{aligned} \tag{2.5}$$

where the *retarded* susceptibility $(\chi^{\mathrm{R}})_{ij}^{\alpha\beta}(t,t')$ is given by the Kubo formula

$$(\chi^{\mathrm{R}})_{ij}^{\alpha\beta}(t,t') = i\theta(t-t')\langle [S_i^\alpha(t), S_j^\beta(t')]\rangle. \tag{2.6}$$

Here, the Heisenberg operators are given by $A(t) = \mathrm{e}^{itH} A e^{-itH}$ with the expectation value $\langle A\rangle = \mathrm{Tr}[A\mathrm{e}^{-\beta H}]/Z$. Assuming no magnetization at zero magnetic field and time-translation invariance, we can write Eq. (2.5) in frequency space as

$$M_j^\alpha(\omega) \approx (\chi^{\mathrm{R}})_{ij}^{\alpha\beta}(\omega) h_j^\beta(\omega), \tag{2.7}$$

where $(\chi^{\mathrm{R}})_{ij}^{\alpha\beta}(\omega) = \int_{-\infty}^{\infty} \mathrm{d}t\ \mathrm{e}^{it\omega} (\chi^{\mathrm{R}})_{ij}^{\alpha\beta}(t)$ and similarly for h and M. Eq. (2.7) says that if we apply a small time-independent magnetic field $h_j(\omega) \sim \delta(\omega)$, the system's response at site i is governed by the *static* susceptibility $\chi_{ij}^{\alpha\beta} \equiv (\chi^{\mathrm{R}})_{ij}^{\alpha\beta}(\omega \to 0)$.

The *retarded* susceptibility can be written using the spectral representation

$$(\chi^{\mathrm{R}})_{ij}^{\alpha\beta}(\omega) = \int \mathrm{d}\omega' \ \frac{\omega' R_{ij}^{\alpha\beta}(\omega')}{\omega + i0^+ - \omega'}, \tag{2.8}$$

where $R_{ij}(\omega')$ is the so-called spin relaxation function, which, just like the fermionic spectral function, is positive semi-definite. Eq. (2.8) is equivalent to the Kramers-Kronig relation for response functions that relates the imaginary part of the retarded susceptibility $\mathrm{Im}[(\chi^{\mathrm{R}})_{ij}^{\alpha\beta}(\omega)] = -\pi\omega R_{ij}^{\alpha\beta}(\omega)$ to its real part [Kro26].

Two related quantities are the Matsubara correlator $(\chi)^{\alpha\beta}(\mathbf{k}, i\omega_n)$ and the dynamic spin structure factor (DSF) $S^{\alpha\beta}(\mathbf{k},\omega)$ given by

$$S^{\alpha\beta}(\mathbf{k},\omega) = \int_{-\infty}^{+\infty} \frac{\mathrm{d}t}{2\pi N} \sum_{ij} \mathrm{e}^{i\omega t - i\mathbf{k}\cdot(\mathbf{r}_i - \mathbf{r}_j)} \left\langle S_i^\alpha(t) S_j^\beta(0)\right\rangle, \tag{2.9}$$

$$\chi^{\alpha\beta}(\mathbf{k}, i\omega_n) = \int_0^\beta \frac{\mathrm{d}\tau}{N} \sum_{ij} \mathrm{e}^{i\omega_n\tau - i\mathbf{k}\cdot(\mathbf{r}_i - \mathbf{r}_j)} \left\langle S_i^\alpha(\tau) S_j^\beta(0) \right\rangle, \tag{2.10}$$

with the imaginary-time Heisenberg operator $A(\tau) = \mathrm{e}^{\tau H} A e^{-\tau H}$ and the Matsubara frequencies $i\omega_n = \frac{2\pi}{\beta} n$ with $n \in \mathbb{Z}$. The Matsubara correlator is connected to the retarted susceptibility by analytic continuation

$$\chi^{\alpha\beta}(\mathbf{k}, i\omega_n \to \omega + i0^+) = (\chi^{\mathrm{R}})^{\alpha\beta}(\mathbf{k}, \omega). \tag{2.11}$$

This is especially interesting for the static susceptibility at $\omega = 0$. Here, the Matsubara correlator at $\omega_n = 0$ and the retarded susceptibility are equal

$$\lim_{\omega \to 0} (\chi^{\mathrm{R}})^{\alpha\beta}(\mathbf{k}, \omega) = \chi^{\alpha\beta}(\mathbf{k}, i\omega_n = 0) \equiv \chi^{\alpha\beta}(\mathbf{k}). \tag{2.12}$$

The DSF is connected to the retared susceptibility by the fluctuation-dissipation theorem [BF04]

$$S^{\alpha\beta}(\mathbf{k}, \omega) = \frac{\omega}{1 - e^{-\omega/T}} R^{\alpha\beta}(\mathbf{k}, \omega) = \frac{-1}{1 - e^{-\omega/T}} \frac{1}{\pi} \mathrm{Im}[(\chi^{\mathrm{R}})^{\alpha\beta}(\mathbf{k}, \omega)]. \tag{2.13}$$

When conducting neutron scattering experiments, the scattering cross section is directly proportional to the dynamic structure factor [Jen04]

$$\frac{\mathrm{d}^2\sigma}{\mathrm{d}E\,\mathrm{d}\Omega} = N \frac{k'}{k} \left(\frac{\hbar\gamma \mathrm{e}^2}{mc^2} \right)^2 \mathrm{e}^{-2W(\kappa)} \left| \frac{1}{2} g F(\kappa) \right|^2 \sum_{\alpha\beta} \left(\delta_{\alpha\beta} - \frac{\kappa^\alpha \kappa^\beta}{\kappa^2} \right) S^{\alpha\beta}(\boldsymbol{\kappa}, \omega). \tag{2.14}$$

Here $\boldsymbol{\kappa} = \mathbf{k} - \mathbf{k}'$ is the momentum transfer vector with magnitude κ, k and k' are the magnitudes of the incident and scattered neutron wave vectors, respectively, N is the number of magnetic ions. The constant γ is the neutron gyromagnetic ratio, e and m denote the electron charge and mass, and c the speed of light. The factor $e^{-2W(\kappa)}$ accounts for thermal motion of the magnetic ions via the Debye–Waller factor [ML71]. g is the Landé g-factor, $F(\kappa)$ the magnetic form factor of the magnetic ions and $(\delta_{\alpha\beta} - \frac{\kappa^\alpha \kappa^\beta}{\kappa^2})$ projects spin components perpendicular to the scattering vector. Equation (2.14) shows that up to known rescaling factors, the inelastic neutron-scattering cross section is fully described by the DSF. At low temperatures, if the spin system is highly susceptible to magnetic order, the main feature of the DSF is a sharp (para)-magnon peak, which is a hallmark of spin-wave quasiparticles with long lifetimes [SS49; ML71]. In contrast, if the system is not ordered magnetically, whether at high temperatures or in low-temperature (topological) paramagnetic phases such as valence bond solids or spin liquids, the DSF is dominated by broad, washed-out features. These can be a sign of spinon excitations or strong spin wave decay. In many cases, both sharp and washed-out features appear together, hinting at a competition between spin waves and spinon excitations.

Experimentally, the DSF is the main observable that provides direct access to the nature of spin excitations and their lifetimes in quantum magnets. It is desirable to have a strong theoretical understanding of all of its features and to be able to make predictions for it. It turns out that obtaining theoretical predictions for $S^{\alpha\beta}(\kappa, \omega)$ is far from trivial. Theoretical predictions for the static susceptibility $\chi^{\alpha\beta}(\mathbf{k}, i\omega_n = 0)$ are, while still non-trivial, easier to obtain than for the DSF because the Matsubara formalism can be used directly. The zero-frequency Matsubara correlator directly corresponds to the static susceptibility via

Eq. (2.12). Unfortunately, there is no established way yet to measure it directly in neutron scattering experiments. This gap could be closed in the future by cold atom experiments that have direct access to the time-dependent magnetization under a time-dependent magnetic field $\frac{\mathrm{d}M_j^\alpha(t)}{\mathrm{d}h_i^\beta(t')}$, which defines the retarded susceptibility in Eq. (2.5).

The main goal of this thesis is to develop methods that can reliably predict both the static susceptibilities and DSFs for general frustrated quantum spin systems such that they can be used to predict neutron scattering data and data from cold atom experiments in the future.

2.2 Majorana Fermions in an Exactly Solvable Spin Liquid

In his seminal paper [Kit06], Kitaev introduced an exactly solvable spin liquid that arises as the ground state of a nearest-neighbor spin model, described by the Hamiltonian

$$H = -J_x \sum_{\langle ij\rangle\in x} S_i^x S_j^x - J_y \sum_{\langle ij\rangle\in y} S_i^y S_j^y - J_z \sum_{\langle ij\rangle\in z} S_i^z S_j^z, \tag{2.15}$$

defined on the honeycomb lattice (see Fig. 2.1(a)), where the spins interact along the x, y, and z bonds. Using the Majorana spin representation

$$S_i^\alpha = i b_i^\alpha c_i, \tag{2.16}$$

with Majorana fermions b^α and c (illustrated in Fig. 2.1(b)), the Hamiltonian can be rewritten as

$$H = \frac{i}{4}\sum_{j,k} \hat{A}_{jk} c_j c_k, \quad \hat{A}_{jk} = \begin{cases} 2J_{\alpha_{jk}}\hat{u}_{jk} & \text{if } j \text{ and } k \text{ are connected,} \\ 0 & \text{otherwise,} \end{cases} \tag{2.17}$$
$$\hat{u}_{jk} = i b_j^{\alpha_{jk}} b_k^{\alpha_{jk}}.$$

The mapping in Eq. (2.16) enlarges the Hilbert space and introduces unphysical states, which can be projected out by the operator $P = \frac{(1+D)}{2}$, where $D = 4b^x b^y b^z c = \pm 1$. Since P commutes with the Hamiltonian, the projected eigenstates of Eq. (2.17) are also eigenstates of the projected Hamiltonian with the same energy. Remarkably, the Hermitian operators $\hat{u}_{jk}$ commute both with the Hamiltonian and with each other. Consequently, the Hilbert space decomposes into common eigenspaces of the $\hat{u}_{jk}$, wherein these operators can be replaced by their eigenvalues $u_{jk} = \pm 1$. This leads to a free Majorana Hamiltonian that can be solved exactly. The resulting free Majorana model can be interpreted as a $\mathbb{Z}_2$ gauge theory, where the u_{jk} act as $\mathbb{Z}_2$ gauge fields. The ground state lies in the sector where all $u_{jk} = 1$. Depending on the coupling constants J_α, the spectrum may be either gapped or gapless (see Fig. 2.1(c)). In the gapless phase, the spectrum features two Dirac cones (see Fig. 2.1(d)) that merge and acquire a mass at the phase boundary, a canonical example of a topological phase transition.

While many interesting details of the model are omitted here, the essential takeaway is the following: The Kitaev honeycomb model hosts an exact $\mathbb{Z}_2$ spin liquid ground state exhibiting both spin fractionalization and topological order, with Majorana fermions emerging as exact quasiparticles via the spin representation Eq. (2.16). This spin liquid arises from a nearest-neighbor spin model that could, in principle, be realized in real materials such as α-$RuCl_3$ [Plu+14; MSK25], although experimental confirmation remains elusive despite extensive efforts [Kas+18; Kee23].

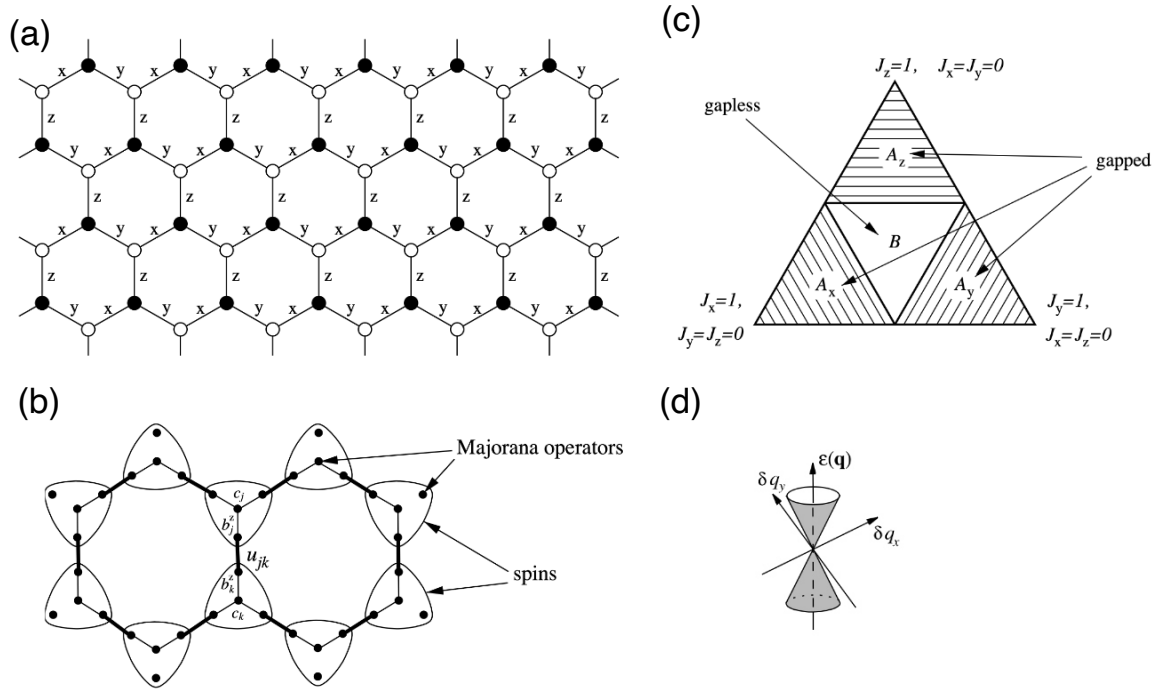

Figure 2.1 Images describing the most important features of the Kitave honeycomb model. a) The honeycomb lattice with bonds labeling the three types of links appearing in the Hamiltonian Eq. (2.15). b) Schematic image of the Majorana representation Eq. (2.16), where each spin is depicted as a triangle with rounded corners. The four dots inside represent the four Majorana flavors. c) Ground state phase diagram. d) Gapless Dirac cones appearing in the gapless phase. Figures reproduced from Ref. [Kit06].

The Kitaev representation Eq. (2.16) is just one among many mappings between spins and fermions. While other models are usually not solvable exactly in terms of these partons, they are hoped to still mimic the model's quasiparticle properties. In the next section, we review several fermionic spin representations that have been widely used in the literature.

2.3 Spin Representations

While in Sec. 2.2 we saw that spin representations in terms of fermions can directly lead to a quasiparticle description of spin Hamiltonians, there are also other practical reasons to consider them. While there exists a path-integral formalism for spins using spin-coherent states [AS10], it contains a topological term that prevents us from using standard path-integral methods. Therefore, if we want to use the standard diagrammatic toolbox like weak-coupling perturbation theory using Wick's theorem, or more advanced methods like functional renormalization group (FRG) [KBS10] or parquet [DM64a; DM64b; NGR69; Bic04], we first have to represent the spins with fermionic or bosonic quasiparticles, the so-called *partons*. What follows is a short overview of the different fermionic spin representations.

In this section, we will focus on the case $S = \frac{1}{2}$. Then our local Hilbert space dimension is 2 and we can use the Pauli matrices that fulfill the algebra $\sigma^\alpha\sigma^\beta = \delta^{\alpha\beta} + i\epsilon^{\alpha\beta\gamma}\sigma^\gamma$ to represent our spins as $S^\alpha = \frac{1}{2}\sigma^\alpha$. Equation (2.2) can then be written as

$$S^\alpha S^\beta = \frac{1}{4}\delta^{\alpha\beta} + \frac{i}{2}\epsilon^{\alpha\beta\gamma}S^\gamma. \tag{2.18}$$

Representing spin with partons generally adds additional states to the Hilbert space. The only requirement for a *faithful* spin-$\frac{1}{2}$ representation is to fulfill Eq. (2.18) after projection to the physica two-dimensional Hilbert space. We will refer to states that lie in the designated two-dimensional Hilbert space as *physical* states and any other states as *unphysical* states. In practice, constructing a representation that fulfills the off-diagonal part of Eq. (2.2) is a lot easier than fulfilling the Hilbert space constraint, which is encoded in the diagonal part proportional to $\delta^{\alpha\beta}$. For this reason, the constraint is often only approximately fulfilled in diagrammatic methods, which makes a representation desirable that is inherently SU(2) symmetric in both the physical and unphysical parts of the Hilbert space.

In the following two sections, we will present parton representations using spinful complex fermions and spinless real Majorana fermions. An overview of those representations can be found in Table 2.1.

2.3.1 Spinful Fermions

A common class of spin representation uses two spinful fermions $f_\uparrow, f_\downarrow$. Each fermionic mode has a two-dimensional Hilbert space, which results in two unphysical states. The most common representation of that kind is the Abrikosov [ALI63] representation

$$\bar{S}^\alpha = \frac{1}{2} f^\dagger \sigma^\alpha f, \tag{2.19}$$

where we used the spinor $f = (f_\uparrow, f_\downarrow)^T$. The spin operators fulfill the following algebra

$$\bar{S}^\alpha \bar{S}^\beta = P\frac{1}{4}\delta^{\alpha\beta} + \frac{i}{2}\epsilon^{\alpha\beta\gamma}\bar{S}^\gamma, \tag{2.20}$$

where we defined $P = \frac{(1+D)}{2}$ and $D = -(2n_\uparrow - 1)(2n_\downarrow - 1)$. Since $D^2 = 1$, P_i fulfills the projector property $P^2 = P$. The spin operators $\bar{S}^\alpha$ live in a local four dimensional Hilbert space spanned by $\{|\uparrow\rangle, |\downarrow\rangle, |\uparrow\downarrow\rangle, |0\rangle\}$. There, we can represent the operators as 2×2 block matrices

$$\bar{S}^\alpha = \begin{pmatrix} S^\alpha & \mathbf{0} \\ \mathbf{0} & \mathbf{0} \end{pmatrix}, \qquad D = \begin{pmatrix} \mathbb{1} & \mathbf{0} \\ \mathbf{0} & -\mathbb{1} \end{pmatrix}, \qquad P = \begin{pmatrix} \mathbb{1} & \mathbf{0} \\ \mathbf{0} & \mathbf{0} \end{pmatrix}. \tag{2.21}$$

This immediately shows that the Abrikosov representation acts as a spin $\frac{1}{2}$ operator on the $|\uparrow\rangle, |\downarrow\rangle$ subspace and a spin 0 operator on the unphysical Hilbert space spanned by $|\uparrow\downarrow\rangle, |0\rangle$. Therefore, spin models written with the Abrikosov representation represent diluted lattices, where each site is either empty or occupied by a spin. The physical spin-$\frac{1}{2}$ Hilbert space is characterized here by the space of states with exactly one fermion such that the number operator equals to $n = 1$. More generally, this corresponds to the constraint $D = 1$. States in the unphysical Hilbert space affect any finite-temperature calculation. However, $n = n_\uparrow + n_\downarrow$ is 1 on average $\langle n \rangle = 1$ due to the particle hole symmetry that is unbroken if we consider Hamiltonians like Eq. (2.1). Together with the fact that an empty site can not lower the energy of the system by interacting with its neighboring spins, a naive estimate gives that the empty and doubly occupied states must be gapped out with a gap of order of the exchange coupling J [RW10] and therefore do not affect ground state properties. While this is true for systems with magnetic order, we challenge this view and give concrete counterexamples in Ref. [P1] for clusters of frustrated spins, where the presence of empty sites can lift frustration effects.

A rigorous way to cancel contributions from the unphysical Hilbert space on all spin expectation values is the Popov-Fedotov trick [PF88; PS11]. It can be shown, that adding the imaginary chemical potential $\mu = \frac{i\pi}{2}T(n-1)$, where T is the temperature, gives contributions from the two degenerate unphysical states $|\uparrow\downarrow\rangle, |0\rangle$ with opposite signs. Therefore, they destructively interfere when calculating the trace over spin observables and do not contribute. μ can be written as the 2×2 block matrix

$$\mu_i = \begin{pmatrix} \mathbb{1} & \mathbf{0} \\ \mathbf{0} & i\pi T S^z \end{pmatrix}. \tag{2.22}$$

While the Abrikosov representation (see Eq. (2.19)) is the most widely known spin-$\frac{1}{2}$ representation, there are three more that are based on fermion bilinears. To make things easier, let us introduce another fermionic spinor $\Psi = (f_\uparrow, f_\downarrow^\dagger)^T$. Following Ref. [FKP18], let us refer to the Abrikosov representation as $\mathrm{SO}(4)_L$ *chiral*. Then the $\mathrm{SO}(4)_R$ *chiral* representation can be defined as

$$\bar{S}^\alpha = \frac{1}{2}\Psi^\dagger \sigma^\alpha \Psi_i = \begin{pmatrix} \mathbf{0} & \mathbf{0} \\ \mathbf{0} & S^\alpha \end{pmatrix}. \tag{2.23}$$

It is equivalent to the Abrikosov representation (Eq. (2.19)) with the physical and unphysical Hilbert spaces exchanged. Therefore, it also fulfills the algebra Eq. (2.2) but with the projection operator projecting onto the zero and doubly occupied space $P = \frac{1-D}{2}$. Here the constraint for the physical Hilbert space is $D = -1$. Another choice is the SO(4) representation

$$\bar{S}^\alpha = \frac{1}{2} f^\dagger \sigma^\alpha f - \frac{1}{2}\Psi^\dagger \sigma^\alpha \Psi = \begin{pmatrix} S^\alpha & \mathbf{0} \\ \mathbf{0} & -S^\alpha \end{pmatrix}, \tag{2.24}$$

which has a time-reversed spin $\frac{1}{2}$ degree of freedom in the unphysical Hilbert space, which fulfills the algebra $\bar{S}^\alpha \bar{S}^\beta = \frac{1}{4}\delta^{\alpha\beta} + D\frac{i}{2}\epsilon^{\alpha\beta\gamma}\bar{S}^\gamma$. Here, the constraint is $D = 1$. As we will see later, it is equivalent to the Kitaev-Majorana representation that was used to solve the Kitaev-Honeycomb model [Kit06].The last representation we are going to mention is the SO(3) representation:

$$\bar{S}^\alpha = \frac{1}{2} f^\dagger \sigma^\alpha f + \frac{1}{2}\Psi^\dagger \sigma^\alpha \Psi = \begin{pmatrix} S^\alpha & \mathbf{0} \\ \mathbf{0} & S^\alpha \end{pmatrix}. \tag{2.25}$$

It fulfills the correct spin algebra on the whole Hilbert space $\bar{S}^\alpha \bar{S}^\beta = \frac{1}{4}\delta^{\alpha\beta} + \frac{i}{2}\epsilon^{\alpha\beta\gamma}\bar{S}^\gamma$. We are free to interpret which subspace is the physical or unphysical one as both $D = \pm 1$ give faithful spin representations. The main advantage of this representation is that no constraint needs to be fulfilled at all. Any spin Hamiltonian written in the SO(3) representation has energy levels that have an unphysical degeneracy. This degeneracy does not influence any observables except for a constant shift of the free energy [NSR21]. However, when we express the Hamiltonian Eq. (2.1) with the representation Eq. (2.25), we get a complicated fermionic theory that breaks particle hole symmetry and does not conserve fermionic particle numbers. This has made its use in diagrammatic approaches unattractive. As we will see below it is equivalent to a simple representation in terms of Majorana fermions with nice and easy to handle properties.

2.3.2 Majorana Representation

Real Majorana fermion operators η fulfill the fermionic anticommutation relations $\{\eta^\alpha, \eta^\beta\} = \delta_{\alpha,\beta}$ and are their own antiparticles $\eta^\dagger = \eta$. Any fermionic degree of freedom can be written in terms of the sum of two Majoranas. For example we can write the transformation:

$$\begin{aligned} f &= \frac{1}{\sqrt{2}}(\eta_1 + i\eta_2), & f^\dagger &= \frac{1}{\sqrt{2}}(\eta_1 - i\eta_2), \\ \eta_1 &= \frac{1}{\sqrt{2}}(f + f^\dagger), & \eta_2 &= \frac{1}{i\sqrt{2}}(f - f^\dagger). \end{aligned} \tag{2.26}$$

Therefore, a Majorana fermion has a formal Hilbert space dimension of $\sqrt{2}$.
One can reproduce the four spin representations from the last section with four Majorana fermions, $\eta^x, \eta^y, \eta^z, \eta^0$ such that operator D is defined by

$$D = 4\eta^0\eta^x\eta^y\eta^z. \tag{2.27}$$

The chiral $\mathrm{SO}(4)_L$ representation can then be written as

$$\bar{S}^\alpha = -\frac{i}{2}(\frac{1}{2}\epsilon^{\alpha\beta\gamma}\eta^\beta\eta^\gamma - \eta^0\eta^\alpha) = \begin{pmatrix} S^\alpha & \mathbf{0} \\ \mathbf{0} & \mathbf{0} \end{pmatrix}, \tag{2.28}$$

with the physical subspace given by $D = 1$. Similarly, the chiral $\mathrm{SO}(4)_R$ representation can be written as

$$\bar{S}^\alpha = -\frac{i}{2}(\frac{1}{2}\epsilon^{\alpha\beta\gamma}\eta^\beta\eta^\gamma + \eta^0\eta^\alpha) = \begin{pmatrix} \mathbf{0} & \mathbf{0} \\ \mathbf{0} & S^\alpha \end{pmatrix}, \tag{2.29}$$

with constraint being $D_i = -1$. The SO(4) representation is

$$\bar{S}^\alpha = i\eta^0\eta^\alpha = \begin{pmatrix} S^\alpha & \mathbf{0} \\ \mathbf{0} & -S^\alpha \end{pmatrix}, \tag{2.30}$$

with constraint being $D_i = 1$. This is exactly the Kitaev representation used to solve Kitaev's honeycomb model (see Sec. 2.2: note that $\eta^\alpha = b^\alpha$ and $\eta^0 = c$) [Kit06]. It has recently been shown that it is also possible to use the SO(3) representation

$$\bar{S}^\alpha = -\frac{i}{2}\epsilon^{\alpha\beta\gamma}\eta^\beta\eta^\gamma = \begin{pmatrix} S^\alpha & \mathbf{0} \\ \mathbf{0} & S^\alpha \end{pmatrix} \tag{2.31}$$

to solve Kitaev's honeycomb model [FKP18]. Notice that Eq. (2.31) only depends on three of the four Majoranas. This reflects the hidden gauge freedom of the SO(3) representation which we discuss below. The SO(3) representation written in terms of Majorana fermions is a lot more practical than its fermionic counterpart (Eq. (2.25)). First introduced in 1959 [Mar59; Tsv92] it has since been used in many different context [HSK13; NSR21; NMR25]. Still, even though the SO(3) representation does not have unphysical states, it is not as popular in the current literature [SB16; FKP18]. This is probably because the classification of topological orders that spin liquids exhibit was historically first described via the projective symmetry-group treatment using Abrikosov fermions [Wen07].

Name	$\mathrm{SO}(4)_L$ (Abrikosov)	$\mathrm{SO}(4)_R$
Fermion Rep.	$\bar{S}^\alpha = \frac{1}{2} f^\dagger \sigma^\alpha f$	$\bar{S}^\alpha = \frac{1}{2} \Psi^\dagger \sigma^\alpha \Psi$
Majorana Rep.	$\bar{S}^\alpha = -\frac{i}{2}\left(\frac{1}{2}\epsilon^{\alpha\beta\gamma}\eta^\beta\eta^\gamma - \eta^0\eta^\alpha\right)$	$\bar{S}^\alpha = -\frac{i}{2}\left(\frac{1}{2}\epsilon^{\alpha\beta\gamma}\eta^\beta\eta^\gamma + \eta^0\eta^\alpha\right)$
Spin Algebra	$\bar{S}^\alpha\bar{S}^\beta = \frac{1+D}{2}\,\frac{1}{4}\delta^{\alpha\beta} + \frac{i}{2}\epsilon^{\alpha\beta\gamma}\bar{S}^\gamma$	$\bar{S}^\alpha\bar{S}^\beta = \frac{1-D}{2}\,\frac{1}{4}\delta^{\alpha\beta} + \frac{i}{2}\epsilon^{\alpha\beta\gamma}\bar{S}^\gamma$
Matrix Rep.	$\bar{S}^\alpha = \left(\begin{smallmatrix} S^\alpha & \mathbf{0} \\ \mathbf{0} & \mathbf{0} \end{smallmatrix}\right)$	$\bar{S}^\alpha = \left(\begin{smallmatrix} \mathbf{0} & \mathbf{0} \\ \mathbf{0} & S^\alpha \end{smallmatrix}\right)$
Constraint	$D = +1$	$D = -1$
Name	SO(4) (Kitaev)	SO(3)
Fermion Rep.	$\bar{S}^\alpha = \frac{1}{2} f^\dagger \sigma^\alpha f - \frac{1}{2}\Psi^\dagger\sigma^\alpha\Psi$	$\bar{S}^\alpha = \frac{1}{2} f^\dagger \sigma^\alpha f + \frac{1}{2}\Psi^\dagger\sigma^\alpha\Psi$
Majorana Rep.	$\bar{S}^\alpha = i\eta^0\eta^\alpha$	$\bar{S}^\alpha = -\frac{i}{2}\epsilon^{\alpha\beta\gamma}\eta^\beta\eta^\gamma$
Spin Algebra	$\bar{S}^\alpha\bar{S}^\beta = \frac{1}{4}\delta^{\alpha\beta} + D\,\frac{i}{2}\epsilon^{\alpha\beta\gamma}\bar{S}^\gamma$	$\bar{S}^\alpha\bar{S}^\beta = \frac{1}{4}\delta^{\alpha\beta} + \frac{i}{2}\epsilon^{\alpha\beta\gamma}\bar{S}^\gamma$
Matrix Rep.	$\bar{S}^\alpha = \left(\begin{smallmatrix} S^\alpha & \mathbf{0} \\ \mathbf{0} & -S^\alpha \end{smallmatrix}\right)$	$\bar{S}^\alpha = \left(\begin{smallmatrix} S^\alpha & \mathbf{0} \\ \mathbf{0} & S^\alpha \end{smallmatrix}\right)$
Constraint	$D = +1$	$D = \pm 1$

Table 2.1 Comparison of four fermionic spin representations. The spinors are defined by $f = (f_\uparrow, f_\downarrow)^T$ and $\Psi = (f_\uparrow, f_\downarrow^\dagger)^T$. The constraint is defined by the operator $D = -(2n_\uparrow - 1)(2n_\downarrow - 1) = 4\eta^0\eta^x\eta^y\eta^z$. The matrix representation is written in the basis $\{|\uparrow\rangle, |\downarrow\rangle, |\uparrow\downarrow\rangle, |0\rangle\}$.

2.3.3 Mixed Representation and Spinless Fermions.

Starting from the SO(3) Majorana representation as $S^z = -i\eta^x\eta^y$, $S^\pm = -i(\eta^x \pm \eta^y)\eta^z$, a transformation from Majoranas to complex fermions $\eta^x = \frac{i}{\sqrt{2}}(c - c^\dagger)$, $\eta^y = \frac{1}{\sqrt{2}}(c + c^\dagger)$ gives

$$S^z = c^\dagger c - \tfrac{1}{2}, \qquad S^+ = i\sqrt{2}\eta^z c, \qquad S^- = i\sqrt{2}\eta^z c^\dagger. \tag{2.32}$$

This mixed representation was first introduced as a "drone-fermion representation" in Refs. [CS70; Mat65; Spe68]. It is similar to the Jordan-Wigner representation [JW28], with the Jordan-Wigner string being represented by the Majorana operator $i\sqrt{2}\eta^z$. As it is inherently U(1)-symmetric, it is especially useful for studying spin systems in a magnetic field [P3].

2.3.4 Gauge Symmetries

As we have discussed above, mapping spins to fermions increases the Hilbert space dimension. Assuming we project onto the physical Hilbert space, any transformation that only acts on the unphysical Hilbert space leaves the spins on the physical Hilbert space invariant. These can therefore be seen as gauge transformations.
The $\mathrm{SO}(4)_L$ (Abrikosov) representation has an SU(2) gauge symmetry that includes all rotations in the $|\uparrow\downarrow\rangle, |0\rangle$ space. These are regularly used in numerical calculations [Bue+19; Reu11] to boost efficiency. They are also the basis of the projective symmetry group calculations laying theoretical basis for topological order of spin liquids [Wen07]. The same SU(2) symmetry exist for the SO(4) (Kitaev) representation. For the $\mathrm{SO}(4)_R$ representation the SU(2) gauge symmetry includes all rotations of the single occupied space. For the SO(3) representation the existence of an SU(2) gauge group is less obvious. Naively the

representation (Eq. (2.31)) only has a $\mathbb{Z}_2$ gauge symmetry that includes multiplication of all local Majorana fermions with a sign $\eta^\alpha \to -\eta^\alpha$. However, this is only part of the full gauge group. When we do not project out the degenerate space, the gauge group includes all rotations between the physical space $\{|\downarrow\rangle, |\uparrow\rangle\}$ and the degenerate space $\{|\uparrow\downarrow\rangle, |0\rangle\}$. This fact has not been considered so far [Tsv92; NSR21; NMR25]. The generators of this $SU(2)$ gauge group are

$$g_1 = \sqrt{2}\eta^0, \qquad g_2 = 2\sqrt{2}\eta_x\eta_y\eta_z, \qquad g_3 = D = 4\eta^0\eta_x\eta_y\eta_z, \tag{2.33}$$

and fulfill the relations

$$[g_\alpha, g_\beta] = 2\epsilon^{\alpha\beta\gamma}g_\gamma, \qquad g_\alpha^2 = 1. \tag{2.34}$$

The SU(2) Gauge transformations can therefore generally be written as

$$\bar{S}^\alpha \to \mathrm{e}^{i\theta\hat{\mathbf{n}}\cdot\mathbf{g}}\bar{S}^\alpha\mathrm{e}^{-i\theta\hat{\mathbf{n}}\cdot\mathbf{g}}, \tag{2.35}$$

where $\mathbf{g} = g_1, g_2, g_3$ and $\hat{\mathbf{n}}$ is a unit vector. Transformations including only g_1 or g_3 can be directly identified with gauge transformations of the real Majoranas themselves. The corresponding U(1) transformations are

$$\eta^\alpha \to e^{i\theta g_1}\eta^\alpha = \cos(\theta)\eta^\alpha + \sqrt{2}i\sin(\theta)\eta^0\eta^\alpha, \tag{2.36a}$$
$$\eta^\alpha \to e^{i\theta g_3}\eta^\alpha = \cos(\theta)\eta^\alpha + i\sin(\theta)\epsilon^{\alpha\beta\gamma}\eta^0\eta^\beta\eta^\gamma. \tag{2.36b}$$

Gauge transformations including g_2 cannot be written so easily as transformations of the *real* Majorana operators, since the right and left Majorana in Eq. (2.31) transform with opposite phases. That the gauge transforms Eq. (2.36) actually leave the spins Eq. (2.31) invariant can be seen by first noticing that both D and η^0 anticommute with η^α. Therefore, $e^{i\theta D}\eta^\alpha\mathrm{e}^{i\theta D} = e^{i\theta D}\mathrm{e}^{-i\theta D}\eta^\alpha = \eta^\alpha$. Together, the two U(1) transfoms in Eq. (2.36) remarkably connect n with $n+2$ objects non-trivially. For example, using both equations for $\theta = \frac{\pi}{2}$ gives the following relation between the local Majorana and the local spin Green's function

$$\langle\eta_i^\alpha(t)\eta_i^\alpha(0)\rangle = 2\langle\bar{S}_i^\alpha(t)\bar{S}_i^\alpha(0)\rangle. \tag{2.37}$$

Similar relations were found in Refs. [SM03; Sch+15; P2] by using constants of motion. This insight could be used to develop a projective symmetry group treatment for U(1) spin liquids working with the SO(3) representation instead of the Abrikosov representation usually used [Wen07].

2.3.5 Summary

To summarize: Historically, the Abrikosov representation has been most widely used due to its simplicity and gauge symmetries. However, the SO(3) is slowly becoming more popular due to its absence of unphysical states and its simplicity when working with Majorana fermions instead of complex fermions. The recent success of the SO(3) Majorana representation has led to the development of generalizations to higher spin values [SR23]. While these Majorana representations seem to have fewer unphysical states than the generalization of the Abrikosov representation to higher spins, the only spin representation that does not add any unphysical states, similar to the SO(3) spin $\frac{1}{2}$ representation, is for $S = \frac{3}{2}$ [YZK09; SR23].

2.4 Functional Methods

In this section, we want to set up the functional renormalization group (FRG) treatment for spin systems. Before diving into the depths of the FRG in Sec. 2.4.2 and its many incarnations in Sec. 2.4.3, let us shortly review the effective-action formalism the method is based upon. The material presented in Sec. 2.4.1 can be found in many textbooks, such as Refs. [DM66; NO98; KBS10] and we include it mainly to define the notation for the rest of the discussion.

2.4.1 1PI Effective Action Formalism

Let us consider a theory described by the classical action $S[\varphi] = \sum_n \frac{1}{n!} V_{a_1 \dots a_n} \varphi^{a_1} \dots \varphi^{a_n}$, where the fields φ^a have fixed statistics and $V_{a_1 \dots a_n}$ are fully (anti)-symmetric tensors representing the bare n-point interactions. The generating functional W of the connected Green's functions is defined as

$$\mathrm{e}^{-W[h]} = \int D\varphi \, e^{-S[\varphi] - h_a \varphi^a}. \tag{2.38}$$

Here, the Einstein's summation convention is used for each contraction of one lower and one upper index. Each index a is a multi-index that can consist of multiple discrete and continuous quantum numbers. For example: $h_a \varphi^a = \sum_i \int \mathrm{d}\tau h_i(\tau) \varphi^i(\tau)$. From W we can calculate connected correlation functions of the fundamental field φ^a via functional derivatives

$$G^{a_1 \dots a_n} \equiv \frac{\delta}{\delta h_{a_1}} \dots \frac{\delta}{\delta h_{a_n}} W[h] = (-1)^{n-1} \langle \varphi^{a_1} \dots \varphi^{a_n} \rangle_c, \tag{2.39}$$

where the average of an arbitrary operator $A[\varphi]$ composed by the φ^a is defined as

$$\langle A[\varphi] \rangle \equiv \mathrm{e}^W \int D\varphi A[\varphi] \mathrm{e}^{-S[\varphi] - h_a \varphi^a}, \tag{2.40}$$

and the subscript c in $\langle \dots \rangle_c$ indicates that only the connected part is taken. $G^{a_1 \dots a_n}$ are represented in Fig. 2.2 as grey circles with n external legs. To not clutter the notation with indices, we might refer to $G^{a_1 \dots a_n}$ as G^n, labeling the Green's function with its number of indices. Calculating the right side of Eq. (2.39) for G^{ab}, we obtain

$$G^{ab} = \bar{\varphi}^a \bar{\varphi}^b - \langle \varphi^a \varphi^b \rangle \equiv G^2, \tag{2.41}$$

where $\bar{\varphi}^a \equiv \frac{\delta W}{\delta h_a} = \langle \varphi^a \rangle$. The 1PI effective action $\Gamma^{1\mathrm{PI}}[\bar{\varphi}]$ is defined as the Legendre transformation of W with respect to the source h_a,

$$\Gamma^{1\mathrm{PI}}[\bar{\varphi}] = W - h_a \bar{\varphi}^a, \tag{2.42}$$

where h_a as a functional of $\bar{\varphi}^a$ is the solution of $\frac{\delta W}{\delta h_a} = \bar{\varphi}^a$. It is well-known [NO98] that $\Gamma^{1\mathrm{PI}}$ is given by a sum of all connected one-particle irreducible (1PI) diagrams with external lines contracted by $\bar{\varphi}^a$, where one-particle irreducible diagram means that one cut of any internal line cannot make the diagram disconnected. The fundamental result of the 1PI effective action formalism is that any connected correlation function $G^{a_1 \dots a_n}$ of order $n > 2$ can be written as a sum of tree diagrams, where the internal lines are one-particle propagators $G^{a_1 a_2}$ and the vertices are functional derivatives of $\Gamma^{1\mathrm{PI}}$ (called 1PI vertices):

$$\Gamma^{1\mathrm{PI}}_{a \dots b} \equiv \frac{\delta}{\delta \bar{\varphi}^a} \dots \frac{\delta}{\delta \bar{\varphi}^b} \Gamma^{1\mathrm{PI}}. \tag{2.43}$$

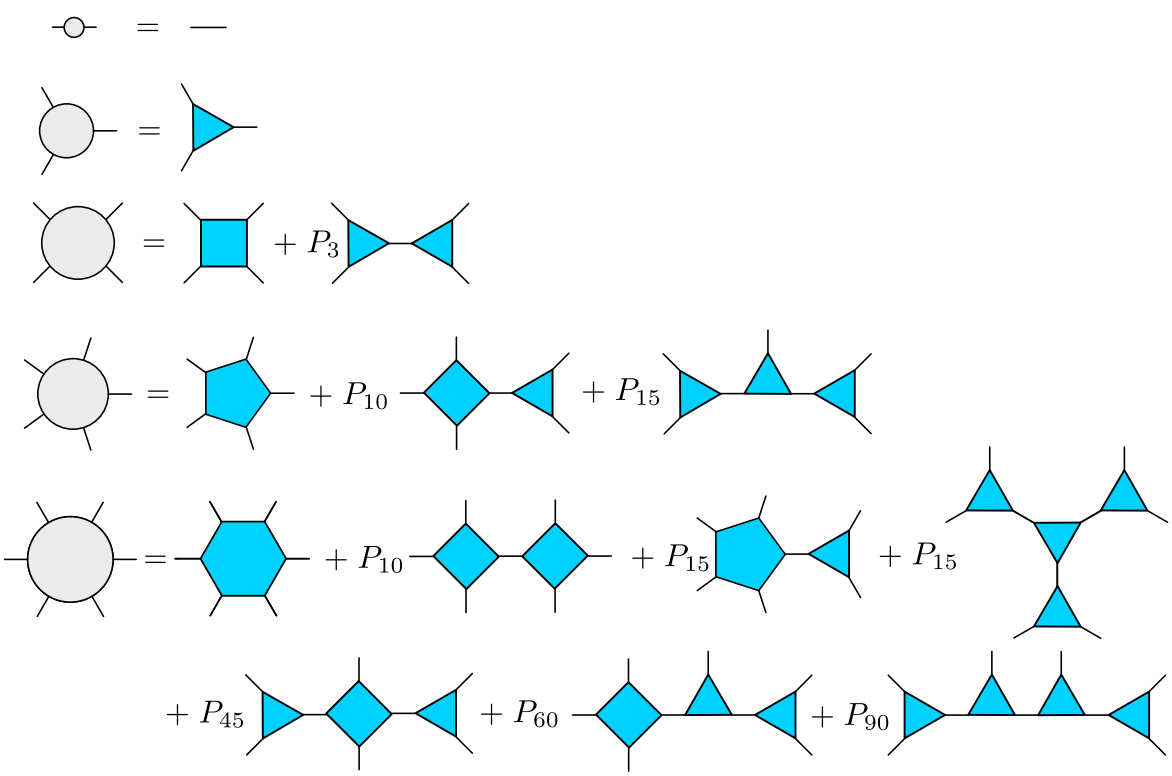

Figure 2.2 Tree expansions of the connected Green's functions. n-point connected Green's functions are represented with gray circles with n external lines. 1PI vertices are represented with cyan polygons with n corners. Each line on the right-hand side represents a two point connected Green's function, as indicated in the first line. P_n denotes a sum over n distinct copies of the diagrams to their right with the same topology but with permuted external lines, such that the sum of these n diagrams is fully crossing-symmetric in all external indices.

This result is the so-called *tree expansion* and derived in full generality in Ref. [KBS10]. A sketch of it is shown in Fig. 2.2, where $\Gamma^{\mathrm{1PI}}_{a\ldots b}$ are represented as cyan polygons.

2.4.2 Functional Renormalization Group

Renormalization-group (RG) methods, originating from Wilson's seminal ideas, have achieved remarkable success in understanding many-body systems [Wil75; Sha94]. The essential concept is to progressively integrate out fluctuations at high energy or length scales, thereby obtaining an effective theory that captures the relevant low-energy physics, which explains the universality of phase transitions. Next to the Wilsonian RG [Wil75; Sha94], which provides critical exponents and characterizes universality classes near phase transitions, the numerical renormalization group (NRG) [BCP08], and the density matrix renormalization group (DMRG) [Sch05] are both numerical implementations of the RG tailored to impurity models and area-law ground-state searches, respectively.

Here, we briefly introduce the functional renormalization group (FRG), a diagrammatic formulation of RG applied to the effective action defined in Eq. (2.42). The FRG yields flow equations for scale-dependent Green's and vertex functions with full frequency and momentum dependence [KBS10; Wet93]. The main idea of the FRG is to take the exact generating functional $W[h]$ (see Eq. (2.38)) of the exact theory and add a scale-dependent cutoff R_Λ to it, that suppresses low-energy dynamics for finite Λ and recovers the exact

physical theory for $\Lambda = 0$:

$$W^{\Lambda}[h] = -\log(\int \mathcal{D}\varphi\, \mathrm{e}^{-S[\varphi]-h_a\varphi^a-\frac{1}{2}\varphi^{a_1}R^{\Lambda}_{a_1a_2}\varphi^{a_2}}), \tag{2.44}$$

where $R^0 = 0$. Just like in Eq. (2.39), functional derivatives of $W^{\Lambda}[h]$ give the scale-dependent connected Green's functionals that reduce to the Green's functions when evaluating them at $h = 0$ and reduce to Green's functions of the physical theory for $\Lambda = 0$. Now, the main idea of FRG is that we can start from a theory at $\Lambda = \Lambda_{\text{init}}$ where we know all correlation functions exactly, and solve the initial value problem given by

$$\frac{\mathrm{d}}{\mathrm{d}\Lambda}W^{\Lambda}[h] = \frac{1}{2}\langle\varphi^{a_1}\dot{R}^{\Lambda}_{a_1a_2}\varphi^{a_2}\rangle, \qquad W^{\Lambda_{\text{init}}}[h] \text{ is known}, \tag{2.45}$$

where the dot indicates derivatives with respect to Λ. Unfortunately, working with the full functional $W^{\Lambda}[h]$ is impossible for most realistic settings. Therefore, it is often expanded in terms of correlation functions or vertices [KBS10]. The former can be done by taking functional derivatives of Eq. (2.45) with respect to h and then setting $h = 0$. This will generate a hierarchy of differential equations for n-point connected Green's functions that depend on $(n+2)$-point connected Green's functions

$$\frac{\mathrm{d}}{\mathrm{d}\Lambda}\langle\varphi^{a_1}\dots\varphi^{a_n}\rangle_c = -\frac{1}{2}\langle\varphi^{a_1}\dots\varphi^{a_n}(\varphi^{b_1}\dot{R}^{\Lambda}_{b_1b_2}\varphi^{b_2})\rangle_c. \tag{2.46}$$

The vertex expansion can be obtained by taking a Legendre transform of Eq. (2.45), which results in the Wetterich equation [Wet93] and then taking functional derivatives with respect to the conjugate variable of h [KBS10] as in Eq. (2.43). Another way is to simply insert the tree-expansion (see Fig. 2.2) into Eq. (2.46). This will generate the vertex flow equations sketched in Fig. 2.3. Note that we give them here for a general theory, where three-point vertices are non-zero. All terms with odd vertices in Fig. 2.3 appear in the spin-FRG formalism [KK19] but drop out in the fermionic parton-FRG approaches discussed in Sec. 2.4.3.

The infinite hierarchy of equations (see Eq. (2.46) or Fig. 2.3) needs to be truncated in practice. This is often done by setting $\frac{\mathrm{d}}{\mathrm{d}\Lambda}\Gamma^{1\text{PI}}_n = 0$ for some $n \geq 5$. This makes the results for $\Lambda = 0$ dependent on the cutoff function R^{Λ}. To minimize unwanted effects of this cut-off dependence, it is advantageous to motivate choices of R^{Λ} physically. The problem of the cut-off dependence motivated the development of the multiloop-FRG scheme which has been shown to be cut-off independent and equivalent to solving the self-consistent parquet equations [KD18a; KD18b]. However, the numerical implementation has shown to be difficult and direct convergence of the parquet equations to be more practical [Ge24; Rit25; Ge25].

2.4.3 Functional Renormalization Group for Partons

The FRG has been applied in many different fields of physics. From predicting the mass of the Higgs-boson [SW10] over studying the flocking behavior of active matter, like birds [JL24], to applications for itinerant fermion systems with, for example, Hubbard-like interactions [HS01; And+04; CHS19; Hil+20]. There, it was used to calculate phase diagrams by identifying instabilities toward magnetic, charge or superconducting order as well as their corresponding susceptibilities. After the seminal paper by Reuther and Wölfle [RW10] the FRG using the Abrikosov representation (see Eq. (2.19)) has been applied to spin models with great success [RTT11; Kie+23; RT14; BT16; HR17; Mül+24; Che+24; Iqb+19; Rit21; Her+22; Noc+23; KZ22; Gre+25]. Due to its use of the pseudo-fermion representation, the method is called pseudo-fermion FRG (pf-FRG). It has been applied to J_1–…–J_n Heisenberg Models [Iqb+19],

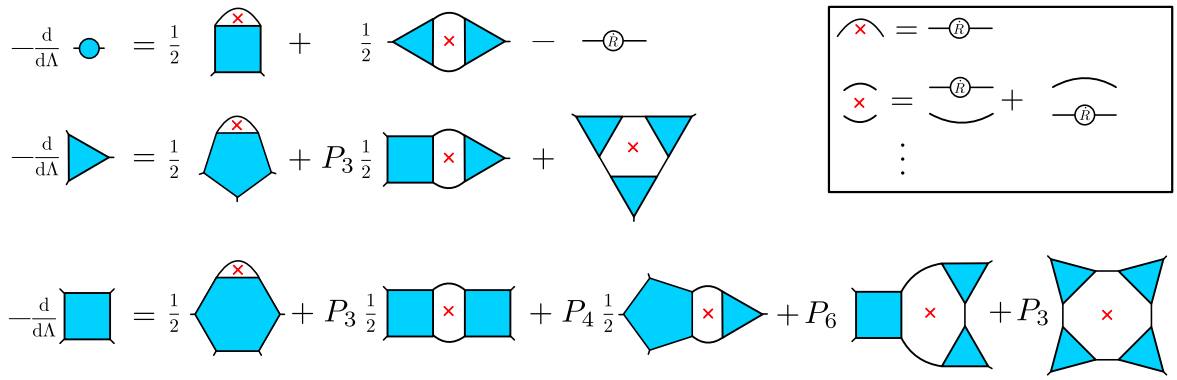

Figure 2.3 Diagrammatic depiction of the one-loop FRG equations Eq. (2.46) after applying the tree expansion (see Fig. 2.2) to represent the connected correlators in terms of vertices. It is assumed that the field expectation value stays zero. Every loop with a red cross is a symmetrized version of the loop where one of the propagators G^2 is replaced by $G^2\dot{R}^\Lambda G^2$ as depicted in the inset. P_n denotes a sum over n distinct copies of the diagrams to their right with the same topology but with permuted external lines, such that the sum of these n diagrams is fully crossing-symmetric in all external vertices.

XYZ models [Che+24], and Dzyaloshinskii-Moriya interactions [HR17; Noc+23] on various 2D and 3D lattices. While it is limited to applications at $T = 0$ due the unphysical states of the Abrikosov representation, its success is based on its ability to give Brillouin-zone resolved correlation functions and identify instabilities to magnetic orders or potentially paramagnetic phases in the thermodynamic limit. The pseudo-fermion action $S[f, f^\dagger]$ corresponding to the Hamiltonian of Eq. (2.1) is

$$S[f, f^\dagger] = \frac{1}{4\pi}\int \mathrm{d}\omega f_j^\dagger(i\omega)G_0^{-1}(i\omega)f_j(-i\omega) - \bar{S}_i^\alpha[f, f^\dagger](i\omega)J_{ij}^{\alpha\beta}\bar{S}_j^\beta[f, f^\dagger](-i\omega), \tag{2.47}$$

with the inverse bare Green's function given by $G_0^{-1}(i\omega) = i\omega\,\mathbb{1}$. To implement the cutoff dependence Λ, a cutoff function $\theta^\Lambda(\omega)$ is often multiplied to the bare Green's function, suppressing dynamics at low frequencies, which is equivalent to the cutoff R^Λ introduced in Eq. (2.44): $(\theta^\Lambda(i\omega)G_0(i\omega))^{-1} \equiv G_0^{-1}(i\omega) + R^\Lambda(i\omega)$. Commonly, $\theta^\Lambda(\omega)$ is chosen to be a Lorentzian

$$\theta^\Lambda(i\omega) = \frac{\omega^2}{\omega^2 + \Lambda^2}, \qquad R^\Lambda(i\omega) = i\frac{\Lambda^2}{\omega}\,\mathbb{1}. \tag{2.48}$$

Despite pf-FRG's success, the method still had a few caveats. Any finite-temperature calculation would be heavily affected by the unphysical states in the Abrikosov representation. Therefore, it was only applicable at zero temperature. Any magnetic instability during the flow would happen at some finite value of Λ where the action does not represent a spin system due to the finite $R_\Lambda(i\omega)$. While some heuristic arguments link $\Lambda \sim T$ [RTT11] it is impossible to rigorously calculate the critical temperatures from finite Λ instabilities. Another downside coming from the fact that no parameter point during the flow corresponds to a physical spin system is that benchmarking the numerical implementations is very hard since ground truth benchmark data is not available. This made large-scale, cross-implementation benchmarking necessary [Rit+22]. We address the finite-temperature and unphysical state problem in Chapter 3.

The benchmark problem can be adressed in the following way [Gün+]: $R(i\omega)$ in Eq. (2.48) has the form of a bath hybridization. Such a term can be achieved by allowing the fermions

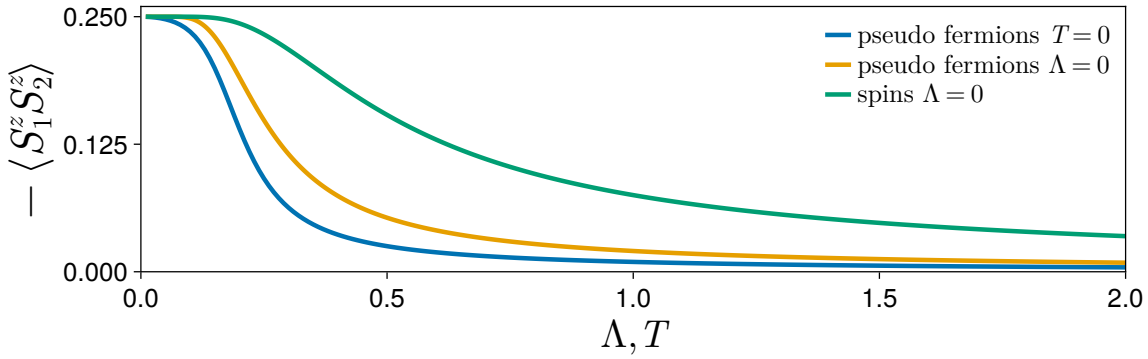

Figure 2.4 The-nonlocal equal-time correlator of the antiferromagnetic Heisenberg spin Dimer ($H = \mathbf{S}_1 \cdot \mathbf{S}_2$) in different settings. The blue line is at $T = 0$ for finite Λ using the Lorenzian cutoff and the Abrikosov representation. The orange line is at finite temperature and $\Lambda = 0$ using the Abrikosov representation. The green line shows the correct finite temperature susceptibility using spin operators. In this case, the finite Λ and finite T pseudo-fermion lines behave similarly and all three lines converge at $T = \Lambda = 0$. We show in Chapter 3 [P1] that this is not always the case.

to hop to a non-interacting bath described by the Hamiltonian

$$H_{\text{bath}} = \epsilon_{\mathbf{k}} c^\dagger_{i\mathbf{k}\alpha} c_{i\mathbf{k}\alpha}, \qquad H_{\text{hyb}} = V_{\mathbf{k}} f^\dagger_{i\alpha} c_{i\mathbf{k}\alpha} + V^*_{\mathbf{k}} c^\dagger_{i\mathbf{k}\alpha} f_{i\alpha}, \tag{2.49}$$

where $\alpha \in \{\uparrow, \downarrow\}$ and $\mathbf{k}$ is the lattice momentum. Since the bath is non-interacting, the c fermions can be integrated out which results in a hybridization term added to the Matsubara action:

$$\sum_{\mathbf{k}} \frac{|V_{\mathbf{k}}|^2}{\epsilon_{\mathbf{k}} - i\omega} f_i^\dagger f_i \equiv R(i\omega) f_i^\dagger f_i. \tag{2.50}$$

The bath corresponding to the Lorenzian cutoff in Eq. (2.48) corresponds to the choice $V_{\mathbf{k}} = \Lambda$, $\epsilon_{\mathbf{k}} = 0$ representing a single zero-energy mode with hopping strength Λ. This allows exact calculations for small spin systems using both the Abrikosov representation and a finite energy cutoff Λ, enabling benchmarking pf-FRG against ground-truth data. We show an example for exact data at finite-Λ in Fig. 2.4. It also emphasizes that the pf-FRG is really computing a Kondo-lattice model [JVW88; LP99] that reduces to a spin model at $\Lambda = 0$. It is therefore indeed possible that, starting the flow from the $T = 0$, $\Lambda = \infty$ Kondo-screened phase, the finite Λ phase transitions observed in pf-FRG have a completely different nature than the finite temperature phase transitions starting from a high temperature paramagnetic phase.

If one is interested in finite-temperature phase transitions, the problem of unphysical states has to be tackled first. This is naturally done by using the SO(3) pseudo-Majorana representation Eq. (2.31). The resulting FRG framework is named pseudo-Majorana FRG (pm-FRG) [NSR21; NRS22; NIR23; Mül+24; SGR25]. It has access to finite temperatures and can reliably detect phase transitions and critical temperatures via finite-size scaling [NSR21]. Due to its quantitative accuracy at high temperatures even for $\Lambda = 0$, benchmarking numerical implementations is a lot easier as well. The corresponding action is very similar to Eq. (2.47):

$$S[\eta] = \frac{T}{2} \sum_{\omega} \eta^\alpha(i\omega)[G_0^{-1}]^{\alpha\alpha}(i\omega)\eta^\alpha(-i\omega) - \bar{S}_i^\alpha[\eta](i\omega) J_{ij}^{\alpha\beta} \bar{S}_j^\beta[\eta](-i\omega). \tag{2.51}$$

In Chapter 3 we present ways to efficiently calculate finite-temperature phase diagrams using the pm-FRG.

2.5 Strong-Coupling Expansion

The strong-coupling diagrammatic technique for general quantum spin-S systems, which was pioneered in the late 1960s [VLP67; VLP68; Sti73b; Sti73a; Sti73c; ISF90] is complementary to the weak-coupling expansions we use in Sec. 2.4.3. While the so-called weak-coupling approaches expand around a theory of free fermions or bosons, the strong-coupling approaches expand around an interacting theory that can not be described by a Gaussian path integral. We will refer to the strong-coupling approach in the spin context as *Spin diagrammatics*. Today, this diagrammatic technique fits into a group of methods designed for strong-coupling regimes and projected Hilbert spaces. While they are all based on the same idea, which we will explain below, they are known by many names like: strong-coupling expansion [Ben+79; Fre+09; PST98], cluster perturbation theory [SPP02], hybridization expansion [WM06], free-graph high-temperature series expansion [OB96], dual fermion approach [RKL08; Rub+09] or linked-cluster expansion [Met91; Kha+14]. Recently, it has served as the basis for the spin-FRG [KK19; Kri19; GRK20; Gol+19; TK21; TK22; Rüc+22; Tar+22] and the Hubbard-X FRG [Rüc+23; AKR25]. These approaches all build on the idea of expanding the generating functional $W[h, J]$ in terms of a parameter J_{ij} which could be fermion hopping or spin-spin interactions and evaluate the trace or functional integral for an interacting reference system described by a H_{loc} that can be solved exactly by some other method, which is often chosen to be exact diagonalization but could also be something like dynamical mean field theory [Rub+09], depending on the context.

Let us give a short introduction of how to obtain such a strong-coupling expansion by considering a Hamiltonian with some non-specified operators O_i that we assume to have bosonic exchange statistics here. In the case of the dual fermion approach O_i would of course be fermionic operators. We consider Hamiltonians of the form

$$H[O] = H_{\text{loc}}[O] + \frac{1}{2} O^{a_1} J_{a_1 a_2} O^{a_2}, \tag{2.52}$$

for any operator O_i, such that all correlation functions for $J_{ij} = 0$ governed by the local Hamiltonian $H_{\text{loc}}[O]$ are known. Following Eq. (2.39), this means that the connected Green's functions are given by

$$G^{a_1 \dots a_n} \equiv \frac{\delta}{\delta h_{a_1}} \dots \frac{\delta}{\delta h_{a_n}} W[h, J] = (-1)^{n-1} \langle \mathcal{T} O^{a_1} \dots O^{a_n} \rangle_c, \tag{2.53}$$

where $W[h, J]$ is the generating functional for connected Green's functions written as a time-ordered exponential

$$W[h, J] = -\ln(\text{Tr}[\mathcal{T} e^{-\int_0^\beta d\tau H_{\text{loc}} + \frac{1}{2} O^{a_1} J_{a_1 a_2} O^{a_2} + h_a O^a}]). \tag{2.54}$$

Here, we have dropped the imaginary time argument of all operators. To not clutter the notation with indices, we might refer to $G^{a_1 \dots a_n}$ as G^n and add a subscript 0 if we assume just the local theory $\lim_{J \to 0} G^n = G_0^n$, where we label the Green's function with the number of its indices.

Hamiltonians of the form of Eq. (2.52) include most extensively studied systems like the Hubbard model, spin models, impurity models, and the t-J model. Regardless of what the operators O_i are, we can cancel the quadratic term by a bosonic or fermionic Hubbard-

Stratonovich transformation

$$\mathbb{1} = \int \mathcal{D}\varphi \, \mathrm{e}^{\frac{1}{2}(\varphi^{a_1} - O^{a_1}) J_{a_1 a_2} (\varphi^{a_2} - O^{a_2})}. \tag{2.55}$$

This way, we can write the whole generating functional as a path integral

$$W[h,J] = -\ln\left(\int \mathcal{D}\varphi \, \mathrm{e}^{\frac{1}{2}\varphi^{\mathrm{a}_1} \mathrm{J}_{\mathrm{a}_1\mathrm{a}_2} \varphi^{\mathrm{a}_2}} \mathrm{Tr}\left[\mathcal{T} e^{-\int_0^\beta d\tau H_{\mathrm{loc}} + O^{a_1}(J_{a_1 a_2}\varphi^{a_2} + h_{a_1})}\right]\right). \tag{2.56}$$

Shifting the field $\varphi^\alpha \to \varphi^{a_1} - (J^{-1})^{a_1 a_2} h_{a_2}$ and exponentiating the trace gives

$$e^{-W[h,J]} = \int \mathcal{D}\varphi \, \mathrm{e}^{\frac{1}{2}\varphi^{\mathrm{a}_1} \mathrm{J}_{\mathrm{a}_1\mathrm{a}_2} \varphi^{\mathrm{a}_2} - \mathrm{h}_{\mathrm{a}} \varphi^{\mathrm{a}} + \frac{1}{2} \mathrm{h}_{\mathrm{a}_1} (\mathrm{J}^{-1})^{\mathrm{a}_1 \mathrm{a}_2} \mathrm{h}_{\mathrm{a}_2} + \ln\left(\mathrm{Tr}\left[\mathcal{T} \mathrm{e}^{-\int_0^\beta \mathrm{d}\tau \mathrm{H}_{\mathrm{loc}} + \mathrm{O}^{\mathrm{a}_1} \mathrm{J}_{\mathrm{a}_1\mathrm{a}_2} \varphi^{\mathrm{a}_2}}\right]\right)}. \tag{2.57}$$

After identifying the log-trace term with the generating functional of the local theory

$$\begin{aligned} W[J_{a_1 a_2}\varphi^{a_2}, 0] =& -\ln[Tr[\mathcal{T} e^{\int_0^\beta d\tau H_{\mathrm{loc}} + O^{a_1} J_{a_1 a_2}\varphi^{a_2}}])] \\ =& \frac{1}{2} G_2^0 (J\varphi)^2 + \frac{1}{3!} G_3^0 (J\varphi)^3 + \frac{1}{4!} G_4^0 (J\varphi)^4 + \dots, \end{aligned} \tag{2.58}$$

where the Hubbard-Stratonovich field appears at the position of the source field h, we arrive at the final result:

$$W[h,J] = -\ln\left(\int \mathcal{D}\varphi \, \mathrm{e}^{\frac{1}{2}\varphi^{\mathrm{a}_1} \mathrm{J}_{\mathrm{a}_1\mathrm{a}_2} \varphi^{\mathrm{a}_2} - \mathrm{h}_{\mathrm{a}} \varphi^{\mathrm{a}} + \frac{1}{2} \mathrm{h}_{\mathrm{a}_1} (\mathrm{J}^{-1})^{\mathrm{a}_1 \mathrm{a}_2} \mathrm{h}_{\mathrm{a}_2} - \mathrm{W}[\mathrm{J}_{\mathrm{a}_1\mathrm{a}_2}\varphi^{\mathrm{a}_2}, 0]}\right). \tag{2.59}$$

We see that the generating functional $W[h,J] = -\ln(\int \mathcal{D}\varphi \, \mathrm{e}^{-S[\varphi] + h\varphi - \frac{1}{2} h J^{-1} h})$ can be written with an action $S[\varphi]$ where the bare vertices are given by the connected Green's functions of the local theory. Supressing the indices, the action can be expanded as

$$S[\varphi] = \frac{1}{2}\varphi(-J + J G_0^2 J)\varphi + \frac{1}{3!} G_0^3 (J\varphi)^3 + \ldots + \frac{1}{n!} G_0^n (J\varphi)^n. \tag{2.60}$$

Now that we have expressed $W[h,J]$ in terms of a canonical field φ, we can use the whole field theory toolbox to calculate correlations functions from it. For example, we can do perturbation theory in J by Taylor expanding $W[h,J]$ or set up an FRG scheme.

Let it be noted that it is not strictly necessary to rewrite the generating functional $W[h,J]$ in terms of a path integral to rigorously define the aforementioned schemes. Working with the time ordered exponential (see Eq. (2.54)) directly is also possible [Kri19; Rüc+23], leading to the exact same diagrammatic schemes. The multitude of spin-FRG approaches presented in Ref. [Kri19] are all based on the strong-coupling approach presented above and differ from each other mainly by the exact definition of the Legendre transform of W in (Eq. (2.42)), which influences the notion of an interaction vertex and, in turn, influences how vertex truncation schemes are realized.

2.6 Perturbation Theory

In this section, we review different approaches to set up strong-coupling perturbative expansions. There are mainly two ways of setting up perturbation theory in J for $W[h,J]$ given by Eq. (2.59). One way is to invoke Wick's theorem [NO98; AS10] and write a diagrammatic expansion in terms of free bosonic propagators and bare vertices, which are given in Eq. (2.60) as

the connected Green's function of the local theory. Equivalently, one can start from the time-ordered exponential Eq. (2.54) and use the generalized Wick's theorem or cumulant expansion.

Another approach is to fulfill the linked cluster theorem explicitly by writing diagrams in terms of full Green's functions and recursively subtracting the disconnected parts of the diagrams [BF04], which we will refer to as the *restricted graph approach*. The Wick's theorem approach is more "standard". It has the advantage that the disconnected parts of each perturbation theory diagram are automatically subtracted, leading to the usual diagrams where each loop corresponds to a momentum and frequency convolution.

The restricted graph approach, however, has its own advantages. It is extensively used in the high-temperature expansion (HTE) community [Bak+67; OB96; SLR11; PBM24; HWT17]. In the context of spin systems, it leads to diagrams where every vertex corresponds to exactly one lattice site and every edge corresponds to exactly one bond joined by the interaction J_{ij}. Instead of momentum integrals, multiplicities of each diagram must be computed by embedding the graph corresponding to the diagram's topology into the graph representing the lattice. Due to efficient graph embedding techniques, this can be simpler than solving the momentum integrals in the Wick's theorem approach. Publications in Chapter 4 present details on the Wick's theorem approach and those in Chapter 5 present details on the restricted graph approach in an HTE context.

We dedicate the rest of this section to setting up the two different approaches. Starting from the generating functional, $W[h, J]$ either given by Eq. (2.54) or Eq. (2.59) , we can write the connected spin-spin expectation value as

$$\langle \mathcal{T} S_r^\alpha(\tau) S_{r'}^{\alpha'}(\tau') \rangle_c = -\frac{\delta^2}{\delta h_{r_1}^{\alpha_1}(\tau_1) \delta h_{r'}^{\alpha'}(\tau')} W[h, J]. \tag{2.61}$$

If we define the spin-spin interaction term as $V(\tau) = \frac{1}{2} S_i^\alpha(\tau) J_{ij}^{\alpha\beta} S_j^\beta(\tau)$, then the expansion of $\langle \mathcal{T} S_r^\alpha(\tau) S_{r'}^{\alpha'}(\tau') \rangle_c$ in terms of J is given by

$$\begin{aligned}
&\langle \mathcal{T} S_r^\alpha(\tau) S_{r'}^{\alpha'}(\tau') \rangle_c \\
&= \sum_{m=0}^{\infty} \frac{1}{m!} \left[\prod_{n=1}^{m} \int_0^\beta \mathrm{d}\tau_n \, J_{i_n j_n}^{\gamma_n \delta_n}(\tau_n) \right] \left[\left(\prod_{n=1}^{m} \frac{\delta}{\delta J_{i_n j_n}^{\gamma_n \delta_n}(\tau_n)} \right) \langle \mathcal{T} S_r^\alpha(\tau) S_{r'}^{\alpha'}(\tau') \rangle_c \right]_{J \to 0} \\
&= \sum_{m=0}^{\infty} \frac{(-1)^m}{m!} \left[\prod_{n=1}^{m} \int_0^\beta \mathrm{d}\tau_n \right] \langle \mathcal{T} S_r^\alpha(\tau) S_{r'}^{\alpha'}(\tau') V(\tau_1) \cdots V(\tau_m) \rangle_{c,0}^{\mathrm{V-con}},
\end{aligned} \tag{2.62}$$

which is just a Taylor expansion written out. The connectedness refers to each (composite) operator in $\langle \ldots \rangle_{c,0}$, so both S and V, and is defined by the functional derivatives of the generating functional. To indicate that the connectedness is with respect to the whole composite operator V and not its constituents, we write $\langle \ldots \rangle^{\mathrm{V-con}}$. The 0 in $\langle \ldots \rangle_{c,0}$ refers to the evaluation at $J = 0$. Equation (2.62) writes the two-point correlator as a sum of

$(m+2)$-point correlators.

$$\int_0^\beta \mathrm{d}\tau\, \mathrm{d}\tau' e^{i(\omega_1\tau+\omega_2\tau')} \langle \mathcal{T} S_r^\alpha(\tau) S_{r'}^{\alpha'}(\tau')\rangle_{c,0} = \sum_{m=0}^{\infty} \frac{(-1)^m}{m!} \int_0^\beta \mathrm{d}\tau\, \mathrm{d}\tau' \left[\prod_{n=1}^{m} \int_0^\beta \mathrm{d}\tau_n\right] e^{i(\omega_1\tau+\omega_2\tau')} \langle \mathcal{T} S_r^\alpha(\tau) S_{r'}^{\alpha'}(\tau') V(\tau_1)\cdots V(\tau_m)\rangle_{c,0}^{\mathrm{V-con}}. \tag{2.63}$$

2.6.1 Generalized Wick's Theorem

When expanding around a free fermionic or bosonic theory, Wick's theorem states that any time-ordered expectation value can be written in terms of a sum of products of connected time-ordered expectation values of at most two fermionic or bosonic operators [Wic50]. When expanding around an interacting theory, this is no longer the case. Then any expectation value can be written as a sum of products of connected time-ordered expectation values with no restriction on the number of operators in the connected expectation value. This is often called the *generalized* Wick's theorem [SP82; VS12].

Applying the generalized Wick's theorem to $\langle \mathcal{T} S_r^\alpha(\tau) S_{r'}^{\alpha'}(\tau') V(\tau_1)\cdots V(\tau_m)\rangle_{c,0}^{\mathrm{V-con}}$ in Eq. (2.63) leads to a sum of products of connected expectation values of equal and lower order. As an example, the first order terms give

$$\begin{aligned}\langle \mathcal{T} S_r^\alpha(\tau) S_{r'}^{\alpha'}(\tau') V(\tau_3)\rangle_{c,0}^{\mathrm{V-con}} =& J_{ij}^{\gamma\delta} \langle \mathcal{T} S_r^\alpha(\tau) S_i^\gamma(\tau_1)\rangle_{c,0} \langle \mathcal{T} S_j^\delta(\tau_1) S_{r'}^{\alpha'}(\tau')\rangle_{c,0} \\ &+ \frac{1}{2} J_{ij}^{\gamma\delta} \langle \mathcal{T} S_r^\alpha(\tau) S_{r'}^{\alpha'}(\tau') S_i^\gamma(\tau_1) S_j^\delta(\tau_1)\rangle_{c,0}.\end{aligned} \tag{2.64}$$

The term in the second line would be 0 by Wick's theorem for canonical bosons or fermions. For spins, both terms can contribute. Using composite indices, the second order can be written as

$$\begin{aligned}\frac{1}{2}\langle \mathcal{T} S_r^\alpha(\tau) S_{r'}^{\alpha'}(\tau') V(\tau_3) V(\tau_4)\rangle_{c,0}^{\mathrm{V-con}} &\equiv \frac{1}{2}\langle \mathcal{T} S_1 S_2 V(3) V(4)\rangle_{c,0}^{\mathrm{V-con}} \\ &= J_3 J_4 \langle \mathcal{T} S_1 S_3\rangle_{c,0} \langle \mathcal{T} S_3 S_4\rangle_{c,0} \langle \mathcal{T} S_4 S_1\rangle_{c,0} + \frac{1}{2} J_3 J_4 \langle \mathcal{T} S_1 S_2 S_3 S_4\rangle_{c,0} \langle \mathcal{T} S_3 S_4\rangle_{c,0} \\ &+ \frac{1}{2} J_3 J_4 \langle \mathcal{T} S_1 S_3 S_4\rangle_{c,0} \langle \mathcal{T} S_2 S_3 S_4\rangle_{c,0} + \frac{1}{8} J_3 J_4 \langle \mathcal{T} S_1 S_2 S_3 S_3 S_4 S_4\rangle_{c,0}.\end{aligned} \tag{2.65}$$

Each term can be interpreted as a diagram with external indices 1 and 2 where vertices correspond to the connected Green's functions and edges correspond to interaction lines J (see Fig. 2.5). All correlation functions in $\langle \ldots\rangle_{c,0}$ are purely local. Therefore, in frequency and momentum space, each diagram loop corresponds to a frequency and momentum integration.

2.6.2 Restricted Graph Aproach

The expansion coefficients in Eq. (2.63) can also be written by recursive subtraction of the disconnected parts from the full correlators $\langle \ldots\rangle_0$, enforcing the result to be connected:

$$\begin{aligned}\langle \mathcal{T} S_r^\alpha(\tau) S_{r'}^{\alpha'}(\tau') V(\tau_1)\cdots V(\tau_m)\rangle_{c,0}^{\mathrm{V-con}} &= \langle \mathcal{T} S_r^\alpha(\tau) S_{r'}^{\alpha'}(\tau') V(\tau_1)\cdots V(\tau_m)\rangle_0 \\ &- \sum_{S\subsetneq\{1,\ldots,m\}} \left\langle \mathcal{T}\left[\prod_{k\in S} V(\tau_k)\right] S_r^\alpha(\tau) S_{r'}^{\alpha'}(\tau')\right\rangle_{c,0}^{\mathrm{V-con}} \left\langle \mathcal{T} \prod_{l\in\{1,..,m\}\setminus S} V(\tau_l)\right\rangle_0,\end{aligned} \tag{2.66}$$

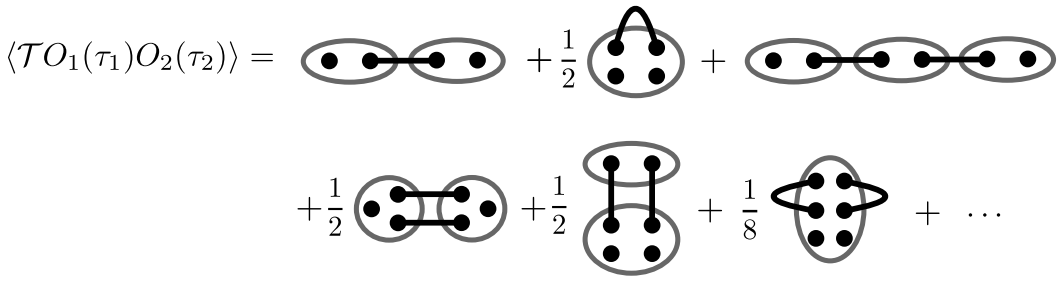

Figure 2.5 Strong-coupling spin diagrams depicting the topology of the first order (see Eq. (2.64)) and second order (see Eq. (2.65)) contributions. Each black dot represents an operator O, each ellipse a time ordered connected expectation value and each line corresponds to a coupling J that connects to operators O. In this section, O is given by the spin operators S^α but the diagrammatics would work exactly the same for any other operators as as long as the Hamiltonian is of the form of Eq. (2.52).

where the sum is over true subsets S of the set $\{1, ..., n\}$ (including the empty set) and the recursion terminates at $\left\langle \mathcal{T} S_r^\alpha(\tau) S_{r'}^{\alpha'}(\tau') \right\rangle_{c,0} \equiv \left\langle \mathcal{T} S_r^\alpha(\tau) S_{r'}^{\alpha'}(\tau') \right\rangle_0$ if no magnetic fields are present. The first-order contribution can therefore be written as

$$\begin{aligned}\langle \mathcal{T} S_r^\alpha(\tau) S_{r'}^{\alpha'}(\tau') V(\tau_1) \rangle_{c,0}^{\mathrm{V-con}} =& \frac{1}{2} J_{ij}^{\alpha\delta} \langle \mathcal{T} S_r^\alpha(\tau) S_{r'}^{\alpha'}(\tau') S_i^\gamma(\tau_1) S_j^\delta(\tau_1) \rangle_0 \\ & - \frac{1}{2} J_{ij}^{\gamma\delta} \langle \mathcal{T} S_r^\alpha(\tau) S_{r'}^{\alpha'}(\tau') \rangle_{c,0} \langle \mathcal{T} S_i^\gamma(\tau_1) S_j^\delta(\tau_1) \rangle_0 . \end{aligned} \tag{2.67}$$

This is the basis for the restricted graph approach used in Chapter 5 and for the high-temperature expansion. It is fully equivalent to the generalized Wick's theorem approach presented above.

2.7 Spectral Representation of Multipoint Green's Functions and its Use in Perturbation Theory

2.7.1 Spectral Representation

The spectral representation, or Lehman representation is a standard way to compute two-point Green's functions [AS10] from a Hamiltonian's eigenenergies and eigenvectors. It represents the two-point Matsubara Green's function as a convolution between a spectral function $A(\omega)$ and a frequency kernel:

$$\int_0^\beta \mathrm{d}\tau_1 \int_0^\beta \mathrm{d}\tau_2 \, \mathrm{e}^{i\tau_1\omega_1 + i\tau_2\omega_2} \langle \mathcal{T} O_1(\tau_1) O_2(\tau_2) \rangle = -\beta \delta_{\omega_1+\omega_2} \int_{-\infty}^{\infty} \mathrm{d}\omega \frac{A(\omega)}{i\omega_1 - \omega}. \tag{2.68}$$

From Eq. (2.68) we can see immediately, that the real-frequency, retarded expectation value can, be obtained by the analytic continuation $i\omega_1 \to \omega_1 + i0^+$, where 0^+ is a positive infinitesimal. Rigorously, this is only possible if the Matsubara correlator is known analytically. Otherwise, the problem of analytic continuation is numerically ill-conditioned. Nevertheless, many numerical analytic continuation schemes have been developed, including stochastic methods [San98], fitting techniques [JG96; HGL23; ZYG24; ZG24], interpolation methods [BG96; FYG21], and also machine learning [YSH18]. All these methods concern only the analytic continuation of two-point functions that are based on their spectral representation. Kugler et al. [KLD21] rigorously extended the notion of a spectral function $A(\omega)$ to multipoint

functions, which made a rigorous extension of analytic continuation of n-point functions possible [Ge+24]. The Fourier transform of the n-point correlator,

$$G^n(i\boldsymbol{\omega}) = \int_0^\beta \mathrm{d}^n\boldsymbol{\tau}\, e^{i\boldsymbol{\omega}\cdot\boldsymbol{\tau}} \langle \mathcal{T} O^1(\tau_1) \dots O^n(\tau_n)\rangle, \tag{2.69}$$

can be written as

$$G^n(i\boldsymbol{\omega}) = \sum_p \int d^n\boldsymbol{\omega}'_p\, \mathcal{K}\left(i\boldsymbol{\omega}_p - \boldsymbol{\omega}'_p\right) \underbrace{\zeta^p \bar{\mathcal{S}}\left[\boldsymbol{\mathcal{O}}_p\right]\left(\boldsymbol{\omega}'_p\right)}_{\mathcal{S}[\boldsymbol{\mathcal{O}}_p](\boldsymbol{\omega}'_p)}, \tag{2.70}$$

where $\boldsymbol{\tau}$ and $\boldsymbol{\omega}$ are vectors of the n imaginary times and Matsubara frequencies, respectively. $\zeta^p = \pm 1$ is the statistical factor of exchanging bosonic or fermionic operators by the n-element permutation $p \in S_n$. $\mathcal{K}$ are the kernel functions, which are Fourier transforms of strings of Heaviside θ functions

$$\mathcal{K}\left(\boldsymbol{\Omega}\right) = \left[\int_0^\beta \mathrm{d}\tau_1\, \mathrm{e}^{\Omega_1\tau_1}\right]\left[\int_0^{\tau_1} \mathrm{d}\tau_2\, \mathrm{e}^{\Omega_2\tau_2}\right] \cdots \left[\int_0^{\tau_{n-2}} \mathrm{d}\tau_{n-1}\, \mathrm{e}^{\Omega_{n-1}\tau_{n-1}}\right]\left[\int_0^{\tau_{n-1}} \mathrm{d}\tau_n\, \mathrm{e}^{\Omega_n\tau_n}\right], \tag{2.71}$$

with complex frequencies $\boldsymbol{\Omega}$, and the partial spectral functions are defined as the Fourier transform of the real-time correlation functions. The so-called *partial spectral functions* are defined as Fourier transforms of real-time expectation values

$$\bar{\mathcal{S}}\left[\boldsymbol{\mathcal{O}}_{\boldsymbol{p}}\right]\left(\boldsymbol{\omega}_p\right) = \int \frac{d^n t}{(2\pi)^n} \mathrm{e}^{i\boldsymbol{\omega}_p\cdot\mathbf{t}_p} \left\langle \mathcal{P} \prod_{i=1}^n O^i_{p(i)}\left(t_{p(i)}\right)\right\rangle, \tag{2.72}$$

where we added a permutation index $p(i)$, that replaces i with the ith position of the permutation p, to each operator. The permutation ordering operator $\mathcal{P}$ is then sorting the operator string by this permutation index; for example,

$$\mathcal{P} O^1_3 O^2_1 O^3_2 = O^2 O^3 O^1. \tag{2.73}$$

Kugler et al. [KLD21] provided the kernels $\mathcal{K}$ for fermionic Matsubara frequencies for two and four-point correlators. In general, they take the following form:

$$\mathcal{K}\left(\boldsymbol{\Omega}\right) \sim \frac{1}{\Omega_1}\frac{1}{\Omega_1+\Omega_2}\cdots\frac{1}{\Omega_1+\ldots+\Omega_n} + \delta_{\Omega_1}\frac{1}{\Omega_2}\ldots. \tag{2.74}$$

This has since been used to compute four-point spectra based on NRG calculations [LKV21; Lih+24; Rit+25; Fra+25]. While the first term in Eq. (2.74), the product of reciprocals, has been known previously, the so-called *anomalous* terms, proportional to Kronecker deltas, sketched as the last term in Eq. (2.74) have only been known for special cases. In Chapter 4, we present a way to calculate $\mathcal{K}$ exactly for fermionic and bosonic theories for any n-point correlator, by solving all imaginary time integrals in Eq. (2.71) exactly, without making any assumptions on Ω_i, therefore including all anomalous terms. This paves the way for using the spectral representation for calculating perturbation-theory diagrams for spin systems presented in Chapter 4 and Chapter 5.

2.7.2 Kernel Trick

One can now use Eq. (2.70) to calculate perturbation theory diagrams in a smart way without having to calculate a single time or frequency integral. This is what we name the *kernel trick*, which we rely upon heavily when calculating the spin diagrams in Chapter 4. While this approach generally applies to any action, like fermionic actions with four-point interactions, we will use it here in the context of strong-coupling spin diagrammatics.

Notice that every term in Eq. (2.63) is of the form of Eq. (2.69) with $\boldsymbol{\omega} = \{\omega_1, \omega_2, \overbrace{0, \ldots, 0}^{\times m}\}$ with the exception that the expectation values are *connected* instead of *full*. As shown in Ref. [KLD21], the connected expectation value has a completely analogous spectral representation. Therefore, we can use Eq. (2.70) to represent Eq. (2.63) in terms of kernels and connected spectral functions $\mathcal{S}_c\left[\boldsymbol{\mathcal{O}}_p\right]$:

$$\begin{aligned}\int_0^\beta \mathrm{d}\tau\, \mathrm{d}\tau'\, \mathrm{e}^{i(\omega_1\tau_1+\omega_2\tau_2)} \langle \mathcal{T} S_r^\alpha(\tau) S_{r'}^{\alpha'}(\tau')\rangle_{c,0} \\ = \sum_{m=0}^{\infty} \frac{1}{m!} \sum_p \int d^{m+2}\boldsymbol{\omega}'_p\, \mathcal{K}\left(i\boldsymbol{\omega}_p - \boldsymbol{\omega}'_p\right) \mathcal{S}_{c,0}\left[\boldsymbol{\mathcal{O}}_p\right]\left(\boldsymbol{\omega}'_p\right),\end{aligned} \tag{2.75}$$

where we used the definition

$$\mathcal{S}_{c,0}\left[\boldsymbol{\mathcal{O}}_{\boldsymbol{p}}\right](\boldsymbol{\omega}_p) = \int \frac{d^n t}{(2\pi)^{m+2}} \mathrm{e}^{i\boldsymbol{\omega}_p\cdot\mathbf{t}_p} \left\langle \mathcal{P} \prod_{i=1}^{m+2} O^i_{p(i)}\left(t_{p(i)}\right)\right\rangle_{c,0}. \tag{2.76}$$

with $\boldsymbol{\mathcal{O}} = \{S_r^\alpha(\tau) S_{r'}^{\alpha'}(\tau'), \overbrace{V, \ldots, V}^{\times m}\}$. The permutation ordering operator $\mathcal{P}$ keeps track of the order of operators when expanding in terms of connected correlators:

$$\begin{aligned}\langle \mathcal{P} O_4 O_2 O_3 O_1\rangle =& \langle \mathcal{P} O_4 O_2\rangle_c \langle \mathcal{P} O_3 O_1\rangle_c + \langle \mathcal{P} O_4 O_3\rangle_c \langle \mathcal{P} O_2 O_1\rangle_c \\ &+ \langle \mathcal{P} O_4 O_1\rangle_c \langle \mathcal{P} O_2 O_3\rangle_c + \langle \mathcal{P} O_4 O_2 O_3 O_1\rangle_c \\ =& \langle O_2 O_4\rangle_c \langle O_1 O_3\rangle_c + \langle O_3 O_4\rangle_c \langle O_1 O_2\rangle_c \\ &+ \langle O_1 O_4\rangle_c \langle O_2 O_3\rangle_c + \langle O_1 O_2 O_3 O_4\rangle_c.\end{aligned} \tag{2.77}$$

Equation (2.75) now has essentially the same form as Eq. (2.63) with a differently defined Fourier transform. Therefore, we can just expand $\left\langle \mathcal{P} \prod_{i=1}^n O^i_{p(i)}\left(t_{p(i)}\right)\right\rangle_{c,0}$ in the same way we expanded $\langle \mathcal{T} S^{\alpha_1}_{r_1}(\tau_1) S^{\alpha_2}_{r_2}(\tau_2) V(\tau_3)\cdots V(\tau_{m+2})\rangle_{c,0}$ in Sec. 2.5 with the generalized Wick's theorem. We end up with the same general diagrams with the following differences:

- Each diagram turns into a sum of $m!$ diagrams, where each summand corresponds to a different permutation.
- The imaginary time-ordered Green's functions are replaced by real-time permutation-ordered expectation values. Therefore, after the Fourier transform, every Matsubara Green's function is replaced by a real-frequency partial-spectral function.
- Each real-frequency diagram is then convolved with the kernel $\mathcal{K}$.

Suppose we expand around a local theory with a few different eigenenergies, like a single spin in a magnetic field. In that case, all partial spectral functions become a sum of a few discrete poles. For a spin without a magnetic field, the partial spectral functions only have poles at $\omega = 0$. This immensely simplifies the convolution with the kernel, which then becomes a

simple multiplication:

$$\mathcal{K}\left(i\boldsymbol{\omega}_p - \boldsymbol{\omega}'_p\right)\mathcal{S}_{c,0}\left[\boldsymbol{\mathcal{O}}_p\right]\left(\boldsymbol{\omega}'_p\right) \to \mathcal{K}\left(i\boldsymbol{\omega}_p\right)\mathcal{S}_{c,0}\left[\boldsymbol{\mathcal{O}}_p\right](0)\,. \tag{2.78}$$

This makes high-order perturbation theory calculations readily accessible when using Eq. (2.75) with both the generalized Wick's theorem and the restricted graph approaches. Details for the generalized Wick's theorem approach can be found in Chapter 4 [P5] and for the restricted graph approach in Chapter 5 [P7].
If we expand around a theory with many poles or even continuous spectra, a difficult-to-evaluate multidimensional real-frequency convolution has to be calculated for each diagram. These could then be sampled using Monte Carlo [VSF21] or alternative methods, such as tensor cross interpolation [Núñ+22].

2.8 Comparison of Spin Diagrams with SO(3) Majorana Diagrams

It is still not properly understood how the diagrammatic schemes using the SO(3) Majorana representation introduced in Sec. 2.3 and Sec. 2.4.3 relate to spin diagrammatics based on the strong-coupling schemes introduced in Sec. 2.5. In this section, we want to shed some light on their connection.

The distinctive feature of the strong-coupling based spin-FRG is that it operates directly with spin operators rather than employing a parton representation [KK19]. This comes at the cost of strong-coupling diagrammatics, with non-zero vertices of every order. When using the pseudo-Majorana representation, one can use diagrammatics for canonical fermions with quartic interactions. This comes at the cost of having "unphysical" degrees of freedom. At first glance, only pairs of Majoranas with different flavors correspond to spin operators like $S^z = -i\eta^x\eta^y$. This means that even though we can calculate four-Majorana vertices to renormalize the four-Majorana expectation values $\langle\eta_i^x(\tau)\eta_i^y(\tau)\eta_j^x(0)\eta_j^y(0)\rangle \sim \langle S_i^z(\tau)S_j^z(0)\rangle$ they only correspond to two-spin expectation values. This naive view is, however, wrong.

By using the gauge freedom (see Eq. (2.36)), it is possible to write down any Majorana diagram in terms of spin operators directly in the same way that Eq. (2.37) was obtained. To give another example, it is possible to write the four-point Majorana Green's function in terms of a four-point spin Green's function

$$\langle\mathcal{T}\eta_i^x(\tau_1)\eta_i^y(\tau_2)\eta_j^x(\tau_3)\eta_j^y(\tau_4)\rangle = 4\langle\mathcal{T}S_i^x(\tau_1)S_i^y(\tau_2)S_j^x(\tau_3)S_j^y(\tau_4)\rangle, \tag{2.79}$$

where the spin operators on the right side of the equation now permute with a fermionic sign under time ordering! Therefore, any diagrammatic scheme written in terms of the SO(3) Majoranas can be directly written in terms of spin operators. Hence, it should be possible to derive the Majorana action (Eq. (2.51)) starting from the generating functional in Eq. (2.54) using $H_{\text{loc}} = 0$ and $O^{\alpha,i} = S_i^\alpha$. We will demonstrate in the following lines how this can be achieved.

Let us first start with the Heisenberg Hamiltonian Eq. (2.1) and rewrite the spin operators using the spin algebra Eq. (2.2) for $S = \frac{1}{2}$

$$H = \frac{1}{2}\sum_{ij}\left(i\epsilon^{\alpha\gamma\delta}S_i^\gamma S_i^\delta\right)J_{ij}^{\alpha\beta}\left(i\epsilon^{\beta\kappa\rho}S_j^\kappa S_j^\rho\right). \tag{2.80}$$

We are now free to insert a $\mathbb{1}$ operator in between the two local pairs of spin operators. We chose to parameterize the $\mathbb{1}$ in terms of Majorana fermions $\mathbb{1} = (\sqrt{2}\eta_i^0)^2$ leading to

$$H = \frac{1}{2}\sum_{ij}\left(\frac{i}{2}\epsilon^{\alpha\gamma\delta}(2S_i^\gamma\eta_i^0)(2S_i^\delta\eta_i^0)\right)J_{ij}^{\alpha\beta}\left(\frac{i}{2}\epsilon^{\beta\kappa\rho}(2S_j^\kappa\eta_j^0)(2S_j^\rho\eta_j^0)\right). \tag{2.81}$$

Notice, that no Majorana representation has been used but an additional Majorana fermion has been invoked that cancels out as it always appears in pairs. We have grouped operators in Eq. (2.81) as $(2S_i^\gamma\eta_i^0)$. On closer inspection we notice that these composite operators mutually fulfill fermionic exchange statistics

$$\{(2S_i^\alpha\eta_i^0),(2S_j^\beta\eta_j^0)\} = \delta_{ij}\delta_{\alpha\beta}. \tag{2.82}$$

This directly follows from the fact that the spin $\frac{1}{2}$ operators anticommute locally but commute non-locally. Since the Majorana η_i^0 anticommutes non-locally and commutes locally, the product of spin and Majorana operator anticommutes everywhere. With $(2S_i^\alpha\eta_i^0)^2 = \frac{1}{2}$, the composite operators have all properties of Majorana fermions themselves. Now, we can just follow a textbook derivation [AS10] to get from the generating functional

$$W[h,J] = \ln(\mathrm{Tr}[\mathcal{T}e^{-\int_0^\beta d\tau\frac{1}{2}\sum_{ij}\left(\frac{i}{2}\epsilon^{\alpha\gamma\delta}(2S_i^\gamma\eta_i^0)(2S_i^\delta\eta_i^0)\right)J_{ij}^{\alpha\beta}\left(\frac{i}{2}\epsilon^{\beta\kappa\rho}(2S_j^\kappa\eta_j^0)(2S_j^\rho\eta_j^0)\right)+h_i^\alpha(2S_i^\alpha\eta_i^0)}]), \tag{2.83}$$

to the fermionic coherent state path integral

$$W[h,J] = \ln(\int\mathcal{D}\eta\ \mathrm{e}^{-S[\eta]+h_i^\alpha\eta_i^\alpha}), \tag{2.84}$$

$$\begin{aligned}S[\eta] &= \frac{1}{2}\sum_i\int_0^\beta d\tau\ \eta_i^\alpha(\tau)\,\partial_\tau\eta_i^\alpha(\tau)\\ &\quad+\frac{1}{8}\int_0^\beta d\tau\ \left(\epsilon^{\alpha\gamma\delta}\,\eta_i^\gamma(\tau)\,\eta_i^\delta(\tau)\right)\,J_{ij}^{\alpha\beta}\,\left(\epsilon^{\beta\kappa\rho}\,\eta_j^\kappa(\tau)\,\eta_j^\rho(\tau)\right).\end{aligned} \tag{2.85}$$

where we have used the symbol

$$\eta_i^\alpha = (2S_i^\alpha\eta_i^0) \tag{2.86}$$

to represent the product of the spin operator with a free Majorana fermion and their corresponding field. Equation (2.84) is exactly equivalent to the pseudo-Majorana action Eq. (2.51). This concludes our derivation.

In this new derivation, we have managed to derive the pseudo-Majorana action starting from the physical spin Hamiltonian, which emphasizes that there are no *unphyscial* degrees of freedom present in the pseudo-Majorana scheme but only degenerate degrees that get introduced by the non-interacting Majoranas η^0. Our exact mapping from spins to fermions was only possible because each spin operator could be written in terms of bilinear products of locally anticommuting and globally commuting matrices. While this is also possible for $S = \frac{3}{2}$ [SR23], it is not possible for higher spin values.

3 Functional Renormalization Group with Fermionic Spin Representations

3.1 Overview

The following series of papers concerns the functional renormalization group methods based on the Abrikosov representation (see Eq. (2.19)) [P1], the SO(3) Majorana representation (see Eq. (2.31)), [P2] and the mixed representation [P3] (see Eq. (2.32)).

In Ref. [P1], we investigate the effect of the unphysical states on correlation functions. Contrary to the often cited argument that the unphysical states must be gapped out at zero temperature, we find that frustrated spin clusters exist where some unphysical states have the same energy as the ground state. Using the Popov-Fedotov trick, we develop an FRG scheme that projects out unphysical contributions, making it possible to access quantities at finite temperature with pf-FRG at $\Lambda = 0$. This also makes reliable detection of critical temperatures possible by finite-size scaling. The Popov-Fedotov trick can be simply added to existing pf-FRG implementations, as it only introduces a chemical potential term at the cost of breaking some gauge symmetries. Using the parquet equation rather than the FRG equations for the investigated systems strongly suppresses the magnetic susceptibilities, rendering a proper scaling analysis impossible. This can be observed even in models known to host a phase transition, such as the Heisenberg antiferromagnet on the cubic lattice. This is a clear example of a case where the one-loop FRG equations produce more reliable results than the parquet equations, even though the FRG equations are cutoff dependent and have *less* diagrammatic content.

Unfortunately, the Popov-Fedotov trick only works reliably for large enough temperatures due to truncation effects in the FRG context. Therefore, the effects of unphysical states can not be entirely removed across all temperature scales. This problem is effectively solved by using the SO(3) Majorana representation, which does not introduce any unphysical states. Here, proper finite-size scaling to detect finite-temperature magnetic phase transitions had already been established [NRS22]. However, numerical costs to map out phase diagrams were still very high, as every temperature point for the scaling needed a full FRG run for different lattice sizes, which could easily add up to over $40 - 100$ FRG runs to estimate the critical temperature for one parameter point.

In Ref. [P2], we solve this problem by introducing an FRG scheme where temperature itself is used as the cutoff parameter Λ. Starting at $T = \infty$, where all Matsubara correlation functions are known exactly, one FRG run gives physical values for correlation functions for all temperatures up to the smallest simulated $\Lambda_{\text{min}} = T_{\text{min}}$. Estimating a critical temperature can therefore be done with an order of 5 FRG runs, each with a different restriction on the maximal correlation length, allowing for a proper finite-size scaling procedure. The temperature flow not only saves a lot of numerical resources, but we find it to be more reliable than the Λ flow. It can detect the phase transition to the $(\pi, \pi, 0)$ phase in the $J_1 - J_2$ Heisenberg model on the cubic lattice which previously failed when investigating the same model with the Λ-Flow in pm-FRG [NRS22]. Let us emphasize that the temperature

flow scheme presented here builds on the fact that all Matsubara correlators are known exactly at $T = \infty$. This, however, is not the case for real-frequency correlators, making a temperature-flow FRG scheme in the Keldysh formalism [Pot+25] unfeasible.

Despite the decade-long development of pf-FRG, including magnetic fields in the studied Hamiltonians proved to be very difficult, such that it was only recently realized in Ref. [NR24]. However, unphysical states still prohibited access to finite temperatures. That is why, motivated by the success of the pm-FRG, we have developed a scheme in Ref. [P3] to include magnetic fields to XXZ Hamiltonians, resulting in XXZ-Z Hamiltonians

$$H = \sum_{ij} J_{ij}^{\perp}(S_i^x S_j^x + S_i^y S_j^y) + J_{ij}^z S_i^z S_j^z + \sum_i h_i S_i^z. \tag{3.1}$$

Setting up an FRG scheme with the SO(3) Majorana representation gives the noninteracting part of the action $\frac{1}{2}\eta^\alpha(i\omega)[G_0^{-1}]^{\alpha\beta}\eta^\beta(-i\omega)$ where G_0^{-1} has off diagonal contributions in the basis $\{\eta^x, \eta^y, \eta^z\}$

$$[G_0^{-1}]^{\alpha\beta} = \begin{pmatrix} i\omega & ih & 0 \\ -ih & i\omega & 0 \\ 0 & 0 & i\omega \end{pmatrix}. \tag{3.2}$$

Working in the basis $\{\frac{1}{\sqrt{2}}(\eta^x + i\eta^y), \frac{1}{\sqrt{2}}(\eta^x - i\eta^y), \eta^z\}$ is more desirable as this gives a diagonal inverse Green's function:

$$[G_0^{-1}]^{\alpha\beta} = \begin{pmatrix} i\omega + h & 0 & 0 \\ 0 & i\omega - h & 0 \\ 0 & 0 & i\omega \end{pmatrix}. \tag{3.3}$$

This basis is equivalent to the mixed representation of Eq. (2.32), which is why we use it in Ref. [P3]. Due to its inherent U(1) symmetry we name the method U(1)-pm-FRG. With it, we were able to almost exactly reproduce the magnetization curves measured for $CeMgAl_{11}O_{19}$ [Gao+24] and calculate the transition temperature of the triangular lattice antiferromagnet with a magnetic field to up-up-down spin solid order that is compatible with previous XTRG results [Xia+24].

[P1] *Taming pseudofermion functional renormalization for quantum spins: Finite temperatures and the Popov-Fedotov trick*
Benedikt Schneider, Dominik Kiese, Björn Sbierski
pages 31–42 / arXiv:2209.13484 Phys. Rev. B 106, 235113 (2022)

[P2] *Temperature flow in pseudo-Majorana functional renormalization for quantum spins*
Benedikt Schneider, Johannes Reuther, Matías G Gonzalez, Björn Sbierski, Nils Niggemann
pages 43–54 / arXiv:2312.14838 Phys. Rev. B 109, 195109 (2024)

[P3] *Pseudo-Majorana functional renormalization for frustrated XXZ spin-$\frac{1}{2}$ models with field or magnetization along the spin-Z direction at finite temperature*
Frederic Bippus, **Benedikt Schneider**, Björn Sbierski
pages 55–69 / arXiv:2411.18198 Phys. Rev. B 111, 054420 (2025)

Taming pseudofermion functional renormalization for quantum spins: Finite temperatures and the Popov-Fedotov trick

Benedikt Schneider [1,2] Dominik Kiese [3,4] and Björn Sbierski [1,2]

[1]*Department of Physics and Arnold Sommerfeld Center for Theoretical Physics, Ludwig-Maximilians-Universität München, Theresienstrasse 37, 80333 Munich, Germany*

[2]*Munich Center for Quantum Science and Technology (MCQST), 80799 Munich, Germany*

[3]*Institute for Theoretical Physics, University of Cologne, 50937 Cologne, Germany*

[4]*Center for Computational Quantum Physics, Flatiron Institute, 162 5th Avenue, New York, New York 10010, USA*

(Received 28 September 2022; accepted 18 November 2022; published 9 December 2022)

The pseudofermion representation for $S = 1/2$ quantum spins introduces unphysical states in the Hilbert space, which can be projected out using the Popov-Fedotov trick. However, state-of-the-art implementation of the functional renormalization group method for pseudofermions have so far omitted the Popov-Fedotov projection. Instead, restrictions to zero temperature were made and the absence of unphysical contributions to the ground state was assumed. We question this belief by exact diagonalization of several small-system counterexamples where unphysical states do contribute to the ground state. We then introduce Popov-Fedotov projection to pseudofermion functional renormalization, enabling finite-temperature computations with only minor technical modifications to the method. At large and intermediate temperatures, our results are perturbatively controlled and we confirm their accuracy in benchmark calculations. At lower temperatures, the accuracy degrades due to truncation errors in the hierarchy of flow equations. Interestingly, these problems cannot be alleviated by switching to the parquet approximation. We introduce the spin projection as a method-intrinsic quality check. We also show that finite-temperature magnetic-ordering transitions can be studied via finite-size scaling.

DOI: 10.1103/PhysRevB.106.235113

I. INTRODUCTION

Many quantum systems of current interest, ranging from frustrated magnets [1] to Rydberg atom arrays [2] can be described by Hamiltonians consisting of spin $S = 1/2$ operators $\mathbf{S} = (S^x, S^y, S^z)$ fulfilling the standard $\mathfrak{su}(2)$ spin algebra [1]. In theoretical treatments, it is often useful to switch to an auxiliary particle representation of the spin operator. An established representation in terms of spinful fermions annihilated by $f_{\alpha=\uparrow,\downarrow}$ goes back to Abrikosov [3],

$$S^\mu \to \bar{S}^\mu = \frac{1}{2}\sum_{\alpha,\alpha'} f^\dagger_\alpha \sigma^\mu_{\alpha\alpha'} f_{\alpha'}. \tag{1}$$

Here, σ^μ are Pauli matrices ($\mu = x, y, z$) and an overbar indicates an operator in the fermionic Hilbert space [4].

The pseudo-fermion (pf) representation (1) allows for a variety of applications. For example, it is one of the pillars of the theory of spin-fractionalization and spin-liquids [5] where pf mean-field states are used to describe highly entangled paramagnetic ground states of frustrated spin systems. On the other hand, the pf representation has been used extensively for numerical methods as it allows to transfer the well-developed diagrammatic toolbox for interacting fermions in equilibrium [6] to quantum spins. These tools are based on the Wick theorem and perturbation theory. Two popular examples for more advanced methods are the diagrammatic Monte Carlo [7–9](pf-diagMC) and the functional renormalization group (pf-fRG) [10] in vertex expansion. Whereas the first method samples diagrams of a perturbative series in J/T (J is the exchange coupling and T the temperature) [11], the second rests on a hierarchy of flow equations for pf vertex functions which flow under the variation of the regularized bare propagator [12,13]. Despite the necessary truncation of this hierarchy, resulting end-of-flow correlation functions contain infinite-order re-summations of certain diagram classes.

Crucially, there is a well-known problem that appears whenever the pf representation (1) is used: While the left hand side acts in the two-dimensional spin Hilbert space spanned by $\{|\uparrow\rangle, |\downarrow\rangle\}$, the basis of the right hand side's Hilbert space is extended, $\{|\uparrow\rangle, |\downarrow\rangle, |\uparrow\downarrow\rangle, |0\rangle\}$ and the pf spin operator is $\bar{S}^\mu = \mathrm{diag}(S^\mu, 0, 0)$. It faithfully represents a spin $S = 1/2$ operator only on the physical subspace $\{|\uparrow\rangle, |\downarrow\rangle\}$ while it acts as a $S = 0$ operator on the empty and doubly-occupied subspaces. As the mentioned fermionic methods are applied in thermal equilibrium, any occupation of the unphysical $S = 0$ subspaces will lead to differences between the physical S^μ correlation functions and the pf ones (using $S^\mu \to \bar{S}^\mu$) as well as between the associated partition functions Z and $\bar{Z}$.

Fortunately, this problem can be circumvented with a trick found by Popov and Fedotov (PF) in the late 1980s [14,15]. We will review the details of the PF trick in Sec. III. In its most simple incarnation it amounts to the addition of an imaginary valued chemical potential term to the pf Hamiltonian, $\bar{H} \to \bar{H} + \bar{H}_{\mathrm{PF}}$, where

$$\bar{H}_{\mathrm{PF}} = \frac{i\pi T}{2}(n_\downarrow + n_\uparrow - 1) \tag{2}$$

and $n_\alpha = f^\dagger_\alpha f_\alpha$ is the pf number operator.

Whereas the PF trick is routinely and straightforwardly employed in pf-diagMC calculations [7–9], this is not the case in the pf-fRG literature where only very limited attention has been paid to the subject [10,16,17]. The justifying narrative for this omission in state-of-the-art pf-fRG [18–26] is that unphysical $S = 0$ states would only occur at energies above the ground state energy and consequently PF projection would be unnecessary if calculations are restricted to $T = 0$. However, this state of affairs comes with a number of problems:

(i) In the following Sec. II, we show that even simple and generic frustrated spin systems like the antiferromagnetic (AFM) Heisenberg trimer have a pf ground state with sizable occupation of unphysical $S = 0$ states if PF projection is omitted. Even if these clusters are usually not the focus of pf-fRG applications, they are basic building blocks of highly relevant lattices like triangular or Kagome. For AFM Heisenberg Hamiltonians on these lattices it is thus questionable if ground states in pf representation without PF projection are indeed in the physical subspace. As these systems have been studied amply with pf-fRG [18,25,27–30], this also questions the quantitative accuracy of these state-of-the-art pf-fRG results.

(ii) Even for systems where the pf ground state is faithful, the unavoidable truncation of the hierarchy of fRG flow equations is an uncontrolled approximation at $T = 0$, where, in the absence of magnetic fields h, neither J/T nor J/h can be used to perturbatively justify the truncation. Existing arguments appealing to the correctness of commonly employed pf-fRG truncations in the large S or large N limit [23,31] [in the sense of generalizing $SU(2)$ to $SU(N)$] are not rigorously helpful in the case $S = 1/2$, $N = 2$ most relevant in applications. At best, it is the presence of the Matsubara cutoff scale Λ which perturbatively controls the pf-fRG: As Λ flows from infinity to zero, only ordering tendencies extracted at $\Lambda \gtrsim J$ tend to be reliable, a point of view not emphasized in the literature before [32]. However, as the physical model is only recovered as $\Lambda \to 0$, quantitatively reliable results for observables cannot be guaranteed by this argument. Another practical difficulty of the pf-fRG at $T = 0$ is the continuous nature of Matsubara frequencies, requiring major numerical efforts for a stable and reliable solution of the flow equations [33], in particular if multiloop schemes are involved [25,26].

In this work, we tame problem (i) and (ii) of the pf-fRG by implementing the PF trick in the pf-fRG framework. We term the resulting method ppf-fRG. We show that this is possible with only minor technical modifications (see Sec. IV) so that most methodological achievements from the last decade [23,25,26,34–37] can be seamlessly adapted. As a result, the ppf-fRG leverages the pf-fRG to finite temperatures T where quantum and thermal fluctuations compete, and the numerical implementation simplifies by the discrete nature of Matsubara frequencies. In addition, we show that the ppf-fRG is now perturbatively justified for small J/T and equipped with a method-intrinsic gauge for the quality of the results.

In Sec. V we benchmark the ppf-fRG using small spin clusters. Although exact results are obtained trivially for these systems, diagrammatic approaches are invoked already at their full complexity, making spin clusters a valuable testbed. We show that the ppf-fRG indeed yields quantitatively reliable results at large and moderate T but cannot be trusted for T smaller than about a third of J, at least for the models studied here. Surprisingly, we find that this situation cannot be improved by considering solutions of the parquet approximation. The latter is known to be in equivalence with the loop-converged limit of the multiloop fRG [38–40] in which the two-particle vertex is correctly obtained up to errors of order J^4, i.e., one order higher than in one-loop fRG.

By applying the ppf-fRG to a translation invariant three-dimensional Heisenberg magnet on the cubic lattice, we show that the study of finite-temperature transitions into symmetry-broken (magnetic) phases becomes possible. In Sec. VI, we conclude and also relate our results to the recently developed pseudo-Majorana fRG (pm-fRG) [41] where *by construction* no unphysical sectors exist in the fermionic Hilbert space.

II. SPIN CONSTRAINT VIOLATION AT $T \geqslant 0$

In this section we substantiate our claim that there exist simple AFM spin clusters with a ground state of the pf Hamiltonian $\bar{H}$ that – without PF projection – partially resides outside of the physical $S = 1/2$ sector. We use exact diagonalization (ED) of the pf Hamiltonian $\bar{H}$ corresponding to the spin Hamiltonian H according to Eq. (1). Our examples serve to demonstrate the need for PF projection along with the pf representation [cf. (i) in Sec. I], but the small system sizes allow to disregard problems related to the solution of $\bar{H}$, i.e. the truncation of the pf-fRG [cf. (ii)].

The most elementary example is the AFM Heisenberg trimer with $N = 3$ spins coupled all-to-all ($J = 1$), see (b) in Fig. 1,

$$H_{\text{trimer}} = J(\mathbf{S}_1 \cdot \mathbf{S}_2 + \mathbf{S}_2 \cdot \mathbf{S}_3 + \mathbf{S}_3 \cdot \mathbf{S}_1). \tag{3}$$

Its degenerate physical ground state manifold is described by two of the spins forming a singlet and the third spin being in any other state. By using the pf representation (1), $H_{\text{trimer}} \to \bar{H}_{\text{trimer}}$, the state with the third spin in an unphysical $S = 0$ configuration has the same energy ($E = -3J/4$) as the physical ground state and is therefore equally populated at $T = 0$. To quantify this further we consider

$$C_i(T) = 4\langle \bar{S}_i^z \bar{S}_i^z \rangle = \langle \bar{P}_i \rangle, \tag{4}$$

first studied in Ref. [25] in the context of pf-fRG. On the right side, the projector to the local $S = 1/2$ sector is

$$\bar{P}_i = n_{i\uparrow} + n_{i\downarrow} - 2n_{i\uparrow}n_{i\downarrow}. \tag{5}$$

Only if the (local) pf configuration is entirely in the physical subspace, $\bar{S}_i^z$ would be a faithful $S = 1/2$ operator squaring to $1/4$ and $C_i(T)$ would be unity. Thus $C_i(T)$ can be interpreted as a measure for the suppression of unphysical states and we refer to it as *spin projection*. Returning to the trimer, we obtain $C_i(T = 0) = 4/5 < 1$ signaling the presence of an admixture of unphysical $S = 0$ states to the ground state manifold. We plot $C_i(T)$ for $\bar{H}_{\text{trimer}}$ over a range of temperatures, see Fig. 1. The spin projection decreases with increasing T reaching $C_i(T \to \infty) = 1/2$, indicating that in the $T = \infty$ state on the pf Hilbert space the occupation of unphysical states equals the occupation of physical states.

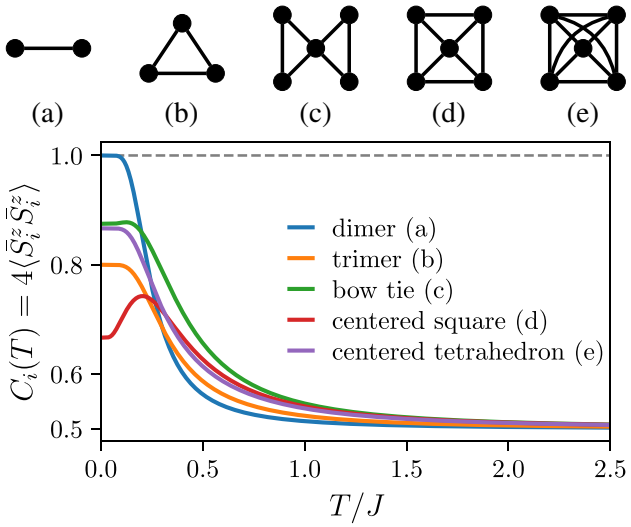

FIG. 1. Spin projection $C_i(T) = 4\langle \bar{S}_i^z \bar{S}_i^z \rangle$ over temperature calculated via exact diagonalization of the pf Hamiltonian $\bar{H}$ for Heisenberg spin-clusters of $N = 2, 3, 5$ sites as shown in the legend. A bond represents an anti-ferromagnetic Heisenberg coupling $J = 1$. For the bow tie and the centered square, with inequivalent sites, the site-label i refers to the center spin. For all clusters except the dimer, the pf ground state manifold contains unphysical states and the $T \to 0$ limit of $C_i(T)$ reduces from the physical value of unity (dashed line) to $\frac{4}{5}$ for the trimer, $\frac{7}{8}$ for the bow tie, $\frac{2}{3}$ for the centered square and $\frac{13}{15}$ for the centered tetrahedron, respectively.

Besides the trimer we found numerous other AFM Heisenberg spin clusters with $N = 5$ where unphysical states poison the pf ground state. This behavior can be generally observed when a physical system cannot lower its ground state energy by adding one more spin and is thus paradigmatic for frustrated systems. In that case, preparing the additional site in a physical $S = 1/2$ or an unphysical $S = 0$ state gives the same ground state energy. In Fig. 1, we show results for the bow tie (c), centered square (d) and centered tetrahedron (e), which are qualitatively similar to the trimer case (b). Since these shapes (including the trimer) are basic building blocks of the triangular, Kagome, face-centered cubic and centered pyrochlore lattice [42], respectively, it is questionable if ground states of AFM Heisenberg pf Hamiltonians $\bar{H}$ on these lattices reside entirely in the physical subspace. Finally, from the clusters considered in Fig. 1, only the $N = 2$ dimer (a) has a pf ground state in the physical subspace.

III. POPOV-FEDOTOV TRICK: A REVIEW

As discussed in Sec. I, the spin operator $\bar{S}^\mu$ in pf representation (1) acts like a spin-1/2 operator on the subspace $\{|\uparrow\rangle, |\downarrow\rangle\}$ but like a spin-0 operator on the subspaces spanned by $|\uparrow\downarrow\rangle$ and $|0\rangle$, respectively. Thermal occupation of the latter two sectors of the fermionic Hilbert space will thus compromise the equivalence between the spin and pf partition functions, $Z \neq \bar{Z} \equiv \operatorname{tr} e^{-\beta \bar{H}}$, respectively. A straightforward projection to the physical subspace using $\bar{P} = \Pi_{i=1,\ldots,N} \bar{P}_i$ with local projectors $\bar{P}_i$ from Eq. (5) becomes unpractical for a large number of spins N.

A more feasible projection scheme was originally proposed by Popov and Fedotov [14] and later generalized by Prokof'ev and Svistunov [15]. It amounts to replacing $\bar{H} \to \bar{H} + \bar{H}_{\mathrm{PF}}^{\phi_{1,2}}$ where

$$\bar{H}_{\mathrm{PF}}^{\phi_{1,2}} = iT[n_\downarrow n_\uparrow \phi_1 + (n_\uparrow - 1)(n_\downarrow - 1)\phi_2] \tag{6}$$

with $\phi_{1,2} \in \mathbb{R}$ and the constraint $e^{i\phi_1} + e^{i\phi_2} = 0$. Now, the partition function in the pf Hilbert space can be split into a sum over the purely physical part of the Hilbert space (equivalent to Z since $\bar{H}_{\mathrm{PF}}^{\phi_{1,2}} = 0$ in the $S = 1/2$ sector) and a part containing the expectation values of a product state with $\mathcal{N} = 1, 2, \ldots, N$ unphysical contributions,

$$\bar{Z} = \operatorname{tr}(e^{-\beta \bar{H} - \beta \bar{H}_{\mathrm{PF}}^{\phi_{1,2}}}) = Z + \sum_{\mathcal{N}=1}^{N} \sum_{\xi_\mathcal{N}} \left(Z_{\xi_\mathcal{N}} \prod_{j \in \xi_\mathcal{N}} F_j^{\phi_{1,2}} \right). \tag{7}$$

Here, $\xi_\mathcal{N}$ counts different configurations of sites with unphysical spin and $Z_{\xi_\mathcal{N}}$ is the physical partition function of the subsystem with the $\mathcal{N}$ unphysical sites removed. Since $\bar{H}$ acts trivially on unphysical states, we can compute the local trace $F_j^{\phi_{1,2}}$ over the unphysical states at site j explicitly,

$$F_j^{\phi_{1,2}} = \langle 0|_j e^{-\beta \bar{H}_{\mathrm{PF}}^{\phi_{1,2}}} |0\rangle_j + \langle \uparrow\downarrow|_j e^{-\beta \bar{H}_{\mathrm{PF}}^{\phi_{1,2}}} |\uparrow\downarrow\rangle_j \tag{8}$$

$$= e^{i\phi_1} + e^{i\phi_2} = 0 \tag{9}$$

and Eq. (7) yields $\bar{Z} = Z$. A similar analytic argument shows the faithfulness of spin correlation functions computed using the pf representation with the PF term (6), in particular $C_i(T) = 1$ for all temperatures.

In the rest of the paper, we make the choice $\phi_1 = -\phi_2 = \frac{\pi}{2}$. This reduces Eq. (6) to Eq. (2), taking the simple non-interacting form of a potential which is, however, imaginary.

We emphasize that the PF trick applies also in the limit $T \to 0$ as easily seen from the fact that in the partition function (for which the PF term is rigorously defined) the Hamiltonian is multiplied by $\beta = 1/T$ and the PF contribution amounts to phase factors independent of T.

IV. SYMMETRIES, CORRELATION FUNCTIONS, AND THE FRG

In this technical section we review the symmetries of the generic pf Hamiltonian $\bar{H}$ following Buessen *et al.* [35]. We then discuss the necessary changes enforced by the addition of the PF potential term (2). The resulting modifications in the parametrization of correlation- (and vertex-) functions are minor and can easily be implemented into established numerical codes solving the pf-fRG flow equations [26,43]. We call the resulting pf-fRG formalism including the PF potential ppf-fRG and restrict our focus to one-loop evaluation of the flow equations (including Katanin truncation) and an iterative solution of the parquet approximation, ppf-PA.

A. Symmetries of the pf Hamiltonian

In analogy to the pf-fRG literature, we restrict our discussion to spin Hamiltonians with two-spin interaction across

bonds (i, j) and disregard magnetic fields,

$$H = \sum_{(i,j)} \sum_{\mu,\nu=x,y,z} J^{\mu\nu}_{(i,j)} S^{\mu}_i S^{\nu}_j. \tag{10}$$

Using Eq. (1), $S^{\mu}_i \to \bar{S}^{\mu}_i$, and the PF potential term $\bar{H}_{\rm PF}$ from Eq. (2), we consider the pf Hamiltonian

$$\bar{H} + \bar{H}_{\rm PF} = \sum_{(i,j)} \sum_{\mu,\nu} J^{\mu\nu}_{(i,j)} \bar{S}^{\mu}_i \bar{S}^{\nu}_j + \frac{i\pi}{2\beta} \sum_j (n_{\uparrow j} + n_{\downarrow j} - 1). \tag{11}$$

For $\bar{H}$ alone, Buessen *et al.* [35] have discussed the following properties: $\bar{H}$ is hermitian (H) and symmetric with respect to local U(1), local particle-hole (lPH) and (anti-unitary) time-reversal (TR) transformation. These symmetries act on $\mathcal{F}_{i\alpha} \equiv (f^{\dagger}_{i\alpha}, f_{i\alpha})^T$ as follows,

$$\mathcal{F}_{i\alpha} \xrightarrow{\rm H} \begin{pmatrix} f_{i\alpha} \\ f^{\dagger}_{i\alpha} \end{pmatrix} \forall i, \qquad \mathcal{F}_{i\alpha} \xrightarrow{\rm U(1)} \begin{pmatrix} e^{i\theta_i} f^{\dagger}_{i\alpha} \\ e^{-i\theta_i} f_{i\alpha} \end{pmatrix},$$
$$\mathcal{F}_{i\alpha} \xrightarrow{\rm lPH} \begin{pmatrix} \alpha f_{i\bar{\alpha}} \\ \alpha f^{\dagger}_{i\bar{\alpha}} \end{pmatrix}, \qquad \mathcal{F}_{i\alpha} \xrightarrow{\rm TR} \begin{pmatrix} e^{i\pi\alpha/2} f^{\dagger}_{i\bar{\alpha}} \\ e^{-i\pi\alpha/2} f_{i\bar{\alpha}} \end{pmatrix} \forall i. \tag{12}$$

Note, that H and TR also involve a complex conjugation when acting on complex numbers. We denote the spin index by $\alpha = \{\uparrow, \downarrow\} = \{+1, -1\}$ and $\bar{\alpha}$ indicates a spin-flip, $\bar{\alpha} = -\alpha$.

The PF-term $\bar{H}_{\rm PF}$ is invariant under the local U(1) symmetry, but changes its sign under hermitian conjugation, global particle-hole (PH) and time-reversal symmetry,

$$\bar{H} + \bar{H}_{\rm PF} \xrightarrow{\rm H,PH,TR} \bar{H} - \bar{H}_{\rm PF}. \tag{13}$$

Therefore, the full Hamiltonian $\bar{H} + \bar{H}_{\rm PF}$ is only symmetric under pairwise combinations of H, PH and TR symmetry. The lPH symmetry ceases to be useful in the presence of $\bar{H}_{\rm PF}$.

Depending on the model-specific $J^{\mu\nu}_{(i,j)}$, we can further find lattice (L) or spin rotation (S) symmetries of $\bar{H}$,

$$J^{\mu\nu}_{(i,j)} \xrightarrow{L} J^{\mu\nu}_{(i',j')}, \qquad J^{\mu\nu}_{(i,j)} \xrightarrow{S} J^{\mu'\nu'}_{(i,j)}. \tag{14}$$

These symmetries are not broken by presence of $\bar{H}_{\rm PF}$.

B. Symmetries of correlation functions

The symmetries of the pf Hamiltonian impose symmetries on the correlation functions, which constitute the basic starting point for the fRG treatment. The single-particle correlation function (or propagator) is

$$G(1';1) = \int_0^{\beta} d\tau' d\tau e^{i\tau'\omega' - i\tau\omega} \langle \mathcal{T}_{\tau} f^{\dagger}_{i'\alpha'}(\tau') f_{i\alpha}(\tau) \rangle, \tag{15}$$

where we used the imaginary time-ordering and operators in the Heisenberg picture. The two-particle correlation function reads

$$G(1', 2'; 1, 2) = \int_0^{\beta} d\tau_{1'} d\tau_{2'} d\tau_1 d\tau_2 e^{i(\tau_{1'}\omega_{1'} + \tau_{2'}\omega_{2'} - \tau_1\omega_1 - \tau_2\omega_2)} \times \langle \mathcal{T}_{\tau} f^{\dagger}_{i_{1'}\alpha_{1'}}(\tau_{1'}) f^{\dagger}_{i_{2'}\alpha_{2'}}(\tau_{2'}) f_{i_1\alpha_1}(\tau_1) f_{i_2\alpha_2}(\tau_2) \rangle. \tag{16}$$

TABLE I. Symmetries of $\bar{H}$ acting on $\bar{H}_{\rm PF}$ and correlation functions: Hermitian (H), local U(1), global particle-hole (PH) and time-reversal (TR) symmetry.

	$\bar{H}_{\rm PF}$	$G(1';1)$	$G(1', 2'; 1, 2)$
H	$-\bar{H}_{\rm PF}$	$G(-1;-1')^*$	$G(-1,-2;-1',-2')^*$
PH	$-\bar{H}_{\rm PF}$	$-\alpha'\alpha G(-\bar{1};-\bar{1}')$	$\alpha_1\alpha_2\alpha'_1\alpha'_2 G(-\bar{1},-\bar{2};-\bar{1}',-\bar{2}')$
TR	$-\bar{H}_{\rm PF}$	$\alpha'\alpha G(-\bar{1}';-\bar{1})^*$	$\alpha_1\alpha_2\alpha'_1\alpha'_2 G(-\bar{1}',-\bar{2}';-\bar{1},-\bar{2})^*$
U(1)	$\bar{H}_{\rm PF}$	$e^{i(\theta_{i'_1} - \theta_{i_1})} G(1';1)$	$e^{i(\theta_{i'_1} + \theta_{i'_2} - \theta_{i_1} - \theta_{i_2})} G(1', 2'; 1, 2)$

On the left-hand side of the above equations, we use multi-indices,

$$1 \equiv (i_1, \quad \omega_1, \alpha_1),$$
$$-1 \equiv (i_1, -\omega_1, \alpha_1),$$
$$\bar{1} \equiv (i_1, \quad \omega_1, \bar{\alpha}_1).$$

Following Ref. [35], we summarize the symmetry constraints on the correlation functions in Table I. For the two particle correlation function, there is the additional crossing symmetry (X) related to anticommuting two fermionic creation or annihilation operators.

$$G(1', 2'; 1, 2) = -G(1', 2'; 2, 1) = G(2', 1'; 2, 1) = -G(2', 1'; 1, 2). \tag{17}$$

C. Parameterization of correlators and vertices

The local U(1) symmetry (12) constrains the single-particle correlator to be site-local and the two-particle correlator to be bi-local in real space. In addition, imaginary time translation symmetry reduces the number of independent frequencies by one. The dependence on the spin indices α can be parameterized by an expansion in Pauli matrices σ^{μ} with $\mu = 0, x, y, z$ and σ^0 the identity matrix. These considerations allow for the parametrization [35]

$$G(1';1) = \delta_{i'i}\delta_{\omega',\omega} \sum_{\mu=0,x,y,z} G^{\mu}_i(\omega) \sigma^{\mu}_{\alpha'\alpha}, \tag{18}$$

and

$$G(1', 2'; 1, 2) = \Big[\Big(\sum_{\mu,\nu=0,x,y,z} G^{\mu\nu}_{i_1 i_2}(s,t,u) \sigma^{\mu}_{\alpha'_1\alpha_1} \sigma^{\nu}_{\alpha'_2\alpha_2} \Big) \delta_{i_{1'}i_1} \delta_{i_{2'}i_2} - (1' \leftrightarrow 2') \Big] \delta_{\omega_{1'}+\omega_{2'},\, \omega_1+\omega_2}, \tag{19}$$

where the bosonic transfer frequencies are

$$s = \omega_{1'} + \omega_{2'} = \omega_1 + \omega_2, \tag{20}$$

$$t = \omega_{1'} - \omega_1 = \omega_2 - \omega_{2'}, \tag{21}$$

$$u = \omega_{1'} - \omega_2 = \omega_1 - \omega_{2'}. \tag{22}$$

The complex numbers $G^{\mu}_i(\omega)$ and $G^{\mu\nu}_{i_1 i_2}(s,t,u)$ can be further constrained using the relations in the first three lines of Table I. This is summarized in Table II.

TABLE II. Constraints on the parameterized pf correlation functions of Eqs. (18) and (19). The constraints are labeled by the symmetries that have been used.

$G_i^{\mu}(\omega) = \xi(\mu) G_i^{\mu}(\omega)$	(H ∘ TR)
$G_i^{\mu}(\omega) = -G_i^{\mu}(\omega)^*$	(TR ∘ PH)
$G_{i_1 i_2}^{\mu\nu}(s,t,u) = \xi(\mu)\xi(\nu) G_{i_1 i_2}^{\mu\nu}(s,-t,u)$	(H ∘ TR)
$G_{i_1 i_2}^{\mu\nu}(s,t,u) = \xi(\mu)\xi(\nu) G_{i_2 i_1}^{\nu\mu}(s,t,-u)$	(X ∘ H ∘ TR)
$G_{i_1 i_2}^{\mu\nu}(s,t,u) = \xi(\mu)\xi(\nu) G_{i_1 i_2}^{\mu\nu}(s,t,u)^*$	(H ∘ PH)

In these relations, we have introduced the sign function

$$\xi(\mu) = \begin{cases} +1 & \text{if } \mu = 0, \\ -1 & \text{otherwise.} \end{cases} \tag{23}$$

Our results indicate that the propagator takes the simple diagonal form

$$G(1', 1) = \delta_{i',i}\delta_{\omega',\omega}\delta_{\alpha',\alpha} G_i(\omega) \tag{24}$$

and we define the real self-energy $\gamma_i(\omega)$ via

$$G_i(\omega) = \frac{1}{i\omega + i\gamma_i(\omega)} \equiv -i g_i(\omega) \in i\mathbb{R}. \tag{25}$$

In comparison to the standard pf-fRG without PF potential term [35], $\gamma_i(\omega)$ is no longer anti-symmetric in ω. Likewise, the two-particle correlator has no symmetry relating $s \leftrightarrow -s$ or $s \leftrightarrow u$. This reduction of symmetries amounts to a factor $\approx$4 in memory and computation time compared to the standard pf-fRG scheme.

Finally, the fRG flow equations in vertex expansion are written in terms of the (one-particle irreducible) vertices defined from the connected correlators via the tree expansion [12]. According to Eq. (25), we have for the self-energy $\Sigma(1';1) = \delta_{i',i}\delta_{\omega',\omega}\delta_{\alpha',\alpha}\{-i\gamma_i(\omega)\}$. The two-particle vertex $\Gamma(1', 2'; 1, 2)$ is defined from the connected part of $-G(1', 2'; 1, 2)$ by amputating external propagators. As the latter take the simple diagonal form (24), the vertex can be parameterized in analogy to the correlator, i.e. Eq. (19) with G replaced by Γ and the symmetries listed in Table II are also applicable to $\Gamma_{i_1 i_2}^{\mu\nu}(s,t,u)$.

So far, we have made no assumptions on the form of the spin-spin interaction $J_{(i,j)}^{\mu\nu}$. If present, spin rotation and lattice symmetries can be used to relate different site and spin indices of $\gamma_i(\omega)$ and $G_{i_1 i_2}^{\mu\nu}$. From now on we focus on the SO(3) symmetric Heisenberg case,

$$J_{(i,j)}^{\mu\nu} = \delta_{\mu,\nu} J_{(i,j)}, \tag{26}$$

for $\mu, \nu = x, y, z$ so that $G_{i_1 i_2}^{00} \equiv G_{i_1 i_2}^{d} \in \mathbb{R}$ and $G_{i_1 i_2}^{xx} = G_{i_1 i_2}^{yy} = G_{i_1 i_2}^{zz} \equiv G_{i_1 i_2}^{s} \in \mathbb{R}$ are the only non-vanishing correlation functions. Analogously, $\Gamma_{i_1 i_2}^{s,d}$ are the only non-vanishing vertices.

D. ppf-fRG

For the (p)pf-fRG, a Matsubara cutoff scheme is applied to the bare propagator $G_j^{(0)}(\omega) = 1/i\omega \to G_j^{(0),\Lambda}(\omega) \equiv \theta^{\Lambda}(\omega) G_j^{(0)}(\omega)$ [10,16] with cutoff function $\theta^{\Lambda}(\omega)$ smoothly interpolating from unity to zero as the magnitude of ω drops below the cutoff scale Λ. When $\Lambda = 0$ the bare propagator, $G_j^{(0),\Lambda=0}(\omega) = 1/i\omega$, is recovered and the action describes the physical system of interest. At $\Lambda = \infty$, however, the modified propagator vanishes and the vertex functions are trivial and frequency independent,

$$\gamma_i^{\Lambda=\infty}(\omega) = \frac{\pi}{2\beta}, \tag{27}$$

$$\Gamma_{i_1 i_2}^{s,\Lambda=\infty}(s,t,u) = J_{(i_1,i_2)}/4, \tag{28}$$

$$\Gamma_{i_1 i_2}^{d,\Lambda=\infty}(s,t,u) = 0. \tag{29}$$

The Wetterich equation [44] describes the flow of all $n-$particle vertex functions under variation of Λ from the trivial starting point $\Lambda = \infty$ to the physical endpoint $\Lambda = 0$. The resulting hierarchy of flow equations can usually not be solved exactly, but has to be truncated, with multiple truncation schemes available. Here, we focus on the established one-loop scheme [12] together with Katanin truncation [45] which partially considers the effect of the three-particle vertex in the flow of the two-particle vertex and constitutes the standard choice in the pf-fRG literature [10]. We refer to Appendix A for the choice of cutoff function and the flow equations which do not differ from the standard pf-fRG case. We use discrete Matsubara grids for all frequency arguments with about $N_w = 30$ (positive) frequencies and ensure that our results are converged in N_w. The ppf-fRG flows are smooth in Λ with features appearing around $\Lambda \sim J$ and a plateau towards $\Lambda \to 0$ from which we obtain the end-of-flow results reported in the following. In Appendix B, we show how imaginary frequency spin susceptibilities $\chi_{i_1 i_2}(\Omega)$ and equal-time spin correlation functions like the spin projection $C_i(T)$ are computed, with a technical subtlety appearing for the bubble contribution in the latter case. In summary, the main difference between the ppf-fRG and the pf-fRG is the slightly reduced symmetry of the vertex functions discussed in the previous subsection, the finite initial condition for the self energy and fRG flows that are smooth and convergent.

E. ppf-PA

Recently, a lot of effort has been put into generalizing the one-loop truncation of general fermionic fRG flows to higher loop orders using multiloop fRG (mfRG) [38–40]. Applications include the Anderson impurity model [46] and the two-dimensional Hubbard model [47,48]. By construction, vertices obtained with mfRG in the limit of infinite loops converge to solutions of the parquet approximation (PA), a complementary diagrammatic formulation of the many-body problem in which the self-energy and frequency-dependent contributions to the two-particle vertex are self-consistently described by the Schwinger-Dyson and three Bethe-Salpeter equations, respectively. In-depth discussions of their structure for pseudo-fermion Hamiltonians can, for example, be found in Refs. [25,26]. In contrast to the full parquet equations, the PA neglects frequency dependent contributions to the fully two-particle irreducible vertex $I_{2\text{PI}}$ which thus reduces to the bare vertex Γ_0, with $\Gamma_0 \sim J$ for pf systems. Deviations from exact vertices set in at fourth order in J/T, corresponding to the so-called *envelope* diagram.

Using the very same initial conditions as in the $\Lambda \to \infty$ limit of ppf-fRG (27)–(29), we numerically converge the algebraic equations of the PA using forward iterations combined

with a mixed update scheme, which determines the input for the next iteration as

$$x_{\text{new}} = (1-\lambda)x_{\text{old}} + \lambda f(x_{\text{old}}), \tag{30}$$

where $x = (\Sigma, \Gamma)$ and f schematically denotes the Schwinger-Dyson and Bethe-Salpeter equations. For $J/T \ll 1$, full updates ($\lambda = 1$) were sufficient to meet the convergence criterion $||f(x_{\text{old}}) - x_{\text{old}}|| < 10^{-6}$ between subsequent iterations ($||.||$ is the maximum norm). For lower temperatures λ had to be reduced from unity in order to obtain converged results. We choose extended Matsubara grids with up to 48×24^2 frequencies in mixed bosonic-fermionic frequency notation to parametrize the two-particle vertex as well as 32 frequencies for the self-energy. For the vertex, we take into account the decomposition of each channel into its respective asymptotic functions K_1, K_2 ($\bar{K}_2$) and R as detailed in Ref. [49]. We checked convergence with respect to the number of frequencies and, in most cases (see Appendix C and D), found no significant changes of our results if more were included.

V. RESULTS

A. Benchmark: Small spin clusters

To benchmark the proposed ppf-fRG and ppf-PA approaches, we consider the AFM Heisenberg dimer $H_{\text{dimer}} = J\mathbf{S}_0 \cdot \mathbf{S}_1$ with $J = 1$ and focus on the static local and non-local susceptibilities and the spin projection C_i as a function of T. Exact ED results of the spin Hamiltonian are shown as solid black lines in Fig. 2, see Ref. [41] for closed-form expressions. The (end-of-flow) ppf-fRG results are denoted by orange symbols. For large and moderate temperatures $T \gtrsim 0.4J$, the exact susceptibilities are accurately reproduced by the ppf-fRG. For lower T, the susceptibilities become unphysically large in magnitude. This breakdown of accuracy is also reflected in C_i which considerably drops below unity with decreasing T.

The inaccuracies at low T are due to the truncation of the ppf-fRG flow equations so that self-energy and (two-particle) vertex are only correct up to order J^2/T, see Appendix C for numerical confirmation. However, the advantage of fRG over naive second-order perturbation theory (SOPT, dotted line in Fig. 2) is the re-summation of certain diagrams to infinite order [16], which is essential for the detection of magnetic ordering tendencies (see below). In the dimer case, the re-summation stabilizes the susceptibilities beyond temperatures where SOPT is applicable.

As the treatment of the full three-particle vertex is prohibitively expensive, an interesting question is if the above truncation problem can be alleviated by invoking higher-loop orders beyond the Katanin truncation. This has been shown to be numerically feasible in the pf-fRG [25,26]. In fact, as explained in Sec. IV, our finite-temperature application makes it even possible to converge the ppf-PA equations equivalent to the loop-converged multi-loop result with an error of order J^4/T^3 and J^5/T^4 for vertex and self-energy, respectively. Surprisingly, our ppf-PA results (green symbols in Fig. 2) show no systematic improvement compared to the ppf-fRG. This unexpected finding also questions the usefulness of multi-loop extensions in the context of pf applications.

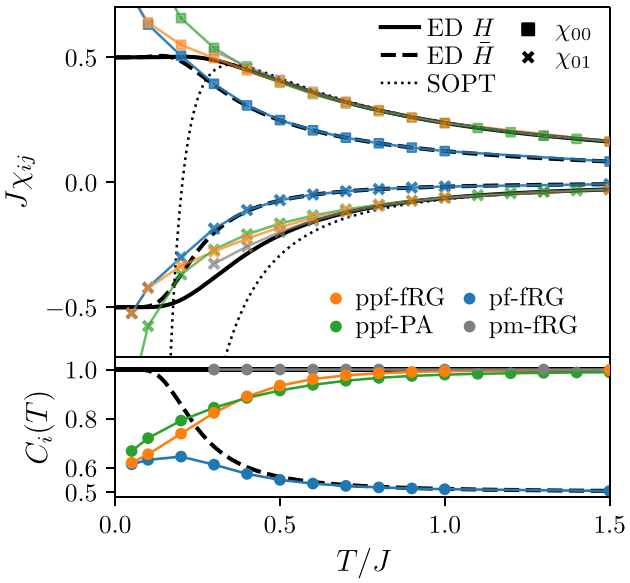

FIG. 2. Heisenberg dimer: Local and non-local susceptibilities (top panel: squares and crosses, respectively) and spin projection $C_i(T) = 4\langle \bar{S}_i^z \bar{S}_i^z \rangle$ (bottom panel) computed with PF projection using the fRG (ppf-fRG) and the parquet approximation (ppf-PA). For comparison, we show the exact results (solid lines), second-order perturbation theory in J (dotted lines), pf-fRG results without PF projection and data from the pseudo-Majorana fRG (pm-fRG) building on a fermionic spin representation without unphysical states.

For completeness, blue symbols in Fig. 2 show results of the standard one-loop pf-fRG applied to $\bar{H}$ (without PF potential $\bar{H}_{\text{PF}}$) which at large T compare well with the exact (but unphysical) ED results obtained from $\bar{H}$ (dashed black line). Like in the ppf-fRG, agreement only holds for $T \gtrsim 0.4J$, suggesting the truncation error in the fRG flow equations is largely independent of $\bar{H}_{\text{PF}}$.

Finally, in Fig. 3 we consider the Heisenberg trimer, Eq. (3), where the ppf-fRG and ppf-PA results are qualitatively similar to the dimer and strengthen the conclusions given above for the latter case. It is interesting to note, that, presumably due to the truncation of the flow equations, the ppf-fRG and pf-fRG converge to the same result for low T even though the ground state of the pf trimer is not in the physical Hilbert space.

B. Finite-temperature magnetization transition in three dimensions

One of the most remarkable properties of spin systems at finite T is the possible appearance of a magnetization transition at a critical temperature T_c. As we consider (short-range coupled) Heisenberg systems with continuous SO(3) spin rotation symmetry, these transitions only occur at dimension three. Despite their classical nature, it is interesting to study magnetic phase transitions in models of – possibly frustrated – quantum spins. Here we investigate if ppf-fRG can detect the Néel transition in a nearest-neighbor cubic lattice Heisenberg AFM ($J_1 = 1$) using finite-size scaling of the correlation ratio

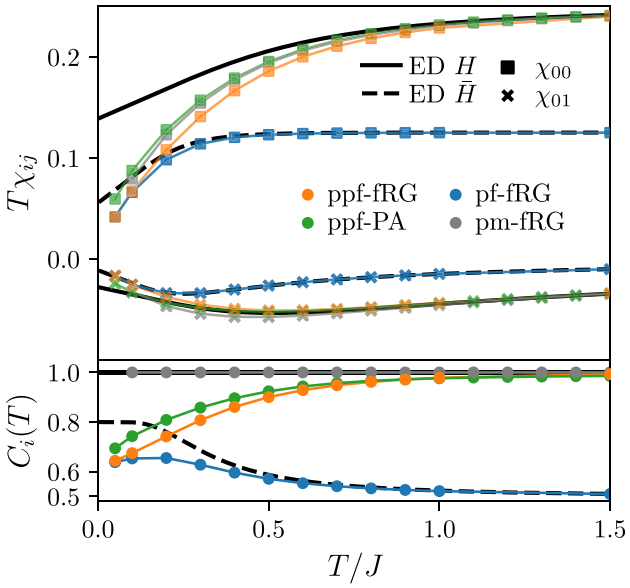

FIG. 3. Heisenberg trimer: The top panel shows the static susceptibilities that diverge as $T \to 0$ and have been multiplied by temperature to obtain finite values at $T = 0$. The bottom panel shows the spin projection $C_i(T)$. The symbols follow the convention of Fig. 2.

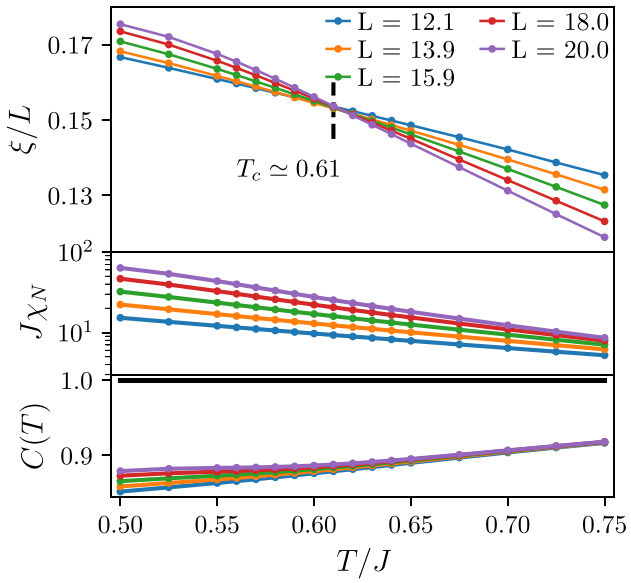

FIG. 4. ppf-fRG: Correlation length ξ, Néel susceptibility χ_N and spin projection C for the nearest neighbor AFM Heisenberg model on the cubic lattice. We find a line crossing at $T_c^{\mathrm{fRG}} \simeq 0.61$. The corresponding scaling collapse can be found in Fig. 5.

[50–52],

$$\xi/L = \frac{1}{2\pi}\sqrt{\chi(\mathbf{Q})/\chi(\mathbf{Q}+\boldsymbol{\delta}) - 1}, \tag{31}$$

where $\chi(\mathbf{q}) = \sum_j e^{-i\mathbf{q}\cdot(\mathbf{r}_i - \mathbf{r}_j)}\chi_{ij}$ is the momentum space static susceptibility, $\mathbf{Q} = (\pi, \pi, \pi)$ is the ordering wave vector, $\boldsymbol{\delta} = (0, 0, 2\pi/L)$ and L is a measure of the system size.

In the ppf-fRG of the cubic lattice AFM we assume a translation invariant infinite system, but limit the range of allowed non-trivial correlations by restricting the vertex functions $\Gamma^{s,d}_{i_1 i_2}$ to $|\mathbf{r}_{i_1} - \mathbf{r}_{i_2}| \leqslant \tilde{L}$ [10]. The length scale $\tilde{L}$ can be used for finite-size scaling [53]. To smooth out discrete-lattice effects, we define $L = 2(\frac{3}{4\pi}N)^{1/3} \simeq 2\tilde{L}$ to be used in Eq. (31), where N is the number of sites to which the reference site is connected by a possible non-trivial vertex (including the on-site vertex). This particular choice of L corresponds to the diameter of the smeared-out *correlation*-sphere including N sites.

Close to the critical temperature T_c, the anticipated scaling form of the AFM spin correlation length ξ is

$$\xi/L \sim g_{\pm}(L|T - T_c|^{\nu}), \tag{32}$$

so that ξ/L becomes independent of L at $T = T_c$, the sign $\pm$ refers to the sign of $T - T_c$ and ν is the universal critical exponent [54]. The ppf-fRG results for the correlation length, Néel susceptibility $\chi_N = \chi(\mathbf{Q})$ and the spin projection $C(T)$ are shown in Fig. 4. We indeed find a clear line-crossing in the ξ/L data indicating $T_c^{\mathrm{fRG}} \simeq 0.61$ significantly below the error controlled quantum Monte-Carlo result $T_c^{\mathrm{QMC}} = 0.946(1)$ [55]. This might be related to an underestimation of the spin projection $C(T)$. The scaling collapse in Fig. 5 shows consistency with the correct three-dimensional Heisenberg universality class with $\nu \simeq 0.71$ [56]. In Appendix D, we further investigate the truncation dependence of these quantities considering analogous simulations using the ppf-fRG without Katanin truncation and in the random phase approximation (RPA) where both $C(T)$ and T_c are overestimated and the critical exponent is consistent with the mean-field value $\nu = 0.5$. We also discuss results obtained from ppf-PA which indicates that this method is not well suited for the assessment of magnetic ordering transitions.

VI. CONCLUSION

In summary, we have considered simple small spin clusters as examples to show that working with the pf representation (1) generally requires the PF projection to the physical $S = 1/2$ subspace at all temperatures. This challenges the existing approach in the pf-fRG literature, which omits the projection

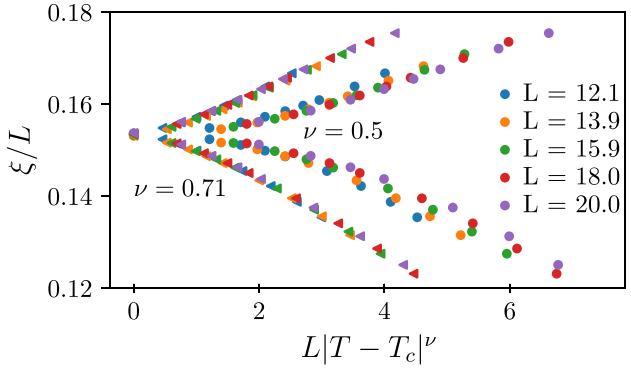

FIG. 5. ppf-fRG: Collapse plot for the data of Fig. 4, assuming the mean-field $\nu = 0.5$ (points) or exact $\nu \simeq 0.71$ (triangles) correlation length critical exponents.

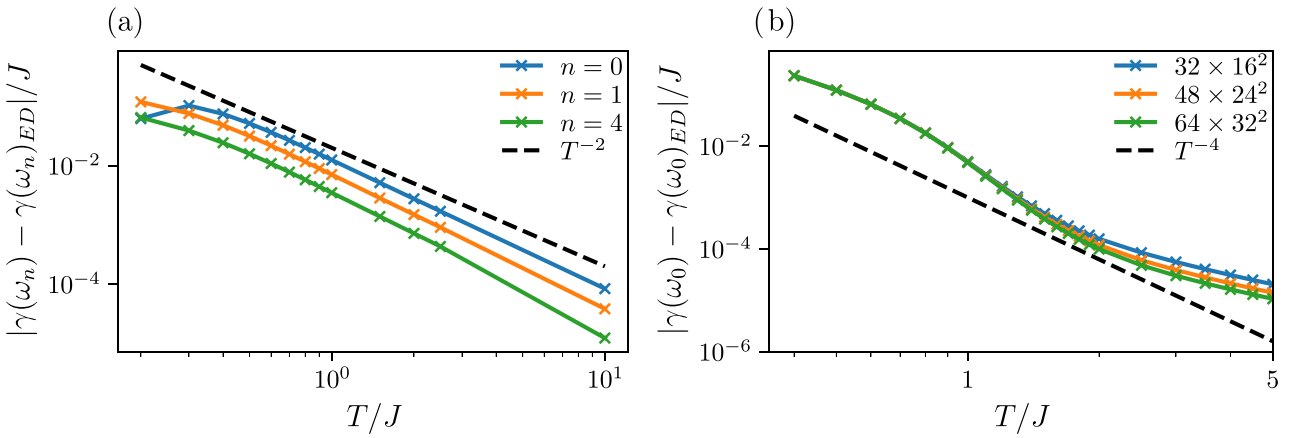

FIG. 6. Error of the pf self energy in the Heisenberg dimer with $J = 1$: (a) In ppf-fRG, the error scales with $\frac{J^3}{T^2}$. For small temperatures, this scaling breaks down because J/T ceases to be a small parameter. (b) In ppf-PA, the observed error scaling depends on the the frequency grid, three choices are indicated by different colors. For larger frequency grids the self-energy error approaches the expected scaling with $\frac{J^3}{T^4}$ more closely.

and focuses on zero temperature. We have leveraged the pf-fRG to include the PF projection in potential form which requires only minor technical modifications and therefore can be readily adopted to existing variants of the method. The discrete nature of finite-temperature Matsubara frequencies simplifies the numerical implementation considerably.

In conclusion, for small benchmark models the proposed ppf-fRG yields quantitatively reliable end-of-flow results at large and intermediate temperatures but fails at small temperatures $T \lesssim 0.4J$ due to the omission of higher-order in J/T diagrams, a problem that also could not be alleviated by adopting a parquet scheme. We note that a detailed understanding for the surprisingly poor performance of the latter is lacking at this point. For forthcoming applications, we suggest that the deviation of the spin projection $C_i(T)$ from the exact value of unity by 10% or more signals the quantitative failure of the ppf-fRG.

This failure of the (p)pf-fRG at low and zero temperature also questions an earlier proposal to remove unphysical contributions of the pf representation in the context of the pf-fRG at $T = 0$. The idea rests on the addition of an on-site term $-J_0 \sum_{\mu=x,y,z} \bar{S}_i^\mu \bar{S}_i^\mu$ [23] with $J_0 > 0$ penalizing the $S = 0$ sector energetically versus the $S = 1/2$ sector. If the treatment of the pf Hamiltonian was exact, the above idea would be a valid $T = 0$ alternative to the PF trick (the latter works at any T). However, due to the unavoidable approximations in the diagrammatic methods at hand, results obtained from the on-site term [23,24] should be considered with appropriate care.

For infinite systems in three dimensions, we have demonstrated that it is possible to robustly detect magnetic ordering by finite-size scaling of the ppf-fRG data. This establishes an alternative to the less physical and implementation dependent concepts of flow-divergence or flow-breakdown at cutoff scale $\Lambda_\star$ which, by mean-field arguments, can be related to T_c [19,22,24]. However, although the correct type of Néel order has been predicted by the ppf-fRG for the nearest-neighbor AFM Heisenberg model on the cubic lattice, it remains unclear why the transition appears at a critical temperature more than 30% below benchmark results. A possible hint might be the spin projection $C_i(T = T_c^{\mathrm{fRG}}) \simeq 0.88$ which is out of the range identified as reliable above.

Finally, there exist two alternatives to the PF projection scheme that we would like to mention. First, in a field theory framework, a functional delta-function representation can be used to constrain the pf operators to the physical subspace. This then leads to the notion of a bosonic gauge field which plays an important role in the (mean-field) theory of spin liquids [5]. On the computational side, however, the introduction of such a bosonic field would require a multitude of additional vertex functions [12], a formidable challenge yet to be faced. Second, it is well known that a faithful quantum spin $S = 1/2$ representation exists in terms of Majorana fermions [57,58]. The associated pseudo-Majorana fRG (pm-fRG) has been developed only recently [41]. The data from pm-fRG applied to the benchmark clusters treated in Sec. V A are shown by the gray lines in Fig. 2 (dimer) and Fig. 3 (trimer). The pm-fRG results are very similar to those of the ppf-fRG, with the same difficulties at small T. However, for the detection of the magnetic phase transition in the cubic lattice case, the pm-fRG determines T_c much more accurately only 5% below the exact result [53].

ACKNOWLEDGMENTS

We thank Johannes Reuther, Nils Niggemann, Jan von Delft, Ronny Thomale, and Marc Ritter for fruitful discussions. The authors gratefully acknowledge the Gauss Centre for Supercomputing e.V. [59] for funding this project by providing computing time through the John von Neumann Institute for Computing (NIC) on the GCS Supercomputer JUWELS at Jülich Supercomputing Centre (JSC). The computations in this work were, in part, run at facilities supported by the Scientific Computing Core at the Flatiron Institute, a division of the Simons Foundation. The authors acknowledge financial support by a MCQST-START fellowship and by the Munich Quantum Valley, which is supported by the Bavarian state government with funds from the Hightech Agenda Bayern Plus.

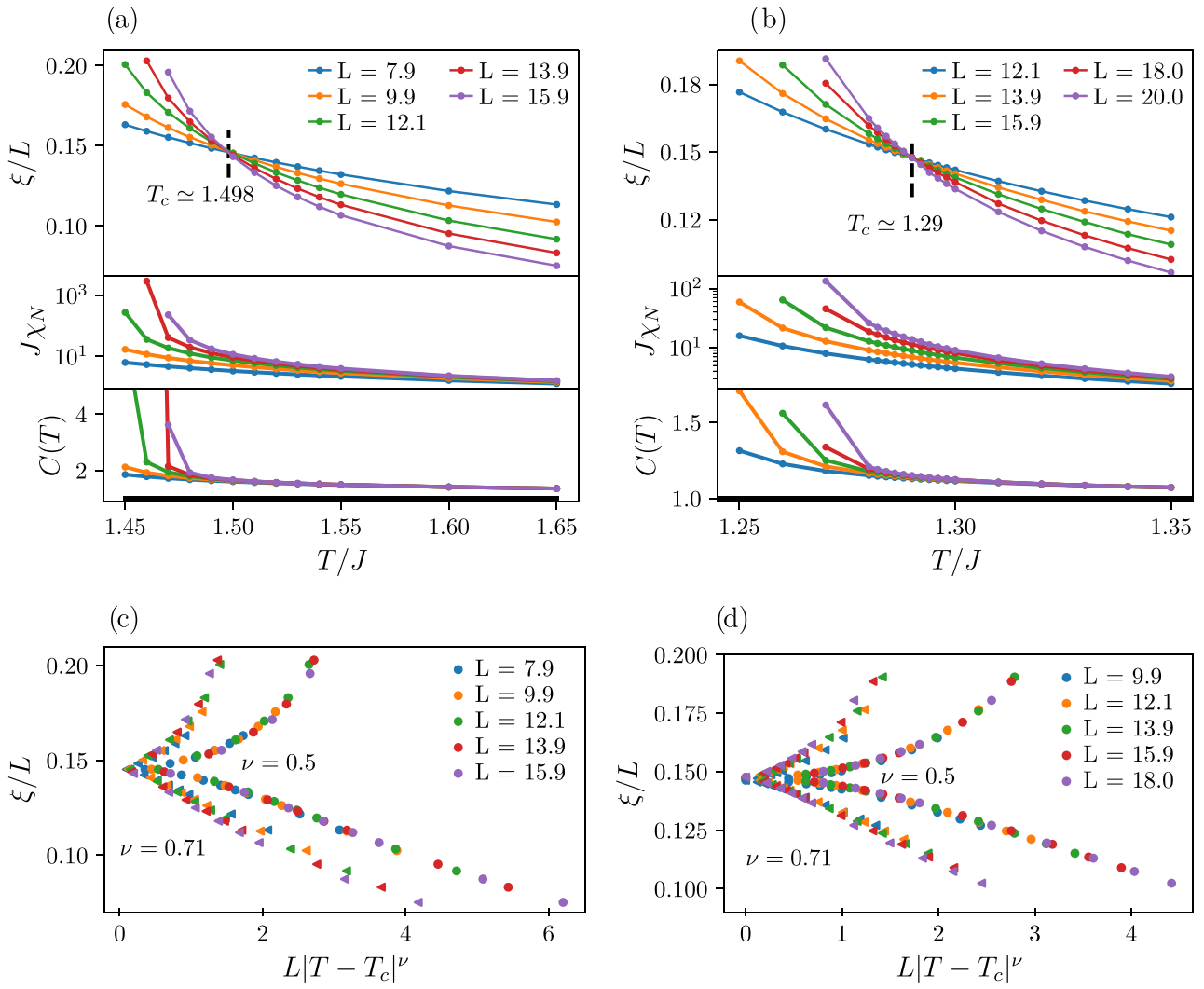

FIG. 7. Correlation length, Néel susceptibility, spin projection and scaling collapse from the calculations on the nearest neighbor AFM Heisenberg model on the cubic lattice. For panel (a) and (c) the flow equations were truncated via the RPA and integrated out numerically. We find $T_c \simeq 1.498$ and a critical exponent consistent with the mean-field value $\nu = 0.5$. The spin projection deviates strongly from the exact result and is greater than 1. For panel (b) and (d) one-loop fRG without Katanin truncation was used. We find $T_c \simeq 1.29$ and a critical exponent also consistent with $\nu = 0.5$. The spin projection exceeds the exact result of $C(T) = 1$.

APPENDIX A: PPF-FRG FLOW EQUATIONS FOR THE HEISENBERG CASE

The one-loop flow equations for the pf-fRG as found in Refs. [16,60] do not rely on the vertex symmetries that are broken by the PF potential term (2), see the discussion in Sec. IV. Here, we write these flow equations for the Heisenberg case where the vertices are parameterized in a density and spin part, Γ^s and Γ^d, see Sec. IV C.

The cutoff dependent propagator is defined as $G_j^\Lambda(\omega) = -ig_j^\Lambda(\omega) = \frac{\theta^\Lambda(\omega)}{i\omega + i\theta^\Lambda(\omega)\gamma_j(\omega)}$ where $\Sigma_j(\omega) = -i\gamma_j(\omega)$ and we chose the regulator to be Lorentzian $\theta^\Lambda(\omega) = \frac{\omega^2}{\omega^2+\Lambda^2}$. The flow equation for the spin part of the vertex reads

$$\begin{aligned}\frac{d}{d\Lambda}\Gamma^{s,\Lambda}_{i_1 i_2}(s,t,u) = T\sum_\omega P^\Lambda_{i_1 i_2}(\omega, s-\omega) \times [-2\Gamma^{s,\Lambda}\Gamma^{s,\Lambda} + \Gamma^{d,\Lambda}\Gamma^{s,\Lambda} + \Gamma^{s,\Lambda}\Gamma^{d,\Lambda}](s, \omega_{1'}-\omega, \omega-\omega_{2'})_{i_1 i_2}(s, \omega-\omega_1, \omega-\omega_2)_{i_1 i_2}\\ - \sum_j P^\Lambda_{jj}(\omega, \omega-t) \times [2\Gamma^{s,\Lambda}\Gamma^{s,\Lambda}](\omega_1+\omega, t, \omega_{1'}-\omega)_{i_1 j}(\omega+\omega_{2'}, t, \omega-\omega_2)_{j i_2}\\ + P^\Lambda_{i_2 i_2}(\omega, \omega-t) \times [\Gamma^{s,\Lambda}\Gamma^{d,\Lambda} - \Gamma^{s,\Lambda}\Gamma^{s,\Lambda}](\omega_1+\omega, t, \omega_{1'}-\omega)_{i_1 i_2}(\omega+\omega_{2'}, \omega-\omega_2, t)_{i_2 i_2}\end{aligned}$$

$$+ P^{\Lambda}_{i_1 i_1}(\omega, \omega - t) \times [\Gamma^{d,\Lambda}\Gamma^{s,\Lambda} - \Gamma^{s,\Lambda}\Gamma^{s,\Lambda}](\omega_1 + \omega, \omega_{1'} - \omega, t)_{i_1 i_1}(\omega + \omega_{2'}, t, \omega - \omega_2)_{i_1 i_2}$$
$$+ P^{\Lambda}_{i_1 i_2}(\omega, \omega + u) \times [2\Gamma^{s,\Lambda}\Gamma^{s,\Lambda} + \Gamma^{d,\Lambda}\Gamma^{s,\Lambda} + \Gamma^{s,\Lambda}\Gamma^{d,\Lambda}](\omega_{1'} + \omega, \omega_2 - \omega, u)_{i_1 i_2}(\omega + \omega_1, \omega - \omega_{2'}, u)_{i_1 i_2} \tag{A1}$$

and the density part flows according to

$$\begin{aligned}\frac{d}{d\Lambda}\Gamma^{d,\Lambda}_{i_1 i_2}(s,t,u) = T\sum_{\omega} P^{\Lambda}_{i_1 i_2}(\omega, s-\omega) \times [\Gamma^{d,\Lambda}\Gamma^{d,\Lambda} + 3\Gamma^{s,\Lambda}\Gamma^{s,\Lambda}](s, \omega_{1'} - \omega, \omega - \omega_{2'})_{i_1 i_2}(s, \omega - \omega_1, \omega - \omega_2)_{i_1 i_2}\\
- \sum_{j} P^{\Lambda}_{jj}(\omega, \omega - t) \times [2\Gamma^{d,\Lambda}\Gamma^{d,\Lambda}](\omega_1 + \omega, t, \omega_{1'} - \omega)_{i_1 j}(\omega + \omega_{2'}, t, \omega - \omega_2)_{j i_2}\\
+ P^{\Lambda}_{i_2 i_2}(\omega, \omega - t) \times [3\Gamma^{d,\Lambda}\Gamma^{s,\Lambda} + \Gamma^{d,\Lambda}\Gamma^{d,\Lambda}](\omega_1 + \omega, t, \omega_{1'} - \omega)_{i_1 i_2}(\omega + \omega_{2'}, \omega - \omega_2, t)_{i_2 i_2}\\
+ P^{\Lambda}_{i_1 i_1}(\omega, \omega - t) \times [3\Gamma^{s,\Lambda}\Gamma^{d,\Lambda} + \Gamma^{d,\Lambda}\Gamma^{d,\Lambda}](\omega_1 + \omega, \omega_{1'} - \omega, t)_{i_1 i_1}(\omega + \omega_{2'}, t, \omega - \omega_2)_{i_1 i_2}\\
+ P^{\Lambda}_{i_1 i_2}(\omega, \omega + u) \times [\Gamma^{d,\Lambda}\Gamma^{d,\Lambda} + 3\Gamma^{s,\Lambda}\Gamma^{s,\Lambda}](\omega_{1'} + \omega, \omega_2 - \omega, u)_{i_1 i_2}(\omega + \omega_1, \omega - \omega_{2'}, u)_{i_1 i_2}\end{aligned} \tag{A2}$$

where

$$P^{\Lambda}_{ij}(\omega, \omega') = \big(-ig^{\Lambda}_i(\omega)\big)S^{\Lambda}_j(\omega') + \big(-ig^{\Lambda}_j(\omega')\big)S^{\Lambda}_i(\omega), \tag{A3}$$

and $S^{\Lambda}_i(\omega)$ is the single scale propagator

$$S^{\Lambda}_j(\omega) = -\frac{\partial}{\partial\Lambda}G^{\Lambda}_j(\omega) = \big(-ig^{\Lambda}_j(\omega)\big)\frac{\partial}{\partial\Lambda}\frac{i\omega}{\theta^{\lambda}(\omega)}\big(-ig^{\Lambda}_j(\omega)\big) = -i\big(g^{\Lambda}_j(\omega)\big)^2\frac{\partial}{\partial\Lambda}\frac{\omega}{\theta^{\lambda}(\omega)}. \tag{A4}$$

Finally, the flow equation for the self energy is

$$\frac{d}{d\Lambda}\gamma^{\Lambda}_i(\omega_1) = T\sum_{\omega_2}\sum_{j}[2\Gamma_d(\omega_1 + \omega_2, 0, \omega_1 - \omega_2)_{ij} - \delta_{ij}(3\Gamma_s + \Gamma_d)(\omega_1 + \omega_2, \omega_1 - \omega_2, 0)_{ii}]S_j(\omega_2). \tag{A5}$$

In the Katanin truncation scheme, the partial derivative in the single scale propagator becomes a full derivative only in the flow equations for the vertex [16],

$$S^{\Lambda}_j(\omega) = -\frac{d}{d\Lambda}G^{\Lambda}_j(\omega) = -i(g^{\Lambda}_j(\omega))^2\left(\frac{\partial}{\partial\Lambda}\frac{\omega}{\theta^{\lambda}(\omega)} + \frac{d}{d\Lambda}\gamma^{\Lambda}_j(\omega)\right). \tag{A6}$$

APPENDIX B: OBSERVABLES FROM VERTEX FUNCTIONS

Following Ref. [25] the susceptibilities $\chi_{ij}(\Omega) \equiv \chi^{zz}_{ij}(\Omega)$ for the Heisenberg case can be computed from the self energy and vertices

$$\chi^{zz}_{ij}(\Omega) = \int_0^{\beta} d\tau e^{i\Omega\tau}\sum_{\alpha_1,\alpha_{1'},\alpha_2,\alpha_{2'}}\frac{1}{4}\sigma^z_{\alpha_1\alpha_{1'}}\sigma^z_{\alpha_2\alpha_{2'}}\langle\mathcal{T}_\tau f^{\dagger}_{i\alpha_1}(\tau)f_{i\alpha_{1'}}(\tau)f^{\dagger}_{j\alpha_2}(0)f_{j\alpha_{2'}}(0)\rangle \tag{B1}$$

$$\begin{aligned}= -\frac{\delta_{ij}}{2\beta}\sum_{\omega}G_i(\omega)G_i(\omega+\Omega) - \frac{\delta_{ij}}{2\beta^2}\sum_{\omega,\omega'}G_i(\omega)G_i(\omega+\Omega)G_i(\omega')G_i(\omega'+\Omega) \times [\Gamma^{s,\Lambda} - \Gamma^{d,\Lambda}](\omega+\omega'+\Omega, \omega-\omega', \Omega)_{ii}\\
-\frac{1}{2\beta^2}\sum_{\omega,\omega'}G_i(\omega)G_i(\omega+\Omega)G_j(\omega')G_j(\omega'+\Omega) \times 2\Gamma^{s,\Lambda}(\omega+\omega'+\Omega, \Omega, \omega-\omega')_{ij}.\end{aligned} \tag{B2}$$

To compute the equal time susceptibility we have to sum over all bosonic Matsubara frequencies Ω and use the infinitesimal positive imaginary time $\delta\tau$,

$$\langle S^z_i S^z_j\rangle = \sum_{\alpha_1,\alpha_{1'},\alpha_2,\alpha_{2'}}\frac{1}{4}\sigma^z_{\alpha_1\alpha_{1'}}\sigma^z_{\alpha_2\alpha_{2'}}\langle\mathcal{T}_\tau f^{\dagger}_{i\alpha_1}(+\delta\tau)f_{i\alpha_{1'}}(+\delta\tau)f^{\dagger}_{j\alpha_2}(0)f_{j\alpha_{2'}}(0)\rangle \tag{B3}$$

$$\begin{aligned}= -\frac{\delta_{ij}}{2\beta^2}\lim_{\delta\tau\to 0}\left[\sum_{\omega}e^{i\delta\tau\omega}G_i(\omega)\right]\left[\sum_{\omega}e^{-i\delta\tau\omega}G_i(\omega)\right]\\
-\frac{\delta_{ij}}{2\beta^3}\sum_{\omega,\omega',\Omega}G_i(\omega)G_i(\omega+\Omega)G_i(\omega')G_i(\omega'+\Omega) \times [\Gamma^{s} - \Gamma^{d}](\omega+\omega'+\Omega, \omega-\omega', \Omega)_{ii}\\
-\frac{1}{2\beta^3}\sum_{\omega,\omega',\Omega}G_i(\omega)G_i(\omega+\Omega)G_j(\omega')G_j(\omega'+\Omega) \times 2\Gamma^{s}(\omega+\omega'+\Omega, \Omega, \omega-\omega')_{ij}.\end{aligned} \tag{B4}$$

In the bubble term, the limit $\delta\tau \to 0$ has to be taken with care and can not be straightforwardly computed numerically. We compute it by adding and subtracting the sum over the bare part of the propagator and calculate the second sum analytically. The remaining sum can be calculated numerically.

$$\begin{aligned}
&\lim_{\delta\tau\to 0}\sum_{\omega} e^{i\delta\tau\omega}G(\omega) \\
&= \underbrace{\sum_{\omega}(G(\omega)+\frac{i}{\omega+T\frac{\pi}{2}})}_{\text{finite}} - \lim_{\delta\tau\to 0}\sum_{\omega} e^{i\delta\tau\omega}\frac{i}{\omega+\frac{\pi}{2\beta}} \\
&= \sum_{\omega}\left(G(\omega)+\frac{i}{\omega+\frac{\pi}{2\beta}}\right) + i\beta\left(\frac{1}{2}-\frac{i}{2}\right). \qquad \text{(B5)}
\end{aligned}$$

APPENDIX C: PERTURBATIVE CHECK FOR PPF-FRG AND PPF-PA AT LARGE TEMPERATURES

When considering large or intermediate temperatures, the one-loop ppf-fRG and the ppf-PA are error controlled with respect to the exact solution. In the one-loop truncation, diagrams of order $\frac{J^3}{T^2}$ and higher are neglected when calculating self energy or vertex. Therefore, the difference of the ED solution with the fRG solution should scale with $\frac{J^3}{T^2}$. This behavior can be seen in Fig. 6(a) for the self-energy of the Heisenberg dimer. For small temperatures, when $\frac{J}{T}$ becomes large, the scaling breaks down. In the ppf-PA, diagrams of order $\frac{J^5}{T^4}$ are neglected for the self energy. Compared to one-loop, this error scaling in ppf-PA is challenging to observe and can only be seen for very large frequency grids and at high temperatures, see Fig. 6(b).

APPENDIX D: FINITE-TEMPERATURE PHASE TRANSITIONS FOR OTHER TRUNCATION SCHEMES

In Sec. V B the ppf-fRG was applied to asess the magnetic phase transition in the cubic lattice AFM Heisenberg model. Here, we additionally investigate the ppf-fRG without Katanin truncation, the RPA [10,16], and the ppf-PA as further benchmark. The numerical RPA calculation is implemented using the ppf-fRG with Katanin truncation but a restriction to the terms including a site-sum $\sum_j$ on the right-hand side of Eqs. (A1), (A2) and (A5). The RPA confirms that the implementation of the PF term can reproduce the analytic spin mean-field result $T_c = 1.5$ and $\nu = 0.5$ for Heisenberg spins, see Figs. 7(a) and 7(c). The one-loop scheme without Katanin truncation yields $T_c = 1.29$ as well as a critical exponent consistent with the mean-field result $\nu = 0.5$, see Figs 7(b) and 7(d). In both the RPA and the one-loop truncation without Katanin, the spin projection exceeds unity.

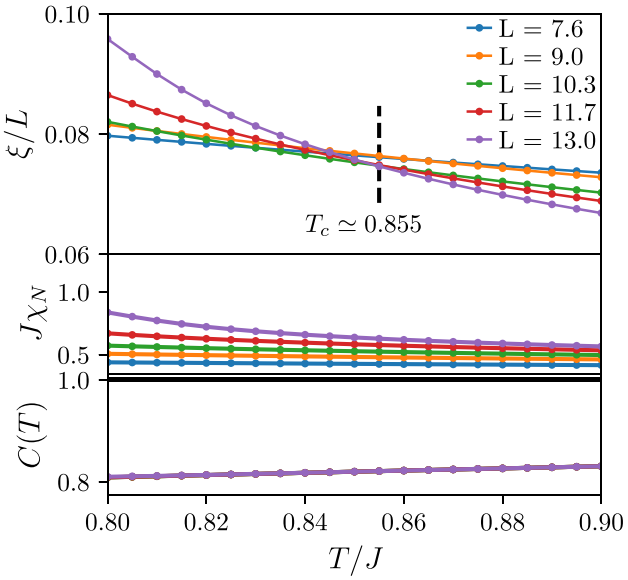

FIG. 8. ppf-PA: Correlation length ξ, Néel susceptibility χ_N and spin projection C for the nearest neighbor AFM Heisenberg model on the cubic lattice. We find a smeared-out line crossing at $T_c^{\text{ppf-PA}} \simeq 0.855$. A corresponding scaling collapse consistent with $\nu = 0.71$ or $\nu = 0.5$ could not be found. For $C(T)$ all five lines lie on top of each other.

We finally consider the ppf-PA formalism. As can be seen in the upper panel of Fig. 8, we indeed find a smeared-out line crossing for ξ/L, with the three largest system sizes crossing at $T_c \simeq 0.855$. However, the corresponding Néel susceptibilities (see the middle panel in Fig. 8) are substantially smaller than those obtained in ppf-fRG and a proper scaling collapse can be found neither for $\nu = 0.5$ nor $\nu = 0.71$. On the numerical side, we find that the rate of convergence drops considerably for $T/J \lesssim 1.0$ and the results, including the location of the intersection point of the ξ-scaling, become highly sensitive to numerical details such as the specific choice of mixing factors and solution algorithm. This could indicate that the ppf-PA fixed points in vicinity of the critical regime are strongly repulsive and hard to access in numerical calculations. In conclusion, for the assessment of magnetic phase transition the ppf-PA seems less reliable and consistent than the one-loop ppf-fRG scheme.

[1] A. Auerbach, *Interacting Electrons and Quantum Magnetism*, Graduate Texts in Contemporary Physics (Springer, New York, NY, 1994).

[2] A. Browaeys and T. Lahaye, Nat. Phys. **16**, 132 (2020).

[3] A. A. Abrikosov, Phys. Phys. Fiz. **2**, 5 (1965).

[4] We skip the overbar for fermionic operators like f_α or $n_\alpha = f_\alpha^\dagger f_\alpha$ where no confusion is possible.

[5] X.-G. Wen, *Quantum Field Theory of Many-Body Systems* (Oxford University Press, Oxford, 2007).

[6] J. W. Negele and H. Orland, *Quantum Many-Particle Systems* (Chapman and Hall/CRC, Boulder, CO, 2018).

[7] S. A. Kulagin, N. Prokof'ev, O. A. Starykh, B. Svistunov, and C. N. Varney, Phys. Rev. B **87**, 024407 (2013).

[8] S. A. Kulagin, N. Prokof'ev, O. A. Starykh, B. Svistunov, and C. N. Varney, Phys. Rev. Lett. **110**, 070601 (2013).

[9] Y. Huang, K. Chen, Y. Deng, N. Prokof'ev, and B. Svistunov, Phys. Rev. Lett. **116**, 177203 (2016).
[10] J. Reuther and P. Wölfle, Phys. Rev. B **81**, 144410 (2010).
[11] K. Van Houcke, E. Kozik, N. Prokof'ev, and B. Svistunov, Phys. Procedia **6**, 95 (2010).
[12] P. Kopietz, L. Bartosch, and F. Schütz, *Introduction to the Functional Renormalization Group*, Lecture Notes in Physics, Vol. 798 (Springer, Berlin, 2010).
[13] W. Metzner, M. Salmhofer, C. Honerkamp, V. Meden, and K. Schönhammer, Rev. Mod. Phys. **84**, 299 (2012).
[14] V. Popov and S. Fedotov, Zh. Eksp. Teor. Fiz **67**, 535 (1988).
[15] N. V. Prokof'ev and B. V. Svistunov, Phys. Rev. B **84**, 073102 (2011).
[16] J. Reuther, Frustrated Quantum Heisenberg Antiferromagnets: Functional Renormalization-Group Approach in Auxiliary-Fermion Representation, Ph.D. thesis, Karlsruher Institut für Technologie, 2011.
[17] D. Roscher, N. Gneist, M. M. Scherer, S. Trebst, and S. Diehl, Phys. Rev. B **100**, 125130 (2019).
[18] J. Reuther and R. Thomale, Phys. Rev. B **83**, 024402 (2011).
[19] J. Reuther, R. Thomale, and S. Trebst, Phys. Rev. B **84**, 100406(R) (2011).
[20] Y. Singh, S. Manni, J. Reuther, T. Berlijn, R. Thomale, W. Ku, S. Trebst, and P. Gegenwart, Phys. Rev. Lett. **108**, 127203 (2012).
[21] J. Reuther and R. Thomale, Phys. Rev. B **89**, 024412 (2014).
[22] Y. Iqbal, R. Thomale, F. Parisen Toldin, S. Rachel, and J. Reuther, Phys. Rev. B **94**, 140408(R) (2016).
[23] M. L. Baez and J. Reuther, Phys. Rev. B **96**, 045144 (2017).
[24] Y. Iqbal, T. Müller, P. Ghosh, M. J. P. Gingras, H. O. Jeschke, S. Rachel, J. Reuther, and R. Thomale, Phys. Rev. X **9**, 011005 (2019).
[25] J. Thoenniss, M. K. Ritter, F. B. Kugler, J. von Delft, and M. Punk, arXiv:2011.01268v1.
[26] D. Kiese, T. Müller, Y. Iqbal, R. Thomale, and S. Trebst, Phys. Rev. Res. **4**, 023185 (2022).
[27] R. Suttner, C. Platt, J. Reuther, and R. Thomale, Phys. Rev. B **89**, 020408(R) (2014).
[28] F. L. Buessen and S. Trebst, Phys. Rev. B **94**, 235138 (2016).
[29] Y. Iqbal, W.-J. Hu, R. Thomale, D. Poilblanc, and F. Becca, Phys. Rev. B **93**, 144411 (2016).
[30] D. Kiese, F. Ferrari, N. Astrakhantsev, N. Niggemann, P. Ghosh, T. Müller, R. Thomale, T. Neupert, J. Reuther, M. J. P. Gingras, S. Trebst, and Y. Iqbal, arXiv:2206.00264.
[31] F. L. Buessen, D. Roscher, S. Diehl, and S. Trebst, Phys. Rev. B **97**, 064415 (2018).
[32] Details will be covered in a forthcoming publication.
[33] M. K. Ritter, D. Kiese, T. Müller, F. B. Kugler, R. Thomale, S. Trebst, and J. von Delft, Eur. Phys. J. B **95**, 102 (2022).
[34] M. Hering and J. Reuther, Phys. Rev. B **95**, 054418 (2017).
[35] F. L. Buessen, V. Noculak, S. Trebst, and J. Reuther, Phys. Rev. B **100**, 125164 (2019).
[36] L. Classen, C. Honerkamp, and M. M. Scherer, Phys. Rev. B **99**, 195120 (2019).
[37] L. Gresista, D. Kiese, and S. Trebst, Eur. Phys. J. B **95**, 119 (2022).
[38] F. B. Kugler and J. von Delft, Phys. Rev. Lett. **120**, 057403 (2018).
[39] F. B. Kugler and J. von Delft, Phys. Rev. B **97**, 035162 (2018).
[40] F. B. Kugler and J. V. Delft, New J. Phys. **20**, 123029 (2018).
[41] N. Niggemann, B. Sbierski, and J. Reuther, Phys. Rev. B **103**, 104431 (2021).
[42] R. Nutakki, R. Röß-Ohlenroth, D. Volkmer, A. Jesche, H.-A. K. von Nidda, A. A. Tsirlin, P. Gegenwart, L. Pollet, and L. D. C. Jaubert, arXiv:2203.08780v1.
[43] F. L. Buessen, SciPost Phys. Codebases **5** (2022).
[44] C. Wetterich, Phys. Lett. B **301**, 90 (1993).
[45] A. A. Katanin, Phys. Rev. B **70**, 115109 (2004).
[46] P. Chalupa-Gantner, F. B. Kugler, C. Hille, J. von Delft, S. Andergassen, and A. Toschi, Phys. Rev. Res. **4**, 023050 (2022).
[47] A. Tagliavini, C. Hille, F. Kugler, S. Andergassen, A. Toschi, and C. Honerkamp, SciPost Phys. **6**, 009 (2019).
[48] C. Hille, F. B. Kugler, C. J. Eckhardt, Y.-Y. He, A. Kauch, C. Honerkamp, A. Toschi, and S. Andergassen, Phys. Rev. Res. **2**, 033372 (2020).
[49] N. Wentzell, G. Li, A. Tagliavini, C. Taranto, G. Rohringer, K. Held, A. Toschi, and S. Andergassen, Phys. Rev. B **102**, 085106 (2020).
[50] A. W. Sandvik, in *Fourteenth Training Course in the Physics of Strongly Correlated Systems*, edited by A. Avella and F. Mancini, AIP Conf. Proc. No. 1297 (AIP, New York, 2010), p. 135.
[51] R. K. Kaul, Phys. Rev. Lett. **115**, 157202 (2015).
[52] S. Pujari, T. C. Lang, G. Murthy, and R. K. Kaul, Phys. Rev. Lett. **117**, 086404 (2016).
[53] N. Niggemann, J. Reuther, and B. Sbierski, SciPost Phys. **12**, 156 (2022).
[54] J. Cardy, *Scaling and Renormalization in Statistical Physics*, 1st ed., (Cambridge University Press, Cambridge, England, 1996).
[55] A. W. Sandvik, Phys. Rev. Lett. **80**, 5196 (1998).
[56] S. M. Chester, W. Landry, J. Liu, D. Poland, D. Simmons-Duffin, N. Su, and A. Vichi, Phys. Rev. D **104**, 105013 (2021).
[57] J. Martin, Proc. R. Soc. London A **251**, 536 (1959).
[58] A. M. Tsvelik, Phys. Rev. Lett. **69**, 2142 (1992).
[59] Please see www.gauss-centre.eu.
[60] M. Hering, New States of Matter in Strongly Frustrated Quantum Magnets, Ph.D. thesis, Freie Universität Berlin, 2019.

Temperature flow in pseudo-Majorana functional renormalization for quantum spins

Benedikt Schneider,[1,2] Johannes Reuther,[3,4,5] Matías G. Gonzalez,[3,4] Björn Sbierski,[1,2,6] and Nils Niggemann[3,4,5]

[1]*Department of Physics and Arnold Sommerfeld Center for Theoretical Physics, Ludwig-Maximilians-Universität München, Theresienstrasse 37, 80333 Munich, Germany*

[2]*Munich Center for Quantum Science and Technology (MCQST), 80799 Munich, Germany*

[3]*Dahlem Center for Complex Quantum Systems and Institut für Theoretische Physik, Freie Universität Berlin, Arnimallee 14, 14195 Berlin, Germany*

[4]*Helmholtz-Zentrum für Materialien und Energie, Hahn-Meitner-Platz 1, 14109 Berlin, Germany*

[5]*Department of Physics and Quantum Centers in Diamond and Emerging Materials (QuCenDiEM) Group, Indian Institute of Technology Madras, Chennai 600036, India*

[6]*Institut für Theoretische Physik, Universität Tübingen, Auf der Morgenstelle 14, 72076 Tübingen, Germany*

(Received 24 January 2024; accepted 1 April 2024; published 3 May 2024)

We implement the temperature flow scheme first proposed by Honerkamp and Salmhofer [Phys. Rev. B **64**, 184516 (2001)] into the pseudo-Majorana functional renormalization group method for quantum spin systems. Since the renormalization group parameter in this approach is a physical quantity, the temperature T, the numerical efficiency increases significantly compared to more conventional renormalization group parameters, especially when computing finite-temperature phase diagrams. We first apply this method to determine the finite-temperature phase diagram of the J_1-J_2 Heisenberg model on the simple cubic lattice, where our findings support claims of a vanishingly small nonmagnetic phase around the high frustration point $J_2 = 0.25J_1$. Perhaps most importantly, we find the temperature flow scheme to be advantageous in detecting finite-temperature phase transitions as, by construction, a phase transition is never encountered at an artificial, unphysical cutoff parameter. Finally, we apply the temperature flow scheme to the dipolar XXZ model on the square lattice, where we find a rich phase diagram with a large nonmagnetic regime down to the lowest accessible temperatures. Wherever a comparison with error-controlled (quantum) Monte Carlo methods is applicable, we find excellent quantitative agreement with less than 5% deviation from the numerically exact results.

DOI: 10.1103/PhysRevB.109.195109

I. INTRODUCTION

Frustrated quantum spin systems are known for their rich phenomenology, allowing for peculiar effects such as order-by-disorder phase transitions [1,2] or magnetically disordered low-temperature phases [3–8]. Examples for the latter are valence bond solids or the highly sought-after quantum spin liquids, in which spin excitations fractionalize into emergent quasiparticles with unusual quantum statistics [9]. Given these desirable properties, there is a high demand for numerical techniques to treat these systems. While a few notable models are amenable to exact solutions [10] or quantum Monte Carlo [11–13], the treatment of general frustrated spin systems is notorious for its difficulty, even if significant approximations are employed.

In the last decade, the pseudo-fermion functional renormalization group (PFFRG) [14,15] has established itself as a useful tool for the numerical treatment of a variety of spin models at zero temperature due to its remarkable flexibility [16–21]. Treating spin operators through a fermionic particle representation to leverage the established functional renormalization group formalism, the PFFRG does not suffer from the sign problem and can treat translational invariant systems with arbitrary lattice geometry and two-body spin interactions. One of its shortcomings, the inclusion of unphysical states in the pseudo-fermion representation, can be circumvented at finite temperatures via the Popov-Fedotov trick [22,23] or by avoiding unphysical states altogether via a faithful spin representation in terms of Majorana fermions in the pseudo-Majorana (PM)-FRG [24,25]. It was found that these approaches accurately capture the interplay between thermal and quantum fluctuations, enabling computations of magnetic phase diagrams and critical temperatures in quantitative agreement to quantum Monte Carlo (whenever the latter is applicable). On the other hand, while PMFRG simulations at finite temperature represent an important method extension and become even perturbatively error controlled at large temperature, the cost of this improvement is significant, as it requires a separate solution of the numerically expensive FRG flow equations at each temperature. The renormalization group parameter is typically implemented through an artificial infrared cutoff Λ in the single-particle Green function, suppressing fermionic propagation with Matsubara frequencies $|\omega_n| \ll \Lambda$. An alternative formulation was first demonstrated by Honerkamp and Salmhofer in Ref. [26] for systems of itinerant fermions where *temperature* was employed as a flow parameter instead. In this approach, a single FRG flow along the physical temperature provides a whole slice through a finite-temperature phase diagram at once. On the other hand, however, the usual notion of the renormalization group (RG)

as a successive integration of UV degrees of freedom is lost [27,28].

Motivated by the above advantages, in this paper we demonstrate an implementation of the temperature flow scheme in the context of the PMFRG. Specifically, in Sec. II we explain the key methodological step in this approach, which amounts to defining rescaled fields and vertex functions. We present flow equations for the rescaled vertices and observables in terms of the rescaled fields in Sec. III. Formally, this temperature flow formulation of the FRG corresponds to an independent method, whose results in the strong coupling limit can differ from the conventional scheme using a Matsubara frequency cutoff (hereafter referred to as the Λ-flow scheme). Hence, we first benchmark our method on the Heisenberg model on the simple cubic lattice in Sec. IV A against error-controlled quantum Monte Carlo and explain crucial differences between the Λ-flow and temperature flow (T-flow) schemes in Sec. IV B. Next, in Sec. V we demonstrate an investigation of a more application-oriented frustrated spin system of high current research interest. Specifically, in Sec. V we treat the square lattice dipolar XXZ model amenable to experimental realizations [29,30], where we exploit the efficiency of the temperature flow formalism in determining the finite-temperature phase diagram. Finally, we summarize our findings in Sec. VI.

II. ACTION AND FIELD RESCALING

We assume a general spin-1/2 Hamiltonian

$$H = \sum_{i,\alpha} h_i^\alpha S_i^\alpha + \frac{1}{2} \sum_{i,j,\alpha_1,\alpha_2} S_i^{\alpha_1} J_{ij}^{\alpha_1\alpha_2} S_j^{\alpha_2}, \tag{1}$$

where S_i^α with $\alpha = x, y, z$ are the components of a spin-1/2 operator on site i, $J_{ij}^{\alpha\beta}$ are general anisotropic spin interactions, and h_i^α is a site-dependent magnetic field. We map H onto a pseudo-Majorana Hamiltonian using the SO(3) representation [31,32]:

$$S_i^x = -i\eta_i^y\eta_i^z,\ S_i^y = -i\eta_i^z\eta_i^x,\ S_i^z = -i\eta_i^x\eta_i^y. \tag{2}$$

This representation's main advantage is the fact that it does not feature unphysical states, and thus we may proceed without the need of any projection.

To solve the corresponding Majorana Hamiltonian, we first consider a general system of interacting Majoranas with the action written in imaginary time τ [24]:

$$\begin{aligned} S = &\frac{1}{2}\int_0^\beta \mathrm{d}\tau\ \eta_{\alpha_1}(\tau)(\delta_{\alpha_1\alpha_2}\partial_\tau + iA_{\alpha_1\alpha_2})\eta_{\alpha_2}(\tau) \\ &+ \frac{1}{4!}\int_0^\beta \mathrm{d}\tau\ V_{\alpha_1\alpha_2\alpha_3\alpha_4}\eta_{\alpha_1}(\tau)\eta_{\alpha_2}(\tau)\eta_{\alpha_3}(\tau)\eta_{\alpha_4}(\tau). \end{aligned} \tag{3}$$

Here, Einstein summation is assumed, $\beta = 1/T$ is the inverse temperature, and $\eta_\alpha(\tau)$ are real and antisymmetric Majorana fields satisfying $\{\eta_\alpha, \eta_\beta\} = \delta_{\alpha\beta}$ and $\eta_\alpha(\tau)^\dagger = \eta_\alpha(-\tau)$, while α refers to indices labeling an arbitrary set of single-particle quantum numbers. The key step in the derivation of a temperature flow FRG scheme is to gather all temperature dependence in the noninteracting part of the Hamiltonian. Here, we do this by introducing a modified Fourier transform,

$$\begin{aligned} \eta(\omega) &= T^{\frac{1}{4}}\int_0^1 \mathrm{d}\tau\ e^{-i\omega\tau}\eta\Big(\frac{\tau}{T}\Big), \\ \eta\Big(\frac{\tau}{T}\Big) &= T^{-\frac{1}{4}}\sum_\omega e^{i\omega\tau}\eta(\omega), \end{aligned} \tag{4}$$

with the dimensionless Matsubara frequencies $\omega = \pi(2n+1)$ and $n \in \mathbb{Z}$, which is more convenient but otherwise equivalent to the rescaling of fields as done by Honerkamp and Salmhofer [26]. In the case of $A_{\alpha_1\alpha_2} = 0$, it is also equivalent to the rescaling introduced in the interaction-flow scheme of Honerkamp *et al.* [28,33]. Crucially, the transformation is chosen in such a way that no implicit temperature dependencies enter through frequencies and the interacting part of the rescaled action. This way, we may express Eq. (3) as

$$\begin{aligned} S = &-\frac{1}{2}\sum_{\substack{\omega_1,\omega_2\\ \alpha_1\alpha_2}} \eta_{\alpha_1}(\omega_1)G^{-1,T}_{0;\alpha_1\alpha_2}(\omega_1,\omega_2)\eta_{\alpha_2}(\omega_2) \\ &+ \frac{1}{4!}\sum_{\substack{\omega_1,\ldots,\omega_4\\ \alpha_1\ldots\alpha_4}} V_{\alpha_1\alpha_2\alpha_3\alpha_4}\delta_{\omega_1+\omega_2+\omega_3+\omega_4,0} \\ &\times \eta_{\alpha_1}(i\omega_1)\eta_{\alpha_2}(i\omega_2)\eta_{\alpha_3}(i\omega_3)\eta_{\alpha_4}(i\omega_4), \end{aligned} \tag{5}$$

where we define

$$G^{-1,T}_{0;\alpha_1\alpha_2}(\omega_1,\omega_2) = \frac{i}{\theta(T)}[\omega_1\delta_{\alpha_1,\alpha_2} - \theta(T)^2 A_{\alpha_1\alpha_2}]\delta_{\omega_1,-\omega_2} \tag{6}$$

as the bare Green function. The crucial insight is that $\theta(T) = T^{-\frac{1}{2}}$ can be seen as a regulator function since it implies a vanishing propagator $G_0^T \to 0$ for $T \to \infty$. In the usual FRG formalism this is achieved by a regulator $G_0 \to \Theta^\Lambda G_0$, where the function Θ^Λ vanishes at the start of the flow at $\Lambda \to \infty$. We note that while this suppression does not by itself act as an infrared cutoff of the Matsubara frequencies, the finite temperature has a similar effect of regularizing infrared divergencies as it shifts the smallest Matsubara frequency away from zero. In Eq. (5), the temperature dependence is fully contained in the regulator $\theta(T)$, which trivially generates the same hierarchy of flow equations as in the standard FRG formalism (see, for example, Ref. [34]) upon simply replacing all derivatives with respect to the artificial cutoff Λ by derivatives with respect to T.

III. FLOW EQUATIONS AND OBSERVABLES

A. General flow equations

The FRG flow equations are derived from the action [Eq. (5)] in full analogy to the standard PMFRG formalism [24]. In this fermionic language, Majorana Green functions are defined as the bare propagator G_0^T, full propagator G^T, and connected two-particle Green function $G_c^{4,T}$:

$$G^T_{1,2} = \langle\eta_2\eta_1\rangle, \tag{7}$$

$$\begin{aligned} G^{4,T}_{c;1,2,3,4} = &\langle\eta_4\eta_3\eta_2\eta_1\rangle - \langle\eta_4\eta_3\rangle\langle\eta_2\eta_1\rangle \\ &+ \langle\eta_4\eta_2\rangle\langle\eta_3\eta_1\rangle - \langle\eta_3\eta_2\rangle\langle\eta_4\eta_1\rangle, \end{aligned} \tag{8}$$

where we have introduced the superlabels $1 = (i_1, \mu_1, \omega_1)$ that collectively describe site, spin, and frequency index,

where the latter emerges after Fourier transforming the associated imaginary-time-ordered correlation functions.

In the FRG formalism, the objects of interest are the self-energy $\Sigma_{1,2}$ and the four-point vertex $\Gamma_{1,2,3,4}$ which are related to Green functions via the Dyson equation and the tree expansion [34]:

$$\Sigma^T_{1,2} = G^{-1,T}_{0;1,2} - G^{-1,T}_{1,2}, \tag{9}$$

$$\Gamma^T_{1,2,3,4} = -\sum_{1',\ldots,4'} G^{-1,T}_{1,1'} G^{-1,T}_{2,2'} G^{-1,T}_{3,3'} G^{-1,T}_{4,4'} G^{4,T}_{c;1',2',3',4'}. \tag{10}$$

As outlined in Ref. [24], in thermal equilibrium the Green functions and vertices are frequency conserving, while due to a local $\mathbb{Z}_2$ gauge symmetry in the Majorana representation [Eq. (2)], the propagator and self-energy are local and the vertex is bilocal:

$$G^T_{1,2} = G^T_{i_1;\alpha_1\alpha_2}(\omega_2)\delta_{i_1,i_2}\delta_{\omega_1,-\omega_2}, \tag{11}$$

$$G^{-1,T}_{0;1,2} = G^{-1,T}_{0;i_1;\alpha_1\alpha_2}(\omega_1)\delta_{i_1,i_2}\delta_{\omega_1,-\omega_2}, \tag{12}$$

$$\Sigma^T_{1,2} = \Sigma^T_{i_1;\alpha_1\alpha_2}(\omega_1)\delta_{i_1,i_2}\delta_{\omega_1,-\omega_2}, \tag{13}$$

$$\begin{aligned}\Gamma^T_{1,2,3,4} = {}& \delta_{\omega_1+\omega_2+\omega_3+\omega_4,0} \\ & \times [\Gamma^T_{i_1 i_3;\alpha_1\alpha_2\alpha_3\alpha_4}(\omega_1,\omega_2,\omega_3,\omega_4)\delta_{i_1,i_2}\delta_{i_3,i_4} \\ & - \Gamma^T_{i_1 i_2;\alpha_1\alpha_3\alpha_2\alpha_4}(\omega_1,\omega_3,\omega_2,\omega_4)\delta_{i_1,i_3}\delta_{i_2,i_4} \\ & + \Gamma^T_{i_1 i_2;\alpha_1\alpha_4\alpha_2\alpha_3}(\omega_1,\omega_4,\omega_2,\omega_3)\delta_{i_1,i_4}\delta_{i_2,i_3}].\end{aligned} \tag{14}$$

In the following we provide the flow equations for the interacting free energy $f_{\text{int}} = F_{\text{int}}/N = -T\log(\frac{Z}{Z_0})$, where N is the number of sites, the self-energy $\Sigma^T_{i_1;\alpha_1,\alpha_2}(\omega_1)$ and vertex $\Gamma^T_{i_1 i_3;\alpha_1\alpha_2\alpha_3\alpha_4}(\omega_1,\omega_2,\omega_3,\omega_4)$ that can be derived equivalently to Ref. [24]. With the transfer frequencies

$$s = \omega_1 + \omega_2 = -\omega_3 - \omega_4, \tag{15}$$

$$t = \omega_1 + \omega_3 = -\omega_2 - \omega_4, \tag{16}$$

$$u = \omega_1 + \omega_4 = -\omega_2 - \omega_3, \tag{17}$$

these flow equations are given by

$$\frac{d}{dT}\frac{f_{\text{int}}}{T} = \frac{1}{2N}\sum_k \sum_\omega \sum_{\beta_1\ldots\beta_4} \left(\frac{\partial}{\partial T} G^T_{0;k;\beta_1\beta_2}(\omega)\right) \Sigma^T_{k;\beta_2\beta_3}(\omega) G^T_{k;\beta_3\beta_4}(\omega) G^{-1,T}_{0;k;\beta_4\beta_1}(\omega), \tag{18}$$

$$\frac{d}{dT}\Sigma^T_{i;\alpha_1\alpha_2}(\omega) = \frac{1}{2}\sum_k \sum_{\omega'} \sum_{\beta_1\beta_2} \Gamma^T_{ki;\beta_2\beta_1\alpha_1\alpha_2}(-\omega',\omega',\omega,-\omega)\frac{\partial}{\partial T}\left[G^T_{k;\beta_1\beta_2}(\omega')\right], \tag{19}$$

$$\frac{d}{dT}\Gamma^T_{ij;\alpha_1\alpha_2\alpha_3\alpha_4}(s,t,u) = X_{ij;\alpha_1,\alpha_2;\alpha_3,\alpha_4}(s,t,u) - \tilde{X}_{ij;\alpha_1,\alpha_3;\alpha_2,\alpha_4}(t,s,u) + \tilde{X}_{ij;\alpha_1,\alpha_4;\alpha_2,\alpha_3}(u,s,t), \tag{20}$$

$$X_{ij;\alpha_1,\alpha_2;\alpha_3,\alpha_4} = \frac{1}{2}\sum_{k,\omega} \sum_{\beta_1\ldots\beta_4} \Gamma^T_{ik;\alpha_1\alpha_2\beta_1\beta_2}(\omega_1,\omega_2,\omega-s,-\omega)\Gamma^T_{kj;\beta_3\beta_4\alpha_3\alpha_4}(\omega,s-\omega,\omega_3,\omega_4)P^T_{kk;\beta_2\beta_3;\beta_4\beta_1}(\omega,\omega-s), \tag{21}$$

$$\tilde{X}_{ij;\alpha_1,\alpha_2;\alpha_3,\alpha_4} = \sum_{\omega} \sum_{\beta_1\ldots\beta_4} \Gamma^T_{ij;\alpha_1\beta_1\alpha_3\beta_3}(\omega_1,-\omega,\omega_2,\omega-s)\Gamma^T_{ij;\beta_2\alpha_2\beta_4\alpha_4}(\omega,\omega_3,s-\omega,\omega_4)P^T_{ij;\beta_1\beta_2;\beta_4\beta_3}(\omega,\omega-s), \tag{22}$$

where we define the single-scale propagator as

$$\begin{aligned}\frac{\partial}{\partial T}G^T_{k;\alpha_1\alpha_2}(\omega) = {}& -\sum_{\beta_1\beta_2} G^T_{k;\alpha_1\beta_1}(\omega)G^T_{k;\beta_2\alpha_2}(\omega) \\ & \times \left(\frac{\partial}{\partial T}G^{-1,T}_{0;k;\beta_1\beta_2}(\omega)\right),\end{aligned} \tag{23}$$

and the bubble propagator as

$$P^T_{ij;\alpha_1\alpha_2;\alpha_3\alpha_4}(\omega,\omega-s) = \frac{\partial}{\partial T}\left[G^T_{i;\alpha_1\alpha_2}(\omega)G^T_{j;\alpha_3\alpha_4}(\omega-s)\right]. \tag{24}$$

The main differences between the flow equations presented here and those of Ref. [24] are the definition of the propagator and the absence of factors T associated with the frequency sums. The initial conditions follow immediately from the fact that the bare propagator G^T_0 vanishes at $T=\infty$ so that the only nonzero vertex at the beginning of the flow is the bare spin interaction:

$$\lim_{T\to\infty}\frac{f_{\text{int}}}{T} = 0, \tag{25}$$

$$\Sigma^{T\to\infty}_{i;\alpha_1\alpha_2}(\omega) = 0, \tag{26}$$

$$\Gamma^{T\to\infty}_{ij,\alpha_1\alpha_2\alpha_3\alpha_4}(s,t,u) = -\sum_{\beta_1\beta_2}\epsilon_{\alpha_1\alpha_2\beta_1}J^{\beta_1\beta_2}_{ij}\epsilon_{\beta_2\alpha_1\alpha_2}, \tag{27}$$

where $\epsilon_{\alpha_1\alpha_2\alpha_4}$ is the fully antisymmetric tensor. Note that by convention the magnetic field is implemented in the off-diagonal elements of the bare inverse Green function in Eq. (6) instead of in the self-energy with $A_{\alpha_1\alpha_2}$ given by

$$A_{\alpha_1\alpha_2} = -\sum_\beta \epsilon_{\alpha_1\alpha_2\beta}h^\beta. \tag{28}$$

In the Katanin truncation scheme [35] that we use for all calculations below, the partial derivative in Eq. (24) is changed to a total derivative, thus including a feedback of the self-energy derivative into the vertex flow equation. This approximation is originally motivated by its inclusion of contributions from the six-point vertex. In this truncation, all ladder-type diagrams and diagrams of the random-phase approximation (RPA) are included [36], and ordering tendencies are dampened that are often overestimated in the bare one-loop approximation [15]. It was previously used to obtain quantitatively accurate critical temperatures and spin-structure factors [25].

We emphasize that the self-energy defined above is related to the Λ-flow self-energy as $\Sigma^{\Lambda=0}(\omega) = T^{1/2}\Sigma^T(\omega)$, while the vertex is unchanged, $\Gamma^{\Lambda=0}_{ij}(s,t,u) = \Gamma^T_{ij}(s,t,u)$ [37]. In practice, one can further reduce the number of independent vertex components by considering the spin and lattice symmetries of the model of interest [24,38].

B. Observables

A feature of the temperature flow is that we have direct access to the differentiated vertices with respect to temperature. Therefore we have direct access to the free energy f and mean energy $U = \langle H\rangle$, while the heat capacity $C = \frac{dU}{dT}$ can be obtained by numerical differentiation. By using the known result for the partition function of free spins-1/2 in a magnetic field $\mathbf{h}_i$,

$$\log(Z_0) = \sum_i \log\left[2\cosh\left(\frac{|\mathbf{h}_i|}{T}\right)\right], \tag{29}$$

we can write them as

$$f = f_{\text{int}} - T\log(Z_0), \tag{30}$$

$$\frac{U}{N} = -T^2\frac{d}{dT}\left(\frac{f_{\text{int}}}{T} - \log(Z_0)\right), \tag{31}$$

$$C = \frac{dU}{dT}. \tag{32}$$

Other observables are the magnetization $M_i^\alpha = \langle S_i^\alpha\rangle$, magnetic susceptibility $\chi_{ij}^{\alpha_1\alpha_2}(\omega) = \int_0^\beta e^{i\omega\tau}\langle S_i^{\alpha_2}(\tau)S_j^{\alpha_1}(0)\rangle$, and the equal-time spin-spin correlator $\langle S_i^{\alpha_2}S_j^{\alpha_1}\rangle$:

$$M_j^\alpha = -iT^{\frac{1}{2}}\sum_\omega\sum_{\beta_1\beta_2}\frac{\epsilon_{\alpha\beta_1\beta_2}}{2}G^T_{j;\beta_2\beta_1}(\omega), \tag{33}$$

$$\left\langle S_i^{\alpha_1}S_j^{\alpha_2}\right\rangle = \frac{1}{\beta}\sum_\omega \chi_{ij}^{\alpha_2\alpha_1}(\omega), \tag{34}$$

$$\chi_{ij}^{\alpha_1\alpha_2}(\omega) = \beta\delta_{0,\omega}M_i^{\alpha_1}M_j^{\alpha_2} + \delta_{ij}\sum_{\substack{\omega_1\\ \alpha\beta\gamma\delta}}\frac{\epsilon_{\alpha_2\beta_1\beta_2}\epsilon_{\alpha_1\beta_3\beta_4}}{4}\left[G^T_{i;\beta_4\beta_1}(\omega_1)G^T_{i;\beta_2\beta_3}(\omega_1+\omega) - G^T_{i;\beta_3\beta_1}(\omega_1)G^T_{i;\beta_2\beta_4}(\omega_1+\omega)\right]$$
$$+\sum_{\substack{\omega_1\omega_2\\ \beta_1\ldots\beta_4\\ \gamma_1\ldots\gamma_4}}\frac{\epsilon_{\alpha_2\beta_1\beta_2}\epsilon_{\alpha_1\beta_3\beta_4}}{4}G^T_{\beta_4\gamma_4}(\omega_1-\nu)G^T_{\gamma_3\beta_3}(\omega_1)G^T_{\beta_2\gamma_2}(\omega_2+\nu)G^T_{\gamma_1\beta_1}(\omega_2)\Gamma^T_{ij;\gamma_4\gamma_3\gamma_2\gamma_1}(-\nu,-\omega_1-\omega_2,\omega_2+\nu-\omega_1). \tag{35}$$

To verify the correctness of our implementation, in Appendix A we consider a simple, exactly solvable model of two interacting spins. Note that this model poses the same methodological challenge to our method as infinite systems and thus provides an excellent benchmark. Overall, we observe similar or better results as compared to the Λ-flow method. Note that as detailed in Appendix B, other checks via exact relations between vertices are also possible but less reliable, as they check only for conservations of specific constants of motions which may be unrelated to quantities of interest.

IV. J_1-J_2 CUBIC LATTICE HEISENBERG MODEL

A. Magnetic phase diagram

As a first nontrivial test of the T-flow PMFRG approach, we revisit the antiferromagnetic J_1-J_2 Heisenberg model on the cubic lattice which was previously treated in the Λ-flow formalism [25]. Here, J_1 and J_2 are the antiferromagnetic exchange interactions on nearest- and next-nearest-neighbor bonds, respectively:

$$H = J_1\sum_{\langle i,j\rangle,\alpha}S_i^\alpha S_j^\alpha + J_2\sum_{\langle\langle i,j\rangle\rangle,\alpha}S_i^\alpha S_j^\alpha. \tag{36}$$

We set $J_1 = 1$ and first consider the case $J_2 = 0$, where the model is unfrustrated and we expect a transition to antiferromagnetic (AFM) Néel order with wave vector $\mathbf{k} = (\pi,\pi,\pi)$ at some finite temperature that can be compared to quantum Monte Carlo. Figure 1(a) displays a critical scaling of the correlation length as indicated by the line crossings of ξ/L, where L is the spatial cutoff distance beyond which vertices are approximated as zero. We detect the critical temperature $T_c \approx 0.97$; for details see Appendix C and Refs. [15,25,39]. Our result is in good agreement with quantum Monte Carlo ($T_c = 0.946$). Incidentally, and perhaps accidentally, we find this result to be marginally better compared to the established Λ-flow PMFRG, which slightly underestimated the critical temperature as $T_c = 0.905$ [25].

In the frustrated regime at finite $J_2 > 0$, Monte Carlo simulations for classical spins ($|\mathbf{S}| = 1$) [40] find order at finite temperatures throughout the phase diagram, with a continuous phase transition to Néel order for $J_2 < 0.25$. For $J_2 > 0.25$ antiferromagnetic stripe order with wave vector $\mathbf{k} = (\pi,\pi,0)$ (and symmetry related wave vectors) is reached via a first-order phase transition, see Fig. 1(c).

In the quantum spin-1/2 case, the possible presence of a small nonmagnetic region around $J_2 = 0.25$ is still debated. At $T = 0$, linear spin wave theory [41] and the coupled cluster method [42] predict antiferromagnetic order from $J_2 = 0$ that transitions into a small paramagnetic phase at $J_2 \approx 0.25$ before undergoing a second phase transition into the antiferromagnetic stripe phase for $J_1/J_2 > 0.25$. On the other hand, nonlinear corrections [41] to spin-wave theory as well as a variational cluster approach [43] predict no paramagnetic phase between the two ordered phases. Using our T-flow PMFRG as outlined above, we determine the finite-temperature phase diagram, detecting critical temperatures down to a minimum simulation temperature of $T \sim 0.05$, with the case $J_2 = 0.31$ shown in Fig. 1(b). The full phase diagram obtained this way is shown in Fig. 1(c). In agreement with

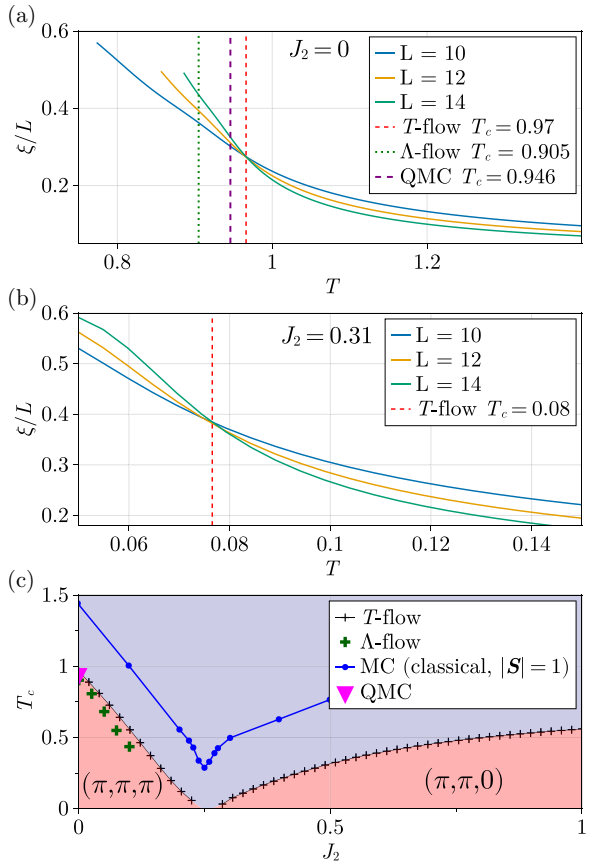

FIG. 1. PMFRG results for the J_1-J_2 Heisenberg model on the cubic lattice. (a) Finite-size scaling of the correlation length using T-flow PMFRG for the simple cubic Heisenberg antiferromagnet at $J_2 = 0$ in comparison the standard Λ-flow PMFRG [25] and quantum Monte Carlo (QMC) [39]. (b) Finite-size scaling of the correlation length using T-flow PMFRG for the simple cubic Heisenberg antiferromagnet at $J_2 = 0.31$. (c) Phase diagram: The transition temperature for the classical model with unit spin length is reproduced from Ref. [40] (blue). The critical temperatures obtained from T-flow (black crosses) predicts slightly larger transition temperatures than the standard Λ-flow PMFRG (green) in the Néel-ordered regime. At $J_2 \gtrsim 0.25$ the T-flow scheme detects critical scaling towards a stripe-ordered phase, in qualitative agreement to the classical model. This critical temperature is not detected in the Λ-flow scheme.

other methods, we find a phase transition to antiferromagnetic Néel order for $J_2 \lesssim 0.25$ and to antiferromagnetic stripe order for $J_2 \gtrsim 0.25$. Due to the observed critical scaling in system size, all phase transitions are of second order. In between, we observe a small regime without any sign of magnetic order. Although intrinsic consistency checks seem to indicate less accurate results at lower temperatures (see Appendix B), our findings support claims that there might be a small region with a paramagnetic phase in between the antiferromagnetic Néel- and stripe-ordered phases.

B. Discussion of the stripe phase transition

As discussed in the previous section, we detect a second-order phase transition towards stripe order in the regime $J_2 \gtrsim 0.25$. Although expected from other methods, this result initially appears incompatible with previous findings in the Λ-flow scheme, which, despite observing large dominant stripe correlations could not detect a critical scaling [25]. We now show that this apparent discrepancy has a simple explanation by further including this artificial infrared cutoff Λ into our temperature flow scheme and interpreting it as an auxiliary parameter.

To compare differences between the two flow schemes, we dress the temperature flow propagator with the usual cutoff of the Λ-flow [24], $\Theta^\Lambda(\omega) = \frac{T^2\omega^2}{T^2\omega^2+\Lambda^2}$, so that

$$G^{-1,T}_{i;\alpha_1\alpha_2}(\omega_1) = \frac{1}{\Theta^\Lambda(\omega_1)} G^{-1,T}_{0;i;\alpha_1\alpha_2}(\omega_1) - \Sigma^T_{i;\alpha_1\alpha_2}(\omega_1). \tag{37}$$

By construction, in the limit $\Lambda = 0$, Eq. (37) reduces to the propagator introduced in the previous section. This propagator is now equal to the Λ-flow propagator in the entire T, Λ parameter space (aside from the trivial prefactors of $T^{1/2}$ due to the rescaling of Majorana fields). Hence, physical observables at large T or Λ will be equal in both approaches. If both $T \lesssim 1$ and $\Lambda \lesssim 1$, however, the approximation of neglecting higher-order vertices becomes uncontrolled, generally allowing for different results between the two methods. Figure 2 shows a comparison of the T-flow scheme (dressed with a Λ cutoff) and the Λ-flow scheme as a function of T and Λ, both at $J_2 = 0$ (Néel order) and $J_2 = 1$ (stripe order). As both T and Λ suppress spin correlations, magnetic order can only be stabilized in a finite region around $T = \Lambda = 0$, as indicated schematically in Figs. 2(a) and 2(b). As displayed further, the conventional Λ-flow scheme approaches the ordered phase along lines of constant T, while the T-flow approaches it along constant Λ.

The remaining panels (c)–(f) display the difference of the rescaled correlation length for the dominant susceptibility,

$$\Delta\tilde{\xi}_{1,2} = \frac{\xi(L_1)}{L_1} - \frac{\xi(L_2)}{L_2}, \tag{38}$$

for two different spatial cutoff distances $L_1 > L_2$. At the phase transition, we have $\xi(L) \propto L$ and thus $\Delta\tilde{\xi} = 0$. Consequently, for large enough $L_{1,2}$, we can identify the region with $\Delta\tilde{\xi} > 0$ ($\Delta\tilde{\xi} < 0$) as the ordered (disordered) phase.

For $J_2 = 0$ [see Figs. 2(c) and 2(d)] both Λ and T-flows find magnetic order at $\Lambda = 0$ for $T \approx 0.9$. Although RG flows can become unphysical below the critical scale of a phase transition, in the Λ-flow the susceptibility and correlation lengths converge to a large but finite plateau value. For small temperatures of $T < 0.3$, on the other hand, we observe a very different behavior of the correlation length, which displays a peak as a function of Λ at a finite $\Lambda \sim 1.25$, indicated by the white circle in Fig. 2(c). This sharp feature, also referred to as a *flow breakdown*, originates from a peak of the maximum susceptibility (see Appendix C) in the renormalization flow. In zero-temperature approaches it is an established signature of a phase transition [14,15,44,45], whose detection, however, can be ambiguous in practice.

Below the critical temperature, the T-flow correlations grow rapidly. Numerically, this requires increasingly smaller steps when solving the flow equations, which we eventually terminate as seen for $J_2 = 0$ in Fig. 2(d). Strikingly, at a finite

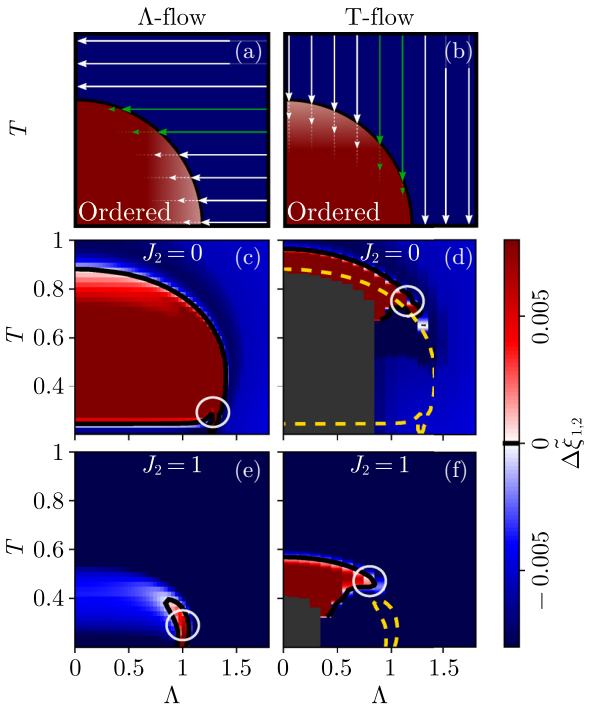

FIG. 2. Magnetic phase diagram for the Λ-flow scheme (left) and the T-flow scheme (right), both as functions of physical temperature T and the artificial infrared cutoff Λ. (a, b) Schematic picture of the phase diagram and the direction of the flow (arrows) for both schemes. Each arrow represents an independent FRG run. Green arrows indicate problematic flow paths along the circumference of the ordered dome close to the phase boundary. (c)–(f) The ordered (paramagnetic) phase is determined by a positive (negative) difference of the rescaled correlation length in Eq. (38) between two runs for $L_1 = 14$ and $L_2 = 12$. Additionally, the phase boundaries given by the contour $\Delta\tilde{\xi} = 0$ are indicated by black lines. In (d) and (f), the phase boundary from the Λ-flow scheme is displayed in yellow. White circles highlight exemplary positions of breakdowns of the PMFRG flow. For better visibility, the color range is limited to a small region around $\Delta\tilde{\xi} = 0$.

value of Λ in Fig. 2(d), the scaling collapse is no longer obtained, leaving the right boundary of the magnetic phase seemingly absent, with similar flow breakdown features as found in the Λ-flow scheme, also indicated via a white circle.

We now move on discussing the T-Λ phase diagrams at $J_2 = 1$ for both the Λ-flow and T-flow schemes in Figs. 2(e) and 2(f), respectively. The T-flow result in Fig. 2(f) resembles the observation in Fig. 2(d) in that a critical scaling is only found at small Λ but disappears as Λ increases. The Λ-flow behavior at $J_2 = 1$ in Fig. 2(e) also resembles Figs. 2(d) and 2(f), *but with the roles of* T *and* Λ *reversed.* While Fig. 2(e) only displays a phase transition at finite $\Lambda \sim 1$ and small $T \lesssim 0.3$, critical scaling is never found in the physically relevant limit $\Lambda = 0$. This makes it impossible to extract a critical temperature in the $J_2 > 0.25$ parameter regime within the Λ-flow scheme.

We interpret these results as follows: Clearly, both Λ-flow and T-flow PMFRG methods are sensitive to ordering tendencies. However, each approach is better suited to detect phase boundaries that do not require a long flow through a critical region close to a magnetic phase. For example, such situations occur when a magnetically ordered phase is only grazed during the renormalization group flow in either Λ or T, shown by green arrows in panels (a) and (b) of Fig. 2. In these critical regions, vertices grow large and the approximation of neglecting higher-order vertices is no longer accurate. Concretely, this means that the Λ-flow scheme is more sensitive to phase boundaries found at finite Λ, while the T-flow is better at detecting the opposite boundary at finite T and small values of Λ. Indeed, one can approximate the shape of the full magnetic phase in the T-Λ space by the complement of both methods. This is visualized by the yellow dashed line in Figs. 2(d) and 2(f).

We see that for $J_1 = 1$ the challenge to resolve magnetic order in the Λ-flow scheme is especially pronounced as the top phase boundary in T-Λ space is particularly flat [see Fig. 2(f)] and the ordering temperature much smaller. To extract physical quantities, the FRG in the Λ-flow scheme needs to be solved all the way down to $\Lambda = 0$, possibly flowing through an ordering transition, where the truncation of flow equations is known to break down. The temperature flow, on the other hand, needs to be followed only slightly beyond the boundary of the phase transition. We can therefore conclude that the T-flow scheme is the favorable method as it approaches the phase boundary from the physically relevant direction.

V. SQUARE LATTICE DIPOLAR XXZ MODEL

In this section we present another application of the T-flow PMFRG, demonstrating that this approach is capable to treat a complex long-range interacting two-dimensional spin model of current research interest and to accurately capture its finite temperature ordering transitions.

If an ordered phase in two dimensions breaks a continuous (spin-rotation) symmetry, a finite T_c is only possible for sufficiently long-ranged interactions [46,47]. Dipolar interactions, decaying with distance as $1/r^3$ are such an example of experimental relevance, as they can be realized in systems of cold atoms and molecules [29,48,49] or Rydberg atom arrays [30]. Here, following the early work of Peter *et al.* [50], we focus on the spin-1/2 square lattice XXZ model with isotropic dipolar interactions and U(1) spin-rotation symmetry,

$$H = \sum_{(i,j)} J^x_{(i,j)} \left(S^x_i S^x_j + S^y_i S^y_j \right) + J^z_{(i,j)} S^z_i S^z_j, \tag{39}$$

where the sum is over all bonds of the square lattice, and $J^x_{(i,j)} = \sin(\theta)/r^3_{ij}$, $J^z_{(i,j)} = \cos(\theta)/r^3_{ij}$ with $r_{ij} = |\mathbf{r}_i - \mathbf{r}_j|$ and $\mathbf{r}_i$ is the position of lattice site i. The angle $\theta \in [0, 2\pi)$ controls the ratio between Ising and in-plane interactions and interpolates between the special cases of AFM-Ising ($\theta = 0$), XY-AFM ($\theta = \pi/2$), Ising-FM ($\theta = \pi$), and XY-FM model ($\theta = 3\pi/2$), see Fig. 3.

For $J_x \leqslant 0$ ($\theta \in [\pi, 2\pi]$) the model is free of the sign problem and thus amenable to quantum Monte Carlo simulation. Results exist for critical temperatures of the Heisenberg-FM and the XY-FM case, $\theta/\pi = 1.25$ and 1.5 [38,51]. For the Ising cases at $\theta = 0, \pi$, classical Monte Carlo simulations are applicable. For the Ising-AFM case, $T_c = 0.296$ was found

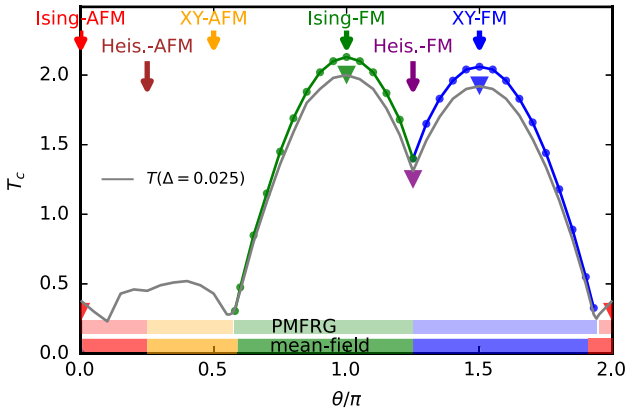

FIG. 3. Finite-temperature phase diagram for the square lattice dipolar XXZ model of Eq. (39). Dots denote the critical temperature found from finite-size scaling of the T-flow PMFRG susceptibility. Lines are guides to the eye. The gray line denotes the lowest accessible temperature below which the internal consistency check for the PMFRG is violated by 2.5%, see Appendix B. The color of the upper horizontal bar denotes the dominant susceptibility (Ising-AFM in red, XY-AFM in orange) at this lowest temperature. The lower bar shows the $T = 0$ mean-field phase boundary determined in Ref. [50], and the arrows with labels on top denote the special cases of the model in Eq. (39). The triangles indicate critical temperatures from classical and quantum Monte Carlo simulations of Refs. [38,51,52] and from Appendix D.

[52]. For the Ising-FM case, where no classical Monte Carlo results were available in the literature, we obtained $T_c = 2.00(1)$. Details are reported in Appendix D. All classical and quantum Monte Carlo results are shown in Fig. 3 as triangles.

In order to complete the phase diagram and find ordering temperatures for all θ (if nonzero and large enough to detect with PMFRG), we apply the PMFRG T-flow method and report the results of a finite-size scaling procedure in Fig. 3 (blue and green dots). Our PMFRG results are usually a few percent above Monte Carlo estimates where the latter are available. The $T_c(\theta)$ corresponding to either Ising- or XY-type FM order forms two domes merging at the Heisenberg FM point ($\theta = 1.25\pi$) at which the T_c is sharply suppressed. Extrapolating the $T_c(\theta)$ to vanishing temperature, we find that the ordered regions are slightly extended beyond the mean-field ground-state phase boundaries of Ref. [50]. The latter are shown by a colored bar in the bottom of Fig. 3.

In the region with dominant AFM interaction, the PMFRG did not find an ordering transition for $\theta/\pi = 1.94...0.57$ down to the lowest accessible temperatures marked by the gray line. This lower bound corresponds to the temperature below which the internal consistency check is violated by 2.5%, see Appendix B. To indicate the type of (short-range) spin correlations in the θ region where no order is detected, the color of the upper vertical bar specifies the dominant susceptibility (red for Ising-AFM, orange for XY-AFM) at this lowest temperature. In the region around the Ising-AFM point where the order breaks a discrete global spin-flip symmetry, a finite T_c, albeit small due to frustration, is expected. Indeed, as mentioned above, classical Monte Carlo [52] finds $T_c \simeq 0.296$, which is just below the temperature accessible to PMFRG. In the region around the XY-AFM point, a Kosterlitz-Thouless transition is anticipated at finite T, with true long-range order only appearing at $T = 0$; see Refs. [30,50] for further discussion. The PMFRG currently is not able to detect the Kosterlitz-Thouless transition, a challenge remaining for future work.

For all θ we find the dominant susceptibilities to be either of XY or Ising type and located at $\mathbf{k} = 0$ or (π, π), as indicated in Fig. 3 by the upper horizontal line. In particular, this means that we do not find any signs of exotic magnetic (e.g., incommensurate) phases. Moreover our results do not rule out paramagnetic behavior down to $T = 0$, which is conceivable close to the mean-field phase boundaries at $\theta/\pi \simeq 0.6$ and 1.9, where the mean-field energies are discontinuous [50]. In summary, our results inform future experiments which could map out the two-dome structure of $T_c(\theta)$ and further explore the nature of the nonmagnetic low-temperature states with dominant XY-AFM interactions. The PMFRG is also capable of treating the case of tilted dipoles, which results in anisotropic spin interactions.

VI. CONCLUSION

Motivated by the efficiency of using a physical flow parameter, in this work we have implemented the temperature flow into the PMFRG framework. Benchmarking our method on the nearest-neighbor simple cubic Heisenberg model, we find this method to have similar or better accuracy as compared to the standard Λ-flow formalism. For the Heisenberg J_1-J_2 model on the simple cubic lattice, we resolve a previous problem about the inability to detect critical scaling at $J_2 > 0.25$ in a Λ-flow study [25]. Our explanation indicates that unphysical renormalization cutoff parameters Λ can suffer from the onset of long-range correlation effects at finite cutoff values, thereby rendering the result in the physical limit at $\Lambda = 0$ inaccurate. The use of the temperature flow also allows us to detect magnetic order at very low critical temperatures $T \sim 0.05$ that were previously out of reach. We demonstrate the substantial improvement in efficiency of the T-flow PMFRG by mapping out the phase diagrams of the Heisenberg J_1-J_2 model on the simple cubic lattice and the dipolar-XXZ model on the square lattice. Both models have points in parameter space where they are amenable to (quantum) Monte Carlo, allowing us to verify the quantitative accuracy of our approach up to a few percent, which gives us confidence in the quantitative accuracy of our critical temperatures even in cases where no Monte Carlo benchmark is available. Combining the efficiency of the zero-temperature Λ-flow approach with the methodological advantages of the finite-temperature formalism, we strongly encourage the use of temperature as the preferred flow parameter.

Our numerical code is available on GitHub [53], where implementations of the T-flow and Λ-flow can be found [54].

ACKNOWLEDGMENTS

We thank L. Pollet and D. Rohe for stimulating discussion. We further acknowledge fruitful discussions with the other participants from the Spin-FRG Mini-workshop 2023

in Berlin during the early stages of this project. N.N. and J.R. acknowledge support from the Deutsche Forschungsgemeinschaft (DFG, German Research Foundation), within Project ID 277101999 CRC 183 (Project A04). B.Sch. and B.Sb. are supported by a MCQST-START fellowship and by the Munich Quantum Valley, which is supported by the Bavarian state government with funds from the Hightech Agenda Bayern Plus. B.Sb. acknowledges support from the DFG through the Research Unit FOR 5413/1, Grant No. 465199066. We acknowledge the use of the JUWELS cluster at the Forschungszentrum Jülich, the Noctua2 cluster at the Paderborn Center for Parallel Computing (PC^2), and the HPC Service of ZEDAT at the Freie Universität Berlin.

APPENDIX A: HEISENBERG DIMER AS BENCHMARK MODEL FOR T-FLOW PMFRG

To benchmark the temperature flow PMFRG, we investigate the Heisenberg dimer $H = \sum_\alpha S_1^\alpha S_2^\alpha$. Despite its apparent simplicity, this model provides a formidable challenge to diagrammatic approaches such as the PMFRG which are oblivious to the size of the Hilbert space. As the low dimensionality renders several crucial mean-field contributions which are fully included in the FRG such as the RPA and ladder-type series insufficient [15], one may consider it as a worst-case benchmark: Generally speaking, the higher-dimensional systems treated in this work are much better described by mean-field contributions and are thus expected to be better behaved. Due to its simple implementation and the availability of exact results, the same dimer system has been studied previously for similar purposes [22,24].

Here, we consider the static spin-spin correlators $\chi_{11}(\omega = 0)$ and $\chi_{12}(\omega = 0)$ as well as the interaction correction to the free energy f_{int}, the energy per site U, and the heat capacity C obtained by Eqs. (30)–(32). Alternatively, the internal energy can also be obtained via $U = \langle H \rangle$, which for the general Hamiltonian in Eq. (1) reads

$$U = \sum_{i,\alpha} h_i^\alpha M_i^\alpha + \frac{1}{2} \sum_{\substack{i,j \\ \alpha\beta}} J_{ij}^{\alpha,\beta} \langle S_i^\alpha S_j^\beta \rangle, \tag{A1}$$

where $M_i^\alpha = 0$ in the present case, since no magnetic field h_i^α is considered. These quantities are compared against the exact solution in Fig. 4 shown as black lines. The interaction correction to the free energy f_{int}, shown in red in panel (a), is obtained from the zero-point vertex in Eq. (18). We observe the temperature flow (solid line) to be closer to the exact result than the Λ-flow result (square markers). From f_{int}, the energy per site U/N may be obtained using Eq. (31) via a numerical derivative with respect to T. Again, we observe the T-flow curve to be closer to the exact result than in Λ-flow in panel (b). In the T-flow scheme, we may avoid inaccuracies from numerical derivatives by inserting the right-hand side of the flow equation in Eq. (18) for $\frac{df_{\text{int}}}{dT}$ in Eq. (31). The result is shown by the blue dashed line. As the numerical accuracy of the solution is rather high with a tolerance of $\sim 10^{-7}$, the result is identical to that obtained via numerical derivatives. Further shown in orange is the T-flow result obtained from spin-spin correlations as defined in Eq. (A1). For intermediate to large temperatures, this quantity is the most accurate but

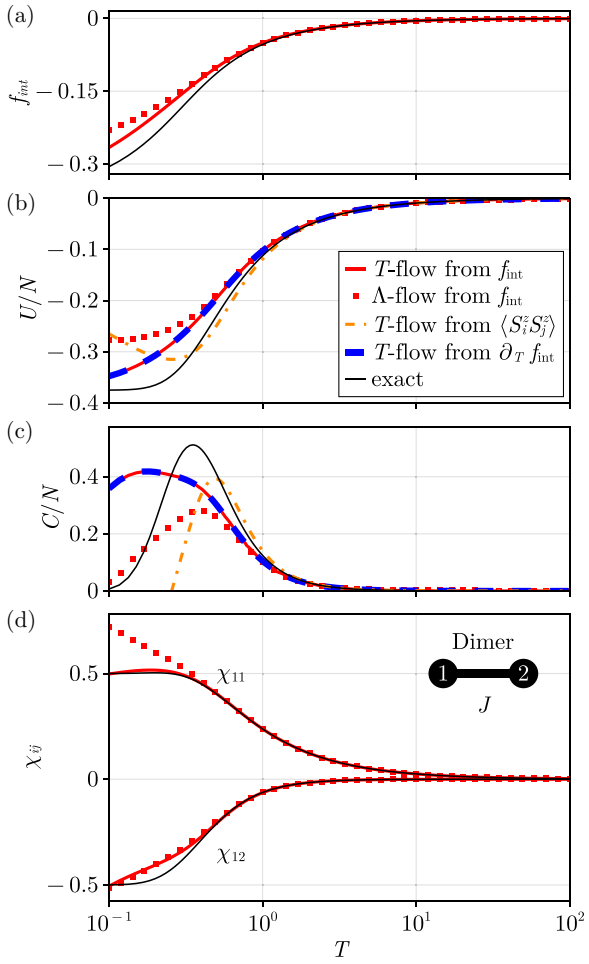

FIG. 4. Thermodynamic quantities for the temperature flow PMFRG on the Heisenberg dimer in comparison to the exact result (black) and the standard Λ-flow PMFRG (squares). (a) Interaction correction to the free energy f_{int} from Eq. (18). For the energy per site U/N [plotted in (b)] and the specific heat C/N [plotted in (c)] the dark red dash-dotted line represents the value obtained via Eq. (A1). The solid red line represents the value obtained via Eq. (32). The same quantity can be obtained directly via the flow equation Eq. (18), shown in blue dashed lines without the need to perform numerical derivatives. (d) The two inequivalent static spin-spin correlators χ_{11} and χ_{12} obtained via Eq. (35).

becomes unphysical around $T \sim 0.25$, showing an increase as the temperature decreases. By taking a numerical derivative, we may also obtain an estimate for the heat capacity C from all these results, shown in panel (c). While the T-flow peak height of the heat capacity is closer to the exact result than the Λ-flow result, its peak location is shifted. We conclude that the energy per site and the heat capacity are strongly affected by truncation errors, since already small errors introduced by neglecting the six-point vertex propagate through the four- and two-point vertex to the zero-point vertex and are then magnified even further upon taking derivatives.

On the other hand, the static spin-spin correlations $\chi_{11}(\omega = 0)$ and $\chi_{12}(\omega = 0)$ are significantly less affected by this problem, as they are obtained directly from the four-point vertex

via Eq. (35). At large temperatures $T \gg J$, where both PMFRG flow approaches are well controlled, they agree well with each other and the exact result. At low temperatures, deviations from the exact result become visible within both the T-flow and standard Λ-flow PMFRG. Somewhat surprisingly, we observe that the local spin correlator $\chi_{11}(\omega = 0)$ appears much more accurate in the temperature flow formalism, while the nonlocal one deviates from the exact result in the same way as in the Λ-flow scheme. We note that this improvement in accuracy may be incidental. In conclusion, we find that both FRG approaches correctly describe correlations in the Heisenberg dimer at high and intermediate temperatures. This holds despite the challenges that the dimer presents to diagrammatic approaches due to its low dimensionality. On the other hand, thermodynamic observables such as the specific heat suffer considerably from error propagation introduced in the derivatives and are thus much less reliable. As a result, in this work we have only relied on results obtained from spin-spin correlators.

APPENDIX B: INTERNAL CONSISTENCY CHECKS FOR PMFRG

The truncation of the flow equation hierarchy by neglecting the six-point vertex is an inherently uncontrolled approximation at low temperatures, making estimates of the exact error bars impossible. Instead, we can rely upon the fulfillment of a Ward identity as a qualitative measure of the truncation error to indicate challenging parameter regimes: All pseudo-Majorana Hamiltonians feature a set of local constants of motion,

$$\theta_j = -2i\eta_j^x\eta_j^y\eta_j^z. \tag{B1}$$

This allows us to derive an exact relation between fully local two- and four-point Majorana correlators [24,55,56]. Hence we may express the static and local spin-spin correlator, which is usually computed from the four-point Majorana vertex [see Eq. (35)] alternatively through the two-point Green function, here shown for the static part at $\omega = 0$:

$$\chi_{jj}^{\alpha_1\alpha_2}(\omega = 0) = \sum_{\omega'} \frac{i}{\omega'\sqrt{T}} G^T_{j;\alpha_1\alpha_2}(\omega'). \tag{B2}$$

This relation must be satisfied for any exact calculation. For the approximate PMFRG, we can use the degree of violation as an internal consistency check and define the quantity

$$\Delta = \left| \frac{\chi_{jj}^{\alpha_1\alpha_2}(0)_1 - \chi_{jj}^{\alpha_1\alpha_2}(0)_2}{\chi_{jj}^{\alpha_1\alpha_2}(0)_1 + \chi_{jj}^{\alpha_1\alpha_2}(0)_2} \right|, \tag{B3}$$

where the subscripts 1 and 2 refer to the two different methods of computing $\chi_{jj}^{\alpha_1\alpha_2}(\omega = 0)$, via Eqs. (B2) and (35), respectively.

In Fig. 5 we show the violation of the consistency condition $\Delta = 0$ for the Heisenberg dimer from Appendix A in the Λ- and T-flow schemes. We notice that Δ is larger in the temperature flow scheme compared to the Λ-flow PMFRG, despite the overall better agreement of the temperature flow with the exact result.

Figure 6 shows the violation of the consistency check Eq. (B3) for the J_1-J_2 Heisenberg model on the simple cubic lattice as a function of temperature and J_2 for the T-flow scheme with the critical temperatures in red corresponding to Fig. 1. At temperatures below $T \sim 0.6$, we find violations of about 5%, steadily growing towards lower temperatures up to 50% at the very lowest temperatures $T = 0.05$. Finally, for the XXZ dipolar model of Sec. V, the temperature at which $\Delta = 0.025$ is shown as a gray line in the phase diagram of Fig. 3.

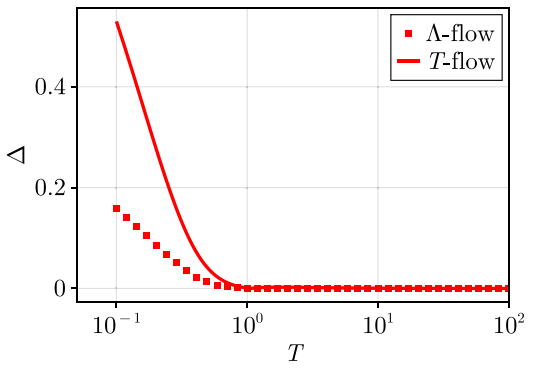

FIG. 5. Violation of the consistency check [Eq. (B3)] for the Heisenberg dimer in the Λ-flow and T-flow PMFRG schemes.

Although Δ cannot replace a real error bar, since it only contains information about the violation of the conservation law for the constant of motion θ_j, a small value of Δ in the few-percent range is an indicator that the truncation of flow equations is still in the well-controlled limit. However, it should be noted that even with a large Δ the method can produce qualitatively and in principle even quantitatively accurate data for quantities which are not directly linked to the conservation of θ_j, which is violated. This is visible in the case of the dimer shown in Fig. 5, where Δ is larger in the T-flow scheme as compared to the Λ-flow result, even though the quantities of interest, primarily the susceptibility, lie closer to the exact result in T-flow.

APPENDIX C: DETECTION OF MAGNETIC PHASE TRANSITIONS

When studying spin systems at finite temperatures, one is commonly interested in phase transitions or the lack thereof. Historically, magnetic phase transitions in the pseudoparticle-

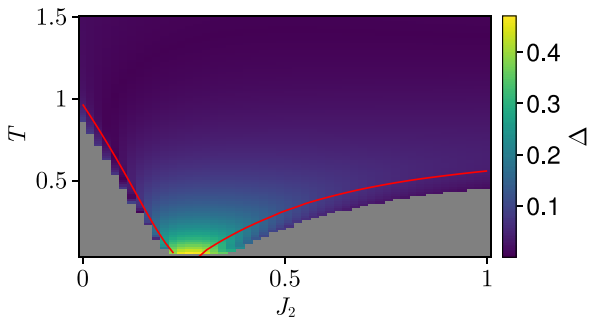

FIG. 6. Consistency check violation Δ, defined by Eq. (B3). The critical temperature is indicated by the red line.

FRG context have been detected as instabilities in the flow equations, where a divergence is often detected as a sharp feature, i.e., "kink" in the corresponding susceptibility. This approach has the disadvantage that the exact point of the feature can heavily depend on numerical parameters such as the maximum correlation length, the frequency discretization, or the accuracy of the ordinary differential equation solver. Moreover, the distinction a weak "kink" from a disordered state is subject to interpretation and thus often of more qualitative nature. As outlined in previous works [22,25,38], finite-size scaling can instead be used as an unbiased and reliable method to extract quantitatively accurate critical temperatures from pseudoparticle-FRG calculations. We approximate the rescaled correlation length by fitting a Lorentz curve with width $\frac{1}{\xi}$ to the largest peak located at wave vector $\mathbf{Q}$ of the Fourier transformed susceptibility $\chi^{\alpha_1\alpha_2}(\mathbf{k})$ [57]:

$$\frac{\xi}{L} = \frac{1}{2\pi} \max_{\delta} \left(\sqrt{\frac{\chi_{\max}(\mathbf{Q})}{\chi_{\max}(\mathbf{Q} + \frac{2\pi}{L}\delta)} - 1} \right), \tag{C1}$$

$$\chi_{\max}(\mathbf{Q}) = \max_{\alpha_1\alpha_2} [\chi^{\alpha_1\alpha_2}(\mathbf{Q})]. \tag{C2}$$

Here, δ is a vector of unit length and L is a measure of system size, and therefore the maximum correlation length. In translationally invariant systems, we need only consider sites i in Σ_i and Γ_{ij} that lie in the first unit cell and set $\Gamma_{ij} = 0$ if the sites i and j are separated by more than L nearest-neighbor bonds. We detect a phase transition by calculating $\frac{\xi}{L}$ for multiple L. In a paramagnetic regime $\frac{\xi}{L}$ decreases with L, while in a magnetic regime $\frac{\xi}{L}$ increases with L. The critical temperature is the temperature at which $\frac{\xi}{L}$ is independent of L.

APPENDIX D: CLASSICAL MONTE CARLO FOR THE SQUARE LATTICE DIPOLAR ISING MODEL

We performed classical Monte Carlo calculations for the ferromagnetic dipolar Ising model [see Eq. (39) for $\theta = \pi$]. We use square systems with periodical boundary conditions containing $N = L \times L$ Ising spins, taking L from 8 and up to 65. Each spin of the system interacts with all other spins through the exchange interaction $J_{(i,j)} = 1/r_{ij}^3$, where r_{ij} is the shortest distance between sites i and j on the torus.

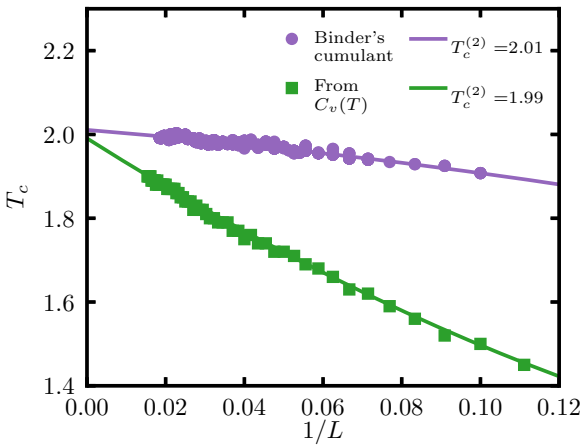

FIG. 7. Scaling of the critical temperature extracted from the specific heat (green squares) and Binder's cumulant (purple circles). The lines correspond to quadratic fits, and the results of T_c for each method are shown in the legend.

To calculate the critical temperature, we use two independent methods. On one hand, we take 201 temperature steps to cool the system down from $T = 3$ to 1 using 10^5 Monte Carlo trials at each temperature. We measure the energy in the second half of each temperature step to obtain $U(T)/N$ and $c_v(T)$. Results are then averaged for ten independent runs. On the other hand, we take 76 steps to cool down from $T = 3$ to 1.5 using 2×10^5 Monte Carlo trials at each temperature. We measure m^2 and m^4 in the same way as before and average over ten independent runs to calculate Binder's cumulant [58], $B = (3 - \langle m^4 \rangle / \langle m^2 \rangle^2)/2$.

Figure 7 shows the temperature at which $c_v(T)$ has a maximum (green squares) and the crossing lines between Binder's cumulants for different lattice sizes (purple circles) as a function of $1/L$. Extrapolating to $L \to \infty$ via two independent quadratic fits yield $T_c = 1.99$ and $T_c = 2.01$, respectively. Thus we can assume that $T_c = 2.00(1)$ is a good estimate of the critical temperature in the thermodynamic limit.

[1] D. Bergman, J. Alicea, E. Gull, S. Trebst, and L. Balents, Order-by-disorder and spiral spin-liquid in frustrated diamond-lattice antiferromagnets, Nat. Phys. **3**, 487 (2007).

[2] A. Mulder, R. Ganesh, L. Capriotti, and A. Paramekanti, Spiral order by disorder and lattice nematic order in a frustrated Heisenberg antiferromagnet on the honeycomb lattice, Phys. Rev. B **81**, 214419 (2010).

[3] J. Wen, S.-L. Yu, S. Li, W. Yu, and J.-X. Li, Experimental identification of quantum spin liquids, npj Quantum Mater. **4**, 12 (2019).

[4] B. Sriram Shastry and B. Sutherland, Exact ground state of a quantum mechanical antiferromagnet, Physica B+C **108**, 1069 (1981).

[5] R. Schäfer, B. Placke, O. Benton, and R. Moessner, Abundance of hard-hexagon crystals in the quantum pyrochlore antiferromagnet, Phys. Rev. Lett. **131**, 096702 (2023).

[6] D. Lozano-Gómez, V. Noculak, J. Oitmaa, R. R. Singh, Y. Iqbal, J. Reuther, and M. J. Gingras, Competing gauge fields and entropically-driven spin liquid to spin liquid transition in non-Kramers pyrochlores, arXiv:2310.16682.

[7] M. Adhikary, A. Ralko, and B. Kumar, Quantum paramagnetism and magnetization plateaus in a kagome-honeycomb Heisenberg antiferromagnet, Phys. Rev. B **104**, 094416 (2021).

[8] R. Pohle, Y. Yamaji, and M. Imada, Ground state of the $S = 1/2$ pyrochlore Heisenberg antiferromagnet: A quantum spin liquid emergent from dimensional reduction, arXiv:2311.11561.

[9] L. Savary and L. Balents, Quantum spin liquids: A review, Rep. Prog. Phys. **80**, 016502 (2017).

[10] A. Kitaev, Anyons in an exactly solved model and beyond, Ann. Phys. **321**, 2 (2006).

[11] A. W. Sandvik and J. Kurkijärvi, Quantum Monte Carlo simulation method for spin systems, Phys. Rev. B **43**, 5950 (1991).

[12] A. W. Sandvik, Stochastic series expansion method with operator-loop update, Phys. Rev. B **59**, R14157 (1999).

[13] O. Benton, O. Sikora, and N. Shannon, Seeing the light: Experimental signatures of emergent electromagnetism in a quantum spin ice, Phys. Rev. B **86**, 075154 (2012).

[14] J. Reuther and P. Wölfle, J_1–J_2 frustrated two-dimensional Heisenberg model: Random phase approximation and functional renormalization group, Phys. Rev. B **81**, 144410 (2010).

[15] T. Müller, D. Kiese, N. Niggemann, B. Sbierski, J. Reuther, S. Trebst, R. Thomale, and Y. Iqbal, Pseudo-fermion functional renormalization group for spin models, Rep. Prog. Phys. **87**, 036501 (2024).

[16] L. E. Chern, F. Desrochers, Y. B. Kim, and C. Castelnovo, A pseudofermion functional renormalization group study of dipolar-octupolar pyrochlore magnets, arXiv:2311.04269.

[17] L. Gresista, C. Hickey, S. Trebst, and Y. Iqbal, Candidate quantum disordered intermediate phase in the Heisenberg antiferromagnet on the maple-leaf lattice, Phys. Rev. B **108**, L241116 (2023).

[18] V. Noculak and J. Reuther, Pseudo-fermion functional renormalization group with magnetic fields, arXiv:2312.12097.

[19] N. Niggemann, Y. Iqbal, and J. Reuther, Quantum effects on unconventional pinch point singularities, Phys. Rev. Lett. **130**, 196601 (2023).

[20] K. Fukui, Y. Kato, and Y. Motome, Ground-state phase diagram of the Kitaev–Heisenberg model on a three-dimensional hyperhoneycomb lattice, J. Phys. Soc. Jpn. **92**, 064708 (2023).

[21] A. Keleş and E. Zhao, Rise and fall of plaquette order in the Shastry-Sutherland magnet revealed by pseudofermion functional renormalization group, Phys. Rev. B **105**, L041115 (2022).

[22] B. Schneider, D. Kiese, and B. Sbierski, Taming pseudofermion functional renormalization for quantum spins: Finite temperatures and the Popov-Fedotov trick, Phys. Rev. B **106**, 235113 (2022).

[23] V. N. Popov and S. A. Fedotov, The functional-integration method and diagram technique for spin systems, Zh. Eksp. Teor. Fiz. **94**, 183 (1988) [Sov. Phys. JETP **67**, 535 (1988)].

[24] N. Niggemann, B. Sbierski, and J. Reuther, Frustrated quantum spins at finite temperature: Pseudo-Majorana functional renormalization group approach, Phys. Rev. B **103**, 104431 (2021).

[25] N. Niggemann, J. Reuther, and B. Sbierski, Quantitative functional renormalization for three-dimensional quantum Heisenberg models, SciPost Phys. **12**, 156 (2022).

[26] C. Honerkamp and M. Salmhofer, Temperature-flow renormalization group and the competition between superconductivity and ferromagnetism, Phys. Rev. B **64**, 184516 (2001).

[27] W. H. C. Platt and R. Thomale, Functional renormalization group for multi-orbital Fermi surface instabilities, Adv. Phys. **62**, 453 (2013).

[28] C. Honerkamp, D. Rohe, S. Andergassen, and T. Enss, Interaction flow method for many-fermion systems, Phys. Rev. B **70**, 235115 (2004).

[29] L. Christakis, J. S. Rosenberg, R. Raj, S. Chi, A. Morningstar, D. A. Huse, Z. Z. Yan, and W. S. Bakr, Probing site-resolved correlations in a spin system of ultracold molecules, Nature (London) **614**, 64 (2023).

[30] C. Chen, G. Bornet, M. Bintz, G. Emperauger, L. Leclerc, V. S. Liu, P. Scholl, D. Barredo, J. Hauschild, S. Chatterjee *et al.*, Continuous symmetry breaking in a two-dimensional Rydberg array, Nature (London) **616**, 691 (2023).

[31] J. Martin, Generalized classical dynamics, and the 'classical analogue' of a fermioscillator, Proc. R. Soc. London A **251**, 536 (1959).

[32] A. M. Tsvelik, New fermionic description of quantum spin liquid state, Phys. Rev. Lett. **69**, 2142 (1992).

[33] This can be seen by setting the interaction flow parameter $g = T^{3/2}$, which results in the same bare Green's function as in Eq. (6).

[34] P. Kopietz, L. Bartosch, and F. Schütz, *Introduction to the Functional Renormalization Group*, Lecture Notes in Physics Vol. 798 (Springer, Berlin, Heidelberg, 2010).

[35] A. A. Katanin, Fulfillment of ward identities in the functional renormalization group approach, Phys. Rev. B **70**, 115109 (2004).

[36] M. Salmhofer, C. Honerkamp, W. Metzner, and O. Lauscher, Renormalization group flows into phases with broken symmetry, Prog. Theor. Phys. **112**, 943 (2004).

[37] Note that the full vertex function $\Gamma^{\Lambda}(\omega_1, \omega_2, \omega_3, \omega_4) \equiv \Gamma^{\Lambda}(s, t, u)\beta\delta_{\omega_1+\omega_2+\omega_3+\omega_4,0}$ has a relative factor of $\beta = 1/T$.

[38] B. Sbierski, M. Bintz, S. Chatterjee, M. Schuler, N. Y. Yao, and L. Pollet, Magnetism in the two-dimensional dipolar XY model, Phys. Rev. B **109**, 144411 (2024).

[39] A. W. Sandvik, Critical temperature and the transition from quantum to classical order parameter fluctuations in the three-dimensional Heisenberg antiferromagnet, Phys. Rev. Lett. **80**, 5196 (1998).

[40] C. Pinettes and H. T. Diep, Phase transition and phase diagram of the $J_1 - J_2$ Heisenberg model on a simple cubic lattice, J. Appl. Phys. **83**, 6317 (1998).

[41] K. Majumdar and T. Datta, Zero temperature phases of the frustrated $J_1 - J_2$ antiferromagnetic spin-1/2 Heisenberg model on a simple cubic lattice, J. Stat. Phys. **139**, 714 (2010).

[42] D. J. J. Farnell, O. Götze, and J. Richter, Ground-state ordering of the J_1–J_2 model on the simple cubic and body-centered cubic lattices, Phys. Rev. B **93**, 235123 (2016).

[43] M. Laubach, D. G. Joshi, J. Reuther, R. Thomale, M. Vojta, and S. Rachel, Quantum disordered insulating phase in the frustrated cubic-lattice Hubbard model, Phys. Rev. B **93**, 041106(R) (2016).

[44] Y. Iqbal, T. Müller, P. Ghosh, M. J. P. Gingras, H. O. Jeschke, S. Rachel, J. Reuther, and R. Thomale, Quantum and classical phases of the pyrochlore Heisenberg model with competing interactions, Phys. Rev. X **9**, 011005 (2019).

[45] Y. Iqbal, R. Thomale, F. Parisen Toldin, S. Rachel, and J. Reuther, Functional renormalization group for three-

dimensional quantum magnetism, Phys. Rev. B **94**, 140408(R) (2016).
[46] N. D. Mermin and H. Wagner, Absence of ferromagnetism or antiferromagnetism in one- or two-dimensional isotropic Heisenberg models, Phys. Rev. Lett. **17**, 1133 (1966).
[47] N. Defenu, T. Donner, T. Macrì, G. Pagano, S. Ruffo, and A. Trombettoni, Long-range interacting quantum systems, Rev. Mod. Phys. **95**, 035002 (2023).
[48] L. Chomaz, I. Ferrier-Barbut, F. Ferlaino, B. Laburthe-Tolra, B. L. Lev, and T. Pfau, Dipolar physics: A review of experiments with magnetic quantum gases, Rep. Prog. Phys. **86**, 026401 (2023).
[49] S. L. Cornish, M. R. Tarbutt, and K. R. A. Hazzard, Quantum computation and quantum simulation with ultracold molecules, arXiv:2401.05086.
[50] D. Peter, S. Müller, S. Wessel, and H. P. Büchler, Anomalous behavior of spin systems with dipolar interactions, Phys. Rev. Lett. **109**, 025303 (2012).
[51] J. Zhao, M. Song, Y. Qi, J. Rong, and Z. Y. Meng, Finite-temperature critical behaviors in 2D long-range quantum Heisenberg model, npj Quantum Mater. **8**, 59 (2023).
[52] E. Rastelli, S. Regina, and A. Tassi, Phase transitions in a square Ising model with exchange and dipole interactions, Phys. Rev. B **73**, 144418 (2006).
[53] Our numerical code can be accessed at GitHub, https://github.com/NilsNiggemann/PMFRG.jl/tree/TemperatureFlow.
[54] N. Niggemann, NilsNiggemann/PMFRG.jl: v2.1.9, Zenodo (2023), https://doi.org/10.5281/zenodo.10255230.
[55] A. Shnirman and Y. Makhlin, Spin-spin correlators in the Majorana representation, Phys. Rev. Lett. **91**, 207204 (2003).
[56] P. Schad, Y. Makhlin, B. Narozhny, G. Schön, and A. Shnirman, Majorana representation for dissipative spin systems, Ann. Phys. **361**, 401 (2015).
[57] A. W. Sandvik, Computational studies of quantum spin systems, AIP Conf. Proc. **1297**, 135 (2010).
[58] K. Binder, Critical properties from Monte Carlo coarse graining and renormalization, Phys. Rev. Lett. **47**, 693 (1981).

Pseudo-Majorana functional renormalization for frustrated XXZ spin-$\frac{1}{2}$ models with field or magnetization along the spin-Z direction at finite temperature

Frederic Bippus [1,2,3] Benedikt Schneider [2,3] and Björn Sbierski [2,3,4]

[1]*Institute of Solid State Physics, TU Wien, 1040 Vienna, Austria*

[2]*Munich Center for Quantum Science and Technology (MCQST), Schellingstraße 4, D-80799 Munich, Germany*

[3]*Department of Physics and Arnold Sommerfeld Center for Theoretical Physics, Ludwig-Maximilians-Universität München, Theresienstraße 37, 80333 Munich, Germany*

[4]*Institut für Theoretische Physik, Universität Tübingen, Auf der Morgenstelle 14, 72076 Tübingen, Germany*

(Received 2 December 2024; revised 24 January 2025; accepted 24 January 2025; published 13 February 2025)

The numerical study of high-dimensional frustrated quantum magnets remains a challenging problem. Here we present an extension of the pseudo-Majorana functional renormalization group to spin-1/2 XXZ-type Hamiltonians with field or magnetization along spin-Z direction at finite temperature. We consider a U(1) symmetry-adapted fermionic spin representation and derive the diagrammatic framework and its renormalization group flow equations. We discuss benchmark results and application to two antiferromagnetic triangular lattice materials recently studied in experiments with applied magnetic fields: First, we numerically reproduce the magnetization data measured for $CeMgAl_{11}O_{19}$ confirming model parameters previously estimated from inelastic neutron spectrum in high fields. Second, we showcase the accuracy of our method by studying the thermal phase transition into the spin solid up-up-down phase of $Na_2BaCo(PO_4)_2$ in good agreement with experiment.

DOI: 10.1103/PhysRevB.111.054420

I. INTRODUCTION

The study of frustrated quantum magnets remains at the forefront of contemporary condensed-matter physics, in particular due to their ability to host collective quantum phases of matter like spin liquids [1,2]. On the theory side, relevant materials can often be described by relatively compact models like the Heisenberg spin Hamiltonian [3]. Based on such models, the objective is to compute order parameters, phase diagrams, and correlation functions. In the context of solid-state quantum magnets, these calculations are usually conducted in thermal equilibrium. However, for frustrated systems like the Heisenberg antiferromagnet (AFM) on the triangular lattice, the well-established quantum Monte Carlo (QMC) approaches are ineffective due to the sign problem [4]. As an alternative, tensor network methods [5] have been applied both in the ground state (at temperature $T = 0$) and, more recently, at finite temperature [6,7]. Here the bottleneck are usually finite-size effects caused by the nonlocal entanglement structure.

An alternative approach to frustrated quantum spins are diagrammatic methods which are oblivious to the sign problem or dimensionality. Although originally developed for interacting fermionic (or bosonic) particles [8], variants of the diagrammatic method working directly with spin operators also have a long history [9] and currently enjoy renewed interest [10–12]. One of the currently most popular diagrammatic methods [13] bridges the gap between spin- and fermionic operators using a pseudofermionic representation of the spin $S = 1/2$ algebra. The resulting interacting fermionic Hamiltonian is then treated with the functional renormalization group (fRG) approach [14,15]. For a recent review on this pseudofermion fRG (pf-fRG), see Ref. [16].

While the original pf-fRG was only applied to $T = 0$ in the hope to avoid unphysical sectors in the pseudofermionic Hilbert space [17], this restriction was alleviated in 2021 when the fRG was combined with a faithful spin-representation building on pseudo-Majorana operators [18]. The resulting finite-temperature pseudo-Majorana fRG (pm-fRG) has since then been successfully applied for frustrated Heisenberg models with short- and long-range interactions [19–23] and was also adapted to models with XXZ-type anisotropy [24].

In this work we generalize the pm-fRG for spin $S = 1/2$ XXZ models where time-reversal symmetry is broken by a field in Z direction, but the U(1) spin-rotation symmetry around this direction remains intact, see Eq. (1) below. We dub our method U(1)-pm-fRG. Importantly, our framework also applies to the field-free case of a Heisenberg model with SU(2) symmetry spontaneously broken to U(1) by magnetization in spin-Z direction. Similar advances have been put forward [25] in the context of pf-fRG at $T = 0$.

On the technical level, in Sec. II, we review a U(1)-symmetry adapted mixed representation that contains one Majorana and one complex fermion per lattice site. This representation is also known as "drone-fermion representation" [26–28]. We discuss the gauge symmetries of the representation and those related to the XXZ-Z Hamiltonian. The associated action and Green's functions are considered in

Sec. III and we provide the expressions for observables like magnetization and susceptibility in Sec. IV. We derive the (one-loop) flow-equations for U(1)-pm-fRG in Sec. V. Various benchmark tests involving small or unfrustrated systems are given in Sec. VI.

As a showcase application to frustrated systems, in Sec. VII we apply the U(1)-pm-fRG to spin-1/2 XXZ-Z models on the triangular lattice inspired by recent experimental studies. First, we revisit the material $CeMgAl_{11}O_{19}$ for which Ref. [29] claimed that the coupling parameters are close to a solvable quantum phase transition point in parameter space. While this argument was made on the basis of neutron-scattering data in high magnetic fields, we bolster this claim by analyzing low field experimental magnetization data at two different temperatures.

Second, we consider the material $Na_2BaCo(PO_4)_2$ in an out-of-plane magnetic field. This material was considered recently [30–34] in the context of spin supersolidity [35–38]. We determine the critical temperature for the transition in the three-sublattice spin solid up-up-down phase confirming experimental results obtained in Ref. [37].

We conclude in Sec. VIII with summary and outlook. Technical details are relegated to various Appendixes.

II. XXZ-Z MODEL, PSEUDO-MAJORANAS, AND THE MIXED REPRESENTATION

We consider the XXZ spin $S = 1/2$ model with an (optional) external field pointing along the spin-Z direction. The Hamiltonian of this XXZ-Z model reads

$$H = H_{\mathrm{XXZ}} + H_Z, \tag{1}$$

where the first term with spin-spin interactions reads

$$H_{\mathrm{XXZ}} = \sum_{i<j}\left[\frac{J^{\perp}_{ij}}{2}(S^+_i S^-_j + S^-_i S^+_j) + J^z_{ij} S^z_i S^z_j\right], \tag{2}$$

with arbitrary exchange couplings and spin raising and lowering operators at site j defined as $S^{\pm}_j \equiv S^x_j \pm iS^y_j$. The Zeeman term for an uniaxial (but not necessarily homogeneous) field is given by

$$H_Z = \sum_j h_j S^z_j. \tag{3}$$

The starting point of the pm-fRG [18,19,22,24] approach developed for Heisenberg and XXZ Hamiltonians is to rewrite the spin-1/2 operators using the SO(3) pseudo-Majorana representation [39,40]. This employs three auxiliary Majorana operators per site, η^{α}_j $(\alpha = x, y, z)$,

$$S^z_j = -i\eta^x_j\eta^y_j, \tag{4a}$$

$$S^{\pm}_j = \left(-i\eta^y_j \mp \eta^x_j\right)\eta^z_j. \tag{4b}$$

The fermionic Majorana operators fulfill $(\eta^{\alpha}_j)^{\dagger} = \eta^{\alpha}_j$, canonical anticommutation relations $\{\eta^{\alpha}_i, \eta^{\beta}_j\} = \delta^{\alpha\beta}\delta_{ij}$ and are normalized as $(\eta^{\alpha}_j)^2 = 1/2$.

The presence of a finite Z field as in Eq. (3) leads to a mixing in flavor space in the noninteracting fermionic Green's function. This complication has so far hindered the application of the pm-fRG calculations in this case. The goal of this work is to introduce a symmetry-adapted variant of the pm-fRG which keeps the complexity of the flow equations at a level tractable for numerical solution.

A. Mixed representation

To simplify calculations including magnetic fields, we diagonalize the noninteracting pseudo-Majorana Hamiltonian by combining η^x_j and η^y_j into a *complex* fermion with creation and annihilation operators $c^{\dagger}_j, c_j$ as follows [41]:

$$\eta^x_j = \frac{i}{\sqrt{2}}(c_j - c^{\dagger}_j), \tag{5a}$$

$$\eta^y_j = \frac{1}{\sqrt{2}}(c_j + c^{\dagger}_j). \tag{5b}$$

The anticommutation relations of the complex fermions are $\{c^{\dagger}_j, c_{j'}\} = \delta_{j,j'}$. We drop the z superscript of the remaining Majorana fermion, $\eta^z_j \equiv \eta_j$ and note that $\{c^{(\dagger)}_j, \eta_{j'}\} = 0$. With this transformation, the spin operators in Eq. (4) become

$$S^+_j = -i\sqrt{2}c_j\eta_j, \tag{6a}$$

$$S^-_j = -i\sqrt{2}c^{\dagger}_j\eta_j, \tag{6b}$$

$$S^z_j = \tfrac{1}{2} - c^{\dagger}_j c_j. \tag{6c}$$

This mixed representation which involves both a complex and a Majorana fermion has first been introduced as "drone-fermion representation" in Refs. [26–28]. We note its similarity to the Jordan-Wigner representation [42]. However, instead of string operators it is the Majorana operator which ensures the correct commutation relations between spin operators at different sites.

In the mixed representation (6), the XXZ-Z model (1) reads

$$H_{\mathrm{XXZ}} = \sum_{i<j}\Bigg[J^{\perp}_{ij}(c^{\dagger}_j c_i\eta_j\eta_i + c^{\dagger}_i c_j\eta_i\eta_j) - J^z_{ij}\left(c^{\dagger}_i c^{\dagger}_j c_i c_j + \frac{1}{2}c^{\dagger}_i c_i + \frac{1}{2}c^{\dagger}_j c_j - \frac{1}{4}\right)\Bigg], \tag{7}$$

$$H_Z = \sum_j h_j\left(\frac{1}{2} - c^{\dagger}_j c_j\right). \tag{8}$$

Now the noninteracting part (8) is diagonal in the fermionic flavor, the magnetic field acts as an on-site potential for the c fermions. This will greatly reduce the effort to include the magnetic Z field in the pm-fRG framework.

B. Symmetries

In the following, we discuss the gauge symmetries of the mixed representation (6) (which leave the spin operators invariant) and those associated to the XXZ-Z model (which leave the Hamiltonian H invariant). Together, they restrict the set of possible nonzero correlation and vertex functions and thus ultimately simplify the fRG flow equations. Spatial symmetries of the underlying lattice are treated as discussed in Ref. [16].

1. Local $\mathbb{Z}_2$ gauge symmetry

The spin operators in Eq. (6) are invariant under a local $\mathbb{Z}_2$ gauge transformation that acts on all fermionic operators at site j as $\Phi_j \equiv (c_j, c_j^\dagger, \eta_j)^T \to -\Phi_j$. This enforces bilocal correlations which means that all correlators with an odd number of fermionic site-j operators vanish. The $\mathbb{Z}_2$ symmetry is associated with an artificial degeneracy of the pseudofermionic eigenstates, with a degeneracy factor of $2^{N/2}$ for N lattice sites [39] reflecting all possible fermion parities for pairs of sites.

2. Antiunitary symmetry

The spin operators in Eq. (6) are further invariant under a global antiunitary symmetry,

$$au: \; i \to -i, \;\; \eta_j \to -\eta_j \; \forall j. \tag{9}$$

This symmetry forces real-valued correlators with an odd number of Majorana operators to vanish. Moreover, it also relates frequencies $\pm\omega$ in Fourier-transformed imaginary time-ordered correlators to be defined below. This is further discussed in Appendix D.

We now turn to the specific symmetries of the Hamiltonian operators, (7) and (8).

3. Global U(1) symmetry

Both parts of the XXZ-Z Hamiltonian (1) are invariant under a global U(1) spin rotation symmetry around the spin-Z axis. In the mixed representation this amounts to

$$\mathrm{U}(1): \; c_j \to e^{i\theta} c_j, \;\; c_j^\dagger \to e^{-i\theta} c_j^\dagger \; \forall j, \tag{10}$$

and corresponds to c-fermion conservation. If the U(1) symmetry is unbroken, then only correlators including $c, c^\dagger$ in a pairwise fashion can exist because

$$\langle c^\dagger c^\dagger \rangle \overset{\mathrm{U}(1)}{=} e^{-2i\theta} \langle c^\dagger c^\dagger \rangle \forall \theta \Rightarrow \langle c^\dagger c^\dagger \rangle = 0. \tag{11}$$

4. $h_j = 0$: Time-reversal and particle-hole symmetry

Without magnetic fields $h_j = 0$, the XXZ Hamiltonian is symmetric under time-reversal $S_j^\alpha \to -S_j^\alpha \; \forall j, \alpha$ which is antiunitary and translates to the mixed representation (6) as follows

$$\mathrm{TR}: \;\; i \to -i, \;\; c \to c^\dagger, \;\; c^\dagger \to c. \tag{12}$$

Moreover, there exists a global particle hole symmetry

$$\mathrm{PH}: \;\; c_j \leftrightarrow c_j^\dagger. \tag{13}$$

In combination with time reversal, this ensures that for $h_j = 0$ all vertices are purely real.

III. GREEN'S FUNCTIONS AND ACTION

In this section, we discuss the Grassmann action [43] for the mixed representation and proceed to define the Green's function objects which are at the core of the diagrammatic method and in particular the fRG. We assume that the symmetries from Sec. II B, except TR and PH, are unbroken. Since we have performed a unitary transformation of the pseudo-Majorana operators, the action formalism for the SO(3) representation [44] can be applied to derive the two local two-point Green's functions $G_{c_i^\dagger c_i}, G_{\eta_i \eta_i}$. A fermionic two-point Matsubara Green's function in thermal equilibrium at temperature $T = 1/\beta$ is defined as

$$\begin{aligned}[\mathbf{G}]_{12} &= \int_0^\beta d\tau_1 d\tau_2 e^{i\omega_1\tau_1 + i\omega_2\tau_2} \langle \xi_2(\tau_2)\xi_1(\tau_1)\rangle \\ &\equiv \langle \xi_2 \xi_1 \rangle = -\langle \xi_1 \xi_2 \rangle = -[\mathbf{G}]_{21} \qquad (14a) \\ &\equiv -\frac{1}{\beta}\delta_{j_1 j_2}\delta_{\omega_1,-\omega_2} G_{12}(\omega_1). \qquad (14b)\end{aligned}$$

Here ξ_1 (and ξ_2) are elements of the Grassmann superfield vector $\Xi_1 = (\psi_1, \bar{\psi}_1, \zeta_1)^T$ related to the coherent states of $c, c^\dagger$ and η, respectively [43]. The multi-index 1 contains all information on particle type, lattice site j_1, and Matsubara frequency ω_1 (short for $\omega_{n_1} = [2n_1 + 1]\pi T, \; n_1 \in \mathbb{Z}$) which appear in the Fourier transformation

$$\xi_1(\tau) \equiv \frac{1}{\beta} \sum_{\omega_1} e^{-i\omega_1 \tau} \xi_1(\omega_1). \tag{15}$$

Note that unlike the standard convention for complex fermions, we use the same sign in the exponent regardless of particle type following Ref. [18].

In the Grassmann field formalism, we write the action as [14]

$$S[\Xi] = S_0[\Xi] + S_I[\Xi], \tag{16a}$$

$$S_0[\Xi] = \frac{1}{\beta}\sum_j \sum_{\omega_1,\omega_2} \left[\frac{1}{2}\Xi_j^T(\omega_1) i\omega_2 \Xi_j(\omega_2) - h_j \; \bar{\psi}_j(\omega_1)\psi_j(\omega_2)\right]\delta_{\omega_1,-\omega_2} \equiv \frac{1}{2\beta^2}\sum_{1,2} \Xi_1^T \left[\mathbf{G}_0^{-1}\right]_{12} \Xi_2, \tag{16b}$$

$$\begin{aligned}S_I[\Xi] = &-\frac{1}{2\beta}\sum_{i<j}\sum_{\omega_1,\omega_2} J_{ij}^z(\bar{\psi}_i(\omega_1)\psi_i(\omega_2) + \bar{\psi}_j(\omega_1)\psi_j(\omega_2))\delta_{\omega_1,-\omega_2} \\ &+ \frac{1}{\beta^3}\sum_{i<j}\sum_{\omega_1,\omega_2,\omega_3,\omega_4}\Big[J_{ij}^\perp(\bar{\psi}_j(\omega_1)\psi_i(\omega_2)\zeta_j(\omega_3)\zeta_i(\omega_4) + \bar{\psi}_i(\omega_1)\psi_j(\omega_2)\zeta_i(\omega_3)\zeta_j(\omega_4)) \\ &- J_{ij}^z \bar{\psi}_i(\omega_1)\bar{\psi}_j(\omega_2)\psi_i(\omega_3)\psi_j(\omega_4)\Big]\delta_{\omega_1+\omega_2,-\omega_3-\omega_4}.\end{aligned} \tag{16c}$$

Here and in the following, constant terms have been neglected. Note that the first line of $S_I[\Xi]$, which is only bilinear in the fields and thus noninteracting, will cancel against the Hartree-like contribution from the last term (see Appendix B 2). Using the Dyson equation $[\mathbf{G}] = [\mathbf{G}_0^{-1} - \mathbf{\Sigma}]^{-1}$ and the choice of $\mathbf{G}_0$ in Eq. (16b), we obtain for the full Green's functions (see Appendix A for details)

$$[\mathbf{G}]_{\psi_1\bar{\psi}_2} = -\frac{1}{\beta}\delta_{j_1 j_2}\delta_{\omega_1,-\omega_2}\frac{1}{i\omega_1 - h_{j_1} + \Sigma_{\bar{\psi}_2\psi_1}(\omega_1)} \equiv -\frac{1}{\beta}\delta_{j_1 j_2}\delta_{\omega_1,-\omega_2}G_{\psi_1\bar{\psi}_2}(\omega_1), \tag{17a}$$

$$[\mathbf{G}]_{\bar{\psi}_1\psi_2} = -\frac{1}{\beta}\delta_{j_1 j_2}\delta_{\omega_1,-\omega_2}\frac{1}{i\omega_1 + h_{j_1} + \Sigma_{\psi_2\bar{\psi}_1}(\omega_1)} \equiv -\frac{1}{\beta}\delta_{j_1 j_2}\delta_{\omega_1,-\omega_2}G_{\bar{\psi}_1\psi_2}(\omega_1), \tag{17b}$$

$$[\mathbf{G}]_{\zeta_1\zeta_2} = -\frac{1}{\beta}\delta_{j_1 j_2}\delta_{\omega_1,-\omega_2}\frac{1}{i\omega_1 + \Sigma_{\zeta_2\zeta_1}(\omega_1)} \equiv -\frac{1}{\beta}\delta_{j_1 j_2}\delta_{\omega_1,-\omega_2}G_{\zeta_1\zeta_2}(\omega_1). \tag{17c}$$

From the antisymmetry of $[\mathbf{G}]_{\psi_1\bar{\psi}_2}$, see Eq. (14a), it follows $G_{\bar{\psi}_1\psi_2}(\omega_1) = -G_{\psi_2\bar{\psi}_1}(-\omega_1)$ and hence also the antisymmetry of the self-energies

$$\Sigma_{\psi_2\bar{\psi}_1}(\omega_1) = -\Sigma_{\bar{\psi}_1\psi_2}(-\omega_1). \tag{18}$$

Here we used the following definitions:

$$[\mathbf{\Sigma}]_{\psi_1\bar{\psi}_2} \equiv \beta\delta_{j_1 j_2}\delta_{\omega_1,-\omega_2}\Sigma_{\psi_1\bar{\psi}_2}(\omega_2), \tag{19a}$$

$$[\mathbf{\Sigma}]_{\bar{\psi}_1\psi_2} \equiv \beta\delta_{j_1 j_2}\delta_{\omega_1,-\omega_2}\Sigma_{\bar{\psi}_1\psi_2}(\omega_2), \tag{19b}$$

$$[\mathbf{\Sigma}]_{\zeta_1\zeta_2} \equiv \beta\delta_{j_1 j_2}\delta_{\omega_1,-\omega_2}\Sigma_{\zeta_1\zeta_2}(\omega_2). \tag{19c}$$

Beyond the above fermionic two-point correlators, we also consider fermionic four-point correlators defined as

$$G_{1234} \equiv \int_0^\beta d\tau_1 d\tau_2 d\tau_3 d\tau_4 (e^{i\omega_1\tau_1 + i\omega_2\tau_2 + i\omega_3\tau_3 + i\omega_4\tau_4} \times \langle \xi_4(\tau_4)\xi_3(\tau_3)\xi_2(\tau_2)\xi_1(\tau_1)\rangle). \tag{20}$$

The one-particle irreducible contributions to G_{1234} are the four-point vertices Γ_{1234}, the formal connection is given via the tree expansion [14]. Of the $3^4 = 81$ possible combinations of field types, most vanish due to U(1) and $\mathbb{Z}_2$ symmetry. Using the antisymmetry under multi-index exchange and the bilocal nature, only five different four-point vertices are independent, $\Gamma_{\bar{\psi}_i\bar{\psi}_i\psi_j\psi_j}$, $\Gamma_{\bar{\psi}_i\bar{\psi}_j\psi_i\psi_j}$, $\Gamma_{\bar{\psi}_i\psi_i\zeta_j\zeta_j}$, $\Gamma_{\bar{\psi}_i\psi_j\zeta_i\zeta_j}$, and $\Gamma_{\zeta_i\zeta_i\zeta_j\zeta_j}$. Moreover, energy conservation is taken into account via reduction to three bosonic transfer frequencies [18],

$$\Gamma_{1234}(s,t,u) \equiv \beta\delta_{0,\omega_1+\omega_2+\omega_3+\omega_4}\Gamma_{1234}(\omega_1,\omega_2,\omega_3,\omega_4), \tag{21}$$

where we define

$$\begin{aligned} s &\equiv \omega_1 + \omega_2 = -\omega_3 - \omega_4, \\ t &\equiv \omega_1 + \omega_3 = -\omega_2 - \omega_4, \\ u &\equiv \omega_1 + \omega_4 = -\omega_2 - \omega_3. \end{aligned} \tag{22}$$

For a lighter notation, we finally drop all redundant labels. For the two-point objects we write

$$\Sigma_{\psi,j}(\omega) \equiv \Sigma_{\bar{\psi}_j\psi_j}(\omega), \tag{23a}$$

$$\Sigma_{\zeta,j}(\omega) \equiv \Sigma_{\zeta_j\zeta_j}(\omega), \tag{23b}$$

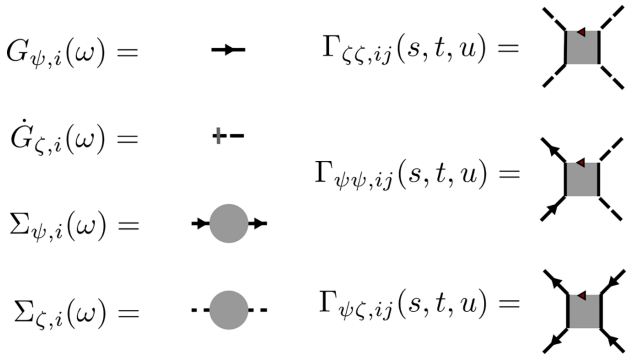

FIG. 1. Diagrammatic representation of the two- and four-point objects defined in Eqs. (23)–(25). Dashed lines correspond to the field ζ representing Majorana operator η, full lines with arrows pointing away (towards) the vertex correspond to $\bar{\psi}$ (ψ) representing the complex fermion. The small arrow at the box boundary points towards the first index of Γ_{1234}, the others follow in an counterclockwise sense.

with ω on the left-hand side referring to the *second* field on the right-hand side, cf. Eq. (19a). Equivalently for the full propagators, with ω referring to the *first* field's frequency [cf. Eq. (14a)], we define

$$G_{\psi,j}(\omega) \equiv G_{\bar{\psi}_j\psi_j}(\omega), \tag{24a}$$

$$G_{\zeta,j}(\omega) \equiv G_{\zeta_j\zeta_j}(\omega). \tag{24b}$$

For the four-point vertices we simplify the notation to account explicitly for their bilocal nature,

$$\Gamma_{\psi\psi,ij}(s,t,u) \equiv \Gamma_{\bar{\psi}_i\bar{\psi}_i\psi_j\psi_j}(s,t,u), \tag{25a}$$

$$\Gamma^{\times}_{\psi\psi,ij}(s,t,u) \equiv \Gamma_{\bar{\psi}_i\bar{\psi}_j\psi_i\psi_j}(s,t,u), \tag{25b}$$

$$\Gamma_{\psi\zeta,ij}(s,t,u) \equiv \Gamma_{\bar{\psi}_i\psi_i\zeta_j\zeta_j}(s,t,u), \tag{25c}$$

$$\Gamma^{\times}_{\psi\zeta,ij}(s,t,u) \equiv \Gamma_{\bar{\psi}_i\psi_j\zeta_i\zeta_j}(s,t,u), \tag{25d}$$

$$\Gamma_{\zeta\zeta,ij}(s,t,u) \equiv \Gamma_{\zeta_i\zeta_i\zeta_j\zeta_j}(s,t,u). \tag{25e}$$

The superscript $\times$ indicates that the *first* and *third* field are site-paired, without the superscript the pairing is between the *first* and *second* field. Furthermore, the antisymmetry under exchange of two fields can be used to restrict the required frequency combinations, see Appendix D. The diagrammatic representation of these objects is given in Fig. 1.

IV. OBSERVABLES IN THE MIXED REPRESENTATION

In this section, we discuss spin observables and their expressions in terms of the two- and four-point functions of the pseudofermionic mixed representations. We focus on the magnetization in Z direction and the static spin susceptibility. As in both cases we are calculating operator averages, $\langle O\rangle = \mathrm{tr}(O\rho)/\mathrm{tr}(\rho)$, the aforementioned $2^{N/2}$-fold degeneracy of the spin representation reflected in the parity sectors of the density matrix $\rho \sim e^{-\beta H}$ is simply canceled between numerator and denominator [18].

A. Magnetization

One main objective of this work is to compute the magnetization in Z direction which is related to the c-fermion two-point function. For site j, we have from Eq. (4),

$$\begin{aligned} M_j \equiv \langle S_j^z \rangle &= \frac{1}{2} - \lim_{\epsilon\to 0} \langle \bar{\psi}_j(\tau+\epsilon)\psi_j(\tau)\rangle \\ &= \frac{1}{2} - \lim_{\epsilon\to 0} \frac{1}{\beta}\sum_\omega e^{i\omega\epsilon}\langle \bar{\psi}_j(\omega)\psi_j(-\omega)\rangle \\ &= \frac{1}{2} - \lim_{\epsilon\to 0} \frac{1}{\beta}\sum_\omega e^{i\omega\epsilon} G_{\psi,j}(\omega), \end{aligned} \tag{26}$$

where the positive infinitesimal ϵ ensures the proper operator ordering. Numerically, such sums over Green's functions converge very poorly [45] and part of the sum should be performed analytically. The convergence generating factor $e^{i\omega\epsilon}$ with $\epsilon \geqslant 0,\ \epsilon \to 0$ is omitted in the following. We use Eq. (17) and split into real and imaginary part,

$$\begin{aligned} &\sum_\omega G_{\psi,j}(\omega) \\ &= \sum_\omega \frac{1}{i\omega + h_j - \Sigma_{\psi,j}(-\omega)} \\ &= \sum_\omega \frac{h_j - \mathrm{Re}[\Sigma_{\psi,j}(\omega)]}{(h_j - \mathrm{Re}[\Sigma_{\psi,j}(\omega)])^2 + (\omega + \mathrm{Im}[\Sigma_{\psi,j}(\omega)])^2} \\ &\quad + i\sum_\omega \frac{\omega + \mathrm{Im}[\Sigma_{\psi,j}(\omega)]}{(h_j - \mathrm{Re}[\Sigma_{\psi,j}(\omega)])^2 + (\omega + \mathrm{Im}[\Sigma_{\psi,j}(\omega)])^2}. \end{aligned} \tag{27}$$

The imaginary part is asymmetric in ω and only the large-ω tail contributes, for which we re-establish the convergence factor. From

$$\lim_{\epsilon\to 0} i\sum_\omega e^{i\omega\epsilon}\frac{1}{\omega} = \frac{\beta}{2}. \tag{28}$$

we observe that this contribution cancels the $1/2$ in Eq. (26). In conclusion,

$$M_j = \frac{1}{\beta}\sum_\omega \frac{\mathrm{Re}[\Sigma_{\psi,j}(\omega)] - h_j}{(h_j - \mathrm{Re}[\Sigma_{\psi,j}(\omega)])^2 + (\omega + \mathrm{Im}[\Sigma_{\psi,j}(\omega)])^2}. \tag{29}$$

In practice it is advisable to extrapolate $\Sigma_{\psi,j}(\omega)$ beyond the numerically computed frequency box, see Appendix D.

B. Spin susceptibilities

The static spin susceptibility defined as $\chi_{ij}^{zz} = -\partial M_i/\partial h_j$ can also be computed from the four-point fermionic correlator. Generalizing to arbitrary directions α, α' in spin space, the definition reads

$$\begin{aligned} \chi_{ij}^{\alpha\alpha'} &= \int_0^\beta d\tau \left\langle S_i^\alpha(\tau) S_j^{\alpha'}(0)\right\rangle_c \\ &= \int_0^\beta d\tau \left\langle \left(S_i^\alpha(\tau) - \langle S_i^\alpha(\tau)\rangle\right)\left(S_j^{\alpha'}(0) - \left\langle S_i^{\alpha'}(0)\right\rangle\right)\right\rangle, \end{aligned} \tag{30}$$

but only the cases $\alpha = \alpha' = z$ and $\alpha = \alpha' = x$ [equal to $\alpha = \alpha' = y$ by U(1) symmetry] are nonzero and independent. Inserting the mixed spin representation (6) and relating the four-point function to the vertices Γ via the tree expansion [14], we arrive at

$$\begin{aligned} \chi_{ij}^{zz} = \frac{1}{\beta^2}\sum_{\omega,\omega'} \big[& G_{\psi,i}^2(\omega) G_{\psi,j}^2(\omega') \\ & \times \Gamma^{\times}_{\psi\psi,ij}(\omega+\omega', 0, \omega-\omega') - \beta\delta_{ij}\delta_{\omega,\omega'} G_{\psi,i}^2(\omega)\big]. \end{aligned} \tag{31}$$

and

$$\begin{aligned} \chi_{ij}^{xx} = \frac{1}{\beta^2}\sum_{\omega\omega'} \big[& -\beta\delta_{ij}\delta_{\omega,\omega'} G_{\psi,i}(\omega) G_{\zeta,i}(\omega) \\ & + G_{\psi,j}(\omega) G_{\psi,i}(-\omega') G_{\zeta,j}(\omega) G_{\zeta,i}(\omega') \\ & \times \Gamma^{\times}_{\psi\zeta,ij}(-\omega-\omega', 0, \omega-\omega')\big]. \end{aligned} \tag{32}$$

Also, it is straightforward to also extract dynamic spin susceptibilities at nonzero bosonic frequency $i\Omega_n$, see Ref. [16]. Then a sum over this frequency would yield the equal-time spin correlator. Although not required in the following, we also note the important role of the spin susceptibilities in a finite-size scaling approach to detect magnetic phase transitions, see, e.g., Refs. [17,19].

V. FRG FLOW EQUATIONS IN THE MIXED REPRESENTATION

The basic idea of the fRG [14,15,46] is to modify the bare propagator $\mathbf{G}_0$ in Eq. (16b) by a deformation (or cutoff) quantified the scalar Λ. Variation of Λ defines a flow. By convention, the starting point is $\Lambda = \infty$ where the action is trivial such that all one-particle irreducible vertices are known exactly. Then a hierarchy of flow equations is derived that govern the variation of the vertices with Λ and in particular allow to compute them in the case $\Lambda = 0$ where we recover the undeformed physical action. However, truncations are necessary to solve the flow equations in practice. In the following, we build on the general superfield formulation of fRG put forward in Ref. [14].

As the main result of this work we here present the fRG flow equations for the XXZ-Z model in the mixed representation. In general, the form of the fRG flow equations are independent of the chosen cutoff, in this work however, we apply a multiplicative Lorentzian cutoff $\mathbf{G}_0^\Lambda = \theta_\Lambda \mathbf{G}_0$ in frequency further detailed in Sec. V A. We proceed with the flow equations of the self-energy and discuss the overall structure of the flow equations for the four-point vertices using one example. The full flow equations of the four-point vertices are given in Appendix B. There we also introduce the Katanin truncation [47] which we use to include parts of the six-point vertex. The initial conditions for the flow are derived in Appendix B 2.

A. Cutoff and single-scale propagator

In this work, we follow Refs. [18,19,24] and apply a Lorentzian cutoff function to smoothly switch off the bare propagator at Matsubara frequencies smaller in magnitude

than Λ,

$$\theta_\Lambda(\omega) = \frac{\omega^2}{\omega^2+\Lambda^2}, \quad \frac{\partial_\Lambda \theta_\Lambda}{\theta_\Lambda^2} = -\frac{2\Lambda}{\omega^2}. \tag{33}$$

The flow equations depend on the single-scale propagators [14], $\dot{\mathbf{G}}^\Lambda \equiv -\mathbf{G}^\Lambda(\partial_\Lambda \mathbf{G}_0^{\Lambda\,-1})\mathbf{G}^\Lambda$, given by

$$\begin{aligned}[\dot{\mathbf{G}}^\Lambda]_{\bar{\psi}_1\psi_2} &= -\frac{\partial_\Lambda\theta_\Lambda}{\beta\theta_\Lambda^2}\frac{\delta_{j_1j_2}\delta_{\omega_1,-\omega_2}\big(i\omega_1 - h_{j_1}\big)}{\big((i\omega_1+h_{j_1})\theta_\Lambda^{-1}(\omega_1)+\Sigma_{\psi_2\bar{\psi}_1}(\omega_1)\big)^2} \\ &\equiv -\frac{1}{\beta}\delta_{j_1j_2}\delta_{\omega_1,-\omega_2}\dot{G}^\Lambda_{\psi,j_1}(\omega_1), \end{aligned} \tag{34a}$$

$$\begin{aligned}[\dot{\mathbf{G}}^\Lambda]_{\zeta_1\zeta_2} &= -\frac{\partial_\Lambda\theta_\Lambda}{\beta\theta_\Lambda^2}\frac{\delta_{j_1j_2}\delta_{\omega_1,-\omega_2} i\omega_1}{\big(i\omega_1\theta_\Lambda^{-1}(\omega_1)+\Sigma_{\zeta_2\zeta_1}(\omega_1)\big)^2} \\ &\equiv -\frac{1}{\beta}\delta_{j_1j_2}\delta_{\omega_1,-\omega_2}\dot{G}^\Lambda_{\zeta,j_1}(\omega_1). \end{aligned} \tag{34b}$$

Here the abbreviated notation is analogous to Eq. (24) for the Green's functions.

B. Self-energy flow

The flow equations for the fermionic self-energy are

$$\begin{aligned}\partial_\Lambda \Sigma^\Lambda_{\psi,i}(-\omega) = \frac{1}{2\beta}\sum_j\sum_{\omega'} &\times\big[-2\dot{G}^\Lambda_{\psi,j}(\omega')\Gamma^{\Lambda\times}_{\psi\psi,ji}(\omega'+\omega,0,\omega'-\omega) \\ &+\dot{G}^\Lambda_{\zeta,j}(\omega')\Gamma^\Lambda_{\psi\zeta,ij}(0,\omega'+\omega,-\omega'+\omega)\big], \end{aligned} \tag{35a}$$

$$\begin{aligned}\partial_\Lambda \Sigma^\Lambda_{\zeta,i}(-\omega) = \frac{1}{2\beta}\sum_j\sum_{\omega'} &\times\big[2\dot{G}^\Lambda_{\psi,j}(\omega')\Gamma^\Lambda_{\psi\zeta,ji}(0,\omega'+\omega,\omega'-\omega) \\ &+\dot{G}^\Lambda_{\zeta,j}(\omega')\Gamma^\Lambda_{\zeta\zeta,ji}(0,\omega'+\omega,\omega'-\omega)\big]. \end{aligned} \tag{35b}$$

The corresponding diagrams are shown in Fig. 2. Note that the mixed four-point vertices involving the ψ and ζ fields appear on the right-hand side of these flow equations. This is also the case for the flow of the four-point vertices discussed next.

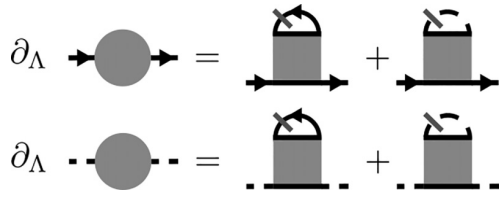

FIG. 2. Diagrammatic representation of $\partial_\Lambda \Sigma^\Lambda_{\zeta,i}$ (35b) and $\partial_\Lambda \Sigma^\Lambda_{\psi,i}$ (35a). According to Fig. 1, connected lines represent fields on the same lattice site. A closed loop corresponds to a sum over internal site and frequency indices.

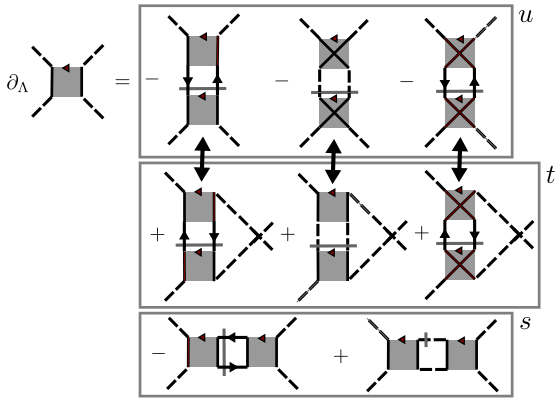

FIG. 3. Diagrammatic representation of $\partial_\Lambda \Gamma^\Lambda_{\zeta\zeta,ij}$ grouped into s, t, u channels characterizing the dependence of the internal propagator loop on the external frequencies. The t and u channel are related by an exchange of external legs. Frequencies and prefactors are omitted here for clarity, they are given in Appendix B 1.

C. Flow equations for four-point vertex

We finally turn to the flow equations for the four-point vertices Γ^Λ where the six-point vertex is approximated to remain at its initial condition which is zero. [However, we involve parts of the six-point vertex using the Katanin truncation, see Appendix B 3.] Here we restrict ourselves to a discussion of $\partial_\Lambda \Gamma^\Lambda_{\zeta\zeta,ij}$ to illustrate the nature of the flow equations, see Fig. 3. We provide the full set of flow equations in Appendix B. The flow equation involves all possible symmetry-allowed combinations of vertices. This includes combinations of pure Majorana vertices but also the mixed vertices. Furthermore terms can be split into three groups, see the boxes in Fig. 3. Terms including internal site sums (third line in Fig. 3) depend on an internal propagator loop characterized by the bosonic frequency s, while those that have crossed (amputated) external legs are characterized by t and all other terms by u, respectively. For pure pm-fRG, terms that depend on u and t are symmetry related by the exchange of external legs. In our formalism, however, this symmetry only exist in flow equations for noncrossed vertices $\partial_\Lambda \Gamma^\Lambda$ and not for crossed vertices $\partial_\Lambda \Gamma^{\Lambda\times}$. If the considered flow-equation is local $i = j$, then further simplifications are possible as crossed and noncrossed vertices are equal in that case.

VI. BENCHMARK TESTS

To test the implementation and capabilities of the U(1)-pm-fRG we now proceed to benchmark it against exact analytical results and QMC. We also checked that the results applied to various Heisenberg models with SU(2) symmetry reproduce data obtained with the standard pm-fRG [18,19]. In the following we use the Katanin truncation of the flow equations, with the results presented in Sec. VI A as the sole exception. Details on the numerical implementation are given in Appendix C.

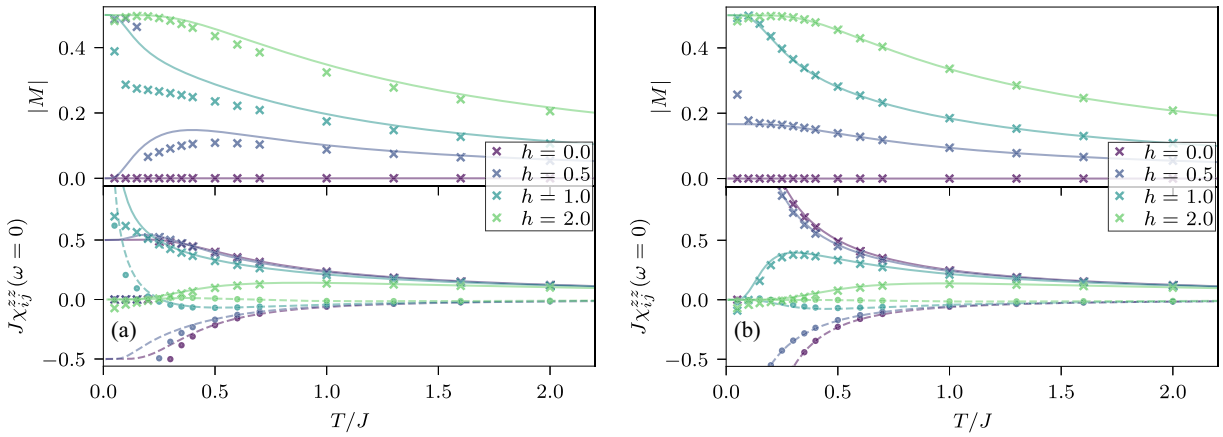

FIG. 4. (a) AFM Heisenberg dimer $J^z = 1,\ J^\perp = 1$: Magnetization $|M|$ (top) and static susceptibility $\chi^{zz}_{ij}(i\omega_m = 0)$ (bottom) as a function of temperature for various external magnetic fields h. Lines correspond to the exact solution while symbols denote fRG results. For the susceptibility we distinguish the local (crosses) and nonlocal (dots) case. (b) The same as in (a) but for the Ising case $J^z = 1,\ J^\perp = 0$.

A. XXZ dimer

Following the practice in the development of pm-fRG [17,18,22] we begin with the simple model of two spins $j = 1, 2$ interacting with Hamiltonian (1). Though analytically solvable, from the viewpoint of pm-fRG this dimer model possesses already the full complexity which makes it an excellent system for benchmarking. In Fig. 4 we show the magnetization and static susceptibilities for the AFM Heisenberg and Ising case in various Z fields, see Figs. 4(a) and 4(b), respectively. As in standard pm-fRG [18] the U(1)-pm-fRG results are excellent at large temperatures $T \gtrsim J$ and start to deviate strongly from the exact solution at model-dependent temperature scales usually around $T \simeq J/3$. In both cases, we also verified the anticipated scaling of the error at large T/J. We observe that the fRG performs better for the Ising than for the Heisenberg model, in the latter deviations are especially severe at low temperatures if the ground state is degenerate (for $h = 1$). As we will show later, better accuracy of the fRG can be expected in higher spatial dimensions by full incorporation of the mean-field equations [16]. Finally, we perform the following consistency check [25] between the static susceptibilities calculated from Eq. (31) using the fermionic four-point vertex and appropriate field derivatives of local magnetizations. We break the dimer's inversion symmetry by small $\Delta h_1 = -\Delta h_2 \equiv \Delta h$ and obtain from $\Delta M \equiv M_1 - M_2$ the following relation valid in the linear response regime $\Delta h \to 0$:

$$\frac{\Delta M}{\Delta h} = \frac{M_1 - M_2}{\Delta h} = \chi^{zz}_{11} - \chi^{zz}_{12} - \chi^{zz}_{21} + \chi^{zz}_{22} \equiv \tilde{\chi}^{zz}. \quad (36)$$

In Fig. 5 we confirm that this relation is indeed fulfilled to few percentages accuracy for a dimer with $J^z = 1$, $J^\perp = 0.5$, $h = 1$, and $\Delta h = 0.002$.

B. FM Heisenberg model on square lattice

We now turn to extended systems and demonstrate the U(1)-pm-fRG's ability to capture magnetization curves $M(T)$. We compare our results for the FM Heisenberg model on the square lattice to error controlled QMC results of Ref. [48]. The fRG result is displayed in Fig. 6 and shows good agreement with QMC until low temperatures where the truncation of higher-order vertices is not justified any longer. We observe that the quality of the fRG results improves with increasing magnetic field h. This is to be expected since a larger h diminishes the relative weight of the interacting term in the Hamiltonian H. Following the line for $h = 0.2$ to low temperatures, a drastic and unphysical dip in $M(T)$ is observed. This is traced back to sharp changes in some vertex components and an associated numerical instability in the fRG flow. Such a behavior often arises when the slope of $M(T)$ is large. This generally occurs at low h and large L.

C. Spontaneous magnetization on cubic lattice Heisenberg model

In three spatial dimensions (short-range) XXZ models can feature long-range order and spontaneous breaking of spin-rotation and time-reversal symmetries below a critical temperature T_c. Previous applications of the pm-fRG [19,22,24] have shown the method's potential to determine T_c within a few percentages accuracy from exact results (when

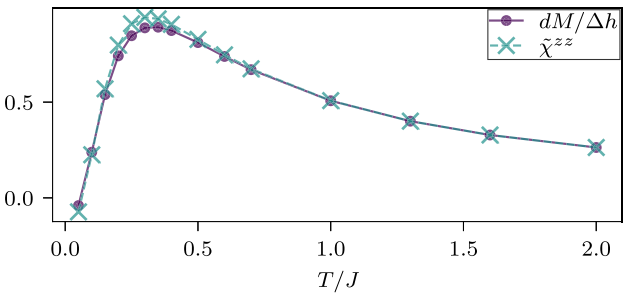

FIG. 5. Confirmation of the relation (36) between field derivatives of the magnetization and the susceptibility computed with U(1)-pm-fRG for the dimer. The model parameters are $J^z = 1,\ J^\perp = 0.5$, $h = 1$ and we set $\Delta h = 0.002$. Lines are guides to the eye.

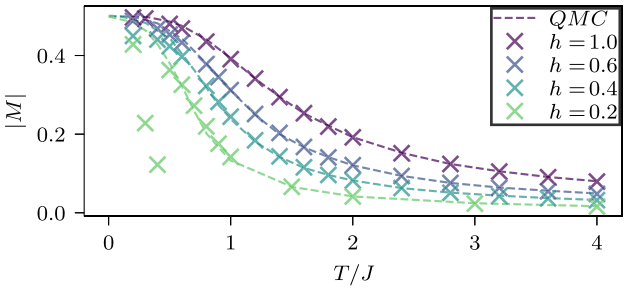

FIG. 6. Magnetization $|M|$ for the FM Heisenberg model on the square lattice for various applied magnetic fields h. Cross markers show fRG results and lines denote QMC results [48].

the latter are available). One of the new features of the U(1)-pm-fRG is the ability to enter the spontaneously ordered phase [if it preserves U(1) spin rotation symmetry] and compute the magnetization $M(T)$ across the phase transition. However, a small but finite symmetry breaking field h is required.

To test these capabilities we turn to the mixed FM-AFM cubic lattice XXZ model with interactions $J^z = -1, J^\perp = 0.3$ and plot the Z magnetization $M(T)$ with various small fields h. The results in Fig. 7 show the expected sharp increase in magnetization around T_c. The onset of magnetization sharpens with decreasing h. For $h = 0.01$ we also compare to QMC results obtained with the worm-type QMC code of Refs. [49,50] and observe good agreement.

VII. APPLICATION: TRIANGULAR LATTICE

We finally apply the U(1)-pm-fRG developed above to real materials studied in recent experiments. In particular, we consider $S = 1/2$ compounds with triangular lattice structure and frustrated in-plane AFM couplings $J^\perp > 0$ not amenable to QMC simulations due to the sign problem [4].

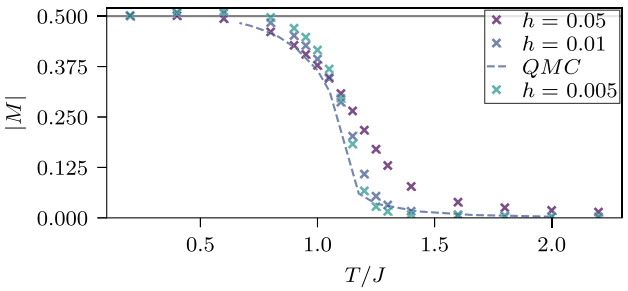

FIG. 7. Magnetization $|M|$ for the XXZ Heisenberg model ($J^z = -1, J^\perp = 0.3$) on the cubic lattice with various small seed fields h. Cross markers show fRG results with $L = 10$ as the radius of the correlation ball. A dashed line shows error controlled QMC results for $h = 0.01$ and a cube of linear extent of ten sites and periodic boundary conditions. Finite-size corrections are negligible on the scale of the plot. The small overshoot $M \gtrsim 0.5$ for small temperatures is a numerical artifact related to truncation of frequency sums.

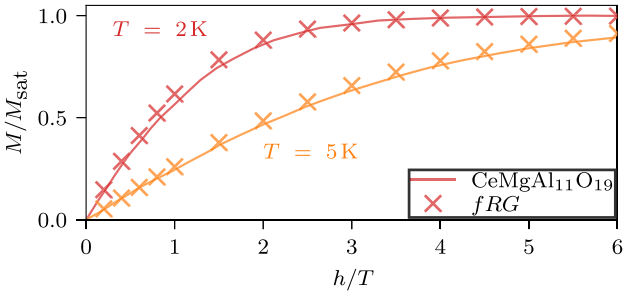

FIG. 8. Consistency check of the proposed XXZ-Z model for $CeMgAl_{11}O_{19}$ using the magnetization data $M(h)$ in units of the saturated magnetization (lines) from Ref. [29]: The crosses show results from the U(1)-pm-fRG applied to the triangular lattice XXZ-Z model with $J^\perp = 0.6469K$, $J^z = -0.2784K$ and $g^z = 3.66$ at temperatures $T = 2$ K and 5 K.

A. Magnetization in $CeMgAl_{11}O_{19}$

Our first application considers the recently investigated rare-earth hexaaluminate material $CeMgAl_{11}O_{19}$. Using inelastic neutron spectra in fully polarizing magnetic out-of-plane fields h, Gao *et al.* [29] determined the Hamiltonian to be well approximated as nearest-neighbor XXZ with $J^\perp = 0.6469K$ and $J^z = -0.2784K$. The large anisotropy is due to spin-orbit coupling. Crucially, the ratio of both couplings is close to the point $J^\perp/J^z = -0.5$ which separates magnetically ordered FM and coplanar 120° phases. At this point, the model features and exactly solvable and highly degenerate "spin-liquid" ground state [51]. In Ref. [29], this insight was used to model the measured $h = 0$ inelastic neutron-scattering spectrum of $CeMgAl_{11}O_{19}$.

Here, by employing the U(1)-pm-fRG we verify that the proposed model indeed accurately reproduces the experimental out-of-plane magnetization data provided in Ref. [29] for $T = 2$ K and 5 K, see Fig. 8. We use the Landé factor $g^z = 3.66$ reported from an ESR measurement [29] to model the Zeeman term as $H_Z = g^z \mu_B \sum_j h S_j^z$, where μ_B is the Bohr magneton.

B. Three-sublattice spin solid in $Na_2BaCo(PO_4)_2$

As a second application of the U(1)-pm-fRG we consider the material $Na_2BaCo(PO_4)_2$ recently studied in Refs. [30–34] and identified to host a spin supersolid phase [37]. The Co^{2+} ions are host to effective $S = 1/2$ spins. The nearest-neighbor XXZ-Z model parameters were estimated as [37] $J^\perp = 0.8K$, $J^z = 1.48K$ with $g^z = 4.89$ the Landé factor.

A spin supersolid is characterized by the simultaneous breaking of lattice translation symmetry and U(1)-spin rotation symmetry. However, in the model at hand this only occurs at very small temperatures <0.2K and thus remains out of reach for the fRG. Instead we consider the transition to three-sublattice up-up-down spin solid order also found experimentally in Ref. [37], see the inset of Fig. 9 for a sketch. We set $h = 2.465K$ (corresponding to $0.75T$) and consider the susceptibility relating the order parameter $(M_a + M_b)/2 - M_c$ to an additional symmetry-breaking seed field $\Delta h_a = \Delta h_b = -\Delta h_c \equiv \Delta h$ (which we keep finite for numerical stability

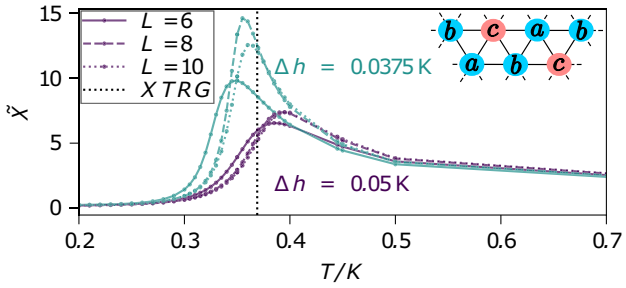

FIG. 9. Susceptibility $\tilde{\chi}^{zz}$ from Eq. (37) detects the transition to three-sublattice order (inset) in the XXZ-Z triangular lattice model for $Na_2BaCo(PO_4)_2$ with $J^{\perp} = 0.8K$, $J^z = 1.48K$, and $h = 2.465K$ studied in Ref. [37]. The two values used for the small symmetry-breaking field Δh are given in the panel. Even smaller symmetry breaking field would cause numerical instabilities in the fRG flow. The vertical line shows the XTRG results from Ref. [37].

across T_c),

$$\tilde{\chi}^{zz} = \sum_j \big[\big(\chi^{zz}_{1_a j_a} + \chi^{zz}_{1_a j_b} - \chi^{zz}_{1_a j_c}\big)/2 + \big(\chi^{zz}_{1_b j_a} + \chi^{zz}_{1_b j_b} - \chi^{zz}_{1_b j_c}\big)/2 - \big(\chi^{zz}_{1_c j_a} + \chi^{zz}_{1_c j_b} - \chi^{zz}_{1_c j_c}\big)\big]. \tag{37}$$

Here j_s labels sublattice sites $s = a, b, c$ for lattice site j and the χ^{zz} on the right-hand side are computed using Eq. (31). In Fig. 9 we show the resulting peak structure of $\tilde{\chi}^{zz}(T)$ which sharpens with increased correlation distance $L = 6, 8, 10$. The center of the peak indicates the transition temperature T_c, does not vary much with Δh and is in good agreement with experimental and exponential tensor renormalization group (XTRG) results [6,37] (vertical line). The main advantage of our U(1)-pm-fRG over the XTRG simulation of Ref. [37] is the ensured convergence in system size. While we use a correlation disk of radius $L \leqslant 10$ embedded in an infinite lattice, the XTRG [37] operates on cylinders of relatively small width $W = 6$.

VIII. SUMMARY AND OUTLOOK

We have introduced a U(1)-pm-fRG scheme based on a symmetry adapted mixed fermionic spin representation for XXZ-Z-type spin $S = 1/2$ models. The advantage of the mixed representation is that it diagonalizes the noninteracting Hamiltonian (and Green's function). This makes fRG calculations with an external magnetic field feasible and allows for the calculation of magnetization and access to the ordered phase. We have derived relevant observables and the fRG flow equations in the usual Katanin truncation with a smooth Matsubara frequency cutoff. The implementation of the more efficient temperature flow scheme recently introduced in the context of pm-fRG [22] is left for future work. Here technical complications are expected since the presence of magnetic fields require large frequency boxes, which could be made feasible by applying vertex compression schemes [52].

We also provided compelling benchmark checks against established exact and QMC results. For applications to real materials, we chose the highly frustrated triangular lattice in magnetic fields. As a first example, in the case of $CeMgAl_{11}O_{19}$ we show excellent agreement of fRG simulations of magnetization curves of the proposed model against experimental results. Second, we reproduced the experimentally determined critical temperature for the transition into the up-up-down three-sublattice spin solid phase in $Na_2BaCo(PO_4)_2$.

We expect that the U(1)-pm-fRG will be especially useful for the application to three-dimensional frustrated XXZ-Z magnets where alternative methods are scarce. In addition, it is also straightforward to adapt our approach to other spin models with U(1) symmetry. This includes, for example, the Jaynes-Cummings model of quantum optics [53] after the bosonic degrees of freedom have been traced out to produce a retarded spin-spin interaction. It would also be interesting to generalize the U(1)-pm-fRG for XXZ-Z models to larger spins, especially to $S = 3/2$ where a faithful pseudo-Majorana representation exists [54]. The pm-fRG was also recently applied to a $S = 1$ model (without magnetic fields) where however the influence of the inevitable unphysical states had to be mitigated [55].

ACKNOWLEDGMENTS

We thank Jan von Delft, Johannes Reuther and the authors of Ref. [29] for discussions. F.B. acknowledges support by the SFB Q-M&S (FWF Project ID F86). B.Sch. and B.Sb. acknowledge support from DFG Grant No. 524270816. B.Sb. acknowledges support from DFG through the Research Unit FOR 5413/1 (Grant No. 465199066). B.Sch. acknowledges funding from the Munich Quantum Valley, supported by the Bavarian state government with funds from the Hightech Agenda Bayern Plus. The authors gratefully acknowledge the Gauss Centre for Supercomputing e.V. [56] for funding this project by providing computing time through the John von Neumann Institute for Computing (NIC) on the GCS Supercomputer JUWELS at Jülich Supercomputing Centre (JSC).

DATA AVAILABILITY

A numerical implementation of the U(1)-pm-fRG is available at [57].

APPENDIX A: DETAILS ON GREEN'S FUNCTIONS

We explain how the expressions for the full Green's function Eq. (17) are obtained from the action in Eq. (16). In the convention of Ref. [14] the matrix components of the noninteracting Green's function in the superfield basis read

$$\big[\mathbf{G}_0^{-1}\big]_{\psi_1\bar{\psi}_2} = \beta\delta_{j_1 j_2}\delta_{\omega_1,-\omega_2}(i\omega_1 - h_{j_1}) \equiv \beta\delta_{j_1 j_2}\delta_{\omega_1,-\omega_2} G^{-1}_{0,\psi_1\bar{\psi}_2}(\omega_1), \tag{A1a}$$

$$\big[\mathbf{G}_0^{-1}\big]_{\bar{\psi}_1\psi_2} = \beta\delta_{j_1 j_2}\delta_{\omega_1,-\omega_2}(i\omega_1 + h_{j_1}) \equiv \beta\delta_{j_1 j_2}\delta_{\omega_1,-\omega_2} G^{-1}_{0,\bar{\psi}_1\psi_2}(\omega_1), \tag{A1b}$$

$$\big[\mathbf{G}_0^{-1}\big]_{\zeta_1\zeta_2} = \beta\delta_{j_1 j_2}\delta_{\omega_1,-\omega_2}(i\omega_1) \equiv \beta\delta_{j_1 j_2}\delta_{\omega_1,-\omega_2} G^{-1}_{0,\zeta_1\zeta_2}(\omega_1). \tag{A1c}$$

The inversion of the above equations requires special care in the frequency and particle sectors,

$$[\mathbf{G}_0]_{\psi_1\bar{\psi}_2} = -\frac{1}{\beta}\delta_{j_1 j_2}\delta_{\omega_1,-\omega_2}\frac{1}{i\omega_1 - h_{j_1}} \equiv -\frac{1}{\beta}\delta_{j_1 j_2}\delta_{\omega_1,-\omega_2}G^0_{\psi_1\bar{\psi}_2}(\omega_1), \tag{A2a}$$

$$[\mathbf{G}_0]_{\bar{\psi}_1\psi_2} = -\frac{1}{\beta}\delta_{j_1 j_2}\delta_{\omega_1,-\omega_2}\frac{1}{i\omega_1 + h_{j_1}} \equiv -\frac{1}{\beta}\delta_{j_1 j_2}\delta_{\omega_1,-\omega_2}G^0_{\bar{\psi}_1\psi_2}(\omega_1), \tag{A2b}$$

$$[\mathbf{G}_0]_{\zeta_1\zeta_2} = -\frac{1}{\beta}\delta_{j_1 j_2}\delta_{\omega_1,-\omega_2}\frac{1}{i\omega_1} \equiv -\frac{1}{\beta}\delta_{j_1 j_2}\delta_{\omega_1,-\omega_2}G^0_{\zeta_1\zeta_2}(\omega_1). \tag{A2c}$$

The propagator matrices are antisymmetric,

$$G^0_{12}(\omega_1) = -G^0_{21}(\omega_2) = -G^0_{21}(-\omega_1). \tag{A3}$$

The full propagator is given by Dyson's equation,

$$[\mathbf{G}]_{12} = [\mathbf{G}^0]_{12} + [\mathbf{G}^0]_{13}[\mathbf{\Sigma}]_{34}[\mathbf{G}]_{42}, \tag{A4}$$

from which we obtain Eq. (17).

APPENDIX B: DETAILED FLOW EQUATIONS

1. Four-point vertex

We present the flow equations of the one-line irreducible four-point vertices. The six-point vertex contributions are truncated due to numerical limitations. A method to partially include them without a significant increase in numerical cost is introduced in Appendix B 3. In the following, we drop all Λ labels for brevity and begin by defining internal propagator pairs,

$$\Pi_{\psi\psi,ij}(\omega,\omega+s) \equiv \frac{1}{2\beta}(\dot{G}_{\psi,i}(\omega)G_{\psi,j}(\omega+s) + G_{\psi,i}(\omega)\dot{G}_{\psi,j}(\omega+s)), \tag{B1a}$$

$$\Pi_{\psi\zeta,ij}(\omega,\omega+s) \equiv \frac{1}{2\beta}(\dot{G}_{\psi,i}(\omega)G_{\zeta,j}(\omega+s) + G_{\psi,i}(\omega)\dot{G}_{\zeta,j}(\omega+s)), \tag{B1b}$$

$$\Pi_{\zeta\zeta,ij}(\omega,\omega+s) \equiv \frac{1}{2\beta}(\dot{G}_{\zeta,i}(\omega)G_{\zeta,j}(\omega+s) + G_{\zeta,i}(\omega)\dot{G}_{\zeta,j}(\omega+s)). \tag{B1c}$$

We group the contributions to the right-hand sides of the four-point vertex flow equations by their properties as follows. Terms with an internal site sum are called X terms. For these terms, the flow equations for the local and bilocal case are equal and need not be distinguished below. In contrast, terms without internal sums are called $\tilde{X}$ terms, for these terms the local case indicated by site indices ii needs to be distinguished from the nonlocal case indicated by site indices ij. For noncrossed $\tilde{X}$ terms t-u symmetries exist, their application to Eqs. (B2b)–(B2d) significantly reduces the numerical cost. For the crossed components ($\times$), this symmetry does not exist. Here we start by stating the flow equations analytically in terms of these components before stating the components explicitly. A diagrammatic representation of the flow equations is displayed in Fig. 10. The nonlocal flow equations (for $i \neq j$) are

$$\partial_\Lambda\Gamma_{\psi\psi,ij}(s,t,u) = X_{\psi\psi,ij}(s,t,u) + \tilde{X}_{\psi\psi,ij}(s,t,u) - \tilde{X}_{\psi\psi,ij}(s,u,t), \tag{B2a}$$

$$\partial_\Lambda\Gamma_{\zeta\zeta,ij}(s,t,u) = X_{\zeta\zeta,ij}(s,t,u) + \tilde{X}_{\zeta\zeta,ij}(s,t,u) - \tilde{X}_{\zeta\zeta,ij}(s,u,t), \tag{B2b}$$

$$\partial_\Lambda\Gamma_{\psi\zeta,ij}(s,t,u) = X_{\psi\zeta,ij}(s,t,u) + \tilde{X}_{\psi\zeta,ij}(s,t,u) - \tilde{X}_{\psi\zeta,ij}(s,u,t), \tag{B2c}$$

$$\partial_\Lambda\Gamma^\times_{\psi\psi,ij}(s,t,u) = X^\times_{\psi\psi,ij}(s,t,u) + \tilde{X}^\times_{\psi\psi,ij}(s,t,u), \tag{B2d}$$

$$\partial_\Lambda\Gamma^\times_{\psi\zeta,ij}(s,t,u) = X^\times_{\psi\zeta,ij}(s,t,u) + \tilde{X}^\times_{\psi\zeta,ij}(s,t,u), \tag{B2e}$$

and the local flow equations are given by

$$\partial_\Lambda\Gamma_{\psi\psi,ii}(s,t,u) = \partial_\Lambda\Gamma^\times_{\psi\psi,ii}(s,t,u) = X_{\psi\psi,ii}(s,t,u) + \tilde{X}_{\psi\psi,ii}(s,t,u) - \tilde{X}_{\psi\psi,ii}(s,u,t), \tag{B2f}$$

$$\partial_\Lambda\Gamma_{\zeta\zeta,ii}(s,t,u) = X_{\zeta\zeta,ii}(s,t,u) + \tilde{X}_{\zeta\zeta,ii}(s,t,u) - \tilde{X}_{\zeta\zeta,ii}(s,u,t), \tag{B2g}$$

$$\partial_\Lambda\Gamma_{\psi\zeta,ii}(s,t,u) = \partial_\Lambda\Gamma^\times_{\psi\zeta,ii}(s,t,u) = X_{\psi\zeta,ii}(s,t,u) + \tilde{X}_{\psi\zeta,ii}(s,t,u) - \tilde{X}_{\psi\zeta,ii}(s,u,t). \tag{B2h}$$

The X contributions to the flow equations read,

$$X_{\psi\psi,ii(j)}(s,t,u) = -\sum_\omega\sum_k \Pi_{\psi\psi,kk}(-\omega,\omega+s)\Gamma_{\psi\psi,ki(j)}(s,-\omega+\omega_3,-\omega+\omega_4)\Gamma_{\psi\psi,ik}(s,-\omega-\omega_2,\omega+\omega_1), \tag{B3a}$$

$$X_{\zeta\zeta,ii(j)}(s,t,u) = 2\sum_\omega\sum_k \Pi_{\psi\psi,kk}(\omega,\omega+s)\Gamma_{\psi\zeta,ki(j)}(s,\omega-\omega_4,\omega-\omega_3)\Gamma_{\psi\zeta,ki}(-s,\omega+\omega_1,\omega+\omega_2) + \sum_\omega\sum_k \Pi_{\zeta\zeta,kk}(\omega,\omega+s)\Gamma_{\zeta\zeta,ki(j)}(s,-\omega+\omega_3,-\omega+\omega_4)\Gamma_{\zeta\zeta,ki}(-s,-\omega-\omega_2,-\omega-\omega_1), \tag{B3b}$$

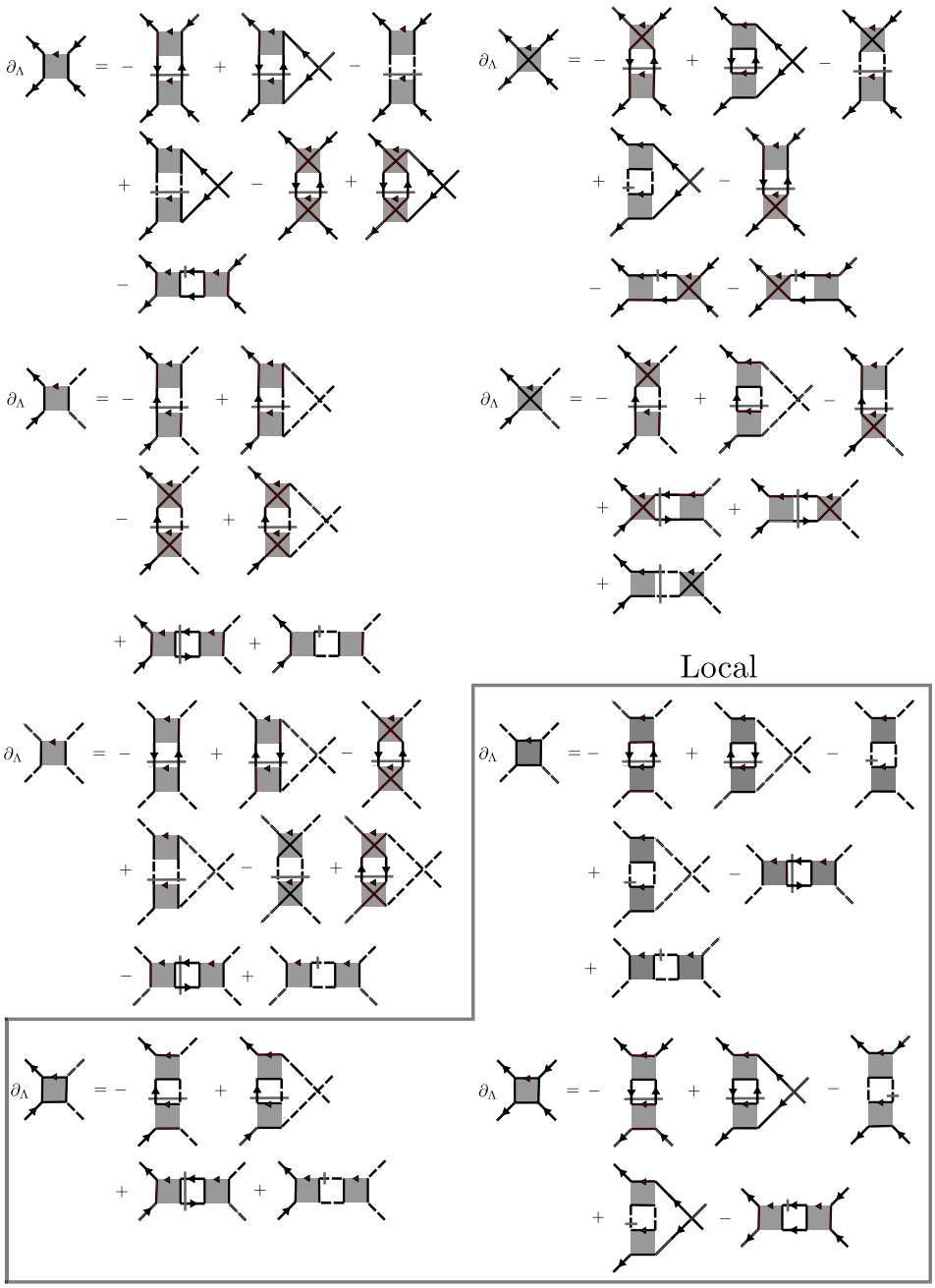

FIG. 10. Diagrammatic representation of the four point flow equations for $\partial_\Lambda \Gamma_{\psi\psi,ij}$, $\partial_\Lambda \Gamma^{\times}_{\psi\psi,ij}$, $\partial_\Lambda \Gamma_{\psi\zeta,ij}$, $\partial_\Lambda \Gamma^{\times}_{\psi\zeta,ij}$, and $\partial_\Lambda \Gamma_{\zeta\zeta,ij}$ and the local terms $\partial_\Lambda \Gamma_{\psi\psi,ii}$, $\partial_\Lambda \Gamma_{\psi\zeta,ii}$, and $\partial_\Lambda \Gamma_{\zeta\zeta,ii}$. Here we skip frequency and site labels as these are given in Eqs. (B1a)–(B2h).

$$X_{\psi\zeta,ii(j)}(s,t,u) = -2\sum_{\omega}\sum_{k} \Pi_{\psi\psi,kk}(\omega,\omega+s)\Gamma_{\psi\zeta,ki(j)}(s,\omega-\omega_4,\omega-\omega_3)\Gamma^{\times}_{\psi\psi,ik}(\omega+\omega_1,s,-\omega-\omega_2)$$
$$+\sum_{\omega}\sum_{k} \Pi_{\zeta\zeta,kk}(\omega,\omega+s)\Gamma_{\zeta\zeta,ki(j)}(s,-\omega+\omega_3,-\omega+\omega_4)\Gamma_{\psi\zeta,ik}(s,-\omega-\omega_2,\omega+\omega_1). \tag{B3c}$$

The $X^{\times}$ contributions are

$$X^{\times}_{\psi\psi,ij}(s,t,u) = -2\sum_{\omega}\sum_{k} \Pi_{\psi\psi,kk}(\omega,\omega-t)\Gamma^{\times}_{\psi\psi,ik}(\omega-\omega_3,t,-\omega+\omega_1)\Gamma^{\times}_{\psi\psi,jk}(\omega+\omega_2,-t,-\omega-\omega_4)$$
$$-\sum_{\omega}\sum_{k} \Pi_{\zeta\zeta,kk}(\omega,\omega-t)\Gamma_{\psi\zeta,ik}(t,\omega-\omega_3,-\omega+\omega_1)\Gamma_{\psi\zeta,jk}(-t,\omega+\omega_2,-\omega-\omega_4), \tag{B3d}$$

$$X^{\times}_{\psi\zeta,ij}(s,t,u) = 2\sum_{\omega}\sum_{k}\Pi_{\psi\zeta,kk}(\omega,\omega-t)\Gamma^{\times}_{\psi\zeta,ik}(-\omega+\omega_1,t,\omega-\omega_3)\Gamma^{\times}_{\psi\zeta,kj}(\omega+\omega_2,t,\omega+\omega_4). \tag{B3e}$$

For the above definitions, local and nonlocal cases have the same expression. For terms without internal lattice site sums $\tilde{X}$, this is not the case. Their nonlocal contributions read

$$\begin{aligned}
\tilde{X}_{\psi\psi,ij}(s,t,u) = \sum_{\omega}\big\{&2\Pi_{\psi\psi,ij}(\omega,\omega-t)\Gamma^{\times}_{\psi\psi,ij}(\omega-\omega_3,-\omega+\omega_1,t)\Gamma_{\psi\psi,ij}(\omega+\omega_2,-t,-\omega-\omega_4)\\
&+2\Pi_{\psi\psi,ji}(\omega,\omega-t)\Gamma_{\psi\psi,ij}(\omega-\omega_3,t,-\omega+\omega_1)\Gamma^{\times}_{\psi\psi,ij}(\omega+\omega_2,-\omega-\omega_4,-t)\\
&+2\Pi_{\zeta\zeta,ij}(\omega,\omega-t)\Gamma^{\times}_{\psi\zeta,ij}(t,-\omega+\omega_1,\omega-\omega_3)\Gamma^{\times}_{\psi\zeta,ij}(-t,\omega+\omega_2,-\omega-\omega_4)\big\},
\end{aligned} \tag{B4a}$$

$$\begin{aligned}
\tilde{X}^{\times}_{\psi\psi,ij}(s,t,u) = \sum_{\omega}\big\{&\Pi_{\psi\psi,ij}(-\omega,\omega+s)\Gamma^{\times}_{\psi\psi,ij}(s,-\omega+\omega_3,-\omega+\omega_4)\Gamma^{\times}_{\psi\psi,ij}(s,\omega+\omega_1,-\omega-\omega_2)\\
&+\Pi_{\psi\psi,ji}(-\omega,\omega+s)\Gamma^{\times}_{\psi\psi,ji}(s,-\omega+\omega_4,-\omega+\omega_3)\Gamma^{\times}_{\psi\psi,ij}(s,-\omega-\omega_2,\omega+\omega_1)\\
&+2\Pi_{\psi\psi,ij}(\omega,\omega+u)\Gamma_{\psi\psi,ji}(\omega-\omega_3,-\omega+\omega_2,-u)\Gamma_{\psi\psi,ij}(\omega+\omega_1,-\omega-\omega_4,u)\\
&+2\Pi_{\psi\psi,ji}(\omega,\omega+u)\Gamma^{\times}_{\psi\psi,ji}(\omega-\omega_3,-\omega+\omega_2,-u)\Gamma^{\times}_{\psi\psi,ij}(\omega+\omega_1,-\omega-\omega_4,u)\\
&+2\Pi_{\zeta\zeta,ij}(\omega,\omega+u)\Gamma^{\times}_{\psi\zeta,ji}(-u,\omega-\omega_3,-\omega+\omega_2)\Gamma^{\times}_{\psi\zeta,ij}(u,\omega+\omega_1,-\omega-\omega_4)\big\},
\end{aligned} \tag{B4b}$$

$$\begin{aligned}
\tilde{X}_{\zeta\zeta,ij}(s,t,u) = \sum_{\omega}\big\{&2\Pi_{\psi\psi,ij}(\omega,\omega-t)\Gamma^{\times}_{\psi\zeta,ji}(-t,\omega-\omega_1,\omega-\omega_3)\Gamma^{\times}_{\psi\zeta,ij}(t,\omega+\omega_2,\omega+\omega_4)\\
&+2\Pi_{\psi\psi,ji}(\omega,\omega-t)\Gamma^{\times}_{\psi\zeta,ij}(-t,\omega-\omega_3,\omega-\omega_1)\Gamma^{\times}_{\psi\zeta,ji}(t,\omega+\omega_4,\omega+\omega_2)\\
&-2\Pi_{\zeta\zeta,ij}(\omega,\omega-t)\,\Gamma_{\zeta\zeta,ij}(-\omega+\omega_1,-\omega+\omega_3,-t)\Gamma_{\zeta\zeta,ji}(-\omega-\omega_2,t,-\omega-\omega_4)\big\},
\end{aligned} \tag{B4c}$$

$$\begin{aligned}
\tilde{X}_{\psi\zeta,ij}(s,t,u) = \sum_{\omega}\big\{&-2\Pi_{\psi\zeta,ij}(\omega,\omega-t)\Gamma_{\psi\zeta,ij}(-\omega+\omega_1,t,\omega-\omega_3)\Gamma_{\psi\zeta,ij}(\omega+\omega_2,\omega+\omega_4,t)\\
&+2\Pi_{\psi\zeta,ji}(\omega,\omega-t)\,\Gamma^{\times}_{\psi\zeta,ij}(-\omega+\omega_1,\omega-\omega_3,t)\Gamma^{\times}_{\psi\zeta,ji}(\omega+\omega_2,\omega+\omega_4,t)\big\},
\end{aligned} \tag{B4d}$$

$$\begin{aligned}
\tilde{X}^{\times}_{\psi\zeta,ij}(s,t,u) = \sum_{\omega}\big\{&2\Pi_{\psi\psi,ji}(\omega,\omega+s)\Gamma^{\times}_{\psi\zeta,ij}(s,\omega-\omega_4,\omega-\omega_3)\Gamma^{\times}_{\psi\psi,ij}(\omega+\omega_1,-\omega-\omega_2,s)\\
&-2\Pi_{\psi\psi,ij}(\omega,\omega+s)\Gamma^{\times}_{\psi\zeta,ji}(s,\omega-\omega_3,\omega-\omega_4)\Gamma_{\psi\psi,ij}(\omega+\omega_1,-\omega-\omega_2,s)\\
&+2\Pi_{\zeta\zeta,ij}(\omega,\omega+s)\Gamma_{\zeta\zeta,ij}(-\omega+\omega_3,s,-\omega+\omega_4)\Gamma^{\times}_{\psi\zeta,ij}(s,\omega+\omega_1,-\omega-\omega_2)\\
&-2\Pi_{\psi\zeta,ji}(\omega,\omega-u)\Gamma_{\psi\zeta,ji}(\omega+\omega_2,\omega+\omega_3,u)\Gamma^{\times}_{\psi\zeta,ij}(-\omega+\omega_1,\omega-\omega_4,u)\\
&+2\Pi_{\psi\zeta,ij}(\omega,\omega-u)\,\Gamma^{\times}_{\psi\zeta,ij}(\omega+\omega_2,\omega+\omega_3,u)\Gamma_{\psi\zeta,ij}(-\omega+\omega_1,u,\omega-\omega_4)\big\}.
\end{aligned} \tag{B4e}$$

The corresponding local contributions are

$$\begin{aligned}
\tilde{X}_{\psi\psi,ii}(s,t,u) &= \tilde{X}^{\times}_{\psi\psi,ii}(s,t,u)\\
&= +\sum_{\omega}\sum_{k}\big\{-2\Pi_{\psi\psi,kk}(\omega,\omega-t)\,\Gamma^{\times}_{\psi\psi,ik}(\omega-\omega_3,t,-\omega+\omega_1)\Gamma^{\times}_{\psi\psi,ik}(\omega+\omega_2,-t,-\omega-\omega_4)\\
&\quad-\Pi_{\zeta\zeta,kk}(\omega,\omega-t)\Gamma_{\psi\zeta,ik}(t,\omega-\omega_3,-\omega+\omega_1)\Gamma_{\psi\zeta,ik}(-t,\omega+\omega_2,-\omega-\omega_4)\big\},
\end{aligned} \tag{B5a}$$

$$\begin{aligned}
\tilde{X}_{\zeta\zeta,ii}(s,t,u) = \sum_{\omega}\sum_{k}\big\{&-2\Pi_{\psi\psi,kk}(\omega,\omega-t)\Gamma_{\psi\zeta,ki}(-t,\omega-\omega_1,\omega-\omega_3)\Gamma_{\psi\zeta,ki}(t,\omega+\omega_4,\omega+\omega_2)\\
&-\Pi_{\zeta\zeta,kk}(\omega,\omega-t)\,\Gamma_{\zeta\zeta,ki}(-t,-\omega+\omega_3,-\omega+\omega_1)\Gamma_{\zeta\zeta,ki}(t,-\omega-\omega_2,-\omega-\omega_4)\},
\end{aligned} \tag{B5b}$$

$$\begin{aligned}
\tilde{X}_{\psi\zeta,ii}(s,t,u) &= \tilde{X}^{\times}_{\psi\zeta,ii}(s,t,u)\\
&= 2\sum_{\omega}\sum_{k}\Pi_{\psi\zeta,kk}(\omega,\omega-t)\Gamma^{\times}_{\psi\zeta,ik}(-\omega+\omega_1,t,\omega-\omega_3)\Gamma^{\times}_{\psi\zeta,ki}(\omega+\omega_2,t,\omega+\omega_4).
\end{aligned} \tag{B5c}$$

2. Initial conditions for the flow

The initial conditions for the flow of the vertices at the initial value $\Lambda=\infty$ are given by the bare vertices [14]. However, for numerical implementations of the flow equations, the integration has to start at finite $\Lambda_i<\infty$ to be chosen much larger than all internal energy scales. For models

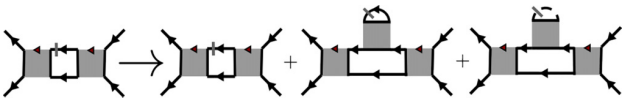

FIG. 11. Katanin truncation for the vertex-flow equation by the replacement $\dot{G} \to \dot{G} + \partial_\Lambda \Sigma$.

that include a Hartree-like contribution care is needed since the contribution from the self-energy flow from $\Lambda = \infty$ to Λ_i is nontrivial [58,59]. To find the initial condition for the self-energy flow, we use the Schwinger-Dyson equation (see Ref. [14]) which at large Λ is approximated as

$$\Sigma^{\Lambda}_{\psi,i}(\omega) = \frac{1}{\beta}\sum_{\omega'}\sum_{j} 2J^z_{ij} G^{\Lambda}_{\psi,j}(\omega'). \tag{B6}$$

In analogy to Sec. IV A, the sum over the $1/\omega'$ tails together with the convergence factor yield

$$\Sigma^{\Lambda_i}_{\psi,i}(\omega) = \sum_j J^z_{ij}. \tag{B7}$$

This cancels the bare self-energy contribution at $\Lambda = \infty$ as read off from Eq. (16b). In summary, at Λ_i, the only nonzero initial conditions are given by [60]

$$\Gamma^{\times}_{\psi\psi,ij} = -J^z_{ij}, \quad \Gamma^{\times}_{\psi\zeta,ij} = J^{\perp}_{ij}. \tag{B8}$$

3. Katanin truncation

So far we have neglected the six-point vertex entirely in our flow equations. However, one can include parts of it at negligible cost [47]. The prescription is to replace the single-scale propagator $\dot{G}$ in the flow equations with the sum of single-scale propagator and self-energy derivative (cf. Fig. 2), $\dot{G} \to \dot{G} + \partial_\Lambda \Sigma$. As shown in Fig. 11 this amounts to the net effect of the six-point vertex at least for nonoverlapping loops and in lowest-order perturbation theory.

APPENDIX C: DETAILS ON NUMERICAL IMPLEMENTATION

The flow equations are solved numerically with the DP5() algorithm of the julia package *DifferentialEquations.jl* [61] ODE solver with a relative and absolute accuracy goal of 10^{-6}. Typically, we set $\Lambda_i = e^{10}$ and report the physical results at a final $\Lambda = e^{-10}$. Further, we truncate the Matsubara frequencies of the vertices at a finite Matsubara index $\pm n_{\max}$. A good compromise between computation times and convergence of the results in $n_{\max}$ is achieved with $n_{\max} = 10$ for the bosonic Matsubara frequencies of the four-point vertices and a three times bigger value for the fermionic Matsubara frequencies of the self-energy. If the right-hand side of the flow equation requires vertices at frequencies outside of the frequency box, then a projection to the last value inside the box is employed.

APPENDIX D: FREQUENCY SYMMETRIES OF THE FOUR-POINT VERTICES

To simplify the numerical treatment of the complex-valued four-point vertices $\Gamma(s,t,u)$ we use antisymmetry under exchange of fermionic fields and the antiunitary symmetry (9) which provide relations between different frequency arguments. This drastically reduces the computational cost since the left-hand side of the flow equations only needs to be evaluated for a fraction of all initially considered frequency combinations. The antiunitary symmetry yields $\Gamma(s,t,u) = \Gamma^{\star}(-s,-t,-u)$ without changing the flavor or site information. This allows us to restrict all vertices to, say, $s \geqslant 0$. In Eq. (D1) we display the frequency relations from (anti-) symmetry under exchange of the indices of Γ_{1234} shown in the left column. Note that sometimes the order of the lattice sites ij are swapped, this is indicated by $(i \leftrightarrow j)$.

	$\Gamma_{\psi\psi,ij}$	$\Gamma^{\times}_{\psi\psi,ij}$	$\Gamma_{\zeta\zeta,ij}$	$\Gamma_{\psi\zeta,ij}$	$\Gamma^{\times}_{\psi\zeta,ij}$
Γ_{1234}	(s,t,u)	(s,t,u)	(s,t,u)	(s,t,u)	(s,t,u)
$-\Gamma_{2134}$	$(s,-u,-t)$		$(s,-u,-t)$		
$-\Gamma_{1243}$	(s,u,t)		(s,u,t)	(s,u,t)	
Γ_{2143}	$(s,-t,-u)$	$(s,-t,-u)$ $(i \leftrightarrow j)$	$(s,-t,-u)$		
Γ_{3412}			$(-s,t,-u)$ $(i \leftrightarrow j)$		
Γ_{4321}			$(-s,-t,u)$ $(i \leftrightarrow j)$		

(D1)

[1] L. Balents, Spin liquids in frustrated magnets, Nature (London) **464**, 199 (2010).

[2] C. Broholm, R. J. Cava, S. A. Kivelson, D. G. Nocera, M. R. Norman, and T. Senthil, Quantum spin liquids, Science **367**, eaay0668 (2020).

[3] A. Auerbach, *Interacting Electrons and Quantum Magnetism*, 1994th ed. (Springer, New York, 1994).

[4] A. W. Sandvik, A. Avella, and F. Mancini, Computational studies of quantum spin systems, AIP Conf. Proc. **1297**, 135 (2010).

[5] U. Schollwöck, The density-matrix renormalization group in the age of matrix product states, Ann. Phys. (NY) **326**, 96 (2011).
[6] B.-B. Chen, L. Chen, Z. Chen, W. Li, and A. Weichselbaum, Exponential thermal tensor network approach for quantum lattice models, Phys. Rev. X **8**, 031082 (2018).
[7] Z. Wang, P. McClarty, D. Dankova, A. Honecker, and A. Wietek, Spectroscopy andcomplex-time correlations using minimally entangled typical thermal states, arXiv:2405.18484.
[8] A. A. Abrikosov, L. P. Gorkov, and I. E. Dzyaloshinski, *Methods of Quantum Field Theory in Statistical Physics* (Dover, Mineola, NY, 2012).
[9] Y. A. Izyumov and Y. N. Skryabin, *Statistical Mechanics of Magnetically Ordered Systems* (Consultants Bureau, New York, 1988).
[10] J. Krieg and P. Kopietz, Exact renormalization group for quantum spin systems, Phys. Rev. B **99**, 060403(R) (2019).
[11] A. Rückriegel, D. Tarasevych, and P. Kopietz, Phase diagram of the J_1-J_2 quantum Heisenberg model for arbitrary spin, Phys. Rev. B **109**, 184410 (2024).
[12] B. Schneider, R. Burkard, B. Olmos, I. Lesanovsky, and B. Sbierski, Dipolar ordering transitions in many-body quantum optics: Analytical diagrammatic approach to equilibrium quantum spins, Phys. Rev. A **110**, 063301 (2024).
[13] J. Reuther and P. Wölfle, J_1-J_2 frustrated two-dimensional Heisenberg model: Random phase approximation and functional renormalization group, Phys. Rev. B **81**, 144410 (2010).
[14] P. Kopietz, L. Bartosch, and F. Schütz, *Introduction to the Functional Renormalization Group* (Springer, Berlin, 2010).
[15] W. Metzner, M. Salmhofer, C. Honerkamp, V. Meden, and K. Schönhammer, Functional renormalization group approach to correlated fermion systems, Rev. Mod. Phys. **84**, 299 (2012).
[16] T. Müller, D. Kiese, N. Niggemann, B. Sbierski, J. Reuther, S. Trebst, R. Thomale, and Y. Iqbal, Pseudo-fermion functional renormalization group for spin models, Rep. Prog. Phys. **87**, 036501 (2024).
[17] B. Schneider, D. Kiese, and B. Sbierski, Taming pseudofermion functional renormalization for quantum spins: Finite temperatures and the Popov-Fedotov trick, Phys. Rev. B **106**, 235113 (2022).
[18] N. Niggemann, B. Sbierski, and J. Reuther, Frustrated quantum spins at finite temperature: Pseudo-Majorana functional renormalization group approach, Phys. Rev. B **103**, 104431 (2021).
[19] N. Niggemann, J. Reuther, and B. Sbierski, Quantitative functional renormalization for three-dimensional quantum Heisenberg models, SciPost Phys. **12**, 156 (2022).
[20] N. Niggemann, N. Astrakhantsev, A. Ralko, F. Ferrari, A. Maity, T. Müller, J. Richter, R. Thomale, T. Neupert, J. Reuther, Y. Iqbal, and H. O. Jeschke, Quantum paramagnetism in the decorated square-kagome antiferromagnet $Na_6Cu_7BiO_4(PO_4)_4Cl_3$, Phys. Rev. B **108**, L241117 (2023).
[21] M. G. Gonzalez, Y. Iqbal, J. Reuther, and H. O. Jeschke, Field-induced spin liquid in the decorated square-kagome antiferromagnet nabokoite $KCu_7TeO_4(SO_4)_5Cl$, arXiv:2410.10385.
[22] B. Schneider, J. Reuther, M. G. Gonzalez, B. Sbierski, and N. Niggemann, Temperature flow in pseudo-Majorana functional renormalization for quantum spins, Phys. Rev. B **109**, 195109 (2024).
[23] Y. Schaden, M. G. Gonzalez, and J. Reuther, Phase diagram of the XXZ pyrochlore model from pseudo-Majorana functional renormalization group, arXiv:2412.14773.
[24] B. Sbierski, M. Bintz, S. Chatterjee, M. Schuler, N. Y. Yao, and L. Pollet, Magnetism in the two-dimensional dipolar XY model, Phys. Rev. B **109**, 144411 (2024).
[25] V. Noculak and J. Reuther, Pseudo-fermion functional renormalization group with magnetic fields, Phys. Rev. B **109**, 174414 (2024).
[26] M. G. Cottam and R. B. Stinchcombe, Thermodynamic properties of a Heisenberg antiferromagnet, J. Phys. C **3**, 2283 (1970).
[27] D. C. Mattis, *The Theory of Magnetism: An Introduction to the Study of Cooperative Phenomena* (Harper & Row, New York, 1965).
[28] H. J. Spencer, Quantum-field-theory approach to the Heisenberg ferromagnet, Phys. Rev. **167**, 434 (1968).
[29] B. Gao, T. Chen, C. Liu, M. L. Klemm, S. Zhang, Z. Ma, X. Xu, C. Won, G. T. McCandless, N. Murai, S. Ohira-Kawamura, S. J. Moxim, J. T. Ryan, X. Huang, X. Wang, J. Y. Chan, S.-W. Cheong, O. Tchernyshyov, L. Balents, and P. Dai, Spin excitation continuum in the exactly solvable triangular-lattice spin liquid $CeMgAl_{11}O_{19}$, arXiv:2408.15957.
[30] R. Zhong, S. Guo, G. Xu, Z. Xu, and R. J. Cava, Strong quantum fluctuations in a quantum spin liquid candidate with a co-based triangular lattice, Proc. Natl. Acad. Sci. USA **116**, 14505 (2019).
[31] N. Li, Q. Huang, X. Y. Yue, W. J. Chu, Q. Chen, E. S. Choi, X. Zhao, H. D. Zhou, and X. F. Sun, Possible itinerant excitations and quantum spin state transitions in the effective spin-1/2 triangular-lattice antiferromagnet $Na_2BaCo(PO_4)_2$, Nat. Commun. **11**, 4216 (2020).
[32] Y. Gao, C. Zhang, J. Xiang, D. Yu, X. Lu, P. Sun, W. Jin, G. Su, and W. Li, Spin supersolid phase and double magnon-roton excitations in a cobalt-based triangular lattice, Phys. Rev. B **110**, 214408 (2024).
[33] Y. Gao, Y.-C. Fan, H. Li, F. Yang, X.-T. Zeng, X.-L. Sheng, R. Zhong, Y. Qi, Y. Wan, and W. Li, Spin supersolidity in nearly ideal easy-axis triangular quantum antiferromagnet $Na_2BaCo(PO_4)_2$, npj Quantum Mater. **7**, 89 (2022).
[34] J. Sheng, L. Wang, A. Candini, W. Jiang, L. Huang, B. Xi, J. Zhao, H. Ge, N. Zhao, Y. Fu, J. Ren, J. Yang, P. Miao, X. Tong, D. Yu, S. Wang, Q. Liu, M. Kofu, R. Mole, G. Biasiol, et al., Two-dimensional quantum universality in the spin-1/2 triangular-lattice quantum antiferromagnet $Na_2BaCo(PO_4)_2$, Proc. Natl. Acad. Sci. USA **119**, e2211193119 (2022).
[35] F. Mila, From RVB to supersolidity: The saga of the Ising-Heisenberg model on the triangular lattice, J. Club Condens. Matter Phys. (2024).
[36] M. Zhu, V. Romerio, N. Steiger, S. D. Nabi, N. Murai, S. Ohira-Kawamura, K. Yu. Povarov, Y. Skourski, R. Sibille, L. Keller, Z. Yan, S. Gvasaliya, and A. Zheludev, Continuum excitations in a spin supersolid on a triangular lattice, Phys. Rev. Lett. **133**, 186704 (2024).
[37] J. Xiang, C. Zhang, Y. Gao, W. Schmidt, K. Schmalzl, C.-W. Wang, B. Li, N. Xi, X.-Y. Liu, H. Jin, G. Li, J. Shen, Z. Chen, Y. Qi, Y. Wan, W. Jin, W. Li, P. Sun, and G. Su, Giant magnetocaloric effect in spin supersolid candidate $Na_2BaCo(PO_4)_2$, Nature (London) **625**, 270 (2024).

[38] T. Chen, A. Ghasemi, J. Zhang, L. Shi, Z. Tagay, L. Chen, E.-S. Choi, M. Jaime, M. Lee, Y. Hao, H. Cao, B. Winn, R. Zhong, X. Xu, N. P. Armitage, R. Cava, and C. Broholm, Phase diagram and spectroscopic evidence of supersolids in quantum ising magnet $K_2Co(SeO_3)_2$, arXiv:2402.15869.

[39] A. M. Tsvelik, New fermionic description of quantum spin liquid state, Phys. Rev. Lett. **69**, 2142 (1992).

[40] J. L. Martin and N. Kemmer, Generalized classical dynamics, and the 'classical analogue' of a Fermioscillator, Proc. R. Soc. Lond. A **251**, 536 (1959).

[41] S. M. Girvin and K. Yang, *Modern Condensed Matter Physics* (Cambridge University Press, Cambridge, UK, 2019).

[42] P. Jordan and E. Wigner, On the Paulian prohibition of equivalence, Z. Phys. **47**, 631 (1928).

[43] A. Altland and B. Simons, *Condensed Matter Field Theory* (Cambridge University Press, Cambridge, UK, 2006).

[44] J. Nilsson and M. Bazzanella, Majorana fermion description of the Kondo lattice: Variational and path integral approach, Phys. Rev. B **88**, 045112 (2013).

[45] G. Roósz, A. Kauch, F. Bippus, D. Wieser, and K. Held, Two-site reduced density matrix from one- and two-particle Green's functions, Phys. Rev. B **110**, 075115 (2024).

[46] C. Wetterich, Exact evolution equation for the effective potential, Phys. Lett. B **301**, 90 (1993).

[47] A. A. Katanin, Fulfillment of ward identities in the functional renormalization group approach, Phys. Rev. B **70**, 115109 (2004).

[48] P. Henelius, A. W. Sandvik, C. Timm, and S. M. Girvin, Monte Carlo study of a two-dimensional quantum ferromagnet, Phys. Rev. B **61**, 364 (2000).

[49] N. Sadoune and L. Pollet, Efficient and scalable path integral Monte Carlo simulations with worm-type updates for Bose-Hubbard and XXZ models, SciPost Phys. Codebases 9 (2022).

[50] N. Sadoune and L. Pollet, Codebaserelease 1.0 for worm algorithm for Bose-Hubbard and XXZ models, SciPost Phys. Codebases 9 (2022).

[51] T. Momoi and M. Suzuki, Ground-state properties and phase diagram of the quantum XXZ antiferromagnet on a triangular lattice, J. Phys. Soc. Jpn. **61**, 3732 (1992).

[52] S. Rohshap, M. K. Ritter, H. Shinaoka, J. von Delft, M. Wallerberger, and A. Kauch, Two-particle calculations with quantics tensor trains – solving the parquet equations, arXiv:2410.22975.

[53] J. Larson and T. Mavrogordatos, *The Jaynes–Cummings Model and Its Descendants: Modern Research Directions*, 2nd ed. (IOP, Philadelphia, PA, 2021).

[54] Y. Schaden and J. Reuther, Bilinear Majorana representations for spin operators with spin magnitudes $S > 1/2$, Phys. Rev. Res. **5**, 023067 (2023).

[55] I. Hagymási, N. Niggemann, and J. Reuther, Phase diagram of the antiferromagnetic J_1-J_2 spin-1 pyrochlore Heisenberg model, arXiv:2405.12745.

[56] www.gauss-centre.eu.

[57] https://gitlab.com/Frederic.Bippus/U1-pm-fRG.git.

[58] C. Karrasch, T. Enss, and V. Meden, Functional renormalization group approach to transport through correlated quantum dots, Phys. Rev. B **73**, 235337 (2006).

[59] C. Karrasch, R. Hedden, R. Peters, T. Pruschke, K. Schönhammer, and V. Meden, A finite-frequency functional renormalization group approach to the single impurity Anderson model, J. Phys.: Condens. Matter **20**, 345205 (2008).

[60] Instead of carrying through the magnetic field in all calculations in Sec. III we could also use h as initial condition for $\Gamma_{\psi,i}$ at $\Lambda \gg J, T$.

[61] C. Rackauckas and Q. Nie, DifferentialEquations.jl—A performant and feature-rich ecosystem for solving differential equations in Julia, J. Open Res. Softw. **5**, 15 (2017).

4 Strong-Coupling Perturbation Theory and Quantum-to-Classical Correspondence

4.1 Overview

While we initially planned to set up a fully numerical FRG scheme based on the strong-coupling expansion (see Sec. 2.5), it was not clear how to truncate the flow equations properly, as a truncation on the level of vertices significantly violates the spin equations of motion. While this problem was seemingly fixed by Rueckriegel et al. [RTK24], their method included heavy approximations of the momentum and frequency dependence of the vertices, where most crossing symmetries of vertices except for the self-energy were lost. Instead of pursuing such an approach, we decided to study the properties of the strong-coupling expansion more closely, which might inform good choices of truncation schemes in the future.

To set up the strong-coupling expansion, we first have to calculate the bare vertices. As described in Sec. 2.5, the bare interaction vertices of strong coupling theories are given by the local connected n-point Green's functions of the local interacting theory. They can be obtained via the spectral representation of the n-point Green's functions introduced in Sec. 2.7. While this is straightforward for few-fermion correlators, this is far from trivial for bosons, due to the appearance of so-called anomalous terms [KLD21; Ge+24]. In Ref. [P4], we solve the problem of calculating n-point Green's functions using their spectral representation in full generality, including a systematic generation of all anomalous terms.

With the bare vertices now available, we use the kernel trick outlined in Chapter 2.7.2 to calculate and tabulate all perturbation theory diagrams in J/T for Ising, Heisenberg, and XX models or J/h for the transverse field Ising model up to fourth order [P5]. We analyze the scaling of diagrams in $1/d$, $\alpha - 2$ where d is the dimension of the lattice and α the exponent of the long range interaction $J_{ij} = \frac{1}{|\mathbf{r}_i - \mathbf{r}_j|^\alpha}$. With the scaling of each diagram known, we are able to systematically improve upon the mean-field solution, which is exact for $d = \infty$ for short-range interactions or $\alpha = d$ for long-range interactions. We are able to show convergence of the critical magnetic field h_c and critical temperature T_c in a $1/d$ expansion from mean-field towards Monte Carlo results for the cubic-lattice transverse-field Ising model and the long-range Heisenberg ferromagnet, respectively. For the Dicke-Ising model at $T = 0$, we show that no diagrams contribute to the correlator beyond the mean-field contributions, rendering mean-field theory exact. All results are given as analytic formulas in terms of momenta, spin length, and Matsubara frequencies, allowing analytic continuation to real frequencies.

The analytic nature of the expansions calculated in Ref. [P5] makes a systematic study of the functional form of the static-spin structure factor possible (see Eq. (2.12))

$$\chi(\mathbf{k}) = \frac{1}{N} \sum_{\mathbf{r},\mathbf{r}'} e^{-i\mathbf{k}\cdot(\mathbf{r}-\mathbf{r}')} \int_0^\beta \mathrm{d}\tau \langle S^z_{\mathbf{r}}(\tau) S^z_{\mathbf{r}'}(0) \rangle, \tag{4.1}$$

which describes the system's response to a time-independent local field. We set out to tackle a long-standing problem in frustrated magnetism: In multiple diagrammatic Monte Carlo studies [Kul+13a; Kul+13b; Wan+20; Hua+16], the site-resolved static structure factor (Eq. (4.1)) of quantum Heisenberg models has been shown to universally match simulations of the same quantity in classical vector-spin models upon a fine-tuned rescaling of the simulation temperature. The match was within Monte Carlo error bars and observed at large and intermediate temperatures down to the convergence limits of the method. This so-called Quantum-to-Classical correspondence (QCC) seems to universally imply that for the static susceptibility, the quantum fluctuations enter on the same level as thermal fluctuations regardless of the lattice geometry, as the QCC has been shown to work for a plethora of lattices in two and three dimensions, with the only known exception being $d = 1$. The underlying reason why such a correspondence exists remained elusive for over a decade. With the expansion from Ref. [P5] we are able to show in Ref. [P6] that in the exact parameterization,

$$[T\chi(\mathbf{k})]^{-1} = f + g\gamma(\mathbf{k}) + \epsilon(\mathbf{k}), \tag{4.2}$$

$\epsilon(\mathbf{k})$ only contributes at fourth order in $\frac{J}{T}$ with a small prefactor for quantum spins and at sixth order for classical spins $S \to \infty$. Here f and g are functions of $\frac{J}{T}$ but independent of momentum, $\gamma(\mathbf{k}) = \frac{1}{z}\sum_{\langle ij\rangle} e^{i(\mathbf{r}_i - \mathbf{r}_j)}$ with the coordination number z, and a rest function $\epsilon(\mathbf{k})$. This leads to an effective description of $\chi(\mathbf{k})$ in terms of f and g warranting the approximation

$$T\chi(\mathbf{k}) \approx \frac{1}{f + g\gamma(\mathbf{k})}, \tag{4.3}$$

which we name *renormalized mean-field* form due to its similarities to susceptibility obtained from mean-field theory

$$T\chi_{\mathrm{MF}}(\mathbf{k}) = \frac{1}{\frac{3}{S(S+1)} + \frac{Jz}{T}\gamma(\mathbf{k})}. \tag{4.4}$$

Because Eq. (4.3) only depends on two parameters, the normalized susceptibility only depends on one parameter, which can then be fine-tuned by changing the simulation temperature of the classical Heisenberg model to match the parameters of the quantum model. Using Eq. (4.3), we reproduce published diagrammatic Monte Carlo susceptibilities for J_1-Heisenberg spin models by fine-tuning the parameters f and g. This is also possible for the $J_1 - \ldots - J_5$ Heisenberg model on the intertwined trillium lattice that describes the langbeinite compound $K_2Ni_2(SO_4)_3$ [Gon+24]. In Ref. [P7] we substantiate this claim by calculating $\epsilon(\mathbf{k})$ up to 12^{th} order in J/T where we observe that it stays about two orders of magnitude lower than g for frustrated lattices to the lowest reachable temperatures $T \sim 0.3J$.

[P4] *Spectral representation of Matsubara n-point functions: Exact kernel functions and applications*
Johannes Halbinger, **Benedikt Schneider**, Björn Sbierski
pages 74–91 / arXiv:2304.03774 SciPost Phys. 15, 183 (2023)

[P5] *Dipolar ordering transitions in many-body quantum optics: Analytical diagrammatic approach to equilibrium quantum spins*
Benedikt Schneider, Ruben Burkard, Beatriz Olmos, Igor Lesanovsky, Björn Sbierski
pages 92–93 / arXiv:2407.18156 Phys. Rev. A 110, 063301 (2024)

[P6] *Taming spin susceptibilities in frustrated quantum magnets: Mean-field form and approximate nature of the quantum-to-classical correspondence*
Benedikt Schneider, Björn Sbierski
pages 108–109 / arXiv:2407.09401 Phys. Rev. Lett. 134, 176502 (2025)

SciPost Phys. 15, 183 (2023)

Spectral representation of Matsubara n-point functions: Exact kernel functions and applications

Johannes Halbinger*, Benedikt Schneider and Björn Sbierski

Department of Physics and Arnold Sommerfeld Center for Theoretical Physics (ASC), Ludwig-Maximilians-Universität München, Theresienstr. 37, München D-80333, Germany
Munich Center for Quantum Science and Technology (MCQST), Schellingstr. 4, D-80799 München, Germany

* johannes.halbinger@physik.uni-muenchen.de

Abstract

In the field of quantum many-body physics, the spectral (or Lehmann) representation simplifies the calculation of Matsubara n-point correlation functions if the eigensystem of a Hamiltonian is known. It is expressed via a universal kernel function and a system- and correlator-specific product of matrix elements. Here we provide the kernel functions in full generality, for arbitrary n, arbitrary combinations of bosonic or fermionic operators and an arbitrary number of anomalous terms. As an application, we consider bosonic 3- and 4-point correlation functions for the fermionic Hubbard atom and a free spin of length S, respectively.

Received 03-05-2023
Accepted 21-08-2023
Published 01-11-2023
doi:10.21468/SciPostPhys.15.5.183

Check for updates

Contents

1 Introduction 2

2 Definition of Matsubara n-point function $G_{A_1\ldots A_n}(\omega_1,\ldots,\omega_n)$ 3

3 Spectral representation of $G_{A_1\ldots A_n}(\omega_1,\ldots,\omega_{n-1})$ 5

4 General kernel function $K_n(\Omega_1,\ldots,\Omega_{n-1})$ 6

5 Explicit kernel functions $K_n(\Omega_1,\ldots,\Omega_{n-1})$ for $n=2,3,4,5$ 8

6 Applications: Hubbard atom and free spin 9
6.1 Fermionic Hubbard atom 9
6.2 Free spin S 11

7 Conclusion 13

A Equivalence to convention of Ref. [21] 14

References 15

1 Introduction

Multi-point correlation functions of n quantum mechanical operators, also known as n-point functions, are a central concept in the study of quantum many-body systems and field theory [1]. They generalize the well-known 2-point functions, which, for the example of electrons in the solid state, are routinely measured by scanning tunneling spectroscopy or angle-resolved photon emission spectroscopy [2]. For magnetic systems, the 2-point spin correlators can be probed in a neutron scattering experiment. Higher order correlation functions with $n = 3, 4, 5...$ can for example be measured in non-linear response settings [3]. In the emerging field of cold atomic quantum simulation, (equal-time) n-point functions are even directly accessible [4].

On the theoretical side the study of higher order correlation functions gains traction as well. One motivation is the existence of exact relations between correlation functions of different order n [5, 6]. Although these exact relations can usually not be solved exactly, they form a valuable starting point for further methodological developments like the parquet approximation [7]. Thus even if the 4-point correlator (or, in that context, its essential part, the one-line irreducible vertex [1]) might not be the primary quantity of interest in a calculation, it appears as a building block of the method. Another example is the functional renormalization group method (fRG) in a vertex expansion [8, 9]. It expresses the many body problem as a hierarchy of differential equations for the vertices that interpolate between a simple solvable starting point and the full physical theory [10]. Whereas experiments measure correlation functions in real time (or frequency), in theory one often is concerned with the related but conceptually simpler versions depending on imaginary time [1]. In the following, we will focus on these Matsubara correlation functions, which, nevertheless feature an intricate frequency dependence.

Whereas the above theoretical methods usually provide only an approximation for the n-point functions, an important task is to calculate these objects exactly. This should be possible for simple quantum many body systems. We consider systems simple if they are amenable to exact diagonalization (ED), i.e. feature a small enough Hilbert space, like few-site clusters of interacting quantum spins or fermions. Also impurity systems, where interactions only act locally, can be approximately diagonalized using the numerical renormalization group [11].

Knowing the exact n-point functions for simple systems is important for benchmark testing newly developed methods before deploying them to harder problems. Moreover, n-point functions for simple systems often serve as the starting point of further approximations like in the spin-fRG [12–14], or appear intrinsically in a method like in diagrammatic extensions of dynamical mean field theory [15] with its auxiliary impurity problems. Another pursuit enabled by the availability of exact n-point functions is to interpret the wealth of information encoded in these objects, in particular in their rich frequency structure. For example, Ref. [16] studied the fingerprints of local moment formation and Kondo screening in quantum impurity models.

In this work we complete the task to calculate exact n-point functions by generalizing the spectral (or Lehmann) representation [1, 17] for Matsubara n-point correlation functions to arbitrary n. We assume that a set of eigenstates and -energies is given. Following pioneering work of Refs. [18–20] and in particular the recent approach by Kugler *et al.* [21], we split the problem of calculating imaginary frequency correlators into the computation of a universal kernel function and a system- and correlator-specific part (called partial spectral function in Ref. [21]). We provide the kernel functions in full generality for an arbitrary number n of bosonic or fermionic frequencies. Previously, these kernel functions were known exactly only up to the 3-point case [18], for the fermionic 4-point case [19–21] or for the general n-point case [21] but disregarding anomalous contributions to the sum that the kernel function con-

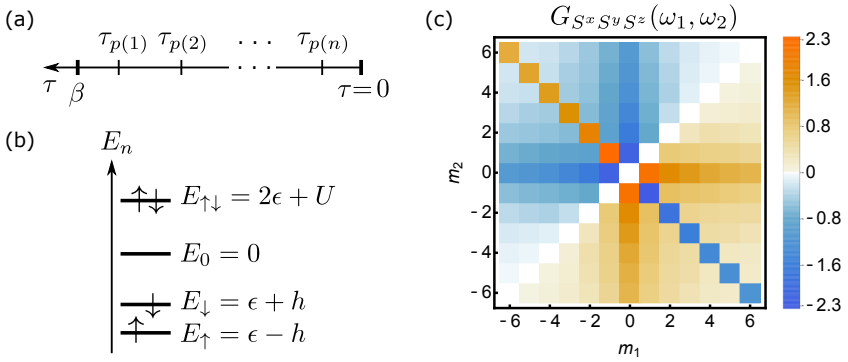

Figure 1: (a) Ordering convention for imaginary times in Eq. (9). (b) Eigenstates and energies of the Hubbard atom. (c) Matsubara correlation function $G_{S^xS^yS^z}(\omega_1,\omega_2)$ with $\omega_j = 2\pi m_j/\beta$ ($m_j \in \mathbb{Z}$, $j = 1,2$) for the Hubbard atom (35) at $\beta = 10$, $h = 0.1$, $\epsilon = -2$, $U = 2$, see Eq. (45). The sharp anti-diagonal ray $\propto \delta_{\omega_1+\omega_2,0}$ represents an anomalous term of order $a = 1$. The other broadened rays become sharp and anomalous for $h \to 0$, see Eq. (49).

sists of. These anomalous contributions are at the heart of the complexity of Matsubara n-point functions. They occur when certain combinations of eigenenergies and external frequencies vanish individually, see the anti-diagonal rays in Fig. 1(c). Physically, they correspond to long-term memory effects, are related to non-ergodicity and, in the case of bosonic two-point functions reflect the difference between static isothermal susceptibilities and the zero-frequency limit of the dynamical Kubo response function [22, 23].

The structure of the paper is as follows: In Sec. 2 we define the Matsubara n-point function $G_{A_1\ldots A_n}(\omega_1,\ldots,\omega_{n-1})$ and review some of its properties. The spectral representation is derived in Sec. 3 with Eq. (15) being the central equation written in terms of the kernel function $K_n(\Omega_1,\ldots,\Omega_{n-1})$. Our main result is an exact closed-form expression of this most general kernel function which is given in Sec. 4. Examples for $n = 2,3,4,5$ are given in Sec. 5 where we also discuss simplifications for the purely fermionic case. We continue with applications to two particular systems relevant in the field of condensed matter theory: In Sec. 6, we consider the Hubbard atom and the free spin of length S, for which we compute n-point functions not previously available in the literature. We conclude in Sec. 7.

2 Definition of Matsubara n-point function $G_{A_1\ldots A_n}(\omega_1,\ldots,\omega_n)$

We consider a set of $n = 2,3,4,\ldots$ operators $\{A_1, A_2, \ldots, A_n\}$ defined on the Hilbert space of a quantum many-body Hamiltonian H. The operators can be fermionic, bosonic or a combination of both types, with the restriction that there is an even number of fermionic operators. As an example, $A_1 = d^\dagger d \equiv n$, $A_2 = d$, $A_3 = d^\dagger$ where $d^\dagger$ and d are canonical fermionic creation and annihilation operators. A subset of operators is called bosonic if they create a closed algebra under the commutation operation. They are called fermionic if the algebra is closed under anti-commutation, see Sec. 1 of Ref. [24]. Spin operators are thus bosonic.

We define the imaginary time-ordered n-point correlation functions for imaginary times $\tau_k \in [0,\beta]$, [25, 26],

$$G_{A_1A_2\ldots A_n}(\tau_1,\tau_2,\ldots,\tau_n) \equiv \langle \mathcal{T} A_1(\tau_1)A_2(\tau_2)\ldots A_n(\tau_n)\rangle \,, \tag{1}$$

where $A_k(\tau_k) = e^{\tau_k H} A_k e^{-\tau_k H}$ denotes Heisenberg time evolution. Here and in the following, $k = 1,2,\ldots,n$. The expectation value is calculated as $\langle\ldots\rangle = \mathrm{tr}[\rho\ldots]$ where $\rho = \exp(-\beta H)/Z$

is the thermal density operator at inverse temperature $\beta = 1/T$ and $Z = \mathrm{tr}\exp(-\beta H)$ is the partition function. Note that other conventions for the n-point function differing by a prefactor are also used in the literature, e.g. Ref. [21] multiplies with $(-1)^{n-1}$. In Eq. (1), the imaginary time-ordering operator $\mathcal{T}$ orders the string of Heisenberg operators,

$$\mathcal{T}A_1(\tau_1)A_2(\tau_2)...A_n(\tau_n) \equiv \zeta(p)A_{p(1)}\left(\tau_{p(1)}\right)A_{p(2)}\left(\tau_{p(2)}\right)...A_{p(n)}\left(\tau_{p(n)}\right), \tag{2}$$

where p is the permutation $p \in S_n$ such that $\tau_{p(1)} > \tau_{p(2)} > ... > \tau_{p(n)}$ [see Fig. 1(a)] and the sign $\zeta(p)$ is -1 if the operator string $A_{p(1)}A_{p(2)}...A_{p(n)}$ differs from $A_1A_2...A_n$ by an odd number of transpositions of fermionic operators, otherwise it is $+1$. The special case $n = 2$, with $\zeta(12) = 1$ and $\zeta(21) = \zeta$ ($\zeta = 1$ for $A_{1,2}$ bosonic, $\zeta = -1$ for $A_{1,2}$ fermionic), simplifies to

$$\mathcal{T}A_1(\tau_1)A_2(\tau_2) = \begin{cases} A_1(\tau_1)A_2(\tau_2), & \tau_1 > \tau_2, \\ \zeta A_2(\tau_2)A_1(\tau_1), & \tau_2 > \tau_1. \end{cases} \tag{3}$$

Imaginary time-ordered correlation functions (1) fulfill certain properties which we review in the following, see e.g. [26] for a more extensive discussion. First, they are invariant under translation of all time arguments,

$$G_{A_1A_2...A_n}(\tau_1, \tau_2, ..., \tau_n) = G_{A_1A_2...A_n}(\tau_1 + \tau, \tau_2 + \tau, ..., \tau_n + \tau), \tag{4}$$

with $\tau \in \mathbb{R}$ such that $\tau_k + \tau \in [0, \beta]$. They also fulfill periodic or anti-periodic boundary conditions for the individual arguments τ_k,

$$G_{A_1...A_n}(\tau_1, ..., \tau_k = 0, ..., \tau_n) = \zeta_k G_{A_1...A_n}(\tau_1, ..., \tau_k = \beta, ..., \tau_n), \tag{5}$$

where $\zeta_k = +1$ or -1 if A_k is from the bosonic or fermionic subset of operators, respectively. This motivates the use of a Fourier transformation,

$$G_{A_1...A_n}(\tau_1, ..., \tau_n) \equiv \beta^{-n} \sum_{\omega_1,...,\omega_n} e^{-i(\omega_1\tau_1+...+\omega_n\tau_n)} G_{A_1...A_n}(\omega_1, ..., \omega_n), \tag{6}$$

$$G_{A_1...A_n}(\omega_1, ..., \omega_n) = \int_0^\beta \mathrm{d}\tau_1 \cdots \int_0^\beta \mathrm{d}\tau_n e^{+i(\omega_1\tau_1+...+\omega_n\tau_n)} G_{A_1...A_n}(\tau_1, ..., \tau_n), \tag{7}$$

where $\omega_k = 2\pi m_k/\beta$ or $\omega_k = 2\pi(m_k + 1/2)/\beta$ with $m_k \in \mathbb{Z}$ are bosonic or fermionic Matsubara frequencies, respectively, and $\sum_{\omega_k}$ is shorthand for $\sum_{m_k\in\mathbb{Z}}$. Note that fermionic Matsubara frequencies are necessarily nonzero, a property that will become important later. As we will not discuss the real-frequency formalisms, we will not write the imaginary unit in front of Matsubara frequencies in the arguments of $G_{A_1...A_n}(\omega_1, ..., \omega_n)$. Again, note that in the literature, different conventions for the Fourier transformation of n-point functions are in use. In particular some authors pick different signs in the exponent of Eq. (7) for fermionic creation and annihilation operators, or chose these signs depending on operator positions.

Time translational invariance (4) implies frequency conservation at the left hand side of Eq. (7),

$$G_{A_1...A_n}(\omega_1, ..., \omega_{n-1}, \omega_n) \equiv \beta\,\delta_{0,\omega_1+...+\omega_n} G_{A_1...A_n}(\omega_1, ..., \omega_{n-1}), \tag{8}$$

where on the right hand side we skipped the n-th frequency entry in the argument list of G. Note that we do not use a new symbol for the correlation function when we pull out the factor β and the Kronecker delta function.

3 Spectral representation of $G_{A_1\ldots A_n}(\omega_1,\ldots,\omega_{n-1})$

The integrals involved in the Fourier transformation (7) generate all $n!$ different orderings of the time arguments τ_k. As in Ref. [21] it is thus convenient to use a sum over all $n!$ permutations $p\in S_n$ and employ a product of $n-1$ step-functions θ, with $\theta(x)=1$ for $x>0$ and 0 otherwise, to filter out the unique ordering for which $\beta>\tau_{p(1)}>\tau_{p(2)}>\ldots>\tau_{p(n-1)}>\tau_{p(n)}>0$, see Fig. 1(a),

$$G_{A_1\ldots A_n}(\tau_1,\ldots,\tau_n)=\sum_{p\in S_n}\zeta(p)\left[\prod_{i=1}^{n-1}\theta(\tau_{p(i)}-\tau_{p(i+1)})\right]\left\langle A_{p(1)}(\tau_{p(1)})A_{p(2)}(\tau_{p(2)})\ldots A_{p(n)}(\tau_{p(n)})\right\rangle . \quad (9)$$

To expose explicitly the time dependence of the Heisenberg operators, we insert n times the basis of eigenstates and -energies of the many-body Hamiltonian H. Instead of the familiar notation $|j_1\rangle, |j_2\rangle,\ldots$ and $E_{j_1}, E_{j_2},\ldots$ we employ $|\underline{1}\rangle, |\underline{2}\rangle,\ldots$ and $E_{\underline{1}}, E_{\underline{2}},\ldots$ for compressed notation and denote operator matrix elements as $A^{\underline{1}\,\underline{2}}=\langle\underline{1}|A|\underline{2}\rangle$. We obtain

$$\begin{aligned}G_{A_1\ldots A_n}(\tau_1,\ldots,\tau_n)&=\sum_{p\in S_n}\zeta(p)\left[\prod_{i=1}^{n-1}\theta(\tau_{p(i)}-\tau_{p(i+1)})\right] \quad (10)\\ &\times\frac{1}{Z}\sum_{\underline{1}\ldots\underline{n}}e^{-\beta E_{\underline{1}}}e^{\tau_{p(1)}E_{\underline{1}}}A^{\underline{1}\,\underline{2}}_{p(1)}e^{(-\tau_{p(1)}+\tau_{p(2)})E_{\underline{2}}}A^{\underline{2}\,\underline{3}}_{p(2)}e^{(-\tau_{p(2)}+\tau_{p(3)})E_{\underline{3}}}\ldots e^{(-\tau_{p(n-1)}+\tau_{p(n)})E_{\underline{n}}}A^{\underline{n}\,\underline{1}}_{p(n)}e^{-\tau_{p(n)}E_{\underline{1}}},\end{aligned}$$

and apply the Fourier transform according to the definition (7),

$$\begin{aligned}G_{A_1\ldots A_n}(\omega_1,\ldots,\omega_n)&=\frac{1}{Z}\sum_{p\in S_n}\zeta(p)\sum_{\underline{1}\ldots\underline{n}}e^{-\beta E_{\underline{1}}}A^{\underline{1}\,\underline{2}}_{p(1)}A^{\underline{2}\,\underline{3}}_{p(2)}\ldots A^{\underline{n}\,\underline{1}}_{p(n)} \quad (11)\\ &\times\left[\int_0^\beta \mathrm{d}\tau_{p(1)}e^{\Omega^{\underline{1}\,\underline{2}}_{p(1)}\tau_{p(1)}}\right]\left[\int_0^{\tau_{p(1)}}\mathrm{d}\tau_{p(2)}e^{\Omega^{\underline{2}\,\underline{3}}_{p(2)}\tau_{p(2)}}\right]\\ &\times\cdots\times\left[\int_0^{\tau_{p(n-2)}}\mathrm{d}\tau_{p(n-1)}e^{\Omega^{\underline{n-1}\,\underline{n}}_{p(n-1)}\tau_{p(n-1)}}\right]\left[\int_0^{\tau_{p(n-1)}}\mathrm{d}\tau_{p(n)}e^{\Omega^{\underline{n}\,\underline{1}}_{p(n)}\tau_{p(n)}}\right],\end{aligned}$$

where we defined

$$\Omega^{\underline{a}\,\underline{b}}_k\equiv i\omega_k+E_{\underline{a}}-E_{\underline{b}}\in\mathbb{C}\,. \quad (12)$$

In Eq. (11), the first line carries all the information of the system and the set of operators $\{A_1,A_2,\ldots,A_n\}$. The remaining terms can be regarded as a universal kernel function defined for general $\{\Omega_1,\Omega_2,\ldots,\Omega_n\}$ probed at $\Omega_k\in\mathbb{C}$ which depends on the system and correlators via (12). Upon renaming the τ-integration variables $\tau_{p(k)}\to\tau_k$, this kernel function is written as follows:

$$\mathcal{K}_n(\Omega_1,\ldots,\Omega_n)\equiv\left[\int_0^\beta\mathrm{d}\tau_1e^{\Omega_1\tau_1}\right]\left[\int_0^{\tau_1}\mathrm{d}\tau_2e^{\Omega_2\tau_2}\right]\ldots\left[\int_0^{\tau_{n-2}}\mathrm{d}\tau_{n-1}e^{\Omega_{n-1}\tau_{n-1}}\right]\left[\int_0^{\tau_{n-1}}\mathrm{d}\tau_ne^{\Omega_n\tau_n}\right] \quad (13)$$

$$\equiv\beta\delta_{0,\Omega_1+\Omega_2+\ldots+\Omega_n}K_n(\Omega_1,\ldots,\Omega_{n-1})+R_n(\Omega_1,\ldots,\Omega_n)\,. \quad (14)$$

In the second line we split $\mathcal{K}_n$ into a part K_n proportional to $\beta\delta_{0,\Omega_1+\Omega_2+\ldots+\Omega_n}$ and the rest R_n. We dropped Ω_n from the argument list of K_n which can be reconstructed from $\{\Omega_1,\ldots,\Omega_{n-1}\}$.

Finally, we express $G_{A_1\ldots A_n}(\omega_1,\ldots,\omega_n)$ of Eq. (11) using the kernel $\mathcal{K}_n$ so that the general $\Omega_k\in\mathbb{C}$ get replaced by $\Omega^{\underline{a}\,\underline{b}}_k$ of Eq. (12). For these, $\Omega^{\underline{1}\,\underline{2}}_{p(1)}+\Omega^{\underline{2}\,\underline{3}}_{p(2)}+\ldots+\Omega^{\underline{n}\,\underline{1}}_{p(n)}=i(\omega_1+\omega_2+\ldots+\omega_n)$,

since the $E_{\underline{k}}$ cancel pairwise. The structure of Eq. (8) (which followed from time translational invariance) implies that the terms proportional to R_n are guaranteed to cancel when summed over permutations $p \in S_n$, so that only the terms proportional to K_n remain. We drop the $\beta\delta_{0,\omega_1+\omega_2+\ldots+\omega_n}$ from both sides [c.f. Eq. (8)] and find the spectral representation of the n-point correlation function in the Matsubara formalism,

$$\boxed{G_{A_1\ldots A_n}(\omega_1,\ldots,\omega_{n-1}) = \frac{1}{Z}\sum_{p\in S_n}\zeta(p)\sum_{\underline{1}\ldots\underline{n}} e^{-\beta E_{\underline{1}}} A^{\underline{1}\underline{2}}_{p(1)} A^{\underline{2}\underline{3}}_{p(2)} \ldots A^{\underline{n}\underline{1}}_{p(n)} \times K_n\left(\Omega^{\underline{1}\underline{2}}_{p(1)}, \Omega^{\underline{2}\underline{3}}_{p(2)}, \ldots, \Omega^{\underline{n-1}\,\underline{n}}_{p(n-1)}\right).} \tag{15}$$

An equivalent expression was derived in the literature before [21], see also Refs. [18–20] for the cases of certain small n. However, kernel functions K_n where previously only known approximately, for situations involving only a low order of anomalous terms, see the discussion in Sec. 5. We define an *anomalous* term of order $a = 1, 2, \ldots n-1$ as a summand contributing to $K_n(\Omega_1,\ldots,\Omega_{n-1})$ that contains a product of a Kronecker delta functions $\delta_{0,x}$, where x is a sum of a subset of $\{\Omega_1,\ldots,\Omega_{n-1}\}$. As can be seen in Fig. 1(c), these anomalous contributions to $G_{A_1\ldots A_n}(\omega_1,\ldots,\omega_{n-1})$ correspond to qualitatively important sharp features.

In the next section, we present a simple, exact expression for general $K_n(\Omega_1,\ldots,\Omega_{n-1})$. Readers not interested in the derivation can directly skip to the result in Eq. (26) or its explicit form for $n = 2, 3, 4, 5$ in Sec. 5.

4 General kernel function $K_n(\Omega_1,\ldots,\Omega_{n-1})$

Assuming the spectrum and matrix elements entering Eq. (15) are known, the remaining task is to find expressions for the kernel function $K_n(\Omega_1,\ldots,\Omega_{n-1})$ defined via Eqns. (13) and (14) as the part of $\mathcal{K}_n(\Omega_1,\Omega_2,\ldots,\Omega_n)$ multiplying $\beta\delta_{0,\Omega_1+\Omega_2+\ldots+\Omega_n}$. To facilitate the presentation in this section, in Eq. (13) we rename the integration variables $\tau_k \to \tau_{n-k+1}$ and define new arguments $z_{n-j+1} = \Omega_j$ for $j = 1, 2, \ldots, n-1$,

$$\begin{aligned}
&\mathcal{K}_n(\Omega_1 = z_n, \Omega_2 = z_{n-1}, \ldots, \Omega_n = z_1) \\
&\quad = \left[\int_0^\beta \mathrm{d}\tau_n e^{z_n\tau_n}\right]\left[\int_0^{\tau_n} \mathrm{d}\tau_{n-1} e^{z_{n-1}\tau_{n-1}}\right]\ldots\underbrace{\left[\int_0^{\tau_3} \mathrm{d}\tau_2 e^{z_2\tau_2}\right]\left[\int_0^{\tau_2} \mathrm{d}\tau_1 \underbrace{e^{z_1\tau_1}}_{\equiv h_1(\tau_1)}\right]}_{\equiv h_2(\tau_2)} \qquad (16)\\
&\quad = \beta\delta_{0,z_1+z_2+\ldots+z_n} K_n(z_n, z_{n-1}, \ldots, z_2) + R_n(z_n, z_{n-1}, \ldots, z_1). \qquad (17)
\end{aligned}$$

As indicated in Eq. (16), we call $h_k(\tau_k)$ the integrand for the $\int_0^{\tau_{k+1}} \mathrm{d}\tau_k$ integral for $k = 1, 2, \ldots, n$. At $k = 1$ this integrand is given by $h_1(\tau_1) = e^{z_1\tau_1}$ and we will find h_k for $k = 2, 3, \ldots, n$ iteratively. For $z \in \mathbb{C}$, we define the abbreviations $\delta_z \equiv \delta_{0,z}$ and

$$\Delta_z \equiv \begin{cases} 0, & \text{if } z = 0, \\ \frac{1}{z}, & \text{if } z \neq 0, \end{cases} \tag{18}$$

and consider the integral (for $p = 0, 1, 2, \ldots$ and $\tilde{\tau} \geq 0$, proof by partial integration and induction)

$$\int_0^{\tilde{\tau}} \mathrm{d}\tau\, \tau^p e^{z\tau} = \left[\frac{\tilde{\tau}^{p+1}}{p+1}\delta_z + p!\,(-1)^p\,\Delta_z^{1+p}\sum_{l=0}^{p}\frac{(-1)^l}{l!}\Delta_z^{-l}\tilde{\tau}^l\right]e^{z\tilde{\tau}} - p!\,(-1)^p\,\Delta_z^{p+1}. \tag{19}$$

Recall that we are only interested in the contribution $K_n(z_n, z_{n-1}, \ldots, z_2)$ that fulfills frequency conservation, see Eq. (17). The $\delta_{z_1+z_2+\ldots+z_n}$ in front of this term arises from the final τ_n integration of $h_n(\tau_n) \propto e^{(z_1+z_2+\ldots+z_n)\tau_n}$ via the first term in Eq. (19). This however requires

that all z_k (except the vanishing ones, of course) remain in the exponent during the iterative integrations. This requirement is violated by the last term in the general integral (19) (which comes from the lower boundary of the integral). All terms in $\mathcal{K}_n$ that stem from this last term in Eq. (19) thus contribute to R_n and can be dropped in the following [21]. Note however, that it is straightforward to generalize our approach and keep these terms if the full $\mathcal{K}_n$ is required.

To define the iterative procedure to solve the n-fold integral in Eq. (16), we make the ansatz

$$h_k(\tau_k) = \sum_{l=0}^{k-1} f_k(l) \tau_k^l e^{(z_k+z_{k-1}+\ldots+z_1)\tau_k}, \tag{20}$$

which follows from the form of the integral (19) and our decision to disregard the terms contributing to R_n. The ansatz (20) is parameterized by the numbers $f_k(l)$ with $l = 0, 1, \ldots, k-1$. These numbers have to be determined iteratively, starting from $f_{k=1}(l=0) = 1$, read off from $h_1(\tau_1) = e^{z_1\tau_1}$, c.f. Eq. (16). Iteration rules to obtain the $f_k(l)$ from $f_{k-1}(l)$ are easily derived from Eqns. (16), (19) and (20). We obtain the recursion relation

$$f_k(l) = \sum_{p=0}^{k-1} \tilde{M}_{k-1}(l,p) f_{k-1}(p). \tag{21}$$

This can be understood as a matrix-vector product of $\mathbf{f}_{k-1} = (f_{k-1}(0), f_{k-1}(1), \ldots, f_{k-1}(k-2))^{\mathrm{T}}$ with the $k \times (k-1)$-matrix

$$\tilde{M}_{k-1}(l,p) = \frac{p!}{l!}\left[\delta_{l,p+1}\tilde{\delta}_{k-1} + \theta(p-l+1/2)(-1)^{l+p}\,\tilde{\Delta}_{k-1}^{1+p-l}\right], \tag{22}$$

where $\tilde{\Delta}_k \equiv \Delta_{z_k+\ldots+z_2+z_1}$, $\tilde{\delta}_k \equiv \delta_{z_k+\ldots+z_2+z_1}$. The tilde on top of the $\tilde{\delta}_k$ and $\tilde{\Delta}_k$ signals the presence of a sum of z_j in the arguments (below we will define related quantities without tilde for the sum of Ω_j). Note that the first (second) term in brackets of Eq. (22) comes from the first (second) term in square brackets of Eq. (19).

The next step is to find $K_n(z_n, z_{n-1}, \ldots, z_2)$. This requires to do the integral $\int_0^\beta \mathrm{d}\tau_n h_n(\tau_n)$ which can be again expressed via Eq. (19) but with the replacement $\tilde{\tau} \to \beta$. Only the first term provides a $\beta\delta_{z_1+z_2+\ldots+z_n}$ and is thus identified with K_n. We find:

$$K_n(z_n, z_{n-1}, \ldots, z_2) = \sum_{l=0}^{n-1} \frac{\beta^l f_n(l)}{l+1}. \tag{23}$$

The argument z_1 that the right hand side of Eq. (23) depends on is to be replaced by $z_1 = -z_2 - z_3 - \ldots - z_n$, in line with the arguments in $K_n(z_n, z_{n-1}, \ldots, z_2)$. Then, to conform with Eq. (15), we reinstate $\Omega_j = z_{n-j+1}$ for $j = 1, 2, \ldots, n-1$. This amounts to replacing the terms $\tilde{\delta}_j$ and $\tilde{\Delta}_j$ that appear in $f_n(l)$ as follows,

$$\tilde{\delta}_j = \delta_{z_j+\ldots+z_2+z_1} = \delta_{\Omega_1+\Omega_2+\ldots+\Omega_{n-j}} \equiv \delta_{n-j}, \tag{24}$$

$$-\tilde{\Delta}_j = -\Delta_{z_j+\ldots+z_2+z_1} = \Delta_{\Omega_1+\Omega_2+\ldots+\Omega_{n-j}} \equiv \Delta_{n-j}, \tag{25}$$

where we used $\Omega_1 + \Omega_2 + \ldots + \Omega_n = 0 = z_n + \ldots + z_2 + z_1$. Finally, we can express Eq. (23) using a product of $n-1$ matrices $\tilde{M}$ multiplying the initial length-1 vector with entry $f_1(0) = 1$. Transferring to the Ω-notation by using Eqns. (24) and (25), we obtain

$$\boxed{\begin{aligned} &K_n(\Omega_1, \ldots, \Omega_{n-1}) \\ &= \sum_{i_{n-1}=0}^{n-1} \sum_{i_{n-2}=0}^{n-2} \cdots \sum_{i_2=0}^{2} \sum_{i_1=0}^{1} \frac{\beta^{i_{n-1}}}{i_{n-1}+1} M_1(i_{n-1}, i_{n-2}) M_2(i_{n-2}, i_{n-3}) \cdots M_{n-2}(i_2, i_1) M_{n-1}(i_1, 0), \end{aligned}} \tag{26}$$

with

$$M_j(l,p) \equiv \frac{p!}{l!}\left[\delta_{l,p+1}\delta_j - \theta\,(p-l+1/2)\,\Delta_j^{1+p-l}\right]. \tag{27}$$

The closed form expression (26) of the universal kernel, to be used in the spectral representation (15), is our main result. By definition it is free of any singularities as the case of vanishing denominators is explicitly excluded in Eq. (18).

5 Explicit kernel functions $K_n(\Omega_1,...,\Omega_{n-1})$ for $n = 2,3,4,5$

While the previous section gives a closed form expression for kernel functions of arbitrary order, we here evaluate the universal kernel functions $K_n(\Omega_1,...,\Omega_{n-1})$ defined in Eq. (14) from Eq. (26) for $n = 2,3,4,5$ and show the results in Tab. 1. In each column, the kernel function in the top row is obtained by first multiplying the entries listed below it in the same column by the common factor in the rightmost column and then taking the sum. The symbols δ_j and Δ_j for $j = 1,2,...,n-1$ which appear in Tab. 1 are defined by

$$\delta_j \equiv \delta_{\Omega_1+\Omega_2+...+\Omega_j,0}\,, \tag{28}$$

$$\Delta_j \equiv \Delta_{\Omega_1+\Omega_2+...+\Omega_j} \equiv \begin{cases} 0\,, & \text{if } \Omega_1+\Omega_2+...+\Omega_j=0\,, \\ \frac{1}{\Omega_1+\Omega_2+...+\Omega_j}\,, & \text{if } \Omega_1+\Omega_2+...+\Omega_j\neq 0\,, \end{cases} \tag{29}$$

compare also to the previous section. As an example, for $n = 2$ and $n = 3$ we obtain from Tab. 1

$$K_2(\Omega_1) = -\Delta_{\Omega_1} + \frac{\beta}{2}\delta_{\Omega_1}\,, \tag{30}$$

$$K_3(\Omega_1,\Omega_2) = +\Delta_{\Omega_1}\Delta_{\Omega_1+\Omega_2} - \frac{\beta}{2}\delta_{\Omega_1}\Delta_{\Omega_2} - \Delta_{\Omega_1}\delta_{\Omega_1+\Omega_2}\left(\frac{\beta}{2}+\Delta_{\Omega_1}\right) + \delta_{\Omega_1}\delta_{\Omega_2}\frac{\beta}{2}\frac{\beta}{3}\,, \tag{31}$$

respectively. The rows of Tab. 1 are organized with respect to the number a of factors δ_l in the summands. Here, $a = 0$ indicates the regular part and $a = 1,2,...,n-1$ indicates anomalous terms. There are $n-1$ *choose* a anomalous terms of order a. Our results are exact and go substantially beyond existing expressions in the literature – these are limited to $n \leq 3$ [18] or to fermionic $n = 4$ [19–21] with $a = 0,1$ (and $a = 2,3$ guaranteed to vanish, see below) or arbitrary n with $a = 0$ [21]. Alternative expressions for the $n = 3,4$ kernel functions with $a \leq 1$ were given in [21], but they are consistent with our kernel functions as they yield the same correlation functions, see the Appendix.

In the case of purely fermionic correlators (all A_k fermionic), individual Matsubara frequencies ω_k cannot be zero and thus the $\Omega_k^{\underline{a}\,\underline{b}} \equiv i\omega_k + E_{\underline{a}} - E_{\underline{b}}$ of Eq. (12) always have a finite imaginary part and are non-zero, regardless of the eigenenergies. In this case, only sums of an even number of frequencies can be zero, and we can simplify $\delta_1 = \delta_3 = \delta_5 = ... = 0$. The expressions for the kernels in Tab. 1, now denoted by $K_n|_F$ for the fermionic case, simplify to

$$K_2(\Omega_1)|_F = -\Delta_1\,, \tag{32}$$

$$K_4(\Omega_1,\Omega_2,\Omega_3)|_F = \Delta_1\Delta_3\left[\delta_2\left(\frac{\beta}{2}+\Delta_1\right) - \Delta_2\right], \tag{33}$$

$$\begin{aligned} K_6(\Omega_1,...,\Omega_5)|_F = \Delta_1\Delta_3\Delta_5\Big\{&-\Delta_2\Delta_4 - \delta_2\delta_4\left[\frac{\beta}{2}\frac{\beta}{3} + (\Delta_1+\Delta_3)\left(\frac{\beta}{2}+\Delta_1\right)\right] \\ &+ \delta_4\Delta_2\left(\frac{\beta}{2}+\Delta_1+\Delta_2+\Delta_3\right) + \delta_2\Delta_4\left(\frac{\beta}{2}+\Delta_1\right)\Big\}. \end{aligned} \tag{34}$$

Table 1: Universal kernel functions $K_n(\Omega_1,...,\Omega_{n-1})$ for $n = 2,3,4,5$ defined in Eq. (14) and calculated from Eq. (26) in Sec. 4. In each column, the kernel function in the top row is obtained by first multiplying the entries listed below it in the same column by the common factor in the rightmost column and then taking the sum, see Eqns. (30) and (31) as examples. The symbols δ_j and Δ_j appearing are defined in Eqns. (28) and (29). The rows are organized with respect to the number a of appearances of δ_j, i.e. the order of the anomalous terms.

#anom.	$K_2(\Omega_1)$	$K_3(\Omega_1,\Omega_2)$	$K_4(\Omega_1,\Omega_2,\Omega_3)$	$K_5(\Omega_1,\Omega_2,\Omega_3,\Omega_4)$	factor for entire row
$a=0$	$-\Delta_1$	$+\Delta_1\Delta_2$	$-\Delta_1\Delta_2\Delta_3$	$+\Delta_1\Delta_2\Delta_3\Delta_4$	1
$a=1$	$+\delta_1$	$-\delta_1\Delta_2$	$+\delta_1\Delta_2\Delta_3$	$-\delta_1\Delta_2\Delta_3\Delta_4$	$\frac{\beta}{2}$
		$-\Delta_1\delta_2$	$+\Delta_1\delta_2\Delta_3$	$-\Delta_1\delta_2\Delta_3\Delta_4$	$\frac{\beta}{2}+\Delta_1$
			$+\Delta_1\Delta_2\delta_3$	$-\Delta_1\Delta_2\delta_3\Delta_4$	$\frac{\beta}{2}+\Delta_1+\Delta_2$
				$-\Delta_1\Delta_2\Delta_3\delta_4$	$\frac{\beta}{2}+\Delta_1+\Delta_2+\Delta_3$
$a=2$		$+\delta_1\delta_2$	$-\delta_1\delta_2\Delta_3$	$+\delta_1\delta_2\Delta_3\Delta_4$	$\frac{\beta}{2}\frac{\beta}{3}$
			$-\delta_1\Delta_2\delta_3$	$+\delta_1\Delta_2\delta_3\Delta_4$	$\frac{\beta}{2}\left(\frac{\beta}{3}+\Delta_2\right)$
			$-\Delta_1\delta_2\delta_3$	$+\Delta_1\delta_2\delta_3\Delta_4$	$\frac{\beta}{2}\frac{\beta}{3}+\Delta_1\left(\frac{\beta}{2}+\Delta_1\right)$
				$+\delta_1\Delta_2\Delta_3\delta_4$	$\frac{\beta}{2}\left(\frac{\beta}{3}+\Delta_2+\Delta_3\right)$
				$+\Delta_1\delta_2\Delta_3\delta_4$	$\frac{\beta}{2}\frac{\beta}{3}+(\Delta_1+\Delta_3)\left(\frac{\beta}{2}+\Delta_1\right)$
				$+\Delta_1\Delta_2\delta_3\delta_4$	$\frac{\beta}{2}\frac{\beta}{3}+(\Delta_1+\Delta_2)\left(\frac{\beta}{2}+\Delta_2\right)+\Delta_1^2$
$a=3$			$+\delta_1\delta_2\delta_3$	$-\delta_1\delta_2\delta_3\Delta_4$	$\frac{\beta}{2}\frac{\beta}{3}\frac{\beta}{4}$
				$-\delta_1\delta_2\Delta_3\delta_4$	$\frac{\beta}{2}\frac{\beta}{3}\left(\frac{\beta}{4}+\Delta_3\right)$
				$-\delta_1\Delta_2\delta_3\delta_4$	$\frac{\beta}{2}\left(\frac{\beta}{3}\frac{\beta}{4}+\Delta_2\left(\frac{\beta}{3}+\Delta_2\right)\right)$
				$-\Delta_1\delta_2\delta_3\delta_4$	$\frac{\beta}{2}\frac{\beta}{3}\frac{\beta}{4}+\Delta_1\left(\frac{\beta}{2}\frac{\beta}{3}+\Delta_1\left(\frac{\beta}{2}+\Delta_1\right)\right)$
$a=4$				$+\delta_1\delta_2\delta_3\delta_4$	$\frac{\beta}{2}\frac{\beta}{3}\frac{\beta}{4}\frac{\beta}{5}$

This concludes the general part of this work. Next, we consider two example systems frequently discussed in the condensed matter theory literature. Using our formalism, we provide analytical forms of correlation functions that to the best of our knowledge were not available before.

6 Applications: Hubbard atom and free spin

6.1 Fermionic Hubbard atom

The Hubbard atom (HA) describes an isolated impurity or otherwise localized system with Hamiltonian

$$H = \epsilon\left(n_\uparrow + n_\downarrow\right) + U n_\uparrow n_\downarrow - h\left(n_\uparrow - n_\downarrow\right), \tag{35}$$

see Fig. 1(b) for a sketch. The HA corresponds to the limit of vanishing system-bath coupling of the Anderson impurity model (AIM), or vanishing hopping in the Hubbard model (HM). The particle number operators $n_\sigma = d_\sigma^\dagger d_\sigma$ count the number of fermionic particles with spin $\sigma \in \{\uparrow,\downarrow\}$, each contributing an onsite energy ϵ shifted by an external magnetic field h in z-direction. An interaction energy U is associated to double occupation.

Due to its simplicity and the four-dimensional Hilbert space, the correlation functions for the HA can be found analytically using the spectral representation. It is therefore often used for benchmarking [3,27,28]. The presence of the interaction term leads to a non-vanishing $n=4$ one-line irreducible vertex function. The HA serves as an important reference point to study and interpret properties of the AIM and HM beyond the one-particle level, for example diver-

gences of two-line irreducible vertex functions [29–32] and signatures of the local moment formation in generalized susceptibilities [16, 33]. Using the fermionic kernels in Eqns. (32) and (33), we have checked that our formalism reproduces the results for the 2-point and 4-point correlators given in Refs. [19, 21, 26] for half-filling, $\epsilon = -U/2$ and $h = 0$.

Correlation functions including bosonic operators describe the asymptotic behaviour of the $n = 4$ fermion vertex for large frequencies [34] or the interaction of electrons by the exchange of an effective boson [35, 36]. These relations involve correlation functions of two bosonic operators or of one bosonic and two fermionic operators, giving rise to expressions possibly anomalous in at most one frequency argument, i.e. $a \leq 1$.

For the HA, AIM and HM, bosonic correlation functions for $n > 2$ have not been considered thoroughly so far. Only recently, steps in this direction were taken, particularly in the context of non-linear response theory [3]. The response of a system to first and second order in an external perturbation is described by 2- and 3-point correlation functions, respectively. For the HA, physically motivated perturbations affect the onsite energy via a term $\delta_\epsilon n$ or take the form of a magnetic field $\boldsymbol{\delta}_h \cdot \mathbf{S}$. Here, the parameters δ_ϵ and $\boldsymbol{\delta}_h$ denote the strength of the perturbation and we define

$$n = n_\uparrow + n_\downarrow\,, \qquad S^x = \frac{1}{2}\left(d_\uparrow^\dagger d_\downarrow + d_\downarrow^\dagger d_\uparrow\right), \quad S^y = \frac{-i}{2}\left(d_\uparrow^\dagger d_\downarrow - d_\downarrow^\dagger d_\uparrow\right), \quad S^z = \frac{1}{2}\left(n_\uparrow - n_\downarrow\right). \tag{36}$$

The resulting changes of the expectation values of the density or magnetization in arbitrary direction are described in second order of the perturbation by the connected parts of the correlation functions $G_{A_1A_2A_3}(\tau_1, \tau_2, \tau_3)$, with $A_i \in \{n, S_x, S_y, S_z\}$, where the time-ordered expectation value is evaluated with respect to the unperturbed system (35) and Fourier transformed to the frequencies of interest. These objects have been studied numerically in Ref. [3]. In the following, we give explicit, analytic expressions of the full correlation functions $G_{A_1A_2A_3}(\omega_1, \omega_2)$ (i.e. including disconnected parts), for arbitrary parameters ϵ, U and h and for all possible operator combinations using the (bosonic) kernel function K_3, see Eq. (31). To the best of our knowledge, these expressions have not been reported before.

The eigenstates of the HA Hamiltonian (35) [see Fig. 1(b)] describe an empty ($|0\rangle$), singly occupied ($d_\uparrow^\dagger|0\rangle = |\uparrow\rangle$, $d_\downarrow^\dagger|0\rangle = |\downarrow\rangle$) or doubly occupied ($d_\uparrow^\dagger d_\downarrow^\dagger|0\rangle = |\uparrow\downarrow\rangle$) impurity with eigenenergies $E_0 = 0$, $E_\uparrow = \epsilon - h$, $E_\downarrow = \epsilon + h$ and $E_{\uparrow\downarrow} = 2\epsilon + U$, respectively. The partition function is $Z = 1 + e^{-\beta(\epsilon-h)} + e^{-\beta(\epsilon+h)} + e^{-\beta(2\epsilon+U)}$. We define

$$s = \frac{e^{-\beta\epsilon}}{Z}\sinh(\beta h)\,, \qquad c = \frac{e^{-\beta\epsilon}}{Z}\cosh(\beta h)\,, \tag{37}$$

and obtain all non-vanishing bosonic 3-point correlation functions (where $\omega_3 = -\omega_1 - \omega_2$):

$$G_{nnn}(\omega_1, \omega_2) = 2\beta^2\delta_{\omega_1}\delta_{\omega_2}\left(\frac{4e^{-\beta(2\epsilon+U)}}{Z} + c\right), \tag{38}$$

$$G_{nnS^z}(\omega_1, \omega_2) = \beta^2\delta_{\omega_1}\delta_{\omega_2}s\,, \tag{39}$$

$$G_{nS^xS^y}(\omega_1, \omega_2) = -\beta\,\delta_{\omega_1}s\frac{\omega_2}{\omega_2^2 + 4h^2}\,, \tag{40}$$

$$G_{nS^xS^x}(\omega_1, \omega_2) = G_{nS^yS^y}(\omega_1, \omega_2) = 2\beta\,\delta_{\omega_1}\frac{h\,s}{\omega_2^2 + 4h^2}\,, \tag{41}$$

$$G_{nS^zS^z}(\omega_1, \omega_2) = \frac{\beta^2}{2}\delta_{\omega_1}\delta_{\omega_2}c\,, \tag{42}$$

$$G_{S^zS^xS^x}(\omega_1, \omega_2) = G_{S^zS^yS^y}(\omega_1, \omega_2) = -s\frac{\omega_2\omega_3 + 4h^2}{(\omega_2^2 + 4h^2)(\omega_3^2 + 4h^2)} + \beta\,\delta_{\omega_1}\frac{h\,c}{\omega_2^2 + 4h^2}\,, \tag{43}$$

$$G_{S^zS^zS^z}(\omega_1,\omega_2) = \frac{\beta^2}{4}\delta_{\omega_1}\delta_{\omega_2 s}\,, \tag{44}$$

$$G_{S^xS^yS^z}(\omega_1,\omega_2) = 2h\,s\frac{\omega_1-\omega_2}{(\omega_1^2+4h^2)(\omega_2^2+4h^2)} - \frac{\beta}{2}\delta_{\omega_3 c}\frac{\omega_1}{\omega_1^2+4h^2}\,. \tag{45}$$

We observe that each conserved quantity, in this case n and S_z, contributes an anomalous term $\propto \delta_{\omega_k}$ in its respective frequency argument ω_k. If an operator A_k is conserved $[H,A_k]=0$, the basis over which we sum in Eq. (15) can be chosen such that both H and A_k are diagonal, $A_k^{\underline{1}\underline{2}} = A_k^{\underline{1}\underline{1}}\delta_{\underline{1},\underline{2}}$. If $A_k^{\underline{1}\underline{1}} \neq 0$ for some state $|\underline{1}\rangle$ the vanishing eigenenergy difference leads to the appearance of an anomalous contribution. If the operators in the correlator additionally commute with each other, in our case for example $[n,S^z]=0$, there exists a basis in which all operators and the Hamiltonian are diagonal, giving rise to correlation functions anomalous in all frequency arguments.

In the limit of vanishing field $h\to 0$, we introduce an additional degeneracy $E_\uparrow = E_\downarrow = \epsilon$ in the system, potentially resulting in additional anomalous contributions. The corresponding correlation functions can then be obtained in two ways. Either we recompute them using the kernel function K_3 or we take appropriate limits, for example

$$\lim_{h\to 0}\frac{h\,\sinh(\beta h)}{\omega_k^2+4h^2} = \frac{\beta}{4}\delta_{\omega_k}\,, \tag{46}$$

resulting in

$$G_{nnn}(\omega_1,\omega_2) = \beta^2\delta_{\omega_1}\delta_{\omega_2}\frac{2\left(4e^{-\beta(2\epsilon+U)}+e^{-\beta\epsilon}\right)}{Z}\,, \tag{47}$$

$$G_{nS^\alpha S^\alpha}(\omega_1,\omega_2) = \beta^2\delta_{\omega_1}\delta_{\omega_2}\frac{e^{-\beta\epsilon}}{2Z} \quad (\alpha\in\{x,y,z\})\,, \tag{48}$$

$$G_{S^xS^yS^z}(\omega_1,\omega_2) = \beta\frac{e^{-\beta\epsilon}}{2Z}\left(-\delta_{\omega_1}\Delta_{\omega_2}+\delta_{\omega_2}\Delta_{\omega_1}-\delta_{\omega_1+\omega_2}\Delta_{\omega_1}\right), \tag{49}$$

with all other correlation functions vanishing. As already pointed out in Ref. [3], only the last correlation function retains a nontrivial frequency dependence due to non-commuting operators.

6.2 Free spin S

We now consider correlation functions of a free spin of length S, without a magnetic field, so that temperature $T = 1/\beta$ is the only energy scale. The operators $\{S^\alpha\}_{\alpha=x,y,z}$ fulfill $S^xS^x + S^yS^y + S^zS^z = S(S+1)$ and the SU(2) algebra $[S^{\alpha_1},S^{\alpha_2}] = i\sum_{\alpha_3=\{x,y,z\}}\epsilon^{\alpha_1\alpha_2\alpha_3}S^{\alpha_3}$, thus they are bosonic. Since the Hamiltonian vanishes and therefore all eigenenergies are zero, every $\Omega_k^{\underline{a}\,\underline{b}}$ in the spectral representation (15) can vanish and a proper treatment of all anomalous terms is essential. As the Heisenberg time dependence is trivial, $S^\alpha(\tau) = S^\alpha$, the non-trivial frequency dependence of the correlators, which can be non-vanishing at any order $n>1$, derives solely from the action of imaginary time-ordering.

The correlators are required, for example, as the non-trivial initial condition for the spin-fRG recently suggested by Kopietz et al., Refs. [13, 37–40]. However, for $n>3$ they are so far only partially available: They are either given for restricted frequency combinations, or for the purely classical case $S^{\alpha_1} = S^{\alpha_2} = \ldots = S^{\alpha_n}$ where the SU(2) algebra does not matter, or for finite magnetic field via an equation of motion [37] or diagrammatic approach [41, 42].

Table 2: Matsubara correlation functions for a free spin-S up to order $n=4$. Here, $\omega_4=-\omega_1-\omega_2-\omega_3$.

$n=2$	$G_{S^+S^-}(\omega)=G_{S^zS^z}(\omega)=\beta\delta_\omega b_1$
$n=3$	$G_{S^+S^-S^z}(\omega_1,\omega_2)=\beta b_1(-\delta_{\omega_1}\Delta_{i\omega_2}+\delta_{\omega_2}\Delta_{i\omega_1}+\delta_{\omega_1+\omega_2}\Delta_{i\omega_2})=-iG_{S^xS^yS^z}(\omega_1,\omega_2)$
$n=4$	$G_{S^zS^zS^zS^z}(\omega_1,\omega_2,\omega_3)=\delta_{\omega_1}\delta_{\omega_2}\delta_{\omega_3}\beta^3 b_3$
	$G_{S^+S^+S^-S^-}(\omega_1,\omega_2,\omega_3)=\beta b_1[2\times\delta_{\omega_1}\delta_{\omega_2}\delta_{\omega_3}\times\frac{\beta^2}{5}\left(3b_1-\frac{1}{3}\right)+r]$
	$G_{S^+S^-S^zS^z}(\omega_1,\omega_2,\omega_3)=\beta b_1[1\times\delta_{\omega_1}\delta_{\omega_2}\delta_{\omega_3}\times\frac{\beta^2}{5}\left(3b_1-\frac{1}{3}\right)-r]$
	$r=\Delta_{i\omega_1}\Delta_{i\omega_2}\left(\delta_{\omega_1+\omega_3}+\delta_{\omega_2+\omega_3}-\delta_{\omega_3}-\delta_{\omega_4}\right)-\left(\delta_{\omega_1}\Delta^2_{i\omega_2}+\delta_{\omega_2}\Delta^2_{i\omega_1}\right)\left(\delta_{\omega_3}+\delta_{\omega_4}\right)$ $-\Delta_{i\omega_3}\Delta_{i\omega_4}\left(\delta_{\omega_1}+\delta_{\omega_2}\right)$

We define the spin raising and lowering operators,

$$S^\pm=(S^x\pm iS^y)/\sqrt{2}, \tag{50}$$

which have to appear in pairs for a non-vanishing correlator due to spin-rotation symmetry. As for the HA, we do not consider connected correlators in this work for brevity. The classical S^z-correlator can be found from its generating functional with source field h [13],

$$\mathcal{G}(y=\beta h)=\frac{\sinh[y(S+1/2)]}{(2S+1)\sinh[y/2]}, \tag{51}$$

$$\left\langle (S^z)^l\right\rangle=\lim_{y\to 0}\partial_y^l\mathcal{G}(y)\equiv b_{l-1}, \tag{52}$$

for example $b_1=\frac{S}{3}(S+1)$ and $b_3=\frac{S}{15}\left(3S^3+6S^2+2S-1\right)$ and vanishing b_l for even l. For all other correlators involving $\alpha_k=\pm$, we adapt Eq. (15) for the free spin case,

$$G_{S^{\alpha_1}S^{\alpha_2}\ldots S^{\alpha_n}}(\omega_1,\ldots,\omega_{n-1})=\sum_{p\in S_n}\langle S^{\alpha_{p(1)}}S^{\alpha_{p(2)}}\ldots S^{\alpha_{p(n)}}\rangle K_n\left(i\omega_{p(1)},i\omega_{p(2)},\ldots,i\omega_{p(n-1)}\right), \tag{53}$$

where we made use of the fact that all eigenenergies are zero and the Heisenberg time evolution is trivial. It is convenient to evaluate the equal-time correlators in Eq. (53) as

$$\langle S^{\alpha_1}S^{\alpha_2}\ldots S^{\alpha_n}\rangle=\frac{1}{2S+1}\sum_{m=-S}^{S}\langle m|S^{\alpha_1}S^{\alpha_2}\ldots S^{\alpha_n}|m\rangle\equiv\frac{1}{2S+1}\sum_{m=-S}^{S}\sum_{l=0}^{n}p_l m^l=p_0+\sum_{l=2}^{n}p_l b_{l-1}, \tag{54}$$

where in the last step we used Eq. (52). We find the real expansion coefficients $\{p_l\}_{l=0,1,\ldots,n}$ iteratively by moving through the string $\alpha_1\alpha_2\ldots\alpha_n$ from the right and start from $p_l=\delta_{0,l}$. Based on the S^z eigenstates $\{|m\rangle\}_{m=-S,\ldots,S-1,S}$ we obtain the iteration rules from $S^z|m\rangle=m|m\rangle$ and $S^\pm|m\rangle=\sqrt{1/2}\sqrt{S(S+1)-m(m\pm1)}|m\pm1\rangle$. We define an auxiliary integer c that keeps track of the intermediate state $|m+c\rangle$, initially $c=0$. Depending on the α_j that we find in step $j=n,n-1\ldots,1$ we take one of the following actions: (i) For $\alpha_j=z$, we update $p_l\leftarrow p_{l-1}+cp_l\ \forall l$ and leave c unchanged. It is understood that $p_{l<0}=0$. (ii) For $\alpha_j=+$, we combine the square-root factor brought by the raising operator with the factor that comes from the necessary $\alpha_{j'}=-$ at another place in the string. We replace $p_l\leftarrow-\frac{1}{2}p_{l-2}-\frac{2c+1}{2}p_{l-1}+\left(\frac{3}{2}b_1-c\frac{c+1}{2}\right)p_l\ \forall l$ and then let $c\leftarrow c+1$. (iii) For $\alpha_j=-$, we update $c\leftarrow c-1$ and keep p_l unchanged, $p_l\leftarrow p_l\ \forall l$.

Our final results for the free spin correlators are reported in Tab. 2. We reproduce the known spin correlators for $n=2,3$ and determine the non-classical correlators $G_{S^+S^+S^-S^-}$ and $G_{S^+S^-S^zS^z}$ at order $n=4$, which to the best of our knowledge were not available in the

literature.[1] We also confirmed the classical result for $G_{S^zS^zS^zS^z}$, which in our full quantum formalism requires some non-trivial cancellations. To arrive at our results, we used the identity

$$\Delta_{a+b}(\Delta_a+\Delta_b)-\Delta_a\Delta_b=\delta_a\Delta_b^2+\delta_b\Delta_a^2-\delta_{a+b}\Delta_a\Delta_b\,. \tag{55}$$

We finally comment on the relation between the $n=3$ free spin-S correlator $G_{S^+S^-S^z}$ from Tab. (2) and the result for $G_{S^xS^yS^z}$ found for the zero-field limit of the HA in Eq. (49). The operators $S^{x,y,z}$ for the Hubbard model [c.f. Eq. (36)] project to the singly-occupied $S=1/2$ subspace spanned by the states $|\uparrow\rangle, |\downarrow\rangle$. Thus, using $G_{S^xS^yS^z}=iG_{S^+S^-S^z}$ and specializing the free spin result from Tab. (2) to $S=1/2$ (where $b_1=1/4$) we find agreement with the HA result (49) up to the factor $2e^{-\beta\epsilon}/Z$. This factor represents the expectation value of the projector to the singly-occupied sector in the HA Hilbert space and goes to unity in the local-moment regime.

7 Conclusion

In summary, we have provided exact universal kernel functions for the spectral representation of the n-point Matsubara correlator. Our results are an efficient alternative to equation-of-motion approaches which often have difficulties to capture anomalous terms related to conserved or commuting operators. We expect our results to be useful for various benchmarking applications, as starting points for emerging many-body methods and for unraveling the physical interpretation of n-point functions in various settings. Our results also apply in the limit $T\to 0$ where the formally divergent anomalous contributions are to be understood as $\beta\delta_{\omega,0}\to 2\pi\delta(\omega)$. Some of these Dirac delta-functions will vanish after subtracting the disconnected contributions, others indicate truely divergent susceptibilities like the $1/T$ Curie law for the spin-susceptiblity of the Hubbard atom in the local moment regime [26]. Although our work has focused on imaginary frequency (Matsubara) correlators, with analytical expressions now at hand, it is also interesting to study the intricacies of analytical continuation to real frequencies and thus to further explore the connection of Matsubara and Keldysh correlators [43].

Acknowledgements

We acknowledge useful discussions with Karsten Held, Friedrich Krien, Seung-Sup Lee, Peter Kopietz, Fabian Kugler, Nepomuk Ritz, Georg Rohringer, Andreas Rückriegel. We thank Andreas Rückriegel for sharing unpublished results on 4-point free spin correlators and pointing out further simplifications of the analytical expressions.

Funding information BS and BS are supported by a MCQST-START fellowship. We acknowledge funding from the International Max Planck Research School for Quantum Science and Technology (IMPRS-QST) for JH, from the Deutsche Forschungsgemeinschaft under Germany's Excellence Strategy EXC-2111 (Project No. 390814868), and from the Munich Quantum Valley, supported by the Bavarian state government with funds from the Hightech Agenda Bayern Plus.

[1] We thank Andreas Rückriegel for sharing unpublished results on 4-point free spin correlators and pointing out further simplifications of the analytical expressions.

A Equivalence to convention of Ref. [21]

In Ref. [21] by Kugler, Lee and von Delft (KLD), only regular ($a=0$) and anomalous terms of order $a=1$ have been considered for $n=3,4$. The corresponding kernel functions were derived from only $(n-1)!$ permutations by setting $\tau_n=0$ and $\tau_{i\neq n}>0$, but still applied to all $n!$ permutations to obtain the correlation functions. For $n=3$, the resulting kernel function (Eq. (46) in Ref. [21]) reads

$$K_{3,\mathrm{KLD}}(\Omega_1,\Omega_2)=\Delta_1\Delta_2-\Delta_1\delta_2\frac{1}{2}(\beta+\Delta_1)-\delta_1\Delta_2\frac{1}{2}(\beta+\Delta_2)\,. \tag{A.1}$$

This can be compared to the corresponding kernel function for $n=3$ found in our Eq. (31) truncated to $a\leq 1$,

$$K_3^{a\leq 1}(\Omega_1,\Omega_2)=\Delta_1\Delta_2-\Delta_1\delta_2\left(\frac{\beta}{2}+\Delta_1\right)-\frac{\beta}{2}\delta_1\Delta_2\,. \tag{A.2}$$

Both approaches are equally valid and should yield the same correlation functions (consistently discarding terms with $a=2$), yet the kernel functions are obviously different. To resolve this issue, we define the difference of the kernel functions

$$K_{3,\mathrm{diff}}(\Omega_1,\Omega_2)=K_{3,\mathrm{KLD}}(\Omega_1,\Omega_2)-K_3^{a\leq 1}(\Omega_1,\Omega_2)=\frac{1}{2}\left(\Delta_1^2\delta_2-\delta_1\Delta_2^2\right), \tag{A.3}$$

and show that the corresponding contributions to the correlation function vanishes when summed over cyclically related permutations $p=123,231,312$. These contributions are given by

$$\begin{aligned}
&\frac{1}{Z}\sum_{p=123,231,312}\zeta(p)\sum_{\underline{123}}e^{-\beta E_{\underline{1}}}A^{\underline{12}}_{p(1)}A^{\underline{23}}_{p(2)}A^{\underline{31}}_{p(3)}K_{3,\mathrm{diff}}(\Omega^{\underline{12}}_{p(1)},\Omega^{\underline{23}}_{p(2)})\\
&=\frac{\zeta(123)}{2Z}\sum_{\underline{123}}e^{-\beta E_{\underline{1}}}A^{\underline{12}}_1A^{\underline{23}}_2A^{\underline{31}}_3\left(\Delta^2_{\Omega^{\underline{12}}_1}\delta_{\Omega^{\underline{12}}_1+\Omega^{\underline{23}}_2}-\delta_{\Omega^{\underline{12}}_1}\Delta^2_{\Omega^{\underline{12}}_1+\Omega^{\underline{23}}_2}\right)\\
&+\frac{\zeta(231)}{2Z}\sum_{\underline{123}}e^{-\beta E_{\underline{1}}}A^{\underline{12}}_2A^{\underline{23}}_3A^{\underline{31}}_1\left(\Delta^2_{\Omega^{\underline{12}}_2}\delta_{\Omega^{\underline{12}}_2+\Omega^{\underline{23}}_3}-\delta_{\Omega^{\underline{12}}_2}\Delta^2_{\Omega^{\underline{12}}_2+\Omega^{\underline{23}}_3}\right)\\
&+\frac{\zeta(312)}{2Z}\sum_{\underline{123}}e^{-\beta E_{\underline{1}}}A^{\underline{12}}_3A^{\underline{23}}_1A^{\underline{31}}_2\left(\Delta^2_{\Omega^{\underline{12}}_3}\delta_{\Omega^{\underline{12}}_3+\Omega^{\underline{23}}_1}-\delta_{\Omega^{\underline{12}}_3}\Delta^2_{\Omega^{\underline{12}}_3+\Omega^{\underline{23}}_1}\right).
\end{aligned} \tag{A.4}$$

Considering the second term of permutation $p=312$ and renaming the summation variables $\underline{2}\to\underline{1}$, $\underline{3}\to\underline{2}$, $\underline{1}\to\underline{3}$ yields

$$\begin{aligned}
&-\frac{\zeta(312)}{2Z}\sum_{\underline{123}}e^{-\beta E_{\underline{1}}}A^{\underline{12}}_3A^{\underline{23}}_1A^{\underline{31}}_2\,\delta_{\Omega^{\underline{12}}_3}\Delta^2_{\Omega^{\underline{12}}_3+\Omega^{\underline{23}}_1}\\
&=-\frac{\zeta(312)}{2Z}\sum_{\underline{123}}e^{-\beta E_{\underline{3}}}A^{\underline{12}}_1A^{\underline{23}}_2A^{\underline{31}}_3\,\delta_{\Omega^{\underline{31}}_3}\Delta^2_{\Omega^{\underline{31}}_3+\Omega^{\underline{12}}_1}\\
&=-\frac{\zeta(123)}{2Z}\sum_{\underline{123}}e^{-\beta E_{\underline{1}}}A^{\underline{12}}_1A^{\underline{23}}_2A^{\underline{31}}_3\,\delta_{\Omega^{\underline{12}}_1+\Omega^{\underline{23}}_2}\Delta^2_{\Omega^{\underline{12}}_1},
\end{aligned} \tag{A.5}$$

where we used $\omega_3=-\omega_1-\omega_2$ and the fact that $\delta_{\Omega^{\underline{31}}_3}=\delta_{\omega_3}\delta_{E_{\underline{1}},E_{\underline{3}}}$ enforces the third operator to be bosonic, such that $\zeta(312)=\zeta(123)$. This term exactly cancels the first contribution of permutation $p=123$ in (A.4). Repeating similar steps for the remaining terms, we find that

the the second term of $p = 123$ and the first term of $p = 231$ as well as the second term of $p = 231$ and the first term of $p = 312$ cancel, leading to

$$\frac{1}{Z}\sum_{p\in\{123,231,312\}}\zeta(p)\sum_{\underline{123}}e^{-\beta E_{\underline{1}}}A^{\underline{12}}_{p(1)}A^{\underline{23}}_{p(2)}A^{\underline{31}}_{p(3)}K_{3,\mathrm{diff}}\left(\Omega^{\underline{12}}_{p(1)},\Omega^{\underline{23}}_{p(2)}\right)=0\,. \tag{A.6}$$

Similarly, summing over the second set of cyclically related permutations $p = 132, 213, 321$ leads to a vanishing result, leading to the conclusion that

$$\frac{1}{Z}\sum_{p\in S_3}\zeta(p)\sum_{\underline{123}}e^{-\beta E_{\underline{1}}}A^{\underline{12}}_{p(1)}A^{\underline{23}}_{p(2)}A^{\underline{31}}_{p(3)}K_{3,\mathrm{diff}}\left(\Omega^{\underline{12}}_{p(1)},\Omega^{\underline{23}}_{p(2)}\right)=0\,. \tag{A.7}$$

Thus we have shown that both kernel functions in Eqns. (A.1) and (A.2) are equivalent as they yield the same correlation functions after summing over all permutations. The same statement holds true for case of $n = 4$ and $a = 1$.

References

[1] J. W. Negele and H. Orland, *Quantum many-particle systems*, CRC Press, Boca Raton, USA, ISBN 9780429497926 (1998), doi:10.1201/9780429497926.

[2] H. Bruus and K. Flensberg, *Many-body quantum theory in condensed matter physics*, Oxford University Press, Oxford, UK, ISBN 9780198566335 (2004).

[3] P. Kappl, F. Krien, C. Watzenböck and K. Held, *Nonlinear responses and three-particle correlators in correlated electron systems exemplified by the Anderson impurity model*, Phys. Rev. B **107**, 205108 (2023), doi:10.1103/PhysRevB.107.205108.

[4] G. Semeghini et al., *Probing topological spin liquids on a programmable quantum simulator*, Science **374**, 1242 (2021), doi:10.1126/science.abi8794.

[5] L. Hedin, *New method for calculating the one-particle Green's function with application to the electron-gas problem*, Phys. Rev. **139**, A796 (1965), doi:10.1103/PhysRev.139.A796.

[6] N. E. Bickers, *Self-consistent many-body theory for condensed matter systems*, in *Theoretical methods for strongly correlated electrons*, Springer, New York, USA, ISBN 9780387217178 (2004), doi:10.1007/0-387-21717-7_6.

[7] B. Roulet, J. Gavoret and P. Nozières, *Singularities in the X-ray absorption and emission of metals. I. First-order parquet calculation*, Phys. Rev. **178**, 1072 (1969), doi:10.1103/PhysRev.178.1072.

[8] P. Kopietz, L. Bartosch and F. Schütz, *Introduction to the functional renormalization group*, Springer, Berlin, Heidelberg, Germany, ISBN 9783642050947 (2010), doi:10.1007/978-3-642-05094-7.

[9] W. Metzner, M. Salmhofer, C. Honerkamp, V. Meden and K. Schönhammer, *Functional renormalization group approach to correlated fermion systems*, Rev. Mod. Phys. **84**, 299 (2012), doi:10.1103/RevModPhys.84.299.

[10] C. Wetterich, *Exact evolution equation for the effective potential*, Phys. Lett. B **301**, 90 (1993), doi:10.1016/0370-2693(93)90726-X.

[11] S.-S. B. Lee, F. B. Kugler and J. von Delft, *Computing local multipoint correlators using the numerical renormalization group*, Phys. Rev. X **11**, 041007 (2021), doi:10.1103/PhysRevX.11.041007.

[12] J. Reuther and R. Thomale, *Cluster functional renormalization group*, Phys. Rev. B **89**, 024412 (2014), doi:10.1103/PhysRevB.89.024412.

[13] J. Krieg and P. Kopietz, *Exact renormalization group for quantum spin systems*, Phys. Rev. B **99**, 060403 (2019), doi:10.1103/PhysRevB.99.060403.

[14] A. Rückriegel, J. Arnold, R. Goll and P. Kopietz, *Spin functional renormalization group for dimerized quantum spin systems*, Phys. Rev. B **105**, 224406 (2022), doi:10.1103/PhysRevB.105.224406.

[15] G. Rohringer, H. Hafermann, A. Toschi, A. A. Katanin, A. E. Antipov, M. I. Katsnelson, A. I. Lichtenstein, A. N. Rubtsov and K. Held, *Diagrammatic routes to nonlocal correlations beyond dynamical mean field theory*, Rev. Mod. Phys. **90**, 025003 (2018), doi:10.1103/RevModPhys.90.025003.

[16] P. Chalupa, T. Schäfer, M. Reitner, D. Springer, S. Andergassen and A. Toschi, *Fingerprints of the local moment formation and its Kondo screening in the generalized susceptibilities of many-electron problems*, Phys. Rev. Lett. **126**, 056403 (2021), doi:10.1103/PhysRevLett.126.056403.

[17] H. Lehmann, *Über Eigenschaften von Ausbreitungsfunktionen und Renormierungskonstanten quantisierter Felder*, Nuovo Cimento **11**, 342 (1954), doi:10.1007/BF02783624.

[18] A. Shvaika, *On the spectral relations for multitime correlation functions*, Condens. Matter Phys. **9**, 447 (2006), doi:10.5488/CMP.9.3.447.

[19] H. Hafermann, C. Jung, S. Brener, M. I. Katsnelson, A. N. Rubtsov and A. I. Lichtenstein, *Superperturbation solver for quantum impurity models*, Europhys. Lett. **85**, 27007 (2009), doi:10.1209/0295-5075/85/27007.

[20] A. Shvaika, *Spectral properties of four-time fermionic Green's functions*, Condens. Matter Phys. **19**, 33004 (2016), doi:10.5488/CMP.19.33004.

[21] F. B. Kugler, S.-S. B. Lee and J. von Delft, *Multipoint correlation functions: Spectral representation and numerical evaluation*, Phys. Rev. X **11**, 041006 (2021), doi:10.1103/PhysRevX.11.041006.

[22] P. C. Kwok and T. D. Schultz, *Correlation functions and Green functions: Zero-frequency anomalies*, J. Phys. C: Solid State Phys. **2**, 1196 (1969), doi:10.1088/0022-3719/2/7/312.

[23] C. Watzenböck, M. Fellinger, K. Held and A. Toschi, *Long-term memory magnetic correlations in the Hubbard model: A dynamical mean-field theory analysis*, SciPost Phys. **12**, 184 (2022), doi:10.21468/SciPostPhys.12.6.184.

[24] A. Tsvelik, *Quantum field theory in condensed matter physics*, Cambridge University Press, Cambridge, UK, ISBN 9780511615832 (2003), doi:10.1017/CBO9780511615832.

[25] G. Rohringer, A. Valli and A. Toschi, *Local electronic correlation at the two-particle level*, Phys. Rev. B **86**, 125114 (2012), doi:10.1103/PhysRevB.86.125114.

[26] G. Rohringer, *New routes towards a theoretical treatment of nonlocal electronic correlations*, PhD thesis, Technische Universität Wien, Wien, Austria (2013) doi:10.34726/hss.2013.21498.

[27] F. Krien and A. Valli, *Parquetlike equations for the Hedin three-leg vertex*, Phys. Rev. B **100**, 245147 (2019), doi:10.1103/PhysRevB.100.245147.

[28] F. Krien, A. Kauch and K. Held, *Tiling with triangles: Parquet and G W γ methods unified*, Phys. Rev. Res. **3**, 013149 (2021), doi:10.1103/PhysRevResearch.3.013149.

[29] T. Schäfer, S. Ciuchi, M. Wallerberger, P. Thunström, O. Gunnarsson, G. Sangiovanni, G. Rohringer and A. Toschi, *Nonperturbative landscape of the Mott-Hubbard transition: Multiple divergence lines around the critical endpoint*, Phys. Rev. B **94**, 235108 (2016), doi:10.1103/PhysRevB.94.235108.

[30] P. Thunström, O. Gunnarsson, S. Ciuchi and G. Rohringer, *Analytical investigation of singularities in two-particle irreducible vertex functions of the Hubbard atom*, Phys. Rev. B **98**, 235107 (2018), doi:10.1103/PhysRevB.98.235107.

[31] P. Chalupa, P. Gunacker, T. Schäfer, K. Held and A. Toschi, *Divergences of the irreducible vertex functions in correlated metallic systems: Insights from the Anderson impurity model*, Phys. Rev. B **97**, 245136 (2018), doi:10.1103/PhysRevB.97.245136.

[32] M. Pelz, S. Adler, M. Reitner and A. Toschi, *Highly nonperturbative nature of the Mott metal-insulator transition: Two-particle vertex divergences in the coexistence region*, Phys. Rev. B **108**, 155101 (2023), doi:10.1103/PhysRevB.108.155101.

[33] S. Adler, F. Krien, P. Chalupa-Gantner, G. Sangiovanni and A. Toschi, *Non-perturbative intertwining between spin and charge correlations: A "smoking gun" single-boson-exchange result*, (arXiv preprint) doi:10.48550/arXiv.2212.09693.

[34] N. Wentzell, G. Li, A. Tagliavini, C. Taranto, G. Rohringer, K. Held, A. Toschi and S. Andergassen, *High-frequency asymptotics of the vertex function: Diagrammatic parametrization and algorithmic implementation*, Phys. Rev. B **102**, 085106 (2020), doi:10.1103/PhysRevB.102.085106.

[35] F. Krien, A. Valli and M. Capone, *Single-boson exchange decomposition of the vertex function*, Phys. Rev. B **100**, 155149 (2019), doi:10.1103/PhysRevB.100.155149.

[36] M. Gievers, E. Walter, A. Ge, J. von Delft and F. B. Kugler, *Multiloop flow equations for single-boson exchange fRG*, Eur. Phys. J. B **95**, 108 (2022), doi:10.1140/epjb/s10051-022-00353-6.

[37] R. Goll, D. Tarasevych, J. Krieg and P. Kopietz, *Spin functional renormalization group for quantum Heisenberg ferromagnets: Magnetization and magnon damping in two dimensions*, Phys. Rev. B **100**, 174424 (2019), doi:10.1103/PhysRevB.100.174424.

[38] R. Goll, A. Rückriegel and P. Kopietz, *Zero-magnon sound in quantum Heisenberg ferromagnets*, Phys. Rev. B **102**, 224437 (2020), doi:10.1103/PhysRevB.102.224437.

[39] D. Tarasevych and P. Kopietz, *Dissipative spin dynamics in hot quantum paramagnets*, Phys. Rev. B **104**, 024423 (2021), doi:10.1103/PhysRevB.104.024423.

[40] D. Tarasevych, A. Rückriegel, S. Keupert, V. Mitsiioannou and P. Kopietz, *Spin functional renormalization group for the $J_1J_2J_3$ quantum Heisenberg model*, Phys. Rev. B **106**, 174412 (2022), doi:10.1103/PhysRevB.106.174412.

[41] V. G. Vaks and S. A. Pikin, *Thermodynamics of an ideal ferromagnetic substance*, Sov. J. Exp. Theor. Phys. **26**, 188 (1968).

[42] V. G. Vaks, A. I. Larkin and S. A. Pikin, *Spin waves and correlation functions in a ferromagnetic*, Sov. J. Exp. Theor. Phys. **26**, 647 (1968).

[43] A. Ge, J. Halbinger, S.-S. B. Lee, J. von Delft and F. B. Kugler, *In preparation*.

Dipolar ordering transitions in many-body quantum optics: Analytical diagrammatic approach to equilibrium quantum spins

Benedikt Schneider,[1,2] Ruben Burkard,[3] Beatriz Olmos,[3] Igor Lesanovsky,[4,5] and Björn Sbierski[3]

[1]*Department of Physics and Arnold Sommerfeld Center for Theoretical Physics, Ludwig-Maximilians-Universität München, Theresienstr. 37, 80333 Munich, Germany*

[2]*Munich Center for Quantum Science and Technology (MCQST), 80799 Munich, Germany*

[3]*Institut für Theoretische Physik, Universität Tübingen, Auf der Morgenstelle 14, 72076 Tübingen, Germany*

[4]*Institut für Theoretische Physik and Center for Integrated Quantum Science and Technology, Universität Tübingen, Auf der Morgenstelle 14, 72076 Tübingen, Germany*

[5]*School of Physics and Astronomy and Centre for the Mathematics and Theoretical Physics of Quantum Non-Equilibrium Systems, The University of Nottingham, Nottingham NG7 2RD, United Kingdom*

(Received 16 August 2024; revised 20 October 2024; accepted 12 November 2024; published 2 December 2024)

Quantum spin models with a large number of interaction partners per spin are frequently used to describe modern many-body quantum optical systems such as arrays of Rydberg atoms, atom-cavity systems, or trapped ion crystals. For theoretical analysis the mean-field (MF) ansatz is routinely applied. However, besides special cases of all-to-all or strong long-range interactions, the MF ansatz provides only approximate results. Here we present a systematic correction to MF theory based on diagrammatic perturbation theory for quantum spin correlators in thermal equilibrium. Our analytic results are universally applicable for any lattice geometry and spin-length S. We provide precomputed and easy-to-use building blocks for Ising, Heisenberg and transverse field Ising models in the symmetry-unbroken regime. We showcase the quality and simplicity of the method by computing magnetic phase boundaries and excitations gaps. We also treat the Dicke-Ising model of ground-state superradiance where we show that corrections to the MF phase boundary vanish.

DOI: 10.1103/PhysRevA.110.063301

I. INTRODUCTION

The past decade has witnessed tremendous progress at the intersection points of cold atomic physics, quantum optics and many-body physics. Atoms and ions can be confined in spatially structured arrangements [1–4] and brought into interaction using tailored potentials or cavity-mediated forces [5–7]. This has opened a new window for the exploration of equilibrium and nonequilibrium phenomena, including phase transitions in arrays of trapped Rydberg atoms [8] and Wigner crystals of trapped ions [9,10], super- and subradiance in dense atomic gases [11,12], or exotic time-crystal phases in atom-cavity systems [13,14].

One commonality of these quantum optical platforms is that their essential physics is often captured by many-body models whose microscopic degrees of freedom are quantum spins. However, the structure of the underlying spin-spin couplings is strikingly different to the short-range interactions encountered in solid-state-based quantum magnetism [15]. This is due to the spatially extended nature of the mode functions of photons (phonons) that mediate the interactions between atoms (ions) and thereby give rise to tunable long-range and even all-to-all spin-spin couplings [16–20], see Fig. 1.

In this theoretical work we are concerned with the treatment of such highly connected spin Hamiltonians, motivated but not limited to the above-discussed quantum optical many-body models. Concretely, we will consider general lattice spin-S Hamiltonians with bilinear couplings, that is,

$$H = -h\sum_i S_i^z + \sum_{i<i'} \sum_{\gamma,\gamma'\in\{+,-,z\}} J_{ii'}^{\gamma\gamma'} S_i^{\gamma} S_{i'}^{\gamma'}, \qquad (1)$$

where S_i^{γ} represents, for the ith spin, its component along the z direction and the spin ladder operators for $\gamma = z$ and $\gamma = +, -$, respectively. Moreover, $J_{ii'}^{\gamma\gamma'}$ are the coupling constants between spins at lattice sites i and i', which may be anisotropic in the spin components and which, in cold atomic experiments, can be controlled by geometry and choice of electronic states. Finally, the homogeneous field h may be generated and controlled, for example, by laser-induced level shifts.

Our goal is to investigate the properties of the equilibrium state of these models. We assume this state to be thermal and characterized by a finite temperature $T \geqslant 0$, see, e.g., Ref. [21] for the demonstration of such a thermometry approach to recent experimental correlation data from a Rydberg-array experiment [22]. This is certainly an approximation for quantum optical spin systems, which are well isolated from the environment (in the sense that they are not embedded in a solid-state matrix). Nevertheless, when preparing ground states and also excited states there is a residual entropy, manifesting in fluctuations, albeit not necessarily thermal.

One recurrent quest in this field is to obtain phase diagrams, which can be probed in experiment, e.g., in Rydberg

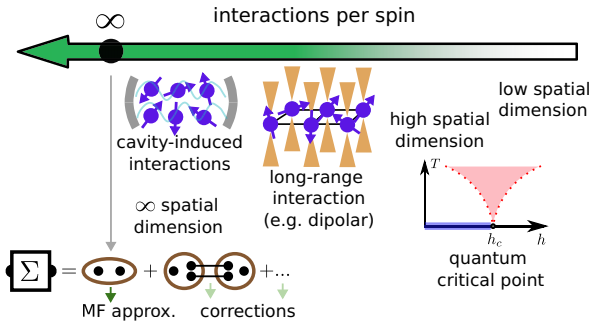

FIG. 1. The validity of the MF approximation in spin systems depends on the number of interactions per spin (green arrow) and is only exact in the limit of infinite connectivity. Corrections to MF can be moderate in systems if the connectivity of spins is large, a common situation in many-body quantum optics, but also in high spatial dimensions or at quantum critical points. In this regime the diagrammatic method proposed in this work provides accurate results at negligible computational cost.

tweezer arrays [22]. More recently, also dynamic quantities such as excitation spectra have come into reach [23]. Theoretically, these and other observables can be obtained from two-point spin correlators, see Eq. (7) below. For example, (second-order) phase transitions are signaled by a divergence of the static correlator [24].

On the computational side, however, a large number of interaction partners per spin often causes considerable difficulties: The plain high-temperature expansion of static correlators [25] becomes ineffective (see, however, Ref. [26]), and approaches relying on finite simulation volumes, e.g., density matrix renormalization group (DMRG) and quantum Monte Carlo (QMC), often suffer from finite-size effects. Furthermore, these methods may be negatively affected by high dimensionality ($d > 1$) or the sign problem [24].

As a complementary and simple method, mean-field (MF) theory is routinely applied. It amounts to approximating the full Hamiltonian (1) by a noninteracting trial Hamiltonian with variational parameters chosen to optimize the free energy [27] (see also Ref. [28] for an insightful discussion). This procedure is often cut short by applying the mnemonically intuitive replacement

$$S_i^\gamma S_{i'}^{\gamma'} \to S_i^\gamma \langle S_{i'}^{\gamma'} \rangle + \langle S_i^\gamma \rangle S_{i'}^{\gamma'} - \langle S_i^\gamma \rangle \langle S_{i'}^{\gamma'} \rangle \tag{2}$$

to the interaction term in Hamiltonian (1), followed by a self-consistent determination of $\langle S_i^\gamma \rangle$.

In the limit of infinite connectivity, the MF approximation is quantitatively exact [29–31]. Examples are all-to-all interactions (e.g., cavity mediated in the limit of an infinite number of spins [32,33]) or the limit of infinite dimension. However, more realistic Hamiltonians feature a large but finite connectivity, so that the MF approximation is expected to be qualitatively correct [34]. This regime, which, as argued above, is naturally realized in many quantum optical spin systems is the main focus of this work. We show that the spin-spin correlator and the derived observables such as phase boundaries or excitation gaps, can be well approximated by a simple and computationally inexpensive spin-diagrammatic approach. This rests on an expansion in powers of a suitably defined small parameter, which varies from one problem to another. Importantly, we show that our approach also works at $T = 0$ where at quantum critical points the (effective) dimensionality is increased [35].

We build on foundations of the diagrammatic technique for general quantum spin-S systems, which were laid starting from the late 1960s [36–41]. In Sec. II, we review the basic idea of the method and introduce an efficient way to evaluate the diagrams to unprecedented order. For concreteness and simplicity, we specialize to specific types of spin-spin interactions in Eq. (1). In Sec. III we provide explicit expressions for the two-point functions of $h = 0$ Heisenberg models and the Ising and transverse-field Ising model (TFIM), the latter at $T = 0$. Throughout we stay in the symmetry unbroken regime for simplicity. In Sec. IV we benchmark our method on the hypercubic lattice with nearest-neighbor interactions. Finally, in Sec. V, we apply our method to two particular quantum optical many-body systems with $S = 1/2$, both on the square lattice: A power-law interacting ferromagnetic (FM) Heisenberg model at $T > 0$ [42] and the Dicke-Ising model at $T = 0$ [43,44]. We conclude in Sec. VI.

II. DIAGRAMMATIC TECHNIQUE FOR QUANTUM SPINS VIA KERNEL FUNCTIONS

A. Models and perturbative expansion

We consider SU(2) quantum spin-S operators $\mathbf{S}_j = (S_j^x, S_j^y, S_j^z)^{\mathrm{T}}$ on a lattice with N sites labeled by index j. The operators obey the spin algebra

$$\left[S_{j_1}^{\alpha_1}, S_{j_2}^{\alpha_2}\right] = i\delta_{j_1 j_2} \epsilon^{\alpha_1 \alpha_2 \alpha_3} S_{j_1}^{\alpha_3} \tag{3}$$

with $\alpha_{1,2,3} \in \{x, y, z\}$ and the spin-length operator constraint $\mathbf{S}_j \cdot \mathbf{S}_j = S(S+1)$. The general bilinear spin Hamiltonian with homogeneous magnetic field h in z direction is given in Eq. (1) where $S^\pm = (S^x \pm iS^y)/\sqrt{2}$ are the spin ladder operators. In the following, it is understood that $\alpha \in \{x, y, z\}$ while $\gamma \in \{+, -, z\}$.

In the following, we specialize Eq. (1) to three important model classes defined by particular combinations of h and the 3×3 matrix $J_{ii'}^{\gamma\gamma'}$ in flavor space. This specialization is not required by methodological restrictions but was chosen to keep the notation and diagrammatic complexity at a level suitable for presentation. Finally, in Sec. V B we consider a model with a more complicated structure.

The three simple choices correspond to the following standard spin models: (i) The Ising model (which is classical and treated mainly for reference)

$$H = \sum_{i<i'} J_{ii'} S_i^z S_{i'}^z \tag{4}$$

is obtained from Eq. (1) by setting $h = 0$ and $J_{ii'}^{\gamma\gamma'} = \delta_{\gamma,z}\delta_{\gamma' z} J_{ii'}$. (ii) The transverse field Ising model (TFIM)

$$H = \sum_{i<i'} J_{ii'} S_i^x S_{i'}^x - h \sum_i S_i^z \tag{5}$$

corresponds to $J_{ii'}^{\gamma\gamma'} = \frac{1}{2}(1 - \delta_{\gamma,z})(1 - \delta_{\gamma',z}) J_{ii'}$. Note that Ising models are usually defined only for $S = 1/2$. (iii) The

Heisenberg model

$$H = \sum_{i<i'} J_{ii'} \mathbf{S}_i \cdot \mathbf{S}_{i'} \tag{6}$$

results from $h = 0$ and $J_{ii'}^{\gamma\gamma'} = \delta_{\bar{\gamma},\gamma'} J_{ii'}$ where we define $\bar{\gamma}$ by $\bar{+} = -$, $\bar{-} = +$, and $\bar{z} = z$. We keep S general and assume vanishing on-site coupling $J_{ii} = 0$ for simplicity.

In the remainder of this work, our computational focus will be on the Matsubara spin-spin correlation function,

$$G_{jj'}^{\alpha\alpha}(i\nu_m) = T \int_0^\beta \mathrm{d}\tau \mathrm{d}\tau' \, e^{i\nu_m(\tau-\tau')} G_{jj'}^{\alpha\alpha}(\tau, \tau'), \tag{7}$$

where τ is (imaginary) time, $\beta = 1/T$ is the inverse temperature, $\nu_m = 2\pi T m$ with $m \in \mathbb{Z}$ a (bosonic) Matsubara frequency, and

$$G_{jj'}^{\alpha\alpha}(\tau, \tau') = \left\langle \mathcal{T} S_j^\alpha(\tau) S_{j'}^\alpha(\tau') \right\rangle = G_{jj'}^{\alpha\alpha}(\tau - \tau') \tag{8}$$

the time-ordered ($\mathcal{T}$) thermal correlation function [41], which only depends on the time difference. Time ordering for spin operators is defined via

$$\mathcal{T} S_j^\alpha(\tau) S_{j'}^{\alpha'}(\tau') = \begin{cases} S_j^\alpha(\tau) S_{j'}^{\alpha'}(\tau') & : \tau > \tau', \\ S_{j'}^{\alpha'}(\tau') S_j^\alpha(\tau) & : \tau' > \tau, \end{cases} \tag{9}$$

and operators in imaginary-time Heisenberg picture are written as $S_j^\alpha(\tau) = e^{H\tau} S_j^\alpha e^{-H\tau}$. Thermal averages are defined as $\langle \ldots \rangle = \mathcal{Z}^{-1} \mathrm{Tr}[e^{-\beta H} \ldots]$ where $\mathcal{Z} = \mathrm{Tr} e^{-\beta H}$ is the partition function.

While dynamic observables are encoded in the analytically continued version of Eq. (7), $G_{jj'}^{\alpha\alpha}(i\nu_m \to \nu \pm i\eta)$, we will be mainly concerned with the detection of magnetic phase transitions of second-order (continuous) nature. Such a transition towards an ordered phase (with $\langle S_i^\alpha \rangle \neq 0$, say) can be conveniently detected coming from the paramagnetic side without spontaneous symmetry breaking, see the black arrow in Fig. 2(a). According to isothermal linear response theory, it is signaled by a divergent spatial Fourier transform (at ordering wave vector $\mathbf{Q}$) of the static Matsubara spin-spin correlator [Eq. (7) with $\nu_m = 0$] also known as spin susceptibility [24]. Note that around first-order (discontinuous) transitions, where the order parameter jumps, the susceptibility is not defined. The analysis or detection of first-order transitions is beyond the scope of this work.

Given these considerations, in the following we will focus on this symmetry-unbroken phase and consider the Matsubara correlator (7) for α for which $\langle S_i^\alpha \rangle = 0$. Among other simplifications on the diagrammatic side to be discussed below, this choice ensures the equality of connected and disconnected two-point correlators.

Next, we review the diagrammatic series expansion of $G_{jj'}^{\alpha\alpha}(i\nu_m)$ in exchange interaction J, originally developed for the case of quantum spins in Refs. [36–40] and summarized in Ref. [41]. Earlier work on the (classical) Ising model can be found in Refs. [29,45,46]. As usual in perturbation theory [27], we start by splitting the Hamiltonian in interacting and noninteracting parts. For the general spin Hamiltonian (1), we thus set $H = H_{0,h} - V$ where

$$H_{0,h} = -h \sum_i S_i^z, \quad V = -\sum_{i<i'} \sum_{\gamma,\gamma' \in \{+,-,z\}} J_{ii'}^{\gamma\gamma'} S_i^\gamma S_{i'}^{\gamma'}. \tag{10}$$

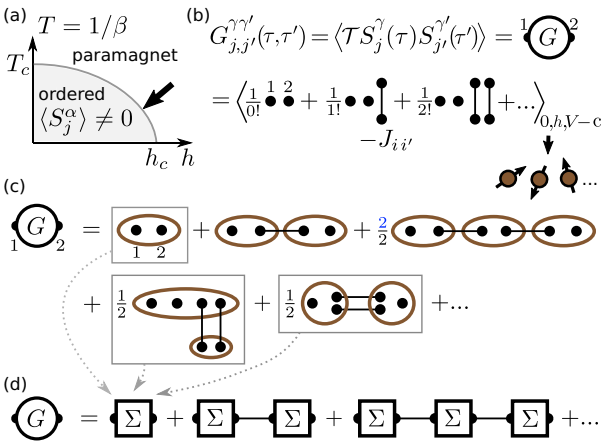

FIG. 2. (a) Schematic of a typical phase diagram for Hamiltonian (1). In this work we approach the magnetic ordering transition from the paramagnetic phase. (b) Diagrammatic representation of the expansion for the spin-spin correlator G in the exchange interaction $-J$ (lines), the orders $n = 0, 1, 2$ are shown explicitly. (c) Diagrammatic representation of the V-connected correlators in (b) in terms of ordinary connected free-spin correlators (brown ellipses). The 1-J-irreducible diagrams of order J^0 and J^2 are marked with boxes, the infinite sum of all these diagrams constitutes Σ, the 1-J-irreducible part of G. (d) The Larkin equation re-combines Σ and J to form G.

The formal series expansion in $V \sim J$ reads [27]

$$G_{jj'}^{\gamma\gamma'}(\tau, \tau') = \sum_{n=0}^{\infty} \frac{1}{n!} \int_0^\beta \mathrm{d}\tau_1 \ldots \mathrm{d}\tau_n \times \left\langle \mathcal{T} V(\tau_1) \ldots V(\tau_n) S_j^\gamma(\tau) S_{j'}^{\gamma'}(\tau') \right\rangle_{0,h,V-c}. \tag{11}$$

Here, the averages and time evolution of operators are governed only by $H_{0,h}$ (we avoid a new symbol since no confusion is possible from here on). For the correlator G, we changed to flavor indices $\gamma, \gamma' \in \{+, -, z\}$ adapted to the U(1) symmetry of $H_{0,h}$. This will prove convenient below. The subscript $V - c$ for the averages on the right-hand side of Eq. (11) excludes vacuum contributions [47] where in a diagrammatic interpretation one or more $V(\tau)$ are not connected to the external indices after performing the average. We refer to Appendix A for a rigorous definition. Note that a formula analogous to Eq. (11) applies for any time-ordered product of Heisenberg-picture operators and in particular also for the local magnetization $\langle \mathcal{T} S_j^\alpha(\tau) \rangle = \langle S_j^\alpha \rangle$. However, as mentioned above, in this work we will focus only on two-point functions.

Finally we perform the τ, τ' integral over Eq. (11) to obtain the Matsubara correlator (7) and also specialize to a fixed expansion order n indicated by a superscript,

$$G_{jj'}^{\gamma\gamma'(n)}(i\nu_m) = T \frac{1}{n!} \int_0^\beta e^{i\nu_m(\tau-\tau')} \mathrm{d}\tau_1 \ldots \mathrm{d}\tau_n \mathrm{d}\tau \mathrm{d}\tau' \times \left\langle \mathcal{T} V(\tau_1) \ldots V(\tau_n) S_j^\gamma(\tau) S_{j'}^{\gamma'}(\tau') \right\rangle_{0,h,V-c}. \tag{12}$$

B. Diagrams, J reducibility, and MF approximation

We proceed with the evaluation of Eq. (12) by a diagrammatic approach [41]. This is conceptually simple, physically

transparent and allows for various subsequent approximation and resummation schemes, one of which will be essential later. In the following, we review the diagrammatic method, the concept of J reducibility and its relation to the MF approximation (2). In the next section, we will propose an evaluation scheme of the diagrams that provides analytical expressions at high orders J^n.

The diagrammatic formulation starts from the graphical representation of Eq. (11) in Fig. 2(b). The dots represent spin operators and for now we do not perform the Fourier transform to Matsubara frequency. The two external spin operators carry multi-indices $1 = (\gamma, j, \tau)$ and $2 = (\gamma', j', \tau')$. All other (internal) spin operators coming from V appear pairwise connected by interaction lines representing $-J_{i_k i'_k}$, $k = 1, 2, \ldots, n$. Flavors, times, and sites of the internal spin operators are summed (or integrated) over and the leading factor $1/n!$ is written explicitly. Interaction lines connect spin operators at the same time (unless retarded, cf. Sec. V B).

Next, the V-connected free spin average in Eq. (11) is taken by colocalizing the $2 + 2n$ spin operators (dots) in any possible way involving blocks of $m = 2, 3, 4, \ldots$ spins shown as brown ellipses, see Fig. 2(c) [41]. These blocks represent connected equal-site time-ordered free spin correlators,

$$\left\langle \mathcal{T} S_i^{\gamma_1}(\tau_1) \ldots S_i^{\gamma_m}(\tau_m) \right\rangle_{0,c,h} = G_{0,c,h}^{\gamma_1 \ldots \gamma_m}(\tau_1, \ldots, \tau_m), \tag{13}$$

which, for the particular noninteracting Hamiltonian $H_{0,h}$ that we consider in Eq. (10), do not depend on the site index i. Connected spin correlators (with subscript c) are defined in analogy to their V-connected counterparts, see Appendix A. Due to our choice of $J_{ii} = 0$, interaction lines cannot start and end at the same block. In Fig. 2(c), the absence of blocks of size $m = 1$ representing single-spin averages (magnetization) is due to our current focus on the three models in question and on $G^{\alpha\alpha}$ for which $\langle S_i^\alpha \rangle = 0$ in the symmetry-unbroken regime. The presence of blocks of order $m > 2$ signals the absence of Wick's theorem [27] for spin operators, ultimately rooted in the operator-valued right-hand side of the commutation relation (3), which differs from the canonical case of bosonic creation and annihilation operators.

The connected time-ordered free spin correlators of Eq. (13), which are central diagrammatic building blocks will be discussed below in generality. For now, we mention the important special case that arises if all m flavor indices are chosen as z such that all involved operators $S_i^z(\tau_n) = S_i^z$ commute. These connected z-spin correlators are then time independent and given via the order-$(m-1)$ derivative of the Brillouin function $b_c(y)$, which describes the magnetization of a free spin $\langle S^z \rangle$ dependent on $y = \beta h$ [41],

$$G_{0,c,h}^{z\ldots z}(\tau_1, \ldots, \tau_m) = b_c^{(m-1)}(\beta h), \tag{14}$$

$$b_c(y) = \left(S + \frac{1}{2}\right) \coth\left[\left(S + \frac{1}{2}\right) y\right] - \frac{1}{2} \coth \frac{y}{2}. \tag{15}$$

For $h \to 0$ we abbreviate $b_c^{(m-1)}(0) \equiv b_{c,m-1}$, e.g., $b_{c,1} = S(S+1)/3$ is the free spin (static) Curie susceptibility that will become important in the following discussion.

Having explained the building blocks of the diagrams in Fig. 2(c), we now turn their topology, i.e., the particular choice of blocks and their connection. Topological multiplicity factors Λ (denoted in blue) appear if the same diagram topology

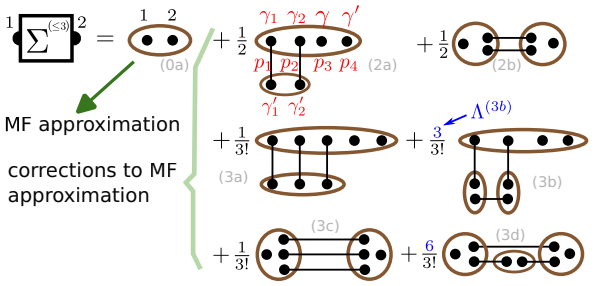

FIG. 3. Diagrams for Σ up to order J^3 for the situation described in the text where magnetization is not relevant. The blue multiplicity factors $\Lambda^{(nx)}$ denote the number of ways to arrive at a given diagram starting from the expansion in Fig. 2(b), e.g., in diagram (3b) there are three choices to pick the bottom line from the three lines available at third-order perturbation theory. The two vertical lines are equivalent and do not enhance the multiplicity as an exchange can be compensated by a permutation of sites within the top ellipse.

can be arrived at by distributing the dots in Fig. 2(b) to the given set of blocks in multiple ways, see, e.g., the last diagram in the first line of Fig. 2(c). Diagrams that only differ by a rearrangement of dots within blocks are not topologically different. Formally, the multiplicity factor can be computed via the number of elements in the automorphism group $\mathcal{A}_x$ of a diagram x of order J^n : $\Lambda = n!/\mathrm{ord}(\mathcal{A}_x)$.

The diagrams in Fig. 2(c) can be classified as either 1-J reducible or 1-J irreducible (1JI). In 1-J reducible diagrams it is possible to separate the external spin operators (single dots) by cutting a single interaction line. If this is not possible, the diagram is 1JI. The infinite sum of all 1JI diagrams is denoted by Σ. For examples, the contributions to Σ of order J^0 and J^2 are indicated with boxes in Fig. 2(c).

All diagrammatic contributions to the spin correlator G that are 1-J reducible can be represented by 1JI diagrams connected by one or more interaction lines, see Fig. 2(d). This diagrammatic expression can be summed exactly and yields the Larkin equation [36,41]. In frequency space, it reads

$$G(i\nu_m) = [1 + \Sigma(i\nu_m) \cdot J]^{-1} \cdot \Sigma(i\nu_m). \tag{16}$$

Here all objects are considered $N \times N$ matrices with two site indices, cf. Eq. (7) and for our purposes the flavors will all be set to a fixed α with $\alpha \in \{x, y, z\}$ for simplicity. Note the similarity of Eq. (16) to Dyson's equation for canonical bosonic or fermionic systems [27], which, however, rests on the concept of cutting free propagator lines (and not interaction lines).

Given the above diagrammatic rules, it is straightforward to write down the 1JI diagrams for Σ at order n indicated by $\Sigma^{(n)}$. The diagrams for $n \leqslant 3$, which include the boxed diagrams of Fig. 2(b) are shown in Fig. 3. We label the different diagram topologies at order n with an additional index $x = a, b, c, \ldots$. Each diagram topology is uniquely identified by (nx). The diagrams for $\Sigma^{(4)}$ have not been systematically collected so far in literature and are given in Fig. 7 of Appendix D. Note that diagrams that combine the two external operators together with one internal operator in a $m = 3$ block are 1JI by our definition. However, for the particular setup and observables that we focus on in this work (see above), these diagrams vanish.

We conclude this section by linking the diagrammatic expansion to the MF approximation for $G^{\alpha\alpha}$. Quite simply, the latter is obtained by using only the lowest-order approximation for Σ (green arrow in Fig. 3)

$$\Sigma^{\alpha\alpha} \to \Sigma^{\alpha\alpha(0)} = G^{\alpha\alpha}_{0,c,h}. \tag{17}$$

For $\alpha = z$, this evaluates to $b_c^{(1)}(\beta h)$, see Eq. (14). We also assumed $\langle S_i^\alpha \rangle = 0$, otherwise h in Eq. (17) would need to be replaced by the Weiss field, see Ref. [41] and Sec. V B. The easiest way to see the correspondence between Eq. (17) and the MF approximation is to recall that the latter is exact for $N \to \infty$ if each spin interacts with all other spins in the system, which requires us to redefine $J \to J/N$. For G and in the limit $N \to \infty$, this means that stringlike diagrams as in the first line of Fig. 2(c) are the only finite contribution. This follows since the site indices of the internal ($m = 2$) blocks can be summed freely over all available sites only in stringlike diagrams while being more restricted in diagrams that contain loops. Finally, the stringlike diagrams are exactly the diagrams that are produced by the replacement $\Sigma \to \Sigma^{(0)}$ in the Larkin equation of Fig. 2(d). It follows that contributions $\Sigma^{(n)}$ with $n > 0$ represent corrections to the MF results, see Figs. 1 and 3.

C. Diagram evaluation via kernel functions

The remaining task is to calculate the analytical expressions encoded in the particular diagrams $\Sigma_{jj'}^{\gamma\gamma'(nx)}(i\nu_m)$, which represent the different contributions of the right-hand side of Eq. (12). Two observations on the simple nature of the chosen models (Ising, TFIM and Heisenberg, cf. Sec. II A) are helpful but by no means crucial for progress: (i) The values for the blocks [brown ellipses, see Eq. (13)] are site independent and (ii) the coupling between any two blocks is characterized by a single number $J_{ii'}$ (unlike for, say, XXZ interactions). Hence we can combine all $J_{ii'}$ [stemming from the insertions of V, cf. Eq. (10)] along with the site sums in a geometry factor $t_{jj'}^{(nx)}[J] \sim J^n$,

$$\Sigma_{jj'}^{\gamma\gamma'(nx)}(i\nu_m) \equiv t_{jj'}^{(nx)}[J] \cdot \sigma^{\gamma\gamma'(nx)}(i\nu_m). \tag{18}$$

This geometry factor captures the dependence of the particular diagram (nx) on j, j' and the underlying $N \times N$ coupling matrix $J_{ii'}$. For example, with regard to Fig. 3, the geometry factor for diagram $(0a)$ is simply $\delta_{jj'}$ whereas for $(2a)$ and $(2b)$ we read off

$$t_{jj'}^{(2a)} = \delta_{jj'} \sum_i J_{ji} J_{ij}, \quad t_{jj'}^{(2b)} = (J_{jj'})^2. \tag{19}$$

The geometry factors for all diagrams of order $n = 0, 2, 3$ are shown in the second column in Table I. In the third column, we provide the momentum space representation for translation invariant lattices with spatial Fourier transform defined by

$$J_{\mathbf{k}} = \sum_{\mathbf{r}_j} e^{-i\mathbf{k}\cdot\mathbf{r}_j} J_{0,\mathbf{r}_j}, \tag{20}$$

and analogous for $G_{\mathbf{k}}$ and $\Sigma_{\mathbf{k}}$. In the fourth column we specialize to the infinite ($N \to \infty$) nearest-neighbor hypercubic lattice model in d spatial dimensions, see the caption of Table I for more details. Geometry factors for the fourth-order diagrams $\Sigma^{(4)}$ are summarized in Table VI of Appendix D.

TABLE I. Geometry factors $t^{(nx)}[J]$ for Σ diagrams of order $n = 0, 2, 3$ and all topologies (for the case $n = 4$ see Table VI). Results in the second column are given in real space [where $J_{jj'}^2$ is understood as $(J_{jj'})^2$ etc.]. The third column shows the same results in momentum space (where we abbreviate $\int_{\mathbf{q}} = 1/N \sum_{\mathbf{q}}$). In the fourth column, momentum space results are specialized for an infinite d-dimensional hypercubic lattice with a lattice constant of unity and nearest-neighbor coupling J_1 where $\tilde{J}_{\mathbf{k}} \equiv 2J_1 \sum_{\mu=1}^d \cos k_\mu$ and accordingly $\tilde{J}_{\mathbf{0}} = 2dJ_1$.

top.	r space $t_{jj'}^{(nx)}$	k space $t_{\mathbf{k}}^{(nx)}$	nn-hyp. $\tilde{t}_{\mathbf{k}}^{(nx)}$
(0a)	$\delta_{jj'}$	1	1
(2a)	$\delta_{jj'}[J \cdot J]_{jj'}$	$\int_{\mathbf{q}} J_{\mathbf{q}}^2$	$J_1 \tilde{J}_{\mathbf{0}}$
(2b)	$J_{jj'}^2$	$\int_{\mathbf{q}} J_{\mathbf{q}-\mathbf{k}} J_{\mathbf{q}}$	$J_1 \tilde{J}_{\mathbf{k}}$
(3a)	$\delta_{jj'} \sum_i J_{ji}^3$	$\int_{\mathbf{p},\mathbf{q}} J_{\mathbf{p}} J_{\mathbf{q}} J_{\mathbf{p}+\mathbf{q}}$	$J_1^2 \tilde{J}_{\mathbf{0}}$
(3b)	$\delta_{jj'}[J \cdot J \cdot J]_{jj}$	$\int_{\mathbf{q}} J_{\mathbf{q}}^3$	0
(3c)	$J_{jj'}^3$	$\int_{\mathbf{q},\mathbf{p}} J_{\mathbf{p}-\mathbf{k}} J_{\mathbf{q}} J_{\mathbf{p}+\mathbf{q}}$	$J_1^2 \tilde{J}_{\mathbf{k}}$
(3d)	$J_{jj'}[J \cdot J]_{jj'}$	$\int_{\mathbf{q}} J_{\mathbf{k}-\mathbf{q}} J_{\mathbf{q}}^2$	0

Beyond the frequency independent geometry factor, the remaining contribution in Eq. (18) denoted as $\sigma^{(nx)}(i\nu_m)$ only depends on the type of spin model (here: Ising, TFIM, Heisenberg). We define it to include the topological multiplicity factor $\Lambda^{(nx)}$ of the diagram (nx). In principle, obtaining $\sigma^{(nx)}$ is straightforward in frequency space [41] where interaction lines proportional to $\delta_{\nu_l+\nu_{l'}}$ connect the blocks, which are temporal Fourier transforms of Eq. (13), $G_{0,c,h}^{\gamma_1\cdots\gamma_m}(\omega_1, \ldots, \omega_{m-1})$. The latter, however, are difficult to calculate in general beyond the case $\gamma_1 = \ldots = \gamma_m = z$ [see Eq. (14)], especially for $h = 0$ where a distinction of cases regarding various frequency combinations is required. Despite recent algorithmic advances [48,49] the general $G_{0,c}^{\gamma_1\cdots\gamma_m}(\omega_1, \ldots, \omega_{m-1})$ (which beyond their appearance in perturbation theory lack physical significance for large m) are currently known analytically up to order $m = 4$ [41]. This would only suffice to compute Σ to order J^2. On the other hand, without the temporal Fourier transform and for a fixed order of times, the blocks representing $\langle \mathcal{T} S^{\gamma_1}(\tau_1) \ldots S^{\gamma_m}(\tau_m) \rangle_{0,c,h}$ [cf. Eq. (13)] simplify to standard connected free-spin equal-time averages $\langle S^{\tilde{\gamma}_1} \ldots S^{\tilde{\gamma}_m} \rangle_{0,c,h}$, which can be efficiently computed for general S, see Sec. 6.2 in Ref. [49].

To make progress, the crucial reformulation detailed in Appendix B expresses $\sigma^{(nx)}$ such that only the simple $\langle S^{\tilde{\gamma}_1} \ldots S^{\tilde{\gamma}_m} \rangle_{0,c,h}$ are required. All the remaining complexity is encapsulated in the universal (model-independent) kernel functions $K_{n+2}(\Omega_1, \ldots, \Omega_{n+2})$ of Ref. [49]. The latter originally appeared in the context of Fourier transforms of time-ordered correlation functions. The key point is that an nth-order perturbative expression as in Eq. (12) can be understood as a Fourier transform of a time-ordered correlation function of order $n + 2$ with n frequencies set to zero.

The translation of diagram (nx) to an expression $\sigma^{(nx)}$ is straightforward. To avoid unnecessary complicated notation,

we just give two examples: For diagram $(2a)$, with the labeling of internal times and flavors in Fig. 3 (red), one obtains

$$\sigma^{\gamma\gamma'(2a)}(i\nu_m) = \Lambda^{(2a)}\frac{(-1)^n}{n!}\sum_{\gamma_{1,\ldots,n}^{(\prime)}}\sum_{p\in S_{n+2}} K_{n+2}(\mathcal{P}\{\Omega_1(p_1),\ldots,\Omega_{n+2}(p_{n+2})\}) \times\left\langle \mathcal{P}S^{\gamma_1}(p_1)S^{\gamma_2}(p_2)S^{\gamma}(p_3)S^{\gamma'}(p_4)\right\rangle_{0,c,h}\left\langle \mathcal{P}S^{\gamma_1'}(p_1)S^{\gamma_2'}(p_2)\right\rangle_{0,c,h}, \tag{21}$$

where $\Lambda^{(2a)} = 1$ and $n = 2$. As another example, diagram (3b) with $\Lambda^{(3b)} = 3$ and $n = 3$ is

$$\sigma^{\gamma\gamma'(3b)}(i\nu_m) = \Lambda^{(3b)}\frac{(-1)^n}{n!}\sum_{\gamma_{1,\ldots,n}^{(\prime)}}\sum_{p\in S_{n+2}} K_{n+2}(\mathcal{P}\{\Omega_1(p_1),\ldots,\Omega_{n+2}(p_{n+2})\}) \times\left\langle \mathcal{P}S^{\gamma_1}(p_1)S^{\gamma_2}(p_2)S^{\gamma}(p_4)S^{\gamma'}(p_5)\right\rangle_{0,c,h}\left\langle \mathcal{P}S^{\gamma_1'}(p_1)S^{\gamma_3}(p_3)\right\rangle_{0,c,h}\left\langle \mathcal{P}S^{\gamma_2'}(p_2)S^{\gamma_3'}(p_3)\right\rangle_{0,c,h}. \tag{22}$$

The internal flavor sums over $\gamma_{1,\ldots,n}^{(\prime)}$ depend on the model, e.g., for the Heisenberg case these sums are over $\{+,-,z\}$ while restricted to $\{z\}$ in the Ising case. The second sum is over the $(n+2)!$ permutations S_{n+2} that determine the ordering of both the argument list of K_{n+2} and the spin operators in the equal-time averages. This is accomplished by the index ordering operator $\mathcal{P}$. This operator applies to operator strings and argument lists alike. It acts like time-ordering, but for discrete indices $(1), (2), \ldots, (n+2)$ that, unlike imaginary time arguments, do not affect the operator, for example $\mathcal{P}S^+(1)S^-(3)S^z(2) = S^-S^zS^+$. Finally, the Ω list is given by

$$\{\Omega_1,\ldots,\Omega_n,\Omega_{n+1},\Omega_{n+2}\} = \{-(\gamma_1+\gamma_1')h,\ldots,-(\gamma_n+\gamma_n')h, i\nu_m-\gamma h, -i\nu_m-\gamma' h\}, \tag{23}$$

where the following replacement rule for flavor labels is understood: $\{z,+,-\}\to\{0,+1,-1\}$.

Closed-form expressions for general kernel functions $K_k(\Omega_1,\ldots,\Omega_k)$ can be found in Ref. [49]. The expressions grow in complexity with k, however, for the current application with the specific form of the Ω list in Eq. (23) and our focus on either $h = 0$ (Ising and Heisenberg models) or $T\to 0$ (for the TFIM), the kernel functions simplify considerably. The resulting expressions are given in Appendix C.

Expressions analogous to Eqs. (21) and (22) can be straightforwardly written for all diagram topologies and should be evaluated via computer algebra for efficiency. In the next section, we provide the expressions for $\sigma^{\gamma\gamma'(nx)}(i\nu_m)$ obtained in this way. Finally, the sum over all topologies yields $\Sigma^{(n)}$ at order J^n,

$$\Sigma_{jj'}^{\gamma\gamma'(n)}(i\nu_m) = \sum_{x=a,b,c,\ldots} t_{jj'}^{(nx)}[J]\sigma^{\gamma\gamma'(nx)}(i\nu_m). \tag{24}$$

III. ANALYTIC RESULTS FOR 1-*J* IRREDUCIBLE DIAGRAMS

In this section we report the analytic results of the diagram evaluation up to third order in J for the Ising model, TFIM at $T = 0$ and the Heisenberg model as defined in Eqs. (4), (5) and (6). Diagrams in fourth order and their analytic results are relegated to Appendix D.

We provide results for the second contribution to Eq. (18), the geometry independent $\sigma^{\gamma\gamma'(nx)}(i\nu_m)$. For the Ising model and TFIM case we consider σ^{zz} and σ^{xx}, respectively, see Table II. In both cases diagrams, which involve blocks of any odd order vanish and are not listed. For the Ising model this is due to spin flip symmetry $S_i^z\to -S_i^z\ \forall i$ in the paramagnetic phase, for the σ^{xx} in the TFIM this follows from the fact that the blocks solely involve S^+ and S^-, which need to appear in equal numbers for any finite contribution in light of U(1) spin rotation symmetry of $H_{0,h}$. For the Ising model only static contributions are finite due to its classical nature.

The results for $\Sigma_{jj'}^{\gamma\gamma'(n)}(i\nu_m)$ computed by summing over topologies [Eq. (24)] have been tested for small clusters of spins, e.g., for the dimer with $N = 2$ and $J_{12} = J_{21} = J_1$ and $J_{11} = J_{22} = 0$. In this case, for moderately large S, the Hilbert space is small and the exact two-point function G can be found using the spectral representation [27]. Hence the exact Σ is obtained via Eq. (16). This exact result is then expanded in J_1 and checked against $\Sigma_{jj'}^{\gamma\gamma'(n)}(i\nu_m)$ computed diagrammatically. As an example, for the TFIM dimer with $J_1 > 0$, $T = 0$ and $S = 1/2$, one confirms

$$\Sigma_{11}^{xx}(i\nu) = \frac{h}{2(h^2+\nu^2)} - J_1^2\frac{5h^2+\nu^2}{64h(h^2+\nu^2)^2} + J_1^4\frac{(43h^4+14h^2\nu^2+3\nu^4)}{4096h^3(h^2+\nu^2)^3} + O\big(J_1^6\big), \tag{25}$$

$$\Sigma_{12}^{xx}(i\nu) = J_1^3\frac{-1}{64h(h^2+\nu^2)^2} + O\big(J_1^5\big). \tag{26}$$

TABLE II. Ising model and TFIM at $T = 0$, both in the symmetric phase: Expansion of the lattice independent parts $\sigma^{(nx)}$ of the diagrams $\Sigma^{(nx)}$ for $n = 0, 2, 3$ [cf. Eq. (18)]. Only topologies with finite $\sigma^{(nx)}$ are shown. The derivatives of the Brillouin function (15) at zero field are denoted by $b_c^{(m)}(0)\equiv b_{c,m}$. Fourth-order results are given in Table VII.

	Ising $T^{1+n}\sigma^{zz(nx)}(i\nu_m = 0)$	TFIM $\sigma^{xx(nx)}(i\nu)\vert_{T=0}$
(0a)	$b_{c,1}$	$\frac{hS}{h^2+\nu^2}$
(2a)	$\frac{1}{2}b_{c,1}b_{c,3}$	$\frac{-S^2(5h^2+\nu^2)}{16h(h^2+\nu^2)^2}$
(3b)	$\frac{-1}{2}b_{c,1}^2b_{c,3}$	$\frac{S^3(4h^2+\nu^2)}{16h^2(h^2+\nu^2)^2}$
(3c)	$\frac{-1}{6}b_{c,3}^2$	$\frac{-S^2}{16(h^2+\nu^2)^2}$

TABLE III. Heisenberg model at $T > 0$ in the paramagnetic phase: Expansion of the lattice independent parts $\sigma^{(nx)}$ of the diagrams $\Sigma^{(nx)}$ for $n = 0, 2, 3$, cf. Eq. (18). Fourth-order results are given in Table VII. The Δ in the dynamic case stands for $1/(2\pi m)$.

$T^{1+n}\sigma^{zz(nx)}$	static ($\nu_m = 0$)	dyn. ($\nu_m \neq 0$)
(0a)	$b_{c,1}$	0
(2a)	$\frac{b_{c,1}^2}{-6}(1 + 6b_{c,1})$	$+2\Delta^2 b_{c,1}^2$
(2b)	$\frac{b_{c,1}^2}{-12}$	$-2\Delta^2 b_{c,1}^2$
(3a)	$\frac{b_{c,1}^2}{-24}(1 + 4b_{c,1})$	$+\frac{1}{2}\Delta^2 b_{c,1}^2$
(3b)	$\frac{b_{c,1}^3}{6}(1 + 6b_{c,1})$	$-2\Delta^2 b_{c,1}^3$
(3c)	$\frac{b_{c,1}^2}{-120}(48b_{c,1}^2 + 16b_{c,1} + 3)$	$-\frac{1}{2}\Delta^2 b_{c,1}^2$
(3d)	0	$+2\Delta^2 b_{c,1}^3$

As some diagrams like (3b) vanish for the dimer geometry it is important to also check the fully connected trimer with $N = 3$ in an analogous fashion.

Finally, we turn to the Heisenberg case at $T > 0$ where the $\sigma^{zz(nx)} = \sigma^{\alpha\alpha(nx)}$ are reported in Table III. We need to distinguish between the static case $\nu_m = 0$ and the dynamic case $\nu_m = 2\pi m T \neq 0$ for which we abbreviate $\Delta = \frac{1}{2\pi m}$. Again, these results have been tested for small spin clusters. Another nontrivial check for the resulting $\Sigma^{(n)}$ is the fulfillment of $\Sigma^{(n)}_{\mathbf{k}=0}(i\nu_m \neq 0) = 0$ required by the constant-of-motion property of $S^z_{\mathbf{k}=0}$ in a Heisenberg system.

IV. HYPERCUBIC LATTICE BENCHMARKS

We now proceed to test the applicability of the diagrammatic expansion for nearest-neighbor models on the hypercubic lattice in d spatial dimensions with AFM coupling $J_1 > 0$. The geometry factors and further details on the lattice can be found in Table I. For the Ising and Heisenberg case we focus on the magnetic ordering temperature T_c and for the TFIM at $T = 0$ we consider the critical field h_c and the excitation gap $\Delta(h)$. The latter serves as an example for a dynamical quantity, which needs to be evaluated via analytical continuation. We will use the inverse dimension $1/d$ as a small control parameter.

The magnetic phase boundary is signaled by the divergence of the static susceptibility, according to Eq. (16),

$$G^{-1}_{\mathbf{k}}(i\nu_m = 0) = 1/\Sigma_{\mathbf{k}}(i\nu_m = 0) + J_{\mathbf{k}} \stackrel{!}{=} 0, \tag{27}$$

with $\mathbf{k}$ replaced by the Néel wave vector $\mathbf{N} = (\pi, \pi, \ldots, \pi)$. Thus the critical coupling is given by the solution of $0 \stackrel{!}{=} 1/\Sigma_{\mathbf{N}} - 2dJ_1$. We specialize to the thermal transition in the Ising case (with $S = 1/2$) or Heisenberg case. First, as stated before, the MF approximation for T_c is found by replacing $\Sigma_{\mathbf{N}} \to \Sigma^{(0)}_{\mathbf{N}} = \beta b_{c,1}$ in the above equation, which yields the well-known MF result $T_c^{(0)} = 2d\, b_{c,1} J_1 \sim d$. We then divide Eq. (27) by T and proceed to obtain corrections to the MF result for T_c. Following pioneering work in Refs. [50,51] we seek a consistent expansion of

$$1/(T\Sigma_{\mathbf{N}}) = 2d\beta J_1 \tag{28}$$

in the parameter $1/d$ assumed to be small. In this case MF is approximately valid so that $X_1 \equiv \beta J_1$ close to criticality is of order $\sim 1/d$. With this in mind we provide the hypercubic geometry factors $\beta^n \tilde{t}^{(nx)}_{\mathbf{k}=\mathbf{N}}$ for all nonvanishing topologies in Table IV. Next to the diagram label we show the leading scaling with $1/d$ of the particular $\beta^n \tilde{t}^{(nx)}_{\mathbf{k}=\mathbf{N}}$ close to the thermal transition, which does depend both on order n and topology x. We can thus expand $1/(T\Sigma_{\mathbf{N}})$ up to order $(1/d)^m$, drop all higher orders and solve numerically for T_c. Since the $\Sigma^{(n)}$ are available up to $n = 4$, we can consider $m = 0, 1, 2$, cf. Table IV. Explicitly, we have

$$\frac{1}{T\Sigma_{\mathbf{N}}} = \frac{1}{T\sigma^{(0)}} - \frac{A_1}{(T\sigma^{(0)})^2} + \frac{A_2}{(T\sigma^{(0)})^3} + O(d^{-3}), \tag{29}$$

$$A_1 = 2dX_1^2 T^3(\sigma^{(2a)} - \sigma^{(2b)}), \tag{30}$$

$$\begin{aligned} A_2 = A_1^2 - T^4\sigma^{(0)}\big[&2dX_1^3(\sigma^{(3a)} - \sigma^{(3c)}) \\ &+ 4d^2X_1^4 T(\sigma^{(4b)} - 2\sigma^{(4e)} + \sigma^{(4f)} + \sigma^{(4h)} \\ &+ 3\sigma^{(4j)} + 3\sigma^{(4l)} - 3\sigma^{(4m)})\big], \end{aligned} \tag{31}$$

where $A_1 \sim 1/d$ and $A_2 \sim 1/d^2$.

We start with the Ising case, where T_c was already obtained in Ref. [50] up to order $1/d^3$. We report the results for $T_c/T_c^{(0)}$ and $d = 3, \ldots, 7$ in Table V. For large d, the quasiexact results from high-order series expansion or Monte Carlo simulations [52–54] are rapidly approached as the order m in $1/d$ is increased. We also compare our results at order $1/d^2$ to other diagrammatic approaches with different resummation strategies: Our results are similar to the spin functional RG approach (spin-fRG) by Krieg and Kopietz [50], only at $d = 3$ the latter has a slight advantage. The dynamical MF theory for spins [55] (spin-DMFT) is not competitive. This is not

TABLE IV. Nonvanishing geometry factors $\beta^n \tilde{t}^{(nx)}_{\mathbf{k}=\mathbf{N}}[J]$ ($n \leqslant 4$) for the nearest-neighbor d-dimensional hypercubic lattice with coupling J_1 as a function of $X_1 = \beta J_1$. The leading-order scaling in powers of $1/d$ close to the thermal ordering transition is provided next to the diagram label. Geometry factors for $n > 4$ (not shown) are of order d^{-3} or smaller.

(0a) $\sim d^0$	(2a) $\sim d^{-1}$	(2b) $\sim d^{-1}$	(3a) $\sim d^{-2}$	(3c) $\sim d^{-2}$
1	$+2dX_1^2$	$-2dX_1^2$	$+2dX_1^3$	$-2dX_1^3$
(4a) $\sim d^{-3}$	(4b) $\sim d^{-2}$	(4c) $\sim d^{-3}$	(4e) $\sim d^{-2}$	(4f) $\sim d^{-2}$
$+2dX_1^4$	$+4d^2X_1^4$	$-2dX_1^4$	$-8d^2X_1^4$	$+4d^2X_1^4$
(4h) $\sim d^{-2}$	(4j) $\sim d^{-2}$	(4l) $\sim d^{-2}$	(4m) $\sim d^{-2}$	
$+4d^2X_1^4$	$6d[2d-1]X_1^4$	$6d[2d-1]X_1^4$	$-6d[2d-1]X_1^4$	

TABLE V. Ising model: Critical temperature $T_c/T_c^{(0)}$ for the d-dimensional nearest-neighbor Ising model ($S = 1/2$) on the hypercubic lattice normalized to the MF transition temperature $T_c^{(0)} = dJ_1/2$. The quasiexact benchmark results in the second column [52–54] are compared to the results obtained from Eq. (29) evaluated up to order $1/d$ and $1/d^2$, respectively. For comparison, the last two columns report results from spin-fRG [50] and spin-DMFT [55].

d	exact	$O(1/d)$	$O(1/d^2)$	spin-fRG [50]	spin-DMFT [55]
3	0.752	0.789	0.740	0.744	0.659
4	0.835	0.854	0.839	0.839	0.807
5	0.878	0.887	0.880	0.880	0.865
6	0.903	0.908	0.904	0.904	
7	0.919	0.923	0.920	0.920	

surprising given DMFT's local approximation of Σ already fails in order J^3 where the nonlocal diagram (3c) appears.[1]

For the Heisenberg model, benchmark checks of T_c suffer from the scarcity of exact results for $d > 3$. The exception is the classical case ($S \to \infty$) for $d = 4$. Here $T_c/T_c^{(0)}$ improves from 0.8536 in order $1/d$ to 0.8315 in order $1/d^2$ with the exact result at 0.822 [56]. For the case $d = 3$ and $S < \infty$, Eq. (28) often yields nonreal solutions at the limited expansion orders available. An exception is the case $d = 3$, $S = 3/2$ for which $T_c/T_c^{(0)}$ improves from 0.769 in order $1/d$ to 0.657 in order $1/d^2$ somewhat closer to the exact result 0.702 [57].

For the TFIM at $T = 0$, the critical field at the ordering transition is given from Eq. (27) as

$$1/\left(d\,\Sigma_{\mathbf{N}}^{xx}\right) \stackrel{!}{=} 2J_1. \tag{32}$$

The MF approximation with $\Sigma_{\mathbf{N}}^{xx} \to S/h$ yields $h_c^{(0)} = 2dSJ_1 \sim d$. Using $\sigma^{xx(nx)}(i\nu = 0)|_{T=0} \sim 1/h^{1+n}$ we again expand the left-hand side for $h \gtrsim h_c$ in orders of $1/d$, which yields expressions similar to Eq. (29). We focus on the case $d = 3$, $S = 1/2$ and report the results for h_c in Fig. 4, see vertical lines. The quasiexact Monte Carlo result $h_c^{(MC)} = 2.57907(3)J_1$ [58] is rapidly approached.

To showcase the advantage of analytical expressions for the Matsubara correlator, we consider the excitation gap $\Delta(h)$ for $h \gtrsim h_c$ which we obtain from the dynamical xx-spin correlator, $G_{\mathbf{k}}^{xx}(i\nu \neq 0)$. The latter contains the dispersion $\omega_{\mathbf{k}}$ of spin waves transversal to the magnetization in the S^z direction determined from the position of the sharp peak in $\mathrm{Im}G_{\mathbf{k}}^{xx,R}(\nu)$. The weight of the peak is the one-particle structure factor. For $h \to h_c$ from above, we expect $\omega_{\mathbf{k}}$ to vanish at $\mathbf{k} = \mathbf{N}$ where the spin wave softens and order sets in. For $h > h_c$, the gap is thus defined as $\Delta(h) = \omega_{\mathbf{N}}$ and we consider

$$G_{\mathbf{N}}^{xx}(i\nu) = \frac{1/d}{\frac{1}{d\,\Sigma_{\mathbf{N}}^{xx}(i\nu)} - 2J_1}. \tag{33}$$

We use an expansion of the denominator similar to above, which we here evaluate to order $1/d$ (and analogously for MF and order $1/d^2$). We find

$$G_{\mathbf{N}}^{xx}(i\nu) \simeq \frac{hS}{h^2 + \frac{5}{8}dSJ_1^2 - 2dShJ_1 - (i\nu)^2\left(1 + \frac{dSJ_1^2}{8h^2}\right)} \tag{34}$$

and after analytic continuation the gap is obtained as

$$\Delta^{(1/d)}(h) = \sqrt{\left(h^2 - 2dShJ_1 + \frac{5}{8}dSJ_1^2\right)\Big/\left(1 + \frac{dSJ_1^2}{8h^2}\right)}. \tag{35}$$

Setting $d = 3$ and $S = 1/2$, this agrees very well with recent iPEPS tensor network simulations in Ref. [59], see Fig. 4 (blue dashed line and dots). For $h \gtrsim h_c$, the iPEPS is actually closer to $\Delta^{(1/d)}(h)$ than to $\Delta^{(1/d^2)}(h)$, we suspect this is an artifact of finite bond dimension of the tensor network.

[1]Note that the lower-order nonlocal diagram (2b) vanishes for the Ising model.

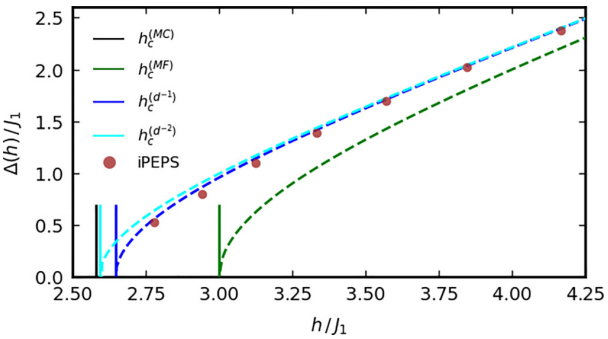

FIG. 4. TFIM on the cubic lattice at $T = 0$ and $S = 1/2$. The vertical lines indicate the critical field h_c in $1/d$ expansion Eq. (32), the quasi-exact result [58] (black) is rapidly approached with increasing expansion order. The same expansion is also used to estimate the spectral gap $\Delta(h)$ shown by dashed lines. The first correction to MF approximation is already in good agreement to the tensor-network (iPEPS) simulation of Ref. [59].

V. APPLICATION TO MODELS FROM MANY-BODY QUANTUM OPTICS

A. Long-range square lattice Heisenberg model

As a first of two applications inspired from many-body quantum optical systems we consider the $S = 1/2$ Heisenberg square lattice model with long-range FM power-law interactions,

$$J_{ii'} = J_1/|\mathbf{r}_i - \mathbf{r}_{i'}|^{\alpha}, \tag{36}$$

with $J_1 < 0$. This model has been recently studied with QMC simulations [42], which are numerically expensive due to the large system sizes required to approximate the infinite system limit. The lattice constant is set to unity and the interesting regime for the power-law exponent is $\alpha \in (2, 4)$ [31]. In this range α is large enough for a well-defined thermodynamic limit but small enough for a finite FM ordering temperature $T_c > 0$ evading the Mermin-Wagner theorem [60]. We abbreviate $J_{\mathbf{r}_j} = J_1/|\mathbf{r}_j|^{\alpha}$.

In analogy to Sec. IV, T_c is determined from

$$-\beta J_{\mathbf{k}=\mathbf{0}} \stackrel{!}{=} 1/(T\,\Sigma_{\mathbf{k}=\mathbf{0}}). \tag{37}$$

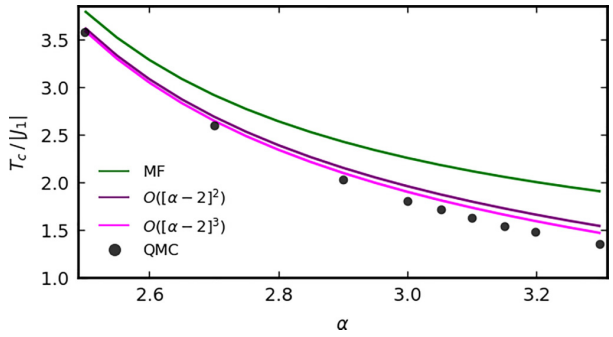

FIG. 5. Ordering temperature for the $S = 1/2$ square lattice Heisenberg FM with couplings decaying as a power law with exponent α, see Eq. (36). Dots denote reference data from QMC taken from Ref. [42]. Colored lines indicate T_c in MF approximation (green), and adding corrections up to order $[\alpha-2]^2$ (purple) and $[\alpha-2]^3$ (magenta), respectively.

To compute the spatial Fourier transform $J_{\mathbf{k}=\mathbf{0}}$ on the left-hand side and for subsequent expansions on the right-hand side, we obtain numerically the lattice sums $I^{(m)} \equiv \sum_{j\neq 0} r_j^{-\alpha m}$ for $m = 1, 2, 3$ and a sufficiently large cutoff. Then $J_{\mathbf{k}=\mathbf{0}} = J_1 I^{(1)}$. To identify a suitable expansion scheme, we consider the integral approximation of $I^{(m)}$ with lower bound $a = O(1)$,

$$I^{(m)} \simeq \int_a^\infty \mathrm{d}r\, r^{1-\alpha m} = \frac{a^{2-m\alpha}}{m\alpha-2} \underset{\alpha\to 2}{\longrightarrow} \begin{cases} \sim \frac{1}{\alpha-2} & : m = 1, \\ \text{const.} & : m > 1. \end{cases} \tag{38}$$

For $\alpha \to 2$ from above, $I^{(m)}$ only diverges for $m = 1$ whereas it is finite for $m > 1$.

From Eq. (37) the MF critical temperature is

$$T_c^{(0)} = |J_1| b_{c,1} I^{(1)} \sim \frac{1}{\alpha-2}, \tag{39}$$

see the green line in Fig. 5. We thus use $\alpha - 2$ as the small parameter for the expansion on the right-hand side of Eq. (37). We consider the geometry factors $\beta^n t^{(nx)}_{\mathbf{k}=\mathbf{0}}$ that play a role for the static Heisenberg case and we limit ourselves to order $n \leqslant 3$. For diagram (3b), we numerically checked that $\sum_{i,j} J_{\mathbf{r}_j} J_{\mathbf{r}_i-\mathbf{r}_j} J_{\mathbf{r}_i} \equiv J_1^3 \tilde{I}^{(3)}$ is nonsingular for $\alpha \to 2$. In summary, this means that $T\Sigma^{(n)} \sim \beta^n \sim [\alpha-2]^n$ around criticality. We expand the right-hand side in Eq. (37) to third order in $\alpha - 2$ and obtain

$$\begin{aligned} b_{c,1}\beta|J_1|I^{(1)} = 1 &- b_{c,1}^{-1}(\beta|J_1|)^2 I^{(2)} T^3 (\sigma^{(2a)} + \sigma^{(2b)}) \\ &+ b_{c,1}^{-1}(\beta|J_1|)^3 T^4 [I^{(3)}(\sigma^{(3a)} + \sigma^{(3c)}) \\ &+ \tilde{I}^{(3)}\sigma^{(3b)}] + \ldots \end{aligned} \tag{40}$$

The results for $S = 1/2$ are shown in Fig. 5 and approach the QMC data quickly if $\alpha - 2$ is sufficiently small.

B. Dicke-Ising model: Ground-state superradiance

As a second application to a many-body quantum optical system we consider the Dicke-Ising model [43,44,61,62]. This also provides an example where single-spin blocks appear in the diagrammatic expansion. This means that the precomputed diagrams of Sec. III cannot be used in the following calculation, see below.

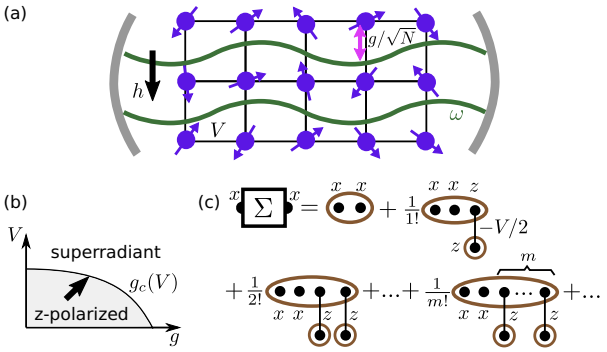

FIG. 6. Dicke-Ising model: (a) Sketch of an experimental square lattice setup with cavity photons at frequency ω coupled to spins with strength $g/\sqrt{N}$, homogeneous z field h and nearest-neighbor AFM Ising interactions V induced via Rydberg dressing. (b) Schematic phase diagram in the vicinity of the z-polarized phase and the adjacent superradiant phase in the presence of AFM Ising interactions V. (c) The diagrammatic expansion for Σ^{xx} in the limit $N \to \infty$ and $T \to 0$ can be summed exactly. This shows that the exact phase boundary in (b) is described by the MF result Eq. (45).

The Hamiltonian features a competition between a homogeneous field $h > 0$ in z direction, a coupling of the total spin x to a cavity photon and a nearest-neighbor AFM Ising zz interaction V, see Fig. 6(a) for a sketch. For concreteness, we specialize to a square lattice geometry. However, our qualitative results below do not depend on this choice. The Hamiltonian is $H = H_x + H_z$ with

$$H_x = \omega a^\dagger a + \frac{g}{\sqrt{N}}(a + a^\dagger)\sum_i S_i^x, \tag{41}$$

$$H_z = -h\sum_i S_i^z + \frac{V}{2}\sum_{\langle i,i'\rangle}\left(S_i^z + \frac{1}{2}\right)\left(S_{i'}^z + \frac{1}{2}\right) \tag{42}$$

$$= -[h - V]\sum_i S_i^z + \frac{V}{2}\sum_{\langle i,i'\rangle} S_i^z S_{i'}^z. \tag{43}$$

Here, the cavity photon at frequency ω is created by $a^\dagger$. The sums go over N sites and the nearest-neighbor bonds, respectively. The cavity-dipole coupling is $g/\sqrt{N} > 0$. This ensures an extensive interacting energy in the infinite system limit $N \to \infty$, which we consider in the following.

The Dicke model (the case $V = 0$) and its phase transition to the symmetry-broken superradiant state (the FM state with $\langle S_i^x\rangle \neq 0$) has been studied thoroughly both in theory [17,32] and experiment [6], the latter in a nonequilibrium setting. However, comparatively little is known about the Dicke-Ising model ($V > 0$) [43,44,61,62], which is yet awaiting experimental implementation. A possible realization for the Ising zz interactions uses the concept of Rydberg dressing [63], which motivated the form of Eq. (42) and leads to a renormalized effective field $h \to h - V$ when rewritten as in Eq. (43).

So far, the model also contains bosonic degrees of freedom in variance to the spin-only formulation in Hamiltonian (1). However, assuming a thermal state we can trace out the photons on the level of the generating functional [64]. This

replaces H_x by an all-to-all retarded (i.e., frequency-dependent) FM spin interaction of the xx type,

$$H_x \to H_{x,\mathrm{ret}} = T \sum_{\nu_m} \frac{1}{2} \sum_{i,i'} S_i^x(-\nu_m) J_{ii'}^{xx}(\nu_m) S_{i'}^x(\nu_m), \quad (44)$$

with $J_{ii'}^{xx}(\nu_m) = -2g^2\omega/[N(\nu_m^2+\omega^2)]$. This is close to Eq. (1), only differing in the frequency dependence and the presence of an on-site term. As we will discuss, this is inconsequential in the following since no xx interactions will appear in the 1JI diagrammatic expansion.

Here, we focus on thermal equilibrium at $T \to 0$ and limit the investigation to the realistic case of small V ($V \ll h$) and its effect on the transition between the z-polarized and superradiant phase. For $V \to 0$, it is well known that the MF approximation is exact for the Dicke model [17] but what happens at $V > 0$? As a first step, in Ref. [43] the phase boundary for the Dicke-Ising model on the square lattice was determined in MF approximation,

$$g_c = \sqrt{\omega(h-2V)}, \quad (45)$$

see Fig. 6(b) for a sketch.

Two questions are in order: First, is the phase transition indeed continuous as in MF approximation? And second, if yes, what are the corrections to the phase boundary beyond the MF prediction?

As shown in Ref. [62] for a simplified and more symmetric version of the Dicke-Ising model with $h - V = 0$ (with no z-polarized phase), the transition between the superradiant and Ising phase is of first order in a chain geometry. However, it is currently unknown if and under which conditions this also holds for the case $V \ll h$ and the phase transition out of the fully polarized phase that we consider.

Making the assumption that the phase transition from the z-polarized to the superradiant phase is continuous (and can thus be detected via a divergence in spin susceptibility) we use the spin diagrammatic technique to show rigorously our main finding of this section: Eq. (45) is already the exact result. This conclusion has been obtained independently in the very recent work of Schellenberger and Schmidt [44] using an alternative algebraic approach.

Analogous to the other examples in this work, we start from the z-polarized symmetry-unbroken phase and approach the boundary of the superradiant phase, see the arrow in Fig. 6(b). We detect the critical light-matter coupling strength g_c from the divergence of the static FM correlator $G_{\mathbf{k}=\mathbf{0}}^{xx}(i\nu = 0)$,

$$1/\Sigma_{\mathbf{k}=\mathbf{0}}^{xx} + J_{\mathbf{k}=\mathbf{0}}^{xx} \stackrel{!}{=} 0. \quad (46)$$

Here and in the following we drop the zero-Matsubara frequency argument from all quantities. The static part of the retarded xx interaction (44) is $J_{\mathbf{k}=\mathbf{0}}^{xx} = -2g^2/(\omega N)$ and Σ^{xx} denotes the J^{xx}-irreducible part of G^{xx}. Next, we expand Σ^{xx} in J^{xx} and V with the noninteracting Hamiltonian being $H_{0,h-V} = -[h-V]\sum_i S_i^z$. The first observation is that due to the limit $N \to \infty$ any occurrence of an interaction $J_{ii'}^{xx} \sim 1/N$ needs to be accompanied with a free site summation. Since these diagrams are necessarily J^{xx}-reducible (cf. the discussion at the end of Sec. II B) they do not occur in Σ^{xx} and only the V interactions $\sim S_i^z S_{i'}^z$ need to be considered. The second observation pertains to z-only blocks $G_{0,c,h-V}^{z\ldots z}(\tau_1,\ldots,\tau_m) = b_c^{(m-1)}(\beta[h-V])$. In the limit $T \to 0$ where the spins are fully polarized, these generalized susceptibilities vanish except for $m = 1$ for which $G_{0,c,h-V}^{z}(\tau_1) = S = 1/2$.

These considerations equate the exact (and local) Σ^{xx} to the infinite sum of diagrams shown in Fig. 6(c). The calculation proceeds without the kernel trick since all diagrammatic objects are free of frequency loops and are easily evaluated at the required zero frequency. We only need $\Sigma^{xx(0)} = 1/(2[h-V])$, see Table II for the TFIM. The fully static mixed-flavor blocks with two S^x operators and m appearances of the S^z operator can be found via a m-fold derivative of $G_{0,c,h-V}^{xx}$ with respect to h (which thus is also used as a source field),

$$G_{0,c,h-V}^{xx\overbrace{z\ldots z}^{m}} = \partial_h^m G_{0,c,h-V}^{xx} = \frac{(-1)^m m!}{2[h-V]^{m+1}}. \quad (47)$$

With these preparations the infinite diagrammatic sum in Fig. 6(c) results in the exact expression

$$\Sigma_{\mathbf{k}=\mathbf{0}}^{xx} = \sum_{m=0}^{\infty} \frac{1}{m!} G_{0,c,h-V}^{xx\overbrace{z\ldots z}^{m}} \cdot \langle S^z \rangle_{0,c}^m \cdot \left(-4\frac{V}{2}\right)^m = \frac{1}{2(h-2V)}. \quad (48)$$

Inserting this in Eq. (46) we obtain that the exact g_c is already given by Eq. (45).

For future work on the Dicke-Ising model, an extension to the complete phase diagram, which includes also a z-AFM and a combined z-AFM and superradiant x-FM phase, would be interesting. According to Ref. [44], MF theory is again exact for the transition between the latter two phases. Likewise, we suggest to consider the experimentally relevant modifications to finite N and the open-system case [65].

VI. CONCLUSION

In summary, we have presented an analytic approach to Matsubara spin-spin correlation functions based on a diagrammatic expansion of their 1-J-irreducible part Σ to nth order in J. We provide closed-form expressions for $n \leqslant 4$ for Ising, TFIM and Heisenberg models of completely general lattice geometry and spin length S. The introduction of the kernel function trick was instrumental in this calculation. The final results are conveniently tabulated for forthcoming application in diverse contexts where other computationally much more involved methods such as tensor networks or QMC are at their limits.

Via many examples and by applying a composite expansion strategy involving the inverse spatial dimension (or similar) as a small parameter, we showed the quantitative success of the diagrammatic approach if applied to models qualitatively described by the MF approximation. We argued that this is often the case in highly connected spin models relevant for state-of-the-art many-body quantum optical experiments. We use a long-range Heisenberg model and the Dicke-Ising model, both on the square lattice, as a showcase. Moreover we provided various benchmark examples for nearest-neighbor models on the (hyper)cubic lattice where our method yields accurate magnetic phase boundaries (both at $T > 0$ for Ising and Heisenberg models and $T = 0$ for

TFIM). We emphasize that due to the analytic nature of our approach, continuation to real frequencies is easily performed. For example we showed competitive results for the gap in the TFIM.

Future work could extend our approach to yet higher orders in J (for which diagram creation can be automated) or a greater variety of spin models, including those with nontrivial unit cells or various forms of disorder. Also spin-spin couplings between sites i, i' that are characterized by two or more nonzero parameters in the 3×3 coupling matrix $J_{ii'}^{\gamma\gamma'}$ [cf. Eq. (1)], e.g., XXZ models [66] could be studied with little extra effort. Another option would be to extend our approach to systems with SU(N) symmetry for $N > 2$ [67,68]. Also, the treatment of the symmetry-broken phase for the study of magnetization and spin-wave properties [48,69] is within reach. Further, it would be interesting to consider analytic continuation beyond the computation of the gap to obtain spectral functions. These are routinely measured in inelastic neutron scattering on solid-state magnets [70] or, more recently via quench spectroscopy in Rydberg tweezer arrays [23]. For the static case, analytic insights offered by our approach proved essential to shed new light [71] onto the puzzle of quantum-to-classical correspondence for static spin correlation functions in $d > 1$ dimensions [72].

Finally, we point out that the combination of the spin-spin correlator's bare series expansion with the kernel function trick [cf. Eq. (B2)] is suitable for evaluation by a diagrammatic Monte Carlo approach [73] similar to the connected determinant method [47]. However, imaginary time integrals are treated exactly via the kernel functions. Implementing these ideas would enhance the available expansion orders in spin diagrammatics and allow for flexible resummation schemes beyond this work.

Note added. Recently, we became aware of independent work in Ref. [74], which computes $\Sigma^{(0,2,3)}$ for the Heisenberg model in the traditional diagrammatic way via frequency integrals. The diagrams were derived from an expansion of spin-fRG flow equations and the five-point free spin correlator was provided analytically. Applications concern the chiral nonlinear susceptibility and estimates of T_c for the $d = 3, 4$ hypercubic case for various S. However, due to the chosen expansion of $1/\Sigma$ in J, the quality of the results for T_c does not improve with expansion order, in contrast to the composite expansion strategies presented in this work.

ACKNOWLEDGMENTS

We thank Marin Bukov, Elio König, Peter Kopietz, Andreas Rückriegel, Achim Rosch, Johannes Reuther, Kai Schmidt, Nils Schopohl, and Sebastian Slama for useful discussions and the authors of Ref. [59] for sharing their iPEPS data. We acknowledge funding from the Deutsche Forschungsgemeinschaft (DFG, German Research Foundation) through the Research Unit FOR 5413/1, Grant No. 465199066. B.Sch. acknowledges funding from the Munich Quantum Valley, supported by the Bavarian state government with funds from the Hightech Agenda Bayern Plus. B.Sb. and B. Schneider are supported by DFG Grant No. 524270816. I.L. acknowledges financing from the Baden-Württemberg Stiftung through Project No. BWST_ISF2019-23.

APPENDIX A: V-CONNECTED CORRELATORS

We define the V-connected correlators [47] (subscript $V-c$) that appear in the formal expansion of the spin correlator in Eq. (11) and the following equations. For brevity, we set $S_j^{\gamma}(\tau)S_{j'}^{\gamma'}(\tau') = A$. Then the V-connected correlators are defined recursively via

$$\langle \mathcal{T} V(\tau_1)\dots V(\tau_n)A\rangle_{0,h,V-c} = \langle \mathcal{T} V(\tau_1)\dots V(\tau_n)A\rangle_{0,h} - \sum_{S\subsetneq\{1,\dots,n\}} \left\langle \mathcal{T}\prod_{j\in S} V(\tau_j)A\right\rangle_{0,h,V-c} \left\langle \mathcal{T}\prod_{k\in\{1,\dots,n\}\setminus S} V(\tau_k)\right\rangle_{0,h}. \tag{A1}$$

Note that the ordering of (bosonic) operators behind imaginary time-ordering operator $\mathcal{T}$ does not matter. Standard connected spin correlators [with subscript c first appearing in Eq. (13)] are defined in analogy to their V-connected counterparts in Eq. (A1) by replacing each $V(\tau_j)$ with a single spin operator and removing the external operators $A \to 1$.

APPENDIX B: EVALUATION OF $\sigma^{\gamma\gamma'(nx)}(i\nu_m)$ VIA KERNEL FUNCTION TRICK

To facilitate all calculations on the right-hand side of Eq. (12) and in particular the evaluation of $\sigma^{(nx)}$ we introduce what we call the kernel function trick. Originally, kernel functions have been introduced to link the Fourier transform of an imaginary time-ordered m-point correlation function $G_{A_1\dots A_m}(i\omega_1,\dots,i\omega_{m-1})$ to eigenstates and -energies $H|\underline{a}\rangle = E_{\underline{a}}|\underline{a}\rangle$ of the many-body Hamiltonian [75]. The m-point correlators are a generalization of Eq. (7) to m arbitrary operators $A_{1,2,\dots,m}$. For the frequency arguments we introduced an abbreviated notation where ω_1 is short for ω_{n_1} and so on. The kernel functions straightforwardly extend the well-known spectral (or Lehmann) representation of the two-point correlator [27] to the m-point case. For bosonic (and spin) operators, the Fourier transform reads [49]

$$G_{A_1\dots A_m}(i\omega_1,\dots,i\omega_{m-1}) = \frac{1}{Z}\sum_{p\in S_m}\sum_{\underline{1}\dots\underline{m}} e^{-\beta E_{\underline{1}}} A_{p(1)}^{\underline{12}} A_{p(2)}^{\underline{23}}\dots A_{p(m)}^{\underline{m1}} K_m \times \left(\Omega_{p(1)}^{\underline{12}}, \Omega_{p(2)}^{\underline{23}},\dots,\Omega_{p(m-1)}^{\underline{m-1m}}\right), \tag{B1}$$

where $A_k^{\underline{ab}} = \langle \underline{a}|A_k|\underline{b}\rangle$ are matrix elements and the argument of the kernel function K_m is a list of m complex numbers $\Omega_k^{\underline{ab}} \equiv i\omega_k + E_{\underline{a}} - E_{\underline{b}}$, which sum to zero so that the last one is often dropped as in Eq. (B1). The kernel function itself are completely universal and do neither depend on the Hamiltonian H nor on the operators A_k in Eq. (B1). For example, $K_2(\Omega_1) = -\Delta_{\Omega_1} + \beta\delta_{\Omega_1}/2$ where $\delta_x = \delta_{0,x}$ and $\Delta_x = (1-\delta_x)/x$. The recent advance in Ref. [49] was the calculation of K_m for general m.

In the context of diagram evaluation, the crucial insight is that Eq. (B1) and nth-order perturbative expressions are naturally connected by interpreting the right-hand side of Eq. (12) as a Fourier transform of a time-ordered correlator of order $n+2$ with the first n frequencies being zero. Hence, as the

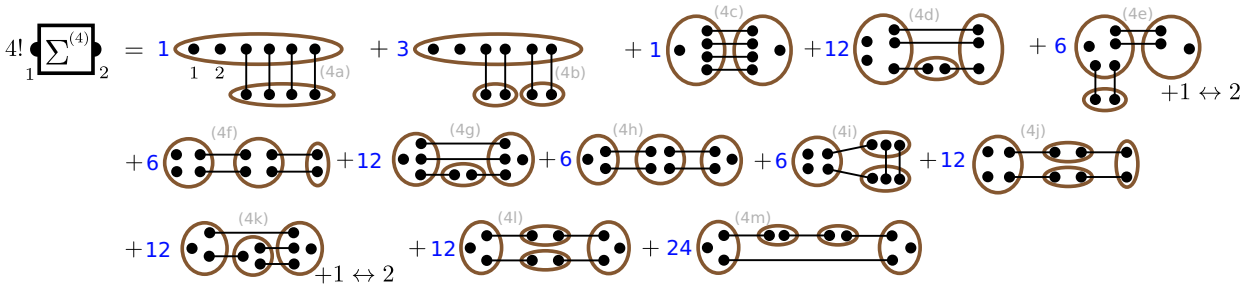

FIG. 7. Diagrams for Σ of order J^4, analogous to Fig. 3. The label $+1 \leftrightarrow 2$ adds the diagram with exchanged external indices.

main technical result of this work, Eq. (12) is expressed as

$$G^{\gamma\gamma'(n)}_{jj'}(i\nu_m) = \frac{(-1)^n}{n!} \sum_{p\in S_{n+2}} \sum_{i_1<i'_1,\ldots,i_n<i'_n} \sum_{\gamma^{(\prime)}_{1,\ldots,n}\in\{+,-,z\}} J^{\gamma_1\gamma'_1}_{i_1 i'_1} \ldots J^{\gamma_n\gamma'_n}_{i_n i'_n} \langle B_{p(1)} B_{p(2)} \ldots B_{p(n+2)}\rangle_{0,h,V\text{–}c} K_{n+2}(\Omega_{p(1)}, \Omega_{p(2)}, \ldots, \Omega_{p(n+1)}). \tag{B2}$$

Here we replaced V using Eq. (10) and defined the following operator and complex-frequency lists

$$\{B_1, \ldots, B_n, B_{n+1}, B_{n+2}\} = \{S^{\gamma_1}_{i_1} S^{\gamma'_1}_{i'_1}, \ldots, S^{\gamma_n}_{i_n} S^{\gamma'_n}_{i'_n}, S^{\gamma}_{j}, S^{\gamma'}_{j'}\}, \tag{B3}$$

$$\{\Omega_1, \ldots, \Omega_n, \Omega_{n+1}, \Omega_{n+2}\} = \{-(\gamma_1+\gamma'_1)h, \ldots, -(\gamma_n+\gamma'_n)h, i\nu_m - \gamma h, -i\nu_m - \gamma' h\}. \tag{B4}$$

Note that the external indices on the left-hand side of Eq. (B2) determine the last two entries of the lists. The Ω list (B4) was already given in Eq. (23). It is to be understood with the following replacement rule of flavor labels by numbers: $\{z, +, -\} \to \{0, +1, -1\}$. The simple structure of $H_{0,h}$ with its many-body (product) eigenstates and ladderlike energies is essential in the derivation of Eq. (B2) as it allows to reduce the complexity of the general Eq. (B1) by rewriting the sum over eigenstates via the equal-time free spin correlator. The point is that the $\Omega^{ab}_k \equiv i\omega_k + E_{\underline{a}} - E_{\underline{b}}$ only depend on the flavor(s) $\{+, -, z\}$ of the (composite) operator B_k.

Further, we rewrite Eq. (B2) using an index ordering operator $\mathcal{P}$. This operator applies to operator strings and argument lists alike. It acts like time-ordering, but for discrete indices $(1), (2), \ldots, (n+2)$ that, unlike imaginary time arguments, do not affect the operator, for example $\mathcal{P}B_1(1)B_2(3)B_3(2) = B_2B_3B_1$. We also reinstate the redundant last argument $\Omega_{p(n+2)}$ of K_{n+2}. We obtain

$$\begin{aligned} G^{\gamma\gamma'(n)}_{jj'}(i\nu_m) = \frac{(-1)^n}{n!} \sum_{p\in S_{n+2}} \sum_{i_1<i'_1,\ldots,i_n<i'_n} \sum_{\gamma^{(\prime)}_{1,\ldots,n}\in\{+,-,z\}} J^{\gamma_1\gamma'_1}_{i_1 i'_1} \ldots J^{\gamma_n\gamma'_n}_{i_n i'_n} \\ \times \langle \mathcal{P}B_1(p_1)B_2(p_2)\ldots B_{n+2}(p_{n+2})\rangle_{0,h,V\text{–}c} K_{n+2}(\mathcal{P}\{\Omega_1(p_1), \Omega_2(p_2), \ldots, \Omega_{n+2}(p_{n+2})\}), \end{aligned} \tag{B5}$$

As the operators $B_1, B_2, \ldots, B_{n+2}$ and their associated $\Omega_1, \Omega_2, \ldots, \Omega_{n+2}$ appear in all possible orderings, this is evidently the same as Eq. (B2).

To calculate $\sigma^{\gamma\gamma'(nx)}(i\nu_m)$ for a particular 1JI diagram (nx) defined by reference site configuration $\{i^{(nx)}_k < i'^{(nx)}_k\}_{k=1,2,\ldots,n}$, we specialize the site sums in Eq. (B5) to this reference configuration and split off the geometry factor $t^{(nx)}[J]$ as explained in Sec. II C. The V-connected average then becomes an ordinary connected equal-time average with respect to $H_{0,h}$, which factorizes according to the blocks of equal sites characteristic for (nx). Examples for diagrams $(2a)$ and $(3b)$ are provided in Eqs. (21) and (22), respectively.

APPENDIX C: SIMPLIFIED KERNEL FUNCTIONS FOR THE SPECIAL CASES $h = 0$ AND $T = 0$

Kernel functions $K_k(\Omega_1, \Omega_2, \ldots, \Omega_k)$ for general complex arguments (obeying $\Omega_1 + \ldots + \Omega_k = 0$) and arbitrary $k = 2, 3, 4, 5, 6\ldots$ are provided in Ref. [49]. However, in the context of this paper, where kernel functions are applied in the framework of spin perturbation theory, we have only two potentially nonreal entries in the Ω list (B4) (the ones at the end, which contain $\pm i\nu_m$ related to the external operators). More importantly, we limit ourselves to two special cases, (i) the case $h = 0$ for the Ising and Heisenberg model and (ii) the limit $T \to 0$ for the TFIM. In these cases substantial simplifications arise.

(i) Case $h = 0$: In Eq. (B5), the arguments of K_k are zero except for a possible nonzero pair of frequencies $\pm i\nu_m = \pm 2m\pi T i$ shuffled to positions $a_{1,2}$ in the list of length $k = n + 2$,

$$\{\Omega_1, \Omega_2, \ldots, \Omega_k\} = (0, 0, \ldots, 0, \underbrace{i\nu_m}_{\text{pos.}a_1}, 0, \ldots, 0, \underbrace{-i\nu_m}_{\text{pos.}a_2}, \underbrace{0, \ldots, 0}_{k-a_2}), \tag{C1}$$

TABLE VI. Geometry factors $t^{(nx)}[J]$ for Σ diagrams of order $n = 4$. See the caption of Table I for remarks.

top.	r space $t^{(nx)}_{jj'}$	k space $t^{(nx)}_{\mathbf{k}}$	nn-hyp. $\tilde{t}^{(nx)}_{\mathbf{k}}$
(4a)	$\delta_{jj'}\sum_i J_{ij}^4$	$\int_{\mathbf{p}_{1,2,3}} J_{\mathbf{p}_1}J_{\mathbf{p}_2}J_{\mathbf{p}_3}J_{\mathbf{p}_1+\mathbf{p}_2+\mathbf{p}_3}$	$J_1^3\tilde{J}_{\mathbf{0}}$
(4b)	$\delta_{jj'}[\sum_i J_{ji}^2]^2$	$[\int_{\mathbf{q}} J_{\mathbf{q}}^2]^2$	$[J_1\tilde{J}_{\mathbf{0}}]^2$
(4c)	$J_{jj'}^4$	$\int_{\mathbf{p}_{1,2,3}} J_{\mathbf{k}-\mathbf{p}_1}J_{\mathbf{p}_2}J_{\mathbf{p}_3}J_{\mathbf{p}_1+\mathbf{p}_2+\mathbf{p}_3}$	$J_1^3\tilde{J}_{\mathbf{k}}$
(4d)	$\delta_{jj'}\sum_i J_{ji}^2[J\cdot J]_{ij}$	$\int_{\mathbf{q},\mathbf{p}} J_{\mathbf{q}}J_{\mathbf{p}}J_{\mathbf{q}+\mathbf{p}}^2$	0
(4e)	$J_{jj'}^2\sum_i[J_{ji}^2+J_{j'i}^2]$	$2[\int_{\mathbf{p}} J_{\mathbf{p}}^2][\int_{\mathbf{q}} J_{\mathbf{k}-\mathbf{q}}J_{\mathbf{q}}]$	$2J_1^2\tilde{J}_{\mathbf{0}}\tilde{J}_{\mathbf{k}}$
(4f)	$\delta_{jj'}\sum_{i_{1,2}} J_{ji_1}^2J_{i_1i_2}^2$	$[\int_{\mathbf{q}} J_{\mathbf{q}}^2]^2$	$[J_1\tilde{J}_{\mathbf{0}}]^2$
(4g)	$J_{jj'}^2[J\cdot J]_{jj'}$	$\int_{\mathbf{q},\mathbf{p}} J_{\mathbf{k}-\mathbf{p}}J_{\mathbf{p}-\mathbf{q}}J_{\mathbf{q}}^2$	0
(4h)	$[J^2\cdot J^2]_{jj'}$	$[\int_{\mathbf{q}} J_{\mathbf{k}-\mathbf{q}}J_{\mathbf{q}}]^2$	$[J_1\tilde{J}_{\mathbf{k}}]^2$
(4i)	$\delta_{jj'}[J\cdot J^2\cdot J]_{jj}$	$\int_{\mathbf{q}}\int_{\mathbf{p}} J_{\mathbf{q}}J_{\mathbf{p}}J_{\mathbf{q}+\mathbf{p}}^2$	0
(4j)	$\delta_{jj'}[J\cdot J\cdot J\cdot J]_{jj}$	$\int_{\mathbf{q}} J_{\mathbf{q}}^4$	$6d[2d-1]J_1^4$
(4k)	$J_{jj'}[J\cdot J^2+J^2\cdot J]_{jj'}$	$2\int_{\mathbf{q}} J_{\mathbf{k}-\mathbf{q}}J_{\mathbf{q}}\int_{\mathbf{p}} J_{\mathbf{q}-\mathbf{p}}J_{\mathbf{p}}$	0
(4l)	$[J\cdot J]_{jj'}^2$	$\int_{\mathbf{q}} J_{\mathbf{k}-\mathbf{q}}^2J_{\mathbf{q}}^2$	$16J_1^4(\frac{d^2}{4}+\frac{1}{8}\sum_{\mu=1}^d\cos(2k_\mu)+\sum_{\mu<\nu}^d\cos k_\mu\cos k_\nu)$
(4m)	$J_{jj'}[J\cdot J\cdot J]_{jj'}$	$\int_{\mathbf{q}} J_{\mathbf{k}-\mathbf{q}}J_{\mathbf{q}}^3$	$3[2d-1]J_1^3\tilde{J}_{\mathbf{k}}$

where we assume $a_1 < a_2$ without loss of generality (see below). For this situation, we define

$$K_k(\Omega_1,\Omega_2,\ldots,\Omega_k) \equiv K_k^{(h=0)}(a_1,a_2,m). \tag{C2}$$

From Ref. [49], we find after some algebra

$$T^{k-1}K_k^{(h=0)}(a_1,a_2,m) = \begin{cases} \frac{1}{k!} & : m=0, \\ (-1)^{a_2-a_1}\sum_{l=a_2-a_1}^{k-a_1}\frac{[\Delta_{2\pi mi}]^l}{(k-l)!}\binom{l-1}{a_2-a_1-1} & : \text{otherwise}, \end{cases} \tag{C3}$$

where $\Delta_x = 1/x$ for nonzero x and zero otherwise. For the case that $-iv_m$ appears first, $a_1 > a_2$, we can flip the sign of m and obtain $K_k(\Omega_1,\Omega_2,\ldots,\Omega_k) = K_k^{(h=0)}(a_2,a_1,-m)$.

(ii) Case $T \to 0$: Here the kernel functions simplify because certain sums are dominated by inverse temperature $\beta \to \infty$. Any $\beta\delta_{\omega_1+\ldots+\omega_l,0}$ that remains must be interpreted as $\beta\delta_{\omega_1+\ldots+\omega_l,0} \overset{T\to 0}{\longrightarrow} 2\pi\delta(\omega_1+\ldots+\omega_l)$, but this does not appear for the particular

TABLE VII. Ising model, TFIM at $T = 0$ and Heisenberg model: The lattice independent part $\sigma^{(nx)}$ for $n = 4$ for all topologies, cf. Eq. (18). The Ising case is purely static.

	Ising $T^{1+n}\sigma^{zz(nx)}$	TFIM $\sigma^{xx(nx)}(iv)\vert_{T=0}$	Heisenberg: $T^{1+n}\sigma^{zz(nx)}(0)$	Heisenberg: $T^{1+n}\sigma^{zz(nx)}(iv_m\neq 0)$
(4a)	$\frac{1}{4!}b_{c,3}b_{c,5}$	$\frac{-S^2(195h^4+38h^2v^2+3v^4)}{512h^3(h^2+v^2)^2(9h^2+v^2)}$	$\frac{b_{c,1}^2}{-240}(192b_{c,1}^3+80b_{c,1}^2+20b_{c,1}+3)$	$\frac{\Delta^2b_{c,1}^2}{15}(4[30\Delta^2+1]b_{c,1}+12b_{c,1}^2+15\Delta^2+2)$
(4b)	$\frac{3}{4!}b_{c,1}^2b_{c,5}$	$\frac{S^3(447h^6+405h^4v^2+93h^2v^4+7v^6)}{256h^3(h^2+v^2)^3(9h^2+v^2)}$	$\frac{b_{c,1}^3}{24}(48b_{c,1}^2+12b_{c,1}+1)$	$\frac{\Delta^2b_{c,1}^3}{-3}(6b_{c,1}+30\Delta^2+1)$
(4c)	0	0	$\frac{b_{c,1}^2}{-120}(12b_{c,1}^2+6b_{c,1}+1)$	$\frac{\Delta^2b_{c,1}^2}{-15}(4[30\Delta^2+1]b_{c,1}+12b_{c,1}^2+15\Delta^2+2)$
(4d)	0	0	$\frac{b_{c,1}^3}{24}(4b_{c,1}+1)$	$\frac{\Delta^2b_{c,1}^3}{-2}$
(4e)	0	0	$\frac{b_{c,1}^3}{48}(4b_{c,1}+1)$	$\frac{\Delta^2b_{c,1}^3}{3}(6b_{c,1}+30\Delta^2+1)$
(4f)	$\frac{6}{4!}b_{c,1}b_{c,3}^2$	$\frac{S^3(21h^2+5v^2)}{256h^3(h^2+v^2)^2}$	$b_{c,1}^3(b_{c,1}^2+\frac{b_{c,1}}{3}+\frac{1}{30})$	$\frac{\Delta^2b_{c,1}^3}{-3}(6b_{c,1}+12\Delta^2+1)$
(4g)	$\frac{12}{4!}b_{c,1}b_{c,3}^2$	$\frac{S^3(21h^2+v^2)}{16h(h^2+v^2)^2(9h^2+v^2)}$	$\frac{b_{c,1}^3}{120}(144b_{c,1}^2+48b_{c,1}+5)$	$\frac{b_{c,1}^3}{3}\Delta^2(12\Delta^2+1)$
(4h)	0	0	$\frac{b_{c,1}^3}{120}$	$-6\Delta^2b_{c,1}^3$
(4i)	0	0	$\frac{b_{c,1}^3}{120}(10b_{c,1}+1)$	$\frac{b_{c,1}^3}{6}\Delta^2(24\Delta^2-1)$
(4j)	$\frac{12}{4!}b_{c,1}^3b_{c,3}$	$\frac{-5S^4(11h^2+3v^2)}{256h^3(h^2+v^2)^2}$	$\frac{b_{c,1}^4}{-6}(6b_{c,1}+1)$	$+2\Delta^2b_{c,1}^4$
(4k)	0	0	$\frac{b_{c,1}^3}{-120}$	$\frac{b_{c,1}^3}{-6}\Delta^2(24\Delta^2-1)$
(4l)	0	0	0	0
(4m)	0	0	0	$-2\Delta^2b_{c,1}^4$

correlators we compute in this work. To express the resulting $K_k^{(T\to 0)}(\Omega_1,\ldots,\Omega_k)$ we define the list of the partial sums

$$\{\Omega_1, \Omega_1+\Omega_2, \Omega_1+\Omega_2+\Omega_3, \ldots, \Omega_1+\ldots+\Omega_{k-1}\} \equiv \{c_1, c_2, \ldots, c_{k-1}\}. \tag{C4}$$

The final expression for $K_k^{(T\to 0)}$ involves a product of all but the l entries of (C4), which are zero,

$$K_k^{(T\to 0)}(\Omega_1,\ldots,\Omega_k) = (-1)^{k+1+l}\frac{\beta^l}{(l+1)!}\prod_{c_m\neq 0}\frac{1}{c_m}. \tag{C5}$$

APPENDIX D: DIAGRAMS AND RESULTS FOR $\Sigma^{(4)}$

In Fig. 7 we provide the diagrams for Σ to order J^4 with geometry factors and $\sigma^{(nx)}$ given in Tables VI and VII.

[1] M. Endres, H. Bernien, A. Keesling, H. Levine, E. R. Anschuetz, A. Krajenbrink, C. Senko, V. Vuletic, M. Greiner, and M. D. Lukin, Atom-by-atom assembly of defect-free one-dimensional cold atom arrays, Science **354**, 1024 (2016).

[2] D. Barredo, S. de Léséleuc, V. Lienhard, T. Lahaye, and A. Browaeys, An atom-by-atom assembler of defect-free arbitrary two-dimensional atomic arrays, Science **354**, 1021 (2016).

[3] J. T. Barreiro, M. Müller, P. Schindler, D. Nigg, T. Monz, M. Chwalla, M. Hennrich, C. F. Roos, P. Zoller, and R. Blatt, An open-system quantum simulator with trapped ions, Nature (London) **470**, 486 (2011).

[4] A. Shankar, E. A. Yuzbashyan, V. Gurarie, P. Zoller, J. J. Bollinger, and A. M. Rey, Simulating dynamical phases of chiral $p+ip$ superconductors with a trapped ion magnet, PRX Quantum **3**, 040324 (2022).

[5] A. Frisk Kockum, A. Miranowicz, S. De Liberato, S. Savasta, and F. Nori, Ultrastrong coupling between light and matter, Nature Rev. Phys. **1**, 19 (2019).

[6] K. Baumann, C. Guerlin, F. Brennecke, and T. Esslinger, Dicke quantum phase transition with a superfluid gas in an optical cavity, Nature (London) **464**, 1301 (2010).

[7] R. Landig, L. Hruby, N. Dogra, M. Landini, R. Mottl, T. Donner, and T. Esslinger, Quantum phases from competing short- and long-range interactions in an optical lattice, Nature (London) **532**, 476 (2016).

[8] A. Browaeys and T. Lahaye, Many-body physics with individually-controlled Rydberg atoms, Nature Phys. **16**, 132 (2020).

[9] C. Monroe, W. C. Campbell, L.-M. Duan, Z.-X. Gong, A. V. Gorshkov, P. W. Hess, R. Islam, K. Kim, N. M. Linke, G. Pagano, P. Richerme, C. Senko, and N. Y. Yao, Programmable quantum simulations of spin systems with trapped ions, Rev. Mod. Phys. **93**, 025001 (2021).

[10] S.-A. Guo, Y.-K. Wu, J. Ye, L. Zhang, W.-Q. Lian, R. Yao, Y. Wang, R.-Y. Yan, Y.-J. Yi, Y.-L. Xu, B.-W. Li, Y.-H. Hou, Y.-Z. Xu, W.-X. Guo, C. Zhang, B.-X. Qi, Z.-C. Zhou, L. He, and L.-M. Duan, A site-resolved two-dimensional quantum simulator with hundreds of trapped ions, Nature (London) **630**, 613 (2024).

[11] W. Guerin, M. O. Araújo, and R. Kaiser, Subradiance in a large cloud of cold atoms, Phys. Rev. Lett. **116**, 083601 (2016).

[12] J. Rui, D. Wei, A. Rubio-Abadal, S. Hollerith, J. Zeiher, D. M. Stamper-Kurn, C. Gross, and I. Bloch, A subradiant optical mirror formed by a single structured atomic layer, Nature (London) **583**, 369 (2020).

[13] P. Kongkhambut, J. Skulte, L. Mathey, J. G. Cosme, A. Hemmerich, and H. Keßler, Observation of a continuous time crystal, Science **377**, 670 (2022).

[14] A. Cabot, F. Carollo, and I. Lesanovsky, Continuous sensing and parameter estimation with the boundary time crystal, Phys. Rev. Lett. **132**, 050801 (2024).

[15] A. Auerbach, *Interacting Electrons and Quantum Magnetism*, 1994th ed. (Springer, New York, 1994).

[16] J. Larson, B. Damski, G. Morigi, and M. Lewenstein, Mott-insulator states of ultracold atoms in optical resonators, Phys. Rev. Lett. **100**, 050401 (2008).

[17] P. Kirton, M. M. Roses, J. Keeling, and E. G. D. Torre, Introduction to the Dicke model: From equilibrium to nonequilibrium, and vice versa, Adv. Quantum Technol. **2**, 1800043 (2019).

[18] F. Mivehvar, F. Piazza, T. Donner, and H. Ritsch, Cavity QED with quantum gases: New paradigms in many-body physics, Adv. Phys. **70**, 1 (2021).

[19] M. B. M. Svendsen and B. Olmos, Modified dipole-dipole interactions in the presence of a nanophotonic waveguide, Quantum **7**, 1091 (2023).

[20] F. Le Kien and A. Rauschenbeutel, Nanofiber-mediated chiral radiative coupling between two atoms, Phys. Rev. A **95**, 023838 (2017).

[21] B. Sbierski, M. Bintz, S. Chatterjee, M. Schuler, N. Y. Yao, and L. Pollet, Magnetism in the two-dimensional dipolar XY model, Phys. Rev. B **109**, 144411 (2024).

[22] C. Chen, G. Bornet, M. Bintz, G. Emperauger, L. Leclerc, V. S. Liu, P. Scholl, D. Barredo, J. Hauschild, S. Chatterjee, M. Schuler, A. M. Läuchli, M. P. Zaletel, T. Lahaye, N. Y. Yao, and A. Browaeys, Continuous symmetry breaking in a two-dimensional Rydberg array, Nature (London) **616**, 691 (2023).

[23] C. Chen, G. Emperauger, G. Bornet, F. Caleca, B. Gély, M. Bintz, S. Chatterjee, V. Liu, D. Barredo, N. Y. Yao, T. Lahaye, F. Mezzacapo, T. Roscilde, and A. Browaeys, Spectroscopy of elementary excitations from quench dynamics in a dipolar XY Rydberg simulator, arXiv:2311.11726.

[24] A. W. Sandvik, Computational studies of quantum spin systems, AIP Conf. Proc. **1297**, 135 (2010).

[25] A. Lohmann, H.-J. Schmidt, and J. Richter, Tenth-order high-temperature expansion for the susceptibility and the specific heat of spin-s Heisenberg models with arbitrary exchange patterns: Application to pyrochlore and kagome magnets, Phys. Rev. B **89**, 014415 (2014).

[26] P. Adelhardt, J. A. Koziol, A. Langheld, and K. P. Schmidt, Monte Carlo based techniques for quantum magnets with long-range interactions, Entropy **26**, 401 (2024).

[27] H. Bruus, K. Flensberg, H. Bruus, and K. Flensberg, *Many-Body Quantum Theory in Condensed Matter Physics: An Introduction*, Oxford Graduate Texts (Oxford University Press, Oxford, 2004).

[28] R. Agra, F. van Wijland, and E. Trizac, On the free energy within the mean-field approximation, Eur. J. Phys. **27**, 407 (2006).

[29] R. Brout, Statistical mechanical theory of ferromagnetism. High density behavior, Phys. Rev. **118**, 1009 (1960).

[30] W. Metzner and D. Vollhardt, Correlated lattice fermions in $d = \infty$, Phys. Rev. Lett. **62**, 324 (1989).

[31] N. Defenu, T. Donner, T. Macrì, G. Pagano, S. Ruffo, and A. Trombettoni, Long-range interacting quantum systems, Rev. Mod. Phys. **95**, 035002 (2023).

[32] K. Hepp and E. H. Lieb, On the superradiant phase transition for molecules in a quantized radiation field: The dicke maser model, Ann. Phys. **76**, 360 (1973).

[33] F. Carollo and I. Lesanovsky, Exactness of mean-field equations for open dicke models with an application to pattern retrieval dynamics, Phys. Rev. Lett. **126**, 230601 (2021).

[34] H. Kleinert and V. Schulte-frohlinde, *Critical Properties of Phi-4-Theories*, 1st ed. (World Scientific, Singapore, 2001).

[35] S. L. Sondhi, S. M. Girvin, J. P. Carini, and D. Shahar, Continuous quantum phase transitions, Rev. Mod. Phys. **69**, 315 (1997).

[36] V. G. Vaks, A. I. Larkin, and S. A. Pikin, Self-consistent field method for the description of phase transitions, Sov. Phys. JETP **24**(1), 240 (1967).

[37] V. G. Vaks and A. I. Larkin, Spin waves and correlation functions in a ferromagnetic, Sov. Phys. JETP **26**(3), 647 (1968).

[38] R. B. Stinchcombe, Thermal and magnetic properties of the transverse Ising model, J. Phys. C **6**, 2507 (1973).

[39] R. B. Stinchcombe, Ising model in a transverse field. I. Basic theory, J. Phys. C **6**, 2459 (1973).

[40] R. B. Stinchcombe, Ising model in a transverse field. II. Spectral functions and damping, J. Phys. C **6**, 2484 (1973).

[41] Y. A. Izyumov and Y. N. Skryabin, *Statistical Mechanics of Magnetically Ordered Systems* (Consultants Bureau, New York, 1988).

[42] J. Zhao, M. Song, Y. Qi, J. Rong, and Z. Y. Meng, Finite-temperature critical behaviors in 2D long-range quantum Heisenberg model, npj Quantum Mater. **8**, 59 (2023).

[43] J. Gelhausen, M. Buchhold, A. Rosch, and P. Strack, Quantum-optical magnets with competing short- and long-range interactions: Rydberg-dressed spin lattice in an optical cavity, SciPost Physics **1**, 004 (2016).

[44] A. Schellenberger and K. P. Schmidt, (Almost) everything is a Dicke model - Mapping non-superradiant correlated light-matter systems to the exactly solvable Dicke model, SciPost Phys. Core **7**, 038 (2024).

[45] G. Horwitz and H. B. Callen, Diagrammatic expansion for the Ising model with arbitrary spin and range of interaction, Phys. Rev. **124**, 1757 (1961).

[46] F. Englert, Linked cluster expansions in the statistical theory of ferromagnetism, Phys. Rev. **129**, 567 (1963).

[47] R. Rossi, Determinant diagrammatic Monte Carlo in the thermodynamic limit, Phys. Rev. Lett. **119**, 045701 (2017).

[48] R. Goll, D. Tarasevych, J. Krieg, and P. Kopietz, Spin functional renormalization group for quantum Heisenberg ferromagnets: Magnetization and magnon damping in two dimensions, Phys. Rev. B **100**, 174424 (2019).

[49] J. Halbinger, B. Schneider, and B. Sbierski, Spectral representation of Matsubara n-point functions: Exact kernel functions and applications, SciPost Phys. **15**, 183 (2023).

[50] J. Krieg and P. Kopietz, Exact renormalization group for quantum spin systems, Phys. Rev. B **99**, 060403(R) (2019).

[51] J. Krieg, Doctoral thesis, Universitätsbibliothek Johann Christian Senckenberg, 2019, https://publikationen.ub.unifrankfurt.de/frontdoor/index/index/year/2020/docId/52628.

[52] A. M. Ferrenberg, J. Xu, and D. P. Landau, Pushing the limits of Monte Carlo simulations for the three-dimensional Ising model, Phys. Rev. E **97**, 043301 (2018).

[53] P. H. Lundow and K. Markström, Critical behavior of the Ising model on the four-dimensional cubic lattice, Phys. Rev. E **80**, 031104 (2009).

[54] P. Butera and M. Pernici, High-temperature expansions of the higher susceptibilities for the Ising model in general dimension d, Phys. Rev. E **86**, 011139 (2012).

[55] J. Otsuki and Y. Kuramoto, Dynamical mean-field theory for quantum spin systems: Test of solutions for magnetically ordered states, Phys. Rev. B **88**, 024427 (2013).

[56] S. McKenzie, C. Domb, and D. L. Hunter, The high-temperature susceptibility of the classical Heisenberg model in four dimensions, J. Phys. A: Math. Gen. **15**, 3909 (1982).

[57] J. Oitmaa and W. Zheng, Curie and Néel temperatures of quantum magnets, J. Phys.: Condens. Matter **16**, 8653 (2004).

[58] H. W. J. Blöte and Y. Deng, Cluster Monte Carlo simulation of the transverse Ising model, Phys. Rev. E **66**, 066110 (2002).

[59] I. V. Lukin, A. G. Sotnikov, J. M. Leamer, A. B. Magann, and D. I. Bondar, Spectral gaps of two- and three-dimensional many-body quantum systems in the thermodynamic limit, Phys. Rev. Res. **6**, 023128 (2024).

[60] N. D. Mermin and H. Wagner, Absence of ferromagnetism or antiferromagnetism in one- or two-dimensional isotropic Heisenberg models, Phys. Rev. Lett. **17**, 1133 (1966).

[61] Y. Zhang, L. Yu, J.-Q. Liang, G. Chen, S. Jia, and F. Nori, Quantum phases in circuit QED with a superconducting qubit array, Sci. Rep. **4**, 4083 (2014).

[62] J. Rohn, M. Hörmann, C. Genes, and K. P. Schmidt, Ising model in a light-induced quantized transverse field, Phys. Rev. Res. **2**, 023131 (2020).

[63] G. Pupillo, A. Micheli, M. Boninsegni, I. Lesanovsky, and P. Zoller, Strongly correlated gases of rydberg-dressed atoms: Quantum and classical dynamics, Phys. Rev. Lett. **104**, 223002 (2010).

[64] M. Weber, Quantum Monte Carlo simulation of spin-boson models using wormhole updates, Phys. Rev. B **105**, 165129 (2022).

[65] E. G. D. Torre, S. Diehl, M. D. Lukin, S. Sachdev, and P. Strack, Keldysh approach for nonequilibrium phase transitions

in quantum optics: Beyond the Dicke model in optical cavities, Phys. Rev. A **87**, 023831 (2013).

[66] D. Peter, S. Müller, S. Wessel, and H. P. Büchler, Anomalous behavior of spin systems with dipolar interactions, Phys. Rev. Lett. **109**, 025303 (2012).

[67] M. A. Cazalilla and A. M. Rey, Ultracold Fermi gases with emergent SU(N) symmetry, Rep. Prog. Phys. **77**, 124401 (2014).

[68] X. Zhang, M. Bishof, S. L. Bromley, C. V. Kraus, M. S. Safronova, P. Zoller, A. M. Rey, and J. Ye, Spectroscopic observation of SU(N)-symmetric interactions in Sr orbital magnetism, Science **345**, 1467 (2014).

[69] Yu. A. Izyumov, N. I. Chaschin, and V. Yu. Yushankhai, Longitudinal spin dynamics in the Heisenberg ferromagnet: Diagrammatic approach, Phys. Rev. B **65**, 214425 (2002).

[70] T. Chen, A. Ghasemi, J. Zhang, L. Shi, Z. Tagay, L. Chen, E.-S. Choi, M. Jaime, M. Lee, Y. Hao, H. Cao, B. Winn, R. Zhong, X. Xu, N. P. Armitage, R. Cava, and C. Broholm, Phase diagram and spectroscopic evidence of supersolids in quantum Ising magnet $K_2Co(SeO_3)_2$, arXiv:2402.15869.

[71] B. Schneider and B. Sbierski, Taming spin susceptibilities in frustrated quantum magnets: Mean-field form and approximate nature of the quantum-to-classical correspondence, arXiv:2407.09401.

[72] S. A. Kulagin, N. Prokof'ev, O. A. Starykh, B. Svistunov, and C. N. Varney, Bold diagrammatic Monte Carlo method applied to fermionized frustrated spins, Phys. Rev. Lett. **110**, 070601 (2013).

[73] R. Burkard *et al.* (unpublished).

[74] A. Rückriegel, D. Tarasevych, J. Krieg, and P. Kopietz, Recursive algorithm for generating high-temperature expansions for spin systems and the chiral nonlinear susceptibility, Phys. Rev. B **110**, 144416 (2024).

[75] F. B. Kugler, S.-S. B. Lee, and J. von Delft, Multipoint correlation functions: Spectral representation and numerical evaluation, Phys. Rev. X **11**, 041006 (2021).

Taming Spin Susceptibilities in Frustrated Quantum Magnets: Mean-Field Form and Approximate Nature of the Quantum-to-Classical Correspondence

Benedikt Schneider[1,2] and Björn Sbierski[3]

[1]*Department of Physics and Arnold Sommerfeld Center for Theoretical Physics, Ludwig-Maximilians-Universität München, Theresienstraße 37, 80333 Munich, Germany*

[2]*Munich Center for Quantum Science and Technology (MCQST), 80799 Munich, Germany*

[3]*Institut für Theoretische Physik, Universität Tübingen, Auf der Morgenstelle 14, 72076 Tübingen, Germany*

(Received 16 August 2024; revised 16 October 2024; accepted 2 April 2025; published 29 April 2025)

In frustrated magnetism, the empirically found quantum-to-classical correspondence (QCC) matches the real-space static susceptibility pattern of a quantum spin-1/2 model with its classical counterpart computed at a certain elevated temperature. This puzzling relation was observed via bold line diagrammatic Monte Carlo simulations in dimensions two and three. The matching was within error bars and seemed valid down to the lowest accessible temperatures T about an order of magnitude smaller than the exchange coupling J. Here, we employ resummed spin diagrammatic perturbation theory to show analytically that the QCC breaks weakly at fourth order in J/T and provide the approximate mapping between classical and quantum temperatures. Our treatment further reveals that QCC is an indication of the surprising accuracy with which static correlators can be approximated by a simple renormalized mean-field form. We illustrate this for all models discussed in the context of QCC so far, including a recent example of the $S = 1$ material $K_2Ni_2(SO_4)_3$. The success of the mean-field form is traced back to partial diagrammatic cancellations.

DOI: 10.1103/PhysRevLett.134.176502

Introduction—Frustrated quantum magnets remain at the forefront of current research in condensed matter physics [1]. In this arena, enhanced spin fluctuations might suppress magnetic ordering and conspire to stabilize delicate highly entangled quantum states characterized by long-range entanglement and fractional excitations at low temperature T [2,3]. But how low is "low"? And which experimental observables reveal the sought-after quantum spin liquid properties unambiguously?

While complete answers to these questions remain elusive even in theory, impressive progress has been made on the numerical front [4–9]. During this endeavor, in 2013, a particularly puzzling empirical observation appeared for the triangular lattice quantum $S = 1/2$ Heisenberg antiferromagnet (AFM) [10]: the bond-resolved spin susceptibility $\chi(\mathbf{r})$ [also known as the static spin correlator, see Eq. (2)] was computed via bold line diagrammatic Monte Carlo (BDMC). For all attainable $T \geq 0.375J$, the intricate and highly featured normalized pattern $\chi(\mathbf{r})/\chi(\mathbf{0})$ (see Fig. 3 left) can be matched by correlation data obtained from the classical ($S = \infty$) vector-spin version of the same model at an empirically obtained elevated temperature $T^{(c)} > T$! This was dubbed the quantum-to-classical correspondence (QCC) [11].

The BDMC [12] is one of the few numerical methods that remains operative for frustrated quantum spin models in high spatial dimensions ($d = 2$, 3) and moderately low $T/J \gtrsim 0.1$. It builds on a complex fermionic representation of spin $S = 1/2$ operators and stochastically samples millions of skeleton Feynman diagrams [13]. Importantly, results for $\chi(\mathbf{r})$ from BDMC are not exact but come with error bars of $\simeq 1\%$. The matching of QCC above is to be understood within these error bars.

In the years following its initial observation on the triangular lattice, QCC was found wherever BDMC was aimed at: the square and kagome lattice in $d = 2$ [10,14] and the pyrochlore lattice in $d = 3$ [15], as well as $J_1 - J_2$ models on the square and anisotropic triangular lattices in $d = 2$ [14]. The corresponding $T^{(c)}(T)$ for various nearest-neighbor models is compiled in Fig. 1 (markers). Recently, QCC was also observed in an $S = 1$ model for the material $K_2Ni_2(SO_4)_3$ consisting of two interconnected $d = 3$ trillium lattices [16]. Here, the quantum data was obtained from the pseudofermion functional renormalization group (PFFRG) [7].

As of today, the QCC remains puzzling with overwhelming empirical evidence but no explanation. Why do the celebrated quantum fluctuations maximized for the smallest spin $S = 1/2$ merely seem to be accounted for classically by an effective heating? And would the QCC break down and reveal an approximate nature if a more

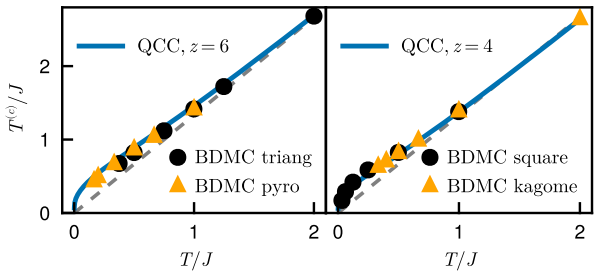

FIG. 1. QCC for systems with nearest-neighbor AFM Heisenberg coupling J, left for triangular and pyrochlore lattice with coordination number $z=6$ and right for kagome and square lattice ($z=4$). The markers are reproduced from the BDMC studies of Refs. [10,14,15] and indicate the temperature $T^{(c)}$ at which the normalized susceptibility pattern of the classical vector-spin model matches the one of the quantum $S=1/2$ model at temperature T within error bars. The solid lines show the analytical prediction for the *approximate* QCC obtained by numerically inverting Eq. (8), the dashed line denotes the high-T limit $T^{(c)}=4T/3$.

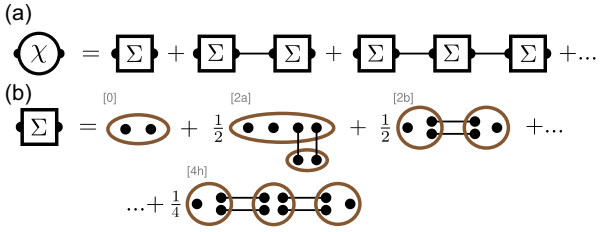

FIG. 2. (a) Diagrammatic representation of the Larkin equation (3). Lines represent the coupling $-J$. (b) Some diagrams contributing to Σ. For details see Ref. [17]. Diagram $[4h]$ and a two-chain $[2b]^2$ contribute to $\Sigma(\mathbf{k})^{-1}$ as $\sim J^4\gamma(\mathbf{k})^2$.

powerful successor of BDMC could reach lower T and smaller error bars? If not, Ref. [10] speculated, could the $T^{(c)}(T)$ curve be extrapolated to $T=0$ such that a classical simulation would reveal properties of highly sought-after quantum ground states?

In this Letter we shed analytical light on the origin of QCC building on recent progress in spin-S diagrammatics [17]. The QCC turns out to be only approximate for all finite S and dimensions d. We quantify QCC's failure at order $[J/T]^4$, provide a closed-form expression of the (approximate) $T^{(c)}(T)$ curve, and reveal a connection between QCC and the surprising success of a renormalized mean-field (MF) ansatz for $\chi(\mathbf{r})$. We also quantitatively explain the failure of QCC for the $d=1$ Heisenberg chain at intermediate temperature, as empirically pointed out already in Ref. [10].

Perturbation theory—We present a resummed perturbative expansion of the susceptibility in spin-S Heisenberg models. For ease of presentation, we here restrict to nearest-neighbor models on N-site Bravais lattices with single atomic bases (e.g., triangular or square lattices),

$$H = J\sum_{\langle \mathbf{r},\mathbf{r}'\rangle} \mathbf{S}_{\mathbf{r}}\cdot\mathbf{S}_{\mathbf{r}'}. \tag{1}$$

For generalizations, see End Matter. The momentum-space susceptibility or static spin correlator (at zero Matsubara frequency) is

$$\chi(\mathbf{k}) = \frac{1}{N}\sum_{\mathbf{r},\mathbf{r}'} e^{-i\mathbf{k}\cdot(\mathbf{r}-\mathbf{r}')}\int_0^\beta \mathrm{d}\tau \langle S^z_{\mathbf{r}}(\tau)S^z_{\mathbf{r}'}(0)\rangle, \tag{2}$$

where $\beta=1/T$ and $S^z_{\mathbf{r}}(\tau)$ is the Heisenberg spin operator at imaginary time τ. The Larkin equation [18,19] expresses Eq. (2) via the set of one-J-irreducible (static) two-legged spin-correlator diagrams $\Sigma(\mathbf{k})$,

$$\chi(\mathbf{k})^{-1} = \Sigma(\mathbf{k})^{-1} + J\gamma(\mathbf{k}), \tag{3}$$

where $\gamma(\mathbf{k}) = (1/N)\sum_{\langle \mathbf{r},\mathbf{r}'\rangle} e^{-i\mathbf{k}\cdot(\mathbf{r}-\mathbf{r}')}$ is the spatial Fourier transform of the real-space coupling pattern normalized to unit strength. A diagrammatic representation of Eq. (3) is shown in Fig. 2(a) and a few low order in J contributions to Σ are depicted in Fig. 2(b).

Replacing the exact Σ in Eq. (3) with its contribution at order J^0, i.e., with the free-spin (Curie) susceptibility $\Sigma^{(0)}=\beta b_1$ [where $b_1=S(S+1)/3$] yields the MF approximation [19]. Consequently, terms of higher order capture corrections beyond MF. It is convenient to parametrize the *exact* (inverse) susceptibility $\chi(\mathbf{k})^{-1}$ of Eq. (3) in terms of a renormalized MF part and a correction $\epsilon(\mathbf{k})$ characterized via its beyond-MF momentum dependence,

$$\beta[\chi(\mathbf{k})]^{-1} = f + g\gamma(\mathbf{k}) + \epsilon(\mathbf{k}). \tag{4}$$

In MF approximation, $f=1/b_1$, $g=\beta J$ and $\epsilon(\mathbf{k})=0$. In that sense the exact f is the (dimensionless) renormalized on-site inverse susceptibility, while g describes the renormalized coupling. We refer to the right-hand side of Eq. (4) with $\epsilon(\mathbf{k})=0$ as renormalized MF form.

Recent methodological progress [17] provides the expansion of Σ in the dimensionless coupling $X=\beta J$ complete to $O(X^4)$ for various spin models and arbitrary lattice geometry. Focusing on the static correlator and the Heisenberg case, the right-hand side of Eq. (4) reads

$$f = \frac{1}{b_1} + z\left(\frac{1}{6}(6b_1+1)X^2 + \frac{1}{24}(4b_1+1)X^3\right) - \frac{I^{(3)}}{6}b_1(6b_1+1)X^3 + O(X^4), \tag{5}$$

$$g = X + \frac{X^2}{12} + \frac{X^3}{120}(48b_1^2+16b_1+3) + O(X^4), \tag{6}$$

$$\epsilon(\mathbf{k}) = -\frac{X^4 b_1}{720}\left[\gamma^2(\mathbf{k}) - z - \frac{I^{(3)}}{z}\gamma(\mathbf{k})\right] + O(X^5). \tag{7}$$

We defined $I^{(n)} = \int_{\mathbf{k}} \gamma^n(\mathbf{k})$. The special case $I^{(2)} = z$ counts the neighbors per site (coordination number). For example, the nearest-neighbor Heisenberg model on the d-dimensional hypercubic lattice is characterized by $\gamma(\mathbf{k}) = 2\sum_{l=1}^{d} \cos k_l$, $z = 2d$ and $I^{(3)} = 0$. The second and third term in brackets of Eq. (7) subtract contributions $\sim\gamma(\mathbf{k})^2$ that can be associated to $O(X^4)$ terms in f and g, respectively.

For all the following arguments, it is crucial that corrections to the renormalized MF form in $\epsilon(\mathbf{k})$ appear only from order X^4 on, meaning they are suppressed at high temperatures. Further, the small prefactor in Eq. (7) results from partial diagrammatic cancellation, $\epsilon(\mathbf{k}) \sim (b_1^{-1}[2\mathrm{b}]^2 - [4\mathrm{h}]) + O(X^5)$; see Fig. 2.

Approximate QCC—To address the QCC puzzle [10] we consider classical (unit-vector) spins via the $S \to \infty$ limit. This is straightforward in our general-S formalism after spin operators in Eqs. (1) and (2) are rescaled by $1/S$. The resulting classical coupling and susceptibility are denoted with superscript (c), hence $\chi^{(c)}(\mathbf{k})^{-1} = \lim_{S\to\infty} S^2\chi(\mathbf{k})^{-1}$ with $X \longrightarrow X^{(c)}/S^2$. Note that b_1 also depends on S, hence the right-hand sides of Eqs. (5) to (7) simplify in the limit $S \to \infty$.

However, as shown above, the susceptibility $\chi(\mathbf{k})$ remains a function of two parameters f, g for all S with $O(X^4)$ corrections. The QCC was discussed for the normalized susceptibility $\chi(\mathbf{k})/\chi(\mathbf{r} = \mathbf{0})$ where $\chi(\mathbf{r} = \mathbf{0}) = \int_{\mathbf{q}} \chi(\mathbf{q})$. The (inverse of the) normalized susceptibility can be computed straightforwardly for both finite S and the classical case. We find an approximate analytic mapping between the two (up to and including order $(X^3) \sim [X^{(c)}]^3$) where f is fixed by the normalization and g can be fixed by relating X to $X^{(c)}$,

$$X = \frac{X^{(c)}}{3b_1} - \frac{(X^{(c)})^2}{108b_1^2} + (X^{(c)})^3 \frac{15b_1 z - 12b_1 - 1}{2430b_1^3} + O(X^4). \tag{8}$$

Equivalently, this relates the temperature $T/J = 1/X$ of the quantum spin-S system to that of the classical system, $T^{(c)}/J = 1/X^{(c)}$. In End Matter we generalize Eq. (8) to $J_1 - J_2 - \cdots$ Heisenberg models with multiple (equivalent) basis sites. For J_1 models on lattices with nontrivial basis (e.g., kagome or pyrochlore), Eq. (8) is not changed. This is our first main result.

In Fig. 1, we plot the numerical inverse of Eq. (8) [without the unknown contribution $O(X^4)$] for various $S = 1/2$ systems (lines). Note that the lattice only enters via the coordination number z. Results are in good agreement with the empirical data points reproduced from the BDMC studies of various $z = 4$ and $z = 6$ models in Refs. [10,14,15].

For all lattices considered here, the corresponding classical temperature is always higher than the quantum temperature. Intuitively, quantum fluctuations heat up the system [10]. However, this is not generally the case with the spin dimer as a counterexample; see End Matter.

Renormalized MF form of susceptibility—The QCC is only approximate and breaks down at order X^4 where first corrections $\epsilon(\mathbf{k})$ to the renormalized MF form appear; see Eq. (7). However, this correction vanishes in the classical limit, $\lim_{S\to\infty} S^2\epsilon(\mathbf{k}) = 0 + O[(X^{(c)})^6]$. Therefore, from fourth order on, the momentum dependence of the quantum and classical $\chi(\mathbf{k})$ is inherently different, making it fundamentally impossible to extend the mapping $X(X^{(c)})$ in Eq. (8) for the full $\chi(\mathbf{k})$ to order X^4. The QCC is therefore always of approximate nature and, contrary to speculations [10], fails for $T \to 0$.

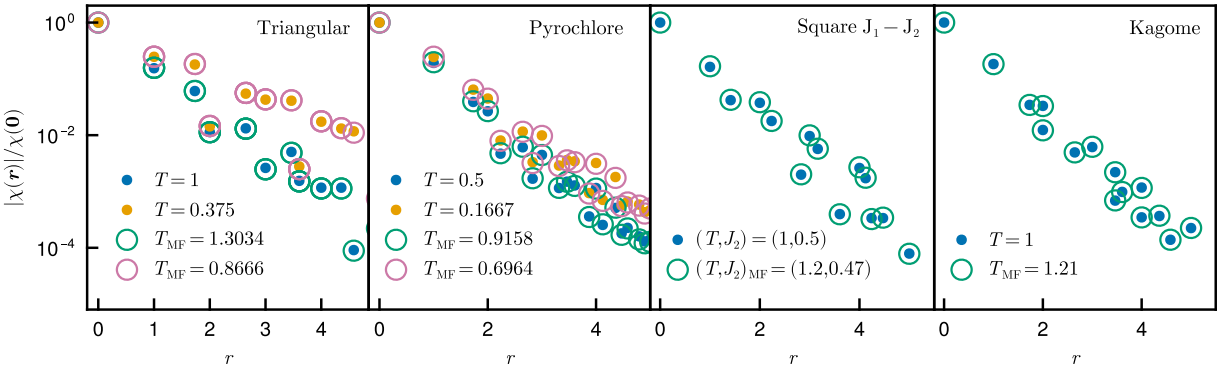

FIG. 3. Absolute values of normalized real-space spin susceptibility for AFM $S = 1/2$ Heisenberg models with $J_1 = 1$ and temperature T (dots, data taken from BDMC calculations of Refs. [10,14,15]) compared to the renormalized MF form (circles) parametrized with temperature T_{MF} (see text) optimized for best agreement. The almost perfect match for a wide range of models and for rather low T shows the accuracy of the renormalized MF form in $d > 1$ dimensions. For pyrochlore, the mean value of $|\chi(\mathbf{r})|$ with the same r is plotted to match the presentation in Fig. 4 of Ref. [15].

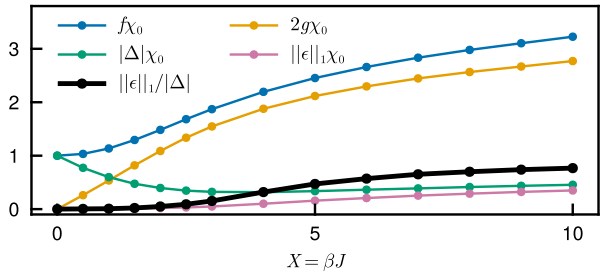

FIG. 4. Parameters of the inverse susceptibility in Eq. (4) for the cyclic $S = 1/2$ AFM Heisenberg chain of length $L = 128$. Lines are guides to the eye. For better visibility f, g, ϵ are multiplied by $\chi_0 \equiv \chi(r = 0)$. Breakdown of the renormalized MF form (and of QCC) is rooted in a non-negligible $\|\epsilon\|_1/\Delta$.

However, it turns out that corrections $\epsilon(\mathbf{k})$ to the renormalized MF form of $[T\chi(\mathbf{k})]^{-1}$ are relatively small even for small T/J (large X). This can be anticipated from the partial cancellation of diagrams as mentioned above, but it can also be inferred empirically by existence of the QCC even for very low T/J, e.g., in the pyrochlore case down to $T/J = 0.1667$ [15]. Formally, the renormalized MF form of $[T\chi(\mathbf{k})]^{-1}$ is a good approximation to the exact value as long as the minimum of the first two terms $\Delta = f - gz$ (the MF gap) is large compared to $\epsilon(\mathbf{k})$, such that $\|\epsilon\|_1/\Delta \ll 1$. Here, we use a L_1 norm in real space, $\|\epsilon\|_1 = \sum_{\mathbf{r}'} |\epsilon_{\mathbf{r},\mathbf{r}'}|$.

In the following we show that for the $d = 2$, 3 models considered in the context of QCC the susceptibility patterns are very accurately approximated by $\epsilon(\mathbf{k}) \approx 0$ well into the cooperative paramagnetic regime $T/J \gtrsim 0.1$. In Fig. 3 we match the $S = 1/2$ BDMC data from various models treated in Refs. [10,14,15] to the renormalized MF form with the empirically optimized MF temperature $T_{\mathrm{MF}} = (fb_1/g)J$. For the $J_1 - J_2$ models with the renormalized MF form $[T\chi(\mathbf{k})]^{-1} \simeq f + g_1\gamma_1(\mathbf{k}) + g_2\gamma_2(\mathbf{k})$ (cf. End Matter), also J_2 is adjusted; see the labels in Fig. 3. In all instances, the renormalized MF and BDMC data fit very well, even at temperatures below which the analytical mapping based on the truncated version of Eq. (8) would yield reasonable results. This is our second main result. Importantly, this goes beyond the empirical QCC [10] since the exact classical susceptibilities, to which the quantum susceptibilities were matched so far, also feature $O([X^{(c)}]^6)$ corrections to the renormalized MF form; cf. the discussion above.

As stated already by Kulagin *et al.* [10] the QCC clearly fails in the $d = 1$ AFM Heisenberg chain. The susceptibility of this model's classical counterpart is exactly described by the renormalized MF form with $f = [(3u^2 + 3)/(1 - u^2)]$, $g = [3u/(1 - u^2)]$, and $\epsilon(\mathbf{k}) = 0$, where $u = \coth(X) - 1/X$ [20]: therefore, QCC can be observed as long as $\|\epsilon\|_1/\Delta \ll 1$ for the quantum correlator. We calculate the susceptibility for the $S = 1/2$ model with quantum MC [21,22]. In Fig. 4 we show that already for $T/J = 0.33$, the corrections to renormalized MF form are sizable, $\|\epsilon\|_1/\Delta \approx 15\%$. This means that the range of T/J where QCC could be observed is significantly smaller in $d = 1$ than in the $d = 2$, 3 models, where no violation was found at the temperatures available to BDMC. This empirical finding can be rationalized in a $1/d$

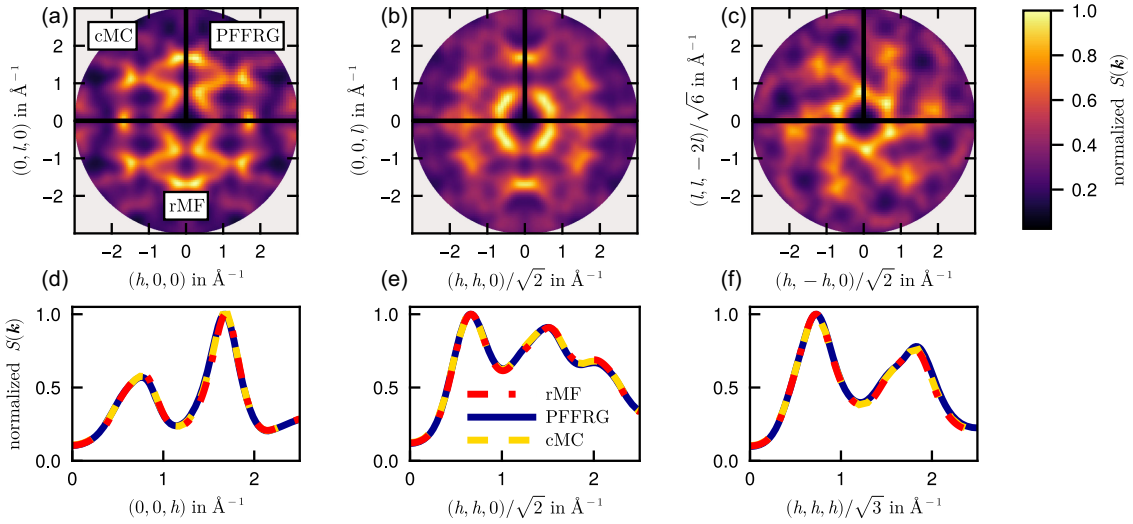

FIG. 5. Static spin structure factor $S(\mathbf{k}) = \sum_{\nu,\nu'} \chi_{\nu,\nu'}(\mathbf{k}) f_{\mathrm{Ni}^{2+}}(\mathbf{k})$ of $K_2Ni_2(SO_4)_3$ along different planes in reciprocal space, where $f_{\mathrm{Ni}^{2+}}(\mathbf{k})$ is the form factor of the Ni^{2+} ions. Panels (a)–(c) show classical MC results at $T = 0.35J_4$ (top left part of each panel), PFFRG results at flow parameter $\Lambda = 0.58J_4$ (top right), and a fit to the renormalized MF form (rMF, lower half) at $T_{\mathrm{MF}} = 0.787J_4$. Panels (d)–(f) display line cuts along three principal directions. The classical MC and PFFRG data were taken from Ref. [16].

expansion [17], where corrections to the renormalized MF form at the MF-critical temperature scale as $\epsilon(\mathbf{k}) \sim (1/d^2)$.

Finally, we test the renormalized MF form for a model of a complex realistic material $K_2Ni_2(SO_4)_3$ where QCC was empirically observed by Gonzalez *et al.* [16]. According to *ab initio* calculations [16], this $d = 3$ material realizes an $S = 1$ Heisenberg model on two interconnected trillium lattices with $\{J_1, J_2, J_3, J_4, J_5\} = \{0.066, -0.026, 0.144, 1, 0.479\}$ with dominant $J_4 = 1$. This model was treated with the ground state PFFRG [7] with results extracted at finite Matsubara frequency cutoff parameter $\Lambda = 0.58J_4$. The latter was argued to act (at least qualitatively) as a finite temperature $T \sim \Lambda$ [23]. Unlike BDMC, the error of PFFRG is uncontrolled. However, empirical confirmation of QCC with $T^{(c)} = 0.35J_4$ found in Ref. [16] suggests that the susceptibility is well described by a renormalized MF form. In Fig. 5 we match the classical MC and PFFRG susceptibilities [16] along multiple planes and cuts in $\mathbf{k}$ space to a renormalized MF form at $T_{\mathrm{MF}} = 0.787J_4$ and all J_m unchanged. The quality could be further improved by also renormalizing the latter.

Conclusion—The approximate description of quantum spin systems with classical theories is a recurring theme [24–27] and cancellations of quantum effects have been observed for various specific spin models on particular lattices [28,29]. However, the so-far empirical QCC for the spin susceptibility on general two- and three-dimensional Heisenberg models [10] revisited in this Letter stands out by its surprising universality and accuracy even for low temperatures T down to about an order of magnitude below J. Using resummed spin diagrammatic perturbation theory, we showed rigorously that the QCC is only approximate and fails at order $(J/T)^4$. At this order, the spatial dependence of the exact susceptibility for $S < \infty$ deviates from a simple renormalized MF form.

In this sense, the QCC can be understood as a symptom of a more fundamental insight put forward in this work: the renormalized MF form almost perfectly accounts for a plethora of spin susceptibility patterns in $d = 2$ and $d = 3$ reported in the literature on the basis of numerically expensive computations. We rationalize this from the partial diagrammatic cancellations of corrections as explicitly observed at order $(J/T)^4$ but likely operative also at higher orders.

The success of the renormalized MF form is surprising, since ordinary MF theory is only valid for high temperatures or lattices with large coordination numbers. For future work, it is thus an interesting question if the renormalized MF ansatz could inform the development of novel theoretical (renormalization) methods or experimental data analysis. The latter could be especially relevant for atom-tweezer array quantum simulators where $\chi(\mathbf{r})$ should be directly accessibly due to single-site control and measurement capabilities [30]. As a first step, it would be useful to extend the analytical (and approximate) QCC mapping of Eq. (8) to higher orders in (J/T) for better estimation of the renormalized MF parameters.

Acknowledgments—We thank Matías G. Gonzalez, Philip Osterholz, Johannes Reuther, Nepomuk Ritz, Lode Pollet, and Manuel Weber for helpful discussions. We acknowledge support from DFG Grant No. 524270816. B. Sb. acknowledges support from DFG through the Research Unit FOR 5413/1 (Grant No. 465199066). B. S. acknowledges funding from the Munich Quantum Valley, supported by the Bavarian state government with funds from the Hightech Agenda Bayern Plus.

[1] C. Lacroix, P. Mendels, and F. Mila, *Introduction to Frustrated Magnetism: Materials, Experiments, Theory*, 2011th ed. (Springer, Berlin Heidelberg, 2011).
[2] A. Kitaev, Anyons in an exactly solved modeland beyond, Ann. Phys. (Amsterdam) **321**, 2 (2006).
[3] L. Savary and L. Balents, Quantum spin liquids: A review, Rep. Prog. Phys. **80**, 016502 (2016).
[4] A. W. Sandvik, A. Avella, and F. Mancini, Computational studies of quantum spin systems, AIP Conf. Proc. **1297**, 135 (2010).
[5] A. Lohmann, H.-J. Schmidt, and J. Richter, Tenth-order high-temperature expansion for the susceptibility and the specific heat of spin-s Heisenberg models with arbitrary exchange patterns: Application to pyrochlore and kagome magnets, Phys. Rev. B **89**, 014415 (2014).
[6] J. Hauschild and F. Pollmann, Efficient numerical simulations with tensor networks: Tensor network Python (TeNPy), SciPost Phys. Lect. Notes 005 (2018).
[7] T. Müller, D. Kiese, N. Niggemann, B. Sbierski, J. Reuther, S. Trebst, R. Thomale, and Y. Iqbal, Pseudo-fermion functional renormalization group for spin models, Rep. Prog. Phys. **87**, 036501 (2024).
[8] W.-Y. Liu, S. Dong, C. Wang, Y. Han, H. An, G.-C. Guo, and L. He, Gapless spin liquid ground state of the spin-1/2 J_1-J_2 Heisenberg model on square lattices, Phys. Rev. B **98**, 241109(R) (2018).
[9] B.-B. Chen, L. Chen, Z. Chen, W. Li, and A. Weichselbaum, Exponential thermal tensor network approach for quantum lattice models, Phys. Rev. X **8**, 031082 (2018).
[10] S. A. Kulagin, N. Prokof'ev, O. A. Starykh, B. Svistunov, and C. N. Varney, Bold diagrammatic Monte Carlo method applied to fermionized frustrated spins, Phys. Rev. Lett. **110**, 070601 (2013).
[11] QCC is not to be confused with the fact that quantum phase transitions in d spatial dimensions can share a universality class with a classical counterpart in $d + 1$ spatial dimensions [31].
[12] S. A. Kulagin, N. Prokof'ev, O. A. Starykh, B. Svistunov, and C. N. Varney, Bold diagrammatic Monte Carlo technique for frustrated spin systems, Phys. Rev. B **87**, 024407 (2013).
[13] N. Prokof'ev and B. Svistunov, Bold diagrammatic Monte Carlo technique: When the sign problem is welcome, Phys. Rev. Lett. **99**, 250201 (2007).

[14] T. Wang, X. Cai, K. Chen, N. V. Prokof'ev, and B. V. Svistunov, Quantum-to-classical correspondence in two-dimensional Heisenberg models, Phys. Rev. B **101**, 035132 (2020).
[15] Y. Huang, K. Chen, Y. Deng, N. Prokof'ev, and B. Svistunov, Spin-ice state of the quantum Heisenberg antiferromagnet on the pyrochlore lattice, Phys. Rev. Lett. **116**, 177203 (2016).
[16] M. G. Gonzalez, V. Noculak, A. Sharma, V. Favre, J.-R. Soh, A. Magrez, R. Bewley, H. O. Jeschke, J. Reuther, H. M. Rønnow, Y. Iqbal, and I. Živković, Dynamics of $K_2Ni_2(SO_4)_3$ governed by proximity to a 3D spin liquid model, Nat. Commun. **15**, 7191 (2024).
[17] B. Schneider, R. Burkard, B. Olmos, I. Lesanovsky, and B. Sbierski, Dipolar ordering transitions in many-body quantum optics: Analytical diagrammatic approach to equilibrium quantum spins, Phys. Rev. A **110**, 063301 (2024).
[18] V. G. Vaks, A. I. Larkin, and S. A. Pikin, Self-consistent field method for the description of phase transitions, Sov. Phys. JETP **24**, 240 (1967).
[19] Y. A. Izyumov and Y. N. Skryabin, *Statistical Mechanics of Magnetically Ordered Systems* (Consultants Bureau, New York, N.Y, 1988).
[20] M. E. Fisher, Magnetism in one-dimensional systems—the Heisenberg model for infinite spin, Am. J. Phys. **32**, 343 (1964).
[21] N. Sadoune and L. Pollet, Efficient and scalable path integral Monte Carlo simulations with worm-type updates for Bose-Hubbard and XXZ models, SciPost Phys. Codebases 9 (2022).
[22] N. Sadoune and L. Pollet, Codebase release 1.0 for worm algorithm for Bose-Hubbard and XXZ models, SciPost Phys. Codebases 9 (2022).
[23] Y. Iqbal, T. Müller, P. Ghosh, M. J. P. Gingras, H. O. Jeschke, S. Rachel, J. Reuther, and R. Thomale, Quantum and classical phases of the pyrochlore Heisenberg model with competing interactions, Phys. Rev. X **9**, 011005 (2019).
[24] S. Chakravarty, B. I. Halperin, and D. R. Nelson, Two-dimensional quantum Heisenberg antiferromagnet at low temperatures, Phys. Rev. B **39**, 2344 (1989).
[25] S. Sachdev, *Quantum Phase Transitions*, 2nd ed. (Cambridge University Press, Cambridge, England, 2011).
[26] D. Dahlbom, F. T. Brooks, M. S. Wilson, S. Chi, A. I. Kolesnikov, M. B. Stone, H. Cao, Y.-W. Li, K. Barros, M. Mourigal, C. D. Batista, and X. Bai, Quantum-to-classical crossover in generalized spin systems: Temperature-dependent spin dynamics of FeI_2, Phys. Rev. B **109**, 014427 (2024).
[27] P. Park, G. Sala, D. M. Pajerowski, A. F. May, J. A. Kolopus, D. Dahlbom, M. B. Stone, G. B. Halász, and A. D. Christianson, Quantum and classical spin dynamics across temperature scales in the $S = 1/2$ Heisenberg antiferromagnet, Phys. Rev. Res. **6**, 033184 (2024).
[28] K.-H. Wu, Tunneling-induced restoration of classical degeneracy in quantum kagome ice, Phys. Rev. B **99**, 134440 (2019).
[29] Z. Wang and L. Pollet, Renormalized classical spin liquid on the ruby lattice, Phys. Rev. Lett. **134**, 086601 (2025).
[30] T. Manovitz, S. H. Li, S. Ebadi, R. Samajdar, A. A. Geim, S. J. Evered, D. Bluvstein, H. Zhou, N. U. Koyluoglu, J. Feldmeier, P. E. Dolgirev, N. Maskara, M. Kalinowski, S. Sachdev, D. A. Huse, M. Greiner, V. Vuletić, and M. D. Lukin, Quantum coarsening and collective dynamics on a programmable simulator, Nature (London) **638**, 86 (2025).
[31] S. L. Sondhi, S. M. Girvin, J. P. Carini, and D. Shahar, Continuous quantum phase transitions, Rev. Mod. Phys. **69**, 315 (1997).

End Matter

Appendix A: Multiparameter models—We generalize the QCC mapping for finite-range multiparameter $J_1 - J_2 - \cdots - J_M$ models on arbitrary lattices. However, we restrict to the case where all lattice sites are equivalent by symmetry so that $\chi(\mathbf{r} = \mathbf{0})$ used for normalization in the QCC is unambiguous. We start with a spin-S Heisenberg Hamiltonian of the type

$$H = \frac{1}{2}\sum_{\mathbf{r}_\nu,\mathbf{r}'_{\nu'}} J_{(\mathbf{r}_\nu,\mathbf{r}'_{\nu'})}\mathbf{S}_{\mathbf{r}_\nu}\cdot\mathbf{S}_{\mathbf{r}'_{\nu'}} \tag{A1}$$

and on a general Bravais lattice spanned by basis vectors $\{\mathbf{e}_1,\ldots,\mathbf{e}_n\}$ with a μ-atomic basis $\{\boldsymbol{\delta}_1,\ldots,\boldsymbol{\delta}_\mu\}$, such that each spin position is uniquely described by $\mathbf{r}_\nu = \sum_i r_i\mathbf{e}_i + \boldsymbol{\delta}_\nu$ with $r_i \in \mathbb{Z}$ and $\nu = 1,2,\ldots,\mu$. We define the matrix-valued susceptibility (or static correlator, at vanishing Matsubara frequency) as

$$\chi_{\nu\nu'}(\mathbf{k}) = \frac{1}{N}\sum_{\mathbf{r},\mathbf{r}'} e^{-i\mathbf{k}\cdot(\mathbf{r}_\nu-\mathbf{r}'_{\nu'})}\int_0^\beta \mathrm{d}\tau\langle S^z_{\mathbf{r}_\nu}(\tau)S^z_{\mathbf{r}'_{\nu'}}(0)\rangle. \tag{A2}$$

Appendix B: Parametrization of the coupling matrix—For each coupling parameter $J_1, J_2, \ldots, J_M$, we define a corresponding unit-strength pattern or coupling matrix,

$$\gamma_{m,\nu\nu'}(\mathbf{r},\mathbf{r}') = \begin{cases} 1 & : J_{(\mathbf{r}_\nu,\mathbf{r}'_{\nu'})} = J_m, \\ 0 & : \text{otherwise}, \end{cases} \tag{B1}$$

which takes bonds $(\mathbf{r}_\nu,\mathbf{r}'_{\nu'})$ as input and outputs unity only if this bond has coupling strength J_m and zero otherwise. With this definition, we obtain with $X_m = \beta J_m$ for $m = 1,2,\ldots,M$,

$$\beta J_{(\mathbf{r}_\nu,\mathbf{r}'_{\nu'})} = \sum_{m=1}^{M} X_m\gamma_{m,\nu\nu'}(\mathbf{r},\mathbf{r}'). \tag{B2}$$

Fourier transforming the expression gives

$$\beta \mathbf{J}(\mathbf{k}) = \beta \sum_{\mathbf{r},\mathbf{r}'} J_{(\mathbf{r}_\nu,\mathbf{r}'_{\nu'})} e^{-i\mathbf{k}\cdot(\mathbf{r}_\nu - \mathbf{r}'_{\nu'})} = \sum_{m=1}^{M} X_m \boldsymbol{\gamma}_m(\mathbf{k}), \tag{B3}$$

where we indicated matrices in sublattice space with bold symbols. The $\boldsymbol{\gamma}_m$ are normalized such that $\boldsymbol{\gamma}_m(\mathbf{k})\delta_{m,n} = \int_{\mathbf{q}} \boldsymbol{\gamma}_m(\mathbf{q}) * \boldsymbol{\gamma}_n(\mathbf{k}-\mathbf{q})$, where $\int_{\mathbf{k}} = (1/V_{BZ}) \int \mathrm{d}\mathbf{k}$ and $*$ is the Hadamard product in sublattice space. Since we assumed that all sites of the lattice are equivalent, the matrices $\gamma_m(\mathbf{k})$ commute $[\boldsymbol{\gamma}_m(\mathbf{k}), \boldsymbol{\gamma}_n(\mathbf{k})] = 0$.

The coordination number z_m with respect to coupling J_m can be expressed via $\int_{\mathbf{k}} \mathrm{Tr}[\boldsymbol{\gamma}_n(\mathbf{k}) \cdot \boldsymbol{\gamma}_m(\mathbf{k})] = \mu z_m \delta_{m,n}$ and the number of three-loops made from couplings l, m, n is $\mu I^{(3)}_{l,m,n} = \int_{\mathbf{k}} \mathrm{Tr}[\boldsymbol{\gamma}_l(\mathbf{k}) \cdot \boldsymbol{\gamma}_m(\mathbf{k}) \cdot \boldsymbol{\gamma}_n(\mathbf{k})]$, respectively. Recall that μ is the number of sublattices. These relations straightforwardly follow from the equivalent expressions in real space.

Appendix C: Examples for coupling matrices—As an example, the J_1-Heisenberg model on the kagome lattice can be described by $\{\mathbf{e}_1, \mathbf{e}_2\} = \{(2,0), (1,\sqrt{3})\}$ and $\{\boldsymbol{\delta}_1, \boldsymbol{\delta}_2, \boldsymbol{\delta}_3\} = \{(1,0), [\frac{1}{2}, (\sqrt{3}/2)], [-\frac{1}{2}, (\sqrt{3}/2)]\}$, where the triangular Bravais lattice sites are in the center of the hexagons. This lattice yields

$$\boldsymbol{\gamma}(\mathbf{k}) = \begin{pmatrix} 0 & 2\cos\left(\frac{k_1}{2} + \frac{\sqrt{3}k_2}{2}\right) & 2\cos\left(\frac{k_1}{2} + \frac{\sqrt{3}k_2}{2}\right) \\ 2\cos\left(\frac{k_1}{2} + \frac{\sqrt{3}k_2}{2}\right) & 0 & 2\cos(k_1) \\ 2\cos\left(\frac{k_1}{2} + \frac{\sqrt{3}k_2}{2}\right) & 2\cos(k_1) & 0 \end{pmatrix}. \tag{C1}$$

For the anisotropic $J_1 - J_2$-triangular lattice with horizontal chains coupled by J_1 and interchain coupling J_2 we have $\{\mathbf{e}_1, \mathbf{e}_2\} = \{(1,0), (1,\sqrt{3})\}$ and $\boldsymbol{\delta}_1 = (0,0)$, which leads to

$$\boldsymbol{\gamma}_1(\mathbf{k}) = 2\cos(k_1), \tag{C2}$$

$$\boldsymbol{\gamma}_2(\mathbf{k}) = 2\cos\left(\frac{k_1}{2} + \frac{\sqrt{3}k_2}{2}\right) + 2\cos\left(\frac{k_1}{2} - \frac{\sqrt{3}k_2}{2}\right). \tag{C3}$$

Appendix D: Perturbative calculation of χ—In matrix form the Larkin equation (3) reads

$$\boldsymbol{\chi}(\mathbf{k})^{-1} = \boldsymbol{\Sigma}(\mathbf{k})^{-1} + \mathbf{J}(\mathbf{k}). \tag{D1}$$

MF theory amounts to using only the $O([\beta J]^0)$ term, $\boldsymbol{\Sigma}^{(0)}(\mathbf{k}) = b_1 \delta_{\nu',\nu}$, with $b_1 = S(S+1)/3$ the first derivative of the Brillouin function at zero field. Combining Eqs. (D1) and (B3), we parametrize the *exact* inverse correlator in analogy to the one-parameter case (4) with

$$[T\boldsymbol{\chi}(\mathbf{k})]^{-1} = f + \sum_m g_m \boldsymbol{\gamma}_m(\mathbf{k}) + \boldsymbol{\epsilon}(\mathbf{k}). \tag{D2}$$

In MF approximation, $f = (1/b_1)$, $g_m = X_m$, and $\boldsymbol{\epsilon}(\mathbf{k}) = 0$. Analogously to the one-parameter case, in the full theory f is the on-site inverse susceptibility, while g_m describes the renormalized MF coupling parameters and $\boldsymbol{\epsilon}(\mathbf{k})$ collects all corrections to the MF form of the correlator.

Using the theory developed in Ref. [17], the inverse static correlator of Eq. (D2) can be expanded in X_m as

$$f = \frac{1}{b_1} + \sum_m z_m \left(\frac{1}{6}(6b_1+1)X_m^2 + \frac{1}{24}(4b_1+1)X_m^3\right) - \frac{1}{6} b_1 (6b_1+1) \sum_{l,m,n} X_m X_l X_n I^{(3)}_{l,m,n} + O(X^4), \tag{D3}$$

$$g_m = X_m + \frac{X_m^2}{12} + \frac{1}{120}(48b_1^2 + 16b_1 + 3)X_m^3 + O(X^4), \tag{D4}$$

$$\boldsymbol{\epsilon}(\mathbf{k}) = -\frac{b_1}{720} \sum_{m,n} (X_m)^2 (X_n)^2 \left(\boldsymbol{\gamma}_m(\mathbf{k}) \cdot \boldsymbol{\gamma}_n(\mathbf{k}) - \delta_{m,n} z_n - \sum_l \frac{I^{(3)}_{l,m,n}}{z_l} \boldsymbol{\gamma}_l(\mathbf{k})\right) + O(X^5). \tag{D5}$$

Appendix E: Analytic calculation of the approximate QCC—Just as in the one-parameter case $\chi(\mathbf{k})^{-1}$ is of renormalized MF form up to third order in X. It is a function of the $M+1$ parameters $f, g_1, g_2, \ldots, g_M$. Therefore, when comparing the inverse correlator $\chi(\mathbf{k})^{-1}\chi(\mathbf{r}=\mathbf{0})$ normalized with the local correlator $\chi(\mathbf{r}=\mathbf{0}) = (1/\mu)\mathrm{Tr}\int_{\mathbf{q}}\chi(\mathbf{q})$, with its classical counterpart, we can find a mapping between the two. f is fixed by the normalization and g_m can be fixed by relating X_m and $X_m^{(c)}$,

$$X_m = \frac{X_m^{(c)}}{3b_1} - \frac{\left(X_m^{(c)}\right)^2}{108b_1^2} + \left(X_m^{(c)}\right)^3 \frac{15b_1 z_m - 12b_1 - 1}{2430b_1^3} + \frac{X_m^{(c)}}{162b_1^2}\sum_{n\neq m} z_n \left(X_n^{(c)}\right)^2 + O(X^4). \tag{E1}$$

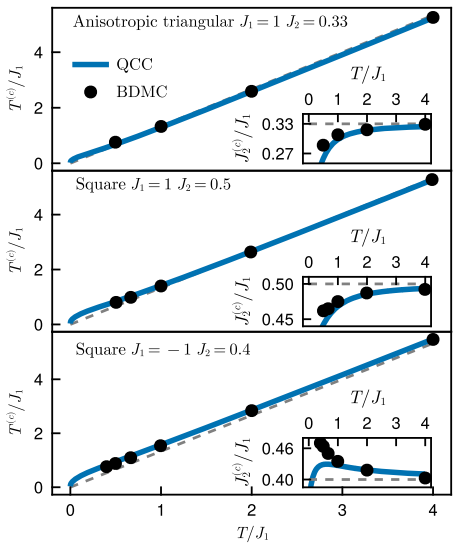

FIG. 6. Mapping between the classical and quantum temperatures for two-parameter models studied by BDMC in Ref. [14]. The solid lines are obtained by inverting Eq. (E1). The markers give the same mapping empirically obtained in Ref. [14]. The dashed line indicates the high temperature asymptotic.

This generalizes Eq. (8) of the main text. As explained there, the mapping is only approximate and ceases to exist rigorously at fourth order in X.

By inverting Eq. (E1) we capture the QCC of the two-parameter $J_1 - J_2$ models studied in Ref. [14]. In analogy to Fig. 1 we compare the empirical data [14] with Eq. (E1); see Fig. 6. The classical temperatures $T^{(c)}$ (from $X_1^{(c)}$) and $J_2^{(c)}$ (from $X_2^{(c)}$) are predicted quite well. Only the $J_2^{(c)}$ couplings of the square lattice $J_1 - J_2$ with ferromagnetic J_1 show a wrong curvature for small quantum temperatures $T/J_1 \lesssim 0.5$. This signals the breakdown of third order perturbation theory.

Appendix F: QCC for the dimer—For J_1-Heisenberg models, QCC generally depends on the correlator being a function of two parameters. Since the Heisenberg dimer $H = J\mathbf{S}_1 \cdot \mathbf{S}_2$ has only two sites and thus just two susceptibilities (local and nonlocal), there exists a trivial, exact QCC. The classical correlator is given by

$$T\chi^{(c)}(k) = \frac{1}{3} + \frac{1}{3}\left[\coth(X^{(c)}) - \frac{1}{X^{(c)}}\right]\cos(k), \tag{F1}$$

where $k \in \{0, \pi\}$ and the quantum correlator reads

$$T\chi(k) = \frac{e^X - 1 + X}{2(e^X + 3)} + \frac{e^X - 1 - X}{2(e^X + 3)}\cos(k). \tag{F2}$$

Therefore, the exact QCC between the two can be found by solving

$$\left[\coth(X^{(c)}) - \frac{1}{X^{(c)}}\right] = \frac{e^X - 1 - X}{e^X - 1 + X}. \tag{F3}$$

Setting $J = 1$, for large temperatures $T^{(c)} \simeq \frac{4}{3}T > T$ the system is heated up by the quantum fluctuation but for low temperatures the classical temperature is exponentially reduced $T^{(c)} = [(2/T^2)e^{-1/T}]T$. This is related to the fact that the quantum dimer is gapped so that susceptibilities decrease to zero at low temperature where the state of the classical system can still be easily perturbed. To make up for this difference, $T^{(c)} < T$ at low temperatures. Other (trivial) examples where the QCC holds exactly are the cyclic spin trimer, and the Heisenberg model in infinite dimensions.

5 Dynamic High Temperature Expansion

5.1 Overview

To improve upon the fourth-order expansion of the dynamic spin-spin correlation function in $\frac{J}{T}$ obtained in Ref. [P5], we use the restricted graph approach (see Sec. 2.6), which is often used in the high temperature expansion community [OB96]. In Ref. [P7], we establish how, by using the kernel-trick introduced in Refs. [P4; P5] (see Sec. 2.7.2), we can generalize the HTE to dynamic and momentum-resolved spin-spin correlators. We name the method *dynamic*-HTE (Dyn-HTE). The results are a simultaneous expansion in $x = J/T$ and inverse Matsubara frequency ω_m of the spin-spin correlator,

$$T\,\langle S_i^\alpha(i\omega_m) S_{i'}^\alpha(-i\omega_m)\rangle = \begin{cases} p_{ii'}^{(0)}(x), & \omega_m = 0, \\ \sum_{r=1}^{r_{\max}} p_{ii'}^{(2r)}(x) \left(\frac{x}{\beta\omega_m}\right)^{2r} + \mathcal{O}(x^{n_{\max}+1}), & \omega_m \neq 0, \end{cases} \tag{5.1}$$

where $p^{(2r)}(x)$ are polynomials of degree $n_{\max} - 2r$. We are able to analytically calculate the value of all $\sim 10 \times 10^6$ graphs that exist up to order $n_{\max} = 12$, for $S \in \{\frac{1}{2}, 1\}$. This only has to be done once and immediately gives access to results on all possible lattice geometries. When a lattice geometry is specified, all $\sim 10 \times 10^6$ graphs are embedded into the lattice, where each vertex of a graph has to be matched one-to-one to a lattice-site and each edge has to be matched with a nearest neighbor bond. This can be done via calculating the number of subgraph isomorphisms of each graph in the lattice. In practice, this is achieved by our high-performance *Julia* code that is publicly available, including a comprehensive documentation and multiple tutorials [P9]. We thoroughly benchmark our code against exact results on finite spin clusters, quantum Monte Carlo results on 1D systems and equal-time correlators from HTE expansions. As a first application, we compute the static susceptibility on the triangular lattice where we find clear deviations from earlier diagrammatic Monte Carlo studies. The good convergence of various Padé approximants of our perturbative series support the validity of our data. Remarkably, the renormalized-mean-field form for the static susceptibility found in Ref. [P6] (see Chapter 4) matches the exact static susceptibility up to 12^{th} order in J/T with astounding accuracy [P7].

While the Dyn-HTE allows us to calculate the Matsubara correlator down to reasonably low T/J, the resulting data at finite Matsubara frequency $i\omega_m \neq 0$ does not directly relate to any physical observable. In contrast, the *real*-frequency dynamic structure factor (DSF) $S(\mathbf{k}, \omega)$ is among the most feature-packed experimental observables for quantum spin systems in equilibrium (see Sec. 2.1). For solid-state samples, the DSF is directly accessible via inelastic neutron scattering in a momentum-resolved manner. However, the DSF is often hard to simulate in an unbiased and accurate way, especially for frustrated and high-dimensional models at intermediate temperature.

In Ref. [P8] we identify a direct correspondence between the polynomials $p_{\mathbf{k}}^{(2r)}(x)$ in the Matsubara correlator's Dyn-HTE (5.1) and the frequency moments of the spin relaxation function $R_{\mathbf{k}}(\omega)$. From the moments, we can reconstruct $R_{\mathbf{k}}(\omega)$ via its continued fraction rep-

resentation with positive definite parameters. Since we only know the HTE of a finite number of moments to a finite expansion order, we resum the first $r_{\max} \simeq 4$ moments using various Padé approximants to recover the first $r_{\max}$ continued fraction parameters. We then follow Ref. [VM94] and extrapolate them linearly to recover a *faithful* continuous, non-negative, and properly symmetric spectral function. This is further detailed in App. A. Benchmarks of the so obtained DSF for the 1D chain against DMRG, show very good agreement down to temperatures $J/4$. For the spin-1 chain, the spectrum reproduces the expected DMRG (para)-magnon dispersion, including temperature-softened signatures of the Haldane gap. In addition, at $T = J/4$ the method correctly captured the (para)-magnon dispersion of the 2D square-lattice antiferromagnet as known from QMC. These results establish the validity of our method.

For applications, we consider spin-$\frac{1}{2}$ triangular lattice antiferromagnet and the spin-1 antiferromagnet on the pyrochlore lattice. The triangular lattice model exhibits 120°-order at $T = 0$. For $\frac{1}{4} \lesssim T/J \lesssim 1$, however, an enigmatic anomaly occurs: As first found by conventional HTE, static properties deviate strongly from renormalized-classical predictions [ESY93; Che+19]. We are able to demonstrate a temperature-frequency scaling of the DSF at the ordering wavevector. This hints that the anomalous temperature regime might be explained by a quantum critical fan, possibly emerging from the quantum critical point of the J_1-J_2 model that is very close in parameter space ($J_2 \gtrsim 0.06 J_1$). The spin-1 pyrochlore material $NaCaNi_2F_7$ is known to be approximately described by a Heisenberg model with possibly smaller corrections like biquadratic interactions. Multiple semiclassical methods have been employed to compute the DSF of the Heisenberg model on this lattice [Zha+19; PS25], but a faithful quantum calculation had not yet been achieved. With the Dyn-HTE, we close this methodological gap.

[P7] *High-temperature series expansion of the dynamic Matsubara spin correlator*
Ruben Burkard, **Benedikt Schneider**, Björn Sbierski
pages 119–133 / arXiv:2505.23699 Phys. Rev. B 113, 075102 (2026)

[P8] *Dynamic correlations of frustrated quantum spins from high-temperature expansion*
Ruben Burkard, **Benedikt Schneider**, Björn Sbierski
pages 134–141 / arXiv:2505.14571 Phys. Rev. Lett. 136, 056501 (2026)

[P9] *Dyn-HTE: Initial Code Release of the Dyn-HTE.Jl Package*
Björn Sbierski, **Benedikt Schneider**, Ruben Burkard Zenodo (2025)

High-temperature series expansion of the dynamic Matsubara spin correlator

Ruben Burkard,[1] Benedikt Schneider,[2,3] and Björn Sbierski[1]

[1]*Institut für Theoretische Physik, Universität Tübingen, Auf der Morgenstelle 14, 72076 Tübingen, Germany*

[2]*Department of Physics and Arnold Sommerfeld Center for Theoretical Physics, Ludwig-Maximilians-Universität München, Theresienstraße 37, 80333 Munich, Germany*

[3]*Munich Center for Quantum Science and Technology (MCQST), 80799 Munich, Germany*

(Received 1 June 2025; revised 25 August 2025; accepted 1 October 2025; published 2 February 2026)

The high-temperature series expansion for quantum spin models is a well-established tool to compute thermodynamic quantities and equal-time spin correlations, in particular for frustrated interactions. We extend the scope of this expansion to the dynamic Matsubara spin-spin correlator and develop an algorithm that yields exact expansion coefficients in the form of rational numbers. We focus on Heisenberg models with a single coupling constant J and spin lengths $S \in \{1/2, 1\}$. The expansion coefficients up to 12th order in J/T are precomputed on all possible $\sim 10^6$ graphs embeddable in arbitrary lattices and are provided in a repository. This enables calculation of static momentum-resolved susceptibilities for arbitrary site pairs or wave vectors. We test our results for the antiferromagnetic $S = 1/2$ chain and triangular lattice model. An important application that we discuss in a companion letter is the calculation of real-frequency dynamic structure factors. This is achieved by identifying the high-frequency expansion coefficients of the Matsubara correlator with frequency moments of the spectral function.

DOI: 10.1103/1l92-z6qd

I. INTRODUCTION

The high-temperature series expansion (HTE) is an invaluable tool for the theoretical analysis of quantum spin systems in thermal equilibrium, for monographs see, e.g., Refs. [1,2]. The HTE is oblivious to frustration and entanglement, is formulated directly in the thermodynamic limit, and remains applicable in high dimensions. Up to now, the HTE can target thermodynamic quantities like entropy, heat capacity, or uniform susceptibility and was also applied to obtain equal-time spin correlation functions $G^{zz}_{ii'} = \langle S^z_i S^z_{i'} \rangle$ for arbitrary site pairs ii'. Key technical advancements of the HTE method included an extension to arbitrary spin length S [3,4], flexible open-source software packages [5], or inclusion of magnetic fields [6]. As the name suggests, the main challenge of HTE is to reach temperatures much below the spin interaction $T \ll J$ when resummation schemes of the bare series give ambiguous and thus nonreliable results. To some extent, these issues can be bypassed if qualitative information on the very low-T behavior is available [7].

HTE has an impressive track-record of achievements: For example, it has first revealed [8] the *anomalous* intermediate-T behavior of the nearest-neighbor $S = 1/2$ Heisenberg AFM on the triangular lattice which cannot be understood in the renormalized-classical picture suggested by the ordered ground state. The latter picture predicts a much smaller entropy and a much larger correlation length than found from HTE. The underlying physical reason of this effect is still not well understood [9,10]. Another example is the accurate quantitative analysis of thermal phase transitions in otherwise challenging three-dimensional frustrated models [11].

However, in order to achieve a better understanding of collective phenomena arising in equilibrium quantum spin systems it is mandatory to also computationally target spin dynamics. Here the most elementary observable is the dynamical spin-spin correlator $G^{zz}_{ii'}(t) = \langle S^z_i(t) S^z_{i'} \rangle$ with $S^z_i(t) = e^{iHt} S^z_i e^{-iHt}$ representing a local spin operator in the Heisenberg picture [12]. The dynamical structure factor which is defined as a spatial and temporal Fourier transform of $G^{zz}_{ii'}(t)$ contains rich information on the dipolar excitation spectrum, the presence and stability of quasiparticles or the fractionalization of spin-flip excitations [13]. It is routinely measured using inelastic neutron scattering [14] in the solid-state context and recently also for cold-atom quantum simulators [15] via Raman spectroscopy. Although the dynamical structure factor can be calculated in various ways for different settings [16] (e.g., via exact diagonalization and linked-cluster methods [17], spin-wave theory [18], and tensor-networks [19]), it is still desirable to approach spin dynamics via the HTE and benefit from its above-mentioned strengths. This is particularly important for (strongly frustrated) spin liquid candidates [20] where the observables available from conventional HTE are often featureless as functions of temperature and momentum. A natural intermediate goal to this endeavor is the extension of the HTE for the dynamical spin correlation function in imaginary time $t \to -i\tau \in i\mathbb{R}$ which is a somewhat simpler task given the benefits of the Matsubara formalism for perturbation theory in equilibrium [12].

In this work, we develop this extension of the HTE to the dynamic imaginary frequency (Matsubara) spin-spin correlator. We term this method dynamic HTE (Dyn-HTE). We lay out the general formalism and apply it to Heisenberg models with a single coupling constant J and spin lengths $S \in \{1/2, 1\}$. The coefficients for the expansion in powers of $x \equiv J/T$ up to order $n_{\max} = 12$ (and in inverse frequency to order $\lfloor n_{\max}/2 \rfloor$) are precomputed exactly in the form of

rational numbers on all possible $\sim 10^6$ graphs and are offered for download along with powerful tools for the creation of arbitrary lattices and efficient graph embeddings [21]. On the technical side Dyn-HTE hinges on the exploitation of the recently developed Kernel trick [22] which solves the $(n+2)$-fold imaginary-time integrals (required at expansion order n) analytically. Interestingly, the numerical cost for the expansion in order n is only modestly increased compared to the conventional HTE for the equal-time correlator. Depending on graph topology the extra effort is by a factor of n in the worst case.

For historic context, early developments of spin-diagrammatic schemes date back to the late 1960s [23,24] where the Wick theorem was generalized for spin operators; see also Ref. [25] for a modern recursive formulation. Recently, these ideas have partially been revived in the development of a functional-renormalization group approach for spin systems [25–27] which in principle can also be used to generate order-by-order expansions of the Matsubara correlator [28]. However, the high expansion orders achieved by Dyn-HTE in this work have not been matched by any other approach.

One experimental observable directly available from Dyn-HTE is the static susceptibility for arbitrary site pairs. We consider the AFM $S = 1/2$ Heisenberg chain and compare the static susceptibility from Dyn-HTE against error-controlled quantum Monte Carlo (QMC). We also report the static susceptibility for the frustrated triangular lattice model. As an application we employ the static susceptibility of Dyn-HTE to showcase the accuracy of a simple approximate parametrization of its momentum dependence as suggested recently under the name renormalized mean-field form.

Finally, as motivated above, a main application of the Matsubara correlator is its analytical continuation to the real-frequency dynamical spin structure factor [12]. A diverse set of methods like QMC or pseudofermion-based diagrammatic approaches [29–33] produce approximate numerical correlator data on a limited set of points on the Matsubara axis. In such a situation, despite recent advances [34–38], this analytical continuation is an ill-conditioned and error-prone procedure. For Dyn-HTE, in contrast, the obtained exact expansion can be regrouped in form of a high-frequency expansion (in inverse Matsubara frequency). In our companion work [39] we show that the associated expansion coefficients can be identified with the frequency moments of the (real-frequency) spectral function from which the dynamical structure factor can be reconstructed by standard methods. This means that Dyn-HTE allows to bypass the standard ill-defined analytical continuation procedure.

II. HEISENBERG SPIN MODEL

We consider a system of length-S quantum spins with operators S_i^α, where $\alpha = x, y, z$. The subscript $i = 1, 2, \ldots, N$ refers to the site at position $\mathbf{r}_i$ of an arbitrary lattice $\mathcal{L}$. The spins interact via Heisenberg exchange characterized by a *single* coupling constant J along an arbitrary subset of all $N(N-1)/2$ site pairs which we call bonds (ii'). This includes the important case of symmetry-related nearest-neighbor interactions but also all-to-all or spatially disordered (but equal) interactions like in a lattice with vacancies. The Hamiltonian reads

$$H = J \sum_{(ii')} \left(S_i^+ S_{i'}^- + S_i^- S_{i'}^+ + S_i^z S_{i'}^z \right) \equiv J \sum_{(ii')} V_{ii'}, \tag{1}$$

where $i < i'$ (no on-site terms). The spin ladder operators are $S_i^\pm = (S_i^x \pm i S_i^y)/\sqrt{2}$. We further assume the absence of external magnetic fields or spontaneously broken symmetries (time reversal and spin rotation). None of these assumptions or the restriction to the model in Eq. (1) are fundamental for Dyn-HTE and can be relaxed in future extensions in parallel to the developments in the history of conventional HTE [2].

We assume thermal equilibrium at temperature $T = 1/\beta$ ($k_B = \hbar = 1$). The density matrix is $\rho = e^{-\beta H}/Z$ with $Z = \operatorname{tr} e^{-\beta H}$ the partition function and thermal averages of operators are given by

$$\langle \ldots \rangle \equiv \operatorname{tr}[\ldots \rho] = \operatorname{tr}[\ldots e^{-\beta H}]/Z. \tag{2}$$

For most applications, we assume translational invariance and place the spins on a regular lattice at positions

$$\mathbf{r}_i = \mathbf{R}_i + \mathbf{b}_i, \tag{3}$$

where the label i selects both the site $\mathbf{R}_i$ of a Bravais lattice and a basis vector $\mathbf{b}_i \in \{\mathbf{b}^{(1)}, \ldots, \mathbf{b}^{(N_b)}\}$. We assume N_c Bravais lattice sites (with periodic boundary conditions) and N_b basis vectors so that $N = N_c N_b$.

III. MATSUBARA SPIN CORRELATOR AND DYN-HTE

The imaginary-frequency (Matsubara) spin-spin correlator is defined as [12]

$$G_{ii'}^{zz}(i\nu_m) = T \int_0^\beta \mathrm{d}\tau \mathrm{d}\tau' \, e^{i\nu_m(\tau-\tau')} \left\langle \mathcal{T} S_i^z(\tau) S_{i'}^z(\tau') \right\rangle, \tag{4}$$

where $\nu_m = 2\pi T m$ with $m \in \mathbb{Z}$ is a (bosonic) Matsubara frequency and $S_i^z(\tau) = e^{H\tau} S_i^z e^{-H\tau}$ denotes *imaginary* time evolution. The operator $\mathcal{T}$ enforces imaginary time ordering, the operator with larger imaginary time argument is moved to the left. Note that the double integral is often replaced by a single integral over the difference $\tau - \tau'$ but the form in (4) will prove useful later. Due to spin rotation symmetry in the Heisenberg Hamiltonian, Eq. (4) also determines correlations for all other spin-flavor combinations, $G^{\alpha\alpha'} = \delta_{\alpha\alpha'} G^{zz}$ and the zz superscript of G^{zz} is dropped in the following to ease notation. The spatial Fourier transform of Eq. (4) reads

$$G_{\mathbf{k}}(i\nu_m) = \frac{1}{N} \sum_{i,i'} e^{-i\mathbf{k}\cdot(\mathbf{r}_i - \mathbf{r}_{i'})} G_{ii'}(i\nu_m). \tag{5}$$

The symmetries of $G_{ii'}(i\nu_m)$ follow from its definition (4) and the Hamiltonian (1): Hermitian conjugation leads to a reality condition $G_{ii'}(i\nu_m) \in \mathbb{R}$ and time-reversal symmetry ensures invariance under frequency flip $G_{ii'}(i\nu_m) = G_{ii'}(-i\nu_m)$. This also implies symmetry under exchange of site indices $G_{ii'}(i\nu_m) = G_{i'i}(i\nu_m)$ which leads to

$$G_{\mathbf{k}}(i\nu_m) = G_{-\mathbf{k}}(i\nu_m)^\star. \tag{6}$$

Hence, with inversion symmetry, $G_{\mathbf{k}}(i\nu_m) \in \mathbb{R}$.

As we show in Sec. IV, the Dyn-HTE of the Matsubara correlator (4) takes the form of a double expansion in $x = J/T$ and inverse Matsubara frequency $1/\nu_m$. To order $n_{\max}$ in x, Dyn-HTE reads

$$TG_{ii'}(i\nu_m) = \begin{cases} p_{ii'}^{(0)}(x) & : m = 0 \\ \sum_{r=1}^{r_{\max}} p_{ii'}^{(2r)}(x)\left(\frac{x}{2\pi m}\right)^{2r} & : m \neq 0 \end{cases} + O\left(x^{n_{\max}+1}\right), \tag{7}$$

where $r_{\max} = \lfloor n_{\max}/2 \rfloor$ is the integer floor of $n_{\max}/2$. The dimensionless polynomials $p_{ii'}^{(2r)}(x)$ for are of degree $n_{\max} - 2r$ with (real) rational coefficients, here $r = 0, 1, 2, \ldots$. Depending on the lattice and site pair ii', some of the polynomial coefficients can be zero. Note that the form (7) is consistent with the symmetries of the Matsubara correlator discussed above.

Our open-source numerical implementation [21] provides the exact polynomial coefficients in Eq. (7) as rational numbers for *arbitrary* lattices $\mathcal{L}$ and all site pairs ii' therein. Currently spin lengths $S \in \{1/2, 1\}$ and maximum expansion order $n_{\max} = 12$ are available.

We conclude this section with a review of the physical content [12] of the Matsubara spin correlator (4). At zero frequency, $m = 0$, the Matsubara correlator yields the static susceptibility $\chi_{ii'}$. The latter is defined as the (negative) linear isothermal response of z magnetization at site i to a static local magnetic field perturbing the Hamiltonian H via $h_{i'}^z S_{i'}^z$ [40],

$$G_{ii'}(i\nu_m = 0) = \chi_{ii'} = -\partial_{h_{i'}^z} \langle S_i^z \rangle \big|_{h_{i'}^z = 0}. \tag{8}$$

At finite frequency $m \neq 0$, the Matsubara correlator does *not* directly represent an observable physical quantity. It is mainly considered for the simplicity of the diagrammatic field-theoretical framework which can be employed for its computation [12]. Usually, numerical data for the Matsubara correlator $G_{ii'}(i\nu_m)$ evaluated at a finite set of frequencies ν_m is linked to its real-frequency version by analytic continuation as discussed in Sec. I. Dyn-HTE allows to take a different and more stable route and never evaluates numerical values for $G_{ii'}(i\nu_m)$: As we show in our companion letter [39], the high-frequency expansion coefficients from Eq. (7) are in direct correspondence to the short-time expansion coefficients of the real-time correlator,

$$p_{ii'}^{(2r)} \sim \partial_t^{2r-1} \langle S_i^z(t) S_{i'}^z \rangle \big|_{t=0}. \tag{9}$$

The object on the right-hand side of Eq. (9) can also be identified with the (real-frequency) moments of the spectral function [41]. Using equations of motion, the moments can be unraveled as equal-time correlators of $2r-1$-fold nested commutators, $\sim\langle [\ldots[S_i^z, H], H], \ldots, H] S_{i'}^z \rangle$. Even for moderate r, these are hard to compute by standard means beyond the case of one dimension and $T = \infty$. This explains the value of Dyn-HTE's access to (the HTE of) $p_{ii'}^{(2r)}$ for these cases. The full spectral function and dynamical structure factor can be reconstructed based on a moderate number of frequency moments via continued fraction representations [41–45]. In our companion letter [39] we discuss this in detail and show benchmarks and applications centered around the dynamical structure factor. In contrast, the remainder of the current work will be concerned with the efficient evaluation of the Dyn-HTE, i.e., the polynomials $p_{ii'}^{(2r)}(x)$ in Eq. (7). Here we also present, benchmark, and discuss results for the Matsubara correlator in imaginary frequency.

IV. DERIVATION OF DYN-HTE

In this central technical section we derive the Dyn-HTE as in Eq. (7) and provide an efficient algorithm for its calculation. To start, we split the Hamiltonian (1) into a noninteracting part $H_0 = 0$ (vanishing in the absence of a magnetic field) and an interacting part V (here the full H) and define the dimensionless expansion coefficients $c_{ii'}^{(n)}(i\nu_m)$ of the Matsubara correlator via

$$TG_{ii'}(i\nu_m) = \sum_{n=0}^{\infty} (-x)^n c_{ii'}^{(n)}(i\nu_m), \quad \left(x = \frac{J}{T}\right). \tag{10}$$

The lowest-order $n = 0$ term represents the Curie susceptibility of a free spin which is local and static (nonzero only for $m = 0$), $c_{ii'}^{(0)}(i\nu_m) = \delta_{ii'}\delta_{0,m} S(S+1)/3$.

A. Expansion coefficients

General perturbation theory for the Matsubara correlator [12] provides an expression for the remaining expansion coefficients in Eq. (10) at order $n = 1, 2, \ldots$,

$$c_{ii'}^{(n)}(i\nu_m) = \frac{T^{n+2}}{n!} \sum_{b_1,\ldots,b_n} \int_0^\beta e^{i\nu_m(\tau-\tau')} \mathrm{d}\tau_1 \ldots \mathrm{d}\tau_n \mathrm{d}\tau \mathrm{d}\tau' \times \left\langle \mathcal{T} V_{b_1}(\tau_1) \ldots V_{b_n}(\tau_n) S_i^z(\tau) S_{i'}^z(\tau') \right\rangle_0^{\text{V-con}}. \tag{11}$$

The sum is over bonds $b_l = (i_l i_l')$ and operator time arguments as in $V_{b_1}(\tau_1)$ now refer to (interaction-picture) evolution with respect to H_0 only. This is trivial for our case, $H_0 = 0$, e.g., $V_{b_1}(\tau_1) = V_{b_1}$. Nevertheless we must keep the time arguments because by virtue of $\mathcal{T}$ they determine the ordering of the string of generally noncommuting operators. These operators are thus distinguishable regardless of the chosen bonds b_l. The $\langle \ldots \rangle_0$ denotes a thermal average with respect to Hamiltonian H_0. Since $H_0 = 0$, the former is simply an (effectively) infinite temperature average or normalized trace over the whole N-site spin Hilbert space, $\langle \ldots \rangle_0 = \mathrm{tr}[\ldots]/(2S+1)^N$, which factorizes according to site index, e.g., $\langle S_1^z S_2^+ S_1^z S_2^- \rangle_0 = \langle S_1^z S_1^z \rangle_0 \langle S_2^+ S_2^- \rangle_0$ with the on-site operator order maintained.

The superscript "V-con" on the right-hand side of Eq. (11) refers to the V-connected correlator which contains all contributions to order V^n, as well as those from the expansion of the partition function Z in the denominator on the right-hand side of Eq. (2). Following Ref. [46], it can be written via recursive subtractions from the "full" correlator

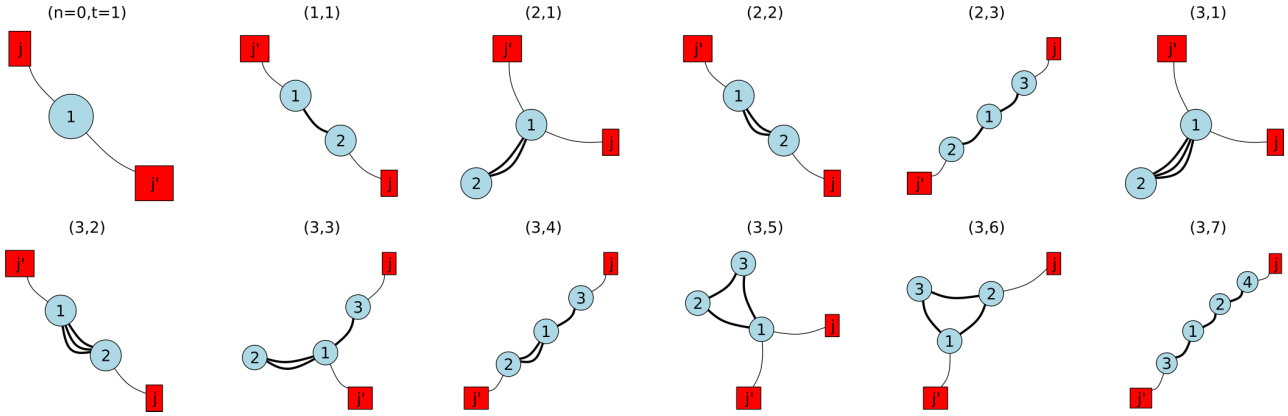

FIG. 1. All required graphs $g_t^{(n)}$ with $n = 0, 1, 2, 3$ edges (black lines) and arbitrary numbered vertices (blue circles). Terminal vertices j, j' (also blue circles) are indicated by their red-square terminal flags attached with thin gray lines. The symmetry factor is $s[g_t^{(n)}] = 1$ for all graphs shown except for $(n, t) = (3, 5)$ where it is two (exchange of vertices $2 \leftrightarrow 3$).

[without V-con, cf. (2)],

$$\left\langle \mathcal{T} V_{b_1}(\tau_1)\cdots V_{b_n}(\tau_n) S_i^z(\tau) S_{i'}^z(\tau')\right\rangle_0^{\text{V-con}} = \left\langle \mathcal{T} V_{b_1}(\tau_1)\cdots V_{b_n}(\tau_n) S_i^z(\tau) S_{i'}^z(\tau')\right\rangle_0 - \sum_{S\subsetneq\{1,\ldots,n\}} \left\langle \mathcal{T}\left[\prod_{k\in S} V_{b_k}(\tau_k)\right] S_i^z(\tau) S_{i'}^z(\tau')\right\rangle_0^{\text{V-con}} \left\langle \mathcal{T} \prod_{l\in\{1,\ldots,n\}\setminus S} V_{b_l}(\tau_l)\right\rangle_0, \tag{12}$$

where the sum is over true subsets S of the set $\{1, \ldots, n\}$ (including the empty set) and the recursion terminates at $\langle \mathcal{T} S_i^z(\tau) S_{i'}^z(\tau')\rangle_0^{\text{V-con}} \equiv \langle \mathcal{T} S_i^z(\tau) S_{i'}^z(\tau')\rangle_0$. We insert Eq. (12) in Eq. (11) and obtain

$$c_{ii'}^{(n)}(i\nu_m) = \sum_{b_1,\ldots,b_n} \frac{T^{n+2}}{n!} \int_0^\beta e^{i\nu_m(\tau-\tau')} \mathrm{d}\tau_1 \ldots \mathrm{d}\tau_n \mathrm{d}\tau \mathrm{d}\tau' \left\{ \left\langle \mathcal{T} V_{b_1}(\tau_1)\cdots V_{b_n}(\tau_n) S_i^z(\tau) S_{i'}^z(\tau')\right\rangle_0 - \sum_{S\subsetneq\{1,\ldots,n\}} \left\langle \mathcal{T}\left[\prod_{k\in S} V_{b_k}(\tau_k)\right] S_i^z(\tau) S_{i'}^z(\tau')\right\rangle_0^{\text{V-con}} \left\langle \mathcal{T} \prod_{l\in\{1,\ldots,n\}\setminus S} V_{b_l}(\tau_l)\right\rangle_0 \right\}. \tag{13}$$

B. Graph-based evaluation of bond sums

Compared to the established HTE for equal-time spin-spin correlators $\langle S_i^z S_{i'}^z\rangle$, the new and challenging aspect in Eq. (13) are the $n+2$-dimensional imaginary time integrals. We relegate the integral evaluation to Sec. IV D. Here we first focus on the bond sums in Eq. (13), which we expose by summarizing the rest as follows:

$$c_{ii'}^{(n)}(i\nu_m) \equiv \sum_{b_1,\ldots,b_n} F_{ii'}^{(n)}(b_1, \ldots, b_n; i\nu_m). \tag{14}$$

Efficient evaluation strategies for these bond sums are well developed in the literature on conventional HTE [2]. The following discussion of the necessary elements of these strategies is self-contained and does not assume any prior knowledge. In a nutshell, our plan is to evaluate the expansion of the Matsubara correlator not directly for a full lattice $\mathcal{L}$, but first for individual lattice snippets with only n bonds which are called graphs, $g^{(n)}$. These are then added up as they fit into the full lattice. Formally speaking, we reorganize the sum over (potentially identical) lattice bonds $\sum_{b_1,\ldots,b_n}$ as a sum over evaluations of $F_{ii'}^{(n)}$ on these graphs,

$$c_{ii'}^{(n)}(i\nu_m) = \sum_{g^{(n)}} e(\mathcal{L}, i, i', g^{(n)}) c_{g^{(n)}}(i\nu_m), \tag{15}$$

$$c_{g^{(n)}}(i\nu_m) = \sum_{\{e_1,\ldots,e_n\}\to\{\tilde{e}_1,\ldots,\tilde{e}_n\}} F_{jj'}^{(n)}(\tilde{e}_1, \ldots, \tilde{e}_n; i\nu_m). \tag{16}$$

A (multi-)graph of order n denoted by $g^{(n)}$ can be thought of as a lattice snippet with n bonds; see Fig. 1. Formally, it is defined by the multiset of n (not necessarily distinct) edges $\{e_1, \ldots, e_n\}$ (thick black lines) connecting its arbitrarily numbered vertices (blue circles) which contain the terminal vertices j, j' (blue circles highlighted by attached red-square flags). The terminal vertices indicate the position of the external operators S_i^z and $S_{i'}^z$. Different graphs are distinguished by graph topology, Fig. 1 shows all topological distinct graphs $g_t^{(n)}$, labeled by $t = 1, 2, \ldots$ with up to $n = 3$ edges that are required for our purpose. As we motivate later, two graphs only differing by the exchange of terminals $j \leftrightarrow j'$ are considered topologically equivalent.

Having defined the graph $g^{(n)}$ as a lattice snippet, we next need to place it into the full lattice $\mathcal{L}$. This is

TABLE I. Embedding factor $e(\mathcal{L}, i, i', g_t^{(n)})$ for various lattices $\mathcal{L}$ and various separations between external sites i, i'. Here "loc" denotes local ($i = i'$) while "(n)nn" denotes (next-) nearest neighbor. A missing entry means $e(\mathcal{L}, i, i', g_t^{(n)}) = 0$.

g	$g_1^{(0)}$	$g_1^{(1)}$	$g_1^{(2)}$	$g_2^{(2)}$	$g_3^{(2)}$	$g_1^{(3)}$	$g_2^{(3)}$	$g_3^{(3)}$	$g_4^{(3)}$	$g_5^{(3)}$	$g_6^{(3)}$	$g_7^{(3)}$
dimer loc	1		1			1						
dimer nn		1		1			1					
trimer loc	1		2			2				1		
trimer nn		1		1	1		1	2	2		1	
chain loc	1		2			2						
chain nn		1		1			1	2				
chain nnn					1				2			
sq. lat. loc	1		4			4						
sq. lat. nn		1		1			1	6				2
tri. lat. loc	1		6			6				6		
tri. lat. nn		1		1	2		1	10	4		2	4

done at the *embedding* step, formally expressed in Eq. (15). Here the embedding factor $e(\mathcal{L}, i, i', g^{(n)}) \in \{0, 1, 2, \dots\}$ counts the number of subgraph isomorphisms from the graph $g^{(n)}$ (with edge-multiplicities ignored) to the lattice $\mathcal{L}$ divided by the graphs' symmetry factor $s[g^{(n)}] \in \{1, 2, \dots\}$ to avoid overcounting due to the arbitrary vertex numbering. The symmetry factor is the number of graph isomorphisms that keep the terminal vertices invariant and respect the edge multiplicities, see the caption of Fig. 1 for examples for $s[g^{(n)}]$.

For the embedding $g^{(n)} \to \mathcal{L}$ we require the assignments $(i, i') \to (j, j')$ or $(i, i') \to (j', j)$ to match the positions of the external operators. Taking into account also the latter assignment $(i, i') \to (j', j)$ allows us to skip graphs which are connected to another graph in the list by an exchange of $j \leftrightarrow j'$. This assignment is not counted if $g^{(n)}$ is mapped to itself under $j \leftrightarrow j'$. As an example, embedding factors for a number of simple lattices are given in Table I. For two- and in particular three-dimensional lattices the embedding step can be numerically demanding. To ensure efficiency, our numerical implementation [21] builds on lattice generating functionalities provided in the software package *SpinMC.jl* [47], relies on space-group symmetries for speedup and uses advanced graph-theoretical algorithms [48,49].

Note that only graphs $g^{(n)}$ with a single connected component provide a nonzero contribution to $c_{ii'}^{(n)}(i\nu_m)$. Indeed, if there are multiple connected components, then the total contribution will vanish in the course of the recursion involved in Eq. (13). Likewise, we skip graphs with (generalized) leaves, which are parts connected to the spline of the graph (the part with the terminal vertices) by a single edge. Such graphs would only contribute for finite field h which we set to zero in the model (1). Similar considerations apply for vacuum graphs to be defined below.

Following these considerations, we have created lists of all required graphs $g^{(n)}$ [with a potential nonzero graph evaluation $c_{g^{(n)}}(i\nu_m)$], for $n = 0, 1, \dots, 12$. The number of graphs per order $n \gtrsim 6$ is roughly a factor 4 larger than for the previous order. At our highest order $n = n_{\max} = 12$ we need to consider 1 273 854 graphs $g^{(12)}$.

TABLE II. Results for the coefficients $c_{t;l}^{(n)}$ in the polynomial (17) of the evaluation of all graphs $g_t^{(n)}$ in Fig. 1 with $n = 0, 1, 2, 3$ edges.

(n, t)	(0,1)	(1,1)	(2,1)	(2,2)	(2,3)	(3,1)
$c_{t;0}^{(n)}$	+1/4	+1/16	−1/96	−1/192	+1/64	+1/384
$c_{t;2}^{(n)}$	0	0	+1/8	−1/8	0	−1/32
(n, t)	(3,2)	(3,3)	(3,4)	(3,5)	(3,6)	(3,7)
$c_{t;0}^{(n)}$	−1/256	−1/384	−1/768	−1/192	0	+1/256
$c_{t;2}^{(n)}$	+1/32	0	0	+1/16	−1/32	0

Finally, we need to consider the quantity which we wanted to evaluate on the lattice snippets defined by a selection of edges $g^{(n)} = \{e_1, \dots, e_n\}$: The HTE of the Matsubara correlator. We call this HTE the graph evaluation $c_{g^{(n)}}(i\nu_m)$. In Eq. (15) the correlator expansion on the full lattice is obtained by a sum over all graph evaluations weighted with the embedding factors. In Eq. (16), the individual graph evaluations are given by a sum $\sum_{\{e_1,\dots,e_n\}\to\{\tilde{e}_1,\dots,\tilde{e}_n\}}$ which associates the multiset of the graph's edges to the time-ordered bond operators in $F_{jj'}^{(n)}(\tilde{e}_1, \dots, \tilde{e}_n; i\nu_m)$ in all $n!/d[g^{(n)}]$ different ways. Here $d[g^{(n)}]$ yields the graph degeneracy which is the product of factorials of all edge weights.

As in the case of conventional HTE [2], the power of our numerical implementation of Dyn-HTE [21] rests on the fact that the lattice-specific embedding factors $e(\mathcal{L}, i, i', g^{(n)})$ can be quickly obtained from advanced graph-theoretical algorithms [48,49], whereas the numerically costly graph evaluations $c_{g^{(n)}}(i\nu_m)$ can be precomputed once and for all. As we will show in the following, they take the form

$$c_{g_t^{(n)}}(i\nu_m) = \delta_{0,m} c_{t;0}^{(n)} + \sum_{l=1}^{n} c_{t;l}^{(n)} \, \Delta_{2\pi m}^{l}, \tag{17}$$

where $\Delta_{2\pi m} \equiv (1 - \delta_{0,m})/(2\pi m)$ is the inverse of dimensionless (nonzero) Matsubara frequencies. As we argue later, after the embedding, all odd l vanish on the right-hand side of Eq. (15) and are thus not computed in the first place. The $c_{t;l}^{(n)}$ for $l = 0, 2, \dots, r_{\max}$ are rational numbers and together with Eq. (10) they give rise to the final form (7). In Table II we provide the values for the evaluations $c_{t;l}^{(n)}$ for all graphs $g^{(n)}$ with $n \leqslant 3$ shown in Fig. 1. The remainder of this section is concerned with the actual calculation of these graph evaluations.

C. Recursive subgraph subtractions

For the (graph-)evaluation of the dynamic spin correlator on graph $g^{(n)}$ denoted by $c_{g^{(n)}}(i\nu_m)$ in Eq. (16) we are required to assign the multiset of the graph's edges $\{e_1, \dots, e_n\}$ to the bond indices of the operators $\{V_{\tilde{e}_1}(\tau_1), \dots, V_{\tilde{e}_n}(\tau_n)\}$ according to $\{e_1, \dots, e_n\} \to \{\tilde{e}_1, \dots, \tilde{e}_n\}$ in all possible ways. The operators are distinguishable by their time arguments even for identical edges. However, recall the iterative definition of the V-con correlator in Eq. (13) which carries over to the graph

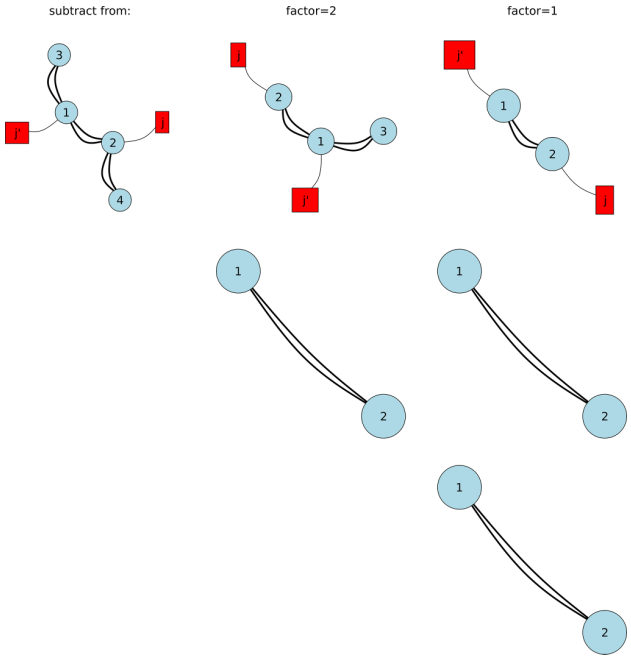

FIG. 2. Subtractions from a graph $g^{(6)}$ shown in the upper left. All connected subgraphs $g^{(k)}$ with $k < 6$ and nonzero graph evaluation are shown in the top row, second to last column. The vacuum graphs $g^{(6)}\backslash g^{(k)} \equiv v$ are shown in the bottom row. These vacuum graphs are possibly disconnected, see third column. The multiplicity factors f for the particular subtraction are also given.

evaluation as follows:

$$c_{g^{(n)}}(i\nu_m) = c^{[\mathrm{full}]}_{g^{(n)}}(i\nu_m) - c^{[\mathrm{sub}]}_{g^{(n)}}(i\nu_m). \tag{18}$$

For the first "full" term, all $n!/d[g^{(n)}]$ assignments are equivalent since the times $\tau_1, \ldots, \tau_n$ can be relabeled and the order of operators behind $\mathcal{T}$ does not matter. We obtain

$$c^{[\mathrm{full}]}_{g^{(n)}}(i\nu_m) = \frac{T^{n+2}}{d[g^{(n)}]} \int_0^\beta e^{i\nu_m(\tau-\tau')} \mathrm{d}\tau_1 \ldots \mathrm{d}\tau_n \mathrm{d}\tau \mathrm{d}\tau' \times \left\langle \mathcal{T} V_{e_1}(\tau_1) \ldots V_{e_n}(\tau_n) S^z_j(\tau) S^z_{j'}(\tau') \right\rangle_0, \tag{19}$$

which we will evaluate further in the next subsection.

For the second "subtracted" term in Eq. (18), we rewrite the $\sum_{S \subsetneq \{1,\ldots,n\}}$ in Eq. (13) as a sum over subgraphs $g^{(k)} \subsetneq g^{(n)}$ with $k < n$ edges. The subgraph $g^{(k)} = \{e'_1, \ldots, e'_k\}$ still needs to be connected and must contain the terminal vertices j, j'. This remaining edges $g^{(n)}\backslash g^{(k)}$ form a vacuum graph without external vertices which is possibly disconnected. There can be more than one ways to get to topologically equivalent $g^{(k)}$, this multiplicity factor is denoted by $f(g^{(n)}, g^{(k)}) \in \{1, 2, \ldots\}$. We refer to Fig. 2 for an example listing all possible nonzero subtractions from a particular graph $g^{(6)}$ with $n = 6$ edges (left) shown in the second and third columns together with their factors $f(g^{(n)}, g^{(k)})$ and the $g^{(k)}$ (top), the vacuum graph $g^{(n)}\backslash g^{(k)}$ is shown in the bottom. Finally, in the second line of Eq. (13) there are $\binom{n}{k}$ possibilities to distribute the imaginary time labels between the first and second average. Hence we obtain

$$c^{[\mathrm{sub}]}_{g^{(n)}}(i\nu_m) = \frac{\binom{n}{k}}{n!} \sum_{g^{(k)} \subsetneq g^{(n)}} f(g^{(n)}, g^{(k)}) T^{n+2} \int_0^\beta e^{i\nu_m(\tau-\tau')} \mathrm{d}\tau_1 \ldots \mathrm{d}\tau_n \mathrm{d}\tau \mathrm{d}\tau' \sum_{g^{(k)}=\{e'_1,\ldots,e'_k\} \to \{\tilde{e}'_1,\ldots,\tilde{e}'_k\}} \left\langle \mathcal{T} V_{\tilde{e}'_1}(\tau_1) \ldots V_{\tilde{e}'_k}(\tau_k) S^z_j(\tau) S^z_{j'}(\tau') \right\rangle_0^{\text{V-con}} \times \sum_{g^{(n)}\backslash g^{(k)}=\{e'_{k+1},\ldots,e'_n\} \to \{\tilde{e}'_{k+1},\ldots,\tilde{e}'_n\}} \left\langle \mathcal{T} V_{\tilde{e}'_{k+1}}(\tau_{k+1}) \ldots V_{\tilde{e}'_n}(\tau_n) \right\rangle_0. \tag{20}$$

The sum in the penultimate line assigns the multiset of graph $g^{(k)}$'s edges $\{e'_1, \ldots, e'_k\}$ in all possible ways to the bond indices of the operators $V_{\tilde{e}'_1}(\tau_1), \ldots, V_{\tilde{e}'_k}(\tau_k)$ and similarly in the last line. We now resolve these assignment sums.

The penultimate line in Eq. (20) appears in the graph-resolved version of Eq. (11) (which only sums over the edges of graph $g^{(k)}$ instead of all bonds $b_1, \ldots, b_n$ of the lattice). Hence we obtain a recursive equation for the graph evaluation $c_{g^{(n)}}(i\nu_m)$

$$c^{[\mathrm{sub}]}_{g^{(n)}}(i\nu_m) = \sum_{g^{(k)} \subsetneq g^{(n)}} f(g^{(n)}, g^{(k)})\, c_{g^{(k)}}(i\nu_m)\, \langle g^{(n)}\backslash g^{(k)} \rangle_0. \tag{21}$$

The last term is the evaluation of the vacuum graph $g^{(n)}\backslash g^{(k)}$ defined from the remaining terms as

$$\langle g^{(n)}\backslash g^{(k)} \rangle_0 = \frac{T^{n-k}}{(n-k)!} \int_0^\beta \mathrm{d}\tau_{k+1} \ldots \mathrm{d}\tau_n \sum_{g^{(n)}\backslash g^{(k)}=\{e'_{k+1},\ldots,e'_n\} \to \{\tilde{e}'_{k+1},\ldots,\tilde{e}'_n\}} \left\langle \mathcal{T} V_{\tilde{e}'_{k+1}}(\tau_{k+1}) \ldots V_{\tilde{e}'_n}(\tau_n) \right\rangle_0 = \frac{1}{d[g^{(n)}\backslash g^{(k)}](n-k)!} \sum_{p \in S_{n-k}} \left\langle V_{e'_{k+p_1}} \ldots V_{e'_{k+p_{n-k}}} \right\rangle_0. \tag{22}$$

In the last step, time integrals together with the time-ordering $\mathcal{T}$ lead to the sum over all permutations p of the numbers $1, 2, \ldots, n-k$, similarly to vacuum graph evaluation for conventional HTE. For disconnected vacuum graphs $g^{(n)}\backslash g^{(k)} \equiv v$ which separate into two connected components $v = v_1 \dot{\cup} v_2$ we have $\langle v \rangle_0 = \langle v_1 \dot{\cup} v_2 \rangle_0 = \langle v_1 \rangle_0 \langle v_2 \rangle_0$ and this generalizes to an arbitrary number of connected components.

In summary, the recursive formulation necessitated by the removal of V-disconnected bond operator configurations in the definition (12) works as follows: Once all the "full" graph

evaluations (19) at order n and vacuum graph evaluations (22) of orders smaller or equal to $n-1$ have been calculated, Eqs. (18) and (21) can be used to find the nth -order graph evaluations via the recursion

$$c_{g^{(n)}}(i\nu_m) = c^{[\mathrm{full}]}_{g^{(n)}}(i\nu_m) - \sum_{g_k \subsetneq g_n} f(g^{(n)}, g^{(k)})\, c_{g^{(k)}}(i\nu_m)\, \langle g^{(n)} \backslash g^{(k)} \rangle_0. \quad (23)$$

This expression is conceptually analogous to a formula popularized in the context of high-order perturbation theory for the fermionic Hubbard model in the diagrammatic Monte Carlo approach (there an expansion in the Hubbard interaction U is used). In this context, Eq. (23) is known as the connected determinant formula and was put forward by Rossi [46]. In the fermionic problem, the averages $\langle \mathcal{T} \dots \rangle_0$ corresponding to our "full" graph evaluations (19) are taken with respect to a noninteracting fermionic (hopping) Hamiltonian H_0 and can thus be obtained via Wick's theorem [12]. This amounts to a determinant evaluation that is numerically efficient. For canonical bosons, the determinant is replaced by a permanent. Then the time integrals are performed stochastically via Markov-chain Monte Carlo.

Crucially, as we are here dealing with spin operators, Wick's theorem is not applicable and the first term on the right-hand side of Eq. (23), $c^{[\mathrm{full}]}_{g^{(n)}}(i\nu_m)$, given in Eq. (19), cannot be written as a determinant or permanent. On the other hand, it turns out that the time dependence of the integrand in our case is much simpler than that encountered in the Hubbard model. These observations lead to a dedicated evaluation strategy which we discuss in the next subsection.

D. Kernel trick for imaginary-time integrals

The central quantity left to be computed is $c^{[\mathrm{full}]}_{g^{(n)}}(i\nu_m)$ in Eq. (19), the full part of the graph evaluation. Its $n+2$-fold time integral can be seen as a $n+2$-dimensional temporal Fourier transform of an (imaginary-)time-ordered $n+2$-point correlator, but with n Matsubara frequencies set to zero. Recently, in Ref. [22] closed-form analytic expressions for these Fourier transforms have been found for arbitrary n, generalizing the Lehmann representation [12] beyond two-point functions [50] (see also Ref. [51] for an earlier solution of the nested time integrals derived in the context of perturbation theory for the Hubbard model). With the help of these "kernel functions," the Fourier transform of a time-ordered $n+2$-point correlator is written exactly in terms of many-body eigenstates, eigenenergies, and matrix elements of the operators involved in the correlation function [22].

In a general case the Hamiltonian cannot be diagonalized and the "kernel trick" is typically not practically applicable. However, in the context of spins, as in Eq. (19), the quantum system of interest is a set of N noninteracting spins ($H_0 = 0$) with trivial product eigenstates and all eigenenergies vanishing. This allows for a tremendous simplification of the analytical expression for Eq. (19) obtained from the kernel trick. For details about the calculation, we refer to our recent work on a complementary spin-diagrammatic scheme tailored for spin systems with close-to-mean-field physics in Ref. [52].

We obtain our main exact and compact result

$$c^{[\mathrm{full}]}_{g^{(n)}}(i\nu_m) = \frac{1}{d[g^{(n)}]} \sum_{p \in S_{n+2}} \tilde{K}_{n+2}(p_{n+1}, p_{n+2}; m) \left\langle \mathcal{P} V^{[p_1]}_{e_1} \dots V^{[p_n]}_{e_n} S^{z[p_{n+1}]}_{j} S^{z[p_{n+2}]}_{j'} \right\rangle_0, \quad (24)$$

where the index ordering operator $\mathcal{P}$ sorts the operator string according to increasing superscript index (in square brackets). For example, in the case $n=2$ and for a particular permutation p it acts as $\mathcal{P} V^{[4]}_{e_1} V^{[1]}_{e_2} S^{z[3]}_{j} S^{z[2]}_{j'} = V_{e_2} S^{z}_{j'} S^{z}_{j} V_{e_1}$.

The dimensionless kernel function $\tilde{K}_{n+2}(p_{n+1}, p_{n+2}; m)$ carries the dependence on external frequency via the Matsubara integer m and depends on the positions p_{n+1}, p_{n+2} of the external operators in the operator string. It relates to the general Kernel function K_{n+2} of Ref. [22] with $n+2$ complex arguments $\Omega_1, \dots, \Omega_{n+2}$ as

$$\tilde{K}_{n+2}(a_+, a_-; m) \equiv T^{n+2} K_{n+2}(0, \dots, 0, \underbrace{+i\nu_m}_{\mathrm{pos.}a_+}, 0, \dots, 0, \underbrace{-i\nu_m}_{\mathrm{pos.}a_-}, 0, \dots, 0), \quad (25)$$

where $a_\pm = 1, 2, \dots, n+2$ mark the position of the frequency entry $i\nu_{\pm m}$ (of arbitrary relative order $a_+ \gtrless a_-$). In Ref. [52], we showed that

$$\tilde{K}_{n+2}(a_+, a_-; m) = \begin{cases} \frac{1}{(n+2)!} & : m = 0, \\ (-1)^{|a_+ - a_-|} \sum_{l=|a_+-a_-|}^{n+2-\min(a_+,a_-)} [\Delta_{2\pi m i}]^l \frac{(\mathrm{sgn}[a_- - a_+])^l}{(n+2-l)!} \binom{l-1}{|a_+ - a_-| - 1} & : m \neq 0, \end{cases} \quad (26)$$

which has the symmetry

$$\tilde{K}_{n+2}(a_+, a_-; m) = \tilde{K}_{n+2}(a_-, a_+; -m) \quad (27)$$

required by the definition (25). We remark that a somewhat similar treatment for a high-temperature expansion in the context of the fermionic Hubbard model (expansion in t/T with t the hopping integral) has been put forward in Ref. [44] but to lower orders and also without the geometric flexibility of the graph-based approach.

In passing, we note a variety of recently suggested approaches that have been developed to solve Matsubara sums (or, equivalently, imaginary-time integrals) that appear in bare or renormalized perturbation theory analytically. These include the discrete-Lehmann representation [53], the intermediate representation [54], and algorithmic Matsubara

integration [55,56]. However, none of these approaches are applicable to perturbation theory diagrams with general bosonic n-point correlators as building blocks, like in the present expansion (which can be understood to be of strong-coupling type in Hubbard-model parlance).

E. Computational aspects for "full" graph evaluations

We finally collect a few algorithmic tricks for efficient numerical evaluation of Eq. (24) which turns out to be the performance bottleneck in the calculation of the complete graph evaluation (23). This can be skipped by the reader unless interested in details of the numerical implementation or the reason for the absence of odd l in the sum (17). With these tricks in place, the evaluations for all graphs up to and including order $n_{\max} = 12$ required on the order of 500.000 core hours for spin length $S = 1/2$.

1. External operator positions

The kernel function in Eq. (24) depends only on the positions p_{n+1} and p_{n+2} of the external operators in the operator string but not on the ordering of the edge operators V_e. We thus simplify Eq. (24) by splitting the sum over permutations p into a sum over permutations of the n edge operator positions and insert the external operator S^z_j *after* a edge operators and the other external operator $S^z_{j'}$ *after* another δa edge operators (and similar for the case that $S^z_{j'}$ appears left of S^z_j),

$$c^{[\mathrm{full}]}_{g^{(n)}}(i\nu_m) = {\sum_{p\in S_n}}' \sum_{a=0}^{n} \sum_{\delta a=0}^{n-a} \tilde{K}_{n+2}(a+1, a+\delta a+2; m) \big\langle \mathcal{P} V^{[p_1]}_{e_1} \dots V^{[p_n]}_{e_n} \xleftarrow{a,\delta a} S^z_j S^z_{j'} \big\rangle_0 + {\sum_{p\in S_n}}' \sum_{a=0}^{n} \sum_{\delta a=0}^{n-a} \tilde{K}_{n+2}(a+\delta a+2, a+1; m) \big\langle \mathcal{P} V^{[p_1]}_{e_1} \dots V^{[p_n]}_{e_n} \xleftarrow{a,\delta a} S^z_{j'} S^z_j \big\rangle_0. \tag{28}$$

The kernels can be precomputed for any combination of $a, \delta a$ and are only multiplied with the accumulated traces ($\sim\langle \dots \rangle_0$) in the very end. In addition, the primed sum $\sum'_{p\in S_n}$ excludes equivalent permutations of the multiset $\{e_1, \dots, e_n\}$ which in Eq. (24) were canceled by the factor $d[g_n]$.

2. Even kernel function

For graphs with $j = j'$ the two traces in the first and second row of Eq. (28) are equivalent,

$$c^{[\mathrm{full}]}_{g^{(n)}}(i\nu_m) = \sum_{a=0}^{n} \sum_{\delta a=0}^{n-a} 2\tilde{K}^{(\mathrm{even})}_{n+2}(a+1, a+\delta a+2; m) \times {\sum_{p\in S_n}}' \big\langle \mathcal{P} V^{[p_1]}_{e_1} \dots V^{[p_n]}_{e_n} \xleftarrow{a,\delta a} S^z_j S^z_{j'} \big\rangle_0, \tag{29}$$

where the even kernel

$$\tilde{K}^{(\mathrm{even})}_{n+2}(a_+, a_-; m) \equiv [\tilde{K}_{n+2}(a_+, a_-; m) + \tilde{K}_{n+2}(a_-, a_+; m)]/2, \tag{30}$$

is given by Eq. (26) with the contributions from odd l removed and is thus real.

The same simplification is also possible for all other graphs with $j \neq j'$. This builds on the insight that graph evaluations $c_{g^{(n)}}(i\nu_m)$ are of little practical relevance for themselves and are only required to find $c^{(n)}_{ii'}(i\nu_m)$ via the embedding in Eq. (15). In the latter, however, embeddings with both $(i, i') \to (j, j')$ and $(i, i') \to (j', j)$ are required. Hence, the rewriting with the even kernel and the vanishing of odd powers of $\Delta_{2\pi m}$ also applies to this case, but only after the embedding. These observations allow us to use Eq. (29) for arbitrary graphs.

3. Cyclicity of trace

Due to the cyclic nature of the trace $\langle \dots \rangle_0$ in Eq. (29), we can always equate the p sum of the latter for any a by setting $a \to 0$. Then the sum over a only has to be taken over the kernel,

$$\tilde{K}^{(\mathrm{even})}_{n+2}(\delta a; m) \equiv \sum_{a=0}^{n-\delta a} \tilde{K}^{(\mathrm{even})}_{n+2}(a+1, a+\delta a+2; m), \tag{31}$$

and Eq. (29) simplifies to

$$c^{[\mathrm{full}]}_{g^{(n)}}(i\nu_m) = 2 \sum_{\delta a=0}^{n} \tilde{K}^{(\mathrm{even})}_{n+2}(\delta a; m) \times {\sum_{p\in S_n}}' \big\langle S^z_j \mathcal{P} V^{[p_1]}_{e_1} \dots V^{[p_n]}_{e_n} \xleftarrow{\delta a} S^z_{j'} \big\rangle_0. \tag{32}$$

Anticipating the two embeddings $(i, i') \to (j, j')$ and $(i, i') \to (j', j)$ as above, we can write the more symmetric expression

$$c^{[\mathrm{full}]}_{g^{(n)}}(i\nu_m) = \sum_{\delta a=0}^{n} \big[\tilde{K}^{(\mathrm{even})}_{n+2}(\delta a, m) + \tilde{K}^{(\mathrm{even})}_{n+2}(n-\delta a, m)\big] \times {\sum_{p\in S_n}}' \big\langle S^z_j \mathcal{P} V^{[p_1]}_{e_1} \dots V^{[p_n]}_{e_n} \xleftarrow{\delta a} S^z_{j'} \big\rangle_0. \tag{33}$$

From this equation, also the general form of the expansions in Eq. (17) [and (7)] follow: From the definition of the kernel (26), after dropping odd powers of $\Delta_{2\pi m}$ in the even kernel, graph evaluations for $g^{(n)}$ with n even contain $\Delta^n_{2\pi m}$ as the highest power. For odd n, naively $\Delta^{n+1}_{2\pi m}$ can occur. However, these terms, which emerge only from the $a = 0$ contribution to $\tilde{K}^{(\mathrm{even})}_{n+2}(\delta a, m)$ mutually cancel out in the square bracket of Eq. (33).

Regarding algorithmic complexity, note that the sum in Eq. (33) has only a factor of n more terms than the analogous

expression for the conventional HTE of the equal-time correlator $\langle S^z_j S^z_{j'}\rangle$ where the two external operators always stay right next to each other due to the absence of time integrals.

4. Flavor sum

So far we have not considered the structure of the edge operators which according to Sec. II are Heisenberg exchange interactions, $V_{e_k} = \sum_{\gamma_k} S^{\gamma_k}_{e_k(1)} S^{\bar{\gamma}_k}_{e_k(2)}$. Here the edge-flavor sum is over $\gamma_k \in \{+,-,z\} \equiv \{+1,-1,0\}$ and $e_k(1)$ and $e_k(2)$ are the two vertices connected by edge e_k. As Eq. (33) involves n of these edge operators, resolving the V_{e_k} for $k = 1,\ldots,n$ naively gives rise to 3^n flavor combinations to be summed over. As mentioned below Eq. (11), the traces $\langle\ldots\rangle_0$ of strings of equal-time spin operators $\in \{S^+_i, S^-_i, S^z_i\}$ appearing in Eq. (33) factorize into traces of spin operators with the same vertex (site) index. The required on-site free spin equal-time correlators for a string of $n' \leqslant n+2$ spin operators are precomputed and saved as a computationally efficient integer after multiplying by a factor $(2S+1)^{n'}$. The product of these factors is to be canceled by global factor $1/(2S+1)^{2n+2}$ which is to be multiplied only at the end.

It turns out that the single free spin n-point correlators vanish for many operator strings. For example in the case $S = 1/2$ and for spin-operator strings of length $n' = 12$, only 8172 out of the $3^{12} = 531\,441$ possible strings have a nonzero trace. Conditions for a zero trace that do not depend on the operator order are a breaking of $U(1)$ spin rotation symmetry (unequal numbers of S^+ and S^- in the string) or a string that is odd under a π-rotation around the spin-x axis. The latter is the case for a string consisting of an odd number of S^z operators, $S^zS^z\ldots S^z$. Such flavor combinations can be skipped already before entering the $\sum'_{p\in S_n}$ sum. We also use the π_x-rotation symmetry in spin space that ensures equality of the traces for flavor strings connected by a global exchange of $S^+ \leftrightarrow S^-$ operators.

Once a given permutation $p \in S_n$ is selected, operator identities like $(S^+)^a = 0$ for $a > 2S$ might render the operator string trivial. Note that this holds also if S^z operators are inserted in between. This is useful since it makes the condition independent of any insertions of external S^z operators done in the δa sum.

V. RESULTS AND APPLICATIONS

A. Tests of expansion coefficients

In a first step, we check the rational coefficients in the polynomials $p^{(n)}_{ii'}(x)$ of Eq. (7) obtained from Dyn-HTE in two settings where they are known by other means; see Appendix for details. In a first test, we consider the Heisenberg four spin cluster ($N = 4$) with all-to-all interactions for which the Matsubara correlator $G_{ii'}(i\nu_m)$ can be found analytically for $S = 1/2$, $S = 1$ and both for the local and nonlocal case. The rational coefficients of a series expansion of these exact results in $x = J/T$ agrees to our graph-embedding based Dyn-HTE result. This test thus involves evaluations for *all* graphs with up to four vertices (as they are embeddable in the $N = 4$ all-to-all cluster). In a second test we focus on extended lattices in two and three dimensions (like kagome, triangular, and pyrochlore) and compute their Dyn-HTE. At each order in x, we take the frequency and site sums to reproduce the conventional HTE expansion of the (purely static) uniform susceptibility χ found in the conventional HTE literature.

B. Benchmark: Heisenberg $S = 1/2$ AFM chain

We proceed to compute numerical values for the Matsubara correlator (4) at finite $x = J/T$ based on the Dyn-HTE expansion (7). We start in this subsection with the (infinite) nearest-neighbor $S = 1/2$ Heisenberg AFM chain. We study the Matsubara correlators both in real and momentum space for various distances $i - i'$ and momenta k; see Fig. 3, left and right columns, respectively. Error controlled QMC benchmark data from the worm algorithm [57,58] are shown as symbols, error bars are smaller than symbol size. We consider the static case $m = 0$ and the two smallest positive Matsubara frequencies $m = 1, 2$, top to bottom row.

The summation of the bare Dyn-HTE series up to order $n = 12$ (gray line) starts to deviate significantly from the exact results at rather high temperature $x = J/T \simeq 2$. This is in close analogy to conventional HTE where it is well known to signal the small radius of convergence of the x series in the complex plane [2]. A standard tool to extract meaningful information from the bare HTE series at smaller temperatures are Padé approximants [2], which are rational functions $[K,L](x) = \frac{P_K(x)}{Q_L(x)}$ with polynomials P_K and Q_L of degree K and L, respectively. For $K + L = n_{\max}$, their coefficients can be determined so that the series expansion of the Padé approximant agrees in the first $n_{\max}$ orders with the bare (Dyn-)HTE series. For the case $[K = 6, L = 6] \equiv [6,6]$, denoted by blue lines in Fig. 3, the agreement with QMC data already extends to $x \simeq 4$, both for the real- and momentum-space correlator. Note that for the latter, we perform the Fourier transform before computing the Padé approximant.

For many combinations of Matsubara integer m and distance $i - i'$ (or momentum k) the [6,6] Padé approximant agrees with the error controlled QMC result to even much larger $x \simeq 8$, most severe deviations occur for the $m = 0$ case with $i - i' = 1$ or $k = \pi$. In real applications (without available benchmark data), the quality of a prediction from Padé approximants is usually gauged by comparison of different $[K,L]$ with $K + L \leqslant n_{\max}$ [2]. Due to the asymptotically constant (and finite) values of $TG_{ii'}(i\nu_m)$ at $x \to \infty$, we limit ourselves to the comparison of the symmetric Padé approximants [6,6] and [5,5] (dashed lines). Indeed, the poor quality of the [6,6] approximants in the two cases mentioned above is reflected in a large disagreement between the two Padé approximants [5,5] and [6,6].

Interestingly, in these cases a transformation from the bare series in x to a series in $u = \tanh(fx)$ and subsequent Padé approximants can help [59]. Indeed, these u-Padé approximants shown by purple lines in Fig. 3 reasonably agree with the QMC benchmark data down to the smallest temperatures ($x = 8$) considered. The free parameter $f = 0.205$ is determined from the condition to have the best possible agreement between the [5,5] and [6,6] u-Padés. In principle, f could be chosen differently for each bare series obtained for the set $(m, i - i')$ [or (m,k)], but we picked a global value here for simplicity. Finally, we note that there are also other resummation techniques like variants of Padé, "integral" approximants

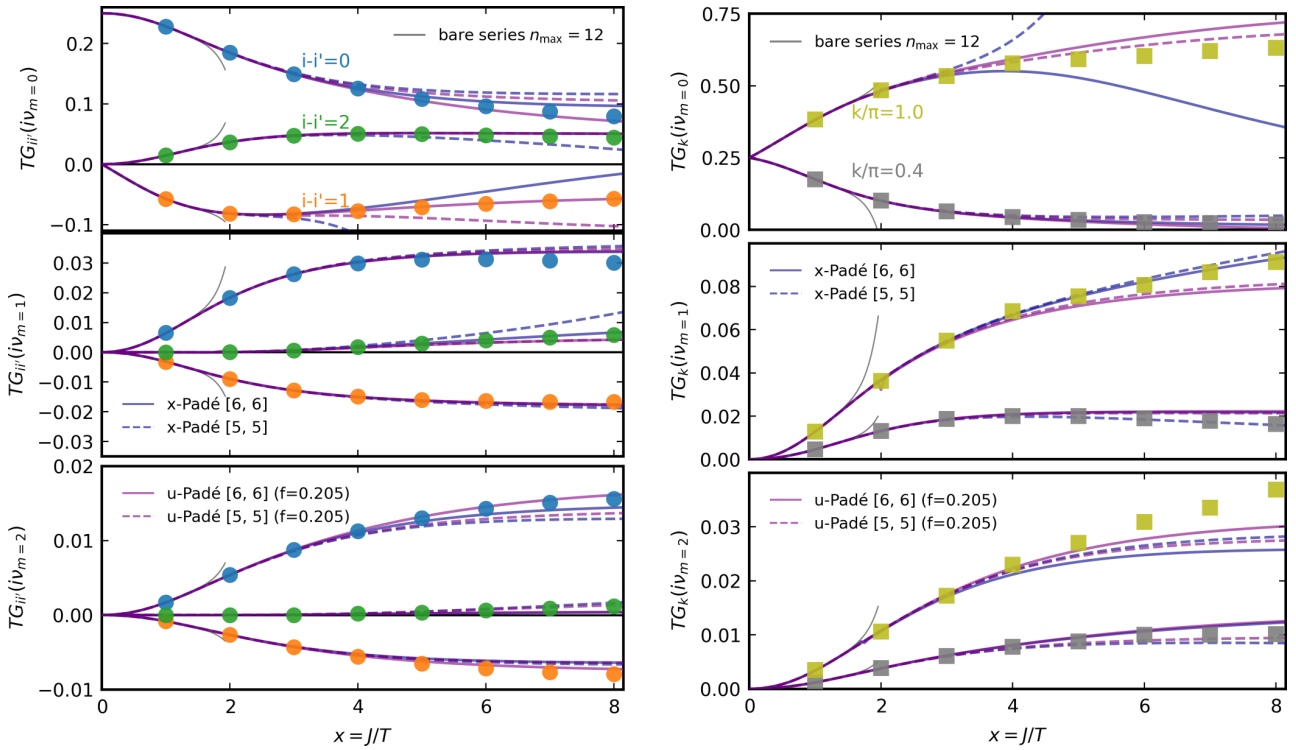

FIG. 3. Matsubara correlators of the Heisenberg $S = 1/2$ AFM chain for real-space distances $i - i' = 0, 1, 2$ (left) and wave vectors $k/\pi = 0.4, 1$ (right) as obtained from Dyn-HTE (lines). The frequencies are $\nu_m = 2\pi mT$ with $m = 0, 1, 2$ (top to bottom). Markers show benchmark results from QMC simulations of a 256-site ring with error bars smaller than the symbol size. The thin gray line denotes the evaluation of the bare Dyn-HTE series truncated at order $n_{max} = 12$. Symmetric Padé approximants ([6,6] and [5,5]) of the x series are shown by blue lines (full and dashed) for the transformed series in $u = \tanh(fx)$ with $f = 0.205$ they are indicated in purple.

[2] or conformal maps [60] that could be tested with Dyn-HTE in future work.

C. Heisenberg $S = 1/2$ AFM on triangular lattice

The Heisenberg $S = 1/2$ AFM on the triangular lattice serves as an example for a frustrated system for which the Matsubara correlator is difficult to study with QMC due to the sign problem. We focus on the static susceptibility of Eq. (8), $G_{\mathbf{k}}(i\nu_m = 0) = \chi_{\mathbf{k}}$, which has been computed previously using the alternative bold-line diagrammatic Monte Carlo (BDMC) method [30] for spin $S = 1/2$. In this approach a fermionic representation is used and standard fermionic skeleton Feynman diagrams are sampled using a Monte Carlo technique. Explicitly, diagrams up to order 7 in the interaction J are taken into account but the self-consistency condition invokes certain diagram classes at all orders.

In Fig. 4 we compare the results of Dyn-HTE (lines) and the BDMC (dots). The top panel reports the T dependence of the static susceptibility at the ground-state ordering wave vector at the corner of the hexagonal Brillouin zone (BZ), known as the K point. The convergence of different Padé approximants denoted by various blue line styles is decent and still improves by using the u series (with $f = 0.25$, purple lines) as in the previous subsection. We are thus confident that the solid purple line (u-Padé [6,6]) gives accurate results in the temperature regime shown with only a few percentages error. In contrast, for $x = J/T \gtrsim 2$ the BDMC obtains inconsistent and much larger values. As the BDMC study [30] does not provide convergence plots of $\chi_{\mathbf{k}=K}$, error bars of the BDMC data are unfortunately not available. As a further complication, the skeleton series is now known for its possibly convergence to unphysical results [61]. In the bottom panel of Fig. 4, we report the static susceptibility for a path through the BZ at various T. Away from the K point already detailed in the top panel, there is good agreement between BDMC (dots) and Dyn-HTE (solid lines) for all temperatures studied.

D. Renormalized mean-field form of static susceptibility

In recent work [62] two of us showed that the static susceptibility $\chi_{\mathbf{k}} = G_{\mathbf{k}}(i\nu_m = 0)$ of a wide selection of Heisenberg models on lattices in dimension higher than one can very well be approximated by a two-parameter function of $\mathbf{k}$, the *renormalized mean-field* form (rMF). The standard mean-field expression for nearest-neighbor models with coupling J reads

$$\left[TG^{\mathrm{MF}}_{\mathbf{k}}(i\nu_m = 0)\right]^{-1} = 1/b_1 + x\gamma_1(\mathbf{k}), \tag{34}$$

where $b_1 = S(S+1)/3$ denotes the dimensionless susceptibility of a free spin and $\gamma_n(\mathbf{k}) = \sum_{\mathbf{r}\in n\text{th NN}} \exp(i\mathbf{k}\cdot\mathbf{r})$ is the spatial Fourier transform of the jth nearest-neighbor coupling pattern [Eq. (34) only involves γ_1]. In the nonsymmetry broken regime, the $\mathbf{k}$-dependence of the exact static susceptibility can always be expanded by using the remaining $\gamma_n(\mathbf{k})$

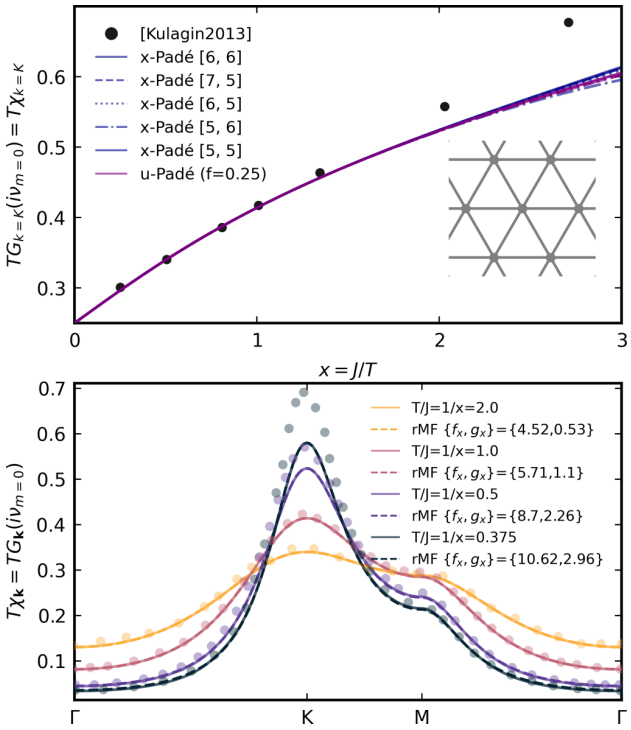

FIG. 4. Static susceptibility $\chi_{\mathbf{k}}$ for the Heisenberg $S = 1/2$ AFM on the triangular lattice. Results from Dyn-HTE (lines) are compared against the bold-line diagrammatic Monte Carlo (BDMC) data obtained by Kulagin *et al.* in Ref. [30] (dots). Top: $\chi_{\mathbf{k}=K}$ at the K point in the corner of the hexagonal Brillouin zone (BZ) versus T. The convergence of various Padé approximants denoted by blue line styles is decent and still improves by using the u series (for $f = 0.25$, purple lines, same Padé approximants as for x series). Bottom: $\chi_{\mathbf{k}}$ for a path through the BZ at various T. The Γ point is the center of the BZ and M denotes the center of the BZ edge. Away from the K point there is good agreement between BDMC (dots) and Dyn-HTE (full lines). Here the [6,6] u-Padé with $f = 0.25$ is shown. The dashed lines represent the best fit of the renormalized mean-field form in Eq. (36) to the Dyn-HTE results. The associated fit parameters $\{f_x, g_x\}$ are given in the legend.

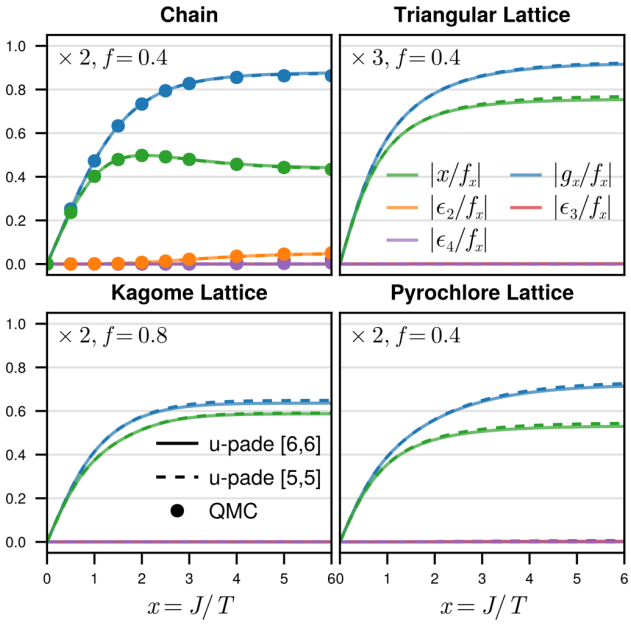

FIG. 5. Amplitudes of parameter ratios of the rMF form (36): x/f_x, g_x/f_x, and the first few corrections $\epsilon_{2,3,4}/f_x$ [cf. Eq. (35)] for the nearest-neighbor $S = 1/2$ Heisenberg AFM model on the chain, triangular, kagome, and pyrochlore lattice from Dyn-HTE. For resummation, we used [6,6] and [5,5] u-Padé approximants. The data are multiplied by the maximum (eigenvalue) of $-\gamma_1(\mathbf{k})$ given in the panels alongside the u-Padé parameter f. For the chain geometry QMC data (dots) [58] matches well with the Dyn-HTE data (lines). For triangular, kagome and pyrochlore lattice $\epsilon_{2,3,4}/f_x$ are of order 10^{-3} rendering the rMF an excellent approximation. Whenever the [6,6] or [5,5] Padé approximant is anomalous (with obvious poles), we use a stable lower-order Padé approximant.

with $n > 1$,

$$[TG_{\mathbf{k}}(iv_m = 0)]^{-1} = f_x + g_x\gamma_1(\mathbf{k}) + \epsilon_2\gamma_2(\mathbf{k}) + \cdots \quad (35)$$

$$\approx f_x + g_x\gamma_1(\mathbf{k}). \quad (36)$$

The approximation in Eq. (36) is the rMF form with parameters f_x and g_x replacing $1/b_1$ and x from Eq. (34), respectively. The expansion in Eq. (35) is defined by inverse Fourier transforms with respect to real-space vectors $\mathbf{r}_{n\text{th NN}}$ pointing to the nth nearest neighbor,

$$f_x = \frac{1}{N_b V_{\text{BZ}}} \int_{\text{BZ}} \mathrm{d}\mathbf{k} [TG_{\mathbf{k}}(iv_m = 0)]^{-1}, \quad (37)$$

$$g_x = \frac{1}{N_b V_{\text{BZ}}} \int_{\text{BZ}} \mathrm{d}\mathbf{k} e^{i\mathbf{k}\cdot\mathbf{r}_{\text{NN}}} [TG_{\mathbf{k}}(iv_m = 0)]^{-1}, \quad (38)$$

$$\epsilon_n = \frac{1}{N_b V_{\text{BZ}}} \int_{\text{BZ}} \mathrm{d}\mathbf{k} e^{i\mathbf{k}\cdot\mathbf{r}_{n\text{th NN}}} [TG_{\mathbf{k}}(iv_m = 0)]^{-1}. \quad (39)$$

Here V_{BZ} is the BZ volume and N_b the number of basis sites.

In Ref. [62] we could show analytically that the HTE of the beyond-rMF terms ϵ_n for $n = 2, 3, \ldots$ start at order $O(x^4)$ with a particularly small prefactor. This lead us to conjecture the excellent validity of the rMF beyond the high-temperature regime which was corroborated by matching the rMF form (36) with published momentum-dependent susceptibilities obtained from the BDMC method [30] and pseudofermion functional renormalization group [63].

Dyn-HTE now offers an alternative and more reliable source of static susceptibility data. For $\chi_{\mathbf{k}}$ of the triangular lattice model shown in Fig. 4 (bottom) we determined the rMF parameters f_x and g_x of Eq. (36) via least-squares fit to the Dyn-HTE data (see legend and dashed lines). The rMF form of the susceptibility describes the Dyn-HTE data remarkably well, with an almost perfect match even for the lowest temperature $T/J = 0.375$.

A quantitative measure of the rMF form's accuracy is provided by the ratio $|\frac{\sum_n \epsilon_n\gamma_n(\mathbf{k})}{f_x + g_x\gamma_1(\mathbf{k})}|$ for which values much smaller than unity indicate the applicability of the approximation. In Fig. 5 we report several ratios of f_x, g_x and the numerically dominant $\epsilon_2, \epsilon_3, \epsilon_4$ for the Heisenberg $S = 1/2$ AFM on various lattices. They are obtained from the u-Padé

approximations for the x-series expansions of the respective ratio found from Dyn-HTE. For the chain (top left panel), the ratios $1/f_x$, g_x/f_x, and ϵ_n/f_x saturate for low T (large x), hence resummation of the ratios with the Padé approximant of the u series works very well as witnessed by comparison to QMC (dots). As ϵ_2 grows sizably for low T, the validity of the rMF approximation is compromised. This was stated before in Ref. [64].

However, for the two- and three-dimensional systems (triangular, kagome, and pyrochlore lattice), the results in Fig. 5 indicate that ϵ_2, ϵ_3, ϵ_4 are negligible as compared to f_x and g_x underlining the validity of the rMF approximation. Remarkably, ϵ_n stays at least two orders of magnitude lower than g_x over the whole accessible temperature range. Therefore, the static susceptibility is accurately described by just g_x and f_x for these models. This also explains the excellent fit to the rMF form in Fig. 4. Other corrections ϵ_n for $n > 4$ (not shown) stay very small as well.

VI. CONCLUSION AND OUTLOOK

We have presented a dynamical extension of the HTE to the Matsubara spin correlator for spin Hamiltonians (Dyn-HTE). Currently, our numerical implementation [21] features an expansion to order $n_{\max} = 12$ and is available for $S \leqslant 1$ Heisenberg Hamiltonians with a single coupling constant J on arbitrary (in particular frustrated and high-dimensional) lattices. The real-frequency dynamic structure factor can be obtained via postprocessing of the Matsubara data as described in our companion letter [39].

For further methodological development of Dyn-HTE it would be worthwhile to reduce the number of graphs by the free-graph expansion technique (where different vertices of a graph can be assigned to the same or different lattice sites) or by the linked-cluster method [2]. In the latter, only graphs (clusters) with simple edges are required on which the observable needs to be expanded in $x = J/T$ or is even determined by exact diagonalization. While this could be a viable way to higher expansion orders for small S, it would also be interesting to extend Dyn-HTE in the form presented in this work to arbitrary S. This could be achieved by building on closed-form expressions for the equal-time free spin correlators [22].

Moreover, possible extensions of Dyn-HTE analogous to achievements in conventional HTE include the application to Heisenberg models with more than one coupling constant, e.g., J_1-J_2 models [5], single-ion anisotropies, or magnetic fields [6]. In the latter case, the kernel trick for the evaluation of the imaginary-time integrals needs to be adapted for the presence of (a few) nonzero many-body eigenenergies of H_0. It would also be interesting to aim Dyn-HTE at more complex correlation functions like three-point correlators encoding higher-order response; see Ref. [28] for pioneering work. Likewise, it would be useful to improve the series convergence beyond the standard Padé approximants by implementing advanced ideas like, e.g., the homotopic action [65].

Beyond the Heisenberg case, Dyn-HTE can be extended to models with broken or reduced spin rotation symmetry like the XXZ case. Likewise, also the fermionic (or bosonic) t-J-model which is prominently realized in cold-atom quantum simulation [66] should be considered. Here existing treatments [44,67] could be extended to higher expansion orders.

ACKNOWLEDGMENTS

We acknowledge useful discussions with Michel Ferrero at several stages of the project and are grateful to Lode Pollet for advise on the QMC worm algorithm [58]. We further thank Nikolay Prokofiev and Boris Svistunov for useful remarks on the manuscript.

The authors acknowledge the Gauss Centre for Supercomputing e.V. for funding this project by providing computing time through the John von Neumann Institute for Computing (NIC) on the GCS Supercomputer JUWELS at Jülich Supercomputing Centre (JSC). The authors also acknowledge support by the state of Baden-Württemberg through bwHPC and the German Research Foundation (DFG) through Grant No. INST 40/575-1 FUGG (JUSTUS 2 cluster). We acknowledge funding from the Deutsche Forschungsgemeinschaft (DFG, German Research Foundation) through the Research Unit FOR 5413/1, Grant No. 465199066. B.Sch. acknowledges funding from the Munich Quantum Valley, supported by the Bavarian state government with funds from the High-tech Agenda Bayern Plus. B.Sb. and B.Sch. are supported by DFG Grant No. 524270816.

DATA AVAILABILITY

The data that support the findings of this article are openly available [21].

APPENDIX: BENCHMARK TESTS FOR EXPANSION OF MATSUBARA CORRELATOR

1. Small spin cluster: $N = 4$ spins with all-to-all coupling

As a first benchmark check on the expansion coefficients of Dyn-HTE in Eq. (7), we consider a cluster with $N = 4$ spins coupled by all-to-all interaction J, for both $S = 1/2$ and $S = 1$. We compute the exact local and nonlocal Matsubara correlators (4) in closed form using diagonalization and the spectral (Lehmann) representation [12]. For $S = 1/2$ they read

$$TG_{11}(i\nu_m) = \begin{cases} \frac{5(x-1)+e^{2x}(9x+8e^x-3)}{8(e^{2x}(2e^x+9)+5)x} = \frac{1}{4} - \frac{x^2}{32} + \frac{x^3}{128} + \frac{23x^4}{2560} + \cdots & : m = 0, \\ \frac{\Delta^2(e^x-1)x(5\Delta^2x^2+e^x(5\Delta^2x^2+e^x(8\Delta^2x^2+2)+5)+5)}{2(e^{2x}(2e^x+9)+5)(4\Delta^4x^4+5\Delta^2x^2+1)} = \frac{3\Delta^2x^2}{8} - \frac{3\Delta^2x^3}{32} - \left(\frac{21\Delta^4}{16} + \frac{11\Delta^2}{128}\right)x^4 + \cdots & : m \neq 0, \end{cases} \tag{A1}$$

$$TG_{12}(i\nu_m) = \begin{cases} \frac{15x+e^{2x}(3x-8e^x+3)+5}{24(e^{2x}(2e^x+9)+5)x} = -\frac{x}{16} + \frac{5x^2}{192} + \frac{3x^3}{256} - \frac{221x^4}{15360} + \cdots & : m = 0, \\ \frac{\Delta^2(e^x-1)x(5\Delta^2x^2+e^x(5\Delta^2x^2+e^x(8\Delta^2x^2+2)+5)+5)}{-6(e^{2x}(2e^x+9)+5)(4\Delta^4x^4+5\Delta^2x^2+1)} = -\frac{\Delta^2x^2}{8} + \frac{\Delta^2x^3}{32} + \left(\frac{7\Delta^4}{16} + \frac{11\Delta^2}{384}\right)x^4 + \cdots & : m \neq 0. \end{cases} \tag{A2}$$

Here we abbreviate $\Delta = \Delta_{2\pi m}$. The straightforward series expansions in x (shown here to order x^4 for brevity) are reproduced via Dyn-HTE based on Eqs. (10), (15), (23), and (24) up to the maximum order $n_{\max} = 12$. The same holds for the case $S = 1$ (the full expressions for $m \neq 0$ are too long to be shown)

$$TG_{11}(i\nu_m) = \begin{cases} \frac{270x+288e^{10x}+108e^{9x}(3x+1)+20e^{7x}(33x-7)+7e^{4x}(66x-25)-81}{216(7e^{4x}+10e^{7x}+6e^{9x}+e^{10x}+3)x} = \frac{2}{3} - \frac{2x^2}{9} + \frac{13x^3}{54} + \frac{181x^4}{1620} + \cdots & : m = 0, \\ \frac{8\Delta^2x^2}{3} - \frac{26\Delta^2x^3}{9} + \left(-\frac{244\Delta^4}{9} - \frac{8\Delta^2}{9}\right)x^4 + \cdots & : m \neq 0, \end{cases} \tag{A3}$$

$$TG_{12}(i\nu_m) = \begin{cases} \frac{810x-288e^{10x}-108e^{9x}(x+1)+140e^{7x}(3x+1)+175e^{4x}(6x+1)+81}{648(7e^{4x}+10e^{7x}+6e^{9x}+e^{10x}+3)x} = -\frac{4x}{9} + \frac{5x^2}{9} + \frac{11x^3}{162} - \frac{3503x^4}{2430} + \ldots & : m = 0, \\ -\frac{8\Delta^2x^2}{9} + \frac{26\Delta^2x^3}{27} + \left(\frac{244\Delta^4}{27} + \frac{8\Delta^2}{27}\right)x^4 + \ldots & : m \neq 0. \end{cases} \tag{A4}$$

2. Consistency with conventional HTE for uniform susceptibility

As mentioned above, the conventional HTE for equal-time correlators and thermodynamic quantities like the uniform susceptibility $\chi \equiv \sum_{i'} \langle S_i^z S_{i'}^z \rangle$ is well established. Here we test Dyn-HTE by reproducing the expansion coefficients of χ calculated to high orders for many lattices. First, we recover the equal-time correlators from the Matsubara correlators by a frequency sum,

$$\left\langle S_i^z S_{i'}^z \right\rangle = \sum_m TG_{ii'}(i\nu_m). \tag{A5}$$

We insert the Dyn-HTE expansion from Eq. (10) on the right-hand side and perform the frequency sums. The numerical values for the sum over even powers of $\Delta_{2\pi m}$ are summarized in Table III for convenience.

As a first nontrivial consistency check, we calculate the uniform susceptibility χ for the triangular lattice Heisenberg $S = 1/2$ AFM and reproduce the expansion coefficients provided in Ref. [68] for all orders $n \leqslant n_{\max} = 12$. Note that this uses all graph evaluations for graphs embeddable in the triangular lattice with their *complete* frequency dependence [only a static contribution must survive after the sum in Eq. (A5)] and thus constitutes a rather nontrivial check.

For the Kagome lattice, we also reproduce the HTE coefficients for the susceptibility [59]. The nth order coefficient of χ in $(-x)$ is given by $a_{n+1}(-1)^n/[(n+1)!\,4^{n+2}]$ where a_n is given in the right column of Table I in Ref. [59]. There, a misprint must be corrected, $a_7 = 2\,711\,296$. This has been also noticed in Ref. [4]. For $S = 1$ we performed the same check for χ against the conventional HTE [4].

Finally, for the Heisenberg $S = 1/2$ AFM on the pyrochlore lattice in three dimensions, we reproduced the HTE coefficients published in Ref. [11].

TABLE III. Frequency sums needed in Eq. (A5).

l	2	4	6	8	10	12	14	16	18
$\Sigma_m \Delta_{2\pi m}^l$	$\frac{1}{12}$	$\frac{1}{720}$	$\frac{1}{30\,240}$	$\frac{1}{1\,209\,600}$	$\frac{1}{47\,900\,160}$	$\frac{691}{1\,307\,674\,368\,000}$	$\frac{1}{74724249600}$	$\frac{3617}{10\,670\,622\,842\,880\,000}$	$\frac{43867}{5\,109\,094\,217\,170\,944\,000}$

[1] C. Domb and M. S. Green, *Phase Transitions and Critical Phenomena*, Series Expansions for Lattice Models (Academic Press, London, 1974), Vol. 3.

[2] J. Oitmaa, C. Hamer, and W. Zheng, *Series Expansion Methods for Strongly Interacting Lattice Models* (Cambridge University Press, Cambridge, UK, 2006).

[3] H.-J. Schmidt, J. Schnack, and M. Luban, Heisenberg exchange parameters of molecular magnets from the high-temperature susceptibility expansion, Phys. Rev. B **64**, 224415 (2001).

[4] A. Lohmann, H.-J. Schmidt, and J. Richter, Tenth-order high-temperature expansion for the susceptibility and the specific heat of spin-s Heisenberg models with arbitrary exchange patterns: Application to pyrochlore and kagome magnets, Phys. Rev. B **89**, 014415 (2014).

[5] A. Hehn, N. Van Well, and M. Troyer, High-temperature series expansion for spin-1/2 Heisenberg models, Comput. Phys. Commun. **212**, 180 (2017).

[6] L. Pierre, B. Bernu, and L. Messio, High temperature series expansions of $S = 1/2$ Heisenberg spin models: Algorithm to include the magnetic field with optimized complexity, SciPost Phys. **17**, 105 (2024).

[7] B. Bernu and G. Misguich, Specific heat and high-temperature series of lattice models: Interpolation scheme and examples on quantum spin systems in one and two dimensions, Phys. Rev. B **63**, 134409 (2001).

[8] N. Elstner, R. R. P. Singh, and A. P. Young, Finite temperature properties of the spin-1/2 Heisenberg antiferromagnet on the triangular lattice, Phys. Rev. Lett. **71**, 1629 (1993).

[9] E. A. Ghioldi, M. G. Gonzalez, S.-S. Zhang, Y. Kamiya, L. O. Manuel, A. E. Trumper, and C. D. Batista, Dynamical structure factor of the triangular antiferromagnet: Schwinger boson theory beyond mean field, Phys. Rev. B **98**, 184403 (2018).

[10] L. Chen, D.-W. Qu, H. Li, B.-B. Chen, S.-S. Gong, J. von Delft, A. Weichselbaum, and W. Li, Two-temperature scales in the triangular-lattice Heisenberg antiferromagnet, Phys. Rev. B **99**, 140404(R) (2019).

[11] M. G. Gonzalez, B. Bernu, L. Pierre, and L. Messio, Finite-temperature phase transitions in $S = 1/2$ three-dimensional Heisenberg magnets from high-temperature series expansions, Phys. Rev. B **107**, 235151 (2023).

[12] H. Bruus, K. Flensberg, H. Bruus, and K. Flensberg, *Many-Body Quantum Theory in Condensed Matter Physics: An Introduction*, Oxford Graduate Texts (Oxford University Press, Oxford, 2004).

[13] M. Mourigal, M. Enderle, A. Klöpperpieper, J.-S. Caux, A. Stunault, and H. M. Rønnow, Fractional spinon excitations in the quantum Heisenberg antiferromagnetic chain, Nat. Phys. **9**, 435 (2013).

[14] J. Khatua, B. Sana, A. Zorko, M. Gomilšek, K. S. M. S. R. Rao, M. Baenitz, B. Schmidt, and P. Khuntia, Experimental signatures of quantum and topological states in frustrated magnetism, Phys. Rep. **1041**, 1 (2023).

[15] M. L. Prichard, Z. Ba, I. Morera, B. M. Spar, D. A. Huse, E. Demler, and W. S. Bakr, Magnon-polarons in the Fermi–Hubbard model, Nat. Phys. (2025).

[16] C. Lacroix, P. Mendels, and F. Mila, *Introduction to Frustrated Magnetism: Materials, Experiments, Theory* (Springer, Berlin, 2011).

[17] N. E. Sherman and R. R. P. Singh, Structure factors of the kagome-lattice Heisenberg antiferromagnets at finite temperatures, Phys. Rev. B **97**, 014423 (2018).

[18] A. Auerbach, *Interacting Electrons and Quantum Magnetism* (Springer, New York, 1994).

[19] M. Drescher, L. Vanderstraeten, R. Moessner, and F. Pollmann, Dynamical signatures of symmetry-broken and liquid phases in an S = 1/2 Heisenberg antiferromagnet on the triangular lattice, Phys. Rev. B **108**, L220401 (2023).

[20] L. Savary and L. Balents, Quantum spin liquids: A review, Rep. Prog. Phys. **80**, 016502 (2016).

[21] B. Sbierski, B. Schneider, and R. Burkard, Dyn-HTE software v1.0: 10.5281/zenodo.17234446 (2025).

[22] J. Halbinger, B. Schneider, and B. Sbierski, Spectral representation of matsubara n-point functions: Exact kernel functions and applications, SciPost Phys. **15**, 183 (2023).

[23] V. G. Vaks and A. I. Larkin, Spin waves and correlation functions in a ferromagnetic, Sov. Phys. JETP **26**, 647 (1968).

[24] Y. A. Izyumov and Y. N. Skryabin, *Statistical Mechanics of Magnetically Ordered Systems* (Consultants Bureau, New York, NY, 1988).

[25] R. Goll, D. Tarasevych, J. Krieg, and P. Kopietz, Spin functional renormalization group for quantum Heisenberg ferromagnets: Magnetization and magnon damping in two dimensions, Phys. Rev. B **100**, 174424 (2019).

[26] J. Krieg and P. Kopietz, Exact renormalization group for quantum spin systems, Phys. Rev. B **99**, 060403(R) (2019).

[27] D. Tarasevych and P. Kopietz, Dissipative spin dynamics in hot quantum paramagnets, Phys. Rev. B **104**, 024423 (2021).

[28] A. Rückriegel, D. Tarasevych, J. Krieg, and P. Kopietz, Recursive algorithm for generating high-temperature expansions for spin systems and the chiral nonlinear susceptibility, Phys. Rev. B **110**, 144416 (2024).

[29] A. W. Sandvik, Computational studies of quantum spin systems, AIP Conf. Proc. **1297**, 135 (2010).

[30] S. A. Kulagin, N. Prokof'ev, O. A. Starykh, B. Svistunov, and C. N. Varney, Bold diagrammatic Monte Carlo technique for frustrated spin systems, Phys. Rev. B **87**, 024407 (2013).

[31] J. Reuther and P. Wölfle, J1-J2 frustrated two-dimensional Heisenberg model: Random phase approximation and functional renormalization group, Phys. Rev. B **81**, 144410 (2010).

[32] N. Niggemann, B. Sbierski, and J. Reuther, Frustrated quantum spins at finite temperature: Pseudo-Majorana functional renormalization group approach, Phys. Rev. B **103**, 104431 (2021).

[33] T. Müller, D. Kiese, N. Niggemann, B. Sbierski, J. Reuther, S. Trebst, R. Thomale, and Y. Iqbal, Pseudo-fermion functional renormalization group for spin models, Rep. Prog. Phys. **87**, 036501 (2024).

[34] J. Fei, C.-N. Yeh, and E. Gull, Nevanlinna analytical continuation, Phys. Rev. Lett. **126**, 056402 (2021).

[35] K. Nogaki and H. Shinaoka, Bosonic Nevanlinna analytic continuation, J. Phys. Soc. Jpn. **92**, 035001 (2023).

[36] L. Huang and C. Yue, Barycentric rational function approximation made simple: A fast analytic continuation method for Matsubara Green's functions, Phys. Rev. B **111**, 125139 (2025).

[37] M. Kliczkowski, L. Keyes, S. Roy, T. Paiva, M. Randeria, N. Trivedi, and M. M. Maska, Autoencoder-based analytic continuation method for strongly correlated quantum systems, Phys. Rev. B **110**, 115119 (2024).

[38] H. Shao and A. W. Sandvik, Progress on stochastic analytic continuation of quantum Monte Carlo data, Phys. Rep. **1003**, 1 (2023).

[39] R. Burkard, B. Schneider, and B. Sbierski, companion paper, Dynamic correlations of frustrated quantum spins from high-temperature expansion, Phys. Rev. Lett. **136**, 056501 (2026).

[40] P. C. Kwok and T. D. Schultz, Correlation functions and Green functions: Zero-frequency anomalies, J. Phys. C **2**, 1196 (1969).

[41] V. S. Viswanath and G. Müller, *The Recursion Method: Application to Many-body Dynamics*, Lecture Notes in Physics Monographs No. 23 (Springer, Berlin, 1994).

[42] H. Mori, A continued-fraction representation of the time-correlation functions, Prog. Theor. Phys. **34**, 399 (1965).

[43] S. Pairault, D. Senechal, and A.-M. S. Tremblay, Strong-coupling perturbation theory of the Hubbard model, Eur. Phys. J. B **16**, 85 (2000).

[44] E. Perepelitsky, A. Galatas, J. Mravlje, R. Žitko, E. Khatami, B. S. Shastry, and A. Georges, Transport and optical conductivity in the Hubbard model: A high-temperature expansion perspective, Phys. Rev. B **94**, 235115 (2016).

[45] S. Bhattacharyya, A. De, S. Gazit, and A. Auerbach, Metallic transport of hard-core bosons, Phys. Rev. B **109**, 035117 (2024).

[46] R. Rossi, Determinant diagrammatic Monte Carlo in the thermodynamic limit, Phys. Rev. Lett. **119**, 045701 (2017).

[47] F. L. Buessen, Fbuessen/SpinMC.Jl (2025).

[48] Graphs.Jl: A performant platform for network and graph analysis in julia (2025).

[49] L. Cordella, P. Foggia, C. Sansone, and M. Vento, A (sub)graph isomorphism algorithm for matching large graphs, IEEE Trans. Pattern Anal. Mach. Intell. **26**, 1367 (2004).

[50] F. B. Kugler, Seung-Sup B. Lee, and J. von Delft, Multipoint correlation functions: Spectral representation and numerical evaluation, Phys. Rev. X **11**, 041006 (2021).

[51] J. Vučičević, P. Stipsić, and M. Ferrero, Analytical solution for time integrals in diagrammatic expansions: Application to real-frequency diagrammatic Monte Carlo, Phys. Rev. Res. **3**, 023082 (2021).

[52] B. Schneider, R. Burkard, B. Olmos, I. Lesanovsky, and B. Sbierski, Dipolar ordering transitions in many-body quantum optics: Analytical diagrammatic approach to equilibrium quantum spins, Phys. Rev. A **110**, 063301 (2024).

[53] J. Kaye, K. Chen, and O. Parcollet, Discrete Lehmann representation of imaginary time Green's functions, Phys. Rev. B **105**, 235115 (2022).

[54] M. Wallerberger, S. Badr, S. Hoshino, S. Huber, F. Kakizawa, T. Koretsune, Y. Nagai, K. Nogaki, T. Nomoto, H. Mori *et al.*, Sparse-ir: Optimal compression and sparse sampling of many-body propagators, SoftwareX **21**, 101266 (2023).

[55] A. Taheridehkordi, S. H. Curnoe, and J. P. F. LeBlanc, Algorithmic Matsubara integration for Hubbard-like models, Phys. Rev. B **99**, 035120 (2019).

[56] M. Burke and J. LeBlanc, TorchAmi: Generalized CPU/GPU implementation of algorithmic Matsubara integration, Comput. Phys. Commun. **308**, 109437 (2025).

[57] N. Sadoune and L. Pollet, Efficient and scalable path integral Monte Carlo simulations with worm-type updates for Bose-Hubbard and XXZ models, SciPost Phys. Codebases **2022**, 9 (2022).

[58] N. Sadoune and L. Pollet, Worm algorithm code, GitHub repository (2023).

[59] N. Elstner and A. P. Young, Spin-1/2 Heisenberg antiferromagnet on the *kagome* lattice: High-temperature expansion and exact-diagonalization studies, Phys. Rev. B **50**, 6871 (1994).

[60] C. Bertrand, S. Florens, O. Parcollet, and X. Waintal, Reconstructing nonequilibrium regimes of quantum many-body systems from the analytical structure of perturbative expansions, Phys. Rev. X **9**, 041008 (2019).

[61] E. Kozik, M. Ferrero, and A. Georges, Nonexistence of the Luttinger-Ward functional and misleading convergence of skeleton diagrammatic series for Hubbard-like models, Phys. Rev. Lett. **114**, 156402 (2015).

[62] B. Schneider and B. Sbierski, Taming spin susceptibilities in frustrated quantum magnets: Mean-field form and approximate nature of the quantum-to-classical correspondence, Phys. Rev. Lett. **134**, 176502 (2025).

[63] M. G. Gonzalez, V. Noculak, A. Sharma, V. Favre, J.-R. Soh, A. Magrez, R. Bewley, H. O. Jeschke, J. Reuther, H. M. Rønnow, Y. Iqbal, and I. Živković, Dynamics of $K_2Ni_2(SO_4)_3$ governed by proximity to a 3D spin liquid model, Nat. Commun. **15**, 7191 (2024).

[64] S. A. Kulagin, N. Prokof'ev, O. A. Starykh, B. Svistunov, and C. N. Varney, Bold diagrammatic Monte Carlo method applied to fermionized frustrated spins, Phys. Rev. Lett. **110**, 070601 (2013).

[65] A. J. Kim, N. V. Prokof'ev, B. V. Svistunov, and E. Kozik, Homotopic action: A pathway to convergent diagrammatic theories, Phys. Rev. Lett. **126**, 257001 (2021).

[66] J. Koepsell, D. Bourgund, P. Sompet, S. Hirthe, A. Bohrdt, Y. Wang, F. Grusdt, E. Demler, G. Salomon, C. Gross, and I. Bloch, Microscopic evolution of doped Mott insulators from polaronic metal to Fermi liquid, Science **374**, 82 (2021).

[67] W. Metzner, Linked-cluster expansion around the atomic limit of the Hubbard model, Phys. Rev. B **43**, 8549 (1991).

[68] J. Oitmaa and E. Bornilla, High-temperature-series study of the spin-1/2 Heisenberg ferromagnet, Phys. Rev. B **53**, 14228 (1996).

Dynamic Correlations of Frustrated Quantum Spins from High-Temperature Expansion

Ruben Burkard,[1] Benedikt Schneider,[2,3] and Björn Sbierski[1]
[1]*Institut für Theoretische Physik, Universität Tübingen, Auf der Morgenstelle 14, 72076 Tübingen, Germany*
[2]*Department of Physics and Arnold Sommerfeld Center for Theoretical Physics, Ludwig-Maximilians-Universität München, Theresienstraße 37, 80333 Munich, Germany*
[3]*Munich Center for Quantum Science and Technology (MCQST), 80799 Munich, Germany*

(Received 1 June 2025; revised 8 November 2025; accepted 7 January 2026; published 2 February 2026)

For quantum spin systems in equilibrium, the dynamic structure factor (DSF) is among the most feature-packed experimental observables. However, from a theory perspective it is often hard to simulate in an unbiased and accurate way, especially for frustrated and high-dimensional models at intermediate temperature. To address this challenge, we compute the DSF from a dynamic extension of the high-temperature expansion to frequency moments. We focus on nearest-neighbor Heisenberg models with spin lengths $S = 1/2$ and 1. We provide comprehensive benchmarks and consider a variety of frustrated two- and three-dimensional antiferromagnets as applications. In particular we shed new light on the anomalous intermediate temperature regime of the $S = 1/2$ triangular lattice model and reproduce the DSF measured recently for the $S = 1$ pyrochlore material $NaCaNi_2F_7$. An open-source numerical implementation for arbitrary lattice geometries is also provided.

DOI: 10.1103/jtjk-x2lw

Introduction—Localized quantum spins with frustrated interactions are ubiquitous in modern condensed matter experiments ranging from solid-state Mott insulators [1] to atom-based analog quantum simulators [2]. A major goal is the realization of exotic correlated and entangled low-energy states like quantum spin liquids (QSLs) [3]. The dynamical structure factor (DSF) defined as spatial and temporal Fourier transform of the equilibrium two-point correlator $\langle S^z_i(t) S^z_{i'} \rangle$ is routinely measured via inelastic neutron scattering (INS) [4] in the solid-state context. For cold-atom setups the DSF is accessible via Raman spectroscopy [5]. The DSF probes collective spin dynamics and contains rich information on (dipolar) excitations, quasiparticles (or the absence thereof), and even entanglement structure [6,7]. From a theory perspective, however, a quantitative and unbiased calculation of the DSF for generic and possibly gapless frustrated quantum spin-S models at low temperature T is often challenging. With exact diagonalization and its derivatives (e.g., finite-T Lanczos method [8]) limited to small systems and quantum Monte Carlo hampered by the sign problem, tensor-network methods like density-matrix renormalization group (DMRG) are state of the art. However, besides in one dimension (1D) [9], current simulations are only feasible for $T = 0$, small S, and are severely affected by finite-size effects and entanglement [10,11]. Diagrammatic approaches that provide spin correlations in imaginary (Matsubara) frequency like pseudofermionic functional renormalization group [12–14] or bold-line diagrammatic Monte Carlo [15] are successful for static correlations down to intermediate J/T with J the spin-spin interaction. However analytic continuation of this approximate Matsubara correlator to the real-frequency DSF is notoriously unstable. A popular bypass is semiclassical approximations of spin dynamics [16–19], which, however, likely miss genuine quantum effects at small S.

Here, we narrow this methodological gap by introducing a dynamic extension of the high-temperature expansion (HTE). Conventional HTE targets equal-time correlations and thermodynamic observables via graph-based expansions in J/T and has been developed for more than five decades [20,21]. It benefits from a formulation in the thermodynamic limit and is oblivious to frustration, entanglement, dimensionality and spin length [22]. Its main limitation is the model-dependent temperature range $T \gtrsim O(J/4)$. Our dynamic HTE (Dyn-HTE) shares the same benefits but applies to frequency moments of the real-frequency dynamic susceptibility from which we reconstruct the DSF [23–25]. Although these moments are considerably more complex than equal-time correlators, the high expansion orders of conventional HTE are maintained. This allows for the computation of four to seven frequency moments, depending on T/J, and goes beyond numerical linked-cluster expansions (NLCE) [26,27] that computed the lowest two moments (Gauss approximation) for some particular $S = 1/2$ models [28].

Our open-source numerical implementation of Dyn-HTE [29] makes it a versatile numerical tool catering directly to experiments. It currently covers $S \in \{1/2, 1\}$ Heisenberg models with arbitrary geometry and a single J; for technical details, see the companion paper [30]. Here, we derive the method and benchmark in 1D. We then obtain DSFs of the

highly frustrated triangular and pyrochlore lattice for $S=1/2$ and $S=1$, respectively. The former sheds new light on the nature of the model's anomalous intermediate-T regime, while the latter is in fair agreement with existing neutron scattering data.

Model and DSF—We consider length-S quantum spins S_i^α with $\alpha = x,\ y,\ z$ and ladder operators $S_i^\pm = (S_i^x \pm iS_i^y)/\sqrt{2}$ at sites $\mathbf{r}_i$ $(i = 1, 2, \ldots, N)$ of an arbitrary lattice $\mathcal{L}$. We focus on the Heisenberg model,

$$H = J\sum_{(ii')} \left(S_i^+ S_{i'}^- + S_i^- S_{i'}^+ + S_i^z S_{i'}^z\right), \tag{1}$$

characterized by a *single* coupling J on arbitrary bonds (ii') with $i < i'$. This includes the important case of symmetry-related nearest-neighbor interactions on which we focus in the following. None of these assumptions or the spin-rotation symmetries of (1) are essential for Dyn-HTE and can be relaxed in future developments analogous to conventional HTE [21,22,31,32]. The DSF for translation invariant $\mathcal{L}$ is defined as

$$S(\mathbf{k},\omega) = \int_{-\infty}^{+\infty} \frac{\mathrm{d}t}{2\pi N} \sum_{i,i'} e^{i\omega t - i\mathbf{k}\cdot(\mathbf{r}_i - \mathbf{r}_{i'})} \langle S_i^z(t) S_{i'}^z \rangle \tag{2}$$

and relates to the imaginary part of the dynamical susceptibility via the fluctuation-dissipation relation [33], $A_\mathbf{k}(\omega) = 2\pi(1 - e^{-\omega/T})S(\mathbf{k},\omega)$. From the Lehmann representation, the exact $A_\mathbf{k}(\omega)$ fulfills $A_\mathbf{k}(\omega > 0) \geq 0$ and $A_\mathbf{k}(\omega) = -A_{-\mathbf{k}}(-\omega)$. We now assume inversion symmetry, and then $A_\mathbf{k}(\omega) = A_{-\mathbf{k}}(\omega)$ is antisymmetric in ω.

Continued fraction and moment expansion—It is well-known [23–25,34,35] that such a "faithful" $A_\mathbf{k}(\omega)$ can be generated from a continued fraction expansion,

$$TA_\mathbf{k}(\omega) = 2w\mathrm{Re}[\tilde{R}_\mathbf{k}(s = iw + 0^+)], \tag{3}$$

$$\tilde{R}_\mathbf{k}(s) = \frac{\delta_{\mathbf{k},0}}{s+} \frac{\delta_{\mathbf{k},1}}{s+} \frac{\delta_{\mathbf{k},2}}{s+} \frac{\delta_{\mathbf{k},3}}{s+} \cdots, \tag{4}$$

with $w = \omega/J$ the dimensionless frequency and the continued fraction parameters $\delta_{\mathbf{k},r} \geq 0$. The first $\delta_{\mathbf{k},r}$ for $r \leq r_{\max}$ can be determined [23,25] from the first $r_{\max}$ (even) frequency moments of the relaxation function $R_\mathbf{k}(w) \equiv TA_\mathbf{k}(\omega)/(2\pi w)$ [24],

$$m_{\mathbf{k},2r} = \int_{-\infty}^{\infty} \mathrm{d}w w^{2r} R_\mathbf{k}(w), \quad r = 0, 1, 2, \ldots. \tag{5}$$

Dropping the $\mathbf{k}$ subscript for brevity, the connection is made via Laplace transform of Eq. (5), $\tilde{R}(s) = \int_{-\infty}^{\infty} \mathrm{d}v\{[R(v)]/(s - iv)\}$, and expansion in the inverse complex argument, $1/s$. Comparison of coefficients [25] leads to $\delta_0 = m_0$, $\delta_1 = m_2/m_0$, $\delta_2 = m_4/m_2 - m_2/m_0$, and $\delta_3 = m_0(m_4^2 - m_2 m_6)/[m_2^3 - m_0 m_2 m_4]$. For $\delta_{4,5,6}$ required in the following, see End Matter. Via a short-time expansion of the spin correlator, the moments can be expressed as equal-time correlators involving a $2r-1$-fold commutator, $J^{2r} m_{\mathbf{k},2r}/(2T) = M_{\mathbf{k},2r-1}$, defined as the spatial Fourier transform of

$$M_{ii',n} = i^n \partial_t^n \langle S_i^z(t) S_{i'}^z \rangle|_{t=0} = \langle [\ldots[[S_i^z, H], H], \ldots, H] S_{i'}^z \rangle. \tag{6}$$

As exact calculation of all $m_{\mathbf{k},2r}$ is not possible for general models, one is limited to finite $r \leq r_{\max}$. We discuss an extrapolation strategy on the level of the $\delta_{\mathbf{k},r}$ below.

Inspection of Eq. (6) shows that the amount of computable moments $r_{\max}$ strongly depends on dimension (controlling the growth of operator support under application of $[\ldots, H]$), spin length S, and temperature. The most simple case is $T = \infty$, where equal-time spin correlators factorize according to site indices. Here, depending on the concrete model, $r_{\max} = O(30)$ can be reached in 1D [36,37], while $r_{\max} \lesssim 10$ in 3D [25]. However, the case of finite T is complicated by the presence of the thermal density matrix $\rho = e^{-H/T}/\mathrm{tr}[e^{-H/T}]$ in Eq. (6). To the best of our knowledge, no method to evaluate even a moderate number of moments at $T/J = O(1)$ for possibly frustrated Heisenberg models beyond 1D is established.

Dyn-HTE for moments—We now present our main conceptual result relevant for finite T: the HTE of moments $m_{\mathbf{k},2r}$ is encoded in the Dyn-HTE of the Matsubara spin correlator. This is significant as the latter treats ρ and imaginary-time evolution $S_i^z(\tau) = e^{H\tau} S_i^z e^{-H\tau}$ on equal footing [33] and allows for an efficient evaluation of *exact* HTE coefficients; see our companion article [30]. The Matsubara correlator at frequency $\nu_m = 2\pi T m$ $(m \in \mathbb{Z})$ and its HTE to order $n_{\max}$ in $x = J/T$ read

$$TG_{ii'}(i\nu_m) = T^2 \int_0^{1/T} \mathrm{d}\tau \mathrm{d}\tau' e^{i\nu_m(\tau - \tau')} \langle \mathcal{T} S_i^z(\tau) S_{i'}^z(\tau') \rangle \tag{7}$$

$$= p_{ii'}^{(0)}(x)\delta_{0,m} + \sum_{r=1}^{r_{\max}} p_{ii'}^{(2r)}(x) x^{2r} \Delta_{2\pi m}^{2r} + O(x^{n_{\max}+1}). \tag{8}$$

Here, $\mathcal{T}$ enforces τ ordering, $\Delta_{2\pi m} \equiv (1 - \delta_{0,m})/(2\pi m)$ and $r_{\max} = \lfloor n_{\max}/2 \rfloor$. The polynomials $p_{ii'}^{(2r)}(x)$ will be linked to the HTE of the moments momentarily. They are of degree $n_{\max} - 2r$ with rational coefficients. Our open-source implementation [29] for $n_{\max} = 12$ provides $p_{ii'}^{(2r)}(x)$ for all site pairs ii' on *arbitrary* lattices $\mathcal{L}$. This flexibility hinges on the preevaluation of Dyn-HTE (8) on generic lattice snippets called "graphs," which are then embedded in arbitrary (and also high-dimensional and frustrated) $\mathcal{L}$ in a postprocessing step as in conventional HTE [21]. Efficient evaluation of *all* $\sim 10^6$ graphs with up to $n_{\max}$ edges [currently for $S \in \{\frac{1}{2}, 1\}$] rests on a recursive

formulation of perturbation theory and the exact solution of the $n_{\max}+2$-fold τ integrals using the kernel trick [38]; see Ref. [30] for details. There we also discuss results for the *static* spin susceptibility, $\sim G_{ii'}(i\nu_m=0)$.

We show that the spatial Fourier transform of the polynomials $p_{ii'}^{(2r)}(x)$ in Eq. (8) is identical to the HTE of the relaxation function's frequency moments $m_{\mathbf{k},2r}$ in Eq. (5) [for $r>0$, there is a relative sign $-(-1)^r$]. To see this, consider the standard integral relation between $A_{\mathbf{k}}(\omega)$ and the Matsubara correlator in momentum space (7),

$$G_{\mathbf{k}}(i\nu_m)=\frac{1}{2\pi}\int_{-\infty}^{\infty}\mathrm{d}\omega\,\frac{A_{\mathbf{k}}(\omega)}{\omega-i\nu_m}. \tag{9}$$

This is strictly correct only for $m\neq 0$ and an additional term quantifying long-term memory effects and nonergodicity appears on the right-hand side for $m=0$ [39–41]. For systems of interest in this Letter, we assume such effects are absent and thus continue with Eq. (9). The claim follows from an expansion of the right-hand side of Eq. (9) in (even) powers of $1/\nu_m\sim\Delta_{2\pi m}$,

$$TG_{\mathbf{k}}(i\nu_m)=\int_{-\infty}^{\infty}\mathrm{d}w R_{\mathbf{k}}(w)\left[\delta_{m,0}-\sum_{r=1,2,\ldots}(iwx\Delta_{2\pi m})^{2r}\right], \tag{10}$$

after comparison to Eqs. (5) and (8).

To lift the assumption of inversion symmetry [under which $A_{\mathbf{k}}(\omega)$ is antisymmetric in ω and $G_{\mathbf{k}}(i\nu_m)$ is real [30]], the above can be straightforwardly generalized using the symmetric and antisymmetric combination $A^{\pm}_{\mathbf{k}}(\omega)\equiv\frac{1}{2}[A_{\mathbf{k}}(\omega)\mp A_{-\mathbf{k}}(-\omega)]$, which fulfills the analog of Eq. (9) with the imaginary and real part of $G_{\mathbf{k}}(i\nu_m)$ on the left-hand side, respectively.

Heisenberg $S=1/2$ AFM chain—As a first example, we turn to the well-studied nearest-neighbor Heisenberg $S=1/2$ antiferromagnet (AFM) in 1D for benchmark. Because of finite expansion order $n_{\max}=12$, the HTE is only available for moments $m_{\mathbf{k},2r}$ with $r\leq r_{\max}=6$. To show how to deal with this restriction, we first consider the infinite-T case ($x=0$), where moments are *exactly* given by the x^0 coefficients of their HTEs. We convert to the δ_r and plot them in Fig. 1(a) for two representative momenta $\mathbf{k}=0.2\pi$ and π (large dots). To avoid sharp Dirac-Delta peaks in $A_{\mathbf{k}}(\omega)$ resulting from an abrupt termination of the continued fraction (4), we follow Ref. [25] and linearly extrapolate $\delta_{r>r_{\max}}=(r-r_{\max})a+b$ for $r>r_{\max}$. Then Eq. (4) can be written as

$$\tilde{R}_{r_{\max}}(s)=\frac{\delta_0}{s+}\frac{\delta_1}{s+}\frac{\delta_2}{s+}\cdots\frac{\delta_{r_{\max}-1}}{s+\delta_{r_{\max}}\Gamma_{a,b}(s)}, \tag{11}$$

where the termination function $\Gamma_{a,b}(s)$ is a fraction of Hermite polynomials [42] (see End Matter) and allows to take the limit 0^+ in Eq. (3) exactly. The different small markers in Fig. 1(a) correspond to various linear extrapolation schemes (cf. Fig. 1 caption). The main features of the resulting DSFs shown in various line styles in Fig. 1(b) are practically insensitive to the chosen extrapolation and are in excellent agreement with DMRG [9] throughout the Brillouin zone (BZ); see Fig. 2, left column.

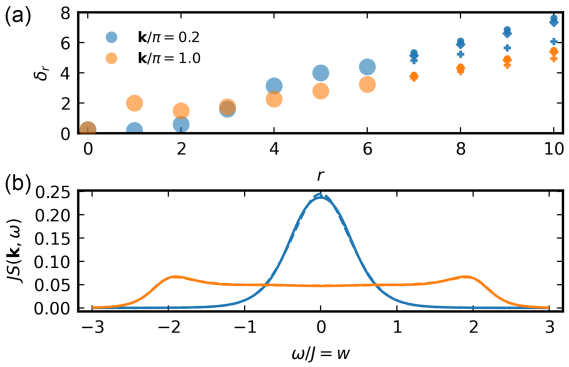

FIG. 1. Heisenberg $S=1/2$ AFM chain at $T=\infty$. (a) Continued fraction parameters δ_r for two momenta $\mathbf{k}$. The large dots denote the exact results for $r=0,1,\ldots,6$ from Dyn-HTE; the small markers depict various linear extrapolation schemes $\delta_{r>6}=(r-6)a+b$ to which the DSF in (b), obtained from the infinite continued fraction [Eq. (11)], is largely insensitive as seen from the overlap of various line styles.

We now turn to $T<\infty$ ($x>0$), where Dyn-HTE has its main advantage. Recall that it provides the expansion of moments $m_{\mathbf{k},2r}(x)$ in x to order $n_{\max}-2r$. Hence, for the interesting regime $x\gtrsim 1$ beyond convergence of the bare HTE series, we apply resummation in form of Padé approximants [21] to $m_{\mathbf{k},2r}(x)$ with $r\leq 3$ and then proceed as above; see End Matter (Fig. 5) for details. Analogous to conventional HTE [21,43] we improve convergence by changing to the auxiliary variable $u=\tanh(fx)$ with tuning parameter f chosen such that different Padé approximants agree. In principle, f should be as small as possible to reach large x and could vary with $\mathbf{k}$ but for the chain a single $f=0.48$ works well. The second and third columns of Fig. 2 compare the DSF at temperatures $x=2$ and 4 from Dyn-HTE (top) to DMRG [9] (middle). Line cuts (bottom) show only minor deviations.

$S=1/2$ Heisenberg AFMs in 2D—While magnetic long-range order is only possible at $T=0$ for nearest-neighbor models, its precursor in the form of spin waves can dominate the DSF already at $T\lesssim J$ [44]. We refer to the End Matter for representative Dyn-HTE results for the DSF of the square lattice model and the frustrated kagome lattice, which lacks long-range magnetic order at $T=0$ and shows broad features in the DSF.

Here, we focus on the triangular lattice model with 120° order at $T=0$ [45]. For $\frac{1}{4}\lesssim T/J\lesssim 1$, however, an enigmatic anomaly occurs: As first found by HTE, static properties deviate strongly from renormalized-classical

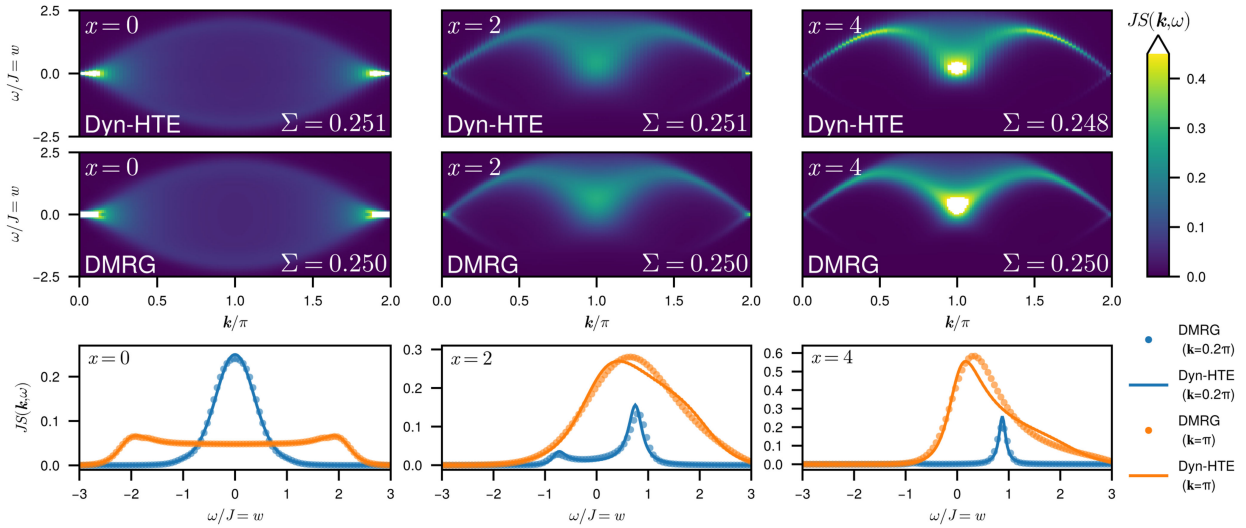

FIG. 2. DSF for the Heisenberg $S = 1/2$ AFM chain at $x = J/T \in \{0, 2, 4\}$, left to right column. Top row: Dyn-HTE results based on extrapolation of moments with $r \leq 6$ ($r \leq 3$ for $x > 0$). Middle row: DMRG data reproduced from Ref. [9]. Bottom row: line shape for $S(\mathbf{k}, \omega)$ at fixed $\mathbf{k} \in \{0.2\pi, \pi\}$. The lattice spacing is set to unity. The values for $\Sigma \equiv [J/(V_{\mathrm{BZ}})] \int_{-\infty}^{\infty} \mathrm{d}\omega \int_{\mathrm{BZ}} \mathrm{d}\mathbf{k}\, S(\mathbf{k}, \omega)$ with V_{BZ} the BZ volume are also indicated and Dyn-HTE fulfills the sum rule $\Sigma = \langle S_i^z S_i^z \rangle = S(S+1)/3 = 1/4$ within $< 1\%$.

spin-wave predictions [46–48]. For example, at $T = J/4$, the correlation length is relatively small (about a lattice constant) and the entropy per spin is large ($\simeq[(\ln 2)/3]$).

The DSF from Dyn-HTE shown in Fig. 3 (see also End Matter for a BZ path at $x = 3$) is ideally suited to shed new light on the still debated nature of this intermediate-T regime. One proposed scenario starts from the $T = 0$ excitation spectrum, which shows a "rotonlike excitation" (RLE) characterized by a dispersion minimum at the M point (center of BZ edge) with gap $\Delta \simeq 0.55J$ [49,50]. Is the intermediate-T region primarily characterized by thermal excitations of these enigmatic RLEs? At $\mathbf{k} = M$, the T dependence of the equal-time structure factor shows a weak maximum around $T \simeq \Delta$ (see Ref. [48]), but the DSF in Fig. 3 (top) does not soften significantly across the intermediate T range with the peak remaining around $\omega_{\mathrm{max}} \simeq J$ [for $S(\mathbf{k} = M, \omega \to 0)$, a weak maximum can, however, be found as T decreases]. Hence, if the RLE at $\mathbf{k} = M$ is responsible for the anomalous behavior, the associated fluctuations are not simple spin waves but must be more complex. One candidate are triangle-based chiral fluctuations [48] but the associated chiral DSF is beyond the scope of this Letter.

An alternative scenario links the anomalous intermediate-T regime to passage through a critical fan [51] of a $T = 0$ quantum phase transition (QPT) at which the 120° order melts [47,52,53]. A hallmark of this scenario is a temperature-frequency scaling relation for the DSF at ordering wave vector $\mathbf{k} = K$ for $|\omega| \lesssim J$,

$$JS(\mathbf{k} = K, \omega)(T/J)^{\alpha} = \Phi(\omega/T), \tag{12}$$

where $\alpha = (2 - \eta)/z$ is determined by the critical exponents of the QPT and $\Phi(\cdot)$ is a scaling function. Interestingly, the $\mathbf{k} = K$ DSF from Dyn-HTE shown in Fig. 3 (bottom) fulfills such a relation for $\alpha = 1.10(2)$ (inset), but the T range for which scaling occurs is relatively narrow. One candidate for the QPT in question is the transition to a Dirac QSL in the $J_1 - J_2$ model at $J_2 \simeq 0.06J_1$ [54]. Although the critical exponents are unknown, Lorentz invariance would imply $z = 1$ and $\eta = O(1)$ has been

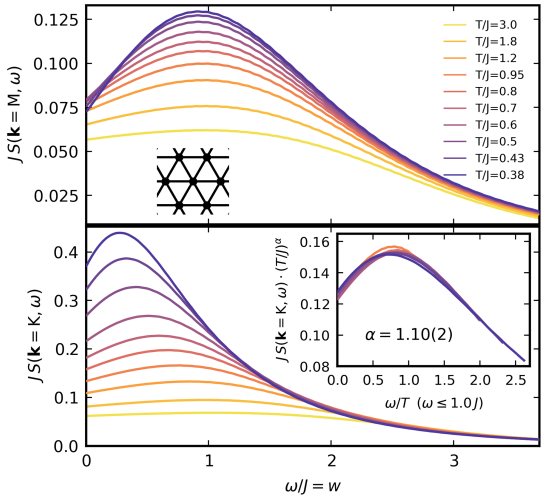

FIG. 3. DSF of triangular lattice $S = 1/2$ Heisenberg AFM at momenta M (top) and K (bottom) from Dyn-HTE with $r_{\mathrm{max}} = 3$ and $f = 0.55$. Inset: ω/T-scaling collapse for $\omega \leq J$ and $0.43 \leq T/J \leq 0.95$ with scaling exponent $\alpha = 1.10(2)$.

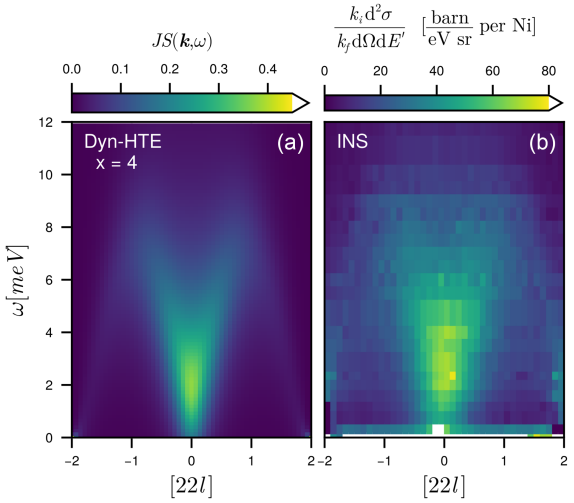

FIG. 4. (a) DSF for the pyrochlore lattice $S = 1$ Heisenberg AFM for $\mathbf{k} = (2, 2, l)$, $J = 2.4$ meV at $x = J/T = 4$ from Dyn-HTE (via u-Padé with $f = 0.6$). (b) Experimental INS data for $NaCaNi_2F_7$ at $x \simeq 15$, from Ref. [58].

found in the potentially related Gross-Neveu-Heisenberg model via large-N_f or $\epsilon = 4 - d$ expansion [55,56]. Our value of α is thus not implausible and can inform further efforts on the field-theory side, although the scaling analysis should be repeated with Dyn-HTE data for the $J_1 - J_2$ model. Other open questions pertain to the incompatible value of $\alpha \simeq 1.73(12)$ found from a similar scaling analysis of INS data from $KYbSe_2$ with finite and slightly subcritical J_2 [57] and an extended scaling analysis taking into account deviations from the ordering wave vector, $\mathbf{k} \neq K$.

$S = 1$ Heisenberg AFMs: Chain and pyrochlore lattice—Finally, we obtain the DSF from Dyn-HTE for spin $S = 1$ Heisenberg AFMs. For the chain at $x = 4$, some aspects like the dispersion maxima or Haldane gap already agree well with ground-state ($x \to \infty$) DMRG results; see End Matter (Fig. 7). The $S = 1$ pyrochlore material $NaCaNi_2F_7$ was reported to approximately realize the nearest-neighbor Heisenberg AFM [16,58] with $J = 2.4$ meV [59]. In Fig. 4, we compare the DSF from Dyn-HTE along the $[22l]$ momentum with experimental INS results [58]. We find fair agreement of the main features, including the size of the "V" shape as well as the height of the dome shape, which was not captured in semiclassical studies [16,59]. In Dyn-HTE, the maximum along the line cut at [220] appears at slightly lower ω compared to INS data. Possible reasons are potential beyond-Heisenberg perturbations in the material and a mismatch in temperature ($x = 4$ in Dyn-HTE versus $x \simeq 15$ in INS). Indeed the peak position in Dyn-HTE has a trend to higher ω with lower T.

Conclusion—Compared to static observables of conventional HTE, the DSF obtained via Dyn-HTE accesses a wealth of additional information on dipolar excitations down to moderately low $T \gtrsim J/4$. On a technical level we achieve this by exploiting a graph-based approach for high-order moment expansions and fine momentum resolution, combined with continued-fraction reconstruction, judiciously chosen resummation schemes all packaged in a single algorithmic recipe [29]. This combination sets our method apart from previous (spin-)diagrammatic approaches in a qualitative manner [35,60–64].

Looking ahead, Dyn-HTE will not only be useful to model INS data but also informs experiments with local probes like muon spin relaxation [4] and inelastic electron tunneling or noise spectroscopy for 2D quantum magnets [65–67]. Other applications include finite-T spin diffusion and the computation of quantum Fisher information as entanglement witness [6,9]. Straightforward extensions of the Dyn-HTE formalism will consider advanced resummation strategies [68], $S > 1$, models with multiple couplings (e.g., $J_1 - J_2$) [69], single-ion anisotropies, or magnetic fields [32]. Another worthwhile extension would be the higher-order dynamic [70,71] or chiral [48,61,72] correlators moving into focus recently.

Acknowledgments—We thank Michel Ferrero, Matías Gonzalez, Lukas Janssen, Wei Li, Johannes Reuther, Alexander Tsirlin, Andreas Weichselbaum, and Kemp Plumb for useful discussions and the latter two for sharing DMRG data from Ref. [9] and INS data from Ref. [58], respectively. The authors acknowledge the Gauss Centre for Supercomputing e.V. for funding this project by providing computing time through the John von Neumann Institute for Computing (NIC) on the GCS Supercomputer JUWELS at Jülich Supercomputing Centre (JSC). The authors also acknowledge support by the state of Baden-Württemberg through bwHPC and the German Research Foundation (DFG) through Grant No. INST 40/575-1 FUGG (JUSTUS 2 cluster). We acknowledge funding from the Deutsche Forschungsgemeinschaft (DFG, German Research Foundation) through the Research Unit FOR 5413/1, Grant No. 465199066. B. Sc. acknowledges funding from the Munich Quantum Valley, supported by the Bavarian state government with funds from the Hightech Agenda Bayern Plus. B. Sb. and B. Sc. are supported by DFG Grant No. 524270816.

Data availability—The data that support the findings of this article are openly available [29].

[1] C. Broholm, R. J. Cava, S. A. Kivelson, D. G. Nocera, M. R. Norman, and T. Senthil, Quantum spin liquids, Science **367**, eaay0668 (2020).
[2] A. Browaeys and T. Lahaye, Many-body physics with individually-controlled Rydberg atoms, Nat. Phys. **16**, 132 (2020).
[3] L. Savary and L. Balents, Quantum spin liquids: A review, Rep. Prog. Phys. **80**, 016502 (2016).

[4] J. Khatua, B. Sana, A. Zorko, M. Gomilšek, K. S. M. S. R. Rao, M. Baenitz, B. Schmidt, and P. Khuntia, Experimental signatures of quantum and topological states in frustrated magnetism, Phys. Rep. **1041**, 1 (2023).

[5] M. L. Prichard, Z. Ba, I. Morera, B. M. Spar, D. A. Huse, E. Demler, and W. S. Bakr, Magnon-polarons in the Fermi–Hubbard model, Nat. Phys. **21**, 1548 (2025).

[6] P. Hauke, M. Heyl, L. Tagliacozzo, and P. Zoller, Measuring multipartite entanglement through dynamic susceptibilities, Nat. Phys. **12**, 778 (2016).

[7] P. Laurell, A. Scheie, E. Dagotto, and D. A. Tennant, Witnessing entanglement and quantum correlations in condensed matter: A review, Adv. Quantum Technol. **8**, 2400196 (2025).

[8] P. Prelovšek, M. Gomilšek, T. Arh, and A. Zorko, Dynamical spin correlations of the kagome antiferromagnet, Phys. Rev. B **103**, 014431 (2021).

[9] L. L. Kish, A. Weichselbaum, D. M. Pajerowski, A. T. Savici, A. Podlesnyak, L. Vasylechko, A. Tsvelik, R. Konik, and I. A. Zaliznyak, High-temperature quantum coherence of spinons in a rare-earth spin chain, Nat. Commun. **16**, 6594 (2025).

[10] M. Drescher, L. Vanderstraeten, R. Moessner, and F. Pollmann, Dynamical signatures of symmetry-broken and liquid phases in an $S = 1/2$ Heisenberg antiferromagnet on the triangular lattice, Phys. Rev. B **108**, L220401 (2023).

[11] N. E. Sherman, M. Dupont, and J. E. Moore, Spectral function of the $J_1 - J_2$ Heisenberg model on the triangular lattice, Phys. Rev. B **107**, 165146 (2023).

[12] J. Reuther and P. Wölfle, $J_1 - J_2$ frustrated two-dimensional Heisenberg model: Random phase approximation and functional renormalization group, Phys. Rev. B **81**, 144410 (2010).

[13] N. Niggemann, B. Sbierski, and J. Reuther, Frustrated quantum spins at finite temperature: Pseudo-Majorana functional renormalization group approach, Phys. Rev. B **103**, 104431 (2021).

[14] T. Müller, D. Kiese, N. Niggemann, B. Sbierski, J. Reuther, S. Trebst, R. Thomale, and Y. Iqbal, Pseudo-fermion functional renormalization group for spin models, Rep. Prog. Phys. **87**, 036501 (2024).

[15] S. A. Kulagin, N. Prokof'ev, O. A. Starykh, B. Svistunov, and C. N. Varney, Bold diagrammatic Monte Carlo technique for frustrated spin systems, Phys. Rev. B **87**, 024407 (2013).

[16] S. Zhang, H. J. Changlani, K. W. Plumb, O. Tchernyshyov, and R. Moessner, Dynamical structure factor of the three-dimensional quantum spin liquid candidate $NaCaNi_2F_7$, Phys. Rev. Lett. **122**, 167203 (2019).

[17] K. Remund, R. Pohle, Y. Akagi, J. Romhányi, and N. Shannon, Semi-classical simulation of spin-1 magnets, Phys. Rev. Res. **4**, 033106 (2022).

[18] D. Dahlbom, H. Zhang, C. Miles, S. Quinn, A. Niraula, B. Thipe, M. Wilson, S. Matin, H. Mankad, S. Hahn, D. Pajerowski, S. Johnston, Z. Wang, H. Lane, Y. W. Li, X. Bai, M. Mourigal, C. D. Batista, and K. Barros, Sunny.jl: A Julia package for spin dynamics, arXiv:2501.13095.

[19] C. Kim and M. Mourigal, Emulation of quantum correlations by classical dynamics in a spin-1/2 Heisenberg chain, Phys. Rev. B **112**, 214437 (2025).

[20] C. Domb and M. S. Green, *Phase Transitions and Critical Phenomena*, Series Expansions for Lattice Models, Phase Transitions and Critical Phenomena Vol. 3 (Academic Press, London, 1974).

[21] J. Oitmaa, C. Hamer, and W. Zheng, *Series Expansion Methods for Strongly Interacting Lattice Models* (Cambridge University Press, Cambridge, England, 2006).

[22] A. Lohmann, H.-J. Schmidt, and J. Richter, Tenth-order high-temperature expansion for the susceptibility and the specific heat of spin-s Heisenberg models with arbitrary exchange patterns: Application to pyrochlore and kagome magnets, Phys. Rev. B **89**, 014415 (2014).

[23] H. Mori, A continued-fraction representation of the time-correlation functions, Prog. Theor. Phys. **34**, 399 (1965).

[24] S. W. Lovesey and R. A. Meserve, Dynamic properties of a one-dimensional Heisenberg magnet, Phys. Rev. Lett. **28**, 614 (1972).

[25] V. S. Viswanath and G. Müller, *The Recursion Method: Application to Many-Body Dynamics*, Lecture Notes in Physics Monographs Vol. 23 (Springer, Berlin, Heidelberg, 1994).

[26] M. Rigol, T. Bryant, and Rajiv R. P. Singh, Numerical linked-cluster algorithms. I. Spin systems on square, triangular, and kagomé lattices, Phys. Rev. E **75**, 061118 (2007).

[27] B. Tang, E. Khatami, and M. Rigol, A short introduction to numerical linked-cluster expansions, Comput. Phys. Commun. **184**, 557 (2013).

[28] N. E. Sherman and R. R. P. Singh, Structure factors of the kagome-lattice Heisenberg antiferromagnets at finite temperatures, Phys. Rev. B **97**, 014423 (2018).

[29] B. Sbierski, B. Schneider, and R. Burkard, Dyn-HTE software v1.0, 2025, 10.5281/zenodo.17234446.

[30] R. Burkard, B. Schneider, and B. Sbierski, companion paper, High-temperature series expansion of the dynamic Matsubara spin correlator, Phys. Rev. B **113**, 075102 (2026).

[31] H. Rosner, R. R. P. Singh, W. H. Zheng, J. Oitmaa, and W. E. Pickett, High-temperature expansions for the $J_1 - J_2$ Heisenberg models: Applications to *ab initio* calculated models for Li_2VOSiO_4 and Li_2VOGeO_4, Phys. Rev. B **67**, 014416 (2003).

[32] L. Pierre, B. Bernu, and L. Messio, High temperature series expansions of $S = 1/2$ Heisenberg spin models: Algorithm to include the magnetic field with optimized complexity, SciPost Phys. **17**, 105 (2024).

[33] H. Bruus, K. Flensberg, H. Bruus, and K. Flensberg, *Many-Body Quantum Theory in Condensed Matter Physics: An Introduction*, Oxford Graduate Texts (Oxford University Press, Oxford, New York, 2004).

[34] S. Pairault, D. Senechal, and A.-M. S. Tremblay, Strong-coupling perturbation theory of the Hubbard model, Eur. Phys. J. B **16**, 85 (2000).

[35] E. Perepelitsky, A. Galatas, J. Mravlje, R. Žitko, E. Khatami, B. S. Shastry, and A. Georges, Transport and optical conductivity in the Hubbard model: A high-temperature expansion perspective, Phys. Rev. B **94**, 235115 (2016).

[36] P. Jung, R. W. Helmes, and A. Rosch, Transport in almost integrable models: Perturbed Heisenberg chains, Phys. Rev. Lett. **96**, 067202 (2006).

[37] J. Wang, M. H. Lamann, R. Steinigeweg, and J. Gemmer, Diffusion constants from the recursion method, Phys. Rev. B **110**, 104413 (2024).
[38] J. Halbinger, B. Schneider, and B. Sbierski, Spectral representation of matsubara n-point functions: Exact kernel functions and applications, SciPost Phys. **15**, 183 (2023).
[39] P. C. Kwok and T. D. Schultz, Correlation functions and Green functions: Zero-frequency anomalies, J. Phys. C **2**, 1196 (1969).
[40] M. Suzuki, Ergodicity, constants of motion, and bounds for susceptibilities, Physica (Utrecht) **51**, 277 (1971).
[41] C. Watzenböck, M. Fellinger, K. Held, and A. Toschi, Long-term memory magnetic correlations in the Hubbard model: A dynamical mean-field theory analysis, SciPost Phys. **12**, 184 (2022).
[42] A. A. Cuyt, V. Petersen, B. Verdonk, H. Waadeland, and W. B. Jones, *Handbook of Continued Fractions for Special Functions* (Springer Science & Business Media, New York, 2008).
[43] N. Elstner and A. P. Young, Spin-1/2 Heisenberg antiferromagnet on the kagome lattice: High-temperature expansion and exact-diagonalization studies, Phys. Rev. B **50**, 6871 (1994).
[44] S. Chakravarty, B. I. Halperin, and D. R. Nelson, Two-dimensional quantum Heisenberg antiferromagnet at low temperatures, Phys. Rev. B **39**, 2344 (1989).
[45] L. Capriotti, A. E. Trumper, and S. Sorella, Long-range Néel order in the triangular Heisenberg model, Phys. Rev. Lett. **82**, 3899 (1999).
[46] N. Elstner, R. R. P. Singh, and A. P. Young, Finite temperature properties of the spin-1/2 Heisenberg antiferromagnet on the triangular lattice, Phys. Rev. Lett. **71**, 1629 (1993).
[47] E. A. Ghioldi, M. G. Gonzalez, S.-S. Zhang, Y. Kamiya, L. O. Manuel, A. E. Trumper, and C. D. Batista, Dynamical structure factor of the triangular antiferromagnet: Schwinger boson theory beyond mean field, Phys. Rev. B **98**, 184403 (2018).
[48] L. Chen, D.-W. Qu, H. Li, B.-B. Chen, S.-S. Gong, J. v. Delft, A. Weichselbaum, and W. Li, Two-temperature scales in the triangular-lattice Heisenberg antiferromagnet, Phys. Rev. B **99**, 140404(R) (2019).
[49] W. Zheng, J. O. Fjærestad, Rajiv R. P. Singh, R. H. McKenzie, and R. Coldea, Anomalous excitation spectra of frustrated quantum antiferromagnets, Phys. Rev. Lett. **96**, 057201 (2006).
[50] O. A. Starykh, A. V. Chubukov, and A. G. Abanov, Flat spin-wave dispersion in a triangular antiferromagnet, Phys. Rev. B **74**, 180403(R) (2006).
[51] S. Sachdev, *Quantum Phase Transitions*, 2nd ed. (Cambridge University Press, Cambridge, England, 2011).
[52] S. Sachdev and J. Ye, Universal quantum-critical dynamics of two-dimensional antiferromagnets, Phys. Rev. Lett. **69**, 2411 (1992).
[53] A. V. Chubukov, S. Sachdev, and T. Senthil, Quantum phase transitions in frustrated quantum antiferromagnets, Nucl. Phys. **B426**, 601 (1994).
[54] Z. Zhu and S. R. White, Spin liquid phase of the S $= 1/2$ $J_1 - J_2$ Heisenberg model on the triangular lattice, Phys. Rev. B **92**, 041105(R) (2015).
[55] N. Zerf, R. Boyack, P. Marquard, J. A. Gracey, and J. Maciejko, Critical properties of the Néel–algebraic-spin-liquid transition, Phys. Rev. B **100**, 235130 (2019).
[56] E. Dupuis, M. B. Paranjape, and W. Witczak-Krempa, Transition from a Dirac spin liquid to an antiferromagnet: Monopoles in a QED3-Gross-Neveu theory, Phys. Rev. B **100**, 094443 (2019).
[57] A. O. Scheie *et al.*, Proximate spin liquid and fractionalization in the triangular antiferromagnet $KYbSe_2$, Nat. Phys. **20**, 74 (2024).
[58] K. W. Plumb, H. J. Changlani, A. Scheie, S. Zhang, J. W. Krizan, J. A. Rodriguez-Rivera, Y. Qiu, B. Winn, R. J. Cava, and C. L. Broholm, Continuum of quantum fluctuations in a three-dimensional $S = 1$ Heisenberg magnet, Nat. Phys. **15**, 54 (2019).
[59] R. Pohle and N. Shannon, Abundance of spin liquids in the $S = 1$ bilinear-biquadratic model on the pyrochlore lattice, and its application to $NaCaNi_2F_7$, arXiv:2503.12776.
[60] V. G. Vaks, A. I. Larkin, and S. A. Pikin, Self-consistent field method for the description of phase transitions, Sov. Phys. JETP **24**, 240 (1967).
[61] A. Rückriegel, D. Tarasevych, J. Krieg, and P. Kopietz, Recursive algorithm for generating high-temperature expansions for spin systems and the chiral nonlinear susceptibility, Phys. Rev. B **110**, 144416 (2024).
[62] B. Schneider, R. Burkard, B. Olmos, I. Lesanovsky, and B. Sbierski, Dipolar ordering transitions in many-body quantum optics: Analytical diagrammatic approach to equilibrium quantum spins, Phys. Rev. A **110**, 063301 (2024).
[63] E. Khatami, E. Perepelitsky, M. Rigol, and B. S. Shastry, Linked-cluster expansion for the Green's function of the infinite-U Hubbard model, Phys. Rev. E **89**, 063301 (2014).
[64] O. A. Starykh, A. W. Sandvik, and R. R. P. Singh, Dynamics of the spin-1/2 Heisenberg chain at intermediate temperatures, Phys. Rev. B **55**, 14953 (1997).
[65] J. Feldmeier, W. Natori, M. Knap, and J. Knolle, Local probes for charge-neutral edge states in two-dimensional quantum magnets, Phys. Rev. B **102**, 134423 (2020).
[66] E. J. König, M. T. Randeria, and B. Jäck, Tunneling spectroscopy of quantum spin liquids, Phys. Rev. Lett. **125**, 267206 (2020).
[67] E. J. Davis, B. Ye, F. Machado, S. A. Meynell, W. Wu, T. Mittiga, W. Schenken, M. Joos, B. Kobrin, Y. Lyu, Z. Wang, D. Bluvstein, S. Choi, C. Zu, A. C. B. Jayich, and N. Y. Yao, Probing many-body dynamics in a two-dimensional dipolar spin ensemble, Nat. Phys. **19**, 836 (2023).
[68] A. J. Kim, N. V. Prokof'ev, B. V. Svistunov, and E. Kozik, Homotopic action: A pathway to convergent diagrammatic theories, Phys. Rev. Lett. **126**, 257001 (2021).
[69] A. Hehn, N. Van Well, and M. Troyer, High-temperature series expansion for spin-1/2 Heisenberg models, Comput. Phys. Commun. **212**, 180 (2017).
[70] D. A. S. Kaib, M. Möller, and R. Valenti, Nonlinear spectroscopy as a magnon breakdown diagnosis and its efficient simulation, arXiv:2502.01746.
[71] Y. Watanabe, S. Trebst, and C. Hickey, Exploring two-dimensional coherent spectroscopy with exact diagonalization: Spinons and confinement in 1D quantum magnets, Phys. Rev. B **110**, 134443 (2024).
[72] G. Bornet, G. Emperauger, C. Chen, F. Machado, S. Chern, L. Leclerc, B. Gély, Y. T. Chew, D. Barredo, T. Lahaye, N. Y. Yao, and A. Browaeys, Enhancing a many-body

dipolar Rydberg tweezer array with arbitrary local controls, Phys. Rev. Lett. **132**, 263601 (2024).
[73] B. Dalla Piazza, M. Mourigal, N. B. Christensen, G. J. Nilsen, P. Tregenna-Piggott, T. G. Perring, M. Enderle, D. F. McMorrow, D. A. Ivanov, and H. M. Rønnow, Fractional excitations in the square-lattice quantum antiferromagnet, Nat. Phys. **11**, 62 (2015).
[74] H. Shao, Y. Q. Qin, S. Capponi, S. Chesi, Z. Y. Meng, and A. W. Sandvik, Nearly deconfined spinon excitations in the square-lattice spin-1/2 Heisenberg antiferromagnet, Phys. Rev. X **7**, 041072 (2017).
[75] Y. Ran, M. Hermele, P. A. Lee, and X.-G. Wen, Projected-wave-function study of the spin-1/2 Heisenberg model on the Kagomé lattice, Phys. Rev. Lett. **98**, 117205 (2007).
[76] Y. Iqbal, F. Becca, S. Sorella, and D. Poilblanc, Gapless spin-liquid phase in the kagome spin-1 2 Heisenberg antiferromagnet, Phys. Rev. B **87**, 060405(R) (2013).
[77] Y.-C. He, M. P. Zaletel, M. Oshikawa, and F. Pollmann, Signatures of Dirac cones in a DMRG study of the Kagome Heisenberg model, Phys. Rev. X **7**, 031020 (2017).
[78] S. Yan, D. A. Huse, and S. R. White, Spin liquid ground state of the $S = 1/2$ Kagome Heisenberg model, Science **332**, 1173 (2011).
[79] S. Depenbrock, I. P. McCulloch, and U. Schollwöck, Nature of the spin-liquid ground state of the $S = 1/2$ Heisenberg model on the Kagome lattice, Phys. Rev. Lett. **109**, 067201 (2012).
[80] W. Zhu, X. Chen, Y.-C. He, and W. Witczak-Krempa, Entanglement signatures of emergent Dirac fermions: Kagome spin liquid & quantum criticality, Sci. Adv. **4**, eaat5535 (2018).
[81] O. Golinelli, T. Jolicoeur, and R. Lacaze, Finite-lattice extrapolations for a Haldane-gap antiferromagnet, Phys. Rev. B **50**, 3037 (1994).
[82] S. R. White and I. Affleck, Spectral function for the $S = 1$ Heisenberg antiferromagetic chain, Phys. Rev. B **77**, 134437 (2008).
[83] J. Becker, T. Köhler, A. C. Tiegel, S. R. Manmana, S. Wessel, and A. Honecker, Finite-temperature dynamics and thermal intraband magnon scattering in Haldane spin-one chains, Phys. Rev. B **96**, 060403(R) (2017).

End Matter

Continued-fraction parameters—The parameters δ_r for $r = 4, 5, 6$ are given in terms of moments $m_0, m_2, \ldots, m_{2r}$,

$$\delta_4 = \frac{m_2(m_4^3 - (2m_2m_6 + m_0m_8)m_4 + m_0m_6^2 + m_2^2m_8)}{(m_2^2 - m_0m_4)(m_2m_6 - m_4^2)} \tag{A1}$$

$$\delta_5 = -\frac{(m_2^2 - m_0m_4)(-m_6^3 + 2m_4m_8m_6 - m_2m_8^2 + (m_2m_6 - m_4^2)m_{10})}{(m_4^2 - m_2m_6)(m_4^3 - (2m_2m_6 + m_0m_8)m_4 + m_0m_6^2 + m_2^2m_8)} \tag{A2}$$

$$\begin{aligned}\delta_6 = {} & [(m_4^2 - m_2m_6)((3m_4m_8 + 2m_2m_{10} + m_0m_{12})m_6^2 - m_6^4 - 2((m_4^2 + m_0m_8)m_{10} + m_2(m_8^2 + m_4m_{12}))m_6 \\ & + m_0m_8^3 - m_4^2m_8^2 - m_2^2m_{10}^2 + m_0m_4m_{10}^2 + 2m_2m_4m_8m_{10} + (m_4^3 + (m_2^2 - m_0m_4)m_8)m_{12})] \\ & /[(m_4^3 - (2m_2m_6 + m_0m_8)m_4 + m_0m_6^2 + m_2^2m_8)(m_6^3 - 2m_4m_8m_6 + m_2m_8^2 + (m_4^2 - m_2m_6)m_{10})]\end{aligned} \tag{A3}$$

Termination function—The infinite continued fraction with linearly growing parameters $\Gamma_{a,b}(s) = [1/(s+)] \times [(1a + b)/(s+)][(2a + b)/(s+)][(3a + b))/(s+)] \cdots$, with $a, b > 0$ fulfills the functional equation $1/\Gamma_{a,b}(s) = s + (1a + b)\Gamma_{a,1a+b}(s)$, which is solved by a fraction of Hermite polynomials $H_\nu(z)$: $\Gamma_{a,b}(s) = \sqrt{2/a} H_{-1-b/a} \times (s/\sqrt{2a})/H_{-b/a}(s/\sqrt{2a})$. The special case $b = 0$ yields $\Gamma_{a,0}(s) = \sqrt{[\pi/(2a)]} e^{\frac{s^2}{2a}}[1 - \mathrm{erf}(s/\sqrt{2a})]$ and analytically continues to a Gaussian $\mathrm{Re}[\Gamma_{a,0}(iw + 0^+)] = \sqrt{[\pi/(2a)]} e^{-\frac{w^2}{2a}}$.

Moments and continued fraction parameters for the Heisenberg $S = 1/2$ AFM chain at $x > 0$—In Fig. 5 we provide details about the resummation of the Dyn-HTE moments $m_{\mathbf{k},2r}(x)$ for $x > 0$ and the parameters $\delta_{\mathbf{k},r}$ underlying the DSF in Fig. 2. We consider $\mathbf{k} = 0.2\pi$ and $\mathbf{k} = \pi$ in the left and right column, respectively. We find it convenient to show $x m_{\mathbf{k},2r}/m_{\mathbf{k},2r}(0)$ (top row); the factor x cancels the T that appears in the definition of the relaxation function and we thus expect a constant value for $x \to \infty$. The bare HTE series of $x m_{\mathbf{k},2r}/m_{\mathbf{k},2r}(0)$ is a polynomial of degree $1 + n_{\max} - 2r = 13 - 2r$, which diverges around $x = 2$ (thin solid lines). Resummation uses Padé approximants after a change of variable $u = \tanh(fx)$; for the chain, $f = 0.48$ shows good agreement between different Padé approximants. Because of the saturation of $\tanh(\cdot)$, x should not be taken larger than $O(2/f)$. In the bottom row we show the associated $\delta_{\mathbf{k},0}, \ldots, \delta_{\mathbf{k},3}$ and the linear extrapolation

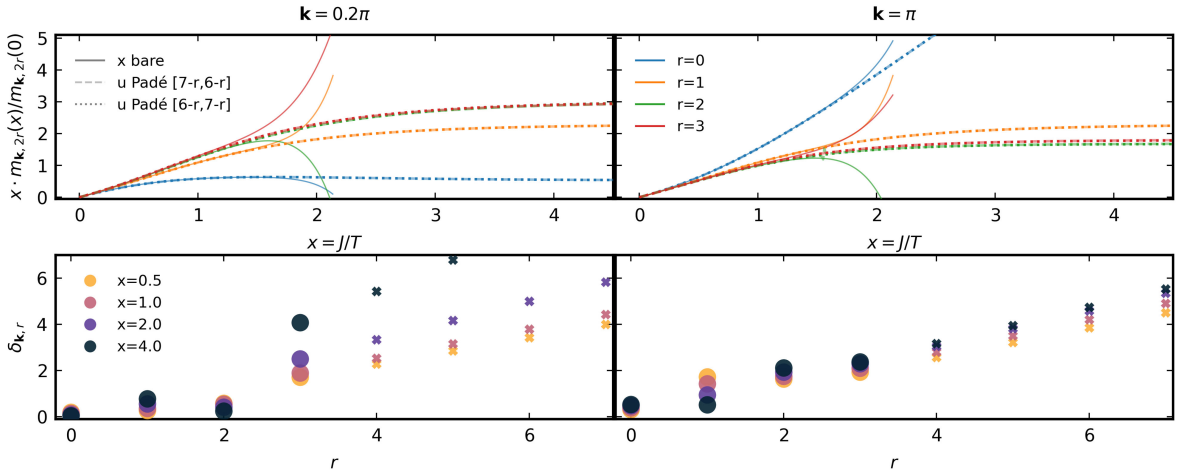

FIG. 5. Heisenberg $S = 1/2$ AFM chain. First four normalized moments $xm_{\mathbf{k},2r}(x)/m_{\mathbf{k},2r}(0)$, $r = 0, 1, 2, 3$ from Dyn-HTE (top) and corresponding continued fraction parameters $\delta_{\mathbf{k},r}$ (bottom) at momenta $\mathbf{k} = 0.2\pi$ (left) and $\mathbf{k} = \pi$ (right). The solid lines represent the bare series, while the dotted and dashed lines are different Padé approximants in the variable $u = \tanh(fx)$. We chose $f = 0.48$ such that the different Padé approximants agree with each other. The bottom row shows the corresponding δ_r of the continued fraction expansion at various temperatures (dots) and their linear extrapolation for $r \geq 4$ (crosses).

for $\delta_{\mathbf{k},4}$ and higher (via a line through $\delta_{\mathbf{k},3}$ and the origin). Note that all $\delta_{\mathbf{k},r}$ are non-negative as required for a faithful $A_{\mathbf{k}}(\omega)$, but this might break for poor moment resummations.

Square-lattice Heisenberg $S = 1/2$ AFM—This model is unfrustrated and known to exhibit long-range Néel order at $T = 0$. At finite T, the spin correlation length becomes finite and the characteristic magnon excitations acquire a lifetime broadening. The DSF of this model has been studied experimentally in a material realization [73] and numerically via quantum Monte Carlo [74]. In Fig. 6 (left) we present the DSF from Dyn-HTE at $x = J/T = 2.0$, where the paramagnons emergent from low ω at $\mathbf{k} = (\pi, \pi)$ are already clearly discernible. The crosses reproduce the energy of the paramagnon mode measured experimentally at $x \simeq 11$ [73]. Despite the difference in T, the agreement is reasonable. Another noteworthy feature of the Dyn-HTE data also observed in experiment is the suppression of the DSF at $(\pi, 0)$ as compared to $(\pi/2, \pi/2)$. However, at temperatures accessible to Dyn-HTE, we fail too see the anomalous non-Gaussian DSF line shape at $(\pi, 0)$, which was proposed as a signature of spinon deconfinement [73].

Kagome lattice Heisenberg $S = 1/2$ AFM—This frustrated nearest-neighbor model is defined by lattice vectors $\mathbf{e}_{1,2} = (1, \pm\sqrt{3})$ and a triatomic basis at the origin and at $(\pm 1, -\sqrt{3})/2$. The nature of the ground state remains under debate with certain evidence for either a gapless U(1) Dirac QSL [75–77] or a gapped $\mathbb{Z}_2$ QSL [78,79]. The DSF at $T = 0$ obtained from DMRG suffers

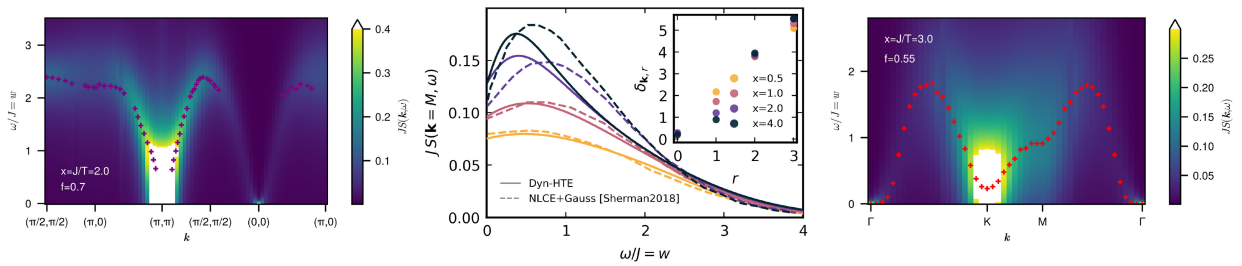

FIG. 6. DSF for $S = 1/2$ nearest-neighbor Heisenberg AFMs in 2D from Dyn-HTE calculated with $r_{\max} = 3$. Left: square lattice model at $x = J/T = 2$ ($f = 0.7$). Crosses denote the energy of the paramagnon mode measured experimentally at $x \simeq 11$ in Ref. [73]. Middle: kagome lattice model, line cuts at momentum M in the extended Brillouin zone from Dyn-HTE with $r_{\max} = 3$ and $f = 0.6$ (lines) and the NLCE results (dashed) from Ref. [28], which use only $r = 0, 1$ (Gaussian approximation). Inset: continued fraction parameters δ_r for the four different temperatures $x = J/T$ from Dyn-HTE. Right: triangular lattice model at $x = 3$ ($f = 0.55$). The red crosses denote the maximum obtained from the Dyn-HTE data at fixed momentum.

from severe finite-size effects [80], especially at small $|\omega|$. For $x = J/T \leq 4$ the DSF has been calculated with NLCE [28] and the Gaussian approximation that constructs $A_{\mathbf{k}}(\omega)$ from moments $r = 0$, 1. We focus on the high-symmetry momentum $M = (0, 2\pi/\sqrt{3})$ and show the DSF from Dyn-HTE using four moments in Fig. 6 (middle panel, full lines). Padé approximants of the u series ($f = 0.6$) allow us to reach $x = 4$. For $x \leq 1$ the Dyn-HTE is close to NLCE results (dashed lines) but for larger x the line shapes deviate significantly. At the K point, the DSF (not shown) closely resembles a slightly scaled up version of the data at the M point.

Triangular lattice Heisenberg $S = 1/2$ AFM—We supplement the line cuts shown in Fig. 3 with a plot of the DSF at $x = 3$ along a BZ path; see Fig. 6 (right panel). For each momentum, we denote the frequency with maximum DSF by a red cross. The shallow dip characterizing the rotonlike excitation at $\mathbf{k} = M$ can already be inferred.

Heisenberg $S = 1$ AFM chain—This model serves as a benchmark for $S = 1$ and features a Haldane gap of $\simeq 0.41J$ [81]. In Fig. 7(a) we show the DSF from Dyn-HTE at $x = 4$ for which the maximum of the dispersion agrees already closely to a ground-state error-controlled DMRG result [82] (red line). The temperature-induced faint intraband magnon scattering signal [83] is not resolved, likely due the low number of moments. A practical insight for postprocessing of Dyn-HTE data is gained from the attempt to compute the real-space on-site structure factor. From ground-state simulations [82] it is expected to feature a double-peak structure that will be softened by temperature. In principle, one could base its calculation on the on-site moments, $m_{ii,2r}$ obtained from the local Matsubara correlator. However, the result is more robust and closer to the expected shape if instead one takes the $\mathbf{k}$ integral over the $\mathbf{k}$-resolved DSF of panel (a); this is shown in Fig. 7(b). The reason is that single-peak shapes [as in $S(k, \omega)$] are more reliably obtained from a limited number of frequency moments $m_{\mathbf{k},2r}$ than more complicated shapes.

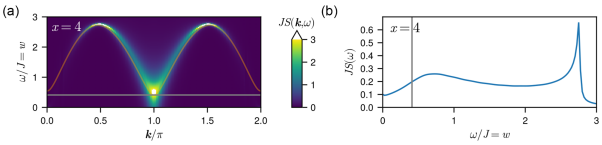

FIG. 7. $S = 1$ AFM Heisenberg chain. (a) DSF for $x = J/T = 4$ from Dyn-HTE with $r_{\max} = 3$ and $f = 0.48$. The red line shows the maxima of the DSF at $T = 0$ obtained from DMRG [82]. (b) On-site DSF $S(\omega) = 1/(2\pi) \int_{-\pi}^{\pi} d\mathbf{k} S(\mathbf{k}, \omega)$ obtained from the data in panel (a). In both panels, the gray lines indicate the Haldane gap of $0.41049(2)J$ [81].

6 Summary and Discussion

In this chapter, we summarize the main results of the thesis and discuss them in the context of the existing literature, giving outlooks for possible future related projects and finally give concluding remarks.

6.1 Functional Renormalization Group for Partons

In Chapter 3 we introduced various state-of-the-art improvements of parton-FRG approaches. Reviewing their impact on recent publications, it is clear that the inclusion of the Popov-Fedotov trick has not become the standard for other pf-FRG codes. This is likely due to the recent slowdown in the development of pf-FRG codes altogether. The pm-FRG has since superseded the pf-FRG with its many advantages (finite temperatures, critical scaling analyses, no unphysical states, ect.). The here devised temperature flow pm-FRG scheme has been shown to be incredibly useful when mapping out complete phase diagrams reproducing accurate transition temperatures down to $\frac{T}{J} \sim 0.5 \times 10^{-2}$ [P2; SGR25].

The pm-FRG has been established to provide quantitatively correct data for high enough temperatures or magnetic fields [NSR21; NRS22; P2; SGR25]. However, the pm-FRG is not suitable for obtaining quantitatively sound, low-temperature or ground-state properties. To find out how far the pm-FRG can be trusted, internal consistency checks of pm-FRG were developed [P2] that typically fail around $T \sim 10^{-1}J$ well before $T = 0$ is reached.

To improve this range of validity inside the FRG framework, another truncation scheme would have to be used than completely truncating the contribution of the six-point vertex. Since taking the full six-point vertex into account is prohibitively numerically expensive, one must resort to taking only parts of the six-point vertex into account. This is usually done by a loop expansion. Taking two-loop contributions into account can improve but also worsen the quantitative nature of the results [NRS22]. A rigorous n-loop expansion has been shown to converge to the parquet equations for $n \to \infty$ [KD18a; KD18b] This is the hard limit, when working only with four-Majorana objects. Unfortunately, the converged parquet equations produce significantly worse results than the 1-loop results [Nig24, Appendix C], indicating that the fully irreducible vertex becomes crucially important.

This raises the question of how else the pm-FRG could be improved. The full six-point vertex would depend on 5 independent frequencies and 2 independent d-dimensional momenta. For three-dimensional lattices, this adds up to an 11 dimensional object, which is far out of reach for a complete numerical treatment. Perhaps intelligent compression algorithms, such as the quantics-TCI method [Rit+24; Roh+25; Fra+25], will address this issue in the future. For now, we are therefore limited to four-Majoran objects. Since every spin is a bilinear of two Majoranas, this only gives us access to the full spin-spin correlation function $\langle S_i^\alpha(i\omega_n) S_j^\beta(-i\omega_n)\rangle$ (and parts of the four spin correlator as explained in Sec. 2.8). To differentiate spin liquids from valence bond solids, higher-order correlators are needed. This motivated investigations into the strong-coupling spin diagrammatics presented in Chapter 4 and Chapter 5.

6.2 Implications of the Connections Between the Pseudo-Majorana and Spin-Diagrams

In Sec. 2.8 we showed that the pseudo-Majorana action can be derived exactly from the time-ordered exponential $W[h, J]$ written in terms of spin-operators without using the Majorana representation. While this mapping of the three spin operators $S^{x,y,z}$ to three flavours of *free*, real (Majorana-) fermions is only possible exactly for $S = \frac{1}{2}$, we propose a way to map $S^{x,y,z}$ to interacting, real (Majorana-) fermions for any spin value $S > \frac{1}{2}$:

To generalize the SO(3) Majorana action to higher spin values, one can follow the derivation outlined in Sec. 2.8 until Eq. (2.83) exactly, with the difference that $2S_i^\alpha \eta_i^0$ are not canonical fermions anymore. Then it is possible to continue without the use of a path integral as established in Ref. [Rüc+23]. This leads to an effective fermionic theory with non-zero local n-point interaction vertices even for non-interacting spins and a bare Green's function with unconventional quasiparticle weight:

$$\langle (2S_i^\alpha \eta_i^0)[i\omega](2S_j^\beta \eta_j^0)[-i\omega]\rangle_0 = \delta_{ij}\delta_{\alpha\beta}\frac{4S(S+1)}{3}\frac{1}{i\omega}, \tag{6.1}$$

where $i\omega$ is a fermionic Matsubara frequency. Notice that Eq. (6.1) reduces to a bare fermionic Green's function for $S = \frac{1}{2}$.

The approach proposed above makes all spin values $\frac{1}{2} \leq S \leq \infty$ available in a three-flavor, Majorana-like, fermionic approach, where the spin algebra is encoded in bare local n-point vertices to all orders. This closes the gap to the bosonic strong-coupling approach used in the spin-FRG where all spin values are naturally available [Kri19]. The main difference between the two approaches is that the local spin algebra gets encoded using either bosons or fermions, which results in different bare n-point vertices.

For $S = \frac{1}{2}$ we could show that the spin-algebra can be exactly represented using free Majorana fermions, resulting in no bare n-point vertices. In contrast, free bosons can not capture the local spin algebra, leading to bare n-point vertices even at $S = \frac{1}{2}$. This leads to much better fulfillment of the equations of motion in the fermionic case when using a simple vertex truncation. In the pm-FRG approach fulfillment of the equations of motion is therefore used as a consistency check [P2], while they have to be fixed by hand in the spin-FRG approach [RW10]. Whether this carries on to higher spin values is unclear. A comprehensive study of such *fermionized* spin diagrammatic approaches for spin values $S > \frac{1}{2}$ and a comparison to their bosonic counterpart is left for future work.

6.3 Spectral Representation and Its Use in Perturbation Theory

In Sec. 2.7 we established how to use the spectral representation for multipoint correlation functions to write Matsubara diagrammatics in terms of spectral functions. Our main result is Eq. (2.75), which has already been an invaluable tool in Refs. [P5; P6; P7; P8] for calculating high-order strong-coupling perturbation theory diagrams without solving a single Matsubara sum. Since Eq. (2.75) retains the analytic dependence on the Matsubara frequencies through the kernel function $\mathcal{K}$, analytic continuation of the results is well defined.

The idea of using the spectral representation to calculate Matsubara diagrammatics is not new, but it is not very widespread either. Therefore, we now discuss our results in the context of the existing literature: The algorithmic Matsubara integration (AMI) algorithm developed by LeBlanc et al. [TCL19; EML22; BL25], first writes down a Matsubara diagram, represents every Matsubara Green's function in terms of its spectral representation, and then iteratively and analytically solves all Matsubara integrals, leaving just a convolution over a kernel with the remaining spectral functions. Up to now, their approach and implementations have only been used for diagrammatics built from two-point Green's functions [BGL23; GL23; LeB+22; FL24; FGL23; McN+22; TCL20b; TCL20a], making them unapplicable here.

A similar approach with a higher focus on approximations with well-defined error measures is the discrete Lehman representation (DLR) [KCP22] , which uses the strong decay of singular values of the Matsubara kernel function to approximate spectral functions systematically. While it has been generalized to three-point functions [Kie+25], systematic treatment of n-point objects used in this thesis is also not available in the DLR framework. The DLR framework is, however, tailored to solving self-consistent perturbation theory [LKH25; She+23; Li+20; Kay+24]. Similar methods were also used to speed up parquet calculations [WSK21]. A lot more similar to our approach are Refs. [VSF21; Kha+14] that also analytically solve the imaginary time integrals (Eq. (2.71)) appearing in fermionic weak-coupling and strong-coupling diagrams.

As mentioned above, the main advantage of our approach to calculate perturbation theory diagrams via the spectral representation is that the results retain an analytic dependence on the Matsubara frequencies, making analytic continuation possible. The main disadvantage, however, is the appearance of the sum over $(n+2)!$ permutations p in Eq. (2.75) that increases numerical costs. In our case, the numerical costs are still a lot lower than calculating the Matsubara sums numerically, since spectral functions of the uncoupled spins only have one pole at zero frequency. However, for applications with spectral functions with many poles, the $(n+2)!$ terms become prohibitive. This is the reason why such analytically continued Matsubara diagrammatics are often used in the context of bold pseudo-particle hybridization expansions [Hua+25; Hau23]. Since these pseudo-particles only contribute for cyclic permutations of one strict time order, the $(n+2)!$ terms reduce to $n+2$ terms, making calculations more tractable. While we only use the spectral representation to calculate two-point functions in this thesis, Eq. (2.75) can be easily generalized for n-point functions where the problem of analytic continuation to access any Keldysh-index or partial spectral function has been solved recently [Ge+24]. This can be used to calculate perturbative expansions of n-point partial spectral functions. Together with the insight that vertex functions themselves can be written as a sum of n-point expectation values, each of which has a spectral representation [Lih+24], the analytic continuation of known functional schemes like the FRG or the parquet equations becomes conceivable. We leave such efforts for future projects.

6.4 Spin-Diagrams Using the Generalized Wick's Theorem

In Ref. [P5], we could achieve convincing results for beyond mean-field corrections to spin correlators already with an expansion up to 4th order, which included the calculation of 20 strong-coupling diagrams. This motivated us to go to higher orders. The number of diagrams quickly grows, such that a numerical implementation is unavoidable. We found that while the calculation of the frequency dependence for higher-order graphs is straightforward, calculating the momentum dependence is hard, as the higher orders lead to very high-dimensional

momentum convolutions. These are solvable analytically in theory, in practice, we lacked the analytic tools to do so generally on arbitrary lattices for the $\sim 10 \times 10^6$ of graphs that appear at 12^{th} order. This is the reason why we have changed strategies in Refs. [P8; P7] to using the restricted graph approach instead of the generalized Wick's theorem to calculate the strong-coupling expansion diagrams, effectively generalizing the high temperature expansion to dynamic quantities. There, the problem of calculating high-dimensional momentum convolutions is translated into calculating subgraph isomorphisms, which can be efficiently calculated by numerical graph theory packages [Fai+21].

If one would like to use generalized Wick's theorem diagrammatics, the problem of calculating general high-dimensional convolutions in momentum space over lattice structure factors would have to be solved with a general and flexible method. This could, for example, be tackled by a Monte Carlo or tensor cross-interpolation method. These would, however, not give analytic results for diagram coefficients, making analytical continuation schemes unstable. However, it is known analytically that the high-dimensional momentum convolutions appearing in the strong-coupling expansion always result in a finite sum of lattice harmonics with integer coefficients. This can be directly seen by transforming the momentum integrals back into real space. Then the site sums count the number of restricted random walks of a fixed length between two lattice sites. Transforming back to momentum space again yields a sum of lattice harmonics, with the integer coefficients being the number of restricted random walks of a fixed length between the corresponding lattice sites. It has been shown in the tensor cross-interpolation context that such integer values can be stably obtained from complicated momentum integrals [Rit+24], making an application in this context conceivable in the future.

6.5 Implications of the Quantum-to-Classical Correspondence

As discussed in Chapter 4 we could show in Ref. [P6] that the quantum-to-classical correspondence observed in diagrammatic Monte Carlo is a direct effect of the static susceptibility having the particularly simple functional form of a mean-field susceptibility with renormalized parameters (see Eq. (4.3)). It is remarkable that such a simple form can universally describe static susceptibilities for Heisenberg models in two and three dimensions, regardless of their lattice geometries. While we could explain why the susceptibilities of Quantum and Classical models can be matched upon rescaling of the simulation temperature, we could not explain why the static susceptibility has such a simple functional form beyond the empirical observation that diagrams contributing to corrections of the renormalized mean field form destructively interfere leading to a strong suppresion of $\epsilon(\mathbf{k})$.

Let us narrow that conceptual gap here by considering the implications if the renormalized mean field form were exact. The Matsubara Spin-Spin correlator

$$G(i\omega, \mathbf{k}) = \frac{1}{N} \sum_{\mathbf{r},\mathbf{r}'} e^{-i\mathbf{k}\cdot(\mathbf{r}-\mathbf{r}')} \int_0^\beta \mathrm{d}\tau e^{i\omega\tau} \langle S^z_{\mathbf{r}}(\tau) S^z_{\mathbf{r}'}(0) \rangle, \tag{6.2}$$

can be written in a single-mode approximation as

$$TG(i\omega, \mathbf{k}) = \frac{m_2(\mathbf{k})}{(\frac{\omega}{J})^2 + \frac{m_2(\mathbf{k})}{T\chi(\mathbf{k})}}, \tag{6.3}$$

where $m_2(\mathbf{k})$ is the second moment of the spin-relaxation function or, equivalently, the term proportional to $(\frac{J}{\omega})^2$ in a high frequency expansion [P8] . This can be checked by setting

$\omega = 0$ giving $G(0, \mathbf{k}) = \chi(k)$ and the first term in the asymptotic expansion is given by $G(i\omega, \mathbf{k}) = \frac{m_2(\mathbf{k})}{\omega^2} + \mathcal{O}(\frac{1}{\omega^4})$, which coincides with the definition of $m_2(\mathbf{k})$. $m_2(\mathbf{k})$ is known exactly from the Heisenberg equations of motion [KW78]

$$m_2(\mathbf{k}) = \frac{4}{3}(1 - \gamma(\mathbf{k}))\frac{(-E)T}{J^2}, \tag{6.4}$$

where $E = \langle H \rangle$ is the energy expectation value.
Plugging this and the renormalized mean-field form for χ into Eq. (6.3) gives

$$TG(i\omega, \mathbf{k}) = \frac{(1 - \gamma(\mathbf{k}))\frac{4}{3}\frac{(-E)T}{J^2}}{(\frac{\omega}{J})^2 + (1 - \gamma(\mathbf{k}))(f + g\gamma(\mathbf{k}))\frac{4}{3}\frac{(-E)T}{J^2}}. \tag{6.5}$$

When inspecting the poles of Eq. (6.5) we find that they describe two harmonic quasiparticles with energies proportional to

$$E_k \sim \pm\sqrt{(1 - \gamma(\mathbf{k}))(1 + \frac{g}{f}\gamma(\mathbf{k}))}. \tag{6.6}$$

In the following, we consider the square lattice with $\gamma(\mathbf{k}) = \frac{1}{2}(\cos(k_1) + \cos(k_2))$. If we now choose $\frac{g}{f} = \pm 1$ for which the static susceptibility gets a divergence at the Γ and M point, the dispersion relations are $E_k \sim 1 - \gamma(\mathbf{k})$ and $E_k \sim \sqrt{1 - \gamma(\mathbf{k})^2}$, respectively. These are exactly the magnon dispersions obtained from linear spin wave theory for the ferro and antiferromagnetic ground states, respectively [Aue94]. Magnon dispersions like Eq. (6.6) can be obtained in linear spin wave theory for non-coplanar or canted orders, where neighboring spins have an angle different from (π) 0 as in the (anti)-ferromagnet. For example, the 120° order of the triangular lattice has the magnon dispersion $E_k \sim \sqrt{(1 - \gamma(\mathbf{k}))(1 + 2\gamma(\mathbf{k}))}$ [CZ09]. Therefore, Eq. (6.6) can be interpreted as a linear paramagnon dispersion on a thermally fluctuating spin-background that causes neighboring spins to have an average angle of $\cos(\theta) \sim \frac{g}{f}$. This semiclassical interpretation is consistent at infinite temperature, where $g = 0$ leads to an average angle of $\theta = \frac{\pi}{2}$, indicating that neighboring spins are uncorrelated as their nearest neighbor expectation value vanishes $\langle \mathbf{S}_i \cdot \mathbf{S}_j \rangle \sim \cos(\theta) \xrightarrow{\theta=\frac{\pi}{2}} 0$. It is also consistent at zero temperature, where spins are aligned (anti)-parallelly $\langle \mathbf{S}_i \cdot \mathbf{S}_j \rangle \sim \cos(\frac{\pi}{2} \pm \frac{\pi}{2}) = \pm 1$ for (anti)-ferromagnetic coupling. Of course, thermal fluctuations would lead to severely suppressed quasiparticle lifetimes at high temperatures, which is not taken into account here. The paramagnons obtained from the single-mode approximation capture the collected spectral weight of the spins for each $\mathbf{k}$ point at a pole located at an average pole position $\bar{\omega} = [\int_0^\infty \mathrm{d}\omega R_{\mathbf{k}}(\omega)\omega] \,/\, \int_0^\infty \mathrm{d}\omega R_{\mathbf{k}}(\omega)$. We illustrate this in Fig. 6.1 where the relaxation function for the triangular lattice Heisenberg model is shown for anti- and ferromagnetic coupling at different temperatures. Here, the average pole position $\bar{\omega}$ and the paramagnon dispersion (Eq. (6.6)) match very well for specific choices of g/f. Minor deviations appear close to the Γ point, where spin-dynamics is governed by spin-diffusion not captured by the single-mode approximation.

In summary, the empirically observed quantum-to-classical correspondence is consistent with a description by linear paramagnons on a thermally fluctuating spin background. It remains a challenge for future work to substantiate the above interpretation and to set up a rigorous linear paramagnon theory that both explains the quantum-to-classical correspondence at high and intermediate temperatures and smoothly interpolates to known low-temperature linear spin wave theory results where applicable. Previous attempts, such as the modified

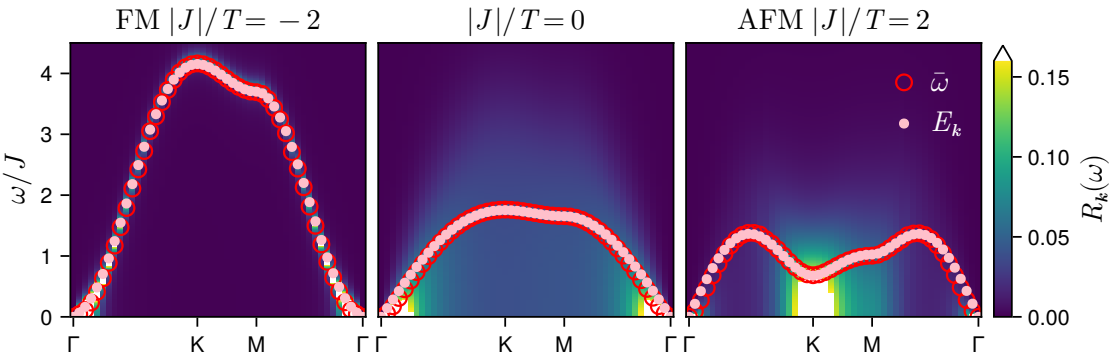

Figure 6.1 Resummed 12th order spin relaxation functions $R_{\mathbf{k}}(\omega)$ for the triangular lattice Heisenberg model calculated with the Dyn-HTE package [P9] at different ratios of $J/T = \{-2, 0, 2\}$ where $J/T = -2$ corresponds to ferromagnetic coupling. Open circles correspond to the weighted average frequency $\bar{\omega} = \left[\int_0^\infty \mathrm{d}\omega R_{\mathbf{k}}(\omega)\omega\right] / \int_0^\infty \mathrm{d}\omega R_{\mathbf{k}}(\omega)$ and filled circles correspond to the paramagnon dispersion $E_{\mathbf{k}}$ (Eq. (6.6)) with parameters $g/f = \{-0.95, 0, 165\}$ from left to right. Deviations from the Eq. (6.6) are largest near $\mathbf{k} = \Gamma$, where the dynamics is governed by spin diffusion, which is not captured by the paramagnon description.

spin-wave theory [Tak89; HT89; NY17], have so far failed to capture the high-temperature limit correctly and only work if the classical ground state is magnetically ordered. Also, the question remains, why the quantum-to-classical correspondence seems to hold exceptionally well for frustrated lattices, where linear spin wave theory is not a good low-temperature description. Such a quasiparticle interpretation may in the future also shed light on the related quantum-to-classical correspondence observed for the DSF [KM25].

6.6 Dynamic High Temperature Series Expansion

As discussed in Chapter 5 we managed to devise a new method [P7] that generalizes the high-temperature series expansion (HTE) to dynamic quantities (Dyn-HTE). We published a well-documented open-source code that can both calculate the expansion coefficients for Heisenberg models with a single coupling parameter and reconstruct the corresponding dynamic structure factors [P9]. Finally, we showed that the so obtained dynamic structure factors both match experimental and theoretical predictions [P8]. The method heavily builds on the advancements made in Ref. [P4] that made the kernel of the spectral representation for multipoint functions (see Sec. 2.7) analytically available for n-point bosonic correlators.

Before the Dyn-HTE, faithful simulations of the DSF for quantum Heisenberg models in three dimensions were entirely out of range, leaving only semiclassical approaches [PS25; Zha+19]. Due to the high flexibility of the Dyn-HTE, which also permits any spin value S, we expect this breakthrough in calculating high and intermediate-temperature DSFs to be an invaluable tool for explaining experimental finite-temperature neutron-scattering data in the future. Since our current implementation is limited to J_1 Heisenberg models, the next logical steps involve generalizing the method to other interaction types and further neighbor coupling to describe interactions in real materials. First steps in that direction have already been explored in the Bachelor theses [B1,B2] that generalized the Heisenberg to an XXZ type interaction, making the coupling parameters of quantum spin-ice materials accessible. Especially interesting would be a proper treatment of the bi-quadratic interactions, which are expected to play a role in the spin-1 pyrochlore magnet $NaCaNi_2F_7$ [PS25]. Other applications could include single-

ion anisotropies or magnetic fields [PBM24], extension to higher-order dynamic [KMV25; WTH24] or chiral [Rüc+24; Che+19; Sch+24] correlators which are recently moving into focus.

A different but just as promising direction are generalizations of the Dyn-HTE to fermionic Hamiltonians of the form of Eq. (2.52). This includes, for example, the Hubbard and t-J models where the Dyn-HTE should be able to yield complementary data to the weak coupling diagrammatic Monte Carlo data [Wie+21]. For these systems, instead of a high-temperature expansion, it would be a strong-coupling expansion in $\frac{t}{U}$ around the local theory using the restricted graph approach, which would also be valid at lower temperatures. Since the strong-coupling expansion is an expansion in terms of local expectation values, it is also possible to fulfill non-trivial local constraints. This makes it, for example, possible to obtain dynamic correlation functions in t-J models that are constrained to have a single hole [Gut+25].

6.7 Concluding Remarks

In this thesis, we set out to improve existing and develop new diagrammatic methods for simulating observables in frustrated spin systems. Along the way, we advanced the pm-FRG into an efficient tool capable of performing large-scale phase-diagram scans, and we constructed high-order strong-coupling / high-temperature expansions. A key methodological achievement was the development of the kernel trick, an approach to evaluate high-dimensional imaginary time integrals used for evaluating perturbation theory diagrams using their spectral representation, which proved invaluable in this work and may have broad applicability well beyond the specific use cases presented here.

Furthermore, we introduced a method to generate faithful finite-temperature quantum dynamic structure factors that can be directly compared to experimental data, and we have made our implementation publicly available to facilitate future research. We also provided new insight into the longstanding puzzle of the quantum-to-classical correspondence, identifying mechanisms that clarify its origin and conditions of validity. In addition, by establishing a connection between pseudo-Majorana and spin diagrammatics, we uncovered a structural correspondence that may enable future generalizations of Majorana-based diagrammatics to higher spin values.

Looking ahead, promising directions include explaining the quantum-to-classical correspondence within a finite-temperature disordered spin-wave theory, extending the Dyn-HTE framework to other models such as the Hubbard model, and generalizing the kernel trick to self-consistent diagrammatic schemes for higher n-point functions. Altogether, the methods and insights developed in this work provide a solid foundation for future studies of frustrated quantum systems and their emergent phenomena.

Appendix A

Linear Extrapolation of Continued Fraction Expansion

In Ref. [P8] we want to reconstruct the spin relaxation function $R_{\mathbf{k}}(w)$ which is closely related to the DSF via the fluctuation dissipation theorem (Eq. (2.13)). Following the classical ansatz of Mori [Mor65], we represent the Laplace transform of R as a continued fraction:

$$\tilde{R}_{\mathbf{k}}(s) \quad = \quad \frac{\delta_{\mathbf{k},0}}{s+}\frac{\delta_{\mathbf{k},1}}{s+}\frac{\delta_{\mathbf{k},2}}{s+}\frac{\delta_{\mathbf{k},3}}{s+}\cdots, \tag{A.1}$$

where the notation $\frac{\delta_{\mathbf{k},0}}{s+}\frac{\delta_{\mathbf{k},1}}{s}$ means $\frac{\delta_{\mathbf{k},0}}{s+\frac{\delta_{\mathbf{k},1}}{s}}$. However, the Dyn-HTE only gives us the first few $\delta_{\mathbf{k},n}$, which is why we need to extrapolate them to recover a smooth dynamic structure factor [VM94]. Results from infinite and finite temperature Lanzos schemes [HWG22] and the so-called operator growth hypothesis predict growing $\delta_{\mathbf{k},r}$ for growing n, where the growth rate is temperature dependent [TWZ24]. In practice, we use the first few $\delta_{\mathbf{k},r}$ and extrapolate them by fitting a linear function to them: $\delta_{r>r_{\max}} = (r - r_{\max})a + b$, which can be written as

$$\tilde{R}_{r_{max}}(s) = \frac{\delta_0}{s+}\frac{\delta_1}{s+}\frac{\delta_2}{s+}\cdots\frac{\delta_{r_{max}-1}}{s+\delta_{r_{max}}\Gamma_{a,b}(s)}, \tag{A.2}$$

where

$$\Gamma_{a,b}(s) = \frac{1}{s+}\frac{(1a+b)}{s+}\frac{(2a+b)}{s+}\frac{(3a+b)}{s+}\cdots \tag{A.3}$$

is a so-called continued fraction termination function defined as a continued fraction depending on the extrapolation parameters a and b.. For $a = 0$ the equation is easily solved by using the identity

$$0 = b\Gamma_{0,b}(s)^2 + s\Gamma_{0,b}(s) - 1, \tag{A.4}$$

which leads to the simple solution

$$\Gamma_{0,b}(s) = \frac{-s \pm \sqrt{4b+s^2}}{2b}. \tag{A.5}$$

For the general case, the identity is a bit more complicated

$$1/\Gamma_{a,b}(s) = s + (1a+b)\Gamma_{a,1a+b}(s). \tag{A.6}$$

and is solved by a fraction of Hermite polynomials $H_\nu(z)$ [Cuy+08]:

$$\Gamma_{a,b}(s) = \sqrt{\frac{2}{a}}\frac{H_{-1-b/a}\left(s/\sqrt{2a}\right)}{/H_{-b/a}\left(s/\sqrt{2a}\right)}. \tag{A.7}$$

The special case $b=0$ yields

$$\Gamma_{a,0}(s)=\sqrt{\frac{\pi}{2a}}e^{\frac{s^2}{2a}}[1-\mathrm{erf}(\frac{s}{\sqrt{2a}})], \tag{A.8}$$

which analytically continues to a Gaussian

$$\mathrm{Re}[\Gamma_{a,0}(iw+0^+)] = \sqrt{\frac{\pi}{2a}}e^{-\frac{w^2}{2a}}. \tag{A.9}$$

Fig. A.1 shows $\mathrm{Re}[\Gamma_{a,0}(iw+0^+)]$ for different values of a and b normalized to its value at $\omega = 0$. We can see that the extrapolation parameters mainly influence the lineshape and width.

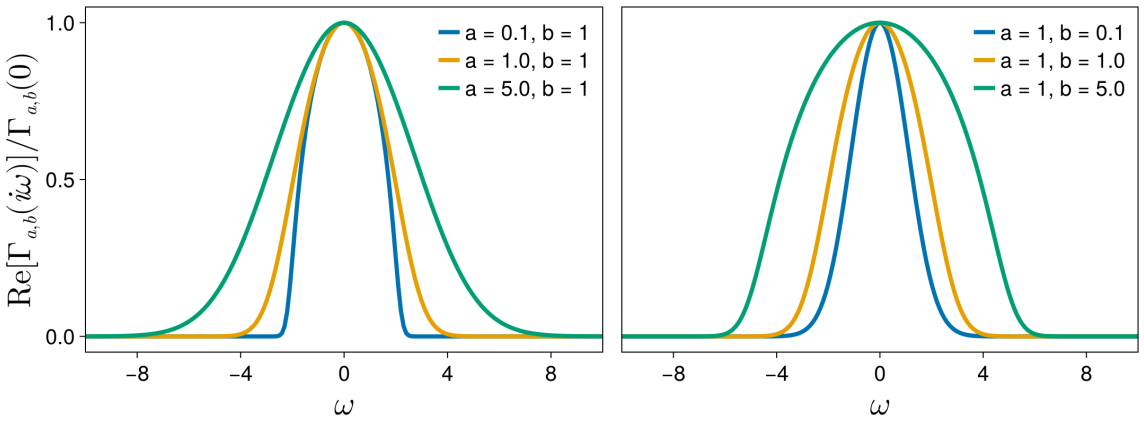

Figure A.1 Analytically continued terminator function $\mathrm{Re}[\Gamma_{a,0}(iw+0^+)]$ for different parameters normalized to its value at $\omega = 0$.

Bibliography

[P1] B. Schneider, D. Kiese, and B. Sbierski. "Taming Pseudofermion Functional Renormalization for Quantum Spins: Finite Temperatures and the Popov-Fedotov Trick." In: *Physical Review B* 106.23 (2022). DOI: 10.1103/PhysRevB.106.235113 (cit. on pp. v, 10, 19, 29, 30).

[P2] B. Schneider, J. Reuther, M. G. Gonzalez, B. Sbierski, and N. Niggemann. "Temperature Flow in Pseudo-Majorana Functional Renormalization for Quantum Spins." In: *Physical Review B* 109.19 (2024). DOI: 10.1103/PhysRevB.109.195109 (cit. on pp. v, 14, 29, 30, 145, 146).

[P3] F. Bippus, B. Schneider, and B. Sbierski. "Pseudo-Majorana Functional Renormalization for Frustrated XXZ Spin-$\frac{1}{2}$ Models with Field or Magnetization along the Spin- Z Direction at Finite Temperature." In: *Physical Review B* 111.5 (2025). DOI: 10.1103/PhysRevB.111.054420 (cit. on pp. v, 13, 29, 30).

[P4] J. Halbinger, B. Schneider, and B. Sbierski. "Spectral Representation of Matsubara N-Point Functions: Exact Kernel Functions and Applications." In: *SciPost Physics* 15.5 (2023). DOI: 10.21468/SciPostPhys.15.5.183 (cit. on pp. v, 71, 73, 117, 150).

[P5] B. Schneider, R. Burkard, B. Olmos, I. Lesanovsky, and B. Sbierski. "Dipolar Ordering Transitions in Many-Body Quantum Optics: Analytical Diagrammatic Approach to Equilibrium Quantum Spins." In: *Physical Review A* 110.6 (2024). DOI: 10.1103/PhysRevA.110.063301 (cit. on pp. v, 27, 71–73, 117, 146, 147).

[P6] B. Schneider and B. Sbierski. "Taming Spin Susceptibilities in Frustrated Quantum Magnets: Mean-Field Form and Approximate Nature of the Quantum-to-Classical Correspondence." In: *Physical Review Letters* 134.17 (2025). DOI: 10.1103/PhysRevLett.134.176502 (cit. on pp. v, 72, 73, 117, 146, 148).

[P7] R. Burkard, B. Schneider, and B. Sbierski. "High-Temperature Series Expansion of the Dynamic Matsubara Spin Correlator." In: *Physical Review B* 113.7 (2026). DOI: 10.1103/1l92-z6qd (cit. on pp. v, 27, 72, 117, 118, 146, 148, 150).

[P8] R. Burkard, B. Schneider, and B. Sbierski. "Dynamic Correlations of Frustrated Quantum Spins from High-Temperature Expansion." In: *Physical Review Letters* 136.5 (2026). DOI: 10.1103/jtjk-x2lw (cit. on pp. v, 117, 118, 146, 148, 150, 153).

[P9] B. Sbierski, B. Schneider, and R. Burkard. *Dyn-HTE: Initial Code Release of the Dyn-HTE.Jl Package*. Zenodo. 2025. DOI: 10.5281/zenodo.17234446 (cit. on pp. v, 117, 118, 150).

[AB12] A. Abragam and B. Bleaney. *Electron paramagnetic resonance of transition ions*. OUP oxford, 2012 (cit. on p. 1).

[AKR25] J. Arnold, P. Kopietz, and A. Rückriegel. *Strong-coupling functional renormalization group: Nagaoka ferromagnetism and non-Fermi liquid physics in the Hubbard model at $U = \infty$*. 2025. DOI: 10.48550/arXiv.2510.01909 (cit. on p. 20).

[ALI63] A. A. Abrikosov, L. P. Gorkov, and I. E. Dzyaloshinski. *Methods Of Quantum Field Theory In Statistical Physics*. eng. 1963 (cit. on p. 10).

[And+04] S. Andergassen, T. Enss, V. Meden, W. Metzner, U. Schollwöck, and K. Schönhammer. "Functional renormalization group for Luttinger liquids with impurities." en. In: *Physical Review B* 70.7 (2004). DOI: 10.1103/PhysRevB.70.075102 (cit. on p. 17).

[And72] P. W. Anderson. "More is different: broken symmetry and the nature of the hierarchical structure of science." In: *Science* 177.4047 (1972) (cit. on p. 1).

[And87] P. W. Anderson. "The Resonating Valence Bond State in La2CuO4 and Superconductivity." In: *Science* 235.4793 (1987). DOI: 10.1126/science.235.4793.1196 (cit. on p. 2).

[Aro+22] D. P. Arovas, E. Berg, S. A. Kivelson, and S. Raghu. "The Hubbard Model." en. In: *Annual Review of Condensed Matter Physics* 13.Volume 13, 2022 (2022). DOI: 10.1146/annurev-conmatphys-031620-102024 (cit. on p. 6).

[AS10] A. Altland and B. D. Simons. *Condensed Matter Field Theory*. 2nd ed. Cambridge: Cambridge University Press, 2010. DOI: 10.1017/CBO9780511789984 (cit. on pp. 9, 21, 24, 28).

[Aue94] A. Auerbach. *Interacting Electrons and Quantum Magnetism*. Graduate Texts in Contemporary Physics. New York, NY: Springer New York, 1994. DOI: 10.1007/978-1-4612-0869-3 (cit. on p. 149).

[Bak+67] G. A. Baker, H. E. Gilbert, J. Eve, and G. S. Rushbrooke. "High-Temperature Expansions for the Spin-½ Heisenberg Model." en. In: *Physical Review* 164.2 (1967). DOI: 10.1103/PhysRev.164.800 (cit. on p. 22).

[Bay62] G. Baym. "Self-Consistent Approximations in Many-Body Systems." en. In: *Physical Review* 127.4 (1962). DOI: 10.1103/PhysRev.127.1391 (cit. on p. 3).

[BCP08] R. Bulla, T. A. Costi, and T. Pruschke. "Numerical renormalization group method for quantum impurity systems." en. In: *Reviews of Modern Physics* 80.2 (2008). DOI: 10.1103/RevModPhys.80.395 (cit. on p. 16).

[BCS57] J. Bardeen, L. N. Cooper, and J. R. Schrieffer. "Theory of Superconductivity." en. In: *Physical Review* 108.5 (1957). DOI: 10.1103/PhysRev.108.1175 (cit. on p. 1).

[Ben+79] C. M. Bender, F. Cooper, G. S. Guralnik, and D. H. Sharp. "Strong-coupling expansion in quantum field theory." en. In: *Physical Review D* 19.6 (1979). DOI: 10.1103/PhysRevD.19.1865 (cit. on p. 20).

[BF04] H. Bruus and K. Flensberg. *Many-Body Quantum Theory in Condensed Matter Physics: An Introduction*. en. OUP Oxford, 2004 (cit. on pp. 6, 7, 22).

[BF83] J. Bricmont and J. Frölich. "An order parameter distinguishing between different phases of lattice gauge theories with matter fields." In: *Physics Letters B* 122.1 (1983). DOI: 10.1016/0370-2693(83)91171-1 (cit. on p. 2).

[BG96] G. A. Baker and P. Graves-Morris. *Padé Approximants*. 2nd ed. Encyclopedia of Mathematics and its Applications. Cambridge: Cambridge University Press, 1996. DOI: 10.1017/CBO9780511530074 (cit. on p. 24).

[BGL23] M. D. Burke, M. Grandadam, and J. P. F. LeBlanc. "Renormalized perturbation theory for fast evaluation of Feynman diagrams on the real frequency axis." en. In: *Physical Review B* 107.11 (2023). DOI: 10.1103/PhysRevB.107.115151 (cit. on p. 147).

[BH20] S. T. Bramwell and M. J. Harris. "The history of spin ice." en. In: *Journal of Physics: Condensed Matter* 32.37 (2020). DOI: 10.1088/1361-648X/ab8423 (cit. on p. 2).

[Bic04] N. E. Bickers. "Self-Consistent Many-Body Theory for Condensed Matter Systems." en. In: *Theoretical Methods for Strongly Correlated Electrons*. Ed. by D. Sénéchal, A.-M. Tremblay, and C. Bourbonnais. New York, NY: Springer, 2004. DOI: 10.1007/0-387-21717-7_6 (cit. on pp. 3, 9).

[BL25] M. D. Burke and J. P. F. LeBlanc. "TorchAmi: Generalized CPU/GPU implementation of algorithmic matsubara integration." In: *Computer Physics Communications* 308 (2025). DOI: 10.1016/j.cpc.2024.109437 (cit. on p. 147).

[BT16] F. L. Buessen and S. Trebst. "Competing magnetic orders and spin liquids in two- and three-dimensional kagome systems: Pseudofermion functional renormalization group perspective." en. In: *Physical Review B* 94.23 (2016). DOI: 10.1103/PhysRevB.94.235138 (cit. on p. 17).

[Bue+19] F. L. Buessen, V. Noculak, S. Trebst, and J. Reuther. "Functional renormalization group for frustrated magnets with nondiagonal spin interactions." en. In: *Physical Review B* 100.12 (2019). DOI: 10.1103/PhysRevB.100.125164 (cit. on p. 13).

[Che+19] L. Chen, D.-W. Qu, H. Li, B.-B. Chen, S.-S. Gong, J. Von Delft, A. Weichselbaum, and W. Li. "Two-temperature scales in the triangular-lattice Heisenberg antiferromagnet." en. In: *Physical Review B* 99.14 (2019). DOI: 10.1103/PhysRevB.99.140404 (cit. on pp. 118, 151).

[Che+24] L. E. Chern, F. Desrochers, Y. B. Kim, and C. Castelnovo. "Pseudofermion functional renormalization group study of dipolar-octupolar pyrochlore magnets." en. In: *Physical Review B* 109.18 (2024). DOI: 10.1103/PhysRevB.109.184421 (cit. on pp. 17, 18).

[CHS19] L. Classen, C. Honerkamp, and M. M. Scherer. "Competing phases of interacting electrons on triangular lattices in moiré heterostructures." en. In: *Physical Review B* 99.19 (2019). DOI: 10.1103/PhysRevB.99.195120 (cit. on p. 17).

[CS70] M. G. Cottam and R. B. Stinchcombe. "Thermodynamic properties of a Heisenberg antiferromagnet." en. In: *Journal of Physics C: Solid State Physics* 3.11 (1970). DOI: 10.1088/0022-3719/3/11/011 (cit. on p. 13).

[Cuy+08] A. A. M. Cuyt, V. Petersen, B. Verdonk, H. Waadeland, and W. B. Jones. *Handbook of Continued Fractions for Special Functions*. en. Springer Science & Business Media, 2008 (cit. on p. 153).

[CZ09] A. L. Chernyshev and M. E. Zhitomirsky. "Spin waves in a triangular lattice antiferromagnet: Decays, spectrum renormalization, and singularities." en. In: *Physical Review B* 79.14 (2009). DOI: 10.1103/PhysRevB.79.144416 (cit. on p. 149).

[DM64a] C. De Dominicis and P. C. Martin. "Stationary Entropy Principle and Renormalization in Normal and Superfluid Systems. I. Algebraic Formulation." en. In: *Journal of Mathematical Physics* 5.1 (1964). DOI: 10.1063/1.1704062 (cit. on pp. 3, 9).

[DM64b] C. De Dominicis and P. C. Martin. "Stationary Entropy Principle and Renormalization in Normal and Superfluid Systems. II. Diagrammatic Formulation." en. In: *Journal of Mathematical Physics* 5.1 (1964). DOI: 10.1063/1.1704064 (cit. on pp. 3, 9).

[DM66] B. S. DeWitt and A. A. Mullin. "Dynamical Theory of Groups and Fields." In: *American Journal of Physics* 34.12 (1966). DOI: 10.1119/1.1953053 (cit. on p. 15).

[Dre+23] M. Drescher, L. Vanderstraeten, R. Moessner, and F. Pollmann. "Dynamical signatures of symmetry-broken and liquid phases in an S = 1 2 Heisenberg antiferromagnet on the triangular lattice." en. In: *Physical Review B* 108.22 (2023). DOI: 10.1103/PhysRevB.108.L220401 (cit. on p. 3).

[Dre+25] M. Drescher, L. Vanderstraeten, R. Moessner, and F. Pollmann. *Spectral Functions of an Extended Antiferromagnetic $S = \frac{1}{2}$ Heisenberg Model on the Triangular Lattice*. 2025. DOI: 10.48550/arXiv.2508.17292 (cit. on p. 3).

[Dys49] F. J. Dyson. "The S Matrix in Quantum Electrodynamics." In: *Physical Review* 75.11 (1949). DOI: 10.1103/PhysRev.75.1736 (cit. on p. 3).

[EML22] H. Elazab, B. D. E. McNiven, and J. P. F. LeBlanc. "LIBAMI: Implementation of algorithmic Matsubara integration." In: *Computer Physics Communications* 280 (2022). DOI: 10.1016/j.cpc.2022.108469 (cit. on p. 147).

[ESY93] N. Elstner, R. R. P. Singh, and A. P. Young. "Finite temperature properties of the spin-1/2 Heisenberg antiferromagnet on the triangular lattice." en. In: *Physical Review Letters* 71.10 (1993). DOI: 10.1103/PhysRevLett.71.1629 (cit. on p. 118).

[Fai+21] J. Fairbanks, M. Besançon, S. Simon, J. Hoffiman, N. Eubank, and S. Karpinski. *JuliaGraphs/Graphs.jl: an optimized graphs package for the Julia programming language*. 2021 (cit. on p. 148).

[FGL23] R. Farid, M. Grandadam, and J. P. F. LeBlanc. "Pairing susceptibility of the two-dimensional Hubbard model in the thermodynamic limit." en. In: *Physical Review B* 107.19 (2023). DOI: 10.1103/PhysRevB.107.195138 (cit. on p. 147).

[FKP18] J. Fu, J. Knolle, and N. B. Perkins. "Three types of representation of spin in terms of Majorana fermions and an alternative solution of the Kitaev honeycomb model." en. In: *Physical Review B* 97.11 (2018). DOI: 10.1103/PhysRevB.97.115142 (cit. on pp. 11, 12).

[FL24] R. Farid and J. P. F. LeBlanc. "Pairing susceptibility in the weakly interacting multilayer Hubbard model evaluated by direct perturbative expansion." en. In: *Physical Review B* 110.14 (2024). DOI: 10.1103/PhysRevB.110.144511 (cit. on p. 147).

[Fra+25] M. Frankenbach, M. Ritter, M. Pelz, N. Ritz, J. v. Delft, and A. Ge. "Compressing local vertex functions from the multipoint numerical renormalization group using quantics tensor cross interpolation." In: *Physical Review Research* 7.4 (2025). DOI: 10.1103/jx7h-lsqk (cit. on pp. 25, 145).

[Fre+09] J. K. Freericks, H. R. Krishnamurthy, Y. Kato, N. Kawashima, and N. Trivedi. "Strong-coupling expansion for the momentum distribution of the Bose-Hubbard model with benchmarking against exact numerical results." en. In: *Physical Review A* 79.5 (2009). DOI: 10.1103/PhysRevA.79.053631 (cit. on p. 20).

[FYG21] J. Fei, C.-N. Yeh, and E. Gull. "Nevanlinna Analytical Continuation." en. In: *Physical Review Letters* 126.5 (2021). DOI: 10.1103/PhysRevLett.126.056402 (cit. on p. 24).

[Gao+24] B. Gao et al. *Spin Excitation Continuum in the Exactly Solvable Triangular-Lattice Spin Liquid CeMgAl11O19*. 2024. DOI: 10.48550/arXiv.2408.15957 (cit. on p. 30).

[Ge+24] A. Ge, J. Halbinger, S.-S. B. Lee, J. von Delft, and F. B. Kugler. "Analytic Continuation of Multipoint Correlation Functions." en. In: *Annalen der Physik* 536.7 (2024). DOI: 10.1002/andp.202300504 (cit. on pp. 25, 71, 147).

[Ge24] A. Ge. "Real-frequency quantum field theory applied to the single-impurity Anderson model." In: *Physical Review B* 109.11 (2024). DOI: 10.1103/PhysRevB.109.115128 (cit. on p. 17).

[Ge25] A. Ge. "Correlator-based approaches in real and imaginary frequencies." de. Text.PhDThesis. Ludwig-Maximilians-Universität München, 2025 (cit. on p. 17).

[Gin11] M. J. P. Gingras. "Spin Ice." en. In: *Introduction to Frustrated Magnetism: Materials, Experiments, Theory*. Ed. by C. Lacroix, P. Mendels, and F. Mila. Berlin, Heidelberg: Springer, 2011. DOI: 10.1007/978-3-642-10589-0_12 (cit. on p. 2).

[GL23] D. Gazizova and J. P. F. LeBlanc. "Emergent nearest-neighbor attraction in the fully renormalized interactions of the single-band repulsive Hubbard model at weak coupling." en. In: *Physical Review B* 108.16 (2023). DOI: 10.1103/PhysRevB.108.165149 (cit. on p. 147).

[GM14] M. J. P. Gingras and P. A. McClarty. "Quantum Spin Ice: A Search for Gapless Quantum Spin Liquids in Pyrochlore Magnets." In: *Reports on Progress in Physics* 77.5 (2014). DOI: 10.1088/0034-4885/77/5/056501 (cit. on p. 2).

[Gol+19] R. Goll, D. Tarasevych, J. Krieg, and P. Kopietz. "Spin functional renormalization group for quantum Heisenberg ferromagnets: Magnetization and magnon damping in two dimensions." In: *Physical Review B* 100 (2019). DOI: 10.1103/PhysRevB.100.174424 (cit. on p. 20).

[Gon+24] M. G. Gonzalez et al. "Dynamics of K2Ni2(SO4)3 governed by proximity to a 3D spin liquid model." en. In: *Nature Communications* 15.1 (2024). DOI: 10.1038/s41467-024-51362-1 (cit. on p. 72).

[Gre+11] K. Gregor, D. A. Huse, R. Moessner, and S. L. Sondhi. "Diagnosing deconfinement and topological order." en. In: *New Journal of Physics* 13.2 (2011). DOI: 10.1088/1367-2630/13/2/025009 (cit. on p. 2).

[Gre+25] L. Gresista, D. Lozano-Gómez, M. Vojta, S. Trebst, and Y. Iqbal. "Quantum effects on pyrochlore higher-rank U(1) spin liquids: Pinch-line singularities, spin nematics, and connections to oxide materials." en. In: *Physical Review Research* 7.3 (2025). DOI: 10.1103/3y39-9ndv (cit. on p. 17).

[GRK20] R. Goll, A. Rückriegel, and P. Kopietz. "Zero-magnon sound in quantum Heisenberg ferromagnets." en. In: *Physical Review B* 102.22 (2020). DOI: 10.1103/PhysRevB.102.224437 (cit. on p. 20).

[Gün+] G. Günal, M. K. Ritter, A. Gleis, B. Schneider, B. Sbierski, and J. Shim. "Benchmarking pf-fRG." In: *unpublished* () (cit. on p. 18).

[Gut+25] T. Guthardt, M. Scheb, J. v. Delft, A. Bohrdt, and F. Grusdt. *Magnetic polarons at finite temperature: One-hole spectroscopy study*. 2025. DOI: 10.48550/arXiv.2504.07701 (cit. on p. 151).

[Hal81] F. D. M. Haldane. "'Luttinger liquid theory' of one-dimensional quantum fluids. I. Properties of the Luttinger model and their extension to the general 1D interacting spinless Fermi gas." en. In: *Journal of Physics C: Solid State Physics* 14.19 (1981). DOI: 10.1088/0022-3719/14/19/010 (cit. on p. 1).

[Hau23] K. Haule. *Strong coupling quantum impurity solver on the real and imaginary axis*. 2023. DOI: 10.48550/arXiv.2311.09412 (cit. on p. 147).

[Hen89] C. L. Henley. "Ordering due to disorder in a frustrated vector antiferromagnet." en. In: *Physical Review Letters* 62.17 (1989). DOI: 10.1103/PhysRevLett.62.2056 (cit. on p. 2).

[Her+22] M. Hering, V. Noculak, F. Ferrari, Y. Iqbal, and J. Reuther. "Dimerization tendencies of the pyrochlore Heisenberg antiferromagnet: A functional renormalization group perspective." en. In: *Physical Review B* 105.5 (2022). DOI: 10.1103/PhysRevB.105.054426 (cit. on p. 17).

[HFB04] M. Hermele, M. P. A. Fisher, and L. Balents. "Pyrochlore Photons: The U(1) Spin Liquid in a $S = \frac{1}{2}$ Three-Dimensional Frustrated Magnet." In: *Physical Review B* 69.6 (2004). DOI: 10.1103/PhysRevB.69.064404 (cit. on p. 2).

[HGL23] Z. Huang, E. Gull, and L. Lin. "Robust analytic continuation of Green's functions via projection, pole estimation, and semidefinite relaxation." en. In: *Physical Review B* 107.7 (2023). DOI: 10.1103/PhysRevB.107.075151 (cit. on p. 24).

[Hil+20] C. Hille, F. B. Kugler, C. J. Eckhardt, Y.-Y. He, A. Kauch, C. Honerkamp, A. Toschi, and S. Andergassen. "Quantitative functional renormalization group description of the two-dimensional Hubbard model." en. In: *Physical Review Research* 2.3 (2020). DOI: 10.1103/PhysRevResearch.2.033372 (cit. on p. 17).

[HR17] M. Hering and J. Reuther. "Functional renormalization group analysis of Dzyaloshinsky-Moriya and Heisenberg spin interactions on the kagome lattice." en. In: *Physical Review B* 95.5 (2017). DOI: 10.1103/PhysRevB.95.054418 (cit. on pp. 17, 18).

[HS01] C. Honerkamp and M. Salmhofer. "Temperature-flow renormalization group and the competition between superconductivity and ferromagnetism." In: *Physical Review B* 64.18 (2001). DOI: 10.1103/PhysRevB.64.184516 (cit. on p. 17).

[HSK13] T. Herfurth, S. Streib, and P. Kopietz. "Majorana spin liquid and dimensional reduction in Cs 2 CuCl 4." en. In: *Physical Review B* 88.17 (2013). DOI: 10.1103/PhysRevB.88.174404 (cit. on p. 12).

[HT89] J. E. Hirsch and S. Tang. "Two-dimensional Heisenberg antiferromagnet with next-nearest-neighbor coupling." en. In: *Physical Review B* 39.4 (1989). DOI: 10.1103/PhysRevB.39.2887 (cit. on p. 150).

[Hua+16] Y. Huang, K. Chen, Y. Deng, N. Prokof'ev, and B. Svistunov. "Spin-Ice State of the Quantum Heisenberg Antiferromagnet on the Pyrochlore Lattice." In: *Physical Review Letters* 116.17 (2016). DOI: 10.1103/PhysRevLett.116.177203 (cit. on p. 72).

[Hua+25] Z. Huang, D. Golež, H. U. R. Strand, and J. Kaye. "Automated evaluation of imaginary time strong coupling diagrams by sum-of-exponentials hybridization fitting." en. In: (2025) (cit. on p. 147).

[HWG22] R. Heveling, J. Wang, and J. Gemmer. "Numerically probing the universal operator growth hypothesis." en. In: *Physical Review E* 106.1 (2022). DOI: 10.1103/PhysRevE.106.014152 (cit. on p. 153).

[HWT17] A. Hehn, N. van Well, and M. Troyer. "High-temperature series expansion for spin-1/2 Heisenberg models." In: *Computer Physics Communications* 212 (2017). DOI: 10.1016/j.cpc.2016.09.003 (cit. on p. 22).

[Iqb+19] Y. Iqbal, T. Müller, P. Ghosh, M. J. P. Gingras, H. O. Jeschke, S. Rachel, J. Reuther, and R. Thomale. "Quantum and Classical Phases of the Pyrochlore Heisenberg Model with Competing Interactions." en. In: *Physical Review X* 9.1 (2019). DOI: 10.1103/PhysRevX.9.011005 (cit. on p. 17).

[ISF90] Y. A. Izyumov, Y. N. Skryabin, and M. E. Fisher. "Statistical Mechanics of Magnetically Ordered Systems." In: *Physics Today* 43.1 (1990). DOI: 10.1063/1.2810417 (cit. on p. 20).

[Jen04] J. Jensen. *Magnetic scattering of neutrons*. 2004 (cit. on p. 7).

[JG96] M. Jarrell and J. E. Gubernatis. "Bayesian inference and the analytic continuation of imaginary-time quantum Monte Carlo data." In: *Physics Reports* 269.3 (1996). DOI: 10.1016/0370-1573(95)00074-7 (cit. on p. 24).

[JL24] P. Jentsch and C. F. Lee. "New Universality Class Describes Vicsek's Flocking Phase in Physical Dimensions." en. In: *Physical Review Letters* 133.12 (2024). DOI: 10.1103/PhysRevLett.133.128301 (cit. on p. 17).

[JVW88] B. A. Jones, C. M. Varma, and J. W. Wilkins. "Low-Temperature Properties of the Two-Impurity Kondo Hamiltonian." en. In: *Physical Review Letters* 61.1 (1988). DOI: 10.1103/PhysRevLett.61.125 (cit. on p. 19).

[JW28] P. Jordan and E. Wigner. "Über das Paulische Äquivalenzverbot." de. In: *Zeitschrift für Physik* 47.9 (1928). DOI: 10.1007/BF01331938 (cit. on p. 13).

[Kas+18] Y. Kasahara et al. "Majorana quantization and half-integer thermal quantum Hall effect in a Kitaev spin liquid." en. In: *Nature* 559.7713 (2018). DOI: 10.1038/s41586-018-0274-0 (cit. on p. 8).

[Kay+24] J. Kaye, Z. Huang, H. U. R. Strand, and D. Golež. "Decomposing Imaginary-Time Feynman Diagrams Using Separable Basis Functions: Anderson Impurity Model Strong-Coupling Expansion." en. In: *Physical Review X* 14.3 (2024). DOI: 10.1103/PhysRevX.14.031034 (cit. on p. 147).

[KBS10] P. Kopietz, L. Bartosch, and F. Schütz. *Introduction to the Functional Renormalization Group*. Vol. 798. Lecture Notes in Physics. Berlin, Heidelberg: Springer Berlin Heidelberg, 2010. DOI: 10.1007/978-3-642-05094-7 (cit. on pp. 3, 9, 15–17).

[KCP22] J. Kaye, K. Chen, and O. Parcollet. "Discrete Lehmann representation of imaginary time Green's functions." en. In: *Physical Review B* 105.23 (2022). DOI: 10.1103/PhysRevB.105.235115 (cit. on p. 147).

[KD18a] F. B. Kugler and J. von Delft. "Multiloop functional renormalization group for general models." en. In: *Physical Review B* 97.3 (2018). DOI: 10.1103/PhysRevB.97.035162 (cit. on pp. 17, 145).

[KD18b] F. B. Kugler and J. von Delft. "Multiloop Functional Renormalization Group That Sums Up All Parquet Diagrams." en. In: *Physical Review Letters* 120.5 (2018). DOI: 10.1103/PhysRevLett.120.057403 (cit. on pp. 17, 145).

[KDG25] O. Kovalska, J. v. Delft, and A. Gleis. *Tangent space Krylov computation of real-frequency spectral functions: Influence of density-assisted hopping on 2D Mott physics*. 2025. DOI: 10.48550/arXiv.2510.07279 (cit. on p. 3).

[Kee23] H.-Y. Kee. "Thermal Hall conductivity of -RuCl3." en. In: *Nature Materials* 22.1 (2023). DOI: 10.1038/s41563-022-01444-6 (cit. on p. 8).

[Kha+14] E. Khatami, E. Perepelitsky, M. Rigol, and B. S. Shastry. "Linked-cluster expansion for the Green's function of the infinite- U Hubbard model." en. In: *Physical Review E* 89.6 (2014). DOI: 10.1103/PhysRevE.89.063301 (cit. on pp. 20, 147).

[Kie+23] D. Kiese et al. "Pinch-points to half-moons and up in the stars: The kagome skymap." In: *Physical Review Research* 5.1 (2023). DOI: 10.1103/PhysRevResearch.5.L012025 (cit. on p. 17).

[Kie+25] D. Kiese, H. U. R. Strand, K. Chen, N. Wentzell, O. Parcollet, and J. Kaye. "Discrete Lehmann representation of three-point functions." en. In: *Physical Review B* 111.3 (2025). DOI: 10.1103/PhysRevB.111.035135 (cit. on p. 147).

[Kit03] A. Y. Kitaev. "Fault-tolerant quantum computation by anyons." en. In: *Annals of Physics* 303.1 (2003). DOI: 10.1016/S0003-4916(02)00018-0 (cit. on p. 2).

[Kit06] A. Kitaev. "Anyons in an exactly solved model and beyond." en. In: *Annals of Physics*. January Special Issue 321.1 (2006). DOI: 10.1016/j.aop.2005.10.005 (cit. on pp. 1, 2, 8, 9, 11, 12).

[KK19] J. Krieg and P. Kopietz. "Exact renormalization group for quantum spin systems." In: *Physical Review B* 99.060403(R) (2019). DOI: 10.1103/PhysRevB.99.060403 (cit. on pp. 4, 17, 20, 27).

[KLD21] F. B. Kugler, S.-S. B. Lee, and J. von Delft. "Multipoint Correlation Functions: Spectral Representation and Numerical Evaluation." In: *Physical Review X* 11.4 (2021). DOI: 10.1103/PhysRevX.11.041006 (cit. on pp. 24–26, 71).

[KM25] C. Kim and M. Mourigal. *Emulation of quantum correlations by classical dynamics in a spin-1/2 Heisenberg chain*. 2025. DOI: 10.48550/arXiv.2503.19975 (cit. on p. 150).

[KMV25] D. A. S. Kaib, M. Möller, and R. Valenti. *Nonlinear Spectroscopy as a Magnon Breakdown Diagnosis and its Efficient Simulation*. 2025. DOI: 10.48550/arXiv.2502.01746 (cit. on p. 151).

[Kri19] J. Krieg. "Functional renormalization group approach to classical and quantum spin systems." en. PhD thesis. 2019 (cit. on pp. 20, 21, 146).

[Kro26] R. d. L. Kronig. "On the Theory of Dispersion of X-Rays." EN. In: *JOSA* 12.6 (1926). DOI: 10.1364/JOSA.12.000547 (cit. on p. 6).

[KRS87] S. A. Kivelson, D. S. Rokhsar, and J. P. Sethna. "Topology of the resonating valence-bond state: Solitons and high- T c superconductivity." en. In: *Physical Review B* 35.16 (1987). DOI: 10.1103/PhysRevB.35.8865 (cit. on p. 2).

[Kul+13a] S. A. Kulagin, N. Prokof'ev, O. A. Starykh, B. Svistunov, and C. N. Varney. "Bold diagrammatic Monte Carlo technique for frustrated spin systems." en. In: *Physical Review B* 87.2 (2013). DOI: 10.1103/PhysRevB.87.024407 (cit. on p. 72).

[Kul+13b] S. A. Kulagin, N. Prokof'ev, O. A. Starykh, B. Svistunov, and C. N. Varney. "Bold Diagrammatic Monte Carlo Method Applied to Fermionized Frustrated Spins." en. In: *Physical Review Letters* 110.7 (2013). DOI: 10.1103/PhysRevLett.110.070601 (cit. on p. 72).

[KW78] C. D. Knight and P. J. Wood. "On the second moment of the relaxation-shape function for a Heisenberg magnet." en. In: *Journal of Physics C: Solid State Physics* 11.3 (1978). DOI: 10.1088/0022-3719/11/3/013 (cit. on p. 149).

[KZ22] A. Keleş and E. Zhao. "Rise and fall of plaquette order in the Shastry-Sutherland magnet revealed by pseudofermion functional renormalization group." en. In: *Physical Review B* 105.4 (2022). DOI: 10.1103/PhysRevB.105.L041115 (cit. on p. 17).

[Lab+16] H. Labuhn, D. Barredo, S. Ravets, S. de Léséleuc, T. Macrì, T. Lahaye, and A. Browaeys. "Tunable two-dimensional arrays of single Rydberg atoms for realizing quantum Ising models." en. In: *Nature* 534.7609 (2016). DOI: 10.1038/nature18274 (cit. on p. 6).

[LeB+22] J. P. F. LeBlanc, K. Chen, K. Haule, N. V. Prokof'ev, and I. S. Tupitsyn. "Dynamic Response of an Electron Gas: Towards the Exact Exchange-Correlation Kernel." en. In: *Physical Review Letters* 129.24 (2022). DOI: 10.1103/PhysRevLett.129.246401 (cit. on p. 147).

[Li+20] J. Li, M. Wallerberger, N. Chikano, C.-N. Yeh, E. Gull, and H. Shinaoka. "Sparse sampling approach to efficient *ab initio* calculations at finite temperature." en. In: *Physical Review B* 101.3 (2020). DOI: 10.1103/PhysRevB.101.035144 (cit. on p. 147).

[Li+22] Q. Li, H. Li, J. Zhao, H.-G. Luo, and Z. Y. Xie. "Magnetization of the spin- 1 2 Heisenberg antiferromagnet on the triangular lattice." en. In: *Physical Review B* 105.18 (2022). DOI: 10.1103/PhysRevB.105.184418 (cit. on p. 2).

[Lih+24] J.-M. Lihm, J. Halbinger, J. Shim, J. Von Delft, F. B. Kugler, and S.-S. B. Lee. "Symmetric improved estimators for multipoint vertex functions." en. In: *Physical Review B* 109.12 (2024). DOI: 10.1103/PhysRevB.109.125138 (cit. on pp. 25, 147).

[LKH25] H. LaBollita, J. Kaye, and A. Hampel. "Stabilizing the calculation of the self-energy in dynamical mean-field theory using constrained residual minimization." In: *Physical Review B* 111.11 (2025). DOI: 10.1103/PhysRevB.111.115155 (cit. on p. 147).

[LKV21] S.-S. B. Lee, F. B. Kugler, and J. Von Delft. "Computing Local Multipoint Correlators Using the Numerical Renormalization Group." en. In: *Physical Review X* 11.4 (2021). DOI: 10.1103/PhysRevX.11.041007 (cit. on p. 25).

[LM01] C. Lhuillier and G. Misguich. "Frustrated Quantum Magnets." en. In: *High Magnetic Fields: Applications in Condensed Matter Physics and Spectroscopy*. Ed. by C. Berthier, L. P. Lévy, and G. Martinez. Berlin, Heidelberg: Springer, 2001. DOI: 10.1007/3-540-45649-X_6 (cit. on p. 2).

[LP99] M. Lavagna and C. Pepin. *The Kondo Lattice Model*. 1999. DOI: 10.48550/arXiv.cond-mat/9903093 (cit. on p. 19).

[Mar59] J. Martin. "Generalized classical dynamics, and the 'classical analogue' of a Fermioscillator." en. In: *Proc. R. Soc. Lond. A* 251.1267 (1959). DOI: 10.1098/rspa.1959.0126 (cit. on p. 12).

[Mat65] D. C. Mattis. *The theory of magnetism: An introduction to the study of cooperative phenomena*. Harper's physics series. New York: Harper & Row, 1965 (cit. on p. 13).

[McN+22] B. D. E. McNiven, H. Terletska, G. T. Andrews, and J. P. F. LeBlanc. "One- and two-particle properties of the weakly interacting two-dimensional Hubbard model in proximity to the van Hove singularity." en. In: *Physical Review B* 106.3 (2022). DOI: 10.1103/PhysRevB.106.035145 (cit. on p. 147).

[Met91] W. Metzner. "Linked-cluster expansion around the atomic limit of the Hubbard model." en. In: *Physical Review B* 43.10 (1991). DOI: 10.1103/PhysRevB.43.8549 (cit. on p. 20).

[ML71] W. Marshall and S. W. Lovesey. "Theory of thermal neutron scattering: the use of neutrons for the investigation of condensed matter." In: *(No Title)* (1971) (cit. on p. 7).

[Mor65] H. Mori. "A Continued-Fraction Representation of the Time-Correlation Functions." In: *Progress of Theoretical Physics* 34.3 (1965). DOI: 10.1143/PTP.34.399 (cit. on p. 153).

[MSK25] Y. Matsuda, T. Shibauchi, and H.-Y. Kee. *Kitaev Quantum Spin Liquids*. 2025. DOI: 10.1103/3m4m-3v59 (cit. on p. 8).

[Mül+24] T. Müller, D. Kiese, N. Niggemann, B. Sbierski, J. Reuther, S. Trebst, R. Thomale, and Y. Iqbal. "Pseudo-fermion functional renormalization group for spin models." en. In: *Reports on Progress in Physics* 87.3 (2024). DOI: 10.1088/1361-6633/ad208c (cit. on pp. 17, 19).

[Née71] L. Néel. "Magnetism and Local Molecular Field." In: *Science* 174.4013 (1971). DOI: 10.1126/science.174.4013.985 (cit. on p. 1).

[NGR69] P. Nozières, J. Gavoret, and B. Roulet. "Singularities in the X-Ray Absorption and Emission of Metals. II. Self-Consistent Treatment of Divergences." en. In: *Physical Review* 178.3 (1969). DOI: 10.1103/PhysRev.178.1084 (cit. on pp. 3, 9).

[Nig24] N. Niggemann. "Investigation of Quantum Spin Systems with Auxiliary Particles." eng. PhD thesis. 2024 (cit. on p. 145).

[NIR23] N. Niggemann, Y. Iqbal, and J. Reuther. "Quantum Effects on Unconventional Pinch Point Singularities." In: *Physical Review Letters* 130.19 (2023). DOI: 10.1103/PhysRevLett.130.196601 (cit. on p. 19).

[NMR25] T. Noblet, L. Messio, and R. Rossi. *Majorana Diagrammatics for Quantum Spin-1/2 Models*. 2025. DOI: 10.48550/arXiv.2508.19734 (cit. on pp. 12, 14).

[NO98] J. W. Negele and H. Orland. *Quantum Many-particle Systems*. Englisch. Reading, MA: CRC Press, 1998 (cit. on pp. 15, 21).

[Noc+23] V. Noculak, D. Lozano-Gómez, J. Oitmaa, R. R. P. Singh, Y. Iqbal, M. J. P. Gingras, and J. Reuther. "Classical and Quantum Phases of the Pyrochlore $S = \frac{1}{2}$ Magnet with Heisenberg and Dzyaloshinskii-Moriya Interactions." In: *Physical Review B* 107.21 (2023). DOI: 10.1103/PhysRevB.107.214414 (cit. on pp. 17, 18).

[NR24] V. Noculak and J. Reuther. "Pseudo-fermion functional renormalization group with magnetic fields." en. In: *Physical Review B* 109.17 (2024). DOI: 10.1103/PhysRevB.109.174414 (cit. on p. 30).

[NRS22] N. Niggemann, J. Reuther, and B. Sbierski. "Quantitative functional renormalization for three-dimensional quantum Heisenberg models." In: *SciPost Physics* 12.5 (2022). DOI: 10.21468/SciPostPhys.12.5.156 (cit. on pp. 19, 29, 145).

[NSR21] N. Niggemann, B. Sbierski, and J. Reuther. "Frustrated quantum spins at finite temperature: Pseudo-Majorana functional renormalization group approach." en. In: *Physical Review B* 103.10 (2021). DOI: 10.1103/PhysRevB.103.104431 (cit. on pp. 3, 11, 12, 14, 19, 145).

[Núñ+22] Y. Núñez Fernández, M. Jeannin, P. T. Dumitrescu, T. Kloss, J. Kaye, O. Parcollet, and X. Waintal. "Learning Feynman Diagrams with Tensor Trains." en. In: *Physical Review X* 12.4 (2022). DOI: 10.1103/PhysRevX.12.041018 (cit. on p. 27).

[NY17] Y. Noriki and S. Yamamoto. "Modified Spin-Wave Theory on Low-Dimensional Heisenberg Ferrimagnets: A New Robust Formulation." In: *Journal of the Physical Society of Japan* 86.3 (2017). DOI: 10.7566/JPSJ.86.034714 (cit. on p. 150).

[OB96] J. Oitmaa and E. Bornilla. "High-temperature-series study of the spin-½ Heisenberg ferromagnet." en. In: *Physical Review B* 53.21 (1996). DOI: 10.1103/PhysRevB.53.14228 (cit. on pp. 3, 20, 22, 117).

[Pac+21] S. D. Pace, S. C. Morampudi, R. Moessner, and C. R. Laumann. "Emergent fine structure constant of quantum spin ice is large." In: *Physical Review Letters* 127.11 (2021) (cit. on p. 2).

[Pae+19] S. Paeckel, T. Köhler, A. Swoboda, S. R. Manmana, U. Schollwöck, and C. Hubig. "Time-evolution methods for matrix-product states." In: *Annals of Physics* 411 (2019). DOI: 10.1016/j.aop.2019.167998 (cit. on p. 3).

[PBM24] L. Pierre, B. Bernu, and L. Messio. "High temperature series expansions of S = 1/2 Heisenberg spin models: Algorithm to include the magnetic field with optimized complexity." en. In: *SciPost Physics* 17.4 (2024). DOI: 10.21468/SciPostPhys.17.4.105 (cit. on pp. 22, 151).

[PF88] V. Popov and S. Fedotov. "The functional-integration method and diagram technique for spin systems." en. In: *Journal of Experimental and Theoretical Physics* 67.3 (1988) (cit. on p. 11).

[Plu+14] K. W. Plumb, J. P. Clancy, L. J. Sandilands, V. V. Shankar, Y. F. Hu, K. S. Burch, H.-Y. Kee, and Y.-J. Kim. "$\alpha - RuCl_3$: A Spin-Orbit Assisted Mott Insulator on a Honeycomb Lattice." In: *Physical Review B* 90.4 (2014). DOI: 10.1103/PhysRevB.90.041112 (cit. on pp. 2, 8).

[Plu+19] K. W. Plumb, H. J. Changlani, A. Scheie, S. Zhang, J. W. Krizan, J. A. Rodriguez-Rivera, Y. Qiu, B. Winn, R. J. Cava, and C. L. Broholm. "Continuum of quantum fluctuations in a three-dimensional S = 1 Heisenberg magnet." en. In: *Nature Physics* 15.1 (2019). DOI: 10.1038/s41567-018-0317-3 (cit. on p. 2).

[Pot+25] J. Potten, Y. Iqbal, R. Thomale, and T. Müller. *Keldysh pseudo-fermion functional renormalization group for quantum magnetism*. 2025. DOI: 10.48550/arXiv.2503.11596 (cit. on p. 30).

[PS11] N. V. Prokof'ev and B. V. Svistunov. "From the Popov-Fedotov case to universal fermionization." en. In: *Physical Review B* 84.7 (2011). DOI: 10.1103/PhysRevB.84.073102 (cit. on p. 11).

[PS25] R. Pohle and N. Shannon. *Abundance of Spin Liquids in the $S = 1$ Bilinear-Biquadratic Model on the Pyrochlore Lattice, and Its Application to* $NaCaNi_2F_7$. 2025. DOI: 10.48550/arXiv.2503.12776 (cit. on pp. 5, 118, 150).

[PST98] S. Pairault, D. Sénéchal, and A.-M. S. Tremblay. "Strong-Coupling Expansion for the Hubbard Model." en. In: *Physical Review Letters* 80.24 (1998). DOI: 10.1103/PhysRevLett.80.5389 (cit. on p. 20).

[Reu11] J. Reuther. "Frustrated Quantum Heisenberg Antiferromagnets: Functional Renormalization-Group Approach in Auxiliary-Fermion Representation." PhD thesis. Karlsruher Institut für Technologie (KIT), 2011 (cit. on p. 13).

[Rit+22] M. K. Ritter, D. Kiese, T. Müller, F. B. Kugler, R. Thomale, S. Trebst, and J. von Delft. "Benchmark calculations of multiloop pseudofermion fRG." en. In: *The European Physical Journal B* 95.7 (2022). DOI: 10.1140/epjb/s10051-022-00349-2 (cit. on p. 18).

[Rit+24] M. K. Ritter, Y. Núñez Fernández, M. Wallerberger, J. Von Delft, H. Shinaoka, and X. Waintal. "Quantics Tensor Cross Interpolation for High-Resolution Parsimonious Representations of Multivariate Functions." en. In: *Physical Review Letters* 132.5 (2024). DOI: 10.1103/PhysRevLett.132.056501 (cit. on pp. 145, 148).

[Rit+25] N. Ritz, A. Ge, M. Frankenbach, M. Pelz, J. Von Delft, and F. B. Kugler. "Testing the parquet equations and the U(1) Ward identity for real-frequency correlation functions from the multipoint numerical renormalization group." en. In: *Physical Review Research* 7.3 (2025). DOI: 10.1103/3jtq-5wf5 (cit. on p. 25).

[Rit21] M. Ritter. *Multiloop Pseudofermion Functional Renormalization Group Study of the Pyrochlore XXZ Model*. 2021 (cit. on p. 17).

[Rit25] N. Ritz. "Dynamic response functions of strongly correlated electrons." de. Text.PhDThesis. Ludwig-Maximilians-Universität München, 2025 (cit. on p. 17).

[RKL08] A. N. Rubtsov, M. I. Katsnelson, and A. I. Lichtenstein. "Dual fermion approach to nonlocal correlations in the Hubbard model." en. In: *Physical Review B* 77.3 (2008). DOI: 10.1103/PhysRevB.77.033101 (cit. on p. 20).

[Roh+25] S. Rohshap, M. K. Ritter, H. Shinaoka, J. Von Delft, M. Wallerberger, and A. Kauch. "Two-particle calculations with quantics tensor trains: Solving the parquet equations." en. In: *Physical Review Research* 7.2 (2025). DOI: 10.1103/PhysRevResearch.7.023087 (cit. on p. 145).

[RT14] J. Reuther and R. Thomale. "Cluster functional renormalization group." en. In: *Physical Review B* 89.2 (2014). DOI: 10.1103/PhysRevB.89.024412 (cit. on p. 17).

[RTK24] A. Rückriegel, D. Tarasevych, and P. Kopietz. "Phase Diagram of the $J_1 - J_2$ Quantum Heisenberg Model for Arbitrary Spin." In: *Physical Review B* 109.18 (2024). DOI: 10.1103/PhysRevB.109.184410 (cit. on p. 71).

[RTT11] J. Reuther, R. Thomale, and S. Trebst. "Finite-temperature phase diagram of the Heisenberg-Kitaev model." en. In: *Physical Review B* 84.10 (2011). DOI: 10.1103/PhysRevB.84.100406 (cit. on pp. 17, 18).

[Rub+09] A. N. Rubtsov, M. I. Katsnelson, A. I. Lichtenstein, and A. Georges. "Dual fermion approach to the two-dimensional Hubbard model: Antiferromagnetic fluctuations and Fermi arcs." en. In: *Physical Review B* 79.4 (2009). DOI: 10.1103/PhysRevB.79.045133 (cit. on p. 20).

[Rüc+22] A. Rückriegel, J. Arnold, R. Goll, and P. Kopietz. "Spin functional renormalization group for dimerized quantum spin systems." In: *Physical Review B* 105 (2022). DOI: 10.1103/PhysRevB.105.224406 (cit. on p. 20).

[Rüc+23] A. Rückriegel, J. Arnold, R. Krämer, and P. Kopietz. "Functional renormalization group without functional integrals: implementing Hilbert space projections for strongly correlated electrons via Hubbard X-operators." In: *Physical Review B* 108.11 (2023). DOI: 10.1103/PhysRevB.108.115104 (cit. on pp. 20, 21, 146).

[Rüc+24] A. Rückriegel, D. Tarasevych, J. Krieg, and P. Kopietz. "Recursive algorithm for generating high-temperature expansions for spin systems and the chiral nonlinear susceptibility." en. In: *Physical Review B* 110.14 (2024). DOI: 10.1103/PhysRevB.110.144416 (cit. on p. 151).

[RW10] J. Reuther and P. Wölfle. "J 1 J 2 frustrated two-dimensional Heisenberg model: Random phase approximation and functional renormalization group." en. In: *Physical Review B* 81.14 (2010). DOI: 10.1103/PhysRevB.81.144410 (cit. on pp. 3, 10, 17, 146).

[San98] A. W. Sandvik. "Stochastic method for analytic continuation of quantum Monte Carlo data." en. In: *Physical Review B* 57.17 (1998). DOI: 10.1103/PhysRevB.57.10287 (cit. on p. 24).

[SB16] L. Savary and L. Balents. "Quantum spin liquids: a review." en. In: *Reports on Progress in Physics* 80.1 (2016). DOI: 10.1088/0034-4885/80/1/016502 (cit. on pp. 2, 12).

[Sbi+24] B. Sbierski, M. Bintz, S. Chatterjee, M. Schuler, N. Y. Yao, and L. Pollet. "Magnetism in the two-dimensional dipolar XY model." en. In: *Physical Review B* 109.14 (2024). DOI: 10.1103/PhysRevB.109.144411 (cit. on p. 2).

[Sch+15] P. Schad, Y. Makhlin, B. N. Narozhny, G. Schön, and A. Shnirman. "Majorana representation for dissipative spin systems." In: *Annals of Physics* 361 (2015). DOI: 10.1016/j.aop.2015.07.006 (cit. on p. 14).

[Sch+22] P. Scholl et al. "Microwave Engineering of Programmable X X Z Hamiltonians in Arrays of Rydberg Atoms." en. In: *PRX Quantum* 3.2 (2022). DOI: 10.1103/PRXQuantum.3.020303 (cit. on p. 6).

[Sch+23] M. Schlosser, S. Tichelmann, D. Schäffner, D. O. De Mello, M. Hambach, J. Schütz, and G. Birkl. "Scalable Multilayer Architecture of Assembled Single-Atom Qubit Arrays in a Three-Dimensional Talbot Tweezer Lattice." en. In: *Physical Review Letters* 130.18 (2023). DOI: 10.1103/PhysRevLett.130.180601 (cit. on p. 2).

[Sch+24] A. O. Scheie et al. "Proximate spin liquid and fractionalization in the triangular antiferromagnet KYbSe2." en. In: *Nature Physics* 20.1 (2024). DOI: 10.1038/s41567-023-02259-1 (cit. on p. 151).

[Sch05] U. Schollwöck. "The density-matrix renormalization group." en. In: *Reviews of Modern Physics* 77.1 (2005). DOI: 10.1103/RevModPhys.77.259 (cit. on p. 16).

[Sem+21] G. Semeghini et al. "Probing Topological Spin Liquids on a Programmable Quantum Simulator." en. In: *Science* 374.6572 (2021). DOI: 10.1126/science.abi8794 (cit. on p. 2).

[SGR25] Y. Schaden, M. G. Gonzalez, and J. Reuther. "Phase diagram of the XXZ pyrochlore model from pseudo-Majorana functional renormalization group." en. In: *Physical Review B* 111.13 (2025). DOI: 10.1103/PhysRevB.111.134442 (cit. on pp. 19, 145).

[Sha+17] H. Shao, Y. Q. Qin, S. Capponi, S. Chesi, Z. Y. Meng, and A. W. Sandvik. "Nearly Deconfined Spinon Excitations in the Square-Lattice Spin- 1 / 2 Heisenberg Antiferromagnet." en. In: *Physical Review X* 7.4 (2017). DOI: 10.1103/PhysRevX.7.041072 (cit. on p. 3).

[Sha94] R. Shankar. "Renormalization-group approach to interacting fermions." en. In: *Reviews of Modern Physics* 66.1 (1994). DOI: 10.1103/RevModPhys.66.129 (cit. on p. 16).

[She+23] N. Sheng, A. Hampel, S. Beck, O. Parcollet, N. Wentzell, J. Kaye, and K. Chen. "Low-rank Green's function representations applied to dynamical mean-field theory." en. In: *Physical Review B* 107.24 (2023). DOI: 10.1103/PhysRevB.107.245123 (cit. on p. 147).

[SLR11] H.-J. Schmidt, A. Lohmann, and J. Richter. "Eighth-order high-temperature expansion for general Heisenberg Hamiltonians." en. In: *Physical Review B* 84.10 (2011). DOI: 10.1103/PhysRevB.84.104443 (cit. on p. 22).

[SM03] A. Shnirman and Y. Makhlin. "Spin-Spin Correlators in the Majorana Representation." en. In: *Physical Review Letters* 91.20 (2003). DOI: 10.1103/PhysRevLett.91.207204 (cit. on p. 14).

[Smi+22] E. M. Smith et al. "Case for a U (1) Quantum Spin Liquid Ground State in the Dipole-Octupole Pyrochlore Ce 2 Zr 2 O 7." en. In: *Physical Review X* 12.2 (2022). DOI: 10.1103/PhysRevX.12.021015 (cit. on p. 2).

[SP82] B. Silvestre-Brac and R. Piepenbring. “Multiphonon theory: Generalized Wick’s theorem and recursion formulas.” en. In: *Physical Review C* 26.6 (1982). DOI: 10.1103/PhysRevC.26.2640 (cit. on p. 23).

[Spe68] H. J. Spencer. “Quantum-Field-Theory Approach to the Heisenberg Ferromagnet.” en. In: *Physical Review* 167.2 (1968). DOI: 10.1103/PhysRev.167.434 (cit. on p. 13).

[SPP02] D. Sénéchal, D. Perez, and D. Plouffe. “Cluster perturbation theory for Hubbard models.” en. In: *Physical Review B* 66.7 (2002). DOI: 10.1103/PhysRevB.66.075129 (cit. on p. 20).

[SR23] Y. Schaden and J. Reuther. “Bilinear Majorana representations for spin operators with spin magnitudes S $>$ 1 / 2.” en. In: *Physical Review Research* 5.2 (2023). DOI: 10.1103/PhysRevResearch.5.023067 (cit. on pp. 14, 28).

[SS49] C. G. Shull and J. S. Smart. “Detection of Antiferromagnetism by Neutron Diffraction.” en. In: *Physical Review* 76.8 (1949). DOI: 10.1103/PhysRev.76.1256.2 (cit. on p. 7).

[ŠSJ22] L. Šmejkal, J. Sinova, and T. Jungwirth. “Emerging Research Landscape of Altermagnetism.” en. In: *Physical Review X* 12.4 (2022). DOI: 10.1103/PhysRevX.12.040501 (cit. on p. 1).

[Sti73a] R. B. Stinchcombe. “Ising model in a transverse field. I. Basic theory.” en. In: *Journal of Physics C: Solid State Physics* 6.15 (1973). DOI: 10.1088/0022-3719/6/15/009 (cit. on p. 20).

[Sti73b] R. B. Stinchcombe. “Ising model in a transverse field. II. Spectral functions and damping.” en. In: *Journal of Physics C: Solid State Physics* 6.15 (1973). DOI: 10.1088/0022-3719/6/15/010 (cit. on p. 20).

[Sti73c] R. B. Stinchcombe. “Thermal and magnetic properties of the transverse Ising model.” en. In: *Journal of Physics C: Solid State Physics* 6.15 (1973). DOI: 10.1088/0022-3719/6/15/011 (cit. on p. 20).

[SW10] M. Shaposhnikov and C. Wetterich. “Asymptotic safety of gravity and the Higgs boson mass.” In: *Physics Letters B* 683.2 (2010). DOI: 10.1016/j.physletb.2009.12.022 (cit. on p. 17).

[Tak89] M. Takahashi. “Modified spin-wave theory of a square-lattice antiferromagnet.” en. In: *Physical Review B* 40.4 (1989). DOI: 10.1103/PhysRevB.40.2494 (cit. on p. 150).

[Tar+22] D. Tarasevych, A. Rückriegel, S. Keupert, V. Mitsiioannou, and P. Kopietz. “Spin-functional renormalization group for the JJJ quantum Heisenberg model.” In: *Physical Review B* 106 (2022). DOI: 10.1103/PhysRevB.106.174412 (cit. on p. 20).

[TCL19] A. Taheridehkordi, S. H. Curnoe, and J. P. F. LeBlanc. “Algorithmic Matsubara integration for Hubbard-like models.” en. In: *Physical Review B* 99.3 (2019). DOI: 10.1103/PhysRevB.99.035120 (cit. on p. 147).

[TCL20a] A. Taheridehkordi, S. H. Curnoe, and J. P. F. LeBlanc. “Algorithmic approach to diagrammatic expansions for real-frequency evaluation of susceptibility functions.” en. In: *Physical Review B* 102.4 (2020). DOI: 10.1103/PhysRevB.102.045115 (cit. on p. 147).

[TCL20b] A. Taheridehkordi, S. H. Curnoe, and J. P. F. LeBlanc. “Optimal grouping of arbitrary diagrammatic expansions via analytic pole structure.” en. In: *Physical Review B* 101.12 (2020). DOI: 10.1103/PhysRevB.101.125109 (cit. on p. 147).

[TK21] D. Tarasevych and P. Kopietz. "Dissipative spin dynamics in hot quantum paramagnets." In: *Physical Review B* 104 (2021). DOI: 10.1103/PhysRevB.104.024423 (cit. on p. 20).

[TK22] D. Tarasevych and P. Kopietz. "Critical spin dynamics of Heisenberg ferromagnets revisited." In: *Physical Review B* 105 (2022). DOI: 10.1103/PhysRevB.105.024403 (cit. on p. 20).

[Tsv92] A. M. Tsvelik. "New fermionic description of quantum spin liquid state." en. In: *Physical Review Letters* 69.14 (1992). DOI: 10.1103/PhysRevLett.69.2142 (cit. on pp. 12, 14).

[TWZ24] C. Tan, Z. Wei, and R. Zhang. *Scaling Relations of Spectrum Form Factor and Krylov Complexity at Finite Temperature*. 2024. DOI: 10.48550/arXiv.2401.10499 (cit. on p. 153).

[Vil79] J. Villain. "Insulating spin glasses." In: *Zeitschrift für Physik B Condensed Matter* 33.1 (1979) (cit. on p. 2).

[VLP67] V. Vaks, A. Larkin, and S. Pikin. "Self-consistent field method for the description of phase transitions." In: *Soviet Physics–JETP* 51 (1967) (cit. on p. 20).

[VLP68] V. Vaks, A. Larkin, and S. Pikin. "Spin waves and correlation functions in a ferromagnetic." In: *Soviet Physics–JETP [translation of Zhurnal Eksperimentalnoi i Teoreticheskoi Fiziki]* 26.3 (1968) (cit. on p. 20).

[VM94] V. S. Viswanath and G. Müller. *The Recursion Method: Application to Many-Body Dynamics*. en. Ed. by H. Araki et al. Vol. 23. Lecture Notes in Physics Monographs. Berlin, Heidelberg: Springer, 1994. DOI: 10.1007/978-3-540-48651-0 (cit. on pp. 118, 153).

[VS12] R. Van Leeuwen and G. Stefanucci. "Wick theorem for general initial states." en. In: *Physical Review B* 85.11 (2012). DOI: 10.1103/PhysRevB.85.115119 (cit. on p. 23).

[VSF21] J. Vučičević, P. Stipsić, and M. Ferrero. "Analytical solution for time integrals in diagrammatic expansions: Application to real-frequency diagrammatic Monte Carlo." en. In: *Physical Review Research* 3.2 (2021). DOI: 10.1103/PhysRevResearch.3.023082 (cit. on pp. 27, 147).

[Wan+20] T. Wang, X. Cai, K. Chen, N. V. Prokof'ev, and B. V. Svistunov. "Quantum-to-classical correspondence in two-dimensional Heisenberg models." en. In: *Physical Review B* 101.3 (2020). DOI: 10.1103/PhysRevB.101.035132 (cit. on p. 72).

[Wan50] G. H. Wannier. "Antiferromagnetism. The Triangular Ising Net." en. In: *Physical Review* 79.2 (1950). DOI: 10.1103/PhysRev.79.357 (cit. on p. 2).

[Wen07] X.-G. Wen. *Quantum Field Theory of Many-Body Systems*. Oxford University Press, 2007 (cit. on pp. 12–14).

[Wet93] C. Wetterich. "Exact evolution equation for the effective potential." en. In: *Physics Letters B* 301.1 (1993). DOI: 10.1016/0370-2693(93)90726-X (cit. on pp. 16, 17).

[Wic50] G. C. Wick. "The Evaluation of the Collision Matrix." en. In: *Physical Review* 80.2 (1950). DOI: 10.1103/PhysRev.80.268 (cit. on p. 23).

[Wie+21] A. Wietek, Y.-Y. He, S. R. White, A. Georges, and E. M. Stoudenmire. "Stripes, Antiferromagnetism, and the Pseudogap in the Doped Hubbard Model at Finite Temperature." en. In: *Physical Review X* 11.3 (2021). DOI: 10.1103/PhysRevX.11.031007 (cit. on p. 151).

[Wil75] K. G. Wilson. “The renormalization group: Critical phenomena and the Kondo problem.” en. In: *Reviews of Modern Physics* 47.4 (1975). DOI: 10.1103/RevModPhys.47.773 (cit. on p. 16).

[WM06] P. Werner and A. J. Millis. “Hybridization expansion impurity solver: General formulation and application to Kondo lattice and two-orbital models.” en. In: *Physical Review B* 74.15 (2006). DOI: 10.1103/PhysRevB.74.155107 (cit. on p. 20).

[WP25] Z. Wang and L. Pollet. “Renormalized Classical Spin Liquid on the Ruby Lattice.” en. In: *Physical Review Letters* 134.8 (2025). DOI: 10.1103/PhysRevLett.134.086601 (cit. on p. 2).

[WSK21] M. Wallerberger, H. Shinaoka, and A. Kauch. “Solving the Bethe-Salpeter equation with exponential convergence.” In: *Physical Review Research* 3.3 (2021). DOI: 10.1103/PhysRevResearch.3.033168 (cit. on p. 147).

[WTH24] Y. Watanabe, S. Trebst, and C. Hickey. “Exploring two-dimensional coherent spectroscopy with exact diagonalization: Spinons and confinement in one-dimensional quantum magnets.” en. In: *Physical Review B* 110.13 (2024). DOI: 10.1103/PhysRevB.110.134443 (cit. on p. 151).

[Xia+24] J. Xiang et al. “Giant magnetocaloric effect in spin supersolid candidate Na2BaCo(PO4)2.” en. In: *Nature* 625.7994 (2024). DOI: 10.1038/s41586-023-06885-w (cit. on p. 30).

[Xio+22] D. Xiong et al. “Antiferromagnetic spintronics: An overview and outlook.” In: *Fundamental Research* 2.4 (2022). DOI: 10.1016/j.fmre.2022.03.016 (cit. on p. 1).

[YSH18] H. Yoon, J.-H. Sim, and M. J. Han. “Analytic continuation via domain knowledge free machine learning.” en. In: *Physical Review B* 98.24 (2018). DOI: 10.1103/PhysRevB.98.245101 (cit. on p. 24).

[YZK09] H. Yao, S.-C. Zhang, and S. A. Kivelson. “Algebraic Spin Liquid in an Exactly Solvable Spin Model.” en. In: *Physical Review Letters* 102.21 (2009). DOI: 10.1103/PhysRevLett.102.217202 (cit. on p. 14).

[Zei+16] J. Zeiher, R. van Bijnen, P. Schauß, S. Hild, J.-y. Choi, T. Pohl, I. Bloch, and C. Gross. “Many-body interferometry of a Rydberg-dressed spin lattice.” en. In: *Nature Physics* 12.12 (2016). DOI: 10.1038/nphys3835 (cit. on p. 6).

[ZG24] L. Zhang and E. Gull. “Minimal pole representation and controlled analytic continuation of Matsubara response functions.” en. In: *Physical Review B* 110.3 (2024). DOI: 10.1103/PhysRevB.110.035154 (cit. on p. 24).

[Zha+19] S. Zhang, H. J. Changlani, K. W. Plumb, O. Tchernyshyov, and R. Moessner. “Dynamical Structure Factor of the Three-Dimensional Quantum Spin Liquid Candidate $NaCaNi_2F_7$.” In: *Physical Review Letters* 122.16 (2019). DOI: 10.1103/PhysRevLett.122.167203 (cit. on pp. 118, 150).

[ZYG24] L. Zhang, Y. Yu, and E. Gull. “Minimal pole representation and analytic continuation of matrix-valued correlation functions.” en. In: *Physical Review B* 110.23 (2024). DOI: 10.1103/PhysRevB.110.235131 (cit. on p. 24).